VOL.29 NO.3
MARCH
2026

AJSTR
of Scientific and Technological Reports

ASEAN JOURNAL

of Scientific and Technological Report

ISSN 2773-8752 (online)

ASEAN
Journal of Scientific and Technological Reports
Online ISSN:2773-8752

ASEAN Journal of Scientific and Technological Reports (AJSTR)

Contact Us Institute of Research and Innovation, Thaksin University
222 M. 2 Ban-Prao sub-district, Pa-Pra-Yom district, Phatthalung province, Thailand
Tel. 0 7460 9600 # 7258, 09 1070 0916, 08 1540 7304, E-mail: aseanjstr@tsu.ac.th

List of Contents

List of Contents

ASEAN
Journal of Scientific and Technological Reports
Online ISSN:2773-8752

ASEAN
Journal of Scientific and Technological Reports
Online ISSN:2773-8752

Research article

Detection and Measurement of Natural and Anthropogenic Disturbances in a Protected Area Using the Rasch Model

Mark Anthony C. Abella[1], and Sherwin E. Balbuena[2*]

[1] Faculty of Department of Agroforestry, College of Agriculture, Dr. Emilio B. Espinosa Sr. Memorial State College of Agriculture and Technology Main Campus, 5411, Philippines
[2] Faculty of Department of Mathematics, College of Education, Dr. Emilio B. Espinosa Sr. Memorial State College of Agriculture and Technology, Main Campus, 5411, Philippines
* Correspondence: macabella@debesmscat.edu.ph

Citation:
Abella, M.A.; Balbuena, S. Detection and Measurement of Natural and Anthropogenic Disturbances in a Protected Area Using the Rasch Model. *ASEAN J. Sci. Tech. Report.* **2026**, *29*(3), e260742. https://doi.org/10.55164/ajstr.v29i3.260742.

Article history:
Received: August 7, 2025
Revised: November 14, 2025
Accepted: December 3, 2025
Available online: February 27 , 2026

Abstract: This study aimed to assess the extent of major threats in the 244.13-hectare Tugbo Natural Biotic Area (TNBA) on Masbate Island, Philippines. Threat-focused patrolling has covered the entire continuum, with a specified recording interval along the protected area (PA), divided into numerous patrol routes. Categorized into human-induced and natural calamities, a total of 27 individual threats were geo-tagged and recorded, with mixed perennial farming as the most frequent threat. Using geo-spatial technologies, the risks were reduced to 10, largely represented by broad expanses of rangelands and invasive monocrop plantations. This paper presents a new methodology for measuring and visualizing threats to protected areas based on the Rasch model. This probabilistic analysis is based on the presence or absence of the threat in each location, disturbance estimates, and the calculation of misfits. The visualization map illustrates that the protected area had an unequal distribution of threats. Most locations have less disturbed areas; hence, the data indicate that the protected area is nearly pristine. This approach is a useful methodology for assessing in-depth environmental disturbance.

Keywords: Disturbance; land-use; protected area; rasch model; threats

1. Introduction

Changes in land use and land cover (LULC) have become a pressing global environmental concern, driving substantial transformations in ecosystems across tropical regions [1]. The increasing global demand for food production and bioenergy has accelerated these changes, raising alarms over their environmental consequences, particularly in relation to climate change and global warming [2]. Human-driven activities—such as the expansion of agriculture, conflicts between humans and wildlife, infrastructure growth, and mining—intensify pressures on land, posing serious risks to biodiversity and the ecological integrity of natural systems [3]. Biodiversity, which underpins ecosystem resilience and supports human well-being, is under mounting threat from anthropogenic stressors including habitat degradation, overexploitation, pollution, and climate change—contributing to alarming extinction rates [4]. Despite efforts to protect biodiversity through conservation policies and designated protected areas, recent studies suggest that species loss continues,

underscoring the ongoing challenges in maintaining ecological balance [5, 6]. In light of these complexities, there is a critical need for research evaluating habitat quality in relation to the diverse, interlinked threats—both human-induced and natural—that affect these dynamic ecosystems.

Geospatial technologies are essential for analyzing land use and land cover (LULC), offering accurate spatial and temporal data for monitoring terrestrial and hydrological dynamics [7]. The use of advanced modeling tools, such as Artificial Intelligence for Environment & Sustainability (ARIES) [8] and Social Values for Ecosystem Services (SoLVES) [9], supports ecological service assessments. However, they often fall short in capturing spatial variability and simulating threat impacts across environmental scenarios [10]. The newly introduced PLUS (Patch-generating Land Use Simulation) model addresses these limitations by integrating machine learning, cellular automata, and spatial policy factors, enabling more realistic LULC simulations—particularly in complex environments such as watersheds and protected areas [11]. The widely used InVEST (Integrated Valuation of Ecosystem Services and Tradeoffs) model offers a robust, spatially explicit framework for habitat quality assessment by integrating temporally dynamic land-use/land-cover data with quantified anthropogenic threat intensities, enabling significant evaluations across transfrontier conservation areas [3, 12] and ecologically sensitive wildlife habitats [13]. Consequently, the CA-Markov hybrid model, which integrates Cellular Automata with Markov Chain analysis, is widely used to simulate and predict spatiotemporal LULC changes in complex watersheds and pasture areas due to its accuracy and efficiency [14, 15]. Recent studies have enhanced this approach by incorporating machine-learning–derived land cover maps as model inputs [16]. Additionally, the CA–Artificial Neural Network model in MOLUSCE offers a more realistic simulation of river basin dynamics by combining spatial patterns and temporal trends within an open-source QGIS framework [17]. The evaluation and prediction of LUCC changes using spatiotemporal data play a vital role in environmental monitoring and in formulating sustainable land management strategies within protected watershed areas.

The introduction of the Rasch probabilistic model [18] is well known for its accuracy and precision in converting categorical item responses to objective-scale measures. It is actually applicable in modern empirical research, often based on parameters from regression models of outcomes represented by a latent variable, such as a person's ability, health, food insecurity, or well-being, as a function of a set of explanatory variables. Simulated data and empirical examples are used to analyze the properties of these processes, demonstrating the utility of the behavioral Rasch selection model for social science study [19]. However, the model has also been successfully used in several applied science studies, demonstrating its practical usefulness across a variety of agricultural and environmental applications. For example, Moral et al. [20] used this method to classify soil fertility potential, map soil production potential, delineate management zones in the field [21], and assess atmospheric pollution levels [22, 23]. While existing LULC modeling frameworks such as PLUS, InVEST, and CA-Markov effectively simulate spatial and temporal transitions in land cover, they operate primarily on deterministic or continuous datasets. These models often assume linearity and visible data inputs, limiting their capacity to represent latent or probabilistic disturbance conditions that arise from overlapping natural and anthropogenic threats [11; 14]. In contrast, the Rasch probabilistic model provides a mathematically rigorous approach for converting dichotomous threat indicators (presence/absence) into a latent continuum of disturbance, expressed in logits [18; 24]. This allows quantifying ecological disturbance as an interval-level construct that integrates multiple independent threat variables into a single, objective scale of environmental pressure [20].

Masbate is an island province in the Philippines, about in the center of the archipelago, between 11°43' north and 123°09' east, and 124°5' east. The province was ranked 9th by the Forest Management Bureau [25], with 6,678 hectares, or 1.17 percent of its total land area, having the least forest cover. Tugbo Natural Biotic Area (TNBA), formerly Tugbo Watershed Forest Reserve (TWFR), was proclaimed under Republic Act No. 11806 in June 2022 as the newest legislated protected area in the country, with a total area of 244.1299 hectares and a length of 19.973 kilometers. It is primarily timberland, with natural forests accounting for more than 50%, while the remaining areas were converted into agricultural and rangeland areas. No comprehensive land-use threat study has been conducted in the watershed, aside from ongoing patrolling and monitoring of the watershed's biodiversity hotspot areas.

There is currently no probabilistic approach that translates qualitative disturbance observations into a statistically validated and reproducible ecological index. By applying the Rasch model, the study introduces a novel analytical framework that integrates spatially heterogeneous field data with psychometric scaling—an innovation rarely applied in ecological or protected-area assessment contexts in the Philippines and Southeast Asia. Information on local-level land-use dynamics is essential for designing sound environmental policies and management. It provides the baseline data required for a proper understanding of how the land was used in the past and the type of changes to be detected in the future [26]. This research, therefore, aimed to visualize the extent of land-use changes across the entire TNBA, using geospatial techniques and a probabilistic model. Specifically, identify and document potential biotic and abiotic threats occurring in the protected area and their spatial distribution; and quantify the magnitude of disturbance using available delineated threat map output and the Rasch model.

2. Materials and Methods

2.1 Study Area

The research took place at the Tugbo Natural Biotic Area (N 120 18. 974' E 1230 37. 019') within the administrative boundaries of Tugbo, Mobo, Masbate, and Tugbo, Masbate City, Philippines (Figure 1). Land-use data for the watershed were obtained from the Land Management Service (LMS) in Legaspi City, Philippines. The study area has a Type III climate, with dry conditions from November to April and wet conditions the rest of the year. The soil textural classes in the area ranged from clay loam to clayey soil with light to medium brown tones [27]. The landscape varied in elevation from mildly undulating to fairly steep slopes (5^0 to 35^0). The downstream portion of the protected area has a closed canopy, while the middle and upper sections have open, fragmented secondary vegetation with pioneer species.

Figure 1. The study area

2.2 Disturbance Monitoring Patrol Routes and Sampling Schedule

Data collection was conducted from March to September 2021, covering both the dry (March–June) and wet southwest monsoon (July–September) seasons in the Philippines. This dual-season coverage was designed to capture seasonal variations in disturbance intensity. This period was purposefully selected because both natural disturbances (e.g., landslides, erosion, typhoon-damaged vegetation) and anthropogenic activities (e.g., farming, charcoal-making, tree cutting) are most active and observable during this time. Threat-focused patrolling in the protected area aimed to identify and document disturbances along designated routes systematically, conducted every 1 to 2 weeks per patrol sector. Patrols followed a planned framework ensuring even coverage and appropriate intensity, with threats recorded every 100 meters. Routes extended from the lowermost catchment areas to the upper boundaries of the protected zone, traversing natural divides such as ridges, midslope terrains, and tributaries. Covering an estimated 80 kilometers across 10 routes, all observed threats were recorded and photo-documented for monitoring and management purposes.

2.3 Calibrating and Recording Potential Threats

The researcher used a GPS installed in a cellphone and a map of the protected area to record pertinent threats as specified in the module. Each threat was recorded individually by entering the specific name of the potential threat and a brief description, while coordinates, distance covered, and altitude were automatically recorded on the phone.

2.4 Ecological Threats in the Protected Area

Environmental threats in TNBA, based on the DENR Lawin Handbook [28], were divided into human-induced and natural calamities. Human-related disturbances include cutting of trees; slash-and-burn farming, hut/house and other infrastructures; annual and perennial farming; a collection of non-timber forest products; charcoal production; wildlife hunting; mining and quarrying; created logging trail; garbage and polluted water; livestock and poultry farming; fire and intentional burning; invasive species while natural phenomena comprise of pest and diseases; landslide and mudslide and typhoon damage.

2.5 Mapping of Land-Use Threats

Google Earth Explorer was used to obtain satellite imagery of land use in the watershed, using updated software based on ground geo-tagging. The 2019 base map from the National Mapping and Resource Information Authority (NAMRIA) [29] was used to locate the hotspot area (e.g., land clearing) and to estimate patches of remaining high-value conservation areas in the study site. Existing land cover was computed to include the total area of annual and perennial farmlands, secondary forest, old-growth forest, invasive plantations, and brushlands/grasslands. GPS-equipped devices were used to install waypoints for a particular land cover at irregular intervals across different sections of the watershed. All encircled waypoints were connected to form a polygon that automatically registered the actual area of a sample land cover. To obtain the percentage cover, similar land covers were combined and added to the total land cover, then divided by the total land area of the PA.

2.6 Data Analysis

Rasch model (RM) analysis was used to estimate the prevalence of anthropogenic disturbance in the area. Response categories were dichotomized so that the presence or absence of a particular threat was coded as 0 or 1, respectively. Following this collapse of categories, a Dichotomous RM was used, and parameters were estimated using a conditional maximum likelihood procedure in R [30]. Misfit items (threat indicators) were assessed using the Outfit and Infit mean square (MSQ) range 0.7 to 1.3. Further analyses were undertaken to show the item (threat) and person (area) locations along the Wright map and to convert the observed total number of threats to log-odds units (logits). Finally, a heatmap of estimated latent disturbance was visualized using ArcGIS symbology.

3. Results and Discussion

3.1 Identified Threats at Tugbo Natural Biotic Area

A total of one hundred twenty-five (125) threats from twenty-seven (27) individual threats were recorded during the conduct of the assessment. The majority of the identified and documented threats as stipulated in the Lawin Handbook were observed in the PA, except for wildlife hunting, collection of minor forest products, garbage and polluted water, and livestock and poultry farming, which was observed in TNBA. Unspecified ecological disturbances considered damaging in the PA were added, including orchards, carabao mud pools, and copra drying huts. In addition, human-induced items, such as houses within the PA, were sub-categorized into houses surrounded by crops and animal corrals; likewise, annual farming was separated from perennial farming.

Table 1. Summary of environmental threats at TNBA

Human-induced Threats	Frequency
1. Cutting of trees	10
2. Slash-and-burn farming (*kaingin*)	2
3. Hut/house within the protected area	12
3a. Hut/house surrounded by crops	10
3b. Hut/house surrounded by animals/corral	2
4. Annual farming	16
4a. Open cultivated area planted with a monocrop	6
4b. Open cultivated area planted with annual/biennial crops	10
5. Mixed perennial farming	18
5a. Farming under perennial	12
5b. Orchard	4
5c.Farming under newly opened/cleared secondary forest	2
6. Grazing/barren lands	11
7. Abandoned formerly cultivated farmlands	7
8. Charcoal production	5
9. Post-mining remnants and pits	5
10. Logging trail	4
11. Intentional fire/burning	3
12. Invasive woody species plantation	8
13. *Carabao* mud pool	6
14. Copra drying hut	4
SUB-TOTAL	110
Natural-caused Threats	
15. Pest and diseases	4
16. Landslide and mudslide	8
17. Typhoon damage to vegetation	6
SUB-TOTAL	18
TOTAL	**125**

During the five months of ground validation, mixed perennial farming, the top land-use threat, was categorized into cultivation under established plantations, permanent orchards, and farming under newly opened secondary forest clearings. These were encountered 18 times during intensive reconnaissance in the high forest conservation zone, as cleared patches planted with cash crops. Annual farming was split into open cultivated areas planted with monocrop and open cultivated areas planted with annual/biennial crops. In contrast, mixed perennial farming was divided into farming under perennials, orchards, and farming under newly opened/cleared secondary forests, with 12 farmlands occupying 12.28 hectares tilled by marginalized farmers. During the transect walk, 12 houses/shanties were occupied by families and occasional cultivators

scattered in the PA out of more than 20 houses built according to the former Protected Area Superintendent (PASu) and validated during the Socio-Economic Assessment and Monitoring Services (SEAMS) team during their actual household survey in the watershed from August to October 2018 [31]. Combined grasslands and barren domains have a delineated area of 41.59 hectares and have been recorded 11 times across various watershed locations, primarily used for grazing carabao (buffalo) and horses by outside dwellers. Tree cutting was observed 10 times, with a total of 29 trees, including displaced logs, with dbh ranging from 15 to 60 cm, cut within the forest reserve.

Table 2. Land cover of TNBA during ground validation

Land Cover	Area (ha)
Secondary forest	83.70
Barren/grasslands	67 .69
Invasive perennial trees /orchard plantation	28.31
Planted native trees	26.26
Cultivated annual crops	21.54
Old-growth forest	16.63
TOTAL	244.13

In the 2020 ground validation result, land use/cover was irregularly distributed within the PA. The NAMRIA-generated map [29] showed that annual crop farmlands occupied the highest land-use with 95.08 has (38.95%), followed by brushlands/grasslands with 72.06 has (29.52%), perennial crops with 58.44 has (23.94%), and grasslands with 6.30 has (2.58%). Patches of grasslands and barren lands (67.69 has, 27.73%), invasive perennial and orchard plantations (28.31 has, 11.60%), and cultivated annual crops (21.54 has, 8.82%) were quantified. Comparing the results of satellite-generated maps and validated ground land use, annual crop cultivation was reduced to 10 percent of the total land area, while barren lands and grasslands were slightly reduced to 10 hectares, owing to effective native tree plantation establishment in the area. Ground validation results provided clearer, more detailed, and updated data on land cover distribution, which may aid local managers in enhancing their current management plans and conservation strategies for the PA.

3.3 Spatial Grid Framework and Threat Distribution Mapping

The study area was initially divided into 18 primary grids (1:400 scale) using Google Earth. Each primary grid was further subdivided into 9 secondary grids (1:130 scale), resulting in 162 grid units. To ensure complete coverage of the protected area's irregular boundaries, an additional 8 grids were added. This produced a total of 170 spatial observation units. Each grid unit was considered a "person" in the Rasch model, with binary-coded disturbance data (1 = present, 0 = absent) across ten threat indicators. Plotting the threats involved locating the coordinates of the 10 clustered threats. Each threat within the grid was counted as 1, meaning several threats may be found in a single grid. These factors were clustered into rangelands/barren lands, invasive mono-crop plantation (including orchards), built-up structures (farmhouse, coconut meat drying hut, charcoal production hole and animal mud pool), annual cultivated crops (newly-opened farmlands and open cultivated farms), perennial with annual intercropped (plantation at sapling stage intercropped with annual crops, under coconut and banana plantation intercropping), cutting of trees (timber poaching, sawn timber), uprooted perennial species (damaged by typhoon, pest and diseases infestation), landslide, post-mining remnants and erosion (including open and abandoned farmlands (formerly cultivated areas), slash-and-burn cultivation (intentional setting of fire and forest burning).

At approximately 100 meters from each threat, a total of 170 threats reemerged during the entire validation period. The highest frequency of large rangeland patches occurred in the southeastern part of the Mobo site, which appeared 32 times. Invasive monocrop plantations dominated by large mahogany and gmelina, irregularly planted in the PA, were commonly observed in the north and south sections of Masbate City site, and in some cases in the opposite site. Other major threats that appeared more than 10 times included built-up structures, annual cultivated crops, perennial crops with annual intercropping, and trees or logs cut, while the rest were considered minor disturbances. Except for natural catastrophes, minute structures are

visible in the understorey, and ecological threats are vividly evident on Google Earth as concrete evidence of how human beings maltreated the PA.

Table 3. Summary of the environmental threat frequency at TNBA

Threat Indicators	Frequency
Rangelands or brushlands (ROB)	32
Invasive monocrop plantation (IMP)	31
Built-up structures (BUS)	24
Annual cultivated crops (ACC)	24
Perennial with annual intercropped (PAI)	20
Cutting of trees (COT)	11
Uprooted perennial species (UPS)	9
Landslide, post-mining cave-in, and soil erosion (LPS)	8
Open and abandoned farmland (OAF)	7
Slash and burn cultivation (SBC)	4
TOTAL	170

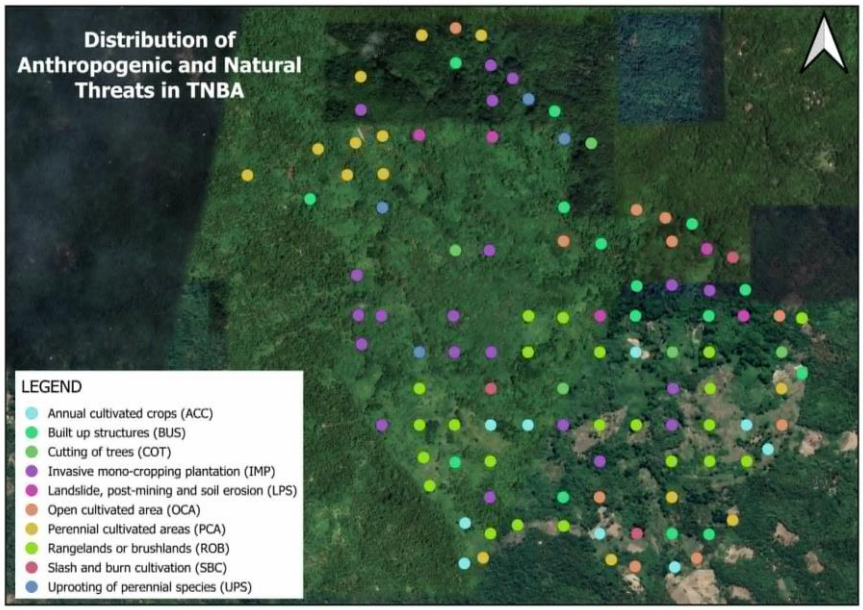

Figure 2. GPS-inputted threats at 100-meter distance interval in TNBA

3.4 Application of the Rasch Model in Measuring the Protected Area Disturbance

The Rasch model can combine data from multiple variables with different metrics into a single scale of a latent variable. In this study, the various threats observed across locations within the TNBA were consolidated into a single scale, referred to as "forest disturbance". Forest disturbance can be considered a latent variable because it cannot be directly observed. It cannot be observed or measured unless the threats that compose it are found to be present or absent. To prepare the dataset for Rasch analysis, all spatial observations were first converted into binary variables indicating the presence (1) or absence (0) of each threat within every grid unit. Threat intensity was originally recorded on a 0–4 ordinal scale; however, preliminary testing using a Partial Credit Model (PCM) revealed disordered category thresholds, indicating that the ordinal responses did not function sequentially along a single latent continuum of disturbance. When such disordered thresholds occur, recoding into fewer categories or into dichotomous form is recommended to restore proper category functioning and uphold Rasch model assumptions [32, 33]. Accordingly, all non-zero ratings were collapsed into a single "presence" category to reflect better the conceptual aim of detecting whether a disturbance exists at all, an approach also found to improve scale performance in other studies [34,35]. This transformation was

implemented to satisfy the requirements of unidimensionality and local independence inherent to Rasch measurement [24]. Following the transformation, model diagnostics were conducted to confirm the appropriateness of the dichotomous specification. A Likelihood Ratio chi-square test showed no significant difference between the PCM and the dichotomous model, $\chi^2(9) = 14.21$, $p = .12$, supporting the simpler dichotomous structure. The dichotomous model exhibited strong measurement precision, with a Person Separation Index (PSI) of 0.82 and item reliability of 0.88 [36]. All threat indicators displayed acceptable fit statistics (infit MSQ 0.876–1.105; outfit MSQ 0.565–1.273), falling within the recommended 0.5–1.5 interval for productive measurement [37]. Threats with fewer than five occurrences across the 170 grids were excluded to avoid unstable parameter estimates, and residual correlations below 0.30 confirmed that the assumption of local independence was met [38]. These diagnostics collectively establish that the dichotomous Rasch model provided a valid and robust basis for estimating watershed disturbance. The line ranges from low to high forest disturbance at each sample location and is operationally defined by the 10 threats. The further to the right a sample point is located, the greater its disturbance (Figure 3). The numerical gradient for this scale is called a logit (log odds) and is established by estimating ordered category threshold parameters for ratings of threat measures that are observed at sampled locations. To estimate threat occurrences and sample location positions, this approach was formally implemented in a dichotomous Rasch model, since the original rating scale (i.e., 0, 1, 2, 3, 4) did not fit the Partial Credit Model due to disordered thresholds. The Rasch analysis in this study is based on the presence (regardless of density) or absence of the threat in each location. It is assumed that the mere presence of destructive human activities in a given location poses an imminent threat to the entire watershed. Using conditional maximum likelihood estimation of the beta and delta parameters in eRm [39], the threat and location disturbance estimates, along with their goodness-of-fit to the Rasch model, were determined. Table 4 presents the threat estimates, their standard errors, and the fit statistics for the threats. The threat estimates ranged from -0.815 to 1.156 logits, indicating that the most frequently observed threat and the rarest are shown in Figure 3. Furthermore, all of the outfit and infit statistics lie between 0.7 and 1.3, except for the outfit of SBC, which lies below the acceptable range. Since the threats did not show consistent misfits (i.e., both outfit and infit are misfits), the data are considered to fit the Rasch model.

Table 4. Threat estimates, standard error and Rasch fit statistics

Threat	Estimate	Std.err	Outfit MSQ	Infit MSQ	Outfit t	Infit t
BUS	-0.815	0.212	0.887	0.935	-0.793	-0.486
GOB	-0.77	0.215	1.11	1.09	0.783	0.709
IMP	-0.725	0.218	1.076	1.05	0.542	0.406
PCA	-0.213	0.259	1.273	1.105	1.226	0.588
OCA	0.023	0.283	0.961	0.975	-0.073	-0.035
ACC	0.114	0.294	0.862	0.943	-0.453	-0.164
COT	0.324	0.32	0.866	0.904	-0.36	-0.271
UPS	0.324	0.32	0.943	0.922	-0.091	-0.203
LPS	0.583	0.358	0.883	0.93	-0.227	-0.12
SBC	1.156	0.462	0.565	0.876	-0.911	-0.148

Table 5. The estimates and standard errors of observed raw scores in the data

Raw score	Estimate	Standard error
0	Negative infinity	NA
1	(approx. -3.3897129 as interpolated) -2.3392	1.069779
2	-1.49443	0.811912
4	-0.44391	0.672329

Location disturbance estimates were also calculated. The raw scores, ranging from 0 to 10 (0 indicating the absence of all threats and 10 indicating the presence of all threats), were transformed into Rasch scores in log-odds units (logits). However, only three raw scores were observed in the data: 1, 2, and 4. The other scores

were not estimated due to the absence of additional threats at each location; however, a linear interpolation may be performed using the existing information, assuming that the relationship between the raw score and the estimate is nearly linear. (For this study, the estimate for 0 was interpolated.) Furthermore, the Rasch model does not provide estimates for extreme scores (i.e., 0 and 10), as the locations with these raw scores are assumed not to contribute to the measurement. Location misfits were also assessed. Of the 170 locations, only 4 were found to misfit the Rasch model. These are found in Location 66 (12°19'09.66''N, 123°37'22.77''E), Location 91 (12°19'02.67''N, 123°37'24.04''E), Location 112 (12°18'54.01''N, 123°36'53.94''E), and Location 161 (12°18'36.70''N, 123°37'11.35''E). These locations did not show a level of disturbance expected by the Rasch model. In the Wright Map in Figure 3, the distribution of the location disturbance estimates is positively skewed. Most locations have lower disturbance, while only a few have higher disturbance. To visualize the levels of disturbance in the watershed, a heat map was generated in ArcGIS. Before the visualization, the raw score estimates were shifted so that the lowest raw score estimate is zero, to satisfy the software's requirement of a positive weight for each location. This was achieved by dividing the shifted estimate by the sum of the estimates for all 170 locations. The latitude and longitude Together with the weight field, they were converted to a shapefile and uploaded to the GIS software for analysis. The visualization output is shown in Figure 4.

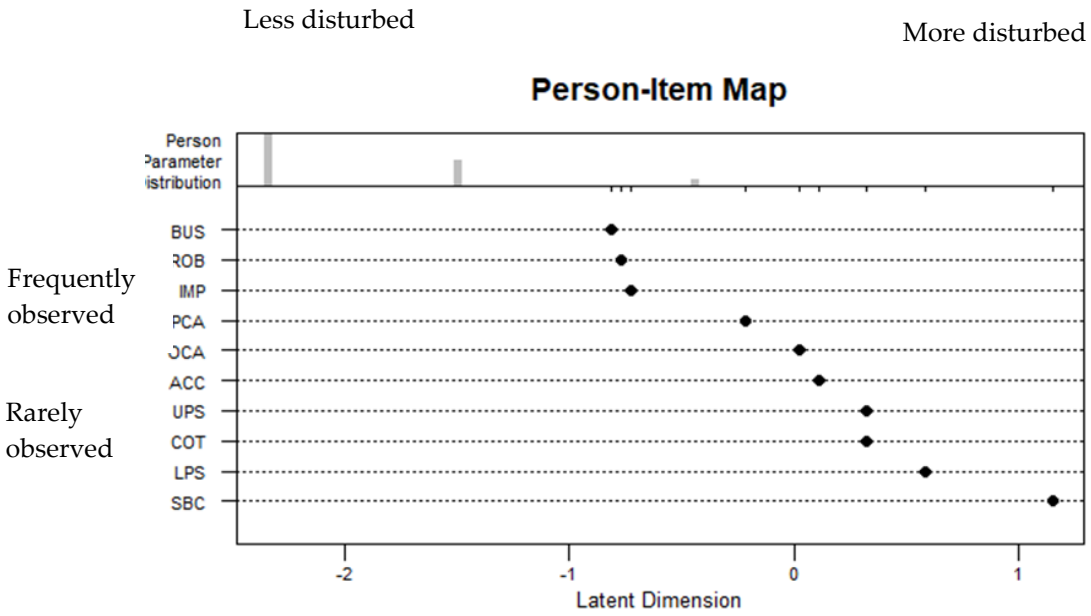

Figure 3. Wright map of the threats and locations estimates in TNBA

To improve the spatial accuracy of the visualization, the logit scores derived from the Rasch model were exported to ArcGIS using the centroid coordinates of the 170 grid units, ensuring consistent spatial resolution throughout the protected area. These logits served as weighted attributes for interpolation, enabling the generation of a continuous disturbance surface rather than discrete point observations. Negative logit values (<-2.00) corresponded to low-disturbance zones, aligning with relatively intact forest areas in the northwestern portion of the watershed. In contrast, logit values exceeding +1.00 identified disturbance hotspots concentrated along agricultural edges, grazing lands, and settlement interfaces. This method enhanced mapping precision by converting binary observations into a spatially coherent disturbance gradient, allowing clearer identification of priority zones for management and rehabilitation.

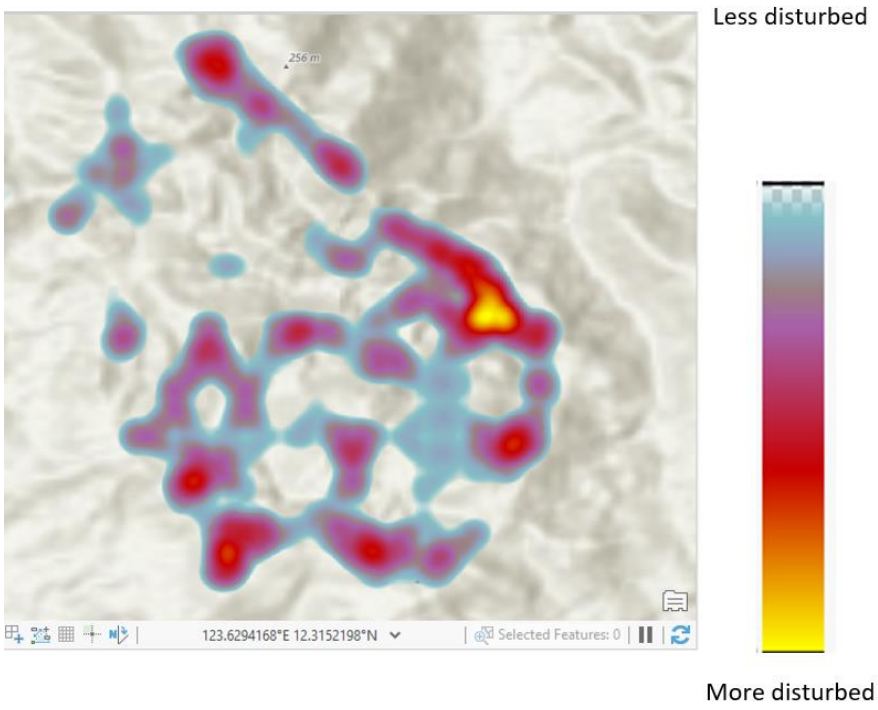

Figure 4. Visualization of threat disturbance at TNBA

Locations in the area were colored according to the level of disturbance observed. The absence of color indicates that the area is pristine. The more the color approaches yellow on the spectrum, the greater the disturbance observed in the area. In the heat map, most of the area, especially the northwestern portion, is undisturbed, while greater disturbance was observed along the boundaries and in the lower half of the area. Median comparisons for the Rasch-based disturbance measures between the two areas (lower and upper) showed that the lower portion of the Mobo area has significantly higher disturbance than the upper portion of the Masbate City area. Most grid locations were positioned below -2.00 logits, indicating low overall disturbance, particularly in the northwestern portion of Masbate City. In contrast, higher disturbance scores—typically exceeding +1.00—were observed in the southern Mobo zone, where rangelands, invasive tree plantations, cultivated farms, and built-up structures are more concentrated.

The test for local independence in the Rasch model showed that no pairs of threat items had significant correlations. The magnitude of local independence was calculated from residual item correlations; correlations above 0.3 indicate dependency between items [24]. In theory, significant correlations among the items after removing the influence of the underlying trait (i.e., disturbance) could indicate a violation of the unidimensionality assumption [38]. This means that the threat indicators used to make the latent trait "disturbance" manifest functioned independently but contributed meaningfully to the measurement of that single trait, thereby satisfying one of the important assumptions of the Rasch model.

Table 6. Threat item residual correlations

	ACC	PCA	OCA	IMP	GOB	COT	SBC	BUS	UPS	LPS
ACC	1	-0.0627	-0.05838	-0.19328	-0.13532	-0.11944	0.193821	-0.11974	-0.11302	-0.09909
PCA	-0.0627	1	-0.11902	-0.18185	-0.17856	-0.10855	-0.08204	-0.22448	-0.10338	-0.08983
OCA	-0.05838	-0.11902	1	-0.13994	-0.13752	-0.11705	0.041018	-0.18146	-0.03783	-0.09707
IMP	-0.19328	-0.18185	-0.13994	1	-0.2826	-0.01362	-0.13405	-0.14073	-0.06901	-0.14523
GOB	-0.13532	-0.17856	-0.13752	-0.2826	1	-0.11287	-0.13098	-0.13642	-0.1071	-0.14225
COT	-0.11944	-0.10855	-0.11705	-0.01362	-0.11287	1	-0.08503	-0.17045	-0.0548	0.007591
SBC	0.193821	-0.08204	0.041018	-0.13405	-0.13098	-0.08503	1	-0.05679	-0.0799	-0.07039
BUS	-0.11974	-0.22448	-0.18146	-0.14073	-0.13642	-0.17045	-0.05679	1	-0.16174	0.030356
UPS	-0.11302	-0.10338	-0.03783	-0.06901	-0.1071	-0.0548	-0.0799	-0.16174	1	-0.08474
LPS	-0.09909	-0.08983	-0.09707	-0.14523	-0.14225	0.007591	-0.07039	0.030356	-0.08474	1

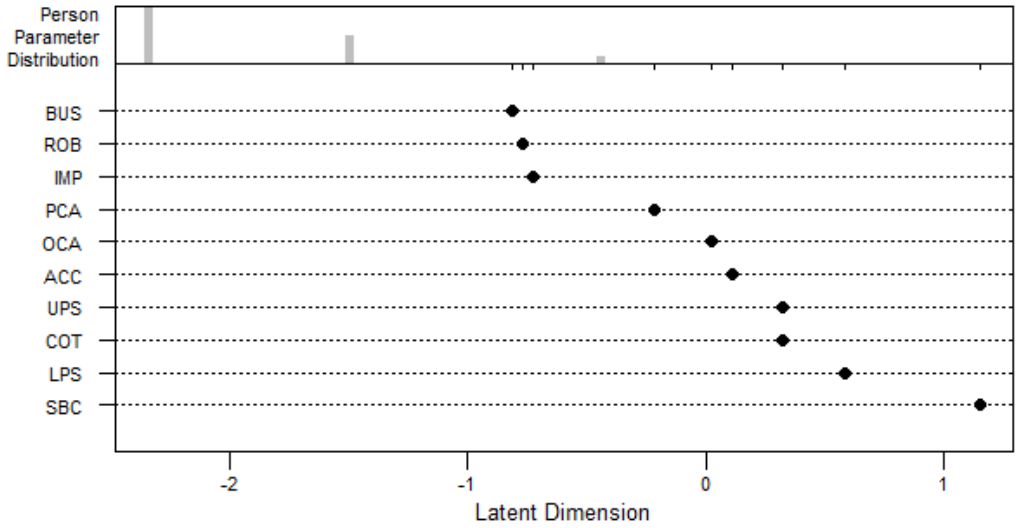

Figure 5. Wright Map on the relative positions of the threat items and locations of disturbance in TNBA

Estimating the threat item and location disturbance parameters led to the construction of the Wright Map (Figure 5). This map illustrates the relative positions of the threat items and location disturbance on the same linear scale (latent dimension). The upper portion of the map shows the distribution of the location disturbance estimates (or Person Parameter Distribution). In contrast, the lower portion shows the positions of the threat items based on their estimated severity (frequency or rarity, in this case, with items on the left more frequently observed and those on the right less frequently observed).

As shown in the person parameter distribution, most locations have disturbance estimates below -2.00, compared with the lowest threat item estimate of -0.815. Since the distributions of threat items and location disturbance did not have the same central tendencies, with the former near 0.00 and the latter near -2.00, the probability that a given threat exists at each location is very low. Hence, the watershed is nearly pristine. In this study, the highest threat item estimate for SBC was 1.156; therefore, a location with disturbance estimates equal to or greater than 1.156 can be considered severely disturbed.

Table 7. Disturbance scale derived using the threat item estimates

Location disturbance estimate		Disturbance level
Lower limit (in logits)	Upper limit (in logits)	
-infinity	-0.815	Very low
-0.815	0.1705	Low
0.1705	1.156	High
1.156	+infinity	Very high

4. Conclusions

A comprehensive assessment of disturbances within the Tugbo Natural Biotic Area emerges from the combined application of ground validation, GIS techniques, and Rasch probabilistic modeling. Ground surveys remain indispensable for documenting fine-scale threats such as timber extraction, mining remnants, charcoal pits, and pest or disease occurrences—factors that are not consistently detected in GIS-based simulations. When integrated with GIS, these data produce a coherent spatial representation of disturbance intensity across the landscape. The Rasch model contributes an innovative measurement component by converting categorical observations into interval-level logits, providing a consistent and objective disturbance index. This triangulated methodology strengthens the scientific basis for adaptive management, enabling protected area managers to identify priority zones and implement targeted conservation interventions. This study confirms that the Tugbo Natural Biotic Area is not entirely pristine but remains largely intact, with localized zones of moderate anthropogenic disturbance. The integration of the Rasch model with GIS offers a novel approach to environmental monitoring by converting qualitative field observations into quantitative interval-level disturbance measures, enabling a more objective evaluation than traditional descriptive or remote–sensing–only approaches. These results can support the Protected Area Management Board in identifying disturbance hotspots, prioritizing zones for rehabilitation, allocating patrolling and monitoring resources more efficiently, and establishing a standardized, repeatable assessment protocol using the same 170-grid framework for long-term ecological monitoring.

5. Acknowledgements

The main author sincerely thanks the K-12 program of the Commission on Higher Education (CHED) for the award of its full scholarship and for providing it with financial support for this report. He also acknowledges DENR RO V, CENRO–Mobo, and the TNBA–PAMB for granting authorization to undertake this research in the protected area. Special mention to Dr. Sherwin E. Balbuena, his co-author and statistician, for conceptualizing the study using the Rasch model, which enabled visualization of environmental disturbance.

Author Contributions: The following are the contributions of each author in this research: Conceptualization: Abella, MAC and Balbuena, SE; Methodology: Abella, MAC and Balbuena, SE; Software: Balbuena, SE; Validation: Abella, MAC; Formal analysis: Balbuena, SE; Investigation: Abella, MAC; Resources: Abella, MAC; Data curation: Balbuena, SE and Abella, MAC; Writing—original draft preparation: Abella, MAC; Writing—review and editing: Abella, MAC and Balbuena, SE; Visualization: Balbuena, SE and Abella, MAC; Supervision: Abella, MAC; Project administration: Abella, MAC; and Funding acquisition: Abella, MAC.

Funding: The main author received a CHED K-12 scholarship.

Conflicts of interest: The authors declare no conflict of interest.

References

[1] Solaimani, K.; Darvishi, S. Comparative Analysis of Land Use Changes Modeling Based-on New Hybrid Models and CA-Markov in the Urmia Lake Basin. *Adv. Space Res.* **2024**, *74*(8), 3749–3764. https://doi.org/10.1016/j.asr.2024.06.078

[2] Roy, P. S.; Ramachandran, R. M.; Paul, O.; Thakur, P. K.; Ravan, S.; Behera, M. D.; Kanawade, V. P. Anthropogenic Land Use and Land Cover Changes—A Review on Its Environmental Consequences and Climate Change. *J. Indian Soc. Remote Sens.* **2022**, *50*(8), 1615–1640. https://doi.org/10.1007/s12524-022-01569-w

[3] Nyathi, N. A.; Musakwa, W.; Krenz, J.; Kuhn, N. J. Spatio-Temporal Dynamics of Habitat Quality Explored with InVEST: The Case of the Greater Limpopo Transfrontier Conservation Area. *Sustain. Environ.* **2025**, *11*(1), 2520642. https://doi.org/10.1080/27658511.2025.2520642

[4] Batool, S.; et al. Nature's Comeback: Case Studies of South Asian Countries Regarding Biodiversity Restoration and Conservation. In *Sustainable Synergy: Harnessing Ecosystems for Climate Resilience*; Choudhury, M., Dixit, G., Majumdar, S., Eds.; Climate Change Management; Springer: Cham, 2025. https://doi.org/10.1007/978-3-031-77957-2_5

[5] Pulido-Chadid, K.; Virtanen, E.; Geldmann, J. How Effective Are Protected Areas for Reducing Threats to Biodiversity? A Systematic Review Protocol. *Environ. Evid.* **2023**, *12*(1). https://doi.org/10.1186/s13750-023-00311-4

[6] Meng, Z.; Dong, J.; Ellis, E. C.; Metternicht, G.; Qin, Y.; Song, X.-P.; Löfqvist, S.; Garrett, R. D.; Jia, X.; Xiao, X. Post-2020 Biodiversity Framework Challenged by Cropland Expansion in Protected Areas. *Nat. Sustain.* **2023**, *6*(7), 758–768. https://doi.org/10.1038/s41893-023-01093-w

[7] Girma, R.; Fürst, C.; Moges, A. Land Use Land Cover Change Modeling by Integrating Artificial Neural Network with Cellular Automata-Markov Chain Model in Gidabo River Basin, Main Ethiopian Rift. *Environ. Chall.* **2022**, *6*, 100419. https://doi.org/10.1016/j.envc.2021.100419

[8] Wang, J.; Wu, Y.; Gou, A. Habitat Quality Evolution Characteristics and Multi-Scenario Prediction in Shenzhen Based on PLUS and InVEST Models. *Front. Earth Sci.* **2023**, *11*. https://doi.org/10.3389/fenvs.2023.1146347

[9] Chen, C.; Liu, J.; Bi, L. Spatial and Temporal Changes of Habitat Quality and Its Influential Factors in China Based on the InVEST Model. *Forests* **2023**, *14*(2), 374. https://doi.org/10.3390/f14020374

[10] Sun, J.; Ongsomwang, S. Optimal Parameters of Random Forest for Land Cover Classification with Suitable Data Type and Dataset on Google Earth Engine. *Front. Earth Sci. (Lausanne)* **2023**, *11*. https://doi.org/10.3389/feart.2023.1188093

[11] Li, X.; Liu, Z.; Li, S.; Li, Y. Multi-Scenario Simulation Analysis of Land Use Impacts on Habitat Quality in Tianjin Based on the PLUS Model Coupled with the InVEST Model. *Sustainability* **2022**, *14*(11), 6923. https://doi.org/10.3390/su14116923

[12] Admasu, S.; Yeshitela, K.; Argaw, M.; Bloor, M. Assessing Habitat Quality Using the InVEST Model in the Dire and Legedadi Watersheds, Central Highland of Ethiopia: Implication for Watershed Management. *Sustain. Environ.* **2023**, *9*(1). https://doi.org/10.1080/27658511.2023.2242137

[13] Nematollahi, S.; Fakheran, S.; Kienast, F.; Jafari, A. Application of InVEST Habitat Quality Module in Spatially Vulnerability Assessment of Natural Habitats (Case Study: Chaharmahal and Bakhtiari Province, Iran). *Environ. Monit. Assess.* **2020**, *192*(8). https://doi.org/10.1007/s10661-020-08460-6

[14] Tahir, Z.; Haseeb, M.; Mahmood, S. A.; Batool, S.; Abdullah-Al-Wadud, M.; Ullah, S.; Tariq, A. Predicting Land Use and Land Cover Changes for Sustainable Land Management Using CA-Markov Modelling and GIS Techniques. *Sci. Rep.* **2025**, *15*(1), 3271. https://doi.org/10.1038/s41598-025-87796-w

[15] Dos Santos, W. P.; Acuña-Guzman, S. F.; de Oliveira, P. T.; Beniaich, A.; Cardoso, D. P.; Silva, M. L.; Avanzi, J. C. CA-Markov Prediction Modeling for the Assessment of Land Use/Land Cover Change in Two Sub-Basins of the Tocantins-Araguaia River Basin. *Environ. Monit. Assess.* **2024**, *196*(6), 499. https://doi.org/10.1007/s10661-024-12673-4

[16] Hakim, A. M. Y.; Santosa, B. H.; Martono, D. N.; Sencaki, D. B.; Prayogi, H.; Arifandri, R.; Steinhausen, M. J. Exploring Land Cover Change Impacts on Ecosystem Services Using Machine Learning Technique and Scenario Simulation: Case Study of the Upper Citarum River Basin, Indonesia. *Mod. Earth Syst. Environ.* **2025**, *11*(3), 211. https://doi.org/10.1007/s40808-025-02352-9

[17] Blissag, B.; Yebdri, D.; Kessar, C. Spatiotemporal Change Analysis of LULC Using Remote Sensing and CA-ANN Approach in the Hodna Basin, NE of Algeria. *Phys. Chem. Earth, Parts A/B/C* **2024**, *133*, 103535. https://doi.org/10.1016/j.pce.2023.103535

[18] Loyd, B. H.; Hoover, H. D. Vertical Equating Using the Rasch Model. *J. Educ. Meas.* **1980**, *17*(3), 179–193.
[19] Rabbitt, M. P. Causal Inference with Latent Variables from the Rasch Model as Outcomes. *Measurement* **2018**, *120*, 193–205. https://doi.org/10.1016/j.measurement.2018.01.044
[20] Moral, F. J.; Terrón, J. M.; Rebollo, F. J. Site-specific Management Zones Based on the Rasch Model and Geostatistical Techniques. *Comput. Electron. Agric.* **2011**, *75*(2), 223–230. https://doi.org/10.1016/j.compag.2010.10.014
[21] Moral, F. J.; Rebollo, F. J.; Terrón, J. M. Analysis of Soil Fertility and Its Anomalies Using an Objective Model. *J. Plant Nutr. Soil Sci.* **2012**, *175*(6), 912–919. https://doi.org/10.1002/jpln.201100361
[22] Moral, F. J.; Álvarez, P.; Canito, J. L. Mapping and Hazard Assessment of Atmospheric Pollution in a Medium Sized Urban Area Using the Rasch Model and Geostatistics Techniques. *Atmos. Environ.* **2006**, *40*(8), 1408–1418. https://doi.org/10.1016/j.atmosenv.2005.10.054
[23] Moral, F. J.; Rebollo, F. J.; Valiente, P.; López, F. Modeling of Atmospheric Pollution in Urban and Rural Sites Using a Probabilistic and Objective Approach. *Appl. Sci.* **2019**, *9*(19), 4009. https://doi.org/10.3390/app9194009
[24] Tennant, A.; Conaghan, P. G. The Rasch Measurement Model in Rheumatology: What Is It and Why Use It? When Should It Be Applied, and What Should One Look for in a Rasch Paper? *Arthritis Care Res.* **2007**, *57*(8), 1358–1362. https://doi.org/10.1002/art.23108
[25] Forest Management Bureau. Top 10 Most Deforested Provinces in the Philippines. *Philippine Forest Cover*. Philstar, March 4, **2018**. https://www.philstar.com/headlines/2018/03/04/1793446/recovering-philippines-forest-cover (accessed 2026-02-23).
[26] Estoque, R. C.; Murayama, Y.; Lasco, R. D.; Myint, S. W.; Pulhin, F. B.; Wang, C.; Hijioka, Y. Changes in the Landscape Pattern of the La Mesa Watershed—The Last Ecological Frontier of Metro Manila, Philippines. *For. Ecol. Manage.* **2018**, *430*, 280–290. https://doi.org/10.1016/j.foreco.2018.08.023
[27] Regional Soils Laboratory. *Soil Test Result Interpretation*; Integrated Laboratory Division, DA-RFU ROV: Naga City, Philippines, **2019**.
[28] Forest Management Bureau. *LAWIN Forest and Biodiversity Protection System. Module 2: Purpose-driven Patrolling*; Forest Conservation Area Planning: **2018**. http://pdf.usaid.gov (accessed 2026-02-23).
[29] National Mapping and Resource Information Authority. *Land Cover Map of Tugbo Watershed Forest Reserve, Province of Masbate*; Land Mapping Division: Legaspi City, Philippines, **2019**.
[30] Mair, P.; Hatzinger, R. CML Based Estimation of Extended Rasch Models with the eRm Package in R. *Psychol. Sci.* **2007**, *49*(1), 26–43.
[31] Provincial Environment and Natural Resources – Community Environment and Natural Resources Office. *Socio-economic Assessment Monitoring System (SEAMS). Tugbo Watershed Forest Reserve*; Masbate City, Philippines, **2018**.
[32] Bond, T. G.; Fox, C. M. *Applying the Rasch Model: Fundamental Measurement in the Human Sciences*, 3rd ed.; Routledge: New York, **2015**.
[33] Boone, W. J.; Staver, J. R.; Yale, M. S. *Rasch Analysis in the Human Sciences*; Springer: Dordrecht, **2014**.
[34] Tsai, C. L.; Wind, S.; Estrada, S. Exploring the Effects of Collapsing Rating Scale Categories in Polytomous Item Response Theory Analyses: An Illustration and Simulation Study. *Meas.: Interdiscip. Res. Perspect.* **2025**, *23*(1), 66–89.
[35] Quan, Y.; Wang, C. Collapsing or Not? A Practical Guide to Handling Sparse Responses for Polytomous Items. *Methodology* **2025**, *21*(1), 46–73.
[36] Linacre, J. M. *Winsteps Rasch Measurement Computer Program User's Guide*, Version 5.1.1; Winsteps.com: **2021**.
[37] Linacre, J. M. What Do Infit and Outfit, Mean-Square and Standardized Mean. *Rasch Meas. Trans.* **2002**, *16*(2), 878.
[38] Lee, Y. W. Examining Passage-related Local Item Dependence (LID) and Measurement Construct Using Q3 Statistics in an EFL Reading Comprehension Test. *Lang. Test.* **2004**, *21*(1), 74–100. https://doi.org/10.1191/0265532204lt260oa
[39] Mair, P.; Hatzinger, R. CML-based Estimation of Extended Rasch Models with the eRm Package in R. *Psychol. Sci.* **2007**, *49*(1), 26–43.

ASEAN
Journal of Scientific and Technological Reports
Online ISSN:2773-8752

Research article

Comparison of Inhibitory Effects between Cetuximab and Cisplatin on Colon Cancer SW480 Cell Line

Barakat Abdulrazzaq Mutar[1*], Azhar Ali Sekhi[2], Zainab Abdulkareem Oleiwi Alfarhani[1], and Arafat A. Muttar[3]

[1] Department of Biology, College of Education, University of Al-Qadisiyah, Iraq
[2] Department of Microbiology, College of Medicine, University of Al-Qadisiyah, Iraq
[3] College of Science, Al-Nahrain University, Iraq
* Correspondence: barakat.abdulrazzaq@qu.edu.iq

Citation:
Mutar, A.B.; Sekhi, A.A.; Alfarhani, A.O.Z.; Muttar, A.A. Comparison of inhibitory effects between cetuximab and cisplatin on colon cancer SW480 cell line. *ASEAN J. Sci. Tech. Report.* **2026**, *29*(3), e262531. https://doi.org/10.55164/ajstr.v29i3.262531.

Article history:
Received: December 22, 2025
Revised: January 3, 2026
Accepted: January 10, 2026
Available online: February 27, 2026

Abstract: Cancer is still one of the more severe diseases that endangers the life of a human being, especially in the present day. Globally, colorectal cancer is a very predominant cancer and the second principal contributor to cancer-related fatalities across all ages, both adults and children. Currently available treatments include surgery, radiotherapy, chemotherapy, and immunotherapy. Chemotherapy is an established modality in the therapy of cancer, and platinum-based drugs demonstrated activity against several tumours. Here, cancer cell lines were grown in ELISA plates in media until ~80% monolayer confluence. Cetuximab (Cetx) was tested for cytotoxicity on the SW480 colon cancer cell line at six serial concentrations ranging from 2.5 to 0.0781 μg/mL. Similarly, the same cell line was exposed to six serial levels of cisplatin (Cisp.), varying from 100 to 3.125 μg/mL, for 24 hours. Cells without any treatment served as controls. Cell viability was monitored by measuring OD with an ELISA reader after staining with crystal violet. The findings revealed a significant result at the statistical level ($P < 0.05$). in the cell-killing impacts of cetuximab and cisplatin in colon cancer cells. These findings emphasize the potential value of cetuximab's anti-tumour activity when used alongside traditional platinum-based chemotherapy and support its use in targeted cancer therapy.

Keywords: Cetuximab; cisplatin; colorectal cancer; SW480 cell line; cytotoxicity

1. Introduction

Colon and rectal disease originate in the colon's tissue, the longest segment of the internal organ. The majority of colon cancers arise in the submucosal layer of the digestive system. Several studies say that lifestyle choices like eating high-fat foods and smoking are to blame, but research has found that inherited traits also play a role in about 25% of cases. Colon cancer is a major contributor to well-known types of cancer internationally and represents the third leading cause of cancer deaths in the US [1, 2]. Its therapy necessitates a multi-methodology model, which involves carefully resecting the growth subsequently treated with chemotherapy and radiotherapy. Notwithstanding significant advances in the treatment of colorectal cancer, there is a need for more advanced therapies and novel approaches that incorporate targeted inhibition of signaling pathways [3]. For people with head and neck cancer, Cetx. Moreover, in general, radiotherapy made them more likely to live for five years than people who had radiotherapy alone [4]. The endurance benefits are related

to Cetx's expansion. Administered as frontline chemotherapy for cutting-edge non-small-cell lung carcinoma in individuals with undeniable EGFR mutations was likewise announced [5].

Moreover, some preclinical investigations propose that Cetx. restrains reduces the expansion of EGFR-positive colorectal cancer cells while enhancing the therapeutic impact of chemo- and radiotherapy [6]. Although these therapy blend choices have worked on the patient's endurance, extra nontoxic designated therapy choices are required in the unmanageable treatment setting of cutting-edge colon cancer. There are many different cis-Diamminedichloroplatinum(II) (Cisp.), but it is one of the most powerful anti-tumour agents. It has many anti-tumour uses, covering clinical management of colorectal pathology [7]. Cellular toxicity arises from its binding to DNA and subsequent generation of DNA damage, which activates various signaling cascades culminating in apoptotic cell death [8, 9]. Be that as it may, it likewise has extremely unfavorable impacts, associated with renal injury, peripheral nerve damage, and auditory toxicity [8, 9,10]. Therefore, continued advancement in innovative drugs and treatment modalities for colorectal cancer is essential. Current investigations largely emphasize combination chemotherapeutic approaches designed to mitigate adverse effects and enhance clinical outcomes [11].

2. Materials and Methods

2.1 Cell Line and Culture Conditions

The College of Medicine, Cancer Research Laboratory, University of Babylon, provides the SW480 cell line, a human colorectal adenocarcinoma cell line. The study involved all cells present in passages 15-25 to make the experiment homogeneous. The cells were grown in RPMI-1640 medium (Gibco, Thermo Fisher Scientific, USA) containing 10% (v/v) fetal bovine serum and penicillin (100 U/mL) and streptomycin (100 μg/mL). Cultures were preserved at 37 °C in a humid atmosphere containing 5% CO2. The medium was refreshed every 2–3 days. When the confluence reached around 8090 percent, cells were dislodged with a 0.25 percent trypsinEDTA solution and then subcultured.

2.2 Reagents and Materials

Cisplatin (cis-Diamminedichloroplatinum (II)) was purchased from a local pharmacy and dissolved in sterile saline to prepare stock solutions. Cetuximab was obtained from the Science Laboratories at the Belarusian State University (College of Belarus). All tissue culture consumables, including 96-well microculture plates, serological pipettes, and cell culture flasks, were obtained from local scientific suppliers. PBS solution and RPMI-1640 growth medium, trypsin-EDTA, crystal violet, paraformaldehyde, methanol, and acetic acid were of analytical grade.

2.3 Cytotoxicity Assay

The crystal violet staining technique was used to assess cell viability. SW480 cells were plated in 96-well culture plates at a cell concentration of 1×10^4 cells per plate in 200 μL of complete, supplemented RPMI-1640 medium. The plates were subsequently preserved at 37 0 C in a humidity-controlled incubator supplemented with 5% CO_2 to allow cell adhesion and the development of an approximately 80% confluent monolayer.

2.3.1 Drug Treatment

After the initial 24-hour incubation period, the cultivation medium was discarded and replaced with a medium containing the test compounds. Cells were treated with cetuximab at six serial values: 2.5, 1.25, 0.625, 0.3125, 0.156, and 0.0781 μg/mL. In parallel experiments, cells were exposed to cisplatin at six values: 100, 50, 25, 12.5, 6.25, and 3.125 μg/mL. All treatments were performed in triplicate. Negative controls were made of untreated cells (culture medium only). The plates were cultured for 24 and 48 h under the same conditions.

2.3.2 Crystal Violet Staining

The drug-containing medium was carefully aspirated after the treatment period (24 and 48 hours), and the cells were washed twice with PBS to remove non-adherent cells and residual medium. To fix the cells, 4% paraformaldehyde (100 μL/well) was added and maintained for 15 minutes at 25°C. Cells were then rinsed with the fixative, followed by incubation with 100 μL/well of 0.1% crystal violet solution solubilized in 20%

methanol at 25°C for 20 minutes. The remaining stain was removed by rinsing the plates with distilled water (3-4 times) until no stain appeared in the wash solution. Plates were put inverted and left to dry overnight at 25°C.

2.3.3 Colorimetric Quantification

The crystal violet retained by the cells was eluted by adding 100 µL of 10% acetic acid to the wells and incubating the wells for 20 minutes with gentle shaking on an orbital platform. Readings were taken at 570 nm and recorded using a microplate ELISA reader (model to be specified if needed). The rate of inhibition (IR%) was computed using the following equation.

$$IR\% = \frac{OD_{control} - OD_{treated}}{OD_{control}} \times 100$$

Where $OD_{control}$ represents the average optical density of untreated control cells, and $OD_{treated}$ represents the mean optical density of drug-treated cells.

2.4 Statistical Analysis

Each experimental procedure was conducted three times, and the findings are reported as mean ± SD. The SPSS software (V 26.0) was used for statistical analysis. The unpaired Student t-test was conducted to compare the cetuximab- and cisplatin-treated groups simultaneously. ANOVA was used to test dose-dependent effects within each treatment group, and the test was examined using post hoc multiple comparisons with the Tukey test. Further, a two-way ANOVA was employed to assess the effects of drug type, drug concentration, and exposure duration on cell viability, along with their interactions. The variation was deemed relevant when the P value was less than 0.05. The graphic representations were produced in Microsoft Excel (Microsoft, USA) and GraphPad Prism software (V 9.0).

3. Results and Discussion

3.1 Cytotoxic Effect of Cetuximab on SW480 Cells

The cytotoxicity of Cetuximab on SW480 colon cancer cells was tested in six serial concentrations (0.07812.5 -3) in 24 and 48 hours of exposure. Cell survival was measured using the crystal violet assay, and the results revealed a clear dose-dependent suppressive effect of cetuximab on the progression of SW480 cells.

3.1.1 Effect at 24 Hours

Cetuximab showed high cytotoxicity against SW480 cells after 24 hours of treatment at all concentrations tested (Table 1; Figure 1). The rate of inhibition increased gradually with increasing drug concentration. A low level of inhibition (13.21) was observed at the lowest concentration (0.0781 µg/mL). The inhibitory effect was significantly higher at higher concentrations, reaching 57.30% at 0.3125 µg/mL and 85.12% at 0.625 µg/mL. The highest reduction rate of 91.24% was observed at 1.25 µg/mL. The maximum concentration tested (2.5 µg/mL) showed a slightly lower inhibition rate (90.82%), suggesting that, in these experimental conditions, the maximum cytotoxic effect was achieved at 1.25 µg/mL.

Table 1. SW480 **cell response to cetuximab after 24 hours.**

Concentration (µg/mL)	Control	0.0781	0.156	0.3125	0.625	1.25	2.5
Mean OD	0.719	0.624	0.537	0.307	0.107	0.063	0.066
IR (%)	—	13.21	25.31	57.30	85.12	91.24	90.82

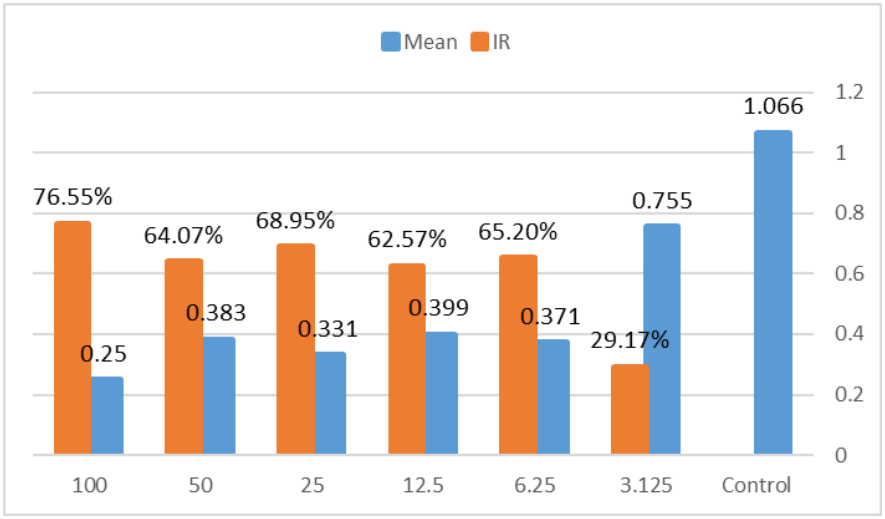

Figure 1. Cetuximab Impact on cell viability of SW480 colon cancer cells in 24 hours. Different concentrations of cetuximab (0.07812.5 µg/mL) were administered to the cells and incubated for 24 hours. The crystal violet assay was used to determine cell viability. Blue bars are the mean optical density (OD 5 0) and orange bars show the inhibition rate (percent). The findings are displayed as the mean ± SD (n = 3).

3.1.2 Effect at 48 Hours

The 48-hour exposure of cetuximab produced better cytotoxicity than the 24-hour exposure (Table 2; Figure 2). The inhibition rates obtained were usually higher across all concentrations tested. The lowest concentration (0.057 µg/mL) showed an inhibition rate of 36.06%, which was significantly higher than the rate at 24 hours. There was a significant cytotoxicity at 0.143 µg/mL (87.13% inhibition) and a maximum cytotoxicity of 97.77 at 0.286 µg/mL. The greater the concentration level (0.625, 1.25, and 2.5 µg/mL), the higher the inhibition rates: 89.79, 93.72, and 93.83, respectively. These findings suggest that the antiproliferative effect of Cetuximab on SW480 cells is enhanced with long-term exposure.

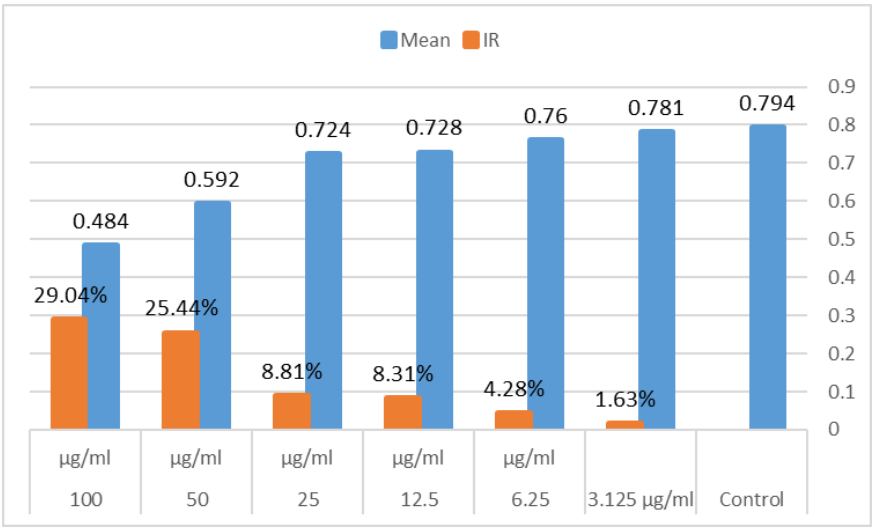

Figure 2. SW480 colon cancer cell viability affected by cisplatin after 24 hours. Different concentrations of cisplatin (3.125-100 mu g/mL) were added to the cells and cultured for 24 h. Cell survival was determined using a crystal violet assay. Blue bars indicate the mean optical density (OD 070) and orange bars indicate the rate of inhibition (percentage). The data are presented as mean ± SD (n = 3).

Table 2. Effects of cisplatin on SW480 cells in 24 hours.

Concentration (µg/mL)	Control	3.125	6.25	12.5	25	50	100
Mean OD	0.794	0.781	0.760	0.728	0.724	0.592	0.484
IR (%)	—	1.64	4.28	8.31	8.82	25.44	39.04

3.2 Cytotoxic Effect of Cisplatin on SW480 Cells

The cytotoxic activity of cisplatin on SW480 cells was tested at six serial doses (3.125-100 µg/mL) after 24 and 48 hours to allow comparison with Cetuximab treatment.

3.2.1 Effect at 24 Hours

The cytotoxicity of cisplatin on SW480 cells was relatively lower after 24 hours of exposure than that of Cetuximab (Table 3; Figure 3). The lowest concentration (3.125 µg/mL) resulted in the lowest inhibition percentage (1.64%), indicating that cell viability was not significantly affected. The concentration of the inhibitory effect rose slowly to 8.31 percent at 12.5 mol/L and 25.44 percent at 50 mol/L. The highest test concentration (100 µg/mL) yielded the highest inhibition rate (39.04%). All these findings imply that, with a shorter incubation period, cisplatin has a lower short-term cytotoxic effect on SW480 cells than cetuximab.

Table 3. Cetuximab effect on the SW480 cells after 48 hours.

Concentration (µg/mL)	Control	0.057	0.143	0.286	0.625	1.25	2.5
Mean OD	0.94	0.601	0.121	0.021	0.096	0.059	0.058
IR (%)	—	36.06	87.13	97.77	89.79	93.72	93.83

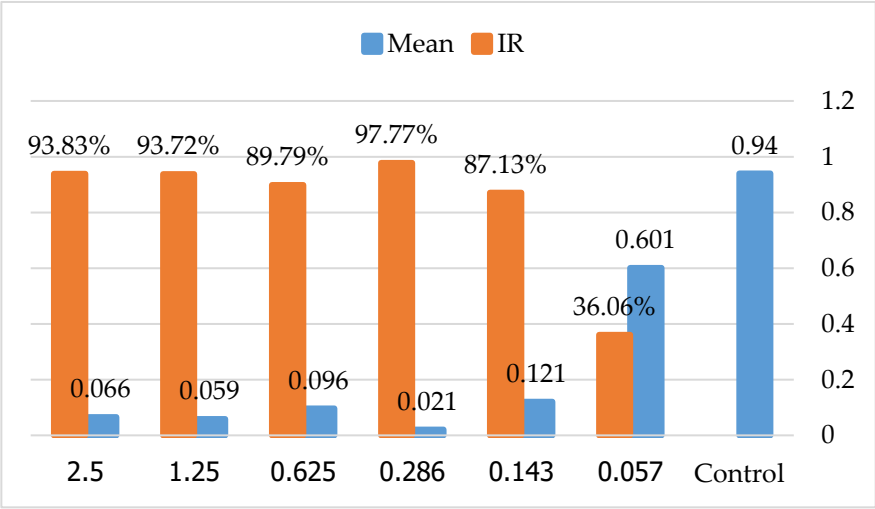

Figure 3. Cetuximab Effect on SW480 colon cancer cell viability after 48 hours. Cells were incubated with different cetuximab (0.057-2.5 µg/mL) concentrations over a period of 48 hrs. The crystal violet assay was used to measure cell viability. Blue bars mean optical density (OD 5 0), and orange bars mean inhibition rate (percent). Statistical values are presented as the mean ± SD (n=3).

3.2.2 Effect at 48 Hours

There was a significant increase in cytotoxicity with extended cisplatin exposure from 24 to 48 hours (Table 4; Figure 4). The lowest inhibition rate (3.125 µg/mL) was 29.17, which is significantly higher than the rate of 1.64 at 24 hours. The antiproliferative activity was enhanced, with inhibition rates of 62.57-68.95 at intermediate concentrations. The highest inhibition percentage, 76.55%, occurred at a concentration of 100 µg/mL. Cisplatin still showed better efficacy at 48 hours, but the maximum inhibition rate (76.55) was still lower than that of cetuximab (97.77) under similar conditions.

Table 4. Effect of Cisplatin on SW480 cells (48 hours).

Concentration (µg/mL)	Control	3.125	6.25	12.5	25	50	100
Mean OD	1.066	0.755	0.371	0.399	0.331	0.383	0.250
IR (%)	—	29.17	65.20	62.57	68.95	64.07	76.55

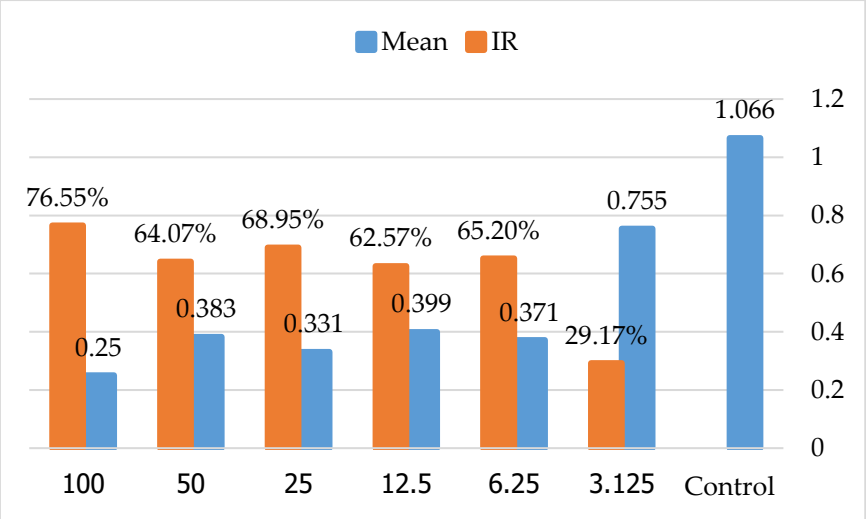

Figure 4. Treatment of SW480 cells in colon cancer with cisplatin after 48 hours. Cells were incubated with different dosages of cisplatin (3.125-100 µg/ml) for 48 hours. The crystal violet assay was used to measure cell viability. Blue bars are the mean optical density (OD 5), and orange bars are the rate of inhibition (percent). The findings are presented as mean ± SD (n = 3).

3.3 Comparative Analysis of Cetuximab and Cisplatin

Statistical analysis revealed a marked variation in the cytotoxic efficacy of cetuximab and cisplatin against colon cancer cells SW480 ($P < 0.05$). Table 5 gives a comparative summary of the major findings.

Table 5. Comparative overview of the cetuximab and cisplatin cytotoxicity on the SW480.

Parameter	Cetuximab	Cisplatin
Concentration range tested	0.0781–2.5 µg/mL	3.125–100 µg/mL
Maximum IR% at 24 hours	91.24% (at 1.25 µg/mL)	39.04% (at 100 µg/mL)
Maximum IR% at 48 hours	97.77% (at 0.286 µg/mL)	76.55% (at 100 µg/mL)
Dose required for >50% inhibition (24h)	0.3125 µg/mL	Not achieved
Dose required for >50% inhibition (48h)	0.143 µg/mL	6.25 µg/mL

Cetuximab showed more than 90% inhibition at concentrations of 1.25 µg/mL and above, whereas cisplatin showed only 39.04% inhibition at the maximum test concentration (100 µg/mL). This is a significant disparity in cytotoxicity, with cetuximab about 80 times more effective at this concentration. The treatment difference was significant ($P < 0.001$). Both drugs showed increased cytotoxicity at 48 hours, but cetuximab was more effective. The maximum inhibition was almost 100% (97.77%) with cetuximab at 0.286 0mL and 76.55% with cisplatin at 100 0mL. The ANOVA showed significant main effects of drug type and concentration ($P < 0.001$ in both cases) and exposure duration ($P < 0.01$). Moreover, the interactions among these variables were statistically significant ($P < 0.05$).

3.4 Discussion

3.4.1 Superior Efficacy of Cetuximab

The outcomes of this study show that cetuximab is much more cytotoxic on the SW480 colon cancer cells than cisplatin. The rapid mechanism of action of cetuximab, with over 90 percent inhibition within the first 24 hours, suggests a powerful mechanism that can kill cancer cells. This is consistent with previous literature indicating that cetuximab represses the proliferation of EGFR-positive colorectal cancer cell lines. Cetuximab is highly effective due to its highly specific and targeted mechanism of action. Cetuximab, a chimeric monoclonal antibody, specifically binds the extracellular domain of EGFR and, as such, blocks further ligand-receptor interaction. This inhibits downstream signaling pathways, including the most important MAPK and PI3K/AKT, which play essential roles in the development, viability, and metastasis of tumor cells. Conversely, the mechanism of action of cisplatin is non-selective, and it involves the formation of DNA adducts that lead to an apoptotic response in cancer and normal cells, a typical feature of its known toxic profile [7, 8].

3.4.2 Dose-Response Relationships

The 2 drugs showed similar dose-dependent cytotoxicity, but their dose-response curves were very different. Cetuximab showed a steep relationship between dose and response, with inhibition levels increasing from 0.156 to 0.625 ug/mL, then leveling off at higher concentrations. This plateau effect implies that the balance regarding the number of EGFR binding sites has been achieved, and subsequent drug supplementation plays no important role. The relationship between dose and response was less steep with cisplatin, with the rate of inhibition increasing gradually across the concentration range used (without necessarily reaching a final plateau at 24 hours).

3.4.3 Time-Dependent Effects

The cytotoxic effects of the two drugs also improved with increasing exposure time, although the rates of increase differed. Cisplatin showed a stronger time-dependent increase in efficacy, with the highest inhibition rates of 39.04% and 76.55% at 24 and 48 hours, respectively. This is consistent with the cisplatin-mediated cytotoxicity mechanism, which involves time to form DNA adducts, interact with cellular repair systems, and activate apoptotic pathways [8, 9]. The improved efficacy of cetuximab was also observed at 48 hours, but the degree of enhancement was not as significant, as the rate of inhibition was high at 24 hours.

3.4.4 Clinical Implications

The current results indicate that Cetuximab is a promising targeted therapy for colorectal cancer. In addition to panitumumab, cetuximab has been granted FDA approval as an EGFR-targeting monoclonal antibody for metastatic colorectal cancer [12]. They are usually used in conjunction with cytotoxic chemotherapy regimens as first- or second-line agents [13]. Previous clinical trials have established that the Cetuximab–irinotecan combination has a better therapeutic impact than single-agent cetuximab in irinotecan-refractory metastatic colorectal carcinoma [12,14,15]. On the same note, when cetuximab was combined with platinum-based chemotherapy, it improved survival in individuals with advanced EGFR-expressing NSCLC [5]. Our preclinical evidence indicates that cetuximab, when combined with cisplatin, can act synergistically or additively in colon cancer cells, allowing a reduction in the cisplatin dose and the elimination of its inherent toxicities, such as nephrotoxicity, peripheral neuropathy, and ototoxicity [8, 9, 10].

3.4.5 Mechanistic Considerations

The increased cytotoxicity of cetuximab observed may be due to mechanisms beyond pure EGFR blockade. Past research has shown that cetuximab suppresses downstream signaling, including the MAPK/ERK pathway, which is important for cell development and viability [6, 16]. Moreover, cetuximab was shown to increase caspase-3 cleavage, thereby activating apoptotic signaling [16]. The oral squamous cell carcinoma models synergize with cetuximab and other agents such as celecoxib, and it can be projected that the same combination strategies will also be effective in colon cancer [16].

3.4.6 Study Limitations

There are various limitations of this study. Firstly, the present research was conducted on a single colon cancer cell line (SW480); therefore, the results could not be extended to other colon cancer cell lines with different genetic backgrounds and EGFR expression levels. Second, this was an in vitro study and therefore did not consider pharmacokinetic factors, tumor-microenvironment interactions, or the involvement of the immune system, which determine drug efficacy in in vivo studies. Third, the cetuximab-cisplatin combination was not under investigation in the study; hence, no information would be available on the potential synergistic effect of the combination. Finally, the mechanisms underlying the observed cytotoxicity had not been examined by molecular methods, such as Western blotting or flow cytometry.

3.4.7 Future Directions

Future research is also needed to evaluate the use of cetuximab at different cisplatin ratios to determine the optimal concentrations of both medications that act synergistically. In addition, experiments across multiple colon cancer cell lines with varying EGFR concentrations would improve the generalizability of these findings. A mechanistic understanding would be gained through molecular analyses of the impact of these therapies on EGFR downstream signaling pathways, and assessment of apoptosis-related and cell cycle–regulatory biomarkers is recommended. Additionally, in vivo xenograft experiments are necessary to substantiate further the therapeutic effectiveness of cetuximab, whether used as a single agent or in combination with platinum-based chemotherapy.

4. Conclusions

The present investigation assessed and compared the cytotoxicity of cetuximab and cisplatin in the human SW480 colorectal cancer cell line using the crystal violet assay. The research results indicate that cetuximab has stronger antiproliferative effects than cisplatin against SW480 cells in vitro. At the low value of 1.25 μg/mL and 0.286 μg/mL, cetuximab recorded maximum inhibition rates of 91.24 per cent and 97.77 per cent at 24 and 48 hours, respectively. Conversely, cisplatin achieved only the highest levels of 39.04 and 76.55 at 24 and 48 hours, respectively, despite being used at much higher concentrations (100 μg/mL). The statistical analysis revealed that the two treatments differ ($P < 0.001$), with cetuximab approximately 80-fold more effective at the required concentration. The speed and the strength of the inhibitory effect of cetuximab are sufficient reasons to consider it a high-quality targeted therapy against EGFR-expressing colorectal cancers. These results are consistent with its established mechanism of action, which entails EGFR inhibition, followed by downstream inhibition of the proliferative signaling pathway. The findings do support the preclinical use of cetuximab in combination with conventional platinum-based chemotherapy. This research, however, was limited to a single cell type and in vitro conditions. Future research must determine the effectiveness of cetuximab across various EGFR levels in colorectal cancer cell lines, investigate whether a cetuximab-cisplatin combination is feasible, and validate the findings in xenograft models. Such studies would also justify the therapeutic potential of a particular EGFR inhibitor in the treatment of colorectal cancer.

5. Acknowledgements

The authors would also like to express their sincere gratitude to the staff of the Cancer Research Laboratory, Babylon Medical School, for providing the SW480 cell line and the laboratory facilities required for conducting this study. The cetuximab used in the research was also provided by the Belarusian State University (College of Belarus) science laboratories.

Authors' Contribution: Conceptualization, [A.A.S.] and [B.A.M.]; methodology, [A.A.S.]; software, [A.A.S.]; validation, [A.A.S.], [B.A.M.] and [Z.A.O.A.]; formal analysis, [A.A.S.]; investigation, [A.A.S.], [B.A.M.]; resources, [Z.A.O.A.]; data curation, [A.A.S.]; writing first draft, [A.A.S.]; review and editing, [B.A.M.] and [Z.A.O.A.]; visualization. Each author has read and agreed to the published version of the manuscript.

Funding: Not applicable.

Conflicts of Interest: The authors declare no conflict of interest.

References

[1] Pai, R.; Soreghan, B.; Szabo, I. L.; Pavelka, M.; Baatar, D.; Tarnawski, A. S. Prostaglandin E2 Transactivates EGF Receptor: A Novel Mechanism for Promoting Colon Cancer Growth and Gastrointestinal Hypertrophy. *Nat. Med.* **2002**, *8*(3), 289–293. https://doi.org/10.1038/nm0302-289

[2] Fahrer, J.; Kaina, B. O6-methylguanine-DNA Methyltransferase in the Defense Against N-nitroso Compounds and Colorectal Cancer. *Carcinogenesis* **2013**, *34*(11), 2435–2442. https://doi.org/10.1093/carcin/bgt275

[3] Sadanandam, A.; Lyssiotis, C. A.; Homicsko, K.; Collisson, E. A.; Gibb, W. J.; Wullschleger, S.; Ostos, L. C. G.; Lannon, W. A.; Grotat, C.; Beer, M.; Mahajan, N.; Gratchev, A.; Venkatasubramanian, M.; Dow, J.; Mitsuiki, M.; Bandyopadhyay, S.; Vermeulen, J. P.; Arumugam, P. U.; Silberert, A.; Vakoc, C. R.; Song, J. S.; Hanahan, D. A Colorectal Cancer Classification System that Associates Cellular Phenotype and Responses to Therapy. *Nat. Med.* **2013**, *19*(5), 619–625. https://doi.org/10.1038/nm.3175

[4] Bonner, J. A.; Harari, P. M.; Giralt, J.; Azarnia, N.; Shin, D. M.; Cohen, R. B.; Jones, C. U.; Sur, R.; Raben, D.; Jassem, J.; Ove, R.; Kies, M. S.; Baselga, J.; Youssoufian, H.; Amellal, N.; Rowinsky, E. K.; Ang, K. K. Radiotherapy Plus Cetuximab for Locoregionally Advanced Head and Neck Cancer: 5-year Survival Data from a Phase 3 Randomized Trial, and Relation Between Cetuximab-induced Rash and Survival. *Lancet Oncol.* **2010**, *11*(1), 21–28. https://doi.org/10.1016/S1470-2045(09)70311-0

[5] Douillard, J. Y.; Pirker, R.; O'Byrne, K. J.; Kerber, A.; Störkel, S.; von Pawel, J.; Gatzemeier, U.; Shepherd, F. A.; Trigo, J. M.; Spigel, D. R.; Boyer, M.; Schirpke, B.; Klingelschmitt, G.; Ochs, J. S. Relationship Between EGFR Expression, EGFR Mutation Status, and the Efficacy of Chemotherapy Plus Cetuximab in FLEX Study Patients with Advanced Non-small-cell Lung Cancer. *J. Thorac. Oncol.* **2014**, *9*(5), 717–724. https://doi.org/10.1097/JTO.0000000000000141

[6] Sridhar, S. S.; Seymour, L.; Shepherd, F. A. Inhibitors of Epidermal-growth-factor Receptors: A Review of Clinical Research with a Focus on Non-small-cell Lung Cancer. *Lancet Oncol.* **2003**, *4*(7), 397–406. https://doi.org/10.1016/S1470-2045(03)01137-9

[7] Siddik, Z. H. Cisplatin: Mode of Cytotoxic Action and Molecular Basis of Resistance. *Oncogene* **2003**, *22*(47), 7265–7279. https://doi.org/10.1038/sj.onc.1206933

[8] Boulikas, T.; Vougiouka, M. Cisplatin and Platinum Drugs at the Molecular Level: A Review. *Oncol. Rep.* **2003**, *10*(6), 1663–1682. https://doi.org/10.3892/or.10.6.1663

[9] Maduro, J. H.; Pras, E.; Willemse, P. H. B.; de Vries, E. G. E. Acute and Long-term Toxicity Following Radiotherapy Alone or in Combination with Chemotherapy for Locally Advanced Cervical Cancer. *Cancer Treat. Rev.* **2003**, *29* (6), 471–488. https://doi.org/10.1016/S0305-7372(03)00117-8

[10] Pinzani, V.; Bressolle, F.; Haug, I. J.; Galtier, M.; Blayac, J. P.; Balmes, P. Cisplatin-induced Renal Toxicity and Toxicity-modulating Strategies: A Review. *Cancer Chemother. Pharmacol.* **1994**, *35*(1), 1–9. https://doi.org/10.1007/BF00686277

[11] Mansouri-Torshizi, H.; Saeidifar, M.; Divsalar, A.; Saboury, A. A. Interaction Studies Between a 1,10-phenanthroline Adduct of Palladium(II) Dithiocarbamate Anti-tumor Complex and Calf Thymus DNA: Synthesis, Spectral, and In-vitro Study. *Spectrochim. Acta, Part A* **2010**, *77*(1), 312–318. https://doi.org/10.1016/j.saa.2010.05.029

[12] Cunningham, D.; Humblet, Y.; Siena, S.; Khayat, D.; Bleiberg, H.; Santoro, A.; Bets, D.; Mueser, M.; Harstrick, A.; Verslype, C.; Chau, I.; Van Cutsem, E. Cetuximab Monotherapy and Cetuximab Plus Irinotecan in Irinotecan-refractory Metastatic Colorectal Cancer. *N. Engl. J. Med.* **2004**, *351*(4), 337–345. https://doi.org/10.1056/NEJMoa033025

[13] Mohelnikova-Duchonova, B.; Melichar, B.; Soucek, P. FOLFOX/FOLFIRI Pharmacogenetics: The Call for a Personalised Approach in Colorectal Cancer Therapy. *World J. Gastroenterol.* **2014**, *20*(30), 10316–10330. https://doi.org/10.3748/wjg.v20.i30.10316

[14] Lim, R.; Sun, Y.; Im, S. A.; Liang, J. T.; Ahn, J. B.; Park, D. J.; Lee, M. A.; Sriuranpong, V.; Mulder, K.; Guo, Y.; Chen, Z.; Thongprasert, S.; Ba, Y.; Li, J.; Kim, T. W.; Yang, L.; Wang, X. W.; Kim, S. Y.; Han, S. W.; Roh, J. K.; Lou, M. A.; Kim, J. H.; Cheng, A. L. Cetuximab Plus Irinotecan in Pretreated Metastatic Colorectal Cancer Patients: The ELSIE Study. *World J. Gastroenterol.* **2011**, *17*(14), 1879–1888. https://doi.org/10.3748/wjg.v17.i14.1879

[15] Prewett, M. C.; Hooper, A. T.; Bassi, R.; Ellis, L. M.; Waksal, H. W.; Hicklin, D. J. Enhanced Anti-tumor Activity of Anti-epidermal Growth Factor Receptor Monoclonal Antibody IMC-C225 in Combination with Irinotecan (CPT-11) Against Human Colorectal Tumor Xenografts. *Clin. Cancer Res.* **2002**, *8*(3), 994–1003.

[16] Qian, M.; Qian, D.; Jing, H.; Li, Y.; Ma, C.; Zhou, Y. Combined Cetuximab and Celecoxib Treatment Exhibits a Synergistic Anti-cancer Effect on Human Oral Squamous Cell Carcinoma In Vitro and In Vivo. *Oncol. Rep.* **2014**, *32*(4), 1681–1688. https://doi.org/10.3892/or.2014.3334

ASEAN
Journal of Scientific and Technological Reports
Online ISSN:2773-8752

Research article

Rhodocista sp. Strain SAIYAI: A Natural Source of Spirilloxanthin and Feed Attractability in Pacific White Shrimp (*Litopenaeus vannamei*)

Agnesia Frisca Damayanti[1], Nion Chirapongsatonkul[1], Suphada Kiriratnikom[2], Masaharu Mizukami[3], Raja Sudhakaran[4], and Kittichon U-taynapun[1*]

[1] Faculty of Agriculture, Rajamangala University of Technology Srivijaya, Nakhon Si Thammarat, 80110, Thailand
[2] Faculty of Technology and Community Development, Thaksin University, Phatthalung, 93210, Thailand
[3] The Research Institute of Marine Bioresources, Fukuyama University, Onomichi, Hiroshima 722-2101, Japan
[4] School of Biosciences and Technology, Vellore Institute of Technology, 632014 Vellore, Tamilnadu, India
* Correspondence: kittichon.u@rmutsv.ac.th

Citation:
Damayanti, A. F.; Chirapongsatonkul, N.; Kiriratnikom, S., Mizukami, M., Sudhakaran, R., U-taynapun, K. *Rhodocista* sp. strain SAIYAI: A natural source of spirilloxanthin and feed attractability in Pacific white shrimp (*Litopenaeus vannamei*). *ASEAN J. Sci. Tech. Report.* **2026**, *29*(3), e260807. https://doi.org/10.55164/ajstr.v29i3.260807.

Article history:
Received: August 12, 2025
Revised: January 8, 2026
Accepted: January 10, 2026
Available online: February 27, 2026

Abstract: This study investigated the potential of isolated photosynthetic bacteria (PSB) as carotenoid producers and assessed their efficacy as a low-cost functional feed additive for Pacific white shrimp (*Litopenaeus vannamei*). Fifteen PSB isolates representing 3 color groups, red, orange, and yellow, were evaluated for total carotenoid content (TCC), and the highest TCC-producing PSB were RP22-4-DPM with 0.82 ± 0.07 mg/g of DW, RP22-OR with 0.38 ± 0.03 mg/g of DW, and RS22-YB with 0.47 ± 0.07 mg/g of DW, respectively. Isolate RP22-4-DPM, further designated as PSB strain SAIYAI, exhibited the highest DPPH scavenging activity (72.65 ± 4.60%) ($p<0.05$); meanwhile, its ABTS scavenging activity (70.7 ± 2.73%) showed no significant difference compared to other strains ($p>0.05$). The predominant pigment and the major carotenoid of this strain were identified as spirilloxanthin by UV-Vis spectrophotometry and APCI LC/MS. Additionally, the attractability was evaluated by coating soybean meal with the lyophilized cell and culture media of the SAIYAI strain at 0.5%, 1%, and 1.5% to Pacific white shrimp. All concentrations significantly increased feed attractability compared to non-coated soybean meal ($p<0.05$), while 0.5% and 1.0% exhibited similar attractability ($p>0.05$). Molecular identification through 16S rRNA sequence analysis and phylogenetic tree construction suggested that strain SAIYAI belongs to the genus *Rhodocista*, which is closely related to *Rhodocista xerospirillum* and *Rhodospirillum centenum*. Accordingly, this study provides evidence that *Rhodocista* sp. strain SAIYAI is a potent spirilloxanthin producer with antioxidant properties and potential as a multifunctional, cost-effective attractant in shrimp feed.

Keywords: *Rhodocista* sp.; photosynthetic bacteria (PSB); spirilloxanthin; attractability; Pacific white shrimp (*Litopenaeus vannamei)*

1. Introduction

Pacific white shrimp (*Litopenaeus vannamei*) is one of the most important crustaceans and a widely farmed species in several countries, including Thailand. Even though shrimp aquaculture is economically significant, the industry faces major hurdles, including disease outbreaks, environmental damage, and rising production costs. As a result, many shrimp ponds have been

abandoned due to unsuccessful cultivation, particularly in the Pak Phanang Basin, which contains a high density of shrimp farms [1]. The condition of these abandoned ponds is typically hypereutrophic, fueled by an abundance of nutrients from the accumulation of particulate organic matter, primarily derived from biological production [2]. This environment enhances the presence of photosynthetic bacteria (PSB), which are considered major decomposers of organic matter, convert organic acids to H_2 and CO_2, and participate in the anoxic carbon cycle [3, 4].

PSB are prokaryotes belonging to the group of phototrophic bacteria that utilize light to generate energy. This group of bacteria is widely distributed in nature, not only in abandoned ponds but also in other environments such as soil, mangrove forests, lakes, reservoirs, and oceans [4]. PSB can be categorized into four primary groups: purple sulfur bacteria (PB), purple non-sulfur bacteria (PNSB), green sulfur bacteria (GSB), and green non-sulfur bacteria (GNB) [5]. The characteristics of each group are distinguished by their bacteriochlorophyll and carotenoid pigments, photosynthetic electron donors, and the composition of their photosynthetic machinery [6]. Carotenoids are natural biomolecules belonging to the isoprenoid subfamily with colors ranging from red, yellow, to orange [7]. Around 100 different carotenoids have been identified in PSB, including spirilloxanthin, lycopene, spheroidenone, β-carotene, zeaxanthin, canthaxanthin, and lutein, each with unique properties [8, 9].

Unlike other common carotenoids such as β-carotene or astaxanthin, spirilloxanthin is uniquely characterized by its long conjugated double-bond system and terminal methoxy groups, which contribute to its robust capacity. It has been demonstrated that spirilloxanthin extracted from *Bacillus licheniformis* RT4M10 exhibits antioxidant scavenging properties [10]. The effects of antioxidant substances have been highlighted across diverse research fields, including aquaculture, where they function in stress reduction or anti-stress, growth stimulation, and immunity improvement [11, 12]. The major bacteria that produce spirilloxanthin are members of the PNSB group, such as *Rhodospirillum rubrum* and *Rhodobacter sphaeroides* [8, 13]. According to Cahoon *et al*. [14], PSB, especially PNSB species, are capable of synthesizing the spirilloxanthin series and exhibit consistent antioxidant properties. In addition, PSB have a shorter antioxidant life cycle and the capability to produce different types of carotenoids with various color shades and desirable biological properties [15]. Therefore, PSB that produces carotenoids with antioxidant activity is a promising candidate for dietary supplementation due to its cost-effectiveness and ease of handling.

PSB, particularly PNSB, has also been studied for its potential as a protein source and growth promoter in shrimp diets and feed additives. Supplementation of these bacteria can enhance growth rates, feed conversion ratios (FCR), survival rates, immune responses, and tolerance to stress [16-19]. Despite these benefits, there is a significant lack of data regarding the attractability effects of PSB in shrimp feed. Attractability in shrimp farming is crucial because it affects feed intake and overall growth performance, which directly influence economic viability [20, 21]. Fish, like other animals, have preferences for certain foods based on their taste, smell, and past experiences. Nutrients and chemosensory cues influence these preferences, the palatability of the food, and the fish's current dietary needs. To improve the appeal of aquafeed, the use of attractants and stimulants has been explored [22, 23]. Addressing attractability issues by incorporating effective attractants is a key consideration for optimizing shrimp farming practices and ensuring sustainable production. PSB, such as marine bacteria, have been demonstrated to play a crucial role in aquaculture by serving as feed attractants for aquatic animals. These bacteria are not only beneficial for their nutritional value but also for their ability to enhance feed palatability and stimulate feeding behavior in aquatic species [24, 25]. Therefore, PSB has shown promising effects on feed intake and is a candidate with high attractability to aquatic animals.

Only limited information about spirilloxanthin utilization and PSB attractability in aquaculture has been demonstrated. As a result, bioprospecting for PSB strains producing high-value substances has garnered considerable attention and is performing better in many fields, especially aquaculture. PSB holds promise as a future multifunctional feed additive for shrimp aquaculture, with potential benefits beyond antioxidant and feed attractant effects. The identification of novel bacterial strains with multifunctional properties represents a significant opportunity for developing integrated approaches to sustainable aquaculture that simultaneously address multiple production challenges. These phototrophic bacteria have been the focus of recent research

because they can utilize elements in wastewater for protein biomass and grow under anaerobic conditions or under anoxygenic photosynthesis [17, 18].

Beyond its antioxidant properties, the metabolic profile of certain PSB, particularly those rich in carotenoids such as spirilloxanthin, is hypothesized to influence chemosensory responses in aquatic animals. In *L. vannamei*, feed attractants are crucial for improving consumption rates and reducing waste in intensive systems. However, the specific role of *Rhodocista* ap. and it's metabolites as dietary attractant remains poorly understood. Therefore, this study was designed to bridge the gap between pigment production and functional feed application. Our objectives were to characterize the spirilloxanthin-producing *Rhodocista* sp. strain SAIYAI isolated from the Pak Phanang Basin and to evaluate its efficacy as both a natural antioxidant source and a feed attractant for Pacific white shrimp. The multi-functional properties of this novel strain could provide a significant contribution to the development of sustainable, cost-effective biological feed additives for the shrimp aquaculture industry.

2. Materials and Methods

2.1 Sampling location and PSB screening

PSB were isolated from water and sediment collected from the coastal area of the Pak Phanang Basin, Nakhon Si Thammarat, Thailand. Five sampling locations included those in coordinate of mangroves: Station (1) 8°31'8.63"/ N 99°58'34.37"/E and Station (2) 8°32'36.62"/ N 99°59'49.18"/E, while Station (3) 8°24'22.63"/N 100°13'36.02"/E, Station (4) 8°17'15.11"/ N 100°15'59.41"/E, and Station (5) 8°19'55.79" N 100°12'0.85"/E represent abandoned shrimp ponds (Figure 1). Water and sediment samples used for bacterial isolation were aseptically collected following the procedures of Higuchi-Takeuchi et al. [26] and Nithya and Pandian [27], with slight modifications. Water samples were taken at a depth of 30 cm above the sediment, while sediment was collected at a depth of 30 cm below the sediment surface to avoid contamination. The samples were collected in sterile tubes and kept cool until transported to the laboratory for further processing. Bacterial isolation was conducted using the basal medium G5 (g/L) containing: peptone, 5.0; yeast extract, 5.0; L-glutamic acid, 4.0; malic acid, 3.5; KH_2PO_4, 0.12; and K_2HPO_4, 0.18. The medium pH was adjusted to 7.0 with 5 M NaOH. For the preparation of solid media G5 agar, 1.5% agar was added to the medium. 1 g of sediment sample was transferred to a sterile test tube with 1 mL autoclaved 1.5% NaCl, vigorously mixed, and then spread onto agar plates. The sediment suspension and water samples were diluted 10-fold in series and spread onto an agar plate in triplicate. All plates were incubated at 37°C for 2-10 days, and color colonies were transferred to a new plate to establish a pure culture. The purified isolates were preserved in Tryptic Soy Broth (TSB, Difco) containing 1.5% NaCl (TSB^+) and 20% glycerol, and kept at -80°C. Selected strains were characterized based on colony and cell morphology. Finally, 5 strains exhibiting distinct characteristics within each color group were chosen for evaluation of total carotenoid content (TCC).

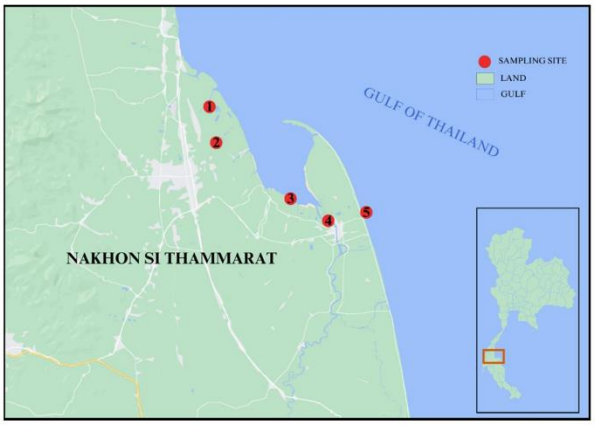

Figure 1. Sampling sites in the Pak Phanang Basin, Nakhon Si Thammarat Province, Thailand. Stations 1 and 2 are in mangrove coordinates, while stations 3, 4, and 5 represent abandoned shrimp ponds.

2.2 Bacteria cultivation

Bacterial cultivation for the downstream studies was performed using a modified method of Sibero *et al.* [28]. Each bacterial isolate was cultured in TSB^+ and shaken at 150 rpm for 48 h at room temperature to serve as a starter for further cultivation. For the assays of pigment profile, antioxidant activity, and attractability, the bacterial production was prepared by adding 100 mL of the starter to the freshly prepared TSB^+ in an Erlenmeyer flask and then culturing under the same conditions as for the starter preparation mentioned above. For the TCC and antioxidant analyses, cells were harvested after shaking for 48 h by centrifugation at 8,000 x g for 15 min and washed twice with 1.5% NaCl. For attractiveness testing, the bacterial cells and culture medium were lyophilized and stored at -80 °C.

2.3 Total carotenoid content (TCC) determination

TCC, from a total of 15 strains (5 strains from each color group: red, orange, and yellow), was determined following the method of Britton *et al*. [29] and Kiriratnikom [30]. Briefly, the cultured bacterial cell was separated into 2 parts for carotenoid quantification and cell mass in terms of dry weight. The first part was extracted with a methanol:acetone solution (2:3 v/v), centrifuged, and the supernatant was collected. The bacterial cell was re-extracted several times until a clear solution was obtained. The volume of extraction liquid was adjusted to achieve appropriate optical densities at OD480 and OD770 for calculating the carotenoid content. For cell mass, the remaining cells from each strain were centrifuged in glass tubes at 8,000 x g at 4 °C for 10 min, washed 3 times with 3% NaCl solution, and dried at 105 °C for 24 h. The dried cell was weighed, and the dry cell mass was calculated as mg dry weight/mL of culture medium. The total carotenoid content formula is:

$$\text{Total carotenoid content (TCC)} = \left(\frac{\text{OD480-0.1OD770}}{\text{DCW (g/L)}}\right) \text{x } 3.85 \text{ x} \frac{\text{B (mL)}}{\text{A (mL)}}$$

DCW: Dry cell weight (mg/g), A: Volume before extraction (mL), B: Volume after extraction (mL).

2.4 In vitro antioxidant activity

The strain with the highest TCC in each color group was further analyzed for antioxidant activity. The pigments were extracted from the bacterial cells by using 99% methanol. Then, the methanolic extract of pigments was centrifuged at 8000 x g for 15 min to separate the residual cells and pigment until the solution was colorless. The antioxidant activity was investigated using the DPPH and ABTS assays.

DPPH free radical scavenging assay was conducted following a modified method of Mukherjee *et al.* [31]. Briefly, 1 mL of the pigment extract was added to 1 mL of a 0.1 mM methanolic solution of DPPH, shaken, and kept in the dark for 30 min, and then measured at 517 nm using a UV/vis spectrophotometer (BioDrop). Methanol was used as a blank solution. The DPPH scavenging effect was determined according to the equation.

$$\text{DPPH scavenging activity (\%)} = \left(\frac{\text{A517 of control- A517 of sample}}{\text{A517 of control}}\right) \text{x } 100\%$$

The ABTS assay was also performed according to the method of Wang *et al.* [24]. ABTS (2,20-azino-bis (3-ethylbenzothiazoline-6-sulfonic acid)) radical-scavenging activity was used to evaluate the antioxidant activity of PSB-extracted pigments. ABTS solution (7 mM) was prepared with 2.45 mM potassium persulfate and was incubated in the dark for 16 h to generate ABTS radicals. The obtained solution was adjusted with 0.01 M PBS buffer (pH 6.8) to achieve an absorbance of approximately 0.7 ± 0.2 at 734 nm. The prepared ABTS solution (600 µL) was added to 50 µL of the sample, and the mixture was incubated in the dark at room temperature for 6 min. The absorbance of the mixture was monitored at 734 nm, and the percentage of ABTS scavenging activity was calculated using the provided equation.

$$\text{ABTS scavenging activity (\%)} = 1 - \left(\frac{\text{Asample}}{\text{Acontrol}}\right) \text{x } 100\%$$

The PSB strain with the highest scavenging activity was selected for further analyses, including determination of the pigment profile, attractability, and bacterial identification.

2.5 Pigment profile

2.5.1 Color extraction and Thin Layer Chromatography analysis

Crude pigment was extracted from the selected PSB strain exhibiting the highest scavenging activity following the modified method of Fang *et al.* [32] by using acetone until the cell pellet was colorless. The color was separated by adding diethyl ether at a 1:1 ratio to the obtained color solution. After the ether phase containing the pigments was obtained, the pigments were separated by Thin Layer Chromatography (TLC) on a silica gel plate (20 cm × 20 cm) using a mixture of diethyl ether and petroleum ether as the mobile phase. The mobile phase ratio was screened until a clear separation of color was observed. The major pigment, expressed as a bold band, was purified by scraping, eluted with diethyl ether, and then dried under N_2 gas to obtain a powder, which was kept at -20 °C until use for profile analysis.

2.5.2 Major carotenoid characterization by mass spectrum analysis

The purified major carotenoid collected from the TLC method was scanned for UV–Vis absorbance spectrum with the wavelength of 400-600 nm by using a spectrophotometer (Biodrop). Moreover, the collected carotenoid powder was eluted with methanol for mass spectrometry (MS) analysis following the method of Ranga *et al*. (2009). The carotenoids were identified using LC-QTOF MS (Agilent Technologies). In brief, the APCI instrument parameters followed the machine protocol, including gas temperature at 350 °C, vaporizer temperature at 400°C, gas flow at 5 L/min, and nebulizer at 60 psig. Scan source parameter followed by VCap 3500, corona positive 4 kv, fragmentor 140, and OctopoleRFPeak at 750. The spectrometer was calibrated in the positive mode, and $[M+H]^+$ ions were recorded. Mass spectra of carotenoids were acquired over an m/z 100-1000 scan range using a diode-array detector and confirmed with respective standards.

2.6 Ethical statement

The Animal Ethics Committee approved the experimental procedures and animal care in this study, Rajamangala University of Technology Srivijaya (Ethics Record No. IAC 01-01-2024), following the guidelines of the Institute of Animal for Scientific Purposes Development, National Research Council, Thailand.

2.7 Attractability assessment

The attractiveness of the aforementioned bacterial strain with the highest scavenging activity was evaluated. Bacterial powder was obtained by freeze-drying the bacterial culture using the modified method of Kim *et al*. [33]. Four g of soybean meal were coated with 0%, 0.5%, 1%, and 1.5% of lyophilized powder and used as trial feeds for Pacific white shrimp. The bacteria-coated soybean meal at all PSB concentrations was air-dried and kept at -20 °C until used. The attractability assessment was conducted following the methods of Suresh et al. [34] and Chirapongsatonkul et al. [35], with slight modifications. Rectangular glass tanks (60 × 50 × 22 cm), with acclimatization and feeding chambers, were used. The tank contained an acclimatization chamber at one end and four feeding chambers at the other, separated by movable shutters (Figure 2). Each feeding chamber was equipped with an aperture to allow shrimp attempting to feed to enter the chamber. Twenty shrimp (1-2 g) were placed in the acclimatization chamber for a 60 min period. Five min before the time period, the trial feed, packed in a sterilized stainless steel mesh tea ball, was placed in the chamber at 3 cm above the bottom. After removing the shutter, shrimp approached the trial feeds in the feeding chambers. A video camera (SONY Zeiss) was set up and recorded for 15 min to collect data throughout the entire experimental duration. Each feed trial underwent random testing 4 times within one of the four designated feeding chambers. The assessment was calculated based on the percentage of shrimp approaching the feeding chamber (%Turn) and the time interval in the chamber (Time), as previously described [35].

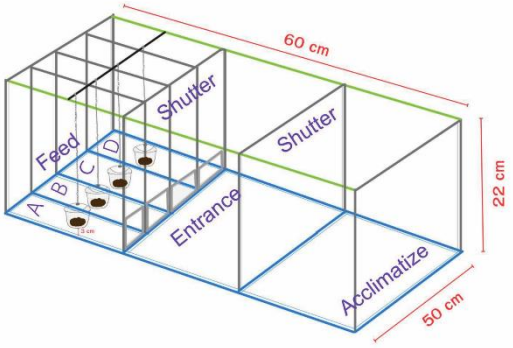

Figure 2. Schematic diagram of the glass tank and its components used for the feed attractability assessment.

2.8 Bacteria identification

The selected strain exhibiting high carotenoid content and the greatest attractability was molecularly identified using conserved 16S rRNA sequencing following the modified method of U-taynapun *et al*. [36]. Bacterial DNA was extracted using the Bacterial DNA Isolation Kit (Geneaid) according to the manufacturer's instructions. DNA concentration was measured by absorbance, and DNA purity was assessed by the 260/280 and 260/230 ratios, with values within 1.8-2.0, indicative of high-quality DNA. The DNA was stored at -80 ˚C until use. The obtained DNA served as a template for 16S rRNA amplification, conducted according to the manufacturer's instructions for Accustart™ II PCR Supermix (Quanta). The primer pairs used for 16S rRNA amplifications were 20F: 5′-AGAGTTTGATCATGGCTCAG-3′ and 1500R: 5′-CGGTTACCTTGTTACGACTT-3′. Bacterial DNA was amplified using a PCR program that included an initial denaturation at 94 ˚C for 3 min, followed by 35 cycles of 30 s at 94 ˚C, 30 s at 60 ˚C, and 1 min at 72 °C, with a final extension of 10 min at 72 ˚C. The PCR product was analyzed by agarose gel electrophoresis at 1.5%. Purification of the PCR product was performed using the Gel/PCR DNA Fragments Kit (Geneaid) according to the manufacturer's instructions. Purified DNA fragment with a size of approximately 1,500 bp was subsequently cloned into the pGEM-T® Easy Vector (Promega), and sequenced. The 16S rRNA gene was deposited in NCBI (National Center for Biotechnology Information). To identify and retrieve homologous sequences, the obtained sequences were subjected to the NCBI BLAST tool. Alignment was manually checked using BioEdit, and the ClustalW algorithm in MEGA 11 was employed for sequence alignment. The measurement (%) of replicate trees in which the associated taxa clustered together in the bootstrap test (1,000 replicates), and MEGA 11 software was used to generate a phylogenetic tree using the Maximum Likelihood [37].

2.9 Statistical analysis

The statistical differences in TCC, antioxidant activity, and attractability were analyzed using one-way analysis of variance (ANOVA) in SPSS Statistics Software version 20.0 (SPSS Inc.). The variance and significant differences among treatments were analyzed using Duncan's Multiple Range Test (DMRT) with a significance level of $p<0.05$.

3. Results and Discussion

3.1 Screening, isolation, and characterization of PSB

Following the isolation of PSB from 5 sampling areas, 30 isolates were obtained on G5 agar plates. The morphology, Gram staining characteristics, and colony appearance were recorded for each isolate. Categorization by colony color: 10, 11, and 9 isolates for red, orange, and yellow, respectively. The majority of bacteria collected in this study were Gram-negative, rod-shaped. Details of all isolates, including sampling area, colony color, characters, and morphology, are summarized in Table 1. Afterwards, these 30 isolates were screened for pigment production based on color shade and morphology. In previous studies, PSB groups have been shown to be carotenoid producers [38-40]. Therefore, a total of 15 isolates, 5 from each color group, were selected for TCC quantification.

3.2 TCC analysis

The TCC from 15 PSB isolates was analyzed and compared within their respective color groups. The results showed that the highest TCC in the red, orange, and yellow groups was found in strains RP22-4-DPM (0.82 ± 0.07 mg/g of DW), RP22-OR (0.38 ± 0.03 mg/g of DW), and RS22-YB (0.47 ± 0.07 mg/g of DW), respectively (Figure 3). Carotenoids produced by PSB are diverse, and most isolates contain high levels of total carotenoids. Previous studies have reported that the biomass production by PNSB varies depending on the species, growth stage, and culture medium used [41]. According to Soon *et al.* [42], bacterial isolates from exposed habitats induce higher dry cell weight (g/L) and total carotenoids production (mg/g dry cell weight) than those from shaded habitats. Three isolates with significantly higher TCC levels ($p<0.05$) than other isolates within the same color group were classified as the highest TCC producers. Among the primary compounds responsible for antioxidant activity are carotenoids, which serve as vital secondary metabolites in microorganisms. These compounds have been demonstrated to play roles in regulating light absorption and preventing photodamage and oxidative stress. due to their antioxidant properties [43]. Consequently, the 3 TCC producers, RP22-4-DPM, RP22-OR, and RS22-YB, were measured for their *in vitro* antioxidant activity.

3.3 Antioxidant assay

Carotenoids exhibit antioxidant potential by neutralizing free radicals through electron transfer, donating hydrogen atoms, or attaching to radicals. The antioxidant activity of carotenoids is significantly influenced by their oxidation potential, which is closely related to the conjugation length and donor/acceptor substituents within the molecule. Shorter conjugation lengths and the incorporation of electron-withdrawing groups result in higher oxidation potentials [44]. In this study, the antioxidant capacity of the crude pigment extracted from the 3 PSB isolates with the highest TCC was evaluated using DPPH and ABTS assays. The results were expressed as the percentage free radical scavenging activity. As shown in Figure 4, each isolate demonstrated different antioxidant levels. Significant differences in DPPH scavenging activity were observed among these 3 isolates ($p<0.05$). Specifically, RP22-4-DPM exhibited the greatest DPPH scavenging activity (72.65 ± 4.60%), followed by GNew4-OC (60 ± 6.94%) and RS22-YB (42.08 ± 4.13%), respectively. In the ABTS assay, although GNew4-OC exhibited the highest scavenging activity (74.16 ± 2.17%), it did not statistically differ from that of RP22-4-DPM (70.7 ± 2.73 %) ($p>0.05$). RS22-YB exhibited the lowest ABTS activity (67.07 ± 2.35%). Based on these findings, the red-pigmented isolate RP22-4-DPM demonstrated the most robust overall antioxidant performance. Given its highest DPPH scavenging capacity and significantly higher TCC compared to the other two strains, RP22-4-DPM was designated as the PSB strain SAIYAI and selected for further investigations.

Table 1. Sample origin, color, character, and morphology of PSB isolated from Pak Phanang Basin.

Number	Isolates	Location	Colony Color	Character		Colony Morphology				
				Gram	Shape	Shape/Form	Margin	Surface	Elevation	Size
1	R3	Station 1	Red	-	Rod	Circular	Entire	Smooth	Flat	Small
2	R4	Station 1	Red	-	Rod	Circular	Filamentous	Wrinkled	Flat	Medium
3	O3	Station 1	Orange	-	Rod	Circular	Entire	Smooth	Flat	Small
4	GNEW4-OC	Station 1	Orange	+	Rod	Circular	Serrate	Concentric	Umbonate	Medium
5	GNEW3-BO	Station 1	Orange	-	Rod	Circular	Entire	Smooth	Raised	Medium
6	Y2	Station 1	Yellow	-	Rod	Circular	Entire	Smooth	Raised	Medium
7	RP22-4-DPM	Station 2	Red	-	Rod	Circular	Entire	Smooth	Flat	Small
8	RP22-4-RM	Station 2	Red	-	Filamentous	Circular	Entire	Smooth	Flat	Small
9	RP22-OR	Station 2	Orange	-	Rod	Circular	Entire	Smooth	Raised	Small
10	RP22-OT	Station 2	Orange	-	Rod	Circular	Entire	Smooth	Flat	Small
11	O1	Station 2	Orange	-	Rod	Circular	Entire	Smooth	Flat	Small
12	RS13-Y	Station 2	Yellow	-	Rod	Circular	Entire	Smooth	Flat	Medium
13	R2	Station 3	Red	-	Rod	Circular	Entire	Smooth	Flat	Small
14	R6	Station 3	Red	-	Rod	Circular	Entire	Smooth	Umbonate	Medium
15	GNEW2-O	Station 3	Orange	-	Rod	Circular	Entire	Smooth	Raised	Small
16	GY22-OB	Station 3	Orange	-	Rod	Circular	Entire	Smooth	Raised	Medium
17	GNEW-BY	Station 3	Yellow	-	Rod	Circular	Entire	Smooth	Flat	Small
18	GNEW2-Y	Station 3	Yellow	-	Rod	Circular	Entire	Smooth	Flat	Small
19	R3B	Station 4	Red	-	Rod	Circular	Entire	Smooth	Raised	Small
20	GNew-OF	Station 4	Orange	-	Rod	Undulate	Concentric	Flat	Undulate	Medium
21	O5	Station 4	Orange	-	Rod	Circular	Entire	Smooth	Umbonate	Medium
22	X1	Station 4	Yellow	-	Rod	Circular	Wavy	Smooth	Flat	Medium
23	RG-DY	Station 4	Yellow	+	Rod	Circular	Entire	Smooth	Flat	Small
24	RG-YB	Station 4	Yellow	-	Rod	Circular	Entire	Smooth	Flat	Small
25	R15	Station 5	Red	-	Rod	Undulate	Concentric	Flat	Undulate	Medium
26	R16	Station 5	Red	-	Rod	Circular	Entire	Smooth	Flat	Small
27	R17	Station 5	Red	-	Rod	Circular	Entire	Smooth	Umbonate	Medium
28	RS22-BO1	Station 5	Orange	-	Rod	Circular	Entire	Smooth	Flat	Large
29	RS4-Y	Station 5	Yellow	-	Rod	Circular	Entire	Smooth	Flat	Small
30	RS22-YB	Station 5	Yellow	+	Rod	Circular	Entire	Smooth	Flat	Small

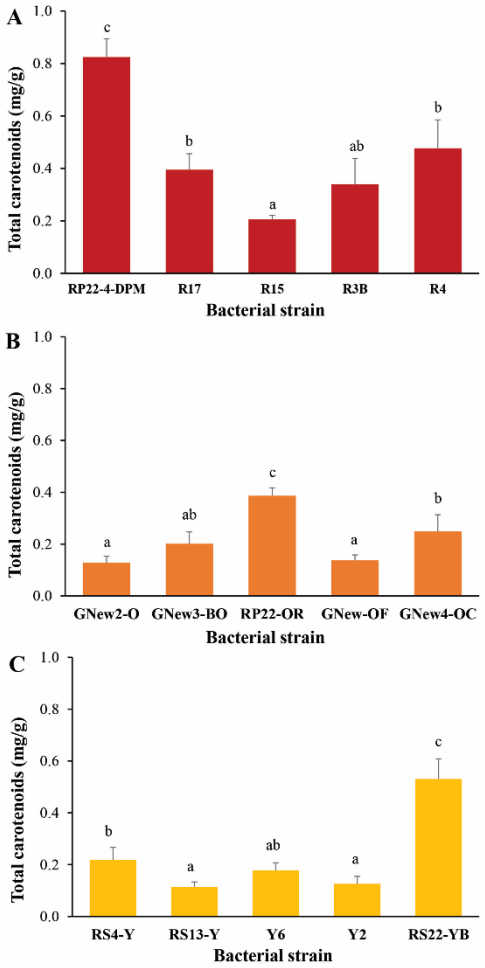

Figure 3. Total carotenoid content (TCC) produced by the selected PSB strains. (A) Red color group, (B) Orange color group, and (C) Yellow color group. Values are means ± SD. Different letters indicate statistically significant differences ($p<0.05$).

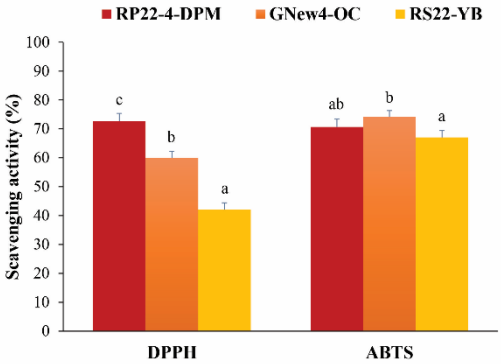

Figure 4. *In vitro* antioxidant activities analyzed by DPPH and ABTS assays of the three PSB strains exhibiting the highest TCC level selected from each colony color group, including RP22-4-DPM (red), GNew4-OC (orange), and RS22-YB (yellow). Values are means ± SD. Different letters indicate statistically significant differences ($p<0.05$).

3.4 Pigment profile

PSB strain SAIYAI, exhibiting a red colony (Figure 5A), was subcultured weekly and maintained on TSA+ agar. Since pigment production occurs during the stationary phase of bacterial growth, pigment was extracted from PSB SAIYAI cells on the fourth day of cultivation. Acetone extraction followed by ether partitioning yielded a deep red solution (Figure 5B). The carotenoid components were separated by TLC using a mixture of diethyl ether and petroleum ether as the mobile phase, varying the ratio until complete separation. A prominent pink band was identified as the major carotenoid (Figure 5C), which was further purified and characterized. The UV-Visible spectrum (400-600 nm) of the purified pigment from the PSB strain SAIYAI showed 3 peaks at 460, 480, and 520 nm, corresponding to the major carotenoid (Figure 6). To elucidate the carotenoid structure, APCI LC/MS was performed. The mass spectrum obtained by the APCI LC/MS revealed a peak at *m*/*z* 597.4662 $[M + H]^+$, with a molecular formula of $C_{42}H_{60}O_2$ (Figure 6). The mass spectrum and predicted structure is presented in Figure 6. Altogether, these data strongly indicate that the major carotenoid from SAIYAI isolate is spirilloxanthin. It has been reported that it is one of the carotenoids most commonly found in PNSB, with the chemical structure $C_{42}H_{60}O_2$ [13]. Indeed, Imhoff [45] reported that carotenoids in the spirilloxanthin series and bacteriochlorophyll a are key photosynthetic pigments of PNSB, including the genus *Rhodocista*. A previous study demonstrated that spirilloxanthin exhibits potent antioxidant properties, consistent with its molecular structure: a relatively long backbone of 13 conjugated double bonds and very weakly polar terminal methoxy groups [14]. Two antioxidant capacity assays have suggested that spirilloxanthin is similar but not superior to lycopene and β-carotene in this regard. In addition, it has been revealed that spirilloxanthin has antioxidant properties and can be applied as a neuroprotective agent, as tested in rats [46]. However, specific applications of spirilloxanthin in aquaculture have not yet been documented. Further antioxidant testing would be necessary for developing spirilloxanthin as a commercial antioxidant product.

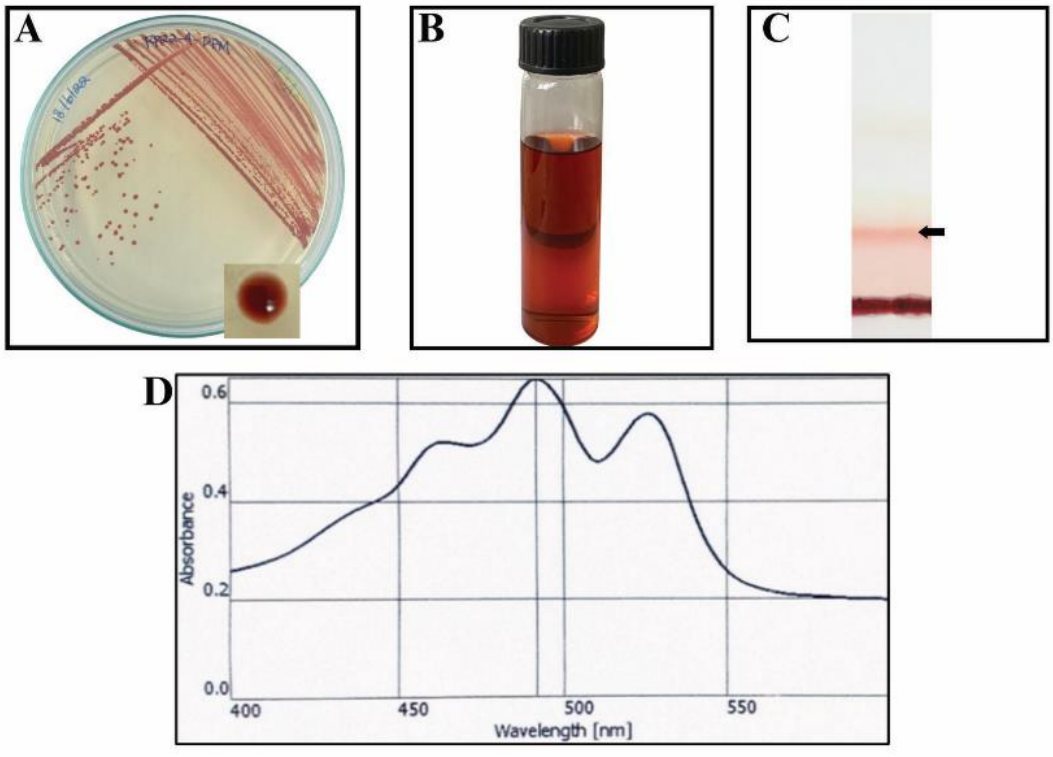

Figure 5. Colony morphology of PSB strain SAIYAI and its produced carotenoids. **(A)** Bacterial colony, **(B)** Crude pigment extracted from the bacterial cells, **(C)** Thin Layer Chromatography (TLC) separation, and **(D)** UV-Vis absorption spectrum of the purified major carotenoid.

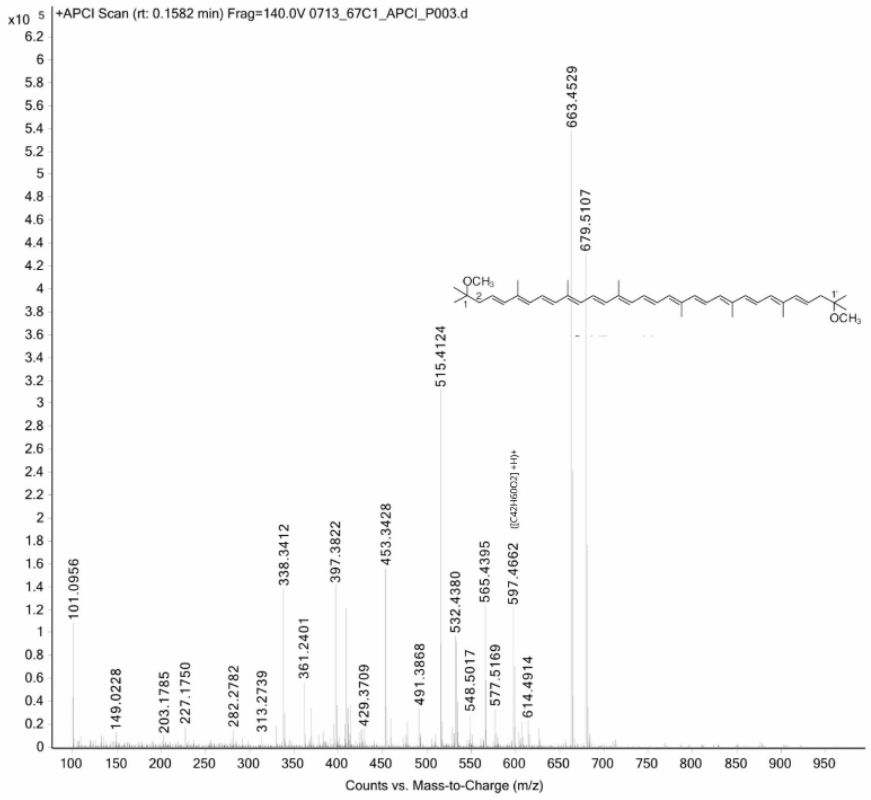

Figure 6. APCI LS/MS profile and the putative structure, spirilloxanthin with the molecular formula of $C_{42}H_{60}O_2$, of the major carotenoids extracted from PSB strain SAIYAI**.**

3.5 Attractability assessment of PSB strain SAIYAI to Pacific white shrimp

The attractability of the trial feeds coated with the PSB SAIYAI strain at 0.5%, 1.0%, and 1.5% showed a significant difference ($p<0.05$) compared to the control (Figure 7). Moreover, 1% SAIYAI-coated soybean meal exhibited the highest attractability in terms of shrimp turning (38% ± 7.83) compared with other concentrations and the control (Figure 7A). Furthermore, the duration shrimp remained in and approached the chamber for the 0.5% and 1% concentrations showed a significant difference ($p<0.05$) compared to the control and 1.5% groups (Figure 7B). These findings suggested that PSB strain SAIYAI can enhance the attractability of soybean meal, which is typically less attractive to Pacific white shrimp. Soybean meal is well known for its lower attractiveness to aquatic organisms, including shrimp [47]. Animals rely on their sensory systems to discriminate between foods that deliver pleasant or unpleasant feelings associated with eating [23]. To improve feed intake, attractants/stimulants have gained significant attention as feed additives. Bardera *et al*. [48] explained that when shrimp exhibit higher attraction to feed, they spend more time and stay longer in the feeding chamber than in the control. This corresponds with a reduction in overall locomotion, evidenced by decreased travel distance and velocity. The shrimp exhibit fewer transitions away from the feeding area, maintaining a closer average proximity to the food source. Similar to our results, PSB strain SAIYAI-coated soybean meal showed a significant, dose-dependent increase in attractiveness compared to the control (non-coated soybean meal). The best concentration of SAIYAI strain-coated soybean meal is 1% with 38% ± 7.83 of shrimp turning and 71 ± 10.06 s of residency time. Shrimp are primarily attracted to dietary components such as amino acids. Low molecular weight and high water solubility allow amino acids to act as efficient attractants, whereas shrimp chemoreceptors are better at detecting soluble compounds and small molecules. These amino acids can trigger a feeding response, which can detect an attractive food source, involving responses such as increased animal activity as the animal explores the area near the food source. Lim *et al*. [49]

have provided evidence of the efficiency of amino acids as chemoattractants for crustaceans, due to reduced food searching and feeding responses. Some amino acids have been demonstrated to act as chemoattractants for crustaceans, helping them reduce food-searching and feeding responses. Alanine, arginine, glycine, histidine, leucine, serine, taurine, and betaine could stimulate swimming crab (*Portunus pelagicus*) to feed, while alanine, serine, and betaine have been reported to have chemoreceptive properties in fiddler crab (*Uca pugilator*) [50]. Some PSB groups have a strong odor, which may also serve as an attraction factor. However, the specific amino acid profiles and odor pathways involved in PSB attractability in Pacific white shrimp require further investigation. To the best of our knowledge, this is the first report regarding the attractiveness of PSB in *L. vannamei*.

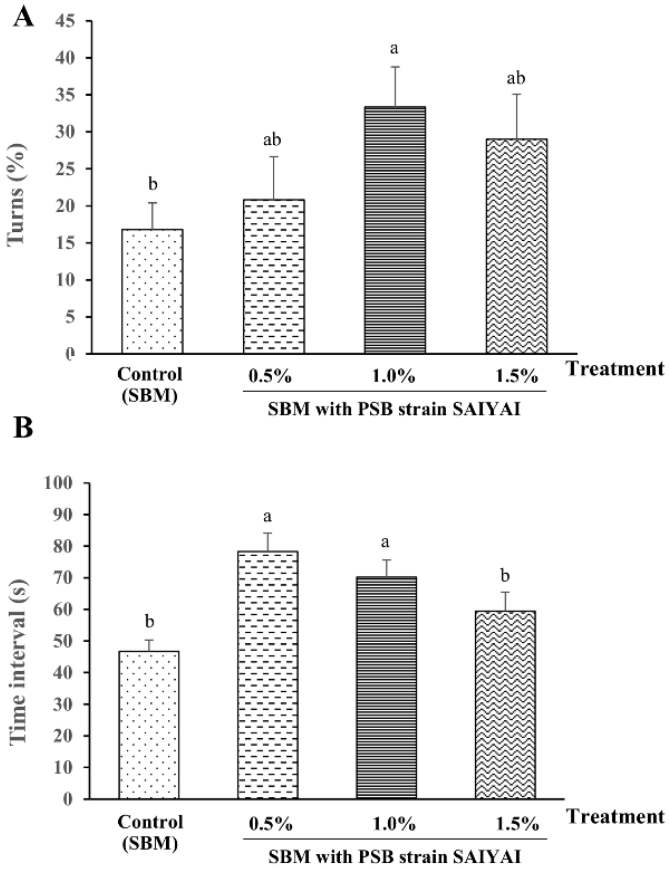

Figure 7. Attraction of soybean meal (SBM) coated with different concentrations of PSB strain SAIYAI to *L. vannamei*. **(A)** Shrimp turning (%) and **(B)** Residency time in the feeding chamber are represented as Time interval. Values are means ± SD. Different letters indicate statistically significant differences ($p<0.05$).

3.6 Bacteria identification by 16S rRNA-based analysis

To identify the PSB strain SAIYAI, molecular characterization was performed using the 16S rRNA sequence. The obtained sequence, 1 ,393 bp long, and its GenBank Accession Number (PQ143229) were compared to the GenBank database. The sequences of 16S rRNA genes from representative isolates and their closest species were used to construct a phylogenetic tree using the Maximum Likelihood method in MEGA 11. The combined dataset comprised 63 taxa (including our strain) representing 12 genera, including 40 species in the family Rhodospirillaceae, 13 species in Rhodobacteraceae, and 7 species in Nitrobacteraceae, which are affiliated with the Alphaproteobacteria class. *Escherichia coli, Aeromonas hydrophila,* and *Pseudomonas aeruginosa*, all from the Gammaproteobacteria class, were used as the outgroup. Bootstrap values, expressed as a percentage of 1000 replicates, are shown at branch points; GenBank Accession Numbers are shown in parentheses. The phylogenetic analysis demonstrated that the PSB strain SAIYAI was most closely related to

Rhodocista xerospirillum, which was clustered within the genus *Rhodocista* in the Alphaproteobacteria class (Figure 8). However, the bootstrap value for the node between them is 73%, indicating that the existing data does not well support this classification. Based on 16S rRNA analysis and phylogenetic tree construction, our target PSB was identified as *Rhodocista* sp. strain SAIYAI, which can be grouped into PNSB. This bacterial group has recently gained increasing focus as multifunctional feed additives and protein sources in aquaculture. Certain PNSB strains, such as *Rhodobacter sphaeroides* SS15 and *Afifella marina* STW181 [16], *Rhodopseudomonas faecalis* PA2 [51], *Rhodopseudomonas palustris*, and *Rhodobacter capsulatus* [17], have proper nutrient content and provide essential nutrients, including amino acids, vitamins, and carotenoids.

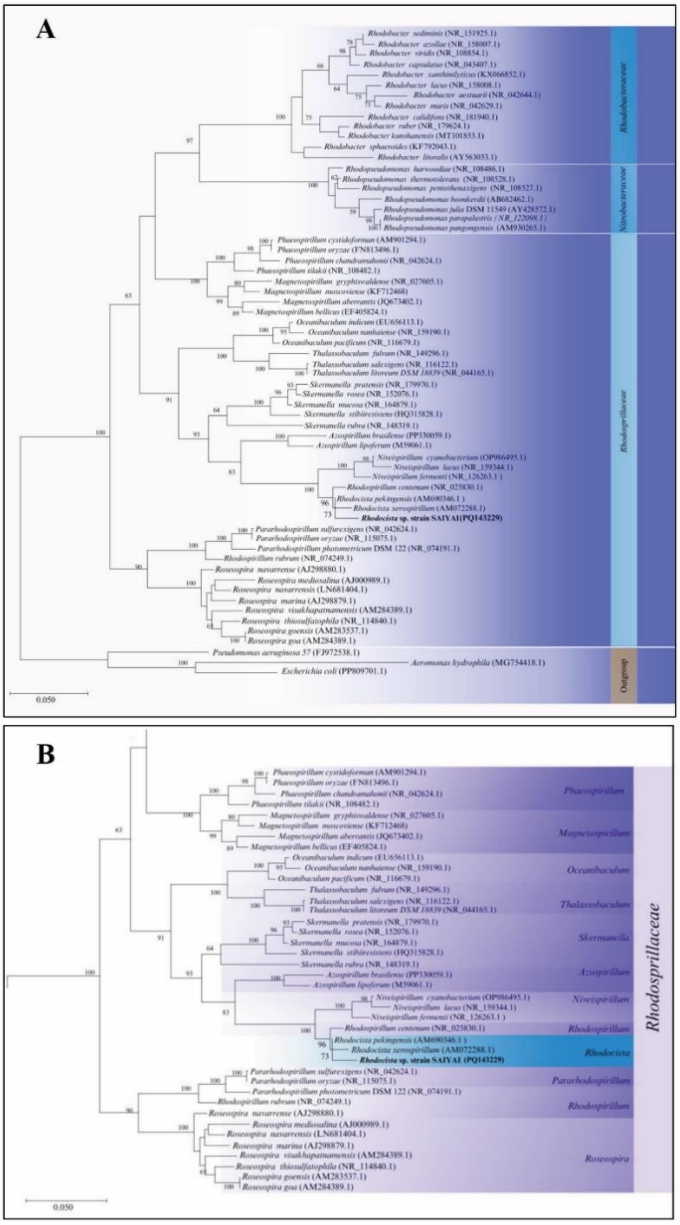

Figure 8. Phylogenetic tree based on 16S rRNA gene sequence of *Rhodocista* sp. strain SAIYAI. **(A)** The respective taxa within the Alphaproteobacteria class and **(B)** Related genera of the Rhodospirillaceae family and the members of genus *Rhodocista.* The phylogenetic tree was constructed using the Maximum Likelihood method with 1,000 bootstrap replicates in MEGA 11. Labels indicate bacterial names and GenBank Accession Numbers.

4. Conclusions

This study demonstrated that *Rhodocista* sp. strain SAIYAI possesses significant potential as a carotenoid producer, a source of spirilloxanthin, and an effective feed attractant for Pacific white shrimp. Spirilloxanthin, the prominent carotenoid produced by this bacterium, exhibits antioxidant efficiency; however, its specific mechanisms of action in aquatic systems warrant further investigation. As a feed additive, this strain has also been considered a low-cost, attractive product and valuable. Future research should explore the multifaceted impacts of *Rhodocista* sp. strain SAIYAI on the growth performance of *L. vannamei* and various quality parameters, including carotenoid-enhanced pigmentation, flesh amino acid composition, and taste. Moreover, investigating the effects of this bacterium on immune responses and gut microbiota would provide valuable insights into its application in sustainable aquaculture practices.

5. Acknowledgements

This research was funded by the National Research Council of Thailand (NRCT) and supported by the Faculty of Agriculture, Rajamangala University of Technology Srivijaya (RUTS). We would also like to thank the members of Aquabiot Laboratory RUTS for their part and valuable assistance throughout this study.

Author Contributions: Conceptualization, formal analysis, investigation, data curation, writing—original draft preparation, A.F.D., N.C., and K.U.; writing—original draft preparation, A.F.D.; writing—review and editing, validation, N.C., S.K., M.M., R.S., and K.U.; methodology, supervision, N.C., S.K., and K.U.; resources, funding acquisition, N.C.; project administration, K.U. All authors have read and agreed to the published version of the manuscript.

Funding: This research was funded by the National Research Council of Thailand (NRCT).

Conflicts of Interest: The authors declare no conflict of interest.

References

[1] Kato, S.; Panitchat, S.; Boonming, S.; Teratnatorn, V.; Saito, N.; Kojima, T.; Matsui, T.; Thanasukarn, P.; Chantrapromma, K.; Aksornkoae, S. Rehabilitation of Abandoned Shrimp Ponds through Mangrove Planting at Nakhon Si Thammarat, Southern Thailand: Investigation of a Food Chain System at a Newly Developed Mangrove Ecosystem. *Walailak J. Sci. Technol.* **2011**, *5*, 137–149.

[2] Yadav, S.; Goyal, V. C. Current Status of Ponds in India: A Framework for Restoration, Policies and Circular Economy. *Wetlands* **2022**, *42*, 107. https://doi.org/10.1007/s13157-022-01624-9

[3] Hallenbeck, P. C.; Benemann, J. R. Biological Hydrogen Production: Fundamentals and Limiting Processes. *Int. J. Hydrogen Energy* **2002**, *27*(11-12), 1185–1193. https://doi.org/10.1016/S0360-3199(02)00131-3

[4] Chen, J.; Wei, J.; Ma, C.; Yang, Z.; Li, Z.; Yang, X.; Wang, M.; Zhang, H.; Hu, J.; Zhang, C. Photosynthetic Bacteria-based Technology is a Potential Alternative to Meet Sustainable Wastewater Treatment Requirement? *Environ. Int.* **2020**, *137*, 105417. https://doi.org/10.1016/j.envint.2019.105417

[5] [5] Lu, H.; Zhang, G.; Zheng, Z.; Meng, F.; Du, T.; He, S. Bio-conversion of Photosynthetic Bacteria from Non-toxic Wastewater to Realize Wastewater Treatment and Bioresource Recovery: A Review. *Bioresour. Technol.* **2019**, *278*, 383–399. https://doi.org/10.1016/j.biortech.2019.01.070

[6] Imhoff, J. F. Systematics of Anoxygenic Phototrophic Bacteria. In *Sulfur Metabolism in Photoorganisms*; Hell, R., Dahl, C., Knaff, D., Leustek, T., Eds.; Springer: Dordrecht, **2008**; pp 269–287. https://doi.org /10.1007/978-1-4020-6863-8_14

[7] Ram, S.; Mitra, M.; Shah, F.; Tirkey, S. R.; Mishra, S. Bacteria as an Alternate Biofactory for Carotenoid Production: A Review of Its Applications, Opportunities and Challenges. *J. Funct. Foods* **2020**, *67*, 103867. https://doi.org/10.1016/j.jff.2020.103867

[8] Wang, G.; Grammel, H.; Abou-Aisha, K.; Sägesser, R.; Ghosh, R. High-level Production of the Industrial Product Lycopene by the Photosynthetic Bacterium *Rhodospirillum rubrum*. *Appl. Environ. Microbiol.* **2012**, *78* (20), 7205–7215. https://doi.org/10.1128/AEM.00545-12

[9] Mapelli-Brahm, P.; Gómez-Villegas, P.; Gonda, M. L.; León-Vaz, A.; León, R.; Mildenberger, J.; Rebours, C.; Saravia, V.; Vero, S.; Vila, E.; Meléndez-Martínez, A. J. Microalgae, Seaweeds and Aquatic Bacteria, Archaea, and Yeasts: Sources of Carotenoids with Potential Antioxidant and Anti-inflammatory Health-promoting Actions in the Sustainability Era. *Mar. Drugs* **2023**, *21*(6), 340. https://doi.org/10.3390/md21060340

[10] Cohen, A. C.; Dichiara, E.; Jofré, V.; Antoniolli, A.; Bottini, R.; Piccoli, P. Carotenoid Profile Produced by *Bacillus licheniformis* RT4M10 Isolated from Grapevines Grown in High Altitude and Their Antioxidant Activity. *Int. J. Food Sci. Technol.* **2018**, *53*(11), 2697–2705. https://doi.org/10.1111/ijfs.13879

[11] Liu, L.; Li, J.; Cai, X.; Ai, Y.; Long, H.; Ren, W.; Huang, A.; Zhang, X.; Xie, Z. Dietary Supplementation of Astaxanthin is Superior to Its Combination with *Lactococcus lactis* in Improving the Growth Performance, Antioxidant Capacity, Immunity and Disease Resistance of White Shrimp (*Litopenaeus vannamei*). *Aquacult. Rep.* **2022**, *24*, 101124. https://doi.org/10.1016/j.aqrep.2022.101124

[12] Yousefi, M.; Nedaei, S.; Farsani, M. N.; Ghafarifarsani, H.; Zhang, M.; Du, Z. Dietary Chrysin Supplementation Improves Growth Performance, Immune Responses, Antioxidant Status, and Resistance against Crowding Stress in Rainbow Trout. *Aquacult. Rep.* **2023**, *32*, 101708. https://doi.org/10.1016/j.aqrep.2023.101708

[13] Niedzwiedzki, D. M.; Dilbeck, P. L.; Tang, Q.; Mothersole, D. J.; Martin, E. C.; Bocian, D. F.; Holten, D.; Hunter, C. N. Functional Characteristics of Spirilloxanthin and Keto-bearing Analogues in Light-harvesting LH2 Complexes from *Rhodobacter sphaeroides* with a Genetically Modified Carotenoid Synthesis Pathway. *Biochim. Biophys. Acta, Bioenerg.* **2015**, *1847*(6-7), 640–655. https://doi.org/10.1016/j.bbabio.2015.04.001

[14] Cahoon, L. B.; Halkides, C. J.; Song, B.; Williams, C. M.; Dubay, G. R.; Fries, A.; Farmer, J.; Fridrich, W.; Brookshire, C. Swine Waste as a Source of Natural Products: A Carotenoid Antioxidant. *Agric. Sci.* **2012**, *3*(6), 806–815. https://doi.org/10.4236/as.2012.36098

[15] Lee, S.; Lur, H.; Liu, C. From Lab to Farm: Elucidating the Beneficial Roles of Photosynthetic Bacteria in Sustainable Agriculture. *Microorganisms* **2021**, *9*(12), 2453. https://doi.org/10.3390/microorganisms9122453

[16] Chumpol, S.; Kantachote, D.; Nitoda, T.; Kanzaki, H. Administration of Purple Nonsulfur Bacteria as Single Cell Protein by Mixing with Shrimp Feed to Enhance Growth, Immune Response and Survival in White Shrimp (*Litopenaeus vannamei*) Cultivation. *Aquaculture* **2018**, *489*, 85–95. https://doi.org/10.1016/j.aquaculture.2018.02.009

[17] Alloul, A.; Wille, M.; Lucenti, P.; Bossier, P.; Van Stappen, G.; Vlaeminck, S. E. Purple Bacteria as Added-value Protein Ingredient in Shrimp Feed: *Penaeus vannamei* Growth Performance, and Tolerance against *Vibrio* and Ammonia Stress. *Aquaculture* **2021**, *530*, 735788. https://doi.org/10.1016/j.aquaculture.2020.735788

[18] Koga, A.; Goto, M.; Hayashi, S.; Yamamoto, S.; Miyasaka, H. Probiotic Effects of a Marine Purple Non-sulfur Bacterium, *Rhodovulum sulfidophilum* KKMI01, on Kuruma Shrimp (*Marsupenaeus japonicus*). *Microorganisms* **2022**, *10* (2), 244. https://doi.org/10.3390/microorganisms10020244

[19] Sudpraseart, C.; Shinn, A. P.; Pooljun, C.; Sirimanapong, W. Efficacy of *Rhodobacter sphaeroides* TISTR 1529 on the Growth Performance, Immune Response, and Amino Acid Profile of Pacific Whiteleg Shrimp, *Penaeus vannamei*. *Aquaculture* **2025**, *599*, 742081.

[20] Smith, D.; Tabrett, S.; Barclay, M.; Irvin, S. The Efficacy of Ingredients Included in Shrimp Feeds to Stimulate Intake. *Aquacult. Nutr.* **2005**, *11*(4), 263–272. https://doi.org/10.1111/j.1365-2095.2005.00349.x

[21] Yuan, Y.; Lawrence, A. L.; Chehade, S. B.; Jensen, K. E.; Barry, R. J.; Fowler, L. A.; Makowsky, R.; Powell, M. L.; Watts, S. A. Feed Intake as an Estimation of Attractability in Pacific White Shrimp *Litopenaeus vannamei*. *Aquaculture* **2021**, *532*, 736041. https://doi.org/10.1016/j.aquaculture.2020.736041

[22] Tantikitti, C. Feed Palatability and the Alternative Protein Sources in Shrimp Feed. *Songklanakarin J. Sci. Technol.* **2014**, *36*(1), 51–55.

[23] Al-Souti, A.; Gallardo, W.; Claereboudt, M.; Mahgoub, O. Attractability and Palatability of Formulated Diets Incorporated with Chicken Feather and Algal Meals for Juvenile Gilthead Seabream, *Sparus aurata*. *Aquacult. Rep.* **2019**, *14*, 100199. https://doi.org/10.1016/j.aqrep.2019.100199

[24] Wang, C.; Chuprom, J.; Wang, Y.; Fu, L. Beneficial Bacteria for Aquaculture: Nutrition, Bacteriostasis and Immunoregulation. *J. Appl. Microbiol.* **2019**, *128* (1), 28–40. https://doi.org/10.1111/jam.14383

[25] Hamza, F.; Zinjarde, S. Use of Marine Microorganisms in Designing Anti-infective Strategies for Sustainable Aquaculture Production. *J. Appl. Microbiol.* **2023**, *134*(6), lxad128. https://doi.org/10.1093/jambio/lxad128

[26] Higuchi-Takeuchi, M.; Morisaki, K.; Numata, K. A Screening Method for the Isolation of Polyhydroxyalkanoate-producing Purple Non-sulfur Photosynthetic Bacteria from Natural Seawater. *Front. Microbiol.* **2016**, *7*, 1509. https://doi.org/10.3389/fmicb.2016.01509

[27] Nithya, C.; Pandian, S. K. Isolation of Heterotrophic Bacteria from Palk Bay Sediments Showing Heavy Metal Tolerance and Antibiotic Production. *Microbiol. Res.* **2010**, *165*(7), 578–593. https://doi.org/10.1016/j.micres.2009.10.004

[28] Sibero, M. T.; Igarashi, Y.; Radjasa, O. K.; Sabdono, A.; Trianto, A.; Zilda, D. S.; Wijaya, Y. J. Sponge-associated Fungi from a Mangrove Habitat in Indonesia: Species Composition, Antimicrobial Activity, Enzyme Screening and Bioactive Profiling. *Int. Aquat. Res.* **2019**, *11*, 173–186. https://doi.org/10.1007/s40071-019-0227-8

[29] Britton, G.; Liaaen-Jensen, S.; Pfender, H. *Carotenoids: Handbook*; Birkhäuser Verlag: Basel, **2004**. https://doi.org/10.1007/978-3-0348-7836-4

[30] Kiriratnikom, S. Evaluation of Possible Application of Photosynthetic Bacteria in Black Tiger Shrimp (*Penaeus monodon*). Ph.D. Thesis, Prince of Songkla University, Songkhla, Thailand, **2006**.

[31] Mukherjee, T.; Bose, S.; Mukhopadhyay, S. K. Antioxidant Properties of the Carotenoid Extracts of Three *Deinococcus-Thermus* Phylum Bacteria, *Meiothermus* sp. Strains RP and TP and *Thermus* sp. Strain YY from Paniphala Hot Spring, India. *Nutrire* **2017**, *42*, 1–11. https://doi.org/10.1186/s41110-017-0032-3

[32] Fang, C.; Ku, K.; Lee, M.; Su, N. Influence of Nutritive Factors on C50 Carotenoids Production by *Haloferax mediterranei* ATCC 33500 with Two-stage Cultivation. *Bioresour. Technol.* **2010**, *101*(16), 6487–6493. https://doi.org/10.1016/j.biortech.2010.03.044

[33] Kim, S.; Jeon, H.; Bai, S. C.; Kim, K.; Lee, S.; Hur, J. W.; Han, H. Effects of Dietary Supplementation with *Arthrobacter bussei* Powder on Growth Performance, Antioxidant Capacity, and Innate Immunity of Pacific White Shrimp (*Litopenaeus vannamei*). *Aquacult. Rep.* **2022**, *25*, 101270. https://doi.org/10.1016/j.aqrep.2022.101270

[34] Suresh, A. V.; Vasagam, K. P. K.; Nates, S. Attractability and Palatability of Protein Ingredients of Aquatic and Terrestrial Animal Origin, and Their Practical Value for Blue Shrimp, *Litopenaeus stylirostris* Fed Diets Formulated with High Levels of Poultry Byproduct Meal. *Aquaculture* **2011**, *319* (1-2), 132–140. https://doi.org/10.1016/j.aquaculture.2011.06.039

[35] Chirapongsatonkul, N.; Srichanun, M.; U-taynapun, K. The Impact of a Mixture of Biofloc Fermentation Medium and Vinasse on Attractability, Palatability, and Antibacterial Properties against Multi-antibiotic Resistant *Aeromonas veronii*. *Int. J. Agric. Technol.* **2019**, *15*(6), 845–858.

[36] U-taynapun, K.; Nganwisuthiphan, T.; Chirapongsatonkul, N. Species Diversity and Existence of Virulence Genes in Clinical *Aeromonas* spp. Causing Motile Aeromonas Septicemia (MAS) Isolated from Cultured Nile Tilapia (*Oreochromis niloticus*). *Int. J. Agric. Technol.* **2020**, *16*(4), 749–760.

[37] Tamura, K.; Stecher, G.; Kumar, S. MEGA11: Molecular Evolutionary Genetics Analysis Version 11. *Mol. Biol. Evol.* **2021**, *38*(7), 3022–3027. https://doi.org/10.1093/molbev/msab120

[38] Maresca, J. A.; Romberger, S. P.; Bryant, D. A. Isorenieratene Biosynthesis in Green Sulfur Bacteria Requires the Cooperative Actions of Two Carotenoid Cyclases. *J. Bacteriol.* **2008**, *190*(19), 6384–6391. https://doi.org/10.1128/JB.00758-08

[39] Vila, E.; Hornero-Méndez, D.; Azziz, G.; Lareo, C.; Saravia, V. Carotenoids from Heterotrophic Bacteria Isolated from Fildes Peninsula, King George Island, Antarctica. *Biotechnol. Rep.* **2019**, *21*, e00306. https://doi.org/10.1016/j.btre.2019.e00306

[40] Sutherland, G. A.; Qian, P.; Hunter, C. N. Swainsbury, D. J.; Hitchcock, A. Engineering Purple Bacterial Carotenoid Biosynthesis to Study the Roles of Carotenoids in Light-harvesting Complexes. *Methods Enzymol.* **2022**, *674*, 137–184. https://doi.org/10.1016/bs.mie.2022.04.001

[41] Kim, J. K.; Lee, B. Mass Production of *Rhodopseudomonas palustris* as Diet for Aquaculture. *Aquacult. Eng.* **2000**, *23*(4), 281–293. https://doi.org/10.1016/S0144-8609(00)00057-1

[42] Soon, T. K.; Al-Azad, S.; Ransangan, J. Isolation and Characterization of Purple Non-sulfur Bacteria, *Afifella marina*, Producing Large Amount of Carotenoids from Mangrove Microhabitats. *J. Microbiol. Biotechnol.* **2014**, *24*(8), 1034–1043. https://doi.org/10.4014/jmb.1308.08072

[43] López, G.-D.; Álvarez-Rivera, G.; Carazzone, C.; Ibáñez, E.; Leidy, C.; Cifuentes, A. Bacterial Carotenoids: Extraction, Characterization, and Applications. *Crit. Rev. Anal. Chem.* **2023**, *53*(6), 1239–1262. https://doi.org/10.1080/10408347.2021.2016366

[44] Gao, Y.; Focsan, A. L.; Kispert, L. D. Antioxidant Activity in Supramolecular Carotenoid Complexes Favored by Nonpolar Environment and Disfavored by Hydrogen Bonding. *Antioxidants* **2020**, *9*(7), 625. https://doi.org/10.3390/antiox9070625

[45] Imhoff, J. F. *Rhodocista*. In *Bergey's Manual of Systematics of Archaea and Bacteria*; Wiley: **2015**; pp 1–5. https://doi.org/10.1002/9781118960608.gbm00895

[46] Dey, A.; Srivastava, N.; Sharma, S.; Verma, V.; Rao, L.; Chaudhary, M.; Jain, S.; Pinapati, K. K. Neuroprotective Effects of Carotenoid Rich *Verbesina encelioides* Flower Extract in Scopolamine Induced Memory Impaired Rats Mimicking Alzheimer's Disease. *Preprints* **2024**, 2024031767. https://doi.org/10.20944/preprints202403.1767.v1

[47] Wu, G.-S.; Chung, Y.-M.; Lin, W.-Y.; Chen, S.-Y.; Huang, C.-H. Effect of Substituting De-hulled or Fermented Soybean Meal for Fish Meal in Diets on Growth of Hybrid Tilapia, *Oreochromis niloticus* and *O. aureus*. *J. Fish. Soc. Taiwan* **2003**, *30*(4), 291–297.

[48] Bardera, G.; Owen, M. A.; Façanha, F. N.; Alcaraz-Calero, J. M.; Sloman, K. A.; Alexander, M. E. Assessing Feed Attractability in Pacific White Shrimp (*Litopenaeus vannamei*) Using an Automated Tracking Software. *Aquaculture* **2020**, *529*, 735692. https://doi.org/10.1016/j.aquaculture.2020.735692

[49] Lim, L.; Liew, K.; Ebi, I.; Shapawi, R.; Lal, M. T. M.; Liew, H. J.; Hamasaki, K.; Masuda, R.; Kawamura, G. Amino Acids as Chemoattractant and Feeding Stimulant for the Commercially Farmed Decapod Crustaceans: A Brief Review. *Aquacult. Res.* **2022**, *53*(2), 333–343. https://doi.org/10.1111/are.15591

[50] Archadale, M. V.; Nakamura, K. Responses to the Swimming Crab *Portunus pelagicus* to Amino Acids and Mono-and Disaccharides. *Nippon Suisan Gakkaishi* **1992**, *58*(2), 165–172. https://doi.org/10.2331/suisan.58.165

[51] Patthawaro, S.; Saejung, C. Production of Single Cell Protein from Manure as Animal Feed by Using Photosynthetic Bacteria. *MicrobiologyOpen* **2019**, *8*(10), e913. https://doi.org/10.1002/mbo3.913

ASEAN
Journal of Scientific and Technological Reports
Online ISSN:2773-8752

Research article

Process Parameter Optimization of Ti-45Nb Titanium Alloy Produced Using the Design of Experiments Technique

Bo Liang[1], Adisak Sangsongfa[1], and Noppadol Amdee[1*]

[1] Faculty of Industrial Technology, Muban Chombueng Rajabhat University, Ratchaburi, 70150, Thailand
* Correspondence: noppadolamd@mcru.ac.th

Citation:
Liang, B.; Sangsongfa, A.; Amdee, N. Process parameter optimization of Ti-45Nb titanium alloy produced using the design of experiments technique. *ASEAN J. Sci. Tech. Report.* **2026**, *29*(3), e260922. https://doi.org/10.55164/ajstr.v29i3.260922.

Article history:
Received: August 12, 2025
Revised: January 8, 2026
Accepted: January 10, 2026
Available online: February 27, 2026

Abstract: The goal of this study is to optimize the production conditions of Ti-45Nb titanium alloy by innovatively introducing the Design of Experiments (DOE) method and using the 2^k method of full factor analysis in DOE, and to improve the chemical heterogeneity of Ti-45Nb titanium alloy by analyzing and optimizing the parameter conditions of the production process and a total of 32 experiments was conducted. Ti-45Nb titanium alloy was produced by vacuum arc remelting (VAR) according to the following process parameters. The titanium alloy products obtained from each production were cut into circular samples with a diameter of 16 cm, and the chemical inhomogeneity was measured by Energy-dispersive X-ray spectroscopy using the 5-point sampling method. Then, the chemical inhomogeneity data values were entered into the previous experimental design, and the appropriate factor levels were determined using the technology provided in the Minitab statistical software package, with a significance level of 0.05 ($\alpha = 0.05$). Through full factorial design (DOE) and residual analysis, a regression model for chemical inhomogeneity was successfully constructed. After optimization, the production conditions of Ti-45Nb titanium alloy are: Smelting current (KA) = 1.7, Current coil (A) = 3.2542, Transform time (S) = 6, Inlet water temperature (°C) = 25, and Water flow (L/min) = 220. The chemical inhomogeneity value of the produced Ti-45Nb titanium alloy is theoretically 10%. It can provide a reference for enterprise production.

Keywords: Ti-45Nb ritanium alloy; chemical inhomogeneity; design of experiments; 2^k full factorial method; parameter optimization

1. Introduction

Titanium is a metal element with excellent mechanical properties and low density. It is widely distributed in various minerals and is abundant in the Earth's crust. Titanium is a chemical element with the symbol Ti and atomic number 22. Sometimes called the "space age metal" [1]. There is probably no material more closely associated with aerospace than titanium and its alloys [2].

Titanium alloys exhibit exceptional physical and mechanical properties [3]. However, many titanium alloys have been developed [4]. Due to their high specific strength and extraordinary corrosion resistance, titanium alloys are widely used in engineering, particularly in the aerospace, automotive, and biomedical fields [5,6]. Currently, the titanium alloy industry appears mature, yet new technologies and applications for these alloys continue to emerge [7]. Despite the utility of titanium alloys, the number of articles addressing the subject has been limited [8]. The development of new titanium alloy materials is

complex, and their production and optimization are even more challenging. Today, the demand for titanium alloys far exceeds their production capacity. The demand for titanium is expected to continue to increase [9]. This inevitably leads to high production costs for titanium alloys, particularly for new materials such as Ti-45Nb.

Ti-45Nb is a titanium alloy composed of titanium (Ti) and niobium (Nb). The alloy typically contains 45% niobium by weight. Because niobium (Nb) is a biocompatible alloying element [10], the new titanium alloy Ti-45Nb was primarily used for biomedical applications upon its invention [11–13]. However, other strategic industries also require advanced titanium alloys. Modern technological advancements are placing increasingly high demands on the functional performance of new structural materials. Currently, titanium and titanium-niobium alloys are key materials in strategic industries such as aerospace, rocket technology, nuclear energy, shipbuilding, medicine, food and chemical engineering, and electronics, and in many cases, are irreplaceable [14–16]. The combination of titanium and niobium in the Ti-45Nb titanium alloy imparts excellent mechanical strength, low density, and corrosion resistance, making it suitable for a variety of applications, from aerospace to medical devices. In the aerospace industry, it is primarily used to manufacture ultra-high-strength components, such as aircraft rivets and engine components. At the same time, titanium alloys have low thermal conductivity and high chemical reactivity, which makes machining more challenging. As a new aviation titanium alloy [17], Ti-45Nb is even more challenging to produce. However, despite its desirable properties, Ti-45Nb is generally perceived as a high-cost material. Producing Ti-45Nb titanium alloy requires significant effort and cost, underscoring the urgent need to improve its manufacturing sustainability.

The vacuum arc remelting method is a promising, innovative approach that combines the benefits of thermochemical and electrochemical processes. This technique has emerged as an economically viable and environmentally friendly solution for titanium production. The vacuum arc remelting method is well-suited to producing the Ti-45Nb titanium alloy. However, because there are too many process parameters to control during the production of this new material, traditional production methods often require experience and experimentation to determine appropriate settings. Multiple tests of each parameter and experience-based judgments are time-consuming, thereby reducing production efficiency and increasing production costs. This is undoubtedly a further blow to the new titanium alloy Ti-45Nb, which is already priced at a premium.

The innovative application of the design of experiments (DOE) method addresses the limitations of traditional experiments in terms of cost and parameter coverage. In this study, a non-factorial design was employed to improve the efficiency of the Ti-45Nb titanium alloy by optimizing process parameters (without structural changes), thereby increasing yield [18].

2. Materials and Methods

This study conducted a production experiment for a novel material, carefully selecting suitable equipment and manufacturing techniques based on widely available raw materials, namely the Ti-45Nb titanium alloy. The objective was to enhance production efficiency through a creative strategy that utilized a newly developed design-of-experiments methodology.

2.1 Materials

The primary materials utilized in this study are titanium and niobium. By welding these metals at a 55% titanium to 45% niobium mass ratio and remelting the resulting alloy, a novel material, Ti-45Nb, is produced.

2.2 Methods

This research investigated the application of a fuzzy logic system to identify suitable parameters to produce the Ti-45Nb titanium alloy. Initially, the variables to be tested were defined, followed by applying the 2^k method within a design-of-experiments framework to estimate and optimize the parameters. The study identified the most effective operating conditions and conducted yield-performance tests. The research methodology was systematically structured, as illustrated in Figure 1. As depicted in Figure 1, the research followed a well-defined sequence of steps summarized below.

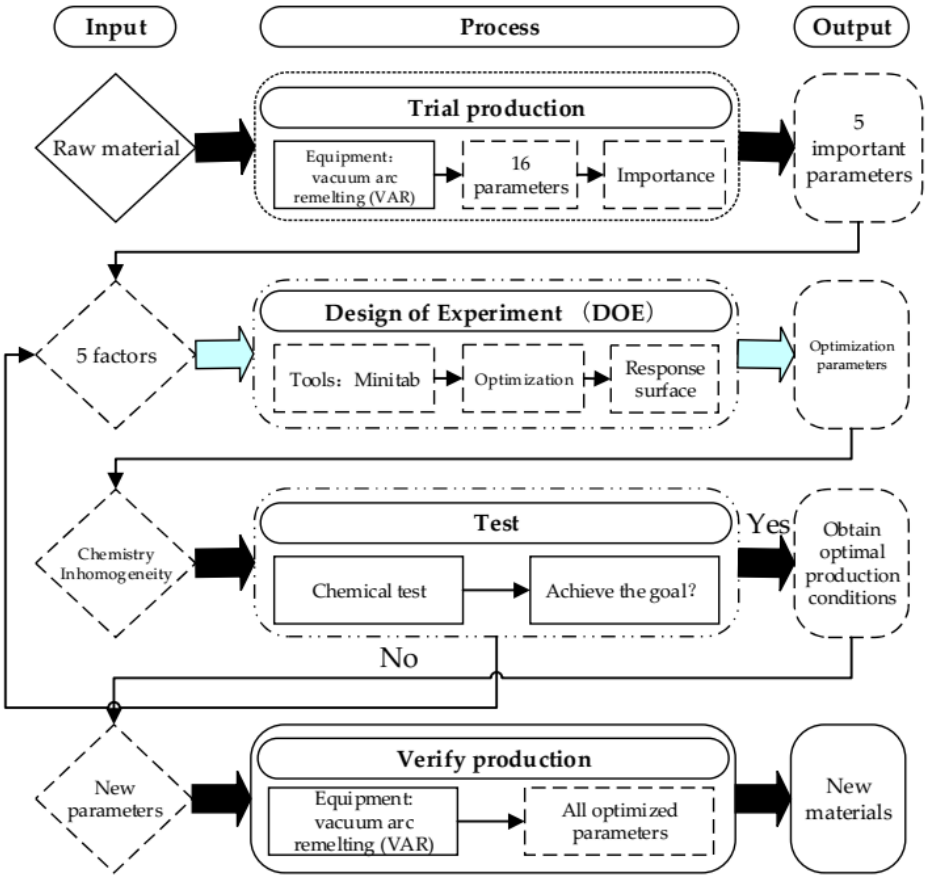

Figure 1. Research path and conceptual framework.

Referring to Figure 1, the path and conceptual framework of this research comprise the following: Input, Process, and Output. The conceptual framework of this research is structured into the following steps. The first step involves input, starting from raw materials and proceeding through the Trial Production process, which is further divided into three steps. The vacuum arc remelting (VAR) equipment is used for trial production, and all 16 parameters are used to determine their importance. This research investigates the factors of smelting current, current coil, transforming time, inlet water temperature, and water flow, as these variables represent the primary controllable parameters governing the energy balance, heat transfer, and melt pool flow dynamics of the smelting process. These factors directly influence the material's homogeneity, defect formation, and microstructural development, and are clearly definable and controllable through the process control system. The selection of these parameters follows established Design of Experiments (DOE) methodology, beginning with a comprehensive review of the literature and process knowledge, complemented by preliminary experimental observations to identify factors with clear mechanistic relevance and observable effects on process outcomes. Subsequently, statistical screening was employed to reduce the dimensionality of the parameter set, yielding a focused set of high-impact factors suitable for interaction analysis under practical constraints on experimental cost, safety, and process stability.

The output comprises 5 essential parameters and serves as input to the second step, which includes 5 factors. In the second step, starting from the input of 5 factors, the specific process is optimized using the Design of Experiment (DOE) method, which is divided into three steps. The Minitab tool is used to optimize and obtain a response. The output is a response parameter that serves as input to the third step, chemist inhomogeneity. In the third step, starting from the input Chemist inhomogeneity, the specific process is tested in two steps. Through chemical tests, it is determined whether the target has been achieved. If achieved, the optimal production conditions are obtained. If it has not been completed, it is returned to the second step for further optimization. In the fourth step, the optimized production parameters are used as inputs. The specific

process involves verifying production, which is divided into two steps. The production is validated using vacuum arc remelting (VAR) equipment, and all optimized parameters are employed to produce output as new materials.

2.2.1 Tool and Equipment

The experimental design was developed in Minitab, and VAR equipment was employed during the process. A pilot trial was conducted with the VAR system to establish preliminary parameters. According to the experimental design, production was performed using the VAR unit, with adjustments to critical process parameters. Raw material inputs and product yields were measured and analyzed both before and after production. This evaluation aimed to assess the feasibility of the treatment method and to identify the optimal process conditions.

2.2.2 Set factor input variables through experimental design

The initial phase involves establishing input variables through an experimental design [19]. There are sixteen smelting process conditions for titanium alloys: Smelting current, Smelting voltage, Welding current, Welding voltage, Current coil, Transform time, Vacuum before welding, Boost rate, Vacuum before smelting, Crucible ratio, Stable arc current, Smelting Vacuum, Inlet water temperature, Outlet water temperature, Water flow, and Cooling time.

Before starting the preliminary trials, first exclude two fixed parameters, such as the Crucible ratio and the Stable arc current. And then exclude welding parameters unrelated to melting, such as welding current and welding voltage, as well as parameters before melting, such as Vacuum before welding and Vacuum before smelting. Then, through preliminary trials, determine the importance, control difficulty, and control effect order of 10 parameters. In the early stages of the trials, it was found that Smelting voltage varies with Smelting current; therefore, the Smelting voltage was excluded from the analysis. Similarly, Outlet water temperature varies with Inlet water temperature; hence, exclusion was also carried out. In subsequent preliminary trials, it was found that the vacuum parameters included the Boost rate and the Smelting Vacuum. In contrast, the Cooling time was difficult to control and had little impact on the product. Therefore, the remaining five parameters were selected for further research. Based on a thorough analysis of parameters and successful trial production, a set of five key parameters was identified from the initial pool of 16 variables. These parameters were selected for their high significance in the process and their controllability, making them ideal input factors. The identified parameters are as follows: Smelting Current, Current Coil, Transform Time, Inlet Water Temperature, and Water Flow. These parameters were selected based on their significant impact on the process and ease of control. By carefully adjusting and optimizing these parameters, manufacturers can improve the quality and performance of the final product. Therefore, setting them as factors. Each factor and their specific details are as follows: Smelting current (KA) with a range of 1.4-2.0, Current coil (A) with a range of 1-4, Transform time (S) with a range of 3-6, Inlet water temperature (°C) with a range of 25-31, and Water flow (L/min) with a range of 160-220.

F = Smelting current, Current coil, Transform time, Inlet water temperature, Water flow.

Factor 1: Smelting current (KA)

Factor 2: Current coil (A)

Factor 3: Transform time (S)

Factor 4: Inlet water temperature (°C)

Factor 5: Water flow (L/min)

These factors are categorized into two levels.

Sc = Smelting current. The Smelting current (Sc) is divided into two levels. The low-level Smelting current is set at 1.4KA, while the high-level Smelting current is set at 2KA.

Cc = Current coil. The Current coil (Cc) is divided into two levels. The low-level Current coil is set at 1A, while the high-level Current coil is set at 4A.

Tt = Transform time. The Transform time (Tt) is divided into two levels. The low-level Transform time is set at 3S, while the high-level Transform time is set at 6S.

Iw = Inlet water temperature. The Inlet water temperature (Iw) is divided into two levels. The low-level Inlet water temperature is set at 25℃, while the high-level Inlet water temperature is set at 31℃.

Wf = Water flow. The Water flow (Wf) is divided into two levels. The low-level Water flow is set to 160 L/min, while the high-level Water flow is set to 220 L/min.

Table 1. Factor settings.

No	Factor	Low	High	Unit
1	Smelting current	1.4	2	KA
2	Current coil	1	4	A
3	Transform time	3	6	S
4	Inlet water temperature	25	31	℃
5	Water flow	160	220	L/min

Table 1 presents the parameter composition and levels, highlighting how the experimental design elucidates the interrelationships among these parameters. By specifying the variables for each trial, a second-order factorial, categorized as low and high [20], is employed to ensure the precision of the experimental design's parameters and levels. This study employed a full factorial design using the 2^k method, with 32 experiments conducted. Subsequent experiments will be structured based on the inputs above. Through these experiments, the experimental variables and levels influencing chemical heterogeneity were identified. The objective is to analyze and optimize operational parameters effectively.

2.2.3 Characterization method

To characterize the process, following the experimental design outlined above, Ti-45Nb titanium alloy was produced in a VAR furnace using a sequential set of process parameters. After each production run, the resulting titanium alloy product was formed into a circular specimen measuring 16 cm in diameter. After surface treatment, chemical inhomogeneity was measured using a five-point sampling method, including the center of the circle, a horizontal and a vertical line passing through the center, and the intersection of five equally divided circles. The specific sampling points are shown in Figures 2 and 3 below:

Figure 2. Ti-45Nb titanium alloy product sample.

According to the test regulations for chemical inhomogeneity, the principle of not measuring the base metal, titanium, in the Ti-45Nb titanium alloy means that its inhomogeneity is not measured. Therefore, this study selects niobium as the target for inhomogeneity measurement. The determination of niobium in metals is performed using energy-dispersive X-ray spectroscopy (EDS), which measures the energy spectrum of X-ray reflections from the material. In energy-dispersive X-ray spectroscopy, ω is usually used to represent the percentage of the element content in the sample. ω refers to the content of an element in a substance calculated

in units of mass fraction, which is the ratio of the maximum mass of a particular component in the substance to the mass of the entire substance.

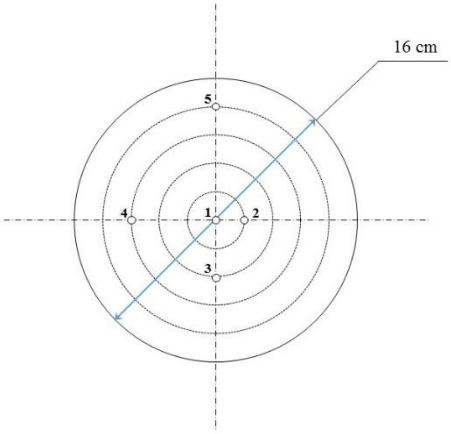

Figure 3. Ti-45Nb titanium alloy product sample test point.

According to the standard for chemical inhomogeneity of titanium alloys, the standard content of niobium in Ti-45Nb titanium alloy is 45. Therefore, the chemical inhomogeneity deviation value of Ti-45Nb titanium alloy in this study is the content of niobium measured by the sample, that is, the absolute value of the difference between the niobium content ω of each sample and 45, and then divided by 45; the chemical inhomogeneity value of Ti-45Nb titanium alloy in this study can be obtained. The specific formula is as follows: Formula 1:

$$CI_i = \frac{\omega_i - 45}{45} \quad (1)$$

In accordance with the previously planned experimental design, production was carried out in the specified sequence. The 32 Ti-45Nb titanium alloy product samples produced were tested using the 5-point sampling method previously defined, and 160 niobium contents (ω) were obtained. Then, they were calculated using formula 4-1 to receive the chemical inhomogeneity values for each sampling point across all products. Then, the chemical inhomogeneity data for the five sampling points of each product were averaged to obtain the chemical inhomogeneity data for the Ti-45Nb titanium alloy produced each time.

3. Results and Discussion

3.1 Results of the experiment

The chemical inhomogeneity data were incorporated into the experimental design, and the effects of the five factors on the chemical inhomogeneity of Ti-45Nb titanium alloy were evaluated using the previously established design method. In an experiment conducted under full-factorial design conditions, the five process parameters affecting the chemical inhomogeneity of Ti-45Nb titanium alloy were analyzed. In 32 experiments, the appropriate factor level was determined using the best technique provided by Minitab, with a significance level of 0.05 (α = 0.05). The full factorial experiment included 32 trials, and the results were used to determine the relationship between the five process parameters and the chemical inhomogeneity of Ti-45Nb titanium alloy, as shown in Table 2. The full factorial design method was used for experimental structure design. Table 2 summarizes the experimental results and highlights the key operational parameters identified. These parameters were evaluated using statistical analysis in Minitab across 32 experiments. The findings provide a foundation for an in-depth analysis of the process parameters and experimental data.

Table 2. Results of the experiment to determine the five process parameters.

Run Order	Std Order	Smelting current	Current coil	Transform time	Inlet water temperature	Water flow	Chemical inhomogeneity
1	25	1.4	1	3	31	220	20.08
2	21	1.4	1	6	25	220	16.98
3	2	2	1	3	25	160	11.46
4	22	2	1	6	25	220	9.03
5	30	2	1	6	31	220	10.05
*	*	*	*	*	*	*	*
*	*	*	*	*	*	*	*
*	*	*	*	*	*	*	*
28	18	2	1	3	25	220	11.04
29	31	1.4	4	6	31	220	13.97
30	8	2	4	6	25	160	5.49
31	11	1.4	4	3	31	160	16.46
32	6	2	1	6	25	160	9.52

3.2 The analysis of experimental results

The first step in the data analysis is to plot the yield residuals. This is illustrated in Figure 4, which shows the residual plot.

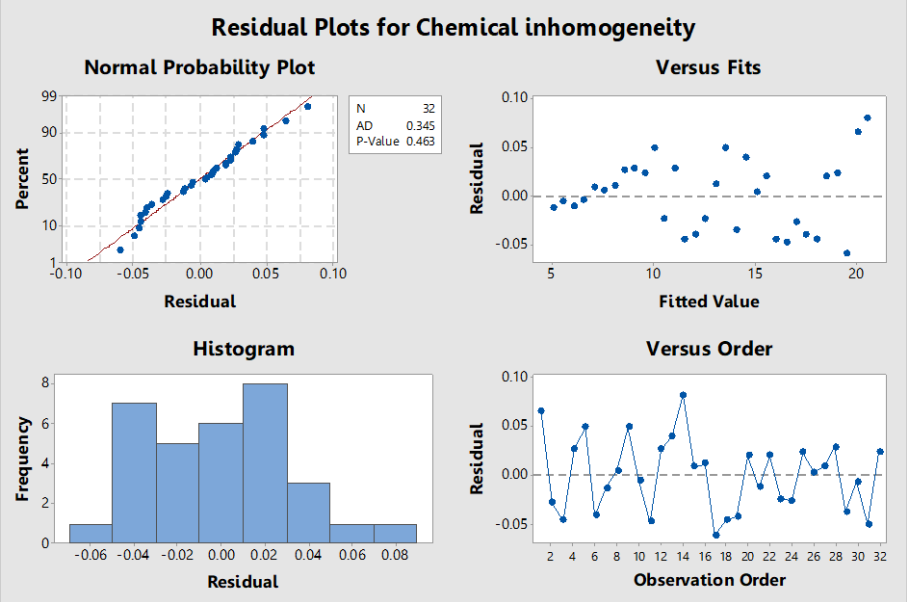

Figure 4. Residual Plots for Chemical Inhomogeneity.

According to the figure, most points are distributed along the diagonal, with only a slight deviation at the end. Specific indicators include N (sample size) is 32, indicating that the sample size is sufficient and the statistical results are credible. The Anderson-Darling (AD) statistic is 0.345, and the sample size is small, indicating good normality. The P-value is 0.463, which exceeds the 0.05 significance level, indicating that the normality assumption cannot be rejected. The histogram of the residuals is approximately symmetrical, bell-shaped, and concentrated near zero. This shows that the residuals are well distributed and supports the standard distribution hypothesis.

The data in this figure are first standardized. Based on the Normal Probability Plot and Histogram, the residuals meet the standard distribution assumption. The Anderson-Darling statistic is small (0.345), and the P-value is greater than 0.05 (0.463), further supporting this conclusion. Second, the research data is independent. From the Residuals vs. Order plot, the residuals are independent of experimental order, and there is no systematic trend or cyclical fluctuation. Third, the data have equal variance. From the Residuals vs Fits plot, the residual distribution appears random and uniform, and the model satisfies the equal-variance assumption. Based on the above conclusions, the model-fitting effect can be analyzed. Residual analysis showed that the model fit the data to some extent. The residuals were normally distributed and showed no apparent pattern, supporting the model's validity. The residuals met the assumptions of normality, independence, and homogeneity of variance, indicating good model fit and high-quality experimental data. The current results support the stability of the experimental design and model, enabling prediction and further optimization of experimental conditions.

Table 3. This is a table. Tables should be placed in the main text near the first time they are cited.

Source	DF	Adj SS	Adj MS	F-Value	P-Value
Model	5	682.851	136.570	87003.39	0.000
Linear	5	682.851	136.570	87003.39	0.000
Smelting current	1	512.640	512.640	326582.42	0.000
Current coil	1	128.000	128.000	81543.64	0.000
Transform time	1	32.281	32.281	20564.68	0.000
Inlet water temperature	1	7.980	7.980	5083.74	0.000
Water flow	1	1.950	1.950	1242.47	0.000
Error	26	0.041	0.002		
Total	31	682.892			

Evaluation of the four operational parameters in the experimental design highlights the factors affecting yield under the specified analysis conditions, as shown in Table 3. According to Table 3, it can be concluded that by comparing the sum of squares of Model and Total, we can see that the model explains almost all the total variation, indicating the model is effective, the sum of squares of error and mean square of error are tiny, proving that the experimental design and model fitting are accurate. The results of the full-factorial experiment, comprising all 32 runs, were also presented within a yield analysis-of-variance framework. Factors influencing yield can be identified at the $\alpha = 0.05$ significance level. When the main factors were considered significant, these factors included Smelting current, Current coil, Transform time, Inlet water temperature, and Water flow. Given the rationality of this experimental design and the favorable results obtained, it is appropriate to incorporate these findings into subsequent production experiments to enhance yield and identify more optimal experimental conditions.

3.3 Response optimizer results

According to the requirements of China's titanium alloy production standard GB/T 3620.2-2023, "Allowable Deviation of Chemical Composition of Titanium and Titanium Alloy Processing Products," and the conventional requirements of titanium alloy production enterprises, the chemical inhomogeneity standard of titanium alloy is usually set at 10%. By incorporating this target value into the optimization, we can determine the optimal production parameters for the Ti-45Nb alloy, thereby meeting the 10% standard. The optimized results are shown in Figure 5, Optimization Plot: From the optimal results shown in Figure 5, by analyzing the production process parameter conditions of Ti-45Nb titanium alloy, it can be concluded that the production process parameters of Ti-45Nb titanium alloy after optimization are as follows: Smelting current (KA) = 1.7, Current coil (A) = 3.2542, Transform time (S) = 6, Inlet water temperature (°C) = 25, and Water flow (L/min) = 220. -optimized towards the target yield.

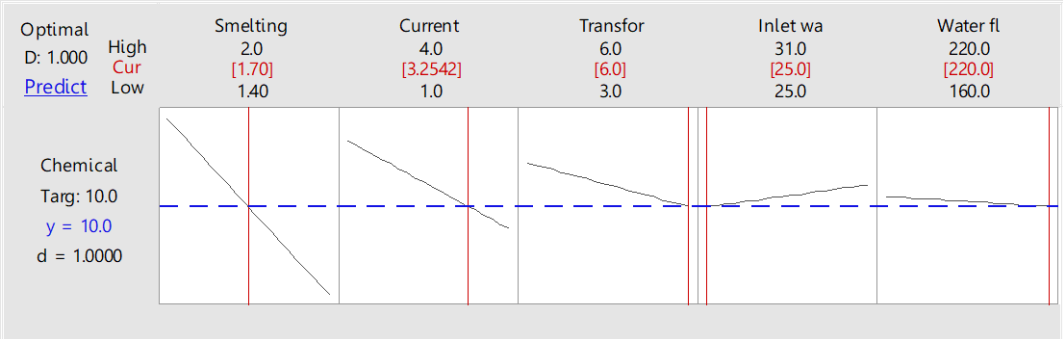

Figure 5. Illustrates an analysis of the yield level at the specified optimal value.

3.4 Verification of research results

Using the optimized production parameter conditions for the Ti-45Nb alloy, the process was repeated, and the resulting product was subjected to a chemical inhomogeneity test using the same method. The results were used to verify whether the final optimization process met the requirements. After production according to the required process parameters, the data results obtained are shown in Table 4 below:

Table 4. The optimized test data.

Run Order	Point 1 data	Point 2 data	Point 3 data	Point 4 data	Point 5 data
After optimization	55.00 %	55.01 %	54.99 %	54.99 %	55.02 %

The data in Table 4 can be used to calculate the chemical inhomogeneity of representative Ti-45Nb titanium alloy products produced with optimized production using Formula 1. The details are shown in Table 5:

Table 5. The average value of data deviation after optimization.

Run Order	Absolute deviation					Average
	Point 1	Point 2	Point 3	Point 4	Point 5	
After optimization	10.00 %	10.01 %	9.99 %	9.99 %	10.02 %	10.002 %

The last column of Table 5 is the average value of the absolute value of all data deviations measured at the five test points of the Ti-45Nb titanium alloy after optimized production, which is the representative data value of the chemical inhomogeneity of the Ti-45Nb titanium alloy after optimized production. The true nature of the chemical inhomogeneity of the Ti-45Nb alloy after optimized production can inform subsequent analyses of production conditions and verification. According to the results, the ω value of the chemical inhomogeneity of the Ti-45Nb titanium alloy after optimized production is 10.002%, which differs by 0.02%

from the theoretical value of 10.00%. Within the error range, the optimized process conditions are considered to meet the set requirements. The optimization results are reasonable and acceptable, demonstrating that the Ti-45Nb titanium alloy production model exhibits good linearity, that the results can be predicted and reproduced, and that the model is correctly and appropriately established.

3.5 Other performance tests of target material products

For the Ti-45Nb titanium alloy products that meet the chemical inhomogeneity requirements after optimization, to further verify whether the products fully meet the performance requirements of Ti-45Nb titanium alloy products, after completing the niobium element detection, comprehensive element detection, and microstructure detection were continued on the Ti-45Nb titanium alloy product samples with the optimized chemical inhomogeneity ω of 10.002%. First, a comprehensive elemental analysis was conducted on the optimized Ti-45Nb titanium alloy samples to determine the contents of impurity elements, including carbon, oxygen, nitrogen, and hydrogen. The specific situation is shown in Table 6, Chemical Element Analysis.

Table 6. The chemical element analysis.

Sample No.	C (ω%)	O (ω%)	N (ω%)	H (ω%)
After optimization	0.012	0.031	0.007	0.0003

According to the data given in the chemical element analysis table in Table 6, in the optimized Ti-45Nb titanium alloy product sample, the carbon content ω is 0.012%, the oxygen content ω is 0.031%, the nitrogen content ω is 0.007%, the hydrogen content ω is 0.0003%, and other elements cannot be detected due to their low content. This result indicates that, following elemental analysis, the optimized Ti-45Nb titanium alloy product sample contains impurity elements at levels below the required lower limit, fully meeting the requirements for titanium alloy products and therefore qualifying. At the same time, it can be shown that the production optimization does not introduce additional interference, that the optimization model is feasible, and that the optimization process is reasonable. Following chemical elemental analysis, the second step is to conduct microstructural characterization of the optimized Ti-45Nb alloy samples. The method involves scanning and imaging the titanium alloy microstructure at 50x and 200x magnifications using a scanning electron microscope. The material's microscopic properties are then assessed based on the lattice distribution observed in the image. The specific microstructure diagram is shown in Figure 6.

Figure 6. Microstructure of the Ti-45Nb titanium alloy sample.

From the microstructural diagram in Figure 6, it can be concluded that the optimized Ti-45Nb alloy sample exhibits a precise microstructure, clear lattice boundaries, and a uniform distribution. This result indicates that the microstructure of the optimized Ti-45Nb alloy sample meets the standard requirements for titanium alloys and fully satisfies the criteria for titanium alloy products, thereby qualifying the product. At

the same time, it can also demonstrate that production optimization has no adverse effects on the microstructure, that the optimization model is correct, and that the optimization process is appropriate.

3.6 Full parameter range expansion optimization method

To broaden the applicability of this research, guide similar studies, and assist other titanium alloy manufacturers in adopting the same techniques and processes, this study will extend the target-point optimization results to cover the entire parameter range of the production process, providing a basis and ideas for further research and production.

3.6.1 Regression equation

The first step is to find the regression equation of the Ti-45Nb titanium alloy production process. The relationships among the parameters can be determined from the previous data analysis, and the regression equation can be derived. The regression equation can evaluate the chemical inhomogeneity of Ti-45Nb titanium alloy products under any conditions.

The regression equation for the uncoded units is given in Formula 2.

$$\text{Chemical inhomogeneity} = 38.6863 - 13.3417\ \text{Smelting current} - 1.33333\ \text{Current coil} - 0.66958\ \text{Transform time} + 0.16646\ \text{Inlet water temperature} - 0.008229\ \text{Water flow}. \quad (2)$$

Formula 2 can be used to derive chemical heterogeneity data for the product obtained under any production parameter conditions during Ti-45Nb production, providing guidance for related research and supporting other titanium alloy production companies.

3.6.2 Interaction plot and Main Effects plot

Based on the previous data analysis and the model established in Formula 2, the second step is to construct the interaction and central-effect diagrams for the production conditions of Ti-45Nb. This diagram illustrates the interactions and influences among various production process parameters and identifies the main effect. The details are shown in the Interaction plot of Figure 7 and the Main Effects plot of Figure 8.

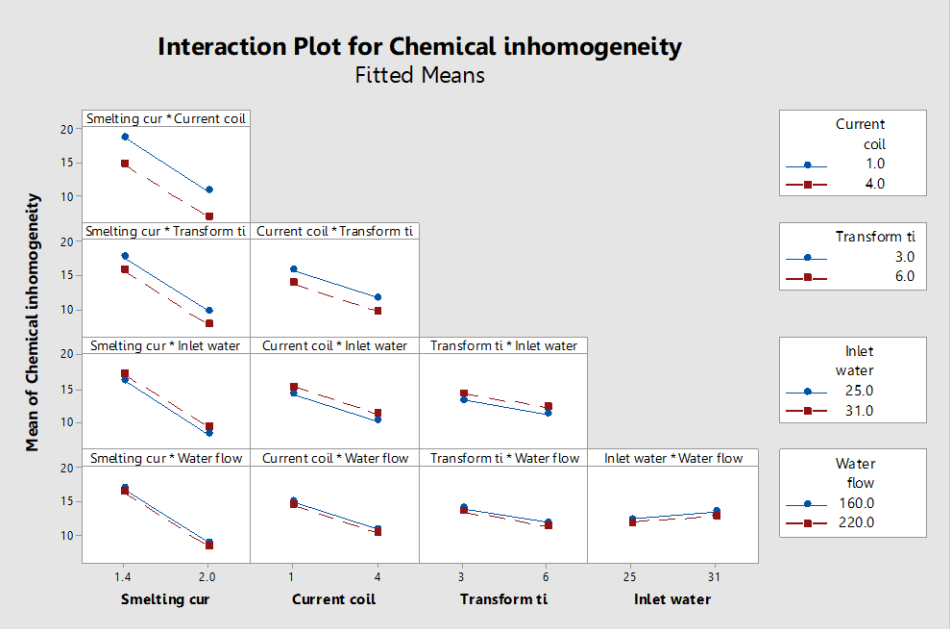

Figure 7. Interaction plot for Chemical inhomogeneity.

According to Figure 7, trends in each process parameter during the production of Ti-45Nb titanium alloy are discernible, and the mutual influence between any two parameters can also be analyzed. Other researchers and titanium alloy manufacturers can obtain the specific ranges and values of each parameter from it.

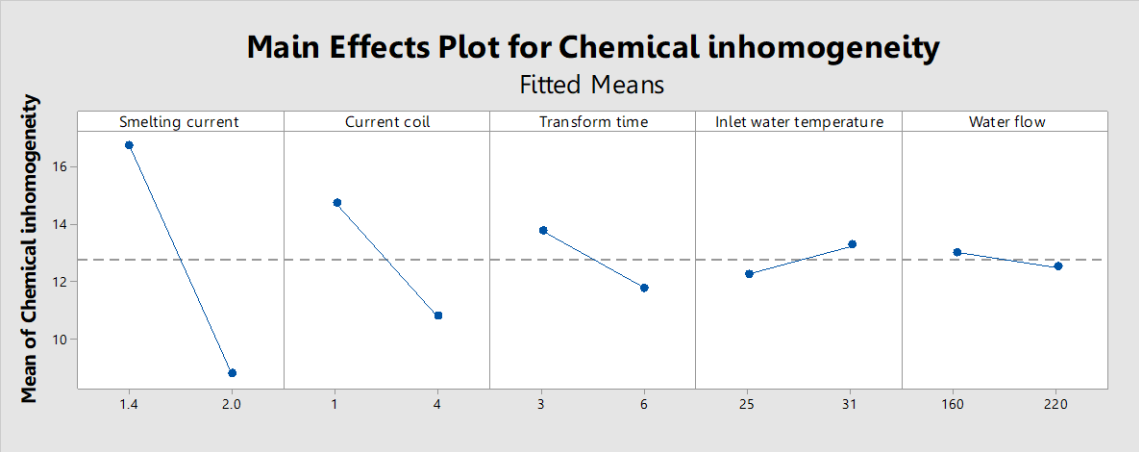

Figure 8. Main Effects of the plot for Chemical inhomogeneity.

Figure 8 shows the details of each process parameter used in the production of the Ti-45Nb titanium alloy, including the parameter's size change and range. According to Figure 17, the slopes of the influence value lines for each parameter differ, with larger slopes indicating greater impact on the product's chemical inhomogeneity and thus a more critical main effect. Based on the slopes of the five parameters, the Smelting current exhibits the largest slope, indicating it is the most significant main effect, followed by the Current coil, Transform time, Inlet water temperature, and Water flow. The effect direction of each process parameter on the result can also be judged according to the inclination direction of each parameter line segment, among which Smelting current, Current coil, Transform time, and Water flow are adverse effects; that is, the larger the parameter, the smaller the chemical inhomogeneity of the product, while Inlet water temperature is a positive effect, that is, the larger the parameter, the greater the chemical inhomogeneity of the product. Different effect directions mean opposite operation directions. Other researchers and manufacturers of titanium alloys can conduct research and operations based on this to avoid wasting time and costs.

3.6.3 Contour plot

According to the model established in Formula 2, the third step is to generate a contour plot of the production conditions for the Ti-45Nb titanium alloy. This map enables a more intuitive assessment of how different parameters influence the product's chemical heterogeneity than the equation, and it provides guidance for titanium alloy research and production based on the information it presents. The specific information is shown in Figure 9-18 below. Among them, Figures 9-12 pertain to Smelting Current. Figures 13 to 15 are related to the Current Coil. Figures 16 and 17 pertain to Transformation Time. Figure 18 is associated with Inlet Water Temperature. Figure 9 shows that the relationship between Current Coil and Smelting Current is proportional, meaning that increasing both parameters reduces Chemical Inhomogeneity. The color blocks in the figure indicate that the closer to dark blue, the smaller the Chemical Inhomogeneity, and the closer to dark green, the larger it is. The optimal position is near blue.

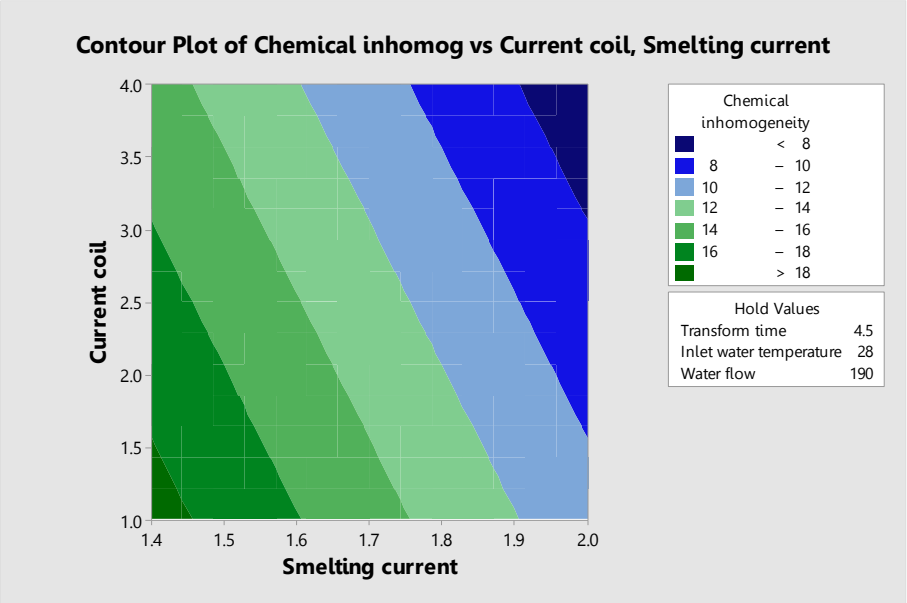

Figure 9. Contour Plot for Current Coil and Smelting Current on Chemical Inhomogeneity.

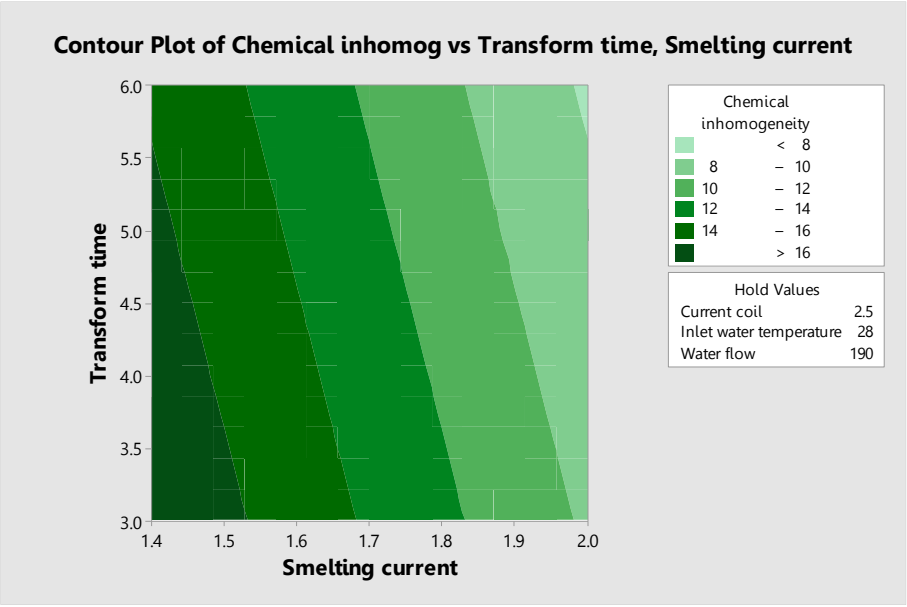

Figure 10. Contour Plot for Transform Time and Smelting Current on Chemical Inhomogeneity.

Figure 10 shows that Transform Time and Smelting Current are directly proportional; increasing both parameters reduces Chemical Inhomogeneity. The color blocks in the figure indicate that the closer to light green, the smaller the Chemical Inhomogeneity, the closer to dark green, the larger the Chemical Inhomogeneity. The optimal position is near light green. Figure 11 shows that the relationship between Inlet Water Temperature and Smelting Current is inversely proportional. That is, increasing Smelting Current and decreasing Inlet Water Temperature can reduce Chemical Inhomogeneity. The color blocks in the figure indicate that the closer to light green, the smaller the Chemical Inhomogeneity, the closer to dark green, the larger the Chemical Inhomogeneity. The optimal position is near light green.

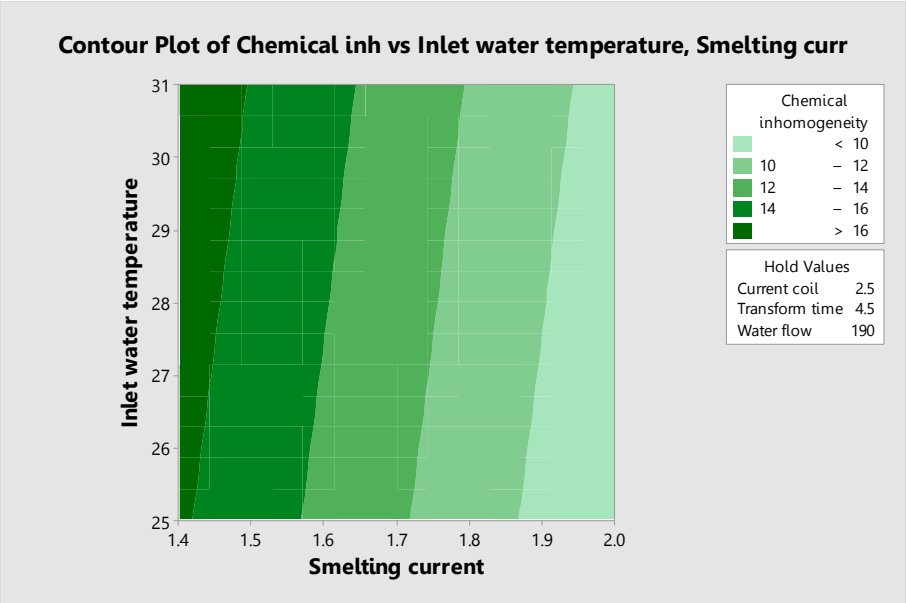

Figure 11. Contour Plot of Inlet Water Temperature and Smelting Current with Respect to Chemical Inhomogeneity.

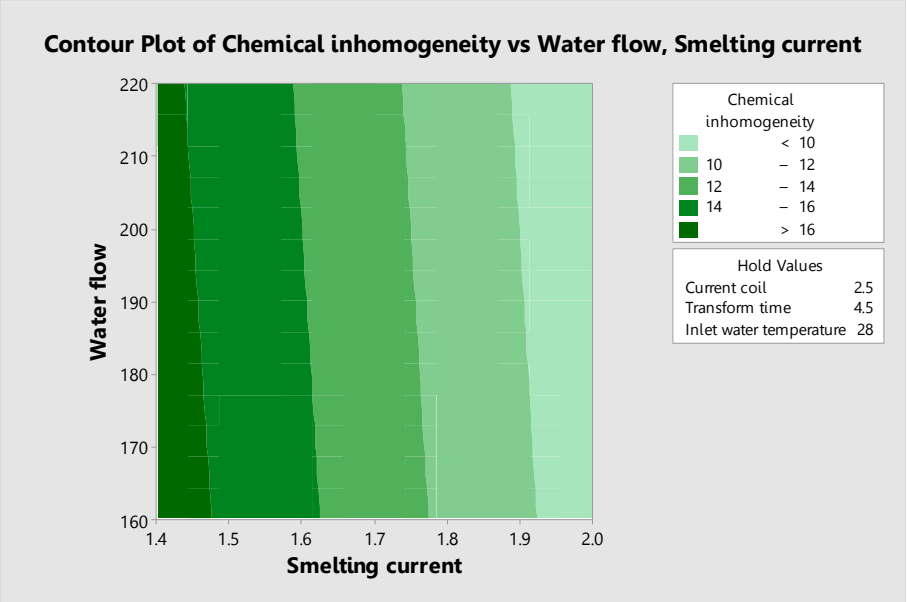

Figure 12. Contour Plot of Water Flow and Smelting Current in the Presence of Chemical Inhomogeneity.

Figure 12 shows that the relationship between Water Flow and Smelting Current is proportional. That is, increasing Smelting Current and Water Flow can reduce Chemical Inhomogeneity. However, the slope is nearly vertical, indicating that the effect of Water Flow is substantially less significant than that of Smelting Current. The color blocks in the figure suggest that the closer to light green, the smaller the Chemical Inhomogeneity, the closer to dark green, the larger the Chemical Inhomogeneity. The optimal position is near light green. The four figures above illustrate the relationship between adjustments to production parameters and the smelting current. They also demonstrate the relationship between other production parameters and smelting current. Except for the inlet water temperature, all other parameters are directly proportional to the smelting current, with varying slopes. The closer the linear relationship is to vertical, the less influential the parameter. Companies can choose production parameter adjustment methods based on chemical inhomogeneity requirements and specific color blocks.

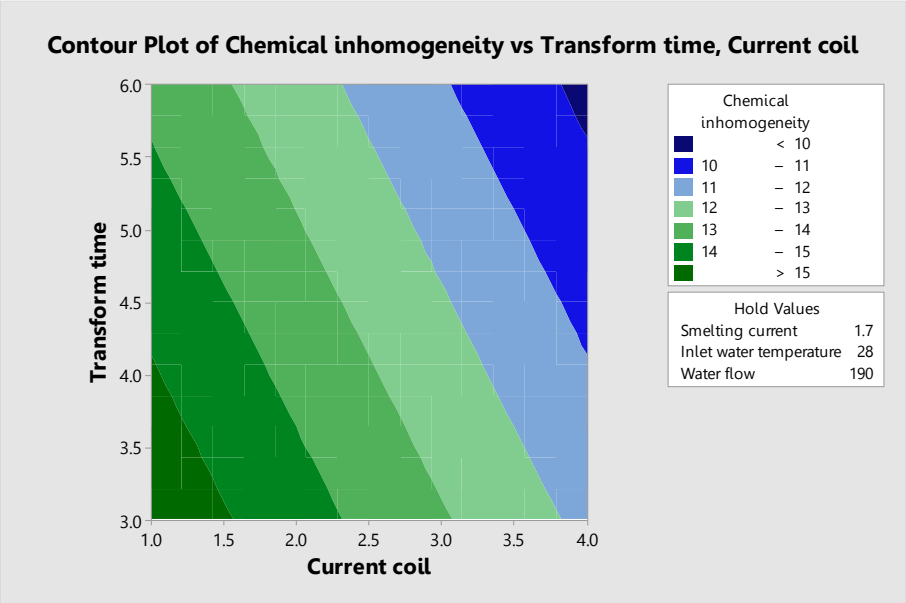

Figure 13. Contour Plot of Transform Time and Current Coil for Chemical Inhomogeneity.

Figure 13 shows that Transformation Time and Current Coil are directly proportional. Increasing the Current Coil and Water Flow reduces Chemical Inhomogeneity. The color blocks in the figure indicate that chemical inhomogeneity decreases as the color approaches dark blue and increases as the color approaches dark green. The optimal value is nearly blue.

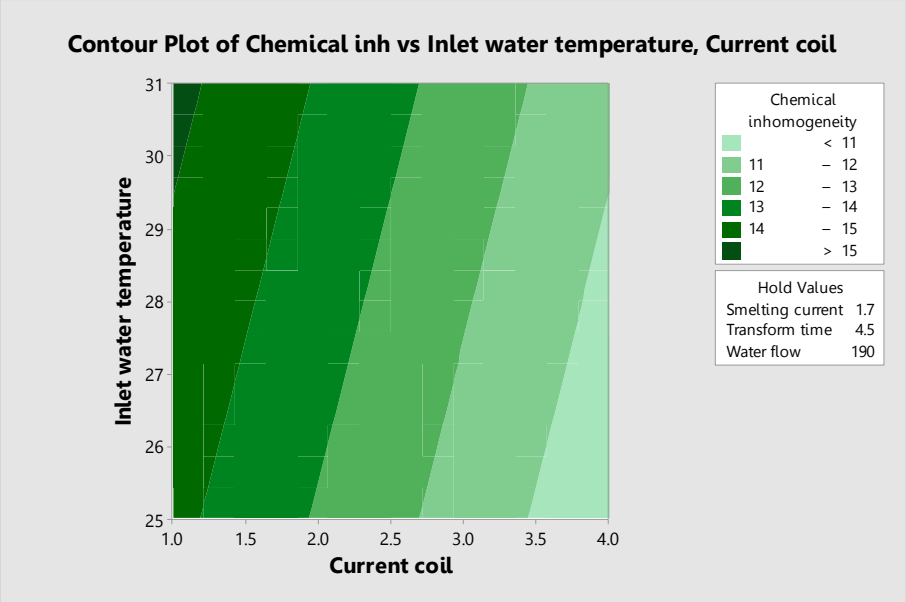

Figure 14. Contour Plot for Inlet Water Temperature and Current Coil on Chemical Inhomogeneity.

Figure 14 shows that the relationship between Inlet Water Temperature and Current Coil is inversely proportional. That is, increasing the Current Coil and decreasing the Inlet Water Temperature can reduce Chemical Inhomogeneity. The color blocks in the figure indicate that the closer the color is to dark green, the smaller the Chemical Inhomogeneity; the farther from dark green, the larger the Chemical Inhomogeneity. The optimal position is near light green.

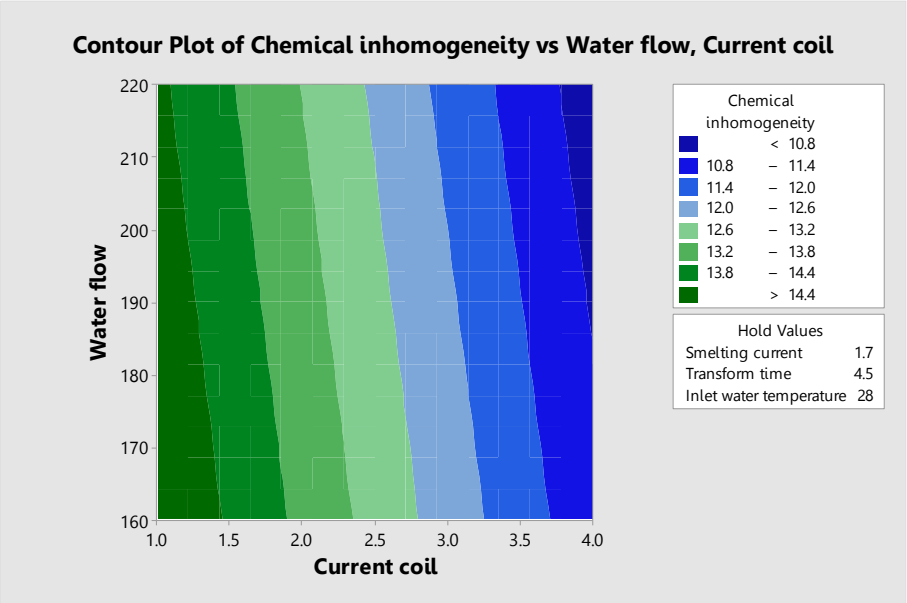

Figure 15. Contour Plot of Water Flow and Current Coil in Chemical Inhomogeneity.

Figure 15 shows that Water Flow and Current Coil are directly proportional. Increasing the Current Coil and Water Flow reduces Chemical Inhomogeneity. Still, the relationship is linear and nearly vertical, indicating that Water Flow has a much smaller impact on Chemical Inhomogeneity than Current Coil. The color blocks in the figure suggest that chemical inhomogeneity decreases as the color approaches dark blue, whereas it increases as the color approaches dark green. The optimal position is near dark blue. The three figures above illustrate the relationship between adjustments to production parameters and the Current Coil. They also demonstrate the relationship between other production parameters and the Current Coil. Except for Inlet Water Temperature, all other parameters are directly proportional to Current Coil, but the slopes of the linear relationships differ. Companies can choose production parameter adjustment methods based on chemical inhomogeneity requirements and the specific color blocks used.

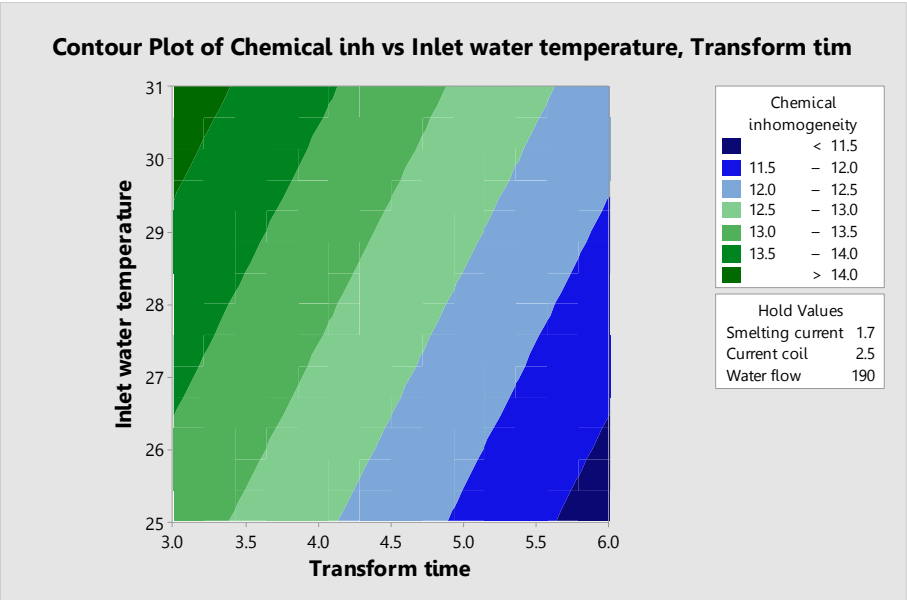

Figure 16. Contour Plot for Inlet Water Temperature and Transformation Time on Chemical Inhomogeneity.

Figure 16 shows that the relationship between inlet water temperature and transformation time is inversely proportional. Increasing transformation time and decreasing inlet water temperature reduce chemical inhomogeneity. The color blocks in the figure indicate that chemical inhomogeneity decreases as the color approaches dark blue and increases as the color approaches dark green. The optimal position is near dark blue.

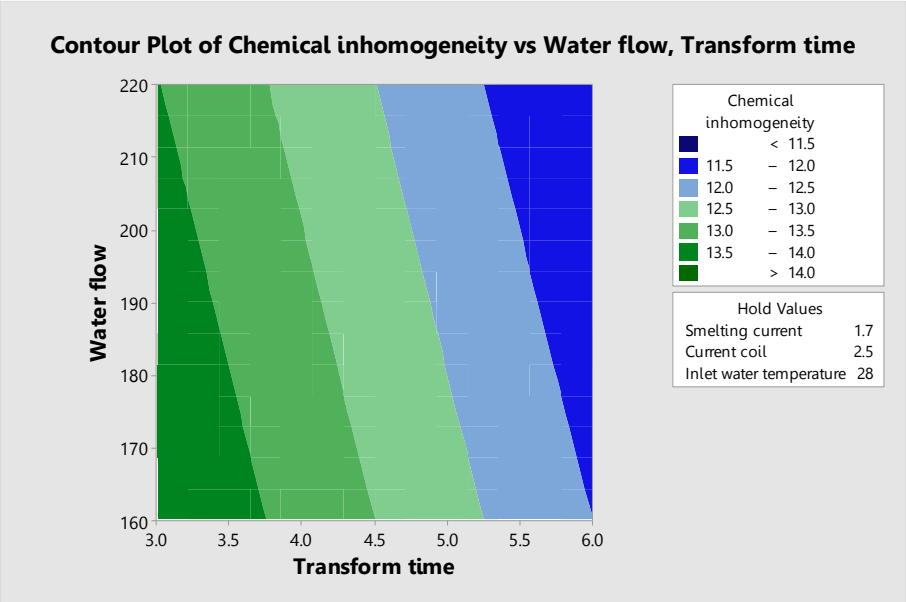

Figure 17. Contour Plot of Water Flow and Transformation Time as a Function of Chemical Inhomogeneity.

Figure 17 shows that Water Flow and Transformation Time are inversely proportional. Increasing Transformation Time and Water Flow reduces Chemical Inhomogeneity. The color blocks in the figure indicate that the closer to dark blue, the lower the Chemical Inhomogeneity, the closer to dark green, the higher the Chemical Inhomogeneity, with the optimal value near dark blue. The two figures above demonstrate the relationship between adjustments to production parameters and Transformation Time. They also illustrate the relationship between other production parameters and Transformation Time. Transformation Time is inversely proportional to Inlet Water Temperature and directly proportional to Water Flow. Analysis of the slopes of these linear relationships indicates that these parameters have essentially the same influence. Companies can select production parameter adjustment methods based on chemical inhomogeneity requirements and specific color blocks. Figure 18 shows that Water Flow and Inlet Water Temperature are inversely proportional. Increasing Water Flow and decreasing Inlet Water Temperature reduce Chemical Inhomogeneity. The color blocks in the figure indicate that chemical inhomogeneity decreases as the color approaches dark blue and increases as the color approaches dark green. The optimal value is near dark blue. The figure above illustrates the relationship between adjustments to production parameters and Inlet Water Temperature. It also demonstrates the relationship between other production parameters and Inlet Water Temperature, which is inversely proportional to Water Flow. Analysis of the slopes of these linear relationships indicates that these parameters have essentially the same influence. Companies can choose production parameter adjustment methods based on chemical inhomogeneity requirements and specific color blocks. As shown in the figures above, the contour map of the Ti-45Nb titanium alloy production conditions clearly illustrates the relationship between the model's production process parameters and the product's chemical heterogeneity. The influence of different parameters on the product and on each other can be observed more intuitively. The trend of product chemical heterogeneity with respect to production process parameters under the corresponding conditions can also be examined for any parameter in the figure, providing a comprehensive foundation and subsequent ideas for related titanium alloy research, as well as detailed parameters and production guidance for other titanium alloy enterprises.

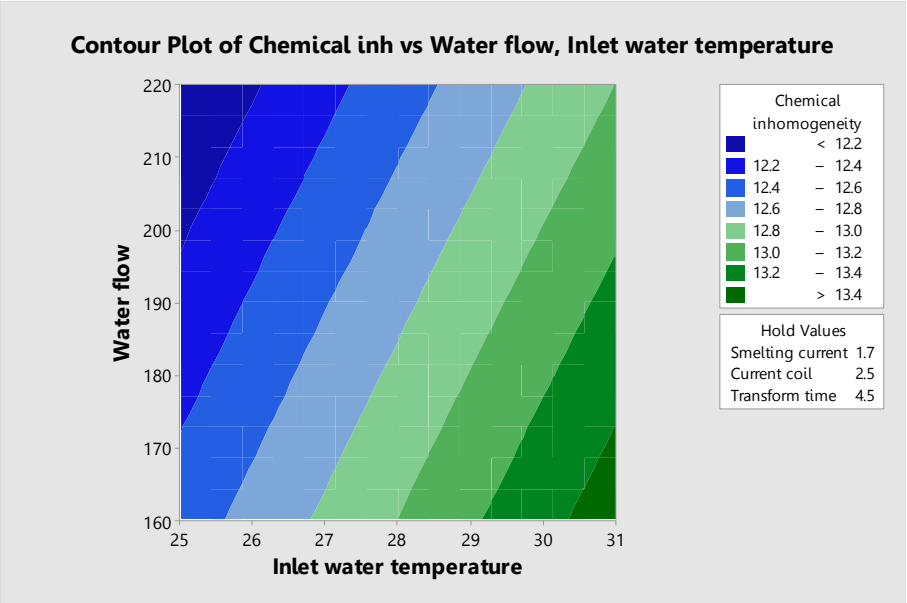

Figure 18. Contour Plot of Water Flow and Inlet Water Temperature with Respect to Chemical Inhomogeneity.

4. Conclusions

The residual plot analysis indicated that the data from the 2^k full factorial experimental design in the DOE were accurate and suitable for analysis, underscoring the applicability of this design for analyzing and optimizing Ti-45Nb titanium alloy production experiments. At a significance level of α = 0.05, the model explains nearly all the total variation, indicating effectiveness; the sum of squares of error and mean square error are small, indicating that the experimental design and model fitting are accurate. Response Optimizer analysis shows that after optimizing target yield, the optimal values of the main factors are as follows: Smelting current (KA) = 1.7, Current coil (A) = 3.2542, Transform time (S) = 6, Inlet water temperature (°C) = 25, and Water flow (L/min) = 220. Under these conditions, the chemical inhomogeneity of the produced Ti-45Nb titanium alloy is theoretically 10%. Manufacturers can use the results of this study, along with yield targets, to determine optimal operating conditions and optimize the production process for the Ti-45Nb alloy.

5. Acknowledgements

The authors would like to thank the Department of Industrial Technology Management, Faculty of Industrial Technology, Muban Chombueng Rajabhat University, for supporting the research tools used in this research.

Author Contributions: B.L: Conceptualization, methodology, literature review, data collection, recording, discussion, interpretation of results, and critiquing; A.S: Conceptualization, methodology, and literature review; N.A: Conceptualization, methodology, literature review, proofreading, validation, and editing. All authors have read and approved the published version of the manuscript.

Funding: This research received no external funding.

Conflicts of Interest: The authors declare no conflict of interest.

References

[1] Gosavi, S.; Gosavi, S.; Alla, R. Titanium: A Miracle Metal in Dentistry. *Trends Biomater. Artif. Organs* **2013**, *27*(1), 42–46.

[2] Peters, M.; Kumpfert, J.; Ward, C. H.; Leyens, C. Titanium Alloys for Aerospace Applications. *Adv. Eng. Mater.* **2003**, *5*(6), 419–427. https://doi.org/10.1002/adem.200310095

[3] Kumpfert, J.; Leyens, C. Orthorhombic Titanium Aluminides: Intermetallics with Improved Damage Tolerance. In *Titanium and Titanium Alloys: Fundamentals and Applications*; Leyens, C., Peters, M., Eds.; Wiley-VCH: Weinheim, Germany, **2003**; pp 59–88. https://doi.org/10.1002/3527602119.ch3

[4] Luo, Y. Biotribology. In *Biotribology*; Davim, J. P., Ed.; ISTE-Wiley: London, **2010**; p 157.

[5] Ribeiro, M. V.; Moreira, M. R.; Ferreira, J. R. Optimization of Titanium Alloy (6Al–4V) Machining. *J. Mater. Process. Technol.* **2003**, *143*, 458–463. https://doi.org/10.1016/S0924-0136(03)00457-6

[6] Rahman, M.; Wang, Z. G.; Wong, Y. S. A Review on High-Speed Machining of Titanium Alloys. *JSME Int. J., Ser. C* **2006**, *49*(1), 11–20. https://doi.org/10.1299/jsmec.49.11

[7] Donachie, M. J. *Titanium: A Technical Guide*, 2nd ed.; ASM International: Materials Park, OH, **2000**.

[8] Veiga, C.; Davim, J. P.; Loureiro, A. J. Properties and Applications of Titanium Alloys: A Brief Review. *Rev. Adv. Mater. Sci.* **2012**, *32*(2), 133–148.

[9] Sverdrup, H. U.; Sverdrup, A. E. An Assessment of the Global Supply, Recycling, Stocks in Use and Market Price for Titanium Using the WORLD7 Model. *Sustain. Horizons* **2023**, *7*, 100067. https://doi.org/10.1016/j.horiz.2023.100067

[10] Hu, N.; Xie, L.; Liao, Q.; Gao, A.; Zheng, Y.; Pan, H.; Tong, L.; Yang, D.; Gao, N.; Starink, M. J.; Chu, P. K. A More Defective Substrate Leads to a Less Defective Passive Layer: Enhancing the Mechanical Strength, Corrosion Resistance and Anti-Inflammatory Response of the Low-Modulus Ti-45Nb Alloy by Grain Refinement. *Acta Biomater.* **2021**, *126*, 524–536. https://doi.org/10.1016/j.actbio.2021.02.045

[11] Zhang, L. C.; Chen, L. Y. A Review on Biomedical Titanium Alloys: Recent Progress and Prospect. *Adv. Eng. Mater.* **2019**, *21*(4), 1801215. https://doi.org/10.1002/adem.201801215

[12] Gepreel, M. A.; Niinomi, M. Biocompatibility of Ti-Alloys for Long-Term Implantation. *J. Mech. Behav. Biomed. Mater.* **2013**, *20*, 407–415. https://doi.org/10.1016/j.jmbbm.2012.11.014

[13] Niinomi, M. Recent Research and Development in Titanium Alloys for Biomedical Applications and Healthcare Goods. *Sci. Technol. Adv. Mater.* **2003**, *4*(5), 445–454. https://doi.org/10.1016/j.stam.2003.09.002

[14] *Titanium and Titanium Alloys: Fundamentals and Applications*; Leyens, C., Peters, M., Eds.; Wiley-VCH: Weinheim, Germany, **2003**. https://onlinelibrary.wiley.com/doi/book/10.1002/3527602119 (accessed 2022-09-26).

[15] Li, Y.; Yang, C.; Zhao, H.; Qu, S.; Li, X.; Li, Y. New Developments of Ti-Based Alloys for Biomedical Applications. *Materials* **2014**, *7*(3), 1709–1800. https://doi.org/10.3390/ma7031709

[16] Patel, D.; Kim, S. H.; Qiu, W.; Maeda, M.; Matsumoto, A.; Nishijima, G.; Kumakura, H.; Choi, S.; Kim, J. H. Niobium-Titanium (Nb-Ti) Superconducting Joints for Persistent-Mode Operation. *Sci. Rep.* **2019**, *9*(1), 14287. https://doi.org/10.1038/s41598-019-50549-7

[17] El Khalloufi, M.; Drevelle, O.; Soucy, G. Titanium: An Overview of Resources and Production Methods. *Minerals* **2021**, *11*(12), 1425. https://doi.org/10.3390/min11121425

[18] Durakovic, B. Design of Experiments Application, Concepts, Examples: State of the Art. *Period. Eng. Nat. Sci.* **2017**, *5*(3), 421–439. https://doi.org/10.21533/pen.v5i3.145

[19] Sreela-or, C.; Tharungsri, P.; Yamkong, S.; Kotam, P.; Jaipong, P. Optimum Conditions of Using Bio-Extract from Urine with Vinasse and Manure Affecting Yields of Marigold. *Life Sci. Environ. J.* **2022**, *23*(2), 283–296 (in Thai). https://doi.org/10.14456/lsej.2022.22

[20] Sonsiri, A.; Palicamin, P.; Amdee, N. Development of Plastic Green Composite for Vacuum Mold Process. *FEAT J. Farm Eng. Autom. Technol. J.* **2021**, *7*(1), 1–9 (in Thai). https://doi.org/10.14456/lsej.2024.25

ASEAN
Journal of Scientific and Technological Reports
Online ISSN:2773-8752

Research article

Humanitarian Logistics Modelling for Flood Disaster Management in Thailand

Rojanee Homchalee[1], Chanipa Uthaipan[2], and Orawich Kumphon[1*]

[1] Faculty of Science, Mahasarakham University, Maha Sarakham, 44150, Thailand
[2] Office of Strategy and Data Analytics, University of the Thai Chamber of Commerce, Bangkok, 10400, Thailand
* Correspondence: orawich.k@msu.ac.th

Citation:
Homchalee, R.; Uthaipan, C.; Kumphon, O. Humanitarian Logistics Modelling for Flood Disaster Management in Thailand. *ASEAN J. Sci. Tech. Report.* **202**6, *29*(3), e261462. https://doi.org/10.55164/ajstr.v29i3.261462.

Article history:
Received: September 23, 2025
Revised: November 29, 2025
Accepted: December 3, 2025
Available online: February 27, 2026

Abstract: Nowadays, many areas in Thailand have experienced severe flood disasters that have widespread effects on life, property, society, economy, and the environment. Therefore, this research aims to develop a mathematical model for humanitarian logistics management in Thailand's flood-affected areas. Two models were developed using mixed-integer nonlinear programming: one to minimize the total cost of disaster relief management, and another to maximize the number of rescued disaster victims, with operating costs as a constraint, because in some situations there was a limited budget for helping victims. The two proposed models provided disaster preparedness planning by identifying optimal shelter locations, determining appropriate quantities of relief supplies to procure, and allocating and distributing those supplies efficiently to affected victims.

Keywords: Humanitarian logistics; flood disaster; mixed integer nonlinear programming

1. Introduction

Disaster is a severe disruption of the functioning of a community or society that has widespread effects on life, property, society, the economy, and the environment, beyond the affected community or society's ability to cope with available resources [1]. Disaster may arise from natural or artificial causes. A flood is a disaster caused by inundation, flash flooding, or water from rivers, streams, or waterways, all driven by excessive water volume, and may occur as flooding, flash floods, or related events. It is a natural disaster that lies largely beyond human control [2, 3]. Thailand has experienced numerous flooding incidents during 2011-2013 and 2024, which have had a significant impact on people and property, especially during the rainy season in lowlands, hillsides, and riverbanks. However, disaster management capacity across government agencies and local communities remains insufficient to cope with such events effectively. Cotes and Cantillo [4] reported that a survey of public opinion on the government's flood management between 2011 and 2013 revealed that assistance to flood victims was duplicated and unevenly distributed. Humanitarian logistics is the management of the logistics process for providing disaster relief. The procurement of products and services is a critical and challenging process for humanitarian organizations, accounting for approximately 65 percent of total relief operation costs [5].

Humanitarian logistics plays a crucial role in disaster relief and resource management and can be divided into two types: continuous aid work and disaster relief, whether natural or man-made. Therefore, humanitarian logistics

is the process of planning, implementing, and controlling the flow of materials and information from the point of origin to the point of need efficiently and cost-effectively to provide relief to those affected [6,7]. Cotes and Cantillo [4] developed a model of facility location for disaster preparedness, aiming to minimize the total social cost. The amount of relief supplies per type is determined in advance and is available in the disaster-affected area during the initial disaster response phase. The model also focuses on the immediate assistance that should be provided within the first 24 hours, using real data from the Caribbean region of Colombia, which was affected by floods in 2010 and 2011. Bozorgi-Amiri et al. [8] presented a robust multi-objective stochastic model for disaster relief logistics that considers uncertain resource demand, procurement costs, and transportation costs. The model objective is to minimize the total cost and the variation in the maximum shortage in the affected area of the earthquake event in Iran. The results showed that the proposed model can support decision-making on location and resource allocation in earthquake relief. In addition, Rodríguez-Espíndola et al. [9] applied logistics to resource management for disaster relief and appropriate operational planning, combining an optimization model with GIS. A bi-objective optimization model was developed to identify the locations of emergency facilities, the amount of stockpiled resources, and the allocation and distribution of resources, along with the number of actors involved in disaster management operations, using real data from the 2013 flood in Acapulco, Mexico.

Rodríguez-Espíndola et al. [10] reviewed a wide range of literature on the application of mathematical models in humanitarian logistics management, finding that most research covers both logistics and supply chain management, and aims to minimize overall costs. Some research aims to minimize processing times, particularly in the transportation of relief goods and disaster victims [11], while other research focuses on developing multi-objective models and applying heuristics [12]. In addition, some research involves simulations or decision support systems to plan for disaster preparedness [13]. A wide range of mathematical models has been applied to disaster management, including single-objective and multi-objective models with nonlinear programming (NLP) [10, 14-16], integer nonlinear programming (INLP), where decision variables are set to integers and the objective function is nonlinear [17], and mixed-integer nonlinear programming (MINLP) [18]. Models for humanitarian logistics management may include either continuous or integer decision variables to determine the location of shelters, the allocation and distribution of relief supplies, and the allocation of resources. Under disaster conditions, this study addresses two research questions: (1) What is the minimum total cost required for effective disaster management? and (2) How can the number of rescued disaster victims be maximized under budgetary constraints?

Accordingly, this research aims to develop a mathematical model for humanitarian logistics management during flooding in Thailand, supporting disaster preparednessby optimizing facility location decisions and resource allocation. The paper is organized as follows: Section 2 introduces the analytical concepts, materials, and methods; Section 3 describes the MINLP models developed for humanitarian logistics. Section 4 applies the models to a real flood-affected area, with accompanying sensitivity analysis, and Section 5 concludes with the key findings and discussion.

2. Materials and Methods

The mathematical models for humanitarian logistics management were developed from two models: Model I aims to minimize the total cost of disaster relief management, and Model II aims to maximize the number of rescued disaster victims. This design concept is not only focused on a single objective but also consistent with the general situation in disaster management, which often has limited budgets. The research procedure is shown in Figure 1. The two proposed models consider constraints on the number of disaster victims and the disaster area, including the habitable disaster-affected area that requires essential relief supplies and the uninhabitable disaster-affected area, where disaster victims must be moved to different temporary shelters. Each shelter can accommodate different numbers of disaster victims. Moreover, the model also considers constraints on the types and capacities of vehicles for transporting disaster victims and relief supplies, as well as on the supply of relief supplies at a given price. The developed mathematical models have an objective function given by Equation (1) and several nonlinear constraints. Therefore, a mixed-integer nonlinear programming (MINLP) approach was used. In Model II, the value of the budget constraints is set

from the objective function result of Model I, and sensitivity analysis is performed with various levels of budget, which vary to decrease for each scenario to consider the effect on the value of the objective function, that is, the number of flood victims rescued and receiving relief supplies. Furthermore, the effect on the decision variables, number of relief supplies procured, and number of shelters open, is also considered. This analysis provides insight into operational trade-offs under financial limitations.

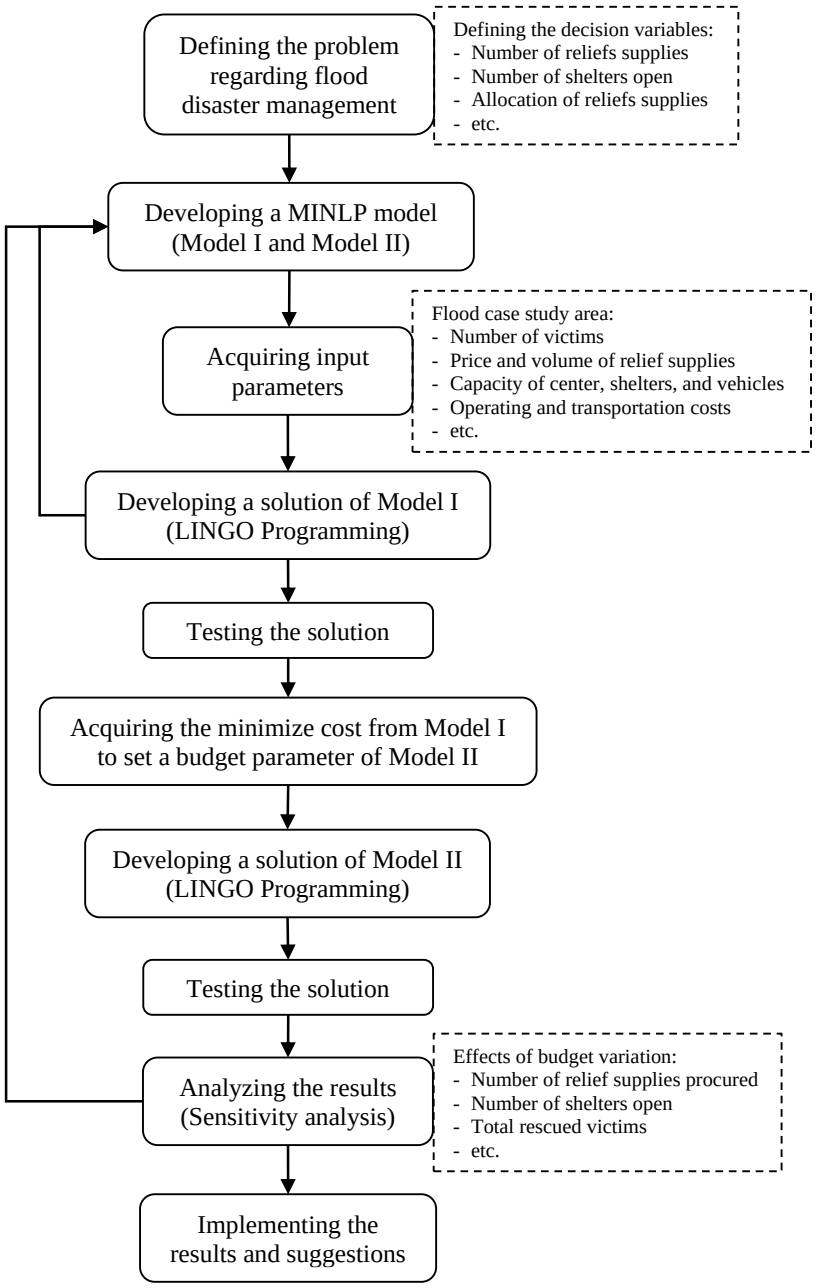

Figure 1. The research procedure.

3. Humanitarian Logistics Models

Two mathematical models for humanitarian logistics management were developed using mixed integer nonlinear programming (MINLP) with the following indexes, decision variables, parameters, and model structure.

Indexes:

i Relief distribution center
j Shelter
k Habitable disaster-affected area
o Uninhabitable disaster-affected area
m Vehicle type for transporting reliefs
n Vehicle type for transporting disaster victims

Decision variables:

Y_j Opening the shelter j
H_i Number of relief supplies to be purchased and stored at the distribution center i (bags)
XK_{ik} Habitable disaster-affected area k that receives relief supplies from the distribution center i
XJ_{ij} Shelters j that receive relief supplies from the distribution center i
Z_k Number of victims in habitable disaster-affected area k that receive relief supplies (people)
Z_j Number of victims in the shelter j that receive relief supplies (people)
NOJ_{ojn} Number of victims in the uninhabitable disaster-affected area o who were transported to the shelter j by vehicle type n (people)
NJ_{ijm} Number of relief supplies transported from the distribution center i to the shelter j by vehicle type m (bags)
NK_{ikm} Number of relief supplies transported from the distribution center i to habitable disaster-affected area k by vehicle type m (bags)

Parameters:

CX_i Operating cost of relief distribution center i (baht)
CY_j Operating cost of shelter j (baht)
Pr Price of relief supplies (baht per bag)
CTM_m Transportation cost of relief supplies by vehicle type m (baht per kilometer)
CTN_n Transportation cost of victims by vehicle type n (baht per kilometer)
NE Number of victims per unit of relief supplies (people)
P_k Number of victims in habitable disaster-affected area k (people)
P_o Number of victims in uninhabitable disaster-affected area o (people)
VOL Volume per bag of relief supplies (m^3)
α Weight per bag of relief supplies (kg)
$CAPX_i$ Capacity of relief distribution center i (m^3)
$CAPY_j$ Capacity of shelter j (people)
$CAPM_m$ Capacity of the vehicle type m used for transporting relief supplies (kg)
$CAPN_n$ Capacity of the vehicle type n used for transporting disaster victims (people)
DXK_{ik} Distance from relief distribution center i to habitable disaster-affected area k (km)
DXY_{ij} Distance from relief distribution center i to shelter j (kilometers)
DOJ_{oj} Distance from uninhabitable disaster-affected area o to shelter j (km)
M The positive large number

3.1 Model I

The objective of the model is to minimize the overall cost of disaster relief management, as shown in Equation (1), which includes the cost of relief goods, the cost of operating relief distribution centers, the cost of operating shelters, the cost of transporting disaster victims, and the cost of transporting relief supplies.

$$\begin{aligned} Minimize\,Total\,Cost \;=\; & \sum_{i=1}^{I} PrH_i + \sum_{i=1}^{I} CX_i + \sum_{j=1}^{J} CY_j Y_j + \sum_{o=1}^{O}\sum_{j=1}^{J}\sum_{n=1}^{N} \frac{CTN_n DOJ_{oj} NOJ_{ojn}}{CAPN_n} \\ & + \sum_{i=1}^{I}\sum_{j=1}^{J}\sum_{m=1}^{M} \frac{CTM_m DXY_{ij}(\alpha NJ_{ijm})}{CAPM_m} + \sum_{i=1}^{I}\sum_{k=1}^{K}\sum_{m=1}^{M} \frac{CTM_m DXK_{ik}(\alpha NK_{ikm})}{CAPM_m} \end{aligned} \tag{1}$$

Subject to

$$\sum_{i=1}^{I} XK_{ik} = 1 \qquad ;\forall k \tag{2}$$

$$\sum_{j=1}^{J} Y_j \geq 1 \tag{3}$$

$$\sum_{i=1}^{I} XJ_{ij} = Y_j \qquad ;\forall j \tag{4}$$

$$H_i VOL \leq CAPX_i \qquad ;\forall i \tag{5}$$

$$\sum_{i=1}^{I} H_i \geq \sum_{i=1}^{I}\sum_{j=1}^{J}\sum_{m=1}^{M} NJ_{ijm} XJ_{ij} + \sum_{i=1}^{I}\sum_{k=1}^{K}\sum_{m=1}^{M} NK_{ikm} \tag{6}$$

$$\sum_{i=1}^{I}\sum_{m=1}^{M} NJ_{ijm} XJ_{ij} \leq M(Y_j) \qquad ;\forall j \tag{7}$$

$$\sum_{j=1}^{J}\sum_{n=1}^{N} NOJ_{ojn} Y_j = P_o \qquad ;\forall o \tag{8}$$

$$\sum_{o=1}^{O}\sum_{n=1}^{N} NOJ_{ojn} \leq CAPY_j(Y_j) \qquad ;\forall j \tag{9}$$

$$\sum_{i=1}^{I}\sum_{m=1}^{M} NJ_{ijm} XJ_{ij} \geq \frac{\sum_{o=1}^{O}\sum_{n=1}^{N} NOJ_{ojn} Y_j}{NE} \qquad ;\forall j \tag{10}$$

$$\sum_{o=1}^{O}\sum_{n=1}^{N} NOJ_{ojn} Y_j \geq Z_j \qquad ;\forall j \tag{11}$$

$$\sum_{i=1}^{I}\sum_{m=1}^{M} NK_{ikm} \geq \frac{Z_k}{NE} \quad ;\forall k \tag{12}$$

$$\sum_{j=1}^{J} Z_j Y_j = \sum_{o=1}^{O} P_o \tag{13}$$

$$Z_k = P_k \quad ;\forall k \tag{14}$$

$$Y_j \in \{0,1\} \quad ;\forall j \tag{15}$$

$$XK_{ik} \in \{0,1\} \quad ;\forall i, \forall k \tag{16}$$

$$XJ_{ij} \in \{0,1\} \quad ;\forall i, \forall j \tag{17}$$

$$H_i \geq 0 \text{ and integer} \quad ;\forall i \tag{18}$$

$$Z_k \geq 0 \text{ and integer} \quad ;\forall k \tag{19}$$

$$Z_j \geq 0 \text{ and integer} \quad ;\forall j \tag{20}$$

$$NOJ_{ojn} \geq 0 \text{ and integer} \quad ;\forall o, \forall j, \forall n \tag{21}$$

$$NJ_{ijm} \geq 0 \text{ and integer} \quad ;\forall i, \forall j, \forall m \tag{22}$$

$$NK_{ikm} \geq 0 \text{ and integer} \quad ;\forall i, \forall k, \forall m \tag{23}$$

The constraint, as Equation (2) shows, is that the habitable disaster-affected area does not receive relief supplies from duplicate distribution centers. Shelters are opened to accommodate the number of victims affected by uninhabitable areas, as shown in Equation (3). Equation (4) shows that relief supplies are transported from distribution centers to open shelters. The number of relief supplies to be purchased must not exceed the storage capacity of each relief distribution center, and the total number of relief supplies to be purchased must be able to meet the relief needs of both the habitable disaster-affected areas and the needs of the shelters, as shown in Equation (5) and Equation (6), respectively. Sufficient relief supplies will be transported to the open shelters as in Equation (7). All victims in the uninhabitable disaster-affected area will be moved to open shelters, and the number of victims that move to the opened shelter must not exceed that shelter's capacity, as shown in Equation (8) and Equation (9), respectively. The constraint, as shown in Equation (10), is that the number of relief supplies transported to the opened shelter must be sufficient to meet the shelter's relief needs. This corresponds to Equation (11), which shows that the number of victims in the uninhabitable disaster-affected areas who have been moved to the opened shelters must receive relief supplies. Equation (12) shows that the number of relief supplies transported to habitable disaster-affected areas must be sufficient to meet that area's relief needs. Moreover, all victims in the uninhabitable disaster-affected areas must have been moved to open shelters and must have received relief supplies. All victims in each habitable disaster-affected area must receive relief supplies, as shown in Equation (13) and Equation (14), respectively. In addition, Equations (14)-(17) show the binary variables, and Equations (18)-(23) show the non-negative integer variables.

3.2 Model II

The objective of the model is to maximize the number of rescued disaster victims under a specified budget constraint, as shown in Equation (24), which refers to the number of disaster victims who receive relief supplies, including both those in habitable disaster-affected areas and those in shelters who have been moved from the uninhabitable disaster-affected areas.

$$Maxmize\ Rescued\ Victims = \sum_{k=1}^{K} Z_k + \sum_{j=1}^{J} Z_j \tag{24}$$

Subject to

Equation (2)-(13), Equation (15)-(23), Equation (25) and Equation (26)

$$\left(\begin{array}{l} \sum_{i=1}^{I} PrH_i + \sum_{i=1}^{I} CX_i + \sum_{j=1}^{J} CY_j Y_j + \sum_{o=1}^{O}\sum_{j=1}^{J}\sum_{n=1}^{N} \frac{CTN_n DOJ_{oj} NOJ_{ojn}}{CAPN_n} \\ + \sum_{i=1}^{I}\sum_{j=1}^{J}\sum_{m=1}^{M} \frac{CTM_m DXY_{ij}(\alpha NJ_{ijm})}{CAPM_m} + \sum_{i=1}^{I}\sum_{k=1}^{K}\sum_{m=1}^{M} \frac{CTM_m DXK_{ik}(\alpha NK_{ikm})}{CAPM_m} \end{array} \right) \leq Budget \tag{25}$$

$$Z_k \leq P_k \qquad ;\forall k \tag{26}$$

In addition, the total cost of disaster relief management is set as a constraint, as in Equation (25). The total cost must not exceed the available budget, which includes the cost of relief supplies, operating relief distribution centers, operating shelters, transporting disaster victims, and transporting relief supplies. Due to limited budgets, appropriate decisions must be made to help victims as much as possible. Moreover, the constraint of Equation (14) is adjusted to Equation (26) to relax the constraint in such a limited budget. Not all victims in each habitable disaster-affected area can receive relief supplies, but all victims in uninhabitable disaster-affected areas must have been moved to open shelters and must receive relief supplies. Other conditions remain the same as in Model I.

4. Case Study and Results

The developed MINLP models were applied to flooding scenarios in Kantharawichai District, Maha Sarakham Province, Thailand. The study area is a water collection point between two reservoirs, which experienced flooding approximately 500 times: 269 floods, 209 overflows, and 22 flash floods during 2012-2020 [19, 20] and consists of 10 sub-districts, 183 villages, and a total population of 82,764. Based on historical disaster records, 180 villages (k1-k180, with 82,194 victims) were classified as habitable disaster-affected areas, while 3 villages (o1-o3, with 570 victims) were classified as uninhabitable and requiring evacuation, as shown in Figure 2. The model parameters are shown in Table 1. The application of the developed MINLP model to the disaster area has the following important assumptions or limitations:

1. There are two centers for distributing relief supplies, namely the Provincial Disaster Prevention and Mitigation Office (i1) and the District Office (i2).

2. There are 19 alternative shelters (j1-j19), which are the locations of various government agencies such as schools and temples.

3. The transportation of disaster victims and relief supplies will be used only by trucks.

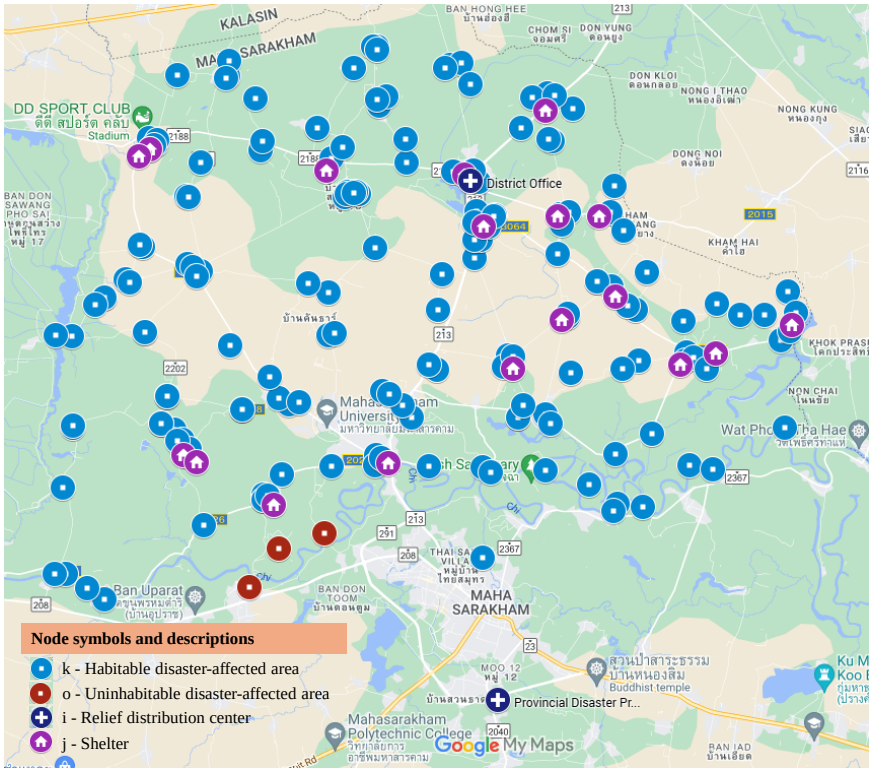

Figure 2. Case study map of flood disaster-affected area in Kantharawichai District, Maha Sarakham Province, Thailand.

Table 1. Model parameter values under flood disaster scenarios in the case study area.

Parameters	Values	Unit	Source
Operating cost of relief distribution centers	25,000-30,000	baht	Department of Disaster Prevention and Mitigation [19, 20]
Operating cost of shelters	28,000-80,000	baht	
Capacity of the relief distribution center	400-500	m^3	
Capacity of shelter	500-1,000	people	
Price of relief supplies	500	baht per bag	
Volume per bag of relief supplies	0.02	m^3	
Number of victims per unit of relief supplies	2	people	
Weight per bag of relief supplies	3	kg	
Capacity of vehicles for transporting relief supplies	1,000-10,000	kg	
The capacity of the vehicle for transporting disaster victims	6-12	people	
Number of victims in the habitable disaster-affected area	97-9,325	people	Department of Provincial Administration [21]
Number of victims in the uninhabitable disaster-affected area	164-216	people	
Transportation cost of relief supplies	11-22.5	baht per km	GIZTIX Co., Ltd. [22]
Transportation cost of victims	11-22.5	baht per km	
Distance from the relief distribution center to the habitable disaster-affected area	0.5-36.3	km	Google maps
Distance from the relief distribution center to the shelter	0.41-30	km	
Distance from the uninhabitable disaster-affected area to the shelter	5-28	km	

4.1 Results of Model I

The developed Model I was processed using LINGO 13.0 by an AMD Ryzen 7 processor (2.00 GHz) with 16.0 GB of RAM. Under the problem size of 1,804 variables and 464 equations constraints, with a computation time of approximately one second, as shown in Figure 3. The optimal solution yielded a minimum total disaster management cost of 20.941 million baht, enabling the provision of relief supplies to all 82,764 victims.

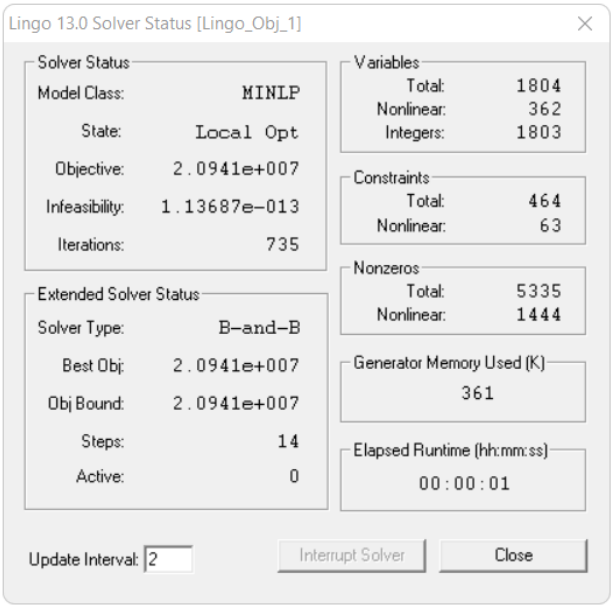

Figure 3. Processing results of Model I.

For the opening of shelters, it was found that three shelters should be opened: 1) Shelter j6, accommodating 164 victims from Village o1; 2) Shelter j11, accommodating 190 victims from Village o2; and 3) Shelter j19, accommodating 216 victims from Village o3. Victims should be transported to shelters by 4-wheel trucks. In addition, the results also found that the relief distribution centers, the Provincial Disaster Prevention and Mitigation Office (i1) and the District Office (i2) should procure 25,000 and 16,428 bags of relief supplies, respectively, totaling 41,428 bags. The i1 and i2 distribution centers distributed relief supplies to the 180 villages that were habitable disaster-affected areas. In comparison, the three villages that were uninhabitable disaster-affected areas received relief goods from the i2 distribution center using 6-wheel and 10-wheel trucks, which had a large capacity to transport relief supplies from the distribution centers to the disaster areas. The results are summarized in Figure 4.

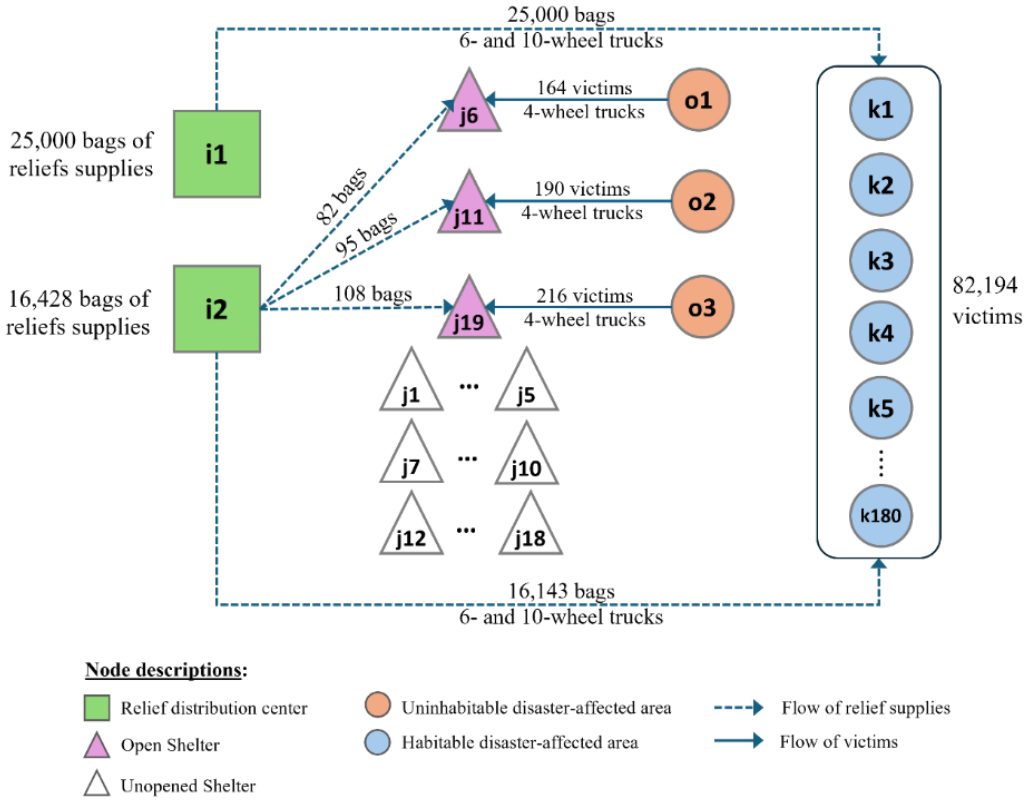

Figure 4. Summary results of Model I.

4.2 Results of Model II

Using the minimum cost from Model I as a budget reference, which has the lowest total disaster management cost of 20.941 million baht, it will be able to help all disaster victims and receive relief supplies. Model II was first solved under a 20 million baht budget, which found that 79,203 disaster victims out of a total of 82,764 could be helped, as shown in Figure 5.

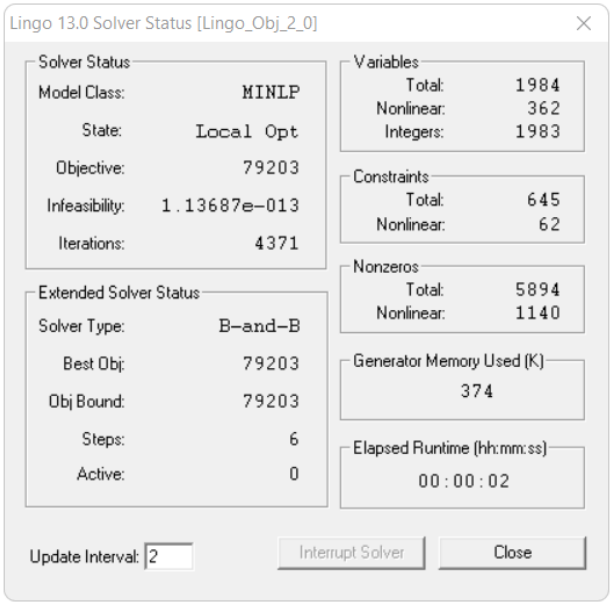

Figure 5. Processing results of Model II with a budget constraint of 20 million baht.

There are 5 villages in the habitable disaster-affected areas that will not be receiving relief supplies: k111, k112, k113, k118, and k120, which are remote villages from the relief distribution center. The result is consistent with the total procurement of relief supplies by the two distribution centers, which was only 39,679 bags. Only one shelter, j18, was opened to accommodate 570 people in the three uninhabitable villages. For transporting disaster victims to shelters, 4-wheel trucks should be used; for transporting relief goods from distribution centers to disaster areas and shelters, 6- and 10-wheel trucks should be used, yielding the same result as Model I. A sensitivity analysis was conducted by reducing the budget by 1 million baht in each scenario (Table 2 and Figures 6-8). As the budget decreased, the number of relief supplies procured declined, and the number of villages not receiving relief increased. However, under the conditions that stipulate all disaster victims in uninhabitable areas must be rescued by moving to appropriate temporary shelters, only one shelter opens, and its location differs in each scenario. The number of victims in habitable disaster-affected areas who did not receive relief supplies has increased, as mentioned above. It was also found that some villages received no relief supplies at all.

Table 2. Summary results of Model I and Model II.

Model	Cost or Budget (Million Baht)	Number of relief supplies procured	Number of shelters open	Number of victims receiving relief supplies			Unrelieved villages
				At shelters	At villages	Total	
Model I	20.941	41,428	3	570	82,194	82,764	-
Model II	20	39,679	1	570	78,633	79,203	5
	19	37,704	1	570	74,764	75,334	11
	18	35,704	1	570	70,768	71,338	21
	17	33,773	1	570	66,910	67,480	30
	16	31,608	1	570	62,645	63,215	38
	15	29,728	1	570	58,821	59,391	39

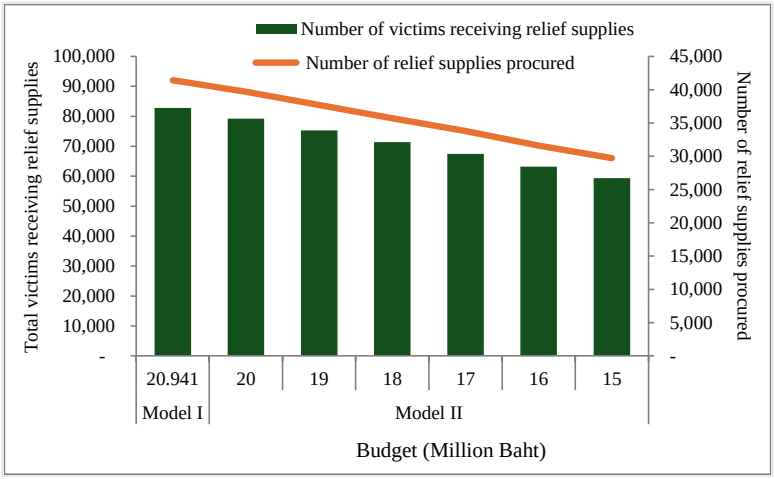

Figure 6. Total victims receiving relief supplies and relief supplies procured when varying the budget.

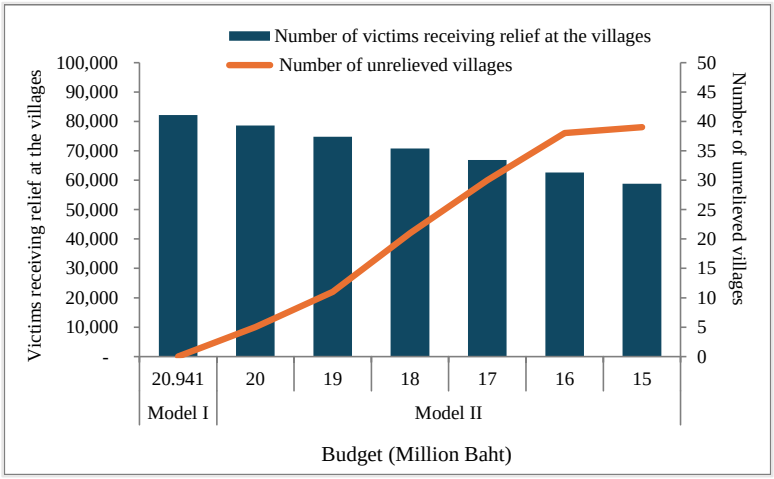

Figure 7. The number of victims receiving relief in villages and in unrelieved villages varies with the budget.

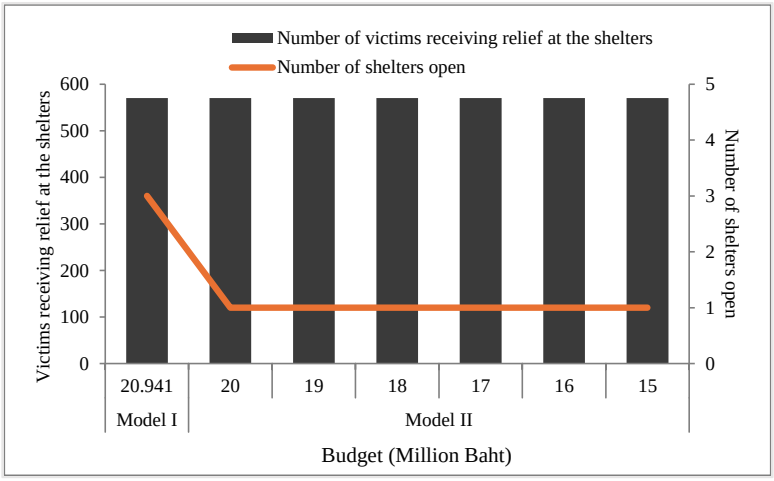

Figure 8. The number of shelters open and the number of victims receiving relief supplies vary with the budget.

To strengthen disaster management under such conditions, flood, fires, or earthquakes [12], several complementary approaches may be considered. First, negotiating lower unit costs of relief supplies with vendors could reduce overall expenditure. Second, adjusting the allocation guideline to allow one relief bag to support two to three individuals instead of one may extend assistance coverage during the initial response phase, particularly during the first two to three days of an event [9, 10]. Additionally, mobilizing monetary donations or in-kind relief supplies, as well as recruiting volunteers to expedite emergency operations, can further enhance response capacity. The proposed models can assist government agencies, humanitarian organizations, and local authorities in preparing effective disaster-response strategies. They can also serve as decision-support tools for shelter planning, supply chain design, and emergency resource allocation. Future research may 1) extend the models to incorporate dynamic decision-making, time-dependent evacuation processes, multi-modal transportation options such as boats, helicopters, or drones during severe flooding [11], and real-time data integration through GIS and advanced analytics. 2) The other metaheuristic methods, Genetic algorithm, Swarm intelligence, etc., can be applied in case of complex problems and take a long time to find the optimal solution. 3) Simulation-based or AI-enhanced approaches could also be explored to increase model adaptability and provide real-time guidance during disaster events. 4) Do comparison; solutions and processing time, with the others using Lingo programming [11].

5. Conclusion

This study developed two MINLP-based models to support humanitarian logistics management in flood disaster settings. The objective of Model I is to minimize the total cost required to fully support all disaster victims, while the objective of Model II is to maximize the number of victims assisted when the available budget is limited. Applied to a real flood-prone district in Thailand, the models provided practical guidance on shelter location, relief-supply procurement, resource allocation, transportation planning, and operational efficiency. The findings indicate that a cost-minimization approach ensures full coverage but may require substantial financial resources, whereas a rescued disaster victims-maximization approach under budget constraints necessitates prioritization and trade-offs. Sensitivity analyses revealed that budget reductions disproportionately affect remote villages in habitable areas, underscoring the need for strategic planning, improved resource mobilization, and targeted support for hard-to-reach communities.

6. Acknowledgements

This research project was financially supported by Mahasarakham University. The facilities for this research were provided by the Applied Statistics Research Unit (Mahasarakham University). LINGO software was supported by the Supply Chain and Logistics Research Center (Khon Kaen University).

Author Contributions: Project administration, supervision, methodology, modelling, validation, and formal analysis, R.H. project resources and data curation, C.U. conceptualization, investigation, and writing original draft preparation, review, and editing, O.K. All authors have read and agreed to the published version of the manuscript.

Funding: The research fund was supported by Mahasarakham University.

Conflicts of Interest: The authors declare no conflict of interest.

References

[1] Department of Disaster Prevention and Mitigation. *Disaster Vocabulary*; 2011. http://www.disaster.go.th/th/ (accessed 2023-02-14).

[2] Thai Meteorological Department. *Meteorological Book*; 2019. https://www.tmd.go.th/info/subpage-info (accessed 2023-05-10).

[3] Carter, W. N. *Disaster Management: A Disaster Management Handbook*; Asian Development Bank: Mandaluyong City, Philippines, **2008**.

[4] Cotes, N.; Cantillo, V. Including Deprivation Costs in Facility Location Models for Humanitarian Relief Logistics. *Socio-Econ. Plann. Sci.* **2019**, *65*, 89–100. https://doi.org/10.1016/j.seps.2018.03.002

[5] Moshtari, M.; Altay, N.; Heikkilä, J.; Gonçalves, P. Procurement in Humanitarian Organizations: Body of Knowledge and Practitioner's Challenges. *Int. J. Prod. Econ.* **2021**, *233*, 108017. https://doi.org/10.1016/j.ijpe.2020.108017

[6] Bhimani, S.; Song, J. S. Gaps Between Research and Practice in Humanitarian Logistics. *J. Appl. Bus. Econ.* **2016**, *18* (1), 11–24.

[7] Yáñez-Sandivari, L.; Cortés, C. E.; Rey, P. A. Humanitarian Logistics and Emergencies Management: New Perspectives to a Sociotechnical Problem and its Optimization Approach Management. *Int. J. Disaster Risk Reduct.* **2021**, *52*, 101952. https://doi.org/10.1016/j.ijdrr.2020.101952

[8] Bozorgi-Amiri, A. J.; Saeed, M.; Al-e-Hashem, S. M. A Multi-objective Robust Stochastic Programming Model for Disaster Relief Logistics Under Uncertainty. *OR Spectrum* **2013**, *35*, 905–933. https://doi.org/10.1007/s00291-011-0268-x

[9] Rodríguez-Espíndola, O.; Albores, P.; Brewster, C. Disaster Preparedness in Humanitarian Logistics: A Collaborative Approach for Resource Management in Floods. *Eur. J. Oper. Res.* **2018**, *264*(3), 978–993. https://doi.org/10.1016/j.ejor.2017.01.021

[10] Rodríguez-Espíndola, O.; Ahmadi, H.; Gastélum-Chavira, D.; Ahumada-Valenzuela, O.; Chowdhury, S.; Dey, P. K.; Albores, P. Humanitarian Logistics Optimization Models: An Investigation of Decision-

maker Involvement and Directions to Promote Implementation. *Socio-Econ. Plann. Sci.* **2023**, *89*, 101669. https://doi.org/10.1016/j.seps.2023.101669

[11] Romero-Mancilla, M. S.; Hernandez-Ruiz, K. E.; Huerta-Muñoz, D. L. A Multi-objective Mathematical Model for a Humanitarian Logistics Multimodal Transportation Problem. *J. Humanit. Logist. Supply Chain Manag.* **2024**, *14*(2), 247–261. https://doi.org/10.1108/JHLSCM-01-2023-0004

[12] Shakibaei, H.; Moosavi, S. A.; Aghsami, A.; Rabbani, M. Designing a Sustainable-resilient Humanitarian Supply Chain for Post-disaster Relief Process, an Earthquake Case Study in Haiti. *J. Humanit. Logist. Supply Chain Manag.* **2024**, *14*(3), 349–368. https://doi.org/10.1108/JHLSCM-08-2023-0071

[13] Cavdur, F.; Sebatli, A. A Decision Support Tool for Allocating Temporary-disaster-response Facilities. *Decis. Support Syst.* **2019**, *127*, 113145. https://doi.org/10.1016/j.dss.2019.113145

[14] Kumar, S. A.; Suresh, N. *Production and Operations Management*; New Age International: New Delhi, **2008**.

[15] Gupta, S.; Starr, M. *Production and Operations Management Systems*; CRC Press: Florida, **2014**. https://doi.org/10.1201/b16470

[16] Render, B.; Stair, R.; Hanna, M. E. *Quantitative Analysis for Management*; Prentice Hall: New Jersey, **2012**.

[17] Soares, I.; Alves, M. J.; Antunes, C. H. A Deterministic Bounding Algorithm vs. a Hybrid Meta-heuristic to Deal with a Bilevel Mixed-integer Nonlinear Optimization Model for Dynamic Electricity Pricing. *Comput. Oper. Res.* **2023**, *155*, 106195. https://doi.org/10.1016/j.cor.2023.106195

[18] Aghsami, A.; Sharififar, S.; Markazi, M. N.; Hazrati, E.; Jolai, F.; Yazdani, R. Strategies for Humanitarian Logistics and Supply Chain in Organizational Contexts: Pre- and Post-Disaster Management Perspectives. *Systems* **2024**, *12*(6), 215. https://doi.org/10.3390/systems12060215

[19] Department of Disaster Prevention and Mitigation. *Citizens' Guide to Preparing for Disaster Safety*; Work Printing Co., Ltd.: Bangkok, **2017**.

[20] Department of Disaster Prevention and Mitigation. *Disaster Prevention and Mitigation Plan, Maha Sarakham Province*; 2020. https://www.disaster.go.th/th/download/download/25 (accessed 2023-05-15).

[21] Department of Provincial Administration. *Disaster Risk Area Information in Maha Sarakham Province*; 2022. https://opendata_tst.dopa.go.th/ (accessed 2023-08-25).

[22] GIZTIX Co., Ltd. *Transportation Service Rates*; 2023. https://giztix.com/pricing (accessed 2023-02-25).

ASEAN
Journal of Scientific and Technological Reports
Online ISSN:2773-8752

Research article

Physicochemical Properties of Carrageenan Extracted from Raw Dried Seaweed of Caluya, Antique, Philippines

Julie Ann Arcales-Quinal[1*], and Reyda Inolino[2]

[1] Faculty of Mercedes Campus, Samar State University, Catbalogan City, Samar, 6700, Philippines
[2] Faculty of New Washington Campus, Aklan State University, New Washington, Aklan, 5610, Philippines
* Correspondence: julieann.arcales@ssu.edu.ph

Citation:
Arcales-Quinal, J.; Inolino, R. Physicochemical properties of carrageenan extracted from raw dried seaweeds of Caluya, Antique, Philippines. *ASEAN J. Sci. Tech. Report.* **2026**, *29*(3), e259655. https://doi.org/10.55164/ajstr.v29i3.259655.

Article history:
Received: June 5, 2025
Revised: December 11, 2025
Accepted: January 11, 2026
Available online: February 27 , 2026

Publisher's Note:
This article has been published and distributed under the terms of Thaksin University.

Abstract: Marine hydrocolloids, such as carrageenan extracted from seaweeds, are widely used in food, industrial, and commercial applications. The Philippines has great potential to export carrageenan, but the industry requires strict quality regulations for the product. The specifications for raw dried seaweeds (RDS), including chemical and gel rheological properties, of *Eucheuma denticulatum* "*Milyon milyon*" and *Kappaphycus striatum* "*Sacol*", collected from Caluya, Antique, Philippines, were investigated and compared to the national standards used by the carrageenan production industry. The RDS (moisture, ash, clean anhydrous weed, impurities) of *E. denticulatum* and *K. striatum* were within the limits of the Philippine National Standards. The chemical properties (moisture, ash, acid-insoluble ash, and sulfate content) of carrageenan extracted from *E. denticulatum* were within the standards, except for the acid-insoluble ash and sulfate content of *K. striatum*, which exceeded the limit. On the other hand, the rheological properties of carrageenan, including gel viscosity, gelling and melting temperatures, and hysteresis, were also within the standard limits. The study suggests using RDS from *E. denticulatum* to produce carrageenan, as it complies with the Philippine National Standards utilized by the seaweed industry.

Keywords: Hydrocolloids; carrageenan; physicochemical properties; rheological properties

1. Introduction

Marine macroalgae, commonly known as seaweed, are primarily found in coastal regions and adhere to rocks and other rigid substrates. Many types of these plant-like organisms thrive in rivers, lakes, seas, and oceans [1]. In Asian nations, including China, Japan, and South Korea, seaweed has long been a staple food. This practice spread to other parts of the world, where eating seaweed is uncommon due to migration [2], prompting a global appreciation for seaweed as a vital component of a healthy diet. The widespread use of seaweed-derived hydrocolloids across dietary, industrial, and commercial applications has driven their growing popularity [3]. The three main hydrocolloids that provide different products with stabilizing, emulsifying, preserving, and textural improvements are agar, alginates, and carrageenan [4]. As a cheap source of these compounds, seaweeds are in worldwide demand. Among the three hydrocolloids, carrageenan is highly favored due to its flexibility and cheapness. This compound accounts for 18% of the global ingredient market, the highest among all [5]. In the local scene,

the Philippines is the leading carrageenan exporter in the world, exporting 94% of its seaweed production as Philippine Natural Grade (PNG) carrageenan, with significant markets in the USA, China, Spain, Russia, and Belgium [6].

A fair proportion of the country's seaweed production has been contributed by Western Visayas, or Region 6 [7]. The Province of Antique is the leading producer and is dubbed the "seaweed basket" of the region, with vast areas of seaweed farms located in the island municipality of Caluya, primarily culturing *Eucheuma* and *Kappaphycus* species [8, 9]. The RDS from the area are then transported to Cebu and Laguna for carrageenan processing. But to our knowledge, no work has been conducted to analyze the physical and chemical attributes of carrageenan extracted from the RDS in Caluya, Antique. Thus, the objective of this study was to determine whether the quality attributes of carrageenan extracted from the commonly cultured and dried seaweeds of Caluya, Antique complied with the Philippine Natural Grade (PNG) standard limit for carrageenan by conducting a physicochemical quality assessment.

2. Materials and Methods

2.1 Raw material

The RDS varieties of *Eucheuma denticulatum* "*Milyon milyon*" and *Kappaphycus striatum* "*Sacol*" were purchased from the island of Caluya, Antique, Philippines, where these species are abundantly cultivated. The seaweeds were grown in natural coastal seawater with an average salinity of 30–34 ppt, temperature of 28–31 °C, and moderate tidal water movement, conditions favorable for carrageenophyte production. Culture was conducted using the monoline hanging method for 1.5 months. Harvesting and sample collection were conducted during the dry season, specifically in March, to minimize the impact of rainfall and excessive moisture on the quality of the raw, dried seaweeds. After harvest, the seaweeds were thoroughly washed with seawater to remove foreign materials and epiphytes, and then dried using the conventional sun-drying method. The secondary information on culture and drying practices was obtained from the seaweed producer. One kilogram of dried samples per variety was packed in clean straw sacks and transported to the Fish Processing Laboratory at the University of the Philippines Visayas, Miagao, Iloilo, for laboratory analyses.

The study focused on the analysis of samples collected from Caluya, Antique, and its limitation was not comparing them to commercially available seaweed powder on the market.

2.2 Characterization of raw dried seaweeds (RDS)

Clean anhydrous seaweed and impurity/debris tests were conducted to determine the specifications of the RDS. The clean anhydrous weed method was used to determine the weight of seaweeds free of impurities and moisture. Impurities determine the total percentage of sand, straw, and other foreign matter attached to the dried seaweed samples. It is essential to consider these factors because they often influence the weight of the dried seaweed products delivered to the seaweed processor. The analyses were based on the Philippine National Standards [10] procedures for RDS. The moisture and ash content of the RDS were determined using methods by the Association of Official Analytical Chemists [11].

2.3 Alkali pretreatment and carrageenan extraction

The RDS were washed thoroughly with distilled water to remove contaminants. These were boiled in a water bath with 10% (w/w) potassium hydroxide (KOH) solution at 60°C for 5 hours. As recommended by Peter McHugh [12] in *A Guide to the Seaweed Industry*, a bleaching step was performed after alkali pretreatment to improve color and for microbial control during the production of processed natural grade (PNG) seaweed. Accordingly, the pretreated seaweeds were soaked in a sodium hypochlorite solution prepared by diluting 0.06 mL of sodium hypochlorite into 500 mL of distilled water, yielding a 0.012% (v/v) solution. Samples were rinsed five times and drained to remove excess water. Then, these were dried in an oven at 60°C for *Eucheuma spp.* and 80°C for *Kappaphycus spp*. for 12-16 hours. The final dried seaweeds were chopped and ground using the laboratory milling machine and stored in a resealable pouch at ambient temperature until further carrageenan analysis was conducted. After bleaching, the samples were rinsed 5 times with distilled water and thoroughly drained to remove excess water. The seaweeds were then oven-dried at 60 °C for *Eucheuma*

spp. and 80 °C for *Kappaphycus* spp. for 12–16 h, or until a constant weight was achieved. The dried samples were finally chopped and milled using a laboratory milling machine, and then stored in resealable polyethylene pouches at ambient temperature until further carrageenan analysis was conducted.

2.4 Chemical properties of carrageenan

Yield, moisture content, and insoluble ash of the gel were determined using the AOAC methods [11]. Sulfate content is a vital factor to monitor in the gel, as it is directly correlated with gel strength, and was determined through a precipitation method using barium chloride [13].

2.5 Gel Rheological properties

Carrageenan extracted from the samples was subjected to gel viscosity analysis, gelling, and melting-point determination. For the gel viscosity, 1.5 g of powdered seaweed was cooked to a viscous solution in 100 ml of distilled water, and its viscosity was analyzed using the gel viscometer (Ametek Brookfield, USA). On the other hand, the gelling and melting points were determined using the method of Rhein-Knudsen et al. through a basic laboratory setup (water bath, thermometer, glass tubes) [14].

2.6 Statistical analysis

The significant differences between variables were determined using a *t*-test. The statistical analysis was conducted using SPSS version 20.

3. Results and Discussion

3.1 Physicochemical properties of RDS

The RDS specifications of *Eucheuma denticulatum* and *Kappaphycus striatum* were presented in Figure 1. The study utilized the parameters based on the Philippine National Standard [10] for the seaweed industry, particularly for RDS production. As can be observed, *E. denticulatum* has a moisture content of 35.98%. These values are within the standard moisture content limit for *Eucheuma* species [10]. The moisture content of *K. striatum* was 40.51%, which is 0.51% higher than the limits for *Kappaphycus* species set by the Philippine National Standards [10] for RDS. The values were not statistically significant among the samples ($p > 0.05$). The ash content of *E. denticulatum* was 34.2%. This falls within the 15-40% standard limit set by FAO JECFA [2] for *Eucheuma* species. The ash content of *K. striatum* was 33.8%, slightly higher than that of *Kappaphycus alvarezii,* which is 28.9%, as studied by Abirami and Kowsalya [15]. There was no significant difference in ash noted among samples ($p>0.05$). For the clean anhydrous weed, which pertains to seaweeds free of moisture, salt, sand, and impurities, the *E. denticulatum* had a content of 35.26%, which is below the 40-45% limit set by the Philippine National Standard [10] for *Eucheuma* species. The *K. striatum* had a content of 23.6%, also lower than the 30-35% limits for *Kappaphycus* species of PNS [10]. There was a significant difference in the *E. denticulatum* samples ($p<0.05$). The *Kappaphycus* and *Eucheuma* species had impurity values lower than the allowable impurity level of 3%, as specified in PNS [10]. *E. denticulatum* had 0.58%, while *K. striatum* had 1.34%. A significant difference was observed between variables, with *K. striatum* showing greater deviation ($p < 0.05$).

Moisture is one of the vital parameters monitored in the industry because it affects manufacturers' final products. For this study, the moisture content of *E. denticulatum* and *K. striatum* is 35.98% and 40.51%, respectively. The moisture content is similar to that reported by Abel and Tolentino [16] for *Eucheuma* and *Kappaphycus*, which range from 35.30% to 38.67%. The standard moisture limit set by PNS [10] specifications for *Eucheuma* and *Kappaphycus* is 30% and 40%, respectively. The *K. striatum* from this study had a moisture content 0.51% above the desired limit, but it is still within the acceptable range and is therefore considered acceptable. The varying drying temperatures and long drying times directly affect the final moisture content of dried seaweeds [17]. Thus, it is essential to maintain the moisture content at the level established by government agencies that govern the industry to prevent the high perishability of seaweeds [18]. Furthermore, it must also be lowered to the standard limit to ensure that the RDS is of good quality [10].

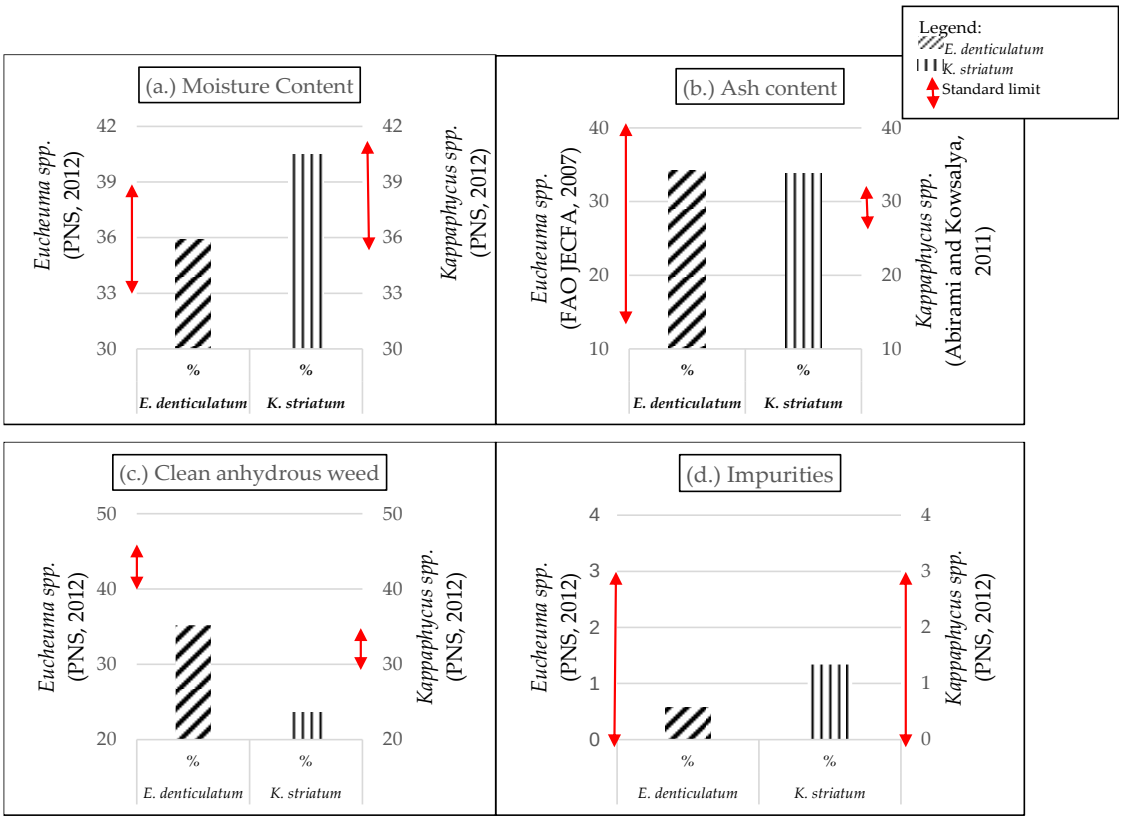

Figure 1. The RDS specifications (a. moisture content; b. ash content; c. clean anhydrous seaweed; d. impurities) of *E. denticulatum* and *K. striatum*.

The ash content represents the total mineral component of the seaweeds [19]. In this study, the ash content of the samples is 34.2% for *E. denticulatum* and 33.8% for *K. striatum*, which are considered acceptable within the FAO JECFA standard range of 15-40% [2]. In comparison, the ash content of *Kappaphycus alvarezii,* studied by Abirami and Kowsalya [15], was 28.9%, which is slightly lower than the result obtained in this study. The ash and mineral content of seaweed are influenced by factors such as drying methods and environmental conditions. Sun-drying is known to cause water leaching and exposure time, which are directly related to lower ash content in dried seaweeds [18]. The high ash content of algae makes it unsuitable for human consumption and limits its application in animal feeds. This is necessary because a high percentage renders seaweed less beneficial for both humans and animals as a food source [20]. The clean anhydrous weed is determined for dried seaweed products because it is used to analyze their salt-free dry matter content [16]. For this study, the seaweeds free of moisture, salt, sand, and impurities, in *E. denticulatum* and *K. striatum*, are 35.26% and 23.6%, respectively. The results are acceptable and fall below the standard limits set by the Philippine National Standard [10] for *Eucheuma* species (40-45%) and for *Kappaphycus* species (30-35%). The lower values obtained from this study indicate that the samples have a more accurate weight when purchased, as dirt and impurities in seaweeds can add extra weight. The impurities collected from the samples included other types of seaweed, plastic straws, dirt, sand, stones, and other foreign materials. The variation in the value of clean, anhydrous seaweed is influenced by the drying method used and the environment in which the seaweed is placed during drying. Drying trays may also affect this value, as well as the position or overlapping, which can cause crystals to form due to low evaporation and allow dirt to adhere easily to seaweed [21].

3.2 Chemical properties of carrageenan

The chemical properties of carrageenan derived from the two samples are presented in Table 1.

Table 1. Chemical properties of extracted carrageenan from *E. denticulatum* and *K. striatum*

Hydrocolloid source	Parameters			
	Yield (%)	**Moisture (%)**	**Insoluble ash (%)**	**Sulfate content (%)**
E. denticulatum	24.84 ± 0.40[a]	22.31 ± 0.04[a]	1.66 ± 0.23[a]	18.22 ± 0.78[a]
K. striatum	11.00 ± 0.47[b]	13.53 ± 0.10[a]	2.12 ± 0.92[a]	38.96 ± 0.08[b]

Values were expressed in mean±standard deviation. Values with different superscripts are statistically significant ($p<0.05$).

The yields of the samples were 24.84% (initial weight: 250 gms; final weight: 62.10 gms) and 11.00% (initial weight: 250 gms; final weight: 27.50 gms) for *E. denticulatum* and *K. striatum*, respectively. The yield value of *K. striatum* is statistically different among samples ($p<0.05$). While the moisture content for *E. denticulatum* was 22.31%, and for *K. striatum* was 13.53%. There was no significant difference among the moisture samples ($p> 0.05$). The acid-insoluble ash content of *E.denticulatum* was 1.66% and 2.12% for *K.striatum*. According to the FAO JECFA [2], the standard limit for acid-insoluble ash of *Eucheuma* species was 1%, similar to the value of acid-insoluble ash of semi-refined carrageenan set by PNS [10]. There was no significant difference noted among samples ($p>0.05$). The sulfate content of *E. denticulatum* was 18.22%, while that of the *K. striatum* was 38.96%. There was a significant difference in sulfate content between *E. denticulatum* and *K. striatum* samples ($p<0.05$). Yield is the ratio of dried carrageenan weight to dried seaweed weight [13]. The yield reported by Freile-Pelegrin and Robledo [22] for *Eucheuma isiforme* was 33.8-43.5%, similar to that of *E. denticulatum*. Mendoza et al. [23] studied *Kappaphycus striatum* and achieved a yield of 56.4%, which is significantly higher than the yield in this study. The yield differences between the same species across studies can be attributed to the methods used for seaweed extraction. The cited research used Aspergillus oryzae for degradation, whereas this study used an alkali pretreatment for extraction. Freile-Pelegrin and Robledo [22] emphasized that carrageenan yield decreases during hot alkaline operations because polysaccharide degradation occurs due to the rigors of processing. Diharmi et al. [24] also noted that carrageenan sourced from various regions exhibits a range of chemical and physical characteristics, particularly those associated with hydrocolloid properties, such as yield.

The moisture content of the carrageenan extracted from *E. denticulatum* was 22.31%, and for *K. striatum* was 13.53%. The values were lower than the PNS standard limit because they were further subjected to various heat applications and had a larger surface area exposed to heat. Thus, the moisture content was lower than the 33-38% limit for *Eucheuma* species and the 35-40% limit for *Kappaphycus* species. Furthermore, the EU requires a moisture content of 8% for food additives, such as carrageenan [25]. Abel and Tolentino [16] reported a moisture content of 16.99% for *E. denticulatum* and 16.65% for *K. alvarezii* in PNG carrageenan. Variation in the moisture content of dried samples can be attributed to factors such as drying temperature, time, method, and speed [26]. The acid-insoluble ash content of carrageenan extracted from *E.denticulatum* was 1.66% and 2.12% for *K. striatum*. Similar to the value of acid-insoluble ash of semi-refined carrageenan set by PNS [10], the standard limit for acid-insoluble ash of *Eucheuma* species was set by FAO JECFA [2] at 1%. The presence of a high acid-insoluble ash content indicates the presence of mineral residue or insoluble metals that remain unaltered during processing [27]. Thus, the drying and sorting processes are important to eliminate impurities in dried seaweeds, which may lead to increased levels of acid-insoluble ash in the final product.

Sulfate groups are important structural substituents of the galactose backbone of carrageenan. The method for its determination is based on the selective hydrolysis of sulfate ester by acid and subsequent selective precipitation of the sulfate ions of barium sulfate [28]. Its value is directly proportional to the gel strength of the hydrocolloid; as potassium hydroxide concentration increases, the value of sulfate decreases, and gel strength increases [13]. According to FAO JECFA [2], the sulfate content of *Eucheuma* species should be 15-40%, which was satisfied by *E. denticulatum* with 18.22%. Meanwhile, Mendoza et al. [23] reported a sulfate content of 23.5% in *K. striatum,* which was lower compared to the result from this study, which was 38.96%. Another survey of the characteristics of carrageenan had reported a sulfate content of 27.33% for *E. denticulatum* and 36.88% for *K. alvarezii* [16]. Commercially available k-carrageenan typically contains 22% (w/w) sulfate, while iota-carrageenan has 32% (w/w) sulfate, and lambda-carrageenan includes 38% (w/w)

sulfate [29]. Parameters such as seasonal variation and environmental conditions are known to affect the chemical composition of carrageenan extracted from dried seaweed products [30].

3.3 Rheological properties of carrageenan

Table 2 presents the rheological properties of the samples. The gel viscosity of *E. denticulatum* was 11.05 cPs, while the *K. striatum* had a gel viscosity of 29.25 cPs. No significant difference was observed among samples ($p>0.05$). The gelling point of *E. denticulatum* was 9.83˚C and 15.67˚C for *K. striatum*. The gelling points were statistically different among the samples ($p < 0.05$). The melting point of *E. denticulatum* was 47.67˚C and 37.67˚C for *K. striatum*. The *K. striatum* was significantly different among the samples ($p < 0.05$). Hysteresis is the difference between the gelling point and the melting point. The hysteresis value for *E. denticulatum* was 37.83˚C, and 22˚C for *K. striatum*, and a significant difference was observed among samples ($p<0.05$).

Table 2. Gel rheological properties of *E. denticulatum* and *K. striatum*

Hydrocolloid source	Parameters			
	Gel viscosity (cPs)	Gelling Temperature (ºC)	Melting Temperature (ºC)	Hysteresis (ºC)
E. denticulatum	11.05 ± 0.78[a]	9.83 ± 0.29[a]	47.67 ± 0.58[a]	37.83 ± 0.29[a]
K. striatum	29.25 ± 0.72[a]	15.67 ± 0.58[b]	37.67 ± 0.58[b]	22.00 ± 0.10[b]

Values were expressed in mean±standard deviation. Values with different superscripts are statistically significant ($p<0.05$).

Gel formation is the most important feature of hydrocolloids; only *kappa* and *iota* carrageenan can form a gel, as other carrageenans lack the essential conformation to gel [31]. Carrageenan forms a highly viscous solution above its coil helix transition temperature. Viscosity increases exponentially with concentration, and adding salts to carrageenan reduces viscosity by shielding the charges on the polymer. It is known to increase with the molecular mass of carrageenan [32]. The gel viscosity of *E. denticulatum* and *K. striatum* is within the limit set by FAO JECFA [2], which is greater than 5 cPs. The results indicate that the correct temperature was used during the drying and extraction process of the RDS, and the extracted carrageenan from the samples was of good quality. The gelling point of *E. denticulatum* was 9.83˚C and 15.67˚C for *K. striatum*. According to Imeson [33], the gelling point of PNG carrageenan ranges from 5-20˚C, and the result of the *E. denticulatum* falls within this range. In comparison, Mendoza et al. [23] reported that the gelling point of *Kappaphycus striatum* was 34.5˚C. At the same time, the melting point of *E. denticulatum* and *K. striatum* was 47.67˚C and 37.67˚C, respectively. The values for *E. denticulatum* fall within the range cited by Imeson [33], which was 40-60˚C, while Mendoza et al. [23] reported a melting point of 56.2˚C for *K. striatum*. Finally, the hysteresis values for *K. striatum* and *E. denticulatum* were 22 °C and 37.83 °C, respectively.

Carrageenan is commonly used in the food sector; therefore, understanding the gelling point is an important consideration when making any food products. It refers to the temperature at which food materials, such as jelly, take on a gel-like consistency. Knowing the gelling point, food manufacturers can calculate the lowest temperature required to maintain the jelly's desired quality. The melting point, on the other hand, can be used to determine the highest temperature at which food items can be stored before consumption. Knowing the melting point enables food manufacturers to establish the temperature restrictions necessary to maintain the food's quality [34-36]. The gelling point of carrageenan from *E. denticulatum* is lower than that of *K. striatum* because it predominantly contains ι-carrageenan, which is more highly sulfated and therefore undergoes coil–helix transition and gelation at lower temperatures [12]. However, the melting point of *E. denticulatum* is higher because ι-carrageenan forms stronger, calcium-mediated ionic cross-links, resulting in a more thermally stable gel network that requires more energy to disrupt. In contrast, *K. striatum*, which is richer in κ-carrageenan, forms a firmer gel at higher temperatures due to its higher 3,6-anhydro-D-galactose content; however, this network is mainly stabilized by potassium ions and weaker intermolecular forces, resulting in a lower melting temperature [37]. Hysteresis, as the temperature difference between gel melting and gel setting, is a well-recognized phenomenon in carrageenan systems and reflects the thermal stability and functional performance

of carrageenan gels [12, 33]. A larger hysteresis value indicates a more thermally stable, strongly cross-linked gel network that requires greater thermal energy to melt once formed. In contrast, a smaller hysteresis suggests a less stable gel structure with weaker intermolecular interactions. In carrageenan, this temperature gap is governed by the degree of sulfation, the 3,6-anhydro-D-galactose content, and the dominant cations (K+ or Ca2+) that stabilize the polymer matrix [37]. Environmental factors and the different physiological and environmental tolerances influence variation in carrageenan content [38]. This phenomenon has been observed in individuals of the same species reared under various environmental conditions [39]. Its properties vary widely depending on harvest time, region, growth conditions (salinity, depth, and nutrient levels), growth stage, extraction method, and other parameters [40]. Thus, it was expected that the results of this study would show both similarities and differences compared with the same or related species. These variations are likely due to differences in internal and external factors that affect seaweeds.

4. Conclusions

Based on the extraction process using the two seaweed species from Caluya, Antique, it can be concluded that *Eucheuma denticulatum* "*Milyon milyon*" exhibited better quality properties than *Kappaphycus striatum* "*Sacol*". Most of its parameters met the industry standards. It was also further observed that the standard drying method for *Kappaphycus* spp. is unsuitable for *Kappaphycus striatum* "*Sacol*" as it negatively affects the final dried product and results in a lower yield than the other variable. Therefore, further studies are needed to optimize the drying temperature for *Kappaphycus striatum* "*Sacol*" and explore its other potential industrial applications.

5. Acknowledgements

All authors are thankful to the Institute of Fish Processing Technology (IFPT) of the University of the Philippines Visayas, Miagao, Iloilo, and the Southeast Asian Fisheries Development Center (SEAFDEC), Tigbauan, Iloilo, for providing the necessary laboratory facilities for this study.

Author Contributions: Conceptualization, J.A.Q. and R.I.; methodology, R.I.; writing-original draft preparation, J.A.Q; writing-review and editing, J.A.Q. and R.I. All authors have read and agreed to the published version of the manuscript.

Funding: This research received no external funding.

Conflicts of Interest: The authors declare no conflict of interest.

References

[1] Islam, M. N.; Tamanna, S.; Pirsa, M. S.; Noman, M. Global Scenarios of Seaweed Cultivation: Science-policy Nexus for Enhancing the Seaweeds and Algae Farming. In *Global Blue Economy*; **2022**; pp 1–32.

[2] Food and Agriculture Organization; World Health Organization. *Joint FAO/WHO Expert Committee on Food Additives Specification (FAO-JECFA)*; Food and Agriculture Organization of the United Nations: **2007**; pp 1–154.

[3] Khalil, H. P. S.; Lai, T. K.; Tye, Y. Y.; Rizal, S.; Chong, E. W. N.; Yap, S. W.; Hamzah, A. A.; Fazita, M. R.; Paridah, M. T. A Review of Extractions of Seaweed Hydrocolloids: Properties and Applications. *eXPRESS Polym. Lett.* **2018**, *12*(4), 296–317. https://doi.org/10.3144/expresspolymlett.2018.27

[4] Pirsa, S.; Hafezi, K. Hydrocolloids: Structure, Preparation Method, and Application in Food and Pharmaceutical Industries. *Res. Sq.* **2022**, 1–32. https://doi.org/10.21203/rs.3.rs-1582020/v1

[5] Narvaez, T. Seaweeds Jobs Value-chain Analysis in Zamboanga Peninsula, Philippines. *Int. J. Oceanogr. Aquacult.* **2018**, *2*(2), 1–7. https://doi.org/10.23880/IJOAC-16000136

[6] Bureau of Fisheries and Aquatic Resources (BFAR). *Seaweed (Kappaphycus) Industry Roadmap 2022-2026*; **2022**; pp 1–169.

[7] Bureau of Fisheries and Aquatic Resources (BFAR). *Philippine Fisheries Profile of 2014*; Department of Agriculture: Quezon City, Philippines, **2014**; pp 1–70.

[8] Arnold, S. Seaweed: The Nature of a Global Cash Crop in the Caluya Islands, Philippines. ChATSEA Working Paper No. 17, **2011**; pp 1–25.
[9] Arnold, S. Seaweed, Power, and Markets: A Political Ecology of the Caluya Islands, Philippines. Master's Thesis, York University: Toronto, Ontario, Canada, **2008**; pp 1–18.
[10] Philippine National Standard (PNS). *Dried Raw Seaweed-specification/Carrageenan – Food Grade – Specification*; Bureau of Agriculture and Fisheries Product Standards: **2012**; pp 1–5.
[11] *AOAC Official Methods of Analysis*, 15th ed.; Helrich, K., Ed.; Association of Official Analytical Chemists: Arlington, VA, **1990**.
[12] McHugh, P. J. *A Guide to the Seaweed Industry*; FAO Fisheries Technical Paper No. 441; Food and Agriculture Organization of the United Nations: Rome, **2003**; pp 1–111.
[13] Distantina, S.; Moh, W.; Rochmadi, F. Carrageenan Properties Extracted from *Eucheuma cottonii* Indonesia. *Int. J. Chem. Mol. Nucl. Mater. Metall. Eng.* **2011**, *5*(6), 487–491.
[14] Rhein-Knudsen, N.; Ale, M. T.; Ajalloueian, F.; Yu, L.; Meyer, A. Rheological Properties of Agar and Carrageenan from Ghanaian Red Seaweeds. *Food Hydrocolloids* **2017**, *63*, 50–58. https://doi.org/10.1016/j.foodhyd.2016.08.023
[15] Abirami, R.; Kowsalya, S. Nutrient and Nutraceutical Potentials of Seaweed Biomass *Ulva lactuca* and *Kappaphycus alvarezii*. *J. Agric. Sci. Technol.* **2011**, *5*(1), 109–115.
[16] Abel, J.; Tolentino, P. D. Characteristics of Carrageenan Extracted from Commercially Important Seaweeds from MIMAROPA Region, Philippines. *Fish. Technol.* **2024**, *61*, 45–52.
[17] Gupta, S.; Cox, S.; Abu-Ghannam, N. Effect of Different Drying Temperatures on the Moisture and Phytochemical Constituents of Edible Irish Brown Seaweed. *LWT--Food Sci. Technol.* **2011**, *44*(5), 1266–1272. https://doi.org/10.1016/j.lwt.2010.12.022
[18] Alfonso, C.; Juliao, D. R.; Pinto, E.; Almeida, A.; Ferreira, I.; Bandarra, N. M.; Cardoso, C. The Effect of Drying Process on Undervalued Brown and Red Seaweed Species: Elemental Composition. *J. Appl. Phycol.* **2022**, *34*, 1749–1761. https://doi.org/10.1007/s10811-022-02741-y
[19] Syad, A. N.; Shunmugiah, K. P.; Kasi, P. D. Seaweeds as Nutritional Supplements: Analysis of Nutritional Profile, Physicochemical Properties and Proximate Composition of *G. acerosa* and *S. wightii*. *Biomed. Prev. Nutr.* **2013**, *3*(2), 139–144. https://doi.org/10.1016/j.bionut.2012.12.002
[20] Alghazeer, R.; El Fatah, H.; Azwai, S.; Elghmasi, S.; Sidati, M.; El Fituri, A.; Althaluti, E.; Gammoudi, F.; Yudiati, E.; Talouz, N.; Shamlan, G.; Al-Farga, A.; Alansari, W.; Eskandrani, A. Nutritional and Non-nutritional Content of Underexploited Edible Seaweeds. *Aquacult. Nutr.* **2022**, 1–8. https://doi.org/10.1155/2022/8422414
[21] Katili, R. A.; Dali, F. A.; Yusuf, N. Quality of Dried Seaweed *Kappaphycus alvarezii* with Traditional Drying Methods from North Gorontalo. *IOP Conf. Ser.: Earth Environ. Sci.* **2019**, *278*, 012039. https://doi.org/10.1088/1755-1315/278/1/012039
[22] Freile-Pelegrin, Y.; Robledo, D. Carrageenan of *Eucheuma isoforme* (Solieriaceae, Rhodophyta) from Nicaragua. *J. Appl. Phycol.* **2007**, *20*(5), 537–541.
[23] Mendoza, W.; Montano, N.; Ganzon-Fortes, E.; Villanueva, R. Chemical and Gelling Profile of Ice-ice Infected Carrageenan from *Kappaphycus striatum* (Schmitz) Doty "Sacol" Strain (Solieriaceae, Gigartinales, Rhodophyta). *J. Appl. Phycol.* **2002**, *14*, 409–418. https://doi.org/10.1023/A:1022178119120
[24] Diharmi, A.; Fardiaz, D.; Andarwulan, N.; Heruwati, E. Chemical and Physical Characteristics of Carrageenan Extracted from *Eucheuma spinosum* Harvested from Three Different Indonesian Coastal Sea Regions. *Phycol. Res.* **2017**, *65*(3), 256–261. https://doi.org/10.1111/pre.12178
[25] European Food Safety Authority (EFSA). Re-evaluation of Carrageenan (E 407) and Processed *Eucheuma* Seaweed (E 407a) as Food Additives. *EFSA J.* **2018**, *16*(4), 5238. https://doi.org/10.2903/j.efsa.2018.5238
[26] Duan, D.; Ma, F.; Zhao, L.; Yin, Y.; Zheng, Y.; Xu, X.; Sun, Y.; Xue, Y. Variation Law and Prediction Model to Determine the Moisture Content in Tea During Hot Air Drying. *J. Food Process Eng.* **2021**, *44*(12), e13966. https://doi.org/10.1111/jfpe.13966

[27] Ismail, B. Ash Content Determination. In *Food Analysis Laboratory Manual*; Springer: Cham, **2017**; pp 117–119. https://doi.org/10.1007/978-3-319-44127-6_11

[28] Food and Agriculture Organization. *Compendium of Food Additive Specifications*; FAO/WHO Joint Expert Committee on Food Additives: Rome, **1992**.

[29] De Ruiter, G. A.; Rudolph, B. Carrageenan Biotechnology. *Trends Food Sci. Technol.* **1997**, *8*(12), 389–395. https://doi.org/10.1016/S0924-2244(97)01091-1

[30] Peña-Rodriguez, A.; Mawhinney, T.; Ricque-Marie, D.; Cruz-Suarez, L. Chemical Composition of Cultivated Seaweed *Ulva clathrata* (Roth) C. Agardh. *Food Chem.* **2011**, *129*(2), 491–498. https://doi.org/10.1016/j.foodchem.2011.04.104

[31] Geonzon, L.; Kobayashi, M.; Tassieri, M.; Bacabac, R.; Adachi, Y.; Matsukawa, S. Microrheological Properties and Local Structure of i-carrageenan Gels Probed by Using Optical Tweezers. *Food Hydrocolloids* **2023**, *137*, 108325. https://doi.org/10.1016/j.foodhyd.2022.108325

[32] Van de Velde, F.; Knutsen, S.; Usov, A.; Rollema, H. S.; Cerezo, A. 1H and 13C High Resolution NMR Spectroscopy of Carrageenans: Application in Research and Industry. *Trends Food Sci. Technol.* **2002**, *13* (3), 73–92. https://doi.org/10.1016/S0924-2244(02)00066-3

[33] Imeson, A. P. Carrageenan. In *Handbook of Hydrocolloids*; Phillips, G. O., Williams, P. A., Eds.; Woodhead Publishing: **2000**; pp 87–102.

[34] Jiang, F.; Liu, Y.; Xiao, Q.; Chen, F.; Weng, H.; Chen, J.; Zhang, Y.; Xiao, A. Eco-friendly Extraction, Structure, and Gel Properties of i-carrageenan Extracted Using Ca(OH)2. *Mar. Drugs* **2022**, *20*(7), 419. https://doi.org/10.3390/md20070419

[35] Darwaman, M.; Utomo, B. S. B.; Mulia, R. A. Y. The Quality of Alkali-treated Cottonii (ATC) Made from *Eucheuma cottonii* Collected from Regions in Indonesia. *Squalene Bull. Mar. Fish. Postharvest Biotechnol.* **2013**, *8* (3), 117–127. https://doi.org/10.15578/squalene.v8i3.37

[36] Necas, J.; Bartosikova, L. Carrageenan: A Review. *Vet. Med. (Prague)* **2013**, *58*(4), 187–205.

[37] Campo, V. L.; Kawano, D.; Silva, D. B.; Carvalho, I. Carrageenans: Biological Properties, Chemical Modifications and Structural Analysis: A Review. *Carbohydr. Polym.* **2009**, *77* (2), 167–180.

[38] Narvarte, B.; Hinaloc, L. A.; Genovia, T.; Gonzaga, S. M.; Tabonda-Nabor, A. M.; Roleda, M. Physiological and Biochemical Characterization of New Wild Strains of *Kappaphycus alvarezii* (Gigartinales, Rhodophyta) Cultivated Under Land-based Hatchery Conditions. *Aquat. Bot.* **2022**, *183*, 103567. https://doi.org/10.1016/j.aquabot.2022.103567

[39] Piriz, M. L.; Cerezo, A. S. Seasonal Variation of Carrageenan in Tetrasporic Cystocarpic and Sterile Stages of *Gigartina skottsbergii* (Rhodophyta, Gigartinales). *Hydrobiologia* **2004**, *226*, 65–69.

[40] Montolalu, R. Effects of Extraction Parameters on Gel Properties of Carrageenan from *Kappaphycus alvarezii*. *J. Appl. Phycol.* **2008**, *20*(5), 525–526. https://doi.org/10.1007/978-1-4020-9619-8_10

ASEAN
Journal of Scientific and Technological Reports
Online ISSN:2773-8752

Research article

Berberine Ameliorates Methionine-Induced Hyperhomocysteinemia and Biochemical Alterations in Male Rats

Aula Talib Zahwar[1*], and Aseel Najah Sabour[1]

[1] Department of Biology, College of Education, University of Al-Qadisiyah, Iraq
* Corresponding Author email: edu.bio.posta108@qu.edu.iq

Citation:
Zahwar, T.A.; Sabour, N.A. Berberine ameliorates methionine-induced hyperhomocysteinemia and biochemical alterations in male rats. *ASEAN J. Sci. Tech. Report.* **2026**, *29*(3), e262094. https://doi.org/10.55164/ajstr.v29i3.262094.

Article history:
Received: October 28, 2025
Revised: December 24, 2025
Accepted: January 13, 2026
Available online: February 27, 2026

Abstract: Hyperhomocysteinemia, characterized by elevated plasma homocysteine levels, is associated with oxidative stress and metabolic dysfunction. This study evaluated the protective effects of berberine, a natural alkaloid compound, against methionine-induced biochemical alterations in male rats. Thirty-two adult male albino rats were randomly divided into four groups (n=8 each) and treated orally for eight weeks: Group 1 (negative control) received standard diet and water; Group 2 (positive control) received methionine (100 mg/kg); Group 3 received methionine (100 mg/kg) plus berberine (40 mg/kg); and Group 4 received berberine (40 mg/kg) alone. Serum samples were analyzed for homocysteine (Hcy), electrolytes (sodium, potassium, chloride), and creatine phosphokinase (CPK) enzyme activity. Methionine treatment significantly elevated homocysteine and CPK levels while reducing sodium and chloride concentrations compared to controls. Co-administration of berberine with methionine markedly decreased homocysteine levels from 76.5 to 12.2 micromole/L and normalized CPK activity. Berberine also restored sodium and chloride concentrations to near-normal levels. The berberine-only group exhibited biochemical parameters comparable to the negative control, confirming its safety profile. These findings demonstrate that berberine effectively mitigates methionine-induced biochemical disturbances through multiple mechanisms, including antioxidant effects, activation of the AMPK pathway, and reduction of reactive oxygen species. Berberine also protected electrolyte homeostasis and mitochondrial function. Therefore, berberine represents a promising natural therapeutic agent for preventing oxidative stress and metabolic complications associated with hyperhomocysteinemia, with potential applications in clinical management of homocysteine-related disorders.

Keywords: Berberine; hyperhomocysteinemia; oxidative stress; AMPK signaling; electrolyte homeostasis

1. Introduction

Methionine is an essential sulfur-containing amino acid that serves as a key substrate in diverse metabolic and biosynthetic pathways across all forms of life [1]. It plays a critical role in protein synthesis and acts as a precursor for S-adenosylmethionine (SAM), the major methyl donor for multiple transmethylation reactions [2]. In normal nutrition, methionine is

predominantly derived from dietary protein sources, including meat, fish, and dairy products, thereby maintaining essential cellular redox status and function [1]. However, when methionine intake exceeds physiological levels, its metabolism is disturbed, leading to the accumulation of homocysteine, an intermediary sulfur-containing molecule normally metabolized via remethylation and transsulfuration pathways [3]. This abnormal elevation in plasma homocysteine levels, termed hyperhomocysteinemia, represents a significant biochemical derangement associated with oxidative stress and endothelial dysfunction [4]. Experimental studies have demonstrated that high methionine intake elevates homocysteine levels in blood and tissues, leading to oxidative stress and disruption of normal cellular function [5, 6].

Elevated plasma homocysteinemia is associated with profound cardiovascular and renal alterations, including disruptions in electrolyte balance involving sodium (Na^+), potassium (K^+), and chloride (Cl^-) ions [7]. These ions are essential for maintaining osmotic balance, membrane potential, and proper nerve and muscle function. Additionally, elevated serum creatine phosphokinase (CPK) activity serves as a biomarker of tissue damage and metabolic dysfunction, reflecting cellular membrane damage caused by excessive oxidative stress and disordered energy metabolism [8, 9]. The pathophysiological mechanisms underlying methionine-induced hyperhomocysteinemia involve the generation of reactive oxygen species (ROS) [10]. High concentrations of methionine promote ROS production, causing lipid, protein, and DNA damage, leading to oxidative stress and potential multi-organ failure [3, 10]. Given these serious health implications, investigational efforts are underway to identify protective agents capable of restoring biochemical homeostasis and mitigating methionine-induced stress. Berberine, a natural isoquinoline alkaloid isolated from plants such as Berberis vulgaris, has emerged as a promising therapeutic candidate [11]. Recent studies have documented berberine's multiple pharmacological activities, including potent antioxidant, anti-inflammatory, and metabolic regulatory effects [12, 13]. Berberine has been shown to activate adenosine monophosphate-activated protein kinase (AMPK) signaling, promoting lipid and methionine metabolism while inhibiting oxidative pathways [12, 6]. Furthermore, berberine increases the expression of antioxidant enzymes, including superoxide dismutase (SOD), catalase (CAT), and glutathione peroxidase (GPx), thereby diminishing oxidative injury [11, 14]. Recent findings also indicate that berberine attenuates mitochondrial dysfunction by improving bioenergetic function and reducing ROS production [13]. Given berberine's multifaceted protective mechanisms and growing evidence of its therapeutic potential in oxidative and metabolic disorders, the present study was designed to evaluate the effects of berberine on selected biochemical indicators—specifically homocysteine, electrolytes (Na^+, K^+, Cl^-), and CPK enzyme activity—in an experimental model of hypermethioninemia-induced hyperhomocysteinemia in male rats.

2. Materials and Methods

2.1 Chemicals and Compounds

Methionine was obtained from HIMEDIA (India) in the form of white crystalline powder and administered orally at a dose of 100 mg/kg body weight [15]. The present study utilized fixed doses of methionine and berberine based on previously published effective concentrations. Future investigations should include dose-response experiments to determine optimal therapeutic doses, establish minimum effective doses, and characterize the dose-dependent effects of berberine. Such studies would enhance translational potential and inform clinical dosing strategies. Berberine was procured from BIO TEST (USA) in capsule form containing yellow powder (500 mg per capsule) and administered orally at a dose of 40 mg/kg body weight [16]. The methionine dose (100 mg/kg) was selected based on established experimental models that reliably induce hyperhomocysteinemia without causing acute systemic toxicity [15]. The berberine dose (40 mg/kg) was chosen based on previous studies demonstrating significant antioxidant and metabolic regulatory effects at this concentration [16], while maintaining a favorable safety profile. This dose corresponds to a human equivalent dose of approximately 450 mg for a 70 kg adult, which falls within the clinically administered range of 500–1500 mg daily.

2.2 Experimental Animals

Adult male albino rats (Rattus norvegicus) aged 12–16 weeks with body weights between 200–300 g were obtained from the College of Veterinary Medicine, University of Al-Qadisiyah, Iraq. Before experimentation,

the animals were acclimatized to laboratory conditions for 2 weeks and subjected to a comprehensive health assessment [1]. Throughout the study, animals were housed under controlled environmental conditions at 22 ± 5 °C with a 12-hour light/12-hour dark cycle. Standard laboratory diet and drinking water were provided ad libitum to all animals [4]. All experimental procedures were conducted in strict accordance with the Institutional Ethical Guidelines for Animal Care and approved by the institutional animal ethics committee [17]. Several limitations should be considered when interpreting these findings. First, the exclusive use of male rats restricts generalizability to female populations. Sex-based differences in homocysteine metabolism are well documented, with estrogen exerting protective effects by enhancing methylation pathway activity. Whether berberine's protective mechanisms operate similarly in females, particularly across different hormonal states (cycling, pregnancy, menopause equivalent), remains to be determined. Second, the single-dose design precludes dose-response characterization. Third, the mechanistic pathways discussed were inferred from existing literature rather than directly measured in this study.

2.3 Experimental Design

A total of 32 adult male rats were randomly divided into four groups, each containing 8 animals. The experimental study period lasted 60 days. The experimental groups were organized as follows: Group 1 (G1) - Negative Control: Eight rats were provided with a standard laboratory diet and water ad libitum throughout the entire experimental period, receiving no chemical treatment [3]. Group 2 (G2) - Positive Control: Eight rats were orally administered methionine at a dose of 100 mg/kg body weight daily for 60 days to induce hypermethioninemia and subsequent hyperhomocysteinemia [15]. Group 3 (G3) - Treatment Group: Eight rats received both methionine (100 mg/kg body weight) and berberine (40 mg/kg body weight) administered orally concurrently throughout the 60-day experimental period [16]. Group 4 (G4) - Berberine Control: Eight rats received berberine (40 mg/kg body weight) orally alone throughout the experimental period to evaluate its safety profile on normal metabolic parameters [12]. All treatments were administered orally daily for the full 60 days using the oral gavage technique [5].

2.4 Blood Collection and Serum Preparation

At the conclusion of the experimental period, all animals were anesthetized using chloroform vapors according to standard laboratory protocols [17]. Blood samples were collected via cardiac puncture into sterile plain collection tubes without anticoagulant [7]. Collected blood samples were allowed to clot naturally for 15–20 minutes at room temperature. Subsequently, samples were centrifuged at 3000 rpm for 15 minutes to obtain serum [2]. The resulting serum was carefully aliquoted into sterile Eppendorf tubes and stored at −20 °C until biochemical analysis [8].

2.5 Biochemical Analysis and Measurements

Serum homocysteine concentrations were determined using a rat-specific enzyme-linked immunosorbent assay (ELISA) kit (BioSource, USA) according to the manufacturer's protocol [13]. The assay was based on a sandwich ELISA methodology utilizing specific antibodies against homocysteine [14]. Briefly, serum samples were incubated in microplate wells coated with capture antibodies. After washing steps, detection antibodies conjugated with horseradish peroxidase (HRP) were added [6]. Optical density (OD) was measured at 450 nm using a microplate reader (LMMR-101) [18]. Homocysteine concentrations were calculated from the kit's standard curves and expressed as micromoles per liter (micromoles/L) [10]. Serum concentrations of sodium (Na^+), potassium (K^+), and chloride (Cl^-) ions were measured using an ion-selective electrode (ISE) module integrated with the Beckman Coulter AU480 automated analyzer (USA) [9]. The system utilizes ion-specific membranes that generate electrical potentials according to the Nernst equation based on the electrochemical gradient across the semipermeable membrane [19]. These potentials are converted to ionic concentrations through the instrument's calibrated software and validated reference materials [13]. The measurement principle involves the formation of a potential difference at the ion-selective electrode surface, which is proportional to the logarithm of the ion concentration [20]. Results were expressed as millimoles per liter (mmol/L) [98]. Serum creatine phosphokinase (CPK) activity was measured using a kinetic enzymatic assay performed on the Beckman Coulter AU480 automated analyzer (USA) [21]. The assay principle is based on the phosphorylation of adenosine diphosphate (ADP) by creatine phosphate in the presence of creatine

kinase enzyme, producing adenosine triphosphate (ATP) [22]. The generated ATP is then coupled with hexokinase (HK) and glucose-6-phosphate dehydrogenase (G6PDH) reactions to generate nicotinamide adenine dinucleotide phosphate (NADPH) [23]. The production of NADPH is proportional to CPK activity and is quantified spectrophotometrically at 340 nm [24]. Enzyme activity was expressed as International Units per liter (IU/L) [21].

2.6 Studied Parameters

The primary physiological and biochemical parameters investigated in this study included Homocysteine (Hcy): Measured as a marker of amino acid metabolism disturbance and oxidative stress burden in methionine-induced hyperhomocysteinemia [25]. Electrolytes (Na^+, K^+, Cl): Measured as indicators of ionic homeostasis, osmotic balance, and cellular membrane function, reflecting renal tubular dysfunction and ion transport capacity [26]. Creatine Phosphokinase (CPK): Measured as a biomarker of tissue damage, myocellular injury, and metabolic dysfunction reflecting membrane integrity and energy metabolism status [9]. These parameters were selected based on their established roles as indicators of oxidative stress, metabolic dysfunction, and cellular membrane integrity in response to methionine-induced hyperhomocysteinemia [27].

2.7 Statistical Analysis

All data obtained were subjected to statistical analysis using one-way analysis of variance (ANOVA) followed by the least significant difference (LSD) post hoc test using SPSS statistical software (version 2010) [28]. Results are presented as mean ± standard deviation (SD) [3]. Statistical significance was established at a probability level of $p \leq 0.05$, while $p > 0.05$ was considered non-significant [4]. Different superscript letters (A, B, C) in tables indicate statistically significant differences between groups at the 5% probability level, while identical letters denote non-significant differences [7].

3. Results and Discussion

3.1 Changes in Serum Homocysteine (Hcy) Levels

The statistical analysis results presented in Table 1 demonstrated a significant increase ($P < 0.05$) in serum homocysteine levels in the positive control group (G2) treated with methionine (76.5 ± 1.06 micromole/L) compared with the negative control group (G1) (7.66 ± 0.26 micromole/L) [5]. This marked elevation in homocysteine levels confirmed the successful induction of hyperhomocysteinemia in the experimental model [55]. In contrast, Group 3 (G3) treated with both methionine and berberine revealed a significant decrease ($P < 0.05$) in homocysteine level (12.2 ± 1.38 micromole/L) compared with Group 2 (G2), representing a reduction of approximately 84% from methionine-induced levels. However, G3 still showed a significant increase ($P < 0.05$) compared with the negative control (G1) [6]. Furthermore, Group 4 (G4) treated with berberine alone showed a significant decrease ($P < 0.05$) in homocysteine level (7.11 ± 0.26 micromole/L) compared with both Groups G2 and G3. Notably, no significant difference ($P > 0.05$) was observed between Group G4 and the negative control group (G1), confirming the safety profile of berberine on normal homocysteine metabolism [12].

3.2 Changes in Creatine Phosphokinase (CPK) Enzyme Activity

The results of the statistical analysis presented in Table 1 revealed a significant increase ($P < 0.05$) in the CPK enzyme level in the positive control group (G2) treated with methionine (442.33 ± 79.34 ng/ml) compared with the negative control group (G1) (230.67 ± 25.8 IU/L), indicating pronounced cellular membrane damage and tissue injury [8]. In contrast, Group 3 (G3) treated with methionine and berberine showed a significant decrease ($P < 0.05$) in CPK enzyme level (270.33 ± 33.06 IU/L) compared with Group G2, with no significant difference ($P > 0.05$) compared with the negative control group (G1). This restoration of CPK activity to near-normal levels indicated that berberine exerts a cytoprotective effect against methionine-induced cellular damage [9]. Additionally, a significant decrease ($P < 0.05$) in CPK enzyme level was observed in Group G4 (berberine only) (233.3 ± 17.67 IU/L) compared with Group G2, whereas no significant difference ($P > 0.05$) was found compared with the negative control group (G1) and Group G3 [13].

3.3 Changes in Serum Electrolyte Levels

As shown in Table 2, a significant decrease ($P < 0.05$) in sodium ion (Na^+) level was observed in the positive control group (G2) treated with methionine (127 ± 0.86 mmol/L) compared with the negative control (G1) (134.67 ± 3.01 mmol/L) [7]. However, Group G3 (methionine + berberine) exhibited a significant increase ($P < 0.05$) in sodium levels (134.17 ± 2.34 mmol/L) compared with Group G2, with no significant difference ($P > 0.05$) compared to Group G1 [18]. Group G4 (berberine only) displayed sodium levels (133.8 ± 3.76 mmol/L) with no significant differences compared with Groups G1 or G3, but exhibited a significant increase ($P < 0.05$) in Na^+ levels compared to Group G2. These results indicate that sodium homeostasis is restored following berberine administration [14]. The results in Table 2 indicated a non-significant decrease in potassium ion (K^+) levels in Group G2 (methionine) (5.05 ± 0.05 mmol/L) compared to Group G1 (5.57 ± 0.27 mmol/L) [1]. Group G3 (methionine + berberine) showed a non-significant decrease (4.60 ± 0.14 mmol/L) compared with G2, but a significant decrease ($P < 0.05$) compared with G1 [4]. Meanwhile, Group G4 (berberine only) displayed a significant decrease ($P < 0.05$) in K^+ level (4.63 ± 0.40 mmol/L) compared to G1, but no significant difference ($P > 0.05$) compared with Groups G2 and G3. These findings suggest a modest regulatory effect of berberine on potassium metabolism [10]. The results in Table 2 demonstrated a significant decrease ($P < 0.05$) in chloride ion (Cl^-) level in the positive control group (G2) (methionine-treated) (90.67 ± 0.88 mmol/L) compared with the negative control (G1) (98.17 ± 1.80 mmol/L) [7]. In contrast, Group G3 (methionine + berberine) showed a non-significant decrease (95.50 ± 3.20 mmol/L) ($P > 0.05$) compared with G2, and no significant difference relative to G1 [2]. Similarly, Group G4 (berberine only) showed no significant differences (94.67 ± 2.23 mmol/L) ($P > 0.05$) compared with the other groups. The restoration of chloride concentrations following berberine treatment indicates recovery of renal tubular reabsorption capacity [3].

Table 1. Effect of Methionine and Berberine on Serum Homocysteine (HCy) and CPK Enzyme Level in Male Albino Rats

Groups	Hcy (micromole/L) Mean ± SE	CPK (IU/L) Mean ± SE
G1	7.66 ± 0.26^{C}	230.67 ± 25.8^{B}
G2	76.5 ± 1.06^{A}	442.33 ± 79.34^{A}
G3	12.2 ± 1.38^{B}	270.33 ± 33.06^{B}
G4	7.11 ± 0.26^{C}	233.3 ± 17.67^{B}
LSD	2.62	135.1

* Different superscript letters indicate statistically significant differences at the 5% probability level ($P < 0.05$); identical letters denote non-significant differences.

Table 2. Effect of Methionine and Berberine on Sodium, Potassium, and Chloride Ion Levels in Male Albino Rats

Groups	K^+ (mmol/L) Mean ± SE	Na^+ (mmol/L) Mean ± SE	Cl^- (mmol/L) Mean ± SE
G1	5.57 ± 0.27^{A}	134.67 ± 3.01^{A}	98.17 ± 1.80^{A}
G2	5.05 ± 0.05^{AB}	127 ± 0.86^{B}	90.67 ± 0.88^{B}
G3	4.60 ± 0.14^{B}	134.17 ± 2.34^{A}	95.50 ± 3.20^{AB}
G4	4.63 ± 0.40^{B}	133.8 ± 3.76^{A}	94.67 ± 2.23^{AB}
LSD	0.823	6.1	6.47

* Different superscript letters indicate significant differences ($P < 0.05$), while identical letters indicate non-significant differences.

Effect size calculations revealed very large treatment effects for all primary outcome measures (Table 3). The Cohen's d for homocysteine reduction in berberine-treated versus methionine-only groups was 52.4, indicating an effect magnitude far exceeding conventional thresholds. Similarly, large effect sizes were observed for CPK normalization ($d = 2.80$), sodium restoration ($d = 4.03$), and chloride recovery ($d = 1.89$). Post-hoc power analysis confirmed that the study achieved statistical power exceeding 0.97 for all primary comparisons, indicating adequate sample size to detect the observed effects. The robustness of findings was further supported by Benjamini-Hochberg correction for multiple comparisons, which maintained significance for all primary outcomes.

Table 3. Effect Size Analysis, Statistical Power, and Clinical Interpretation of Treatment Effects

Comparison	Parameter	Mean Diff	Cohen's d	95% CI	Power (1-β)	Effect Size	Context
Methionine-Induced Biochemical Alterations (G2 vs G1 - Negative Control)							
G2 vs G1	Homocysteine	68.84	89.20	[58.28, 120.12]	0.99	Very large	Methionine-induced elevation
G2 vs G1	CPK	211.66	3.59	[2.00, 5.17]	0.99	Very large	Methionine-induced elevation
G2 vs G1	Sodium (Na^+)	-7.67	3.47	[1.92, 5.01]	0.99	Very large	Methionine-induced decrease
G2 vs G1	Chloride (Cl^-)	-7.50	5.29	[3.21, 7.37]	0.99	Very large	Methionine-induced decrease
Berberine Protective Effects (G3 vs G2 - Positive Control)							
G3 vs G2	Homocysteine	-64.30	52.26	[34.12, 70.39]	0.99	Very large	Berberine protective effect
G3 vs G2	CPK	-172.00	2.83	[1.44, 4.22]	0.99	Very large	Berberine protective effect
G3 vs G2	Sodium (Na^+)	7.17	4.07	[2.35, 5.78]	0.99	Very large	Berberine restoration
G3 vs G2	Chloride (Cl^-)	4.83	2.06	[0.85, 3.27]	0.98	Very large	Berberine restoration
Berberine Safety Profile (G4 vs G1 - Negative Control)							
G4 vs G1	Homocysteine	-0.55	2.12	[0.89, 3.34]	0.99	Very large	Berberine alone vs control
G4 vs G1	CPK	2.63	0.12	[0.00, 1.10]	0.04	Negligible	Berberine alone vs control
G4 vs G1	Sodium (Na^+)	-0.87	0.26	[0.00, 1.24]	0.07	Small	Berberine alone vs control
G4 vs G1	Chloride (Cl^-)	-3.50	1.73	[0.58, 2.88]	0.93	Very large	Berberine alone vs control

Notes: Effect size interpretation based on Cohen's conventions: Negligible ($d < 0.2$), Small ($d = 0.2–0.49$), Medium ($d = 0.5–0.79$), Large ($d = 0.8–1.19$), Very large ($d \geq 1.2$).
Cohen's d calculated as: $d = |M_1 - M_2| / SD_{pooled}$, where $SD_{pooled} = \sqrt{[(SD_1^2 + SD_2^2)/2]}$.
95% CI calculated using standard error approximation: $SE(d) \approx \sqrt{[(n_1+n_2)/(n_1 \times n_2) + d^2/(2(n_1+n_2))]}$.
Statistical power (1-β) calculated for $\alpha = 0.05$, two-tailed test, with n = 8 per group.
G1 = Negative control; G2 = Methionine (100 mg/kg); G3 = Methionine + Berberine (40 mg/kg); G4 = Berberine alone (40 mg/kg).

Abbreviations: CPK, creatine phosphokinase; CI, confidence interval; Diff, difference.

3.4 Methionine-Induced Hyperhomocysteinemia and Biochemical Alterations

The present study demonstrated that methionine treatment in male rats resulted in marked changes in biochemical findings, comprising significant increases in serum homocysteine (Hcy) levels (from 7.66 to 76.5 micromole/L) and creatine phosphokinase (CPK) levels (from 230.67 to 442.33 ng/ml), alongside decreases in sodium (Na^+) and chloride (Cl^-) concentrations. These results demonstrated that abnormal amino acid metabolism resulting from excessive methionine intake leads to hyperhomocysteinemia and oxidative stress [5]. The marked elevation of plasma homocysteine levels in the methionine-supplemented group is supported by previous studies, which showed that high methionine intake disrupts both the transsulfuration and remethylation pathways, the two major pathways involved in homocysteine metabolism [6]. This biochemical disturbance results in the accumulation of homocysteine in plasma and tissues, with deleterious effects on redox homeostasis and endothelial function [4]. The simultaneous increase in CPK activity corroborates the presence of oxidative stress and cellular damage since, upon sarcolemmal membrane rupture, CPK leaks into the serum, serving as a reliable indicator of muscle and tissue injury [8]. High homocysteine induces auto-oxidation reactions, resulting in the production of reactive oxygen species (ROS), which damage cellular lipids, proteins, and DNA through mechanisms including lipid peroxidation and protein carbonylation, ultimately leading to tissue injury and multi-organ dysfunction [10]. The disturbances in electrolyte balance observed in the methionine-treated group, particularly the decreases in Na^+ and Cl^- ions, indicate that hyperhomocysteinemia-induced oxidative damage is the primary cause of renal tubular dysfunction and ion transport disturbances [3]. These electrolyte alterations suggest impaired renal function and disrupted regulation of membrane potential, which can have serious physiological consequences [7].

3.5 Berberine's Protective Mechanisms Against Methionine-Induced Hyperhomocysteinemia

Co-administration of berberine with methionine in treated animals (G3) notably decreased serum homocysteine levels by approximately 84% and restored CPK activity to near-normal levels, indicating profound cytoprotective effects. This beneficial effect can be attributed to multiple interconnected mechanisms involving berberine's modulation of key metabolic and signaling pathways [12]. One of the primary protective mechanisms of berberine is its activation of the Adenosine Monophosphate-Activated Protein Kinase (AMPK) signaling pathway, a cellular energy sensor that plays crucial roles in metabolic regulation [20]. Berberine's modulating effect on hepatic AMPK signaling promotes lipid and methionine metabolism while simultaneously inhibiting oxidative pathways that generate harmful reactive oxygen species [12]. AMPK activation improves mitochondrial biogenesis and enhances cellular energy production, thereby reducing metabolic burden and cellular stress [13]. Berberine increases the expression of multiple antioxidant enzymes, including superoxide dismutase (SOD), catalase (CAT), and glutathione peroxidase (GPx), thus providing a multi-layered defense against oxidative injury [14]. These antioxidant enzymes work synergistically to neutralize reactive oxygen species: SOD catalyzes the conversion of superoxide radicals to hydrogen peroxide, CAT converts hydrogen peroxide to water and oxygen, and GPx reduces hydrogen peroxide and lipid hydroperoxides [11]. By upregulating these enzymatic defenses, berberine effectively mitigates the oxidative stress imposed by methionine-induced hyperhomocysteinemia [19]. The decrease in CPK levels in berberine-treated rats provides additional evidence regarding its stabilizing and cytoprotective effect on mitochondria and cellular membranes [9]. Recent research has demonstrated that berberine attenuates mitochondrial dysfunction by improving bioenergetic function and reducing reactive oxygen species (ROS) production within the mitochondrial matrix [13]. By maintaining mitochondrial integrity and function, berberine preserves cellular energy production and prevents the membrane rupture that leads to CPK leakage into the serum [21]. In combination, berberine's protective effects involve inhibition of NF-κB-induced inflammation, a key transcription factor that promotes the expression of pro-inflammatory cytokines and adhesion molecules [20]. By reducing inflammatory signaling, berberine minimizes tissue damage and protects against the secondary inflammatory consequences of oxidative stress [26].

3.6 Restoration of Electrolyte Homeostasis

The restoration of Na^+ and Cl^- content after berberine treatment suggests a recovery of renal tubular reabsorption capacity and improved regulation of membrane potential [7]. Berberine has been reported to

protect Na^+/K^+-ATPase activity, an enzyme critical for maintaining the sodium-potassium gradient across cell membranes [21]. This Na^+/K^+-ATPase protection demonstrates berberine's antioxidative capacity and its ability to uphold electrolyte homeostasis despite oxidative stress [18]. The Na^+/K^+-ATPase pump, located on cell membranes, is highly vulnerable to oxidative damage due to its high metabolic activity and its location in lipid-rich membranes that are susceptible to peroxidation [19]. By protecting this crucial enzyme through its antioxidant mechanisms, berberine maintains the active transport of sodium and potassium ions, thereby preserving cellular osmotic balance and membrane potential [7]. The fairly modest influence of berberine on potassium content reported in this investigation suggests a regulation rather than an overstimulating effect of berberine on K^+ channels and transporters [12]. This nuanced regulatory effect prevents ionic penalties or electrolyte imbalance that could result from excessive modulation of potassium metabolism [14]. The comprehensive results demonstrate that berberine mediates a multi-targeted biochemical defense against methionine-induced stress through the coordinated action of several mechanisms [20]. The restoration of homocysteine levels indicates improved methionine metabolism via both remethylation and transsulfuration pathways [6]. The normalization of CPK levels reflects protection of cellular membranes and mitochondrial integrity. The restoration of electrolyte concentrations demonstrates recovery of renal function and ion transport capacity [3]. This combined protective response accounts for the concomitant normalization of homocysteine, electrolyte balance, and CPK enzyme activity observed in the present study. The synergistic activation of AMPK signaling, enhancement of antioxidant defense systems, mitochondrial stabilization, and anti-inflammatory effects create a comprehensive protective environment that counteracts the multifaceted toxic effects of methionine-induced hyperhomocysteinemia [13].

3.7 Comparison with Existing Literature and Clinical Relevance

The findings of the present study are in accordance with worldwide investigations on the biological effects of berberine. Internationally, multiple studies have reported that berberine is a multi-targeted metabolic modulator and potent antioxidant, with demonstrated capacity to maintain mitochondrial stability and protect cells [11]. Neag and colleagues reported comprehensive evidence for berberine's relevance in cardiovascular, metabolic, hepatic, and renal disorders [11]. Fang and colleagues documented berberine's research-validated capacity to improve mitochondrial bioenergetic function and reduce reactive oxygen species production through multiple molecular pathways [13]. Chang and colleagues demonstrated that berberine effectively reduced hyperhomocysteinemia and associated hyperlipidemia in rats fed long-term high-fat diets [14]. These consistent results from worldwide studies highlight the robustness of berberine's pharmacological properties and suggest its considerable potential medical value in oxidative and metabolic pathologies [11]. Additionally, several studies have documented berberine's protective effects in diverse disease models, including diabetic kidney disease, gentamicin-induced nephrotoxicity, doxorubicin-induced cardiotoxicity, and renal ischemia-reperfusion injury [21]. The protective mechanism observed in these studies consistently involves reducing oxidative stress, enhancing antioxidant defenses, and preserving cellular and organ function [26]. The berberine-only treatment group (G4) exhibited biochemical parameters comparable to the negative control group, confirming the safety profile of berberine at the administered dose (40 mg/kg) on normal metabolic processes [12]. This finding is critical for therapeutic development, as it demonstrates that berberine does not induce adverse metabolic effects in the absence of pathological conditions [16]. The effectiveness of berberine in ameliorating methionine-induced hyperhomocysteinemia suggests potential therapeutic applications in clinical settings where hyperhomocysteinemia represents a health risk [3]. Elevated plasma homocysteine is an established independent risk factor for cardiovascular disease, thrombosis, cognitive decline, and renal dysfunction [4]. Natural compounds such as berberine can effectively reduce homocysteine levels while simultaneously enhancing antioxidant defenses and protecting organ function, representing valuable therapeutic options, particularly for patients seeking complementary or alternative approaches to managing hyperhomocysteinemia-associated disorders [10]. The multi-targeted nature of berberine's protective effects suggests its potential utility in complex metabolic disorders involving multiple pathogenic mechanisms [20]. Rather than targeting a single pathway, berberine simultaneously addresses oxidative stress, mitochondrial dysfunction, inflammatory signaling, and metabolic dysregulation, providing more comprehensive protection than agents targeting single mechanisms [13].

4. Conclusions

This study successfully demonstrated that berberine effectively ameliorates methionine-induced hyperhomocysteinemia and associated biochemical alterations in male rats through multiple interconnected protective mechanisms. The administration of berberine alongside methionine markedly reduced serum homocysteine levels by approximately 84%, normalized creatine phosphokinase enzyme activity, and restored electrolyte homeostasis (sodium and chloride concentrations) to near-normal levels. These comprehensive biochemical improvements indicate the restoration of cellular and metabolic homeostasis following berberine treatment. The protective effects of berberine were mediated through several key mechanisms, including activation of the AMPK signaling pathway, enhancement of antioxidant enzyme expression (SOD, CAT, and GPx), mitochondrial stabilization, and inhibition of pro-inflammatory signaling pathways. Importantly, berberine administration alone did not produce adverse metabolic effects, confirming its safety profile at the tested dose of 40 mg/kg body weight. These findings provide compelling evidence that berberine is a natural therapeutic compound with significant potential to protect against oxidative stress and metabolic disturbances associated with hyperhomocysteinemia. The multi-targeted protective mechanisms of berberine make it a particularly valuable candidate for managing complex metabolic disorders characterized by multiple pathogenic pathways. Future clinical investigations should explore berberine's efficacy in human populations with hyperhomocysteinemia and its potential therapeutic applications in cardiovascular disease, renal dysfunction, and other hyperhomocysteinemia-related conditions. Additionally, dose-optimization studies and long-term safety assessments would further establish berberine as a promising natural compound for clinical therapeutic interventions in metabolic and oxidative disorders.

5. Acknowledgements

The authors would like to express their sincere gratitude to the Department of Biology, College of Education, University of Al-Qadisiyah, Iraq, for providing the laboratory facilities and technical support necessary to carry out this research. Special thanks are extended to the laboratory staff for their assistance during animal handling and biochemical analyses.

Author Contributions: A.T.Z. and A.N.S. contributed to conceptualization. A.T.Z. was responsible for methodology, software, resources, data curation, formal analysis, investigation, drafting the original manuscript, and visualization. Supervision and administration of the project, validation was performed by A.N.S. Funding acquisition was carried out by A.T.Z. All authors have reviewed and validated the submitted draft of the manuscript.

Funding: This research received no external funding

Conflicts of Interest: The authors declare no conflict of interest.

References

[1] Brosnan, J. T.; Brosnan, M. E.; Bertolo, R. F.; Brunton, J. A. Methionine: A Metabolically Unique Amino Acid. *Livest. Sci.* **2007**, *112* (1–2), 2–7. https://doi.org/10.1016/j.livsci.2007.07.005

[2] Mato, J. M.; Martínez-Chantar, M. L.; Lu, S. C. S-adenosylmethionine Metabolism and Liver Disease. *Ann. Hepatol.* **2013**, *12*(2), 183–189. https://doi.org/10.1016/S1665-2681(19)31355-9

[3] Long, Y.; Nie, J. Homocysteine in Renal Injury. *Kidney Dis.* **2016**, *2*(2), 80–87. https://doi.org/10.1159/000444900

[4] Bellamy, M.; McDowell, I.; Ramsey, M.; Brownlee, M.; Bones, C.; Newcombe, R.; Lewis, M. Hyperhomocysteinemia After an Oral Methionine Load Acutely Impairs Endothelial Function in Healthy Adults. *Circulation* **1998**, *98*(18), 1848–1852. https://doi.org/10.1161/01.CIR.98.18.1848

[5] Derouiche, F.; Djemil, R.; Sebihi, F. Z.; Douaouya, L.; Maamar, H.; Benjemana, K. High Methionine Diet Mediated Oxidative Stress and Proteasome Impairment Causes Toxicity in Liver. *Sci. Rep.* **2024**, *14*, 5555. https://doi.org/10.1038/s41598-024-55857-1

[6] Wu, N.; Sarna, L. K.; Siow, Y. L.; O, K. Regulation of Hepatic Cholesterol Biosynthesis by Berberine During Hyperhomocysteinemia. *Am. J. Physiol. Regul. Integr. Comp. Physiol.* **2011**, *300*(3), R635–R643. https://doi.org/10.1152/ajpregu.00441.2010

[7] Okediran, B. S.; Amid, S.; Suleiman, K.; Adah, A.; Olaifa, F.; Sanusi, F. Electrolytes Changes in Male Rats Deprived of Feed and Water. *Assiut Vet. Med. J.* **2021**, *67*(169), 202–208. https://doi.org/10.21608/avmj.2021.188865

[8] Xiong, C.; Wu, Y.-Z.; Zhang, Y.; Wu, Z.-X.; Chen, X.-Y.; Jiang, P.; Guo, J.-J. Protective Effect of Berberine on Acute Cardiomyopathy Associated with Doxorubicin Treatment. *Oncol. Lett.* **2018**, *15* (4), 5721–5729. https://doi.org/10.3892/ol.2018.8020

[9] Zhang, Y.; Ma, X.-J.; Guo, C.-Y.; Wang, M.-M.; Kou, N.; Qu, H.; Mao, H.-M.; Shi, D.-Z. Pretreatment with a Combination of Ligustrazine and Berberine Improves Cardiac Function in Rats with Coronary Microembolization. *Acta Pharmacol. Sin.* **2016**, *37*(4), 463–472. https://doi.org/10.1038/aps.2015.147

[10] Veeranki, S.; Tyagi, S. C. Defective Homocysteine Metabolism: Potential Implications for Skeletal Muscle Malfunction. *Int. J. Mol. Sci.* **2013**, *14*(7), 15074–15091. https://doi.org/10.3390/ijms140715074

[11] Neag, M. A.; Mocan, A.; Echeverría, J.; Pop, R. M.; Bocsan, C. I.; Crişan, G.; Buzoianu, A. D. Berberine: Botanical Occurrence, Traditional Uses, Extraction Methods, and Relevance in Cardiovascular, Metabolic, Hepatic, and Renal Disorders. *Front. Pharmacol.* **2018**, *9*, 557. https://doi.org/10.3389/fphar.2018.00557

[12] Yin, J.; Ye, J.; Jia, W. Effects and Mechanisms of Berberine in Diabetes Treatment. *Acta Pharm. Sin. B* **2012**, *2*(4), 327–334. https://doi.org/10.1016/j.apsb.2012.06.003

[13] Fang, X.; Wu, H.; Wei, J.; Miao, R.; Zhang, Y.; Tian, J. Research Progress on the Pharmacological Effects of Berberine Targeting Mitochondria. *Front. Endocrinol.* **2022**, *13*, 982145. https://doi.org/10.3389/fendo.2022.982145

[14] Chang, X.-X.; Yan, H.-M.; Xu, Q.; Xia, M.-F.; Bian, H.; Zhu, T.-F.; Gao, X. The Effects of Berberine on Hyperhomocysteinemia and Hyperlipidemia in Rats Fed with a Long-term High-fat Diet. *Lipids Health Dis.* **2012**, *11*, 86. https://doi.org/10.1186/1476-511X-11-86

[15] Garlick, P. J. Toxicity of Methionine in Humans. *J. Nutr.* **2006**, *136*(6), 1722S–1725S. https://doi.org/10.1093/jn/136.6.1722S

[16] Adil, M.; Kandhare, A. D.; Dalvi, G.; Ghosh, P.; Venkata, S.; Raygude, K. S.; Bodhankar, S. L. Ameliorative Effect of Berberine Against Gentamicin-induced Nephrotoxicity in Rats via Attenuation of Oxidative Stress, Inflammation, Apoptosis and Mitochondrial Dysfunction. *Renal Failure* **2016**, *38*(6), 996–1006. https://doi.org/10.3109/0886022X.2016.1165120

[17] National Research Council. *Guide for the Care and Use of Laboratory Animals*, 8th ed.; National Academies Press: Washington, DC, **2011**.

[18] Dhondup, T.; Qian, Q. Acid-Base and Electrolyte Disorders in Patients with and without Chronic Kidney Disease: An Update. *Kidney Dis.* **2017**, *3* (4), 136–148. https://doi.org/10.1159/000479968

[19] Tanase, D. M.; Gosav, E. M.; Anton, M. I.; Floria, M.; Seritean Isac, P. N.; Hurjui, L. L.; Tarniceriu, C. C.; Costea, C. F.; Ciocoiu, M.; Rezus, C. Oxidative Stress and NRF2/KEAP1/ARE Pathway in Diabetic Kidney Disease (DKD): New Perspectives. *Biomolecules* **2022**, *12*(9), 1227. https://doi.org/10.3390/biom12091227

[20] Ai, X.; Yu, P.; Peng, L.; Luo, L.; Liu, J.; Li, S.; Lai, X.; Luan, F.; Meng, X. Berberine: A Review of its Pharmacokinetics Properties and Therapeutic Potentials in Diverse Vascular Diseases. *Front. Pharmacol.* **2021**, *12*, 762654. https://doi.org/10.3389/fphar.2021.762654

[21] Kumaş, M.; Eşrefoğlu, M.; Karataş, E.; Duymaç, N.; Kanbay, S.; Ergün, I. S.; Üyüklü, M.; Koçyiğit, A. Investigation of Dose-dependent Effects of Berberine Against Renal Ischemia/Reperfusion Injury in Experimental Diabetic Rats. *Nefrologia* **2019**, *39* (4), 411–423. https://doi.org/10.1016/j.nefro.2018.10.006

[22] Abd El-Mottaleb, N.; Abd-Elhady, H.; Hassanin, K.; Khaleel, A.; Mostafa, E. Role of Berberine in Diabetic Adult Male Rats. *Bull. Egypt. Soc. Physiol. Sci.* **2014**, *34*(1), 200–219. https://doi.org/10.21608/besps.2014.34793

[23] Shoob, H. D.; Thompson, S. J.; Drane, J. W.; Tocharoen, A.; Sargent, R. G.; Best, R. G. Dietary Methionine is Involved in the Etiology of Neural Tube Defect-affected Pregnancies in Humans. *J. Nutr.* **2001**, *131*(10), 2653–2658. https://doi.org/10.1093/jn/131.10.2653

[24] Yang, F.; Gao, R.; Luo, X.; Liu, R.; Xiong, D. Berberine Influences Multiple Diseases by Modifying Gut Microbiota. *Front. Nutr.* **2023**, *10*, 1187718. https://doi.org/10.3389/fnut.2023.1187718

[25] Huyut, Z.; Yildizhan, K.; Altındağ, F. The Effects of Berberine and Curcumin on Cardiac, Lipid Profile and Fibrosis Markers in Cyclophosphamide-induced Cardiac Damage: The Role of the TRPM2 Channel. *J. Biochem. Mol. Toxicol.* **2024**, *38*(6), e23783. https://doi.org/10.1002/jbt.23783

[26] Goudarzi, M.; Kalantar, M.; Malayeri, A.; Basir, Z.; Karamallah, M. H.; Kalantar, H. Berberine Alleviates Sodium Arsenite-induced Renal and Liver Toxicity by Regulating Oxidative Stress and Inflammation in Rats. *Toxicol. Environ. Health Sci.* **2023**, *15*(2), 157–172. https://doi.org/10.1007/s13530-023-00168-7

[27] Willke, T. Methionine Production—A Critical Review. *Appl. Microbiol. Biotechnol.* **2014**, *98*(24), 9893–9914. https://doi.org/10.1007/s00253-014-6156-y

[28] IBM Corp. *IBM SPSS Statistics for Windows*, Version 19.0; IBM Corp.: Armonk, NY, **2010**.

ASEAN
Journal of Scientific and Technological Reports
Online ISSN:2773-8752

Research article

Effect of Recycled Coarse Aggregate Quality on Compressive Strength of Concrete at Different Replacement Levels

Arusmalem Ginting[1*], One Selfiana Fitri Winarno[1], and Prasetya Adi[1]

[1] Department of Civil Engineering, Janabadra University, Yogyakarta, Indonesia
* Correspondence: aginting@janabadra.ac.id

Citation:
Ginting, A.; Winarno, O.S.F.; Adi, P. The effect of concrete cylinder testing waste quality as a replacement for natural coarse aggregate on the compressive strength of new concrete. *ASEAN J. Sci. Tech. Report.* **2026**, *29*(3), e261091. https://doi.org/10.55164/ajstr.v29i3.261091.

Article history:
Received: September 1, 2025
Revised: January 24, 2026
Accepted: January 24, 2026
Available online: February 27, 2026

Abstract: Recycled Coarse Aggregate (RCA) is produced from the processing of construction and demolition waste and is used as a replacement for Natural Coarse Aggregate (NCA). Waste concrete cylinders from compressive-strength testing in precast concrete factories are readily available but have not been optimally utilized. One potential solution for utilizing this waste is to recycle it into RCA. In previous studies, the quality of the RCA used was generally not known with certainty; therefore, its effect on Recycled Aggregate Concrete (RAC) remains to be further investigated. This study aims to determine the effect of RCA quality on the compressive strength of new concrete. The RCA used in this research consists of six quality levels: RCA67 (f'c = 67 MPa), RCA58 (f'c = 58 MPa), RCA50 (f'c = 50 MPa), RCA30 (f'c = 30 MPa), RCA25 (f'c = 25 MPa), and RCA20 (f'c = 20 MPa). NCA was replaced with RCA at two replacement levels: 50% and 100%. The tests included aggregate properties, slump, compressive strength, and unit weight. The results showed that the compressive strength of Natural Aggregate Concrete (NAC) with 100% NCA was higher than that of RAC with either 50% or 100% RCA. Compared to NAC, the compressive strength of RAC decreased by 14.11%–43.58% with 100% RCA and by 1.53%–13.75% with 50% RCA. The compressive strength of RAC decreased as the quality of RCA decreased. RCA quality had a significant effect on concrete compressive strength at both replacement levels.

Keywords: Recycled coarse aggregate; natural coarse aggregate; natural aggregate concrete; recycled aggregate concrete; compressive strength

1. Introduction

Recycled Coarse Aggregates (RCA) are produced by processing construction and demolition waste, primarily from old concrete structures, to serve as a replacement for Natural Coarse Aggregates (NCA) in new concrete mixes. Their use supports environmental sustainability by reducing landfill waste and conserving natural resources [1,2]. Waste concrete specimens from laboratory testing can be crushed and recycled for use as coarse aggregates in new concrete [3,4]. RCA, obtained from construction and demolition waste, has a specific gravity of 2.21-2.66, a density of 1270-1487 kg/m^3, and an abrasion value of approximately 37%. Generally, the compressive, tensile, and flexural strengths of Recycled Aggregate Concrete (RAC) are about 10%–20% lower compared to those of Natural Aggregate Concrete (NAC) [5]. The water absorption of RAC increases with increasing NCA replacement by RCA [6–8]. The manufacturing process of RCA generally involves the following main

steps: collection of construction and demolition waste, crushing, cleaning and sorting, grading, and quality control [9]. RCA can be used as a partial or full replacement for NCA in concrete mixes, with performance impacts varying with the replacement level and application [10].

Tran et al. [11] conducted a study on RAC with NCA replaced by RCA at levels of 25%, 50%, 75%, and 100%. The workability of RAC decreased with increasing RCA content. The compressive strength of RAC was 5.0–9.3% lower than that of NAC, primarily due to a weaker interfacial transition zone (ITZ). The elastic modulus of RAC was also lower than that of NAC, with a difference of 7.7% at 100% RCA content. Qasim et al. [12] used RCA from construction waste to replace NCA at levels of 0%, 10%, 20%, 30%, 40%, 50%, 60%, 70%, 80%, 90%, and 100%. The workability of RAC decreased with increasing NCA replacement, due to the RCA's rough surface texture. The compressive strength also decreased as the NCA replacement level increased. Al-Shamaa et al. [13] used building rubble as RCA to replace NCA at 0%, 35%, 65%, and 100% levels. Replacing NCA with 100% RCA resulted in lower slump values. NAC had an average density of 2390 kg/m^3, while RAC, with 100% RCA, had a significantly lower density of 2116 kg/m^3 (11% lower). Compared to NAC, RAC with 100% RCA showed a 64% decrease in compressive strength, a 71% decrease in tensile strength, a 62% decrease in flexural strength, and a 12% decrease in density. Buller et al. [14] used demolished concrete as RCA to replace 50% of the NCA in concrete mixes. The RCA had a water absorption of 3.90%, which was 120% higher than that of NCA. Its specific gravity was 2.40, approximately 5% lower than that of NCA. The density of RAC was 1960 kg/m^3, 11% lower than that of NAC. The compressive strength of RAC was 6.95% lower than that of NAC. Halahla et al. [15] used demolished concrete waste as Recycled Coarse Aggregate (RCA) for 100% replacement of NCA. The RCA had significantly higher water absorption, almost twice that of NCA, which must be considered in concrete mix design. The compressive strength of RAC was approximately 10% lower than that of NAC, while its splitting tensile strength was about 4% lower. Hassan [16] used RCA to replace NCA at levels of 20%, 40%, 60%, 80%, and 100%. Increasing the RCA percentage decreased the slump. However, replacing NCA with RCA at these levels had little effect on the concrete's compressive strength.

Demolished column waste was used as RCA to replace NCA at levels of 10%, 20%, 30%, 40%, 50%, and 100%. The compressive, flexural, and splitting tensile strengths of the concrete were reduced as the proportion of demolished column waste in the mixture increased [17]. Concrete pile waste was used as RCA to replace 100% of the NCA. The resulting RAC exhibited greater compressive strength than the NAC [18]. The company's recycled coarse aggregate was used as RCA to replace NCA at 0%, 30%, 40%, and 50%. The slump values achieved met the target requirements. Replacement of NCA with RCA was feasible up to 50%, with the compressive strength of RAC being equal to or exceeding that of NAC [19]. Crushed tested cylinders were used as RCA to replace NCA at levels of 0%, 20%, 40%, 60%, 80%, and 100%. Substituting NCA with varying proportions of RCA had no adverse effect on the consistency of the concrete mixture. In the case of Normal Strength Concrete (NSC), the incorporation of RCA led to an average decrease of 9.8% in compressive strength, 13.5% in splitting tensile strength, and 11% in elastic modulus. For High Strength Concrete (HSC), the reductions averaged 11% for compressive strength, 10.3% for splitting tensile strength, 10.8% for flexural strength, and 11.3% for elastic modulus [20].

In precast concrete factories, concrete cylinder waste from compressive-strength testing is abundant but is not optimally utilized. One potential solution to maximize the benefits of this waste is to recycle it for use as a replacement for NCA in new concrete mixes. Utilizing concrete cylinder waste in this manner can reduce the demand for NCA and minimize waste accumulation. In previous studies, the quality of RCA used as an NCA replacement was often unknown, necessitating investigation of its effect on the properties of new concrete. In precast concrete factories, concrete cylinder waste can be classified by original concrete strength. This study aims to evaluate the correlation of RCA quality, as a replacement for NCA, to the compressive strength of RAC. This study hypothesizes that RCA quality influences the compressive strength of RAC.

2. Materials and Methods

2.1 Concrete components

2.1.1 Cement

This study utilized Type I Ordinary Portland Cement (OPC), which has a specific gravity of 3.15, a fineness of 160 m^2/kg, a minimum initial setting time of 60 minutes, and a maximum final setting time of 600 minutes.

2.1.2 Sand

The sand used in this study was sourced from Srumbung, Magelang, Indonesia. The tests performed included silt content analysis [21], specific gravity and absorption [22], unit weight [23], water content [24], fineness modulus, and gradation [25]. The results of the sand tests are presented in Table 1. The sand is classified as rather coarse, falling within Zone II, as shown in Figure 1.

Table 1. Test results of sand.

Types of testing	Results	Unit
Silt content	2.300	%
Specific gravity	2.558	-
Absorption	2.776	%
Unit weight	1.379	g/cm^3
Water content	4.146	%
Fineness modulus	2.806	-

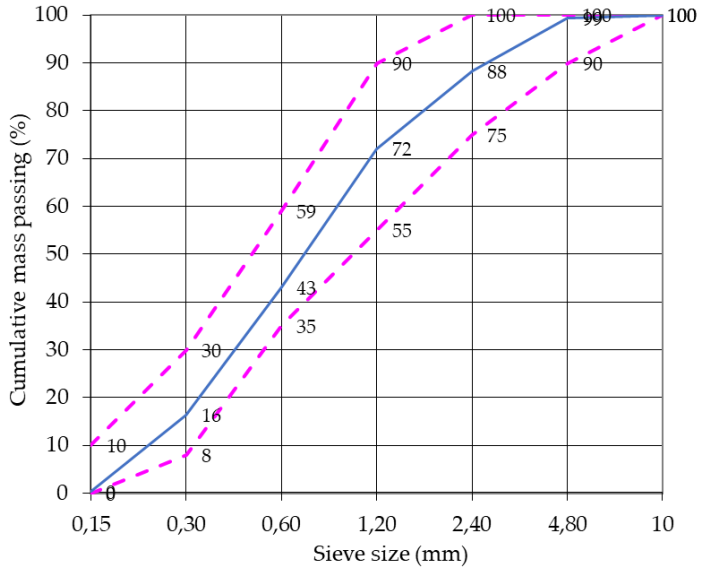

Figure 1. Gradation of sand.

2.1.3 Natural Coarse Aggregate (NCA)

In this study, the NCA was produced from crushed stone supplied by a quarry in Clereng, Kulon Progo, Yogyakarta, Indonesia. The tests performed included silt content analysis [21], specific gravity and absorption [26], unit weight [23], water content [24], fineness modulus, abrasion value, and gradation [25]. The results of the NCA tests are presented in Table 2. The maximum particle size of the NCA is 20 mm, as shown in Figure 2.

Table 2. Test results of NCA.

Types of testing	Results	Unit
Silt content	0.550	%
Specific gravity	2.635	-
Absorption	2.145	%
Unit weight	1.319	g/cm^3
Water content	1.199	%
Fineness modulus	6.766	-
Abrasion value	22.880	%

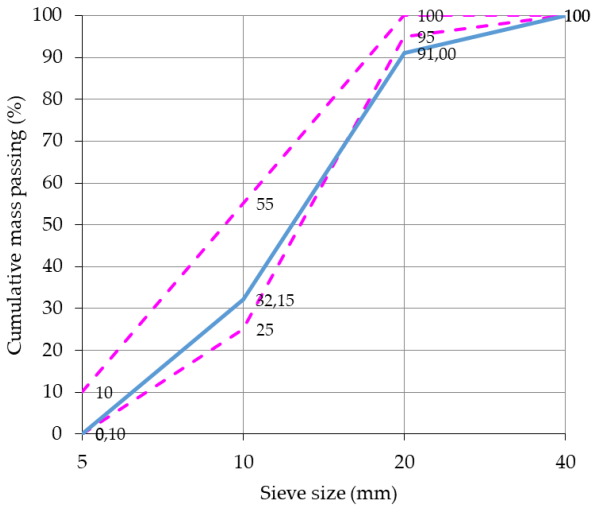

Figure 2. Gradation of NCA.

2.1.4 Recycled Coarse Aggregates (RCA)

The RCA used in this study was derived from concrete cylinder waste obtained from compressive strength testing, as shown in Figure 3. The waste cylinders were crushed at a stone-crushing plant and then sieved. The RCA was classified into six categories based on different mix designs: 67 MPa (RCA67), 58 MPa (RCA58), 50 MPa (RCA50), 30 MPa (RCA30), 25 MPa (RCA25), and 20 MPa (RCA20). The results of the RCA tests are presented in Table 3. The maximum particle size of the RCA is 20 mm, as shown in Figure 4.

Figure 3. Concrete cylinder waste: A) Before crushing, B) After crushing.

Table 3. Test results of RCA.

Types of testing	RCA67	RCA58	RCA50	RCA30	RCA25	RCA20	Unit
Silt content	0.60	1.00	0.95	2.65	2.10	2.80	%
Specific gravity	2.577	2.506	2.469	2.439	2.387	2.457	-
Absorption	2.723	3.735	3.040	4.604	4.064	4.336	%
Unit weight	1.331	1.280	1.297	1.268	1.267	1.267	g/cm^3
Water content	0.452	0.503	0.898	1.200	0.503	0.751	%
Fineness modulus	6.686	6.730	6.654	6.521	6.476	6.546	-
Abrasion value	26.900	27.220	27.180	36.960	40.240	39.660	%

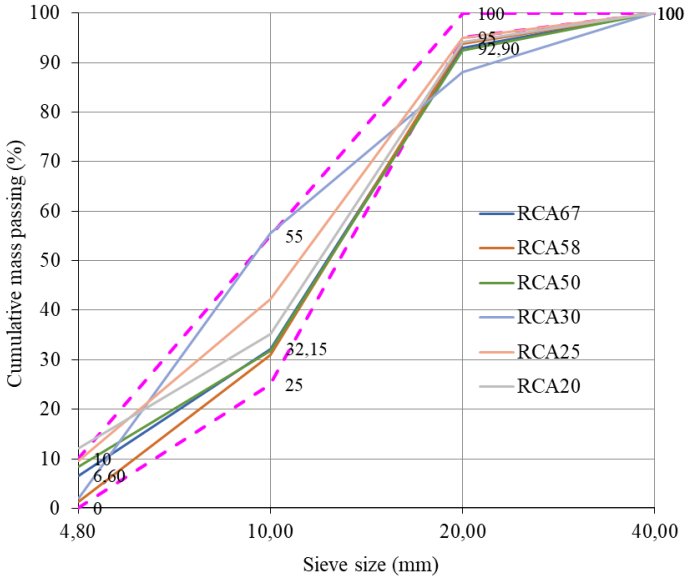

Figure 4. Gradation of RCA.

2.2 Mix design

The mix design was prepared in accordance with the Indonesian National Standard SNI 03-2834-2000. [25] The mix design followed the methods for normal concrete mix design as specified in the Indonesian National Standard SNI 03-2834-2000, for 1 m^3 of concrete with a target compressive strength of 25 MPa at 28 days, the mix proportions were as follows: 205 liters of water, 477 kg of cement, 652 kg of fine aggregate, 1019 kg of coarse aggregate, and a water–cement ratio of 0.43. The target slump value was 60–180 mm. The water and aggregate requirements in the mix design were based on saturated surface-dry (SSD) conditions. The aggregates used were air-dry condition, so the water volume and weight of the aggregates were adjusted based on the absorption value and actual water content of the aggregates. The test specimens were concrete cylinders with a diameter of 150 mm and a height of 300 mm. NCA was replaced with RCA at 50% and 100% replacement levels, with the specimen variations presented in Table 4.

Table 4. Test specimens.

Mix Code	f'c of RCA (MPa)	NCA (%)	RCA (%)	Number of test specimens	Material requirements for 1 m³ of concrete				
					Cement (kg)	Sand (kg)	NCA (kg)	RCA (kg)	Water (L)
100NCA	-	100	0	3	477	660	1009	0	206
100RCA67	67	0	100	3	477	651	0	981	219
100RCA58	58	0	100	3	477	640	0	955	228
100RCA50	50	0	100	3	477	633	0	956	217
100RCA30	30	0	100	3	477	628	0	937	229
100RCA25	25	0	100	3	477	621	0	923	231
100RCA20	20	0	100	3	477	632	0	940	231
50RCA67	67	50	50	3	477	655	501	494	212
50RCA58	58	50	50	3	477	650	497	485	217
50RCA50	50	50	50	3	477	647	494	488	212
50RCA30	30	50	50	3	477	644	492	480	218
50RCA25	25	50	50	3	477	640	489	476	219
50RCA20	20	50	50	3	477	646	494	480	219

2.3 Concrete cylinder testing

Compressive strength testing of the concrete cylinders was conducted after 28 days of curing, in accordance with the Indonesian National Standard SNI 1974-2011 [27]. The curing method used was water curing at 23 ± 1.7 °C. The compressive strength testing machine used had a capacity of 2000 kN, with a loading rate of 0.15-0.35 MPa/s.

3. Results and Discussion

3.1 Coarse aggregate test results

3.1.1 Silt content

The results of the silt content test are shown in Figure 5.

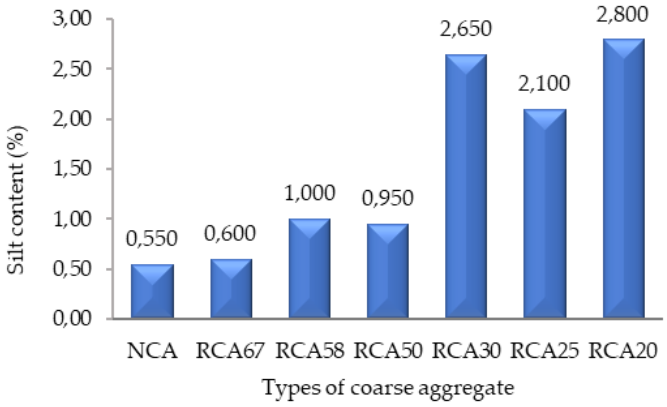

Figure 5. Silt content.

Figure 5 shows that the silt content, defined as the proportion of material passing the No. 200 sieve (0.075 mm), is lower for NCA compared to RCA. A decreasing RCA quality or original compressive strength corresponds to an increase in silt content. This is attributed to the higher amount of residual mortar or adhered old concrete, which tends to disintegrate during the recycling process. Based on the analysis of variance (ANOVA), the obtained F-value was 9.1429 with degrees of freedom (5,6) and a p-value of 0.0089, indicating that the quality of RCA significantly affects silt content.

3.1.2 Specific gravity

The results of the specific gravity test are presented in Figure 6. The specific gravity of NCA is higher than that of RCA. Furthermore, a decrease in RCA quality or compressive strength corresponds to a reduction in its specific gravity.

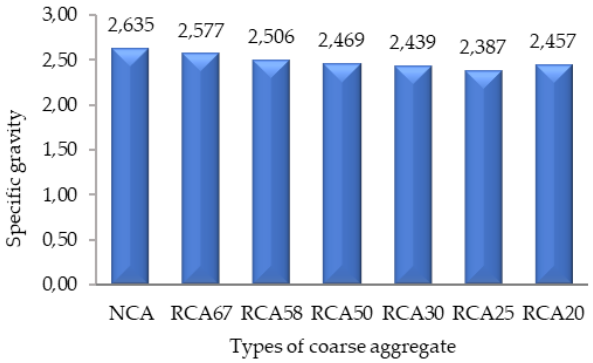

Figure 6. Specific gravity.

Based on the results of the analysis of variance (ANOVA), the obtained F-value was 16.0764 with degrees of freedom (5,6) and a p-value of 0.002, indicating that the quality of RCA has a significant effect on specific gravity.

3.1.3 Absorption

Figure 7 presents the results of the absorption test, showing that NCA exhibits lower water absorption compared to RCA. This higher absorption in RCA is primarily due to residual mortar or old adhered concrete on its surface, which increases its water-uptake capacity.

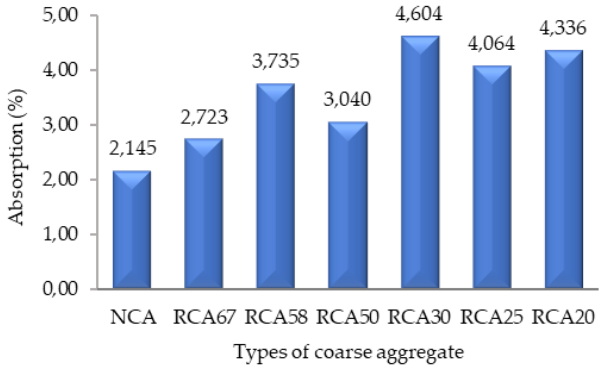

Figure 7. Absorption.

Based on the analysis of variance (ANOVA), the obtained F-value was 2.0248 with degrees of freedom (5,6) and a p-value of 0.2077, indicating that the quality of RCA does not have a significant effect on absorption.

3.1.4 Unit weight

The results of the unit weight test are presented in Figure 8. Overall, the unit weight of NCA is higher than that of RCA.

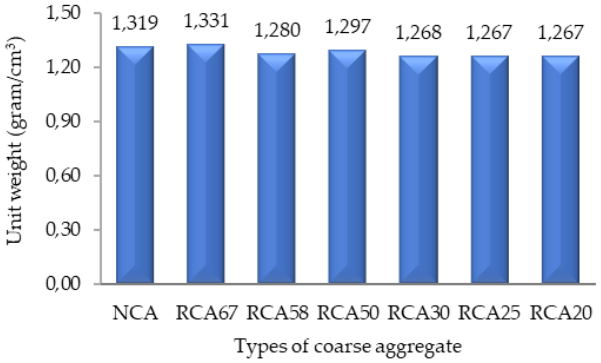

Figure 8. Unit weight.

Based on the results of the analysis of variance (ANOVA), the obtained F-value was 1.7014 with degrees of freedom (5,6) and a p-value of 0.2673, indicating that the quality of RCA does not have a significant effect on unit weight.

3.1.5 Fineness modulus

The results of the fineness modulus test are presented in Figure 9. The fineness modulus of NCA is nearly the same as that of RCA, indicating that the coarseness of both aggregates used in this study is comparable.

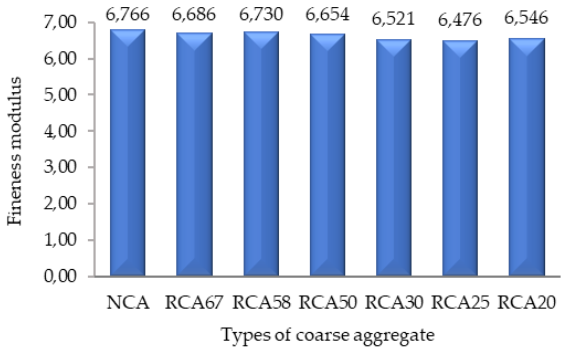

Figure 9. Fineness modulus.

3.1.6 Abrasion value

Figure 10 illustrates the results of the abrasion test, showing that the abrasion value of NCA is lower than that of RCA, indicating that NCA has greater resistance to wear. Additionally, the data indicate that a reduction in RCA quality or compressive strength is associated with an increase in its abrasion value.

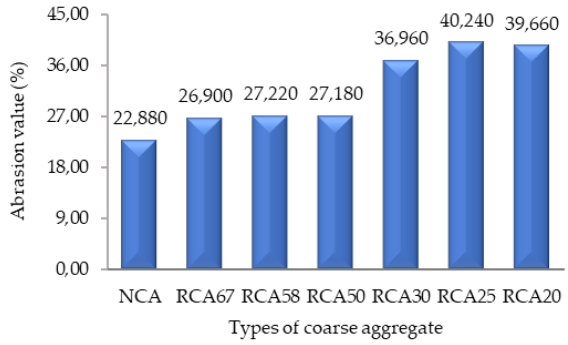

Figure 10. Abrasion value.

3.2. Slump value

The results of the slump value test are presented in Figure 11. The figure illustrates the slump values of mixtures containing NCA, RCA, and a combination of NCA and RCA. All mixtures achieved slump values within the target range of 60–180 mm. Although RCA exhibits higher water absorption than NCA, this does not significantly affect the slump value, provided that water content adjustments are made to the mixture in accordance with the aggregate's absorption capacity and moisture condition.

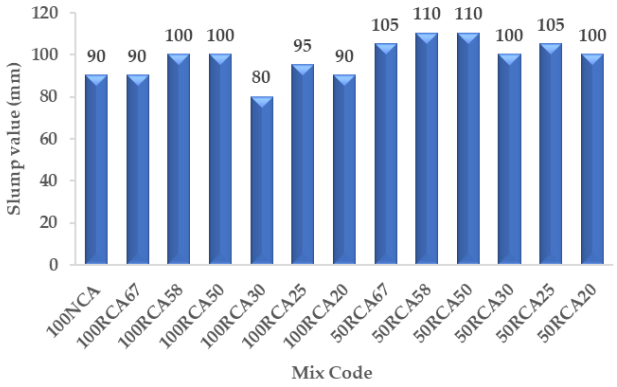

Figure 11. Slump value.

3.3 Compressive strength

The compressive strength test outcomes are displayed in Table 5, Figure 12, and Figure 13. As indicated in Table 5 and Figure 12, the compressive strength of NAC made with 100% NCA is greater than that of RAC composed entirely of RCA. Furthermore, the compressive strength of RAC declines as RCA quality decreases. The mix incorporating 100% RCA with a compressive strength rating of 67 MPa (100RCA67) attained 85.89% of the strength achieved by the 100% NCA mix (100NCA), surpassing the findings reported by Noshin et al. [28] at 84.21%, and Hassan et al. [29] at 73.65%. The compressive strength of concrete containing 100% RCA with compressive strength classes of 58 MPa, 50 MPa, 30 MPa, 25 MPa, and 20 MPa reached 72.87%, 66.28%, 58.38%, 54.17%, and 56.42%, respectively, of the compressive strength of concrete containing 100% NCA. These values are lower than those reported by Noshin et al. [28] (84.21%) and Hassan et al. [29] (73.65%).

Table 5. Compressive strength.

Mix Code	f'c of RCA (MPa)	NCA (%)	RCA (%)	Average compressive strength		Std. Dev.	F-value	P-Value
				MPa	%			
100NCA	-	100	0	33.38	100	2.6695		
100RCA67	67	0	100	28.68	85.89	4.6879	10.541	0.00046
100RCA58	58	0	100	24.33	72.87	1.3400		
100RCA50	50	0	100	22.13	66.28	1.1002		
100RCA30	30	0	100	19.49	58.38	1.1505		
100RCA25	25	0	100	18.08	54.17	1.2053		
100RCA20	20	0	100	18.84	56.42	0.3592		
50RCA67	67	50	50	32.87	98.47	1.2354	4.25	0.01863
50RCA58	58	50	50	32.18	96.41	2.2266		
50RCA50	50	50	50	32.64	97.78	0.2650		
50RCA30	30	50	50	31.19	93.42	1.0725		
50RCA25	25	50	50	28.79	86.25	0.8657		
50RCA20	20	50	50	30.10	90.16	1.5516		

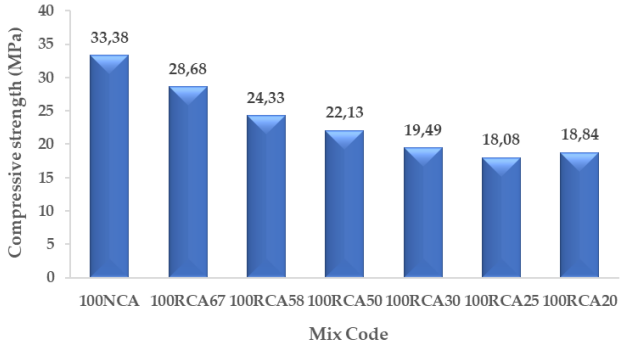

Figure 12. Compressive strength of concrete with 100% RCA.

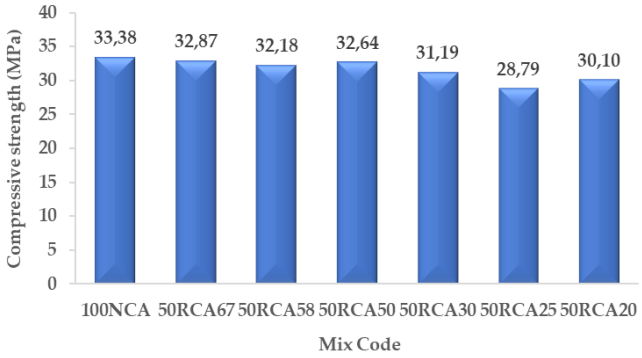

Figure 13. Compressive strength of concrete with 50% RCA.

Based on Table 5 and Figure 13, the compressive strength of NAC containing 100% NCA is higher than that of RAC containing 50% RCA. For RAC, compressive strength decreases as RCA quality decreases. The compressive strength of concrete incorporating 50% RCA with compressive strength classes of 67 MPa, 58 MPa, 50 MPa, 30 MPa, 25 MPa, and 20 MPa reached 98.47%, 96.41%, 97.78%, 93.42%, 86.25%, and 90.16%, respectively, of the compressive strength of concrete made with 100% NCA. These values are either higher or lower than those reported by Noshin et al. [28] of 94.26%. The analysis of variance (ANOVA) for 100% replacement of natural coarse aggregate (NCA) with recycled concrete aggregate (RCA) yielded an F-value of 10.541 with degrees of freedom (5,12) and a p-value of 0.00046, indicating that the quality of RCA has a statistically significant effect on the compressive strength of concrete when NCA is fully replaced by RCA. Similarly, for 50% replacement of NCA with RCA, the ANOVA yielded an F-value of 4.25 with degrees of freedom (5,12) and a p-value of 0.01863, indicating that the quality of RCA also has a statistically significant effect on the compressive strength of concrete at a 50% replacement level. The coefficient of determination, along with the regression equations for concrete compressive strength at 100% and 50% NCA replacement levels, is presented in Figures 14 and 15.

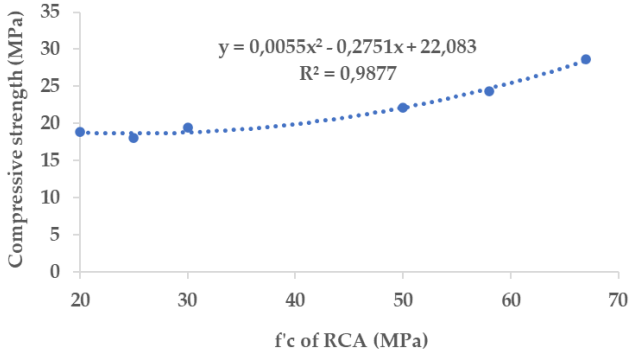

Figure 14. The coefficient of determination for **the** compressive strength of concrete with 100% RCA.

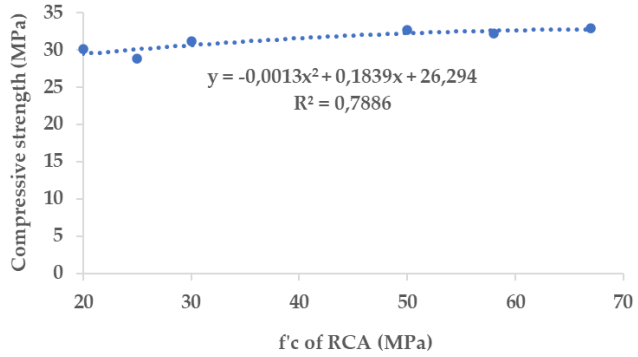

Figure 15. The coefficient of determination for **the** compressive strength of concrete with 50% RCA.

From Figure 14, the high coefficient of determination (R^2 = 0.9877) indicates a statistically strong relationship between RCA quality and concrete compressive strength for mixtures with 100% replacement of NCA, where 98.77% of the variability in compressive strength is explained by the regression model $y = 0.0055x^2 - 0.2751x + 22.083$. From Figure 15, the coefficient of determination (R^2 = 0.7886) indicates a statistically strong relationship between RCA quality and concrete compressive strength for mixtures with 50% replacement of NCA, where 78.86% of the variability in compressive strength is explained by the regression model y = -0,0013x2 + 0,1839x + 26,294.

3.4 Unit weight

The unit weight results are presented in Figure 16. As shown, the unit weight of NAC made with 100% NCA is higher than that of RAC produced with either 100% or 50% RCA.

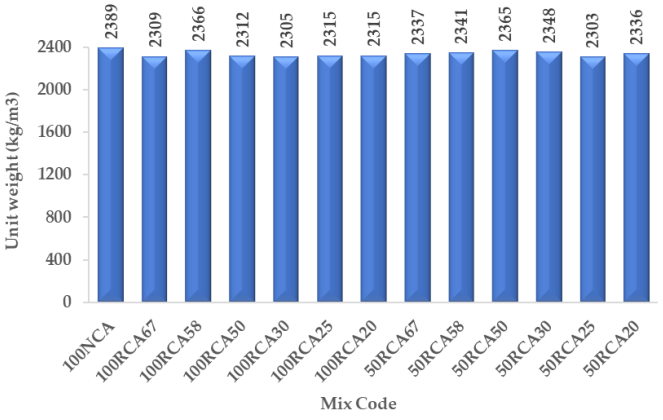

Figure 16. Unit weight.

The analysis of variance (ANOVA) for 100% replacement of natural coarse aggregate (NCA) with recycled concrete aggregate (RCA) yielded an F-value of 0.91 with degrees of freedom (5,12) and a p-value of 0.50623 ($p > 0.05$), indicating that the quality of RCA does not have a significant effect on unit weight. Similarly, for 50% replacement of NCA with RCA, the ANOVA yielded an F-value of 1.117 with degrees of freedom (5,12) and a p-value of 0.40191 ($p > 0.05$), indicating that the quality of RCA does not have a significant effect on unit weight at a 50% replacement level.

4. Conclusions

This research examines the effect of RCA quality when used as a substitute for NCA on concrete compressive strength. The findings demonstrate that NAC produced entirely with NCA achieves higher compressive strength than RAC incorporating 100% or 50% RCA. Furthermore, the compressive strength of RAC declines proportionally as the quality of RCA decreases. Statistical evaluation confirms that RCA quality

significantly influences the compressive strength of concrete at both 100% and 50% replacement levels. To achieve the minimum compressive strength of 20 MPa for structural concrete, a minimum RCA quality of 50 MPa is required for full NCA replacement, while a minimum RCA quality of 20 MPa is adequate for 50% replacement. Suggestions for further research include using a wider range of RCA quality levels and increasing the number of test specimens for each variation to improve the statistical robustness and reliability of the results.

5. Acknowledgements

The authors gratefully acknowledge the Faculty of Engineering and Janabadra University, for providing the facilities and technical assistance that supported the completion of this research.

Author Contributions: Conceptualization and experimental design: A.G., O.S.F.W., and P.A.; experimental work and data acquisition: A.G., O.S.F.W., and P.A.; writing-original draft preparation and editing: A.G. and O.S.F.W. All authors have read and approved the final version of the manuscript.

Funding: This research was funded by the Faculty of Engineering and Janabadra University.

Conflicts of Interest: The authors declare no conflict of interest.

References

[1] Kumar, V.; Kumar, E. R.; Singh, G. Utilization of Recycled Coarse Aggregates (RCA) for Development of Concrete: Review. *Int. J. Creat. Res. Thoughts* **2024**, *12*(3), 139–144.

[2] Sadik, M. N.; Akter, T.; Proma, P. D.; Prodhan, M. A. R.; Momotaj, M. Impact of Recycled Coarse Aggregates on the Mechanical Properties and Durability of Concrete. *Eur. J. Theor. Appl. Sci.* **2024**, *2*(5), 738–759. https://doi.org/10.59324/ejtas.2024.2(5).66

[3] Benito, E. K. D.; et al. Durability Performance of Concrete Containing Recycled Coarse Aggregates Derived from Laboratory-tested Specimens. *World J. Eng.* **2024**, *21*(3), 604–614. https://doi.org/10.1108/WJE-02-2023-0033

[4] Bilal, H.; Ali, D. Overview of Studies on the Effect of Recycled Aggregates Sourced from Tested Cylinders on Concrete Material and Structural Properties. *MATEC Web Conf.* **2017**, *120*, 03007. https://doi.org/10.1051/matecconf/201712003007

[5] Neupane, R. P.; Imjai, T.; Makul, N.; Garcia, R.; Kim, B.; Chaudhary, S. Use of Recycled Aggregate Concrete in Structural Members: A Review Focused on Southeast Asia. *J. Asian Archit. Build. Eng.* **2025**, *24* (3), 1197–1220. https://doi.org/10.1080/13467581.2023.2270029

[6] Ayub, T.; Khan, A.-R.; Mahmood, W. Effect of Recycled Concrete Aggregates on Compressive Strength and Water Permeability of Concrete. *Int. J. Energy Environ.* **2020**, *14*, 25–32. https://doi.org/10.46300/91012.2020.14.6

[7] Xiao, Q.; Liu, X.; Qiu, J.; Li, Y. Capillary Water Absorption Characteristics of Recycled Concrete in Freeze-Thaw Environment. *Adv. Mater. Sci. Eng.* **2020**, *2020*, 1620914. https://doi.org/10.1155/2020/1620914

[8] Gao, Q.; Ma, Z.; Xiao, J.; Li, F. Effects of Imposed Damage on the Capillary Water Absorption of Recycled Aggregate Concrete. *Adv. Mater. Sci. Eng.* **2018**, *2018*, 2890931. https://doi.org/10.1155/2018/2890931

[9] Prasittisopin, L.; Tuvayanond, W.; Kang, T. H. K.; Kaewunruen, S. Concrete Mix Design of Recycled Concrete Aggregate (RCA): Analysis of Review Papers, Characteristics, Research Trends, and Underexplored Topics. *Resources* **2025**, *14*(2), 21. https://doi.org/10.3390/resources14020021

[10] Shawais, Z. A.; Abdulhaleem, K. N.; Ahmed, S. H.; Hamada, H. M.; Mohammed, V. R. Influence of Recycled Coarse Aggregate and Steel Fiber on the Workability and Strength of Self-Compacting Concrete. *IOP Conf. Ser.: Earth Environ. Sci.* **2024**, *1374*(1), 012084. https://doi.org/10.1088/1755-1315/1374/1/012084

[11] Tran, D. V. P.; Allawi, A.; Albayati, A.; Cao, T. N.; El-zohairy, A.; Nguyen, Y. T. H. Recycled Concrete Aggregate for Medium-Quality Concrete. *Materials* **2021**, *14*(16), 4612. https://doi.org/10.3390/ma14164612

[12] Qasim, O. A.; Hilal, N.; Al Biajawi, M. I.; Sor, N. H.; Tawfik, T. A. Studying the Usability of Recycled Aggregate to Produce New Concrete. *J. Eng. Appl. Sci.* **2024**, *71*(1), 1–24. https://doi.org/10.1186/s44147-024-00463-1

[13] Al-shamaa, M. F. K.; Ali, A. A.; Al-mulla, I. F. A. Mechanical Characteristics of Structural Concrete Using Building Rubbles as Recycled Coarse Aggregate. *J. Mech. Behav. Mater.* **2024**, *33*(1), 20240001. https://doi.org/10.1515/jmbm-2024-0001

[14] Buller, A. H.; Husain, N.; Buller, A. S.; Channa, I. A.; Ali, T.; Shabbir, S. Effect of Recycled Aggregates on Physical and Mechanical Performance of Green Concrete Mix. *Teh. Vjesn.* **2025**, *32*(1), 306–312.

[15] Halahla, A. M.; Akhtar, M.; Almasri, A. H. Utilization of Demolished Waste as Coarse Aggregate in Concrete. *Civ. Eng. J.* **2019**, *5*(3), 540–551. https://doi.org/10.28991/cej-2019-03091266

[16] Hassan, S. S. Effects of Recycled Concrete Aggregate on Some Mechanical Properties of High Strength Concrete. *IOP Conf. Ser.: Mater. Sci. Eng.* **2018**, *433*, 012033. https://doi.org/10.1088/1757-899X/433/1/012033

[17] Hegde, R.; Rao, K. S.; Shashank, H.; Madar, S. H.; Jakathi, A. H.; Vijaykumar, P. V. A Study on Strength Characteristics of Concrete by Replacing Coarse Aggregate by Demolished Column Waste. *Int. J. Eng. Res. Technol.* **2018**, *7* (6), 386–395. https://doi.org/10.17577/IJERTV7IS060213

[18] Jantarachot, K.; Yodsudjai, W.; Nokkaew, N.; Prayongphan, S. Compressive Strength of Recycled Aggregated Concrete From Concrete Waste and Plastic Waste. *Int. J. GEOMATE* **2023**, *25*(108), 72–80. https://doi.org/10.21660/2023.108.3857

[19] Yoon, S.; Choi, W.; Jeon, C. Effects of the Recycled Coarse Aggregate Mixing Ratio on the Characteristics of Concrete with Different Design Strengths. *J. Mater. Cycles Waste Manag.* **2024**, *26*(5), 2792–2803. https://doi.org/10.1007/s10163-024-02007-4

[20] Hamad, B. S.; Dawi, A. H. Sustainable Normal and High Strength Recycled Aggregate Concretes Using Crushed Tested Cylinders as Coarse Aggregates. *Case Stud. Constr. Mater.* **2017**, *7*, 228–239. https://doi.org/10.1016/j.cscm.2017.08.006

[21] Badan Standarisasi Nasional Indonesia. *Metode Pengujian Jumlah Bahan dalam Agregat yang Lolos Saringan No. 200 (0,075 mm)*. SNI 03-4142-1996; Jakarta, 1996.

[22] Badan Standarisasi Nasional Indonesia. *Cara Uji Berat Jenis dan Penyerapan Air Agregat Halus*. SNI 1970:2016; Jakarta, 2016.

[23] Badan Standarisasi Nasional Indonesia. *Test Methods for Unit Weight and Voids in Aggregates*. SNI 03-4804-1998; Jakarta, 1998.

[24] Badan Standarisasi Nasional Indonesia. *Metode Pengujian Kadar Air Agregat*. SNI 03-1971-1990; Jakarta, 1990.

[25] Badan Standarisasi Nasional Indonesia. *Tata Cara Pembuatan Rencana Campuran Beton Normal*. SNI 03-2834-2000; Jakarta, 2000.

[26] Badan Standarisasi Nasional Indonesia. *Cara Uji Berat Jenis dan Penyerapan Air Agregat Kasar*. SNI 1969:2006; Jakarta, 2016.

[27] Badan Standarisasi Nasional Indonesia. *Cara Uji Kuat Tekan Beton dengan Benda Uji Silinder*. SNI-1974-2011; Jakarta, 2011.

[28] Noshin, S.; Aslam, M. S.; Kanwal, H.; Khan, M. A.; Ahmad, A. Effects on Compressive and Tensile Strength of Concrete by Replacement of Natural Aggregates with Various Percentages of Recycled Aggregates. *Mehran Univ. Res. J. Eng. Technol.* **2022**, *41*(1), 195–201.

[29] Hassan, H. A.; El Moghazy, M.; El-Tehawy, E. Reusing Egyptian In-situ Construction & Demolition Waste (CDW) to Produce Sustainable Concrete: Investigation of Compressive & Bond Strengths Using Steel & Glass Fiber Reinforced Polymer (GFRP) Rebars. *HBRC J.* **2024**, *20*(1), 301–316. https://doi.org/10.1080/16874048.2024.2314884

ASEAN
Journal of Scientific and Technological Reports
Online ISSN:2773-8752

Research article

An IoT-Based Real-Time Human Fall Detection and Notification System with Instance Segmentation Deep Learning

Wiwat Su-hren[1], Tanawat Srirugsa[1,4], Saowanee Singsarothai[1], Supachai Kaewpoung[1,4] and Tawat Chuchit[1,4*]

[1] Faculty of Engineering, Thaksin University, Phatthalung 93210, Thailand
[4] Center of Excellence for Agricultural Innovation and Bioproducts of Thaksin University, Thaksin University, Phatthalung, 93210, Thailand
* Correspondence: tawat.c@tsu.ac.th; (T. Chuchit)

Citation:
Suhren, W., Srirugsa, T., Singsarothai, S., Kaewpoung, S., Chuchit, T., An IoT-based real-time human fall detection and notification system with instance segmentation eeep learning. *ASEAN J. Sci. Tech. Report.* **2026**, *29*(3), e260412. https://doi.org/10.55164/ajstr. v29i3.260412.

Article history:
Received: July 19, 2025
Revised: January 6, 2026
Accepted: January 11, 2026
Available online: February 28, 2026

Abstract: This research presents a person fall detection system based on deep learning using the Instance Image Segmentation technique with the YOLOv11-seg model, which achieves high speed and accuracy in object detection. The developed system aims to individually detect a person's posture in an image, enabling accurate analysis of their falling posture characteristics. And there is a notification in the application to the administrator or relevant person within 10 seconds, allowing quick help. Using a dataset of 10,169 images, 8622 for training, 994 for inspection, and 553 for testing (with a ratio of 85:10:5 for training, inspection, and testing). The system performs impressively by using all 3 YOLOv11-seg models: YOLOv11s-seg, YOLOv11n-seg, and YOLOv11m-seg. The training dataset showed excellent performance with a YOLOv11s-seg model, achieving a precision of 0.966, a recall of 0.910, and an F1 Score of 0.88. The results show that the developed system can detect falls and issue real-time alerts via an IoT-based framework. It improves safety and reduces the risk for the elderly or patients at risk of falling.

Keywords: Instance segmentation; deep learning; human fall detection system; YOLO; IoT-based framework

1. Introduction

Fall-related injuries are a major problem affecting the quality of life of the elderly and high-risk patients. According to the World Health Organization (WHO), falls are the leading cause of severe injuries and a major factor in premature deaths among the elderly [1], with the trend of an increasing elderly population around the world. This problem has attracted increased attention in the research community, leading to the development of systems that can detect falls and provide timely assistance. Falling detection with computer vision and artificial intelligence (AI) technology has become popular because it is a non-intrusive method and can be widely applied in the real world. Especially when deep learning technology is used to help analyze human movement behavior. This significantly increases the detection accuracy. One technique that has gained attention is Instance Segmentation, which can segment and classify individual objects in an image at the pixel level [2]. It enables more effective detection of falling behavior than traditional methods based on Object Detection or Pose Estimation. In some cases, there is overlap among individuals or a complex environment. Past research has shown that using pose skeletons rather than boundaries can effectively improve the efficiency of individual discrimination [3]. In addition, approaches based on image sequence analysis with 3D CNNs and temporal models such as LSTMs have become increasingly

popular [4,5]. These techniques can temporarily extract movement data to help better distinguish falling behavior from normal movement. Meanwhile, Techniques that use skeleton-based detection in conjunction with temporal networks, such as Two-stage Temporal Convolutional Networks (TCN) and models that integrate OpenPose with high-performance networks, have been developed to meet the needs of real-time detection [6,7]. However, past research has identified an important trend: integrating deep learning techniques with multi-perspective visual data and temporal motion analysis, which is the main direction of fall detection technology today. [8].

The main goal of this research is to create a system that can be used in a variety of environments. It supports real-time processing and helps enhance the safety of the elderly and patients at high risk of falling in their daily lives. This research aims to present a new approach to applying Deep Learning and Instance Segmentation in healthcare and accident surveillance in the future.

2. Materials and Methods

2.1 Instance segmentation

In the past decade, the rapid advancement of Artificial Intelligence (AI) has driven significant progress in computer vision, particularly in image understanding and object segmentation. Among various techniques, instance segmentation has emerged as one of the most important and widely adopted approaches, integrating the strengths of object detection and semantic segmentation. While object detection provides coarse localization through bounding boxes and semantic segmentation assigns class labels to pixels without distinguishing individual objects, instance segmentation enables the precise localization and delineation of each object instance at the pixel level. This capability is particularly important for applications that require accurate spatial understanding, such as human posture analysis and fall detection. Instance segmentation techniques were initially popularized by the Mask R-CNN framework, which extends the Faster R-CNN architecture by introducing a parallel branch for pixel-level mask prediction, as illustrated in Figure 1. In Mask R-CNN, region proposals generated by the Region Proposal Network (RPN) are processed simultaneously by a classification branch and a mask branch. A fixed-size feature representation is passed through a SoftMax function to produce class probabilities, while a Fully Connected Layer followed by deconvolution layers generates a binary segmentation mask corresponding to the detected object at its original spatial resolution. Although this design achieves high segmentation accuracy, it incurs relatively high computational complexity, which limits its suitability for real-time and edge-based applications [9]. To overcome the limitations of two-stage architectures, one-stage detection models, such as YOLO (You Only Look Once), have been extensively developed. YOLO is well known for its real-time detection capability, as it performs object localization and classification in a single forward pass. The YOLO family has evolved continuously, and the latest variant, YOLOv11-seg, extends the original detection framework to support instance segmentation while maintaining high inference speed. This characteristic makes YOLOv11-seg particularly suitable for applications that require real-time processing and low-latency deployment.

YOLOv11-seg adopts a one-stage architecture composed of three main components: a backbone, a neck, and a head. The backbone is responsible for feature extraction and is built on an improved Cross Stage Partial (CSP) bottleneck structure that enhances feature reuse while reducing computational redundancy. The neck incorporates modules such as Spatial Pyramid Pooling–Fast (SPPF) to aggregate multi-scale contextual information, enabling robust object detection across varying sizes under diverse scene conditions. In addition, integrating a Convolutional block with Parallel Spatial Attention (C2PSA) enables the network to focus more effectively on informative spatial regions within the input image. The instance segmentation capability of YOLOv11-seg is realized through a Protonet-based mask generation module integrated into the detection head. This module generates a set of shared prototype masks from high-level feature maps. For each detected object, the network predicts a set of mask coefficients that linearly combine these prototypes to produce an instance-specific segmentation mask. This mechanism is conceptually similar to that employed in the YOLACT model; however, it is optimized to integrate seamlessly with the YOLO architecture, thereby enabling faster inference and improved suitability for real-time applications. Deconvolution and up-sampling operations are subsequently applied to align the generated masks with the original image resolution, ensuring accurate object

boundaries and a faithful representation of object shapes [10,11]. By leveraging instance segmentation with YOLOv11-seg, the proposed system can obtain fine-grained pixel-level representations of human posture, which are essential for reliably distinguishing between standing and falling states. This detailed spatial information enhances robustness in challenging scenarios, such as partial occlusions, overlapping individuals, and varying illumination conditions. Consequently, YOLOv11-seg provides an effective and computationally efficient foundation for real-time human fall detection systems deployed on edge and IoT-based platforms.

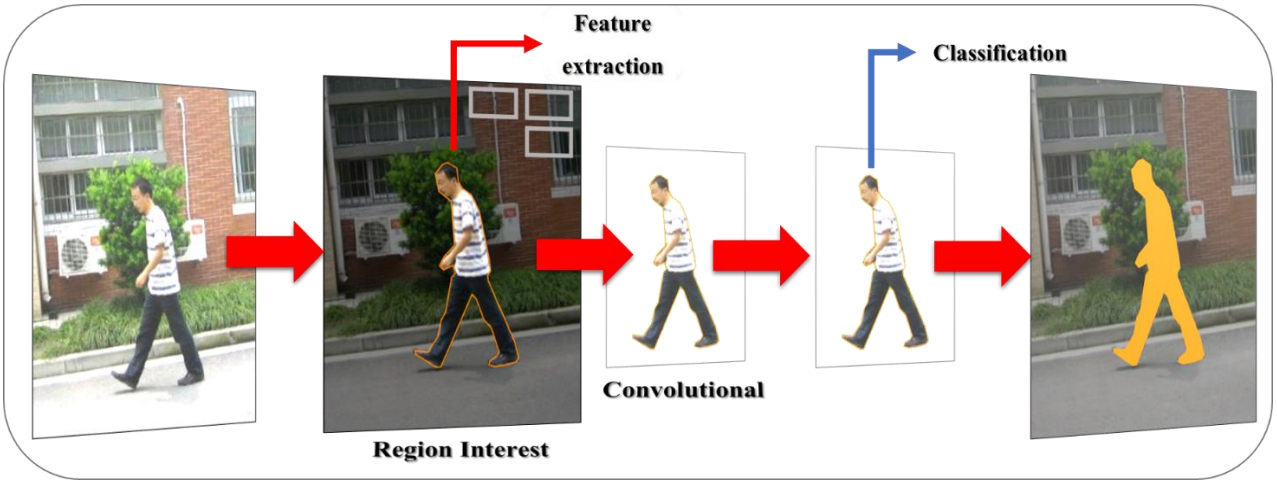

Figure 1. Principle of Mask R-CNN

2.2 ROBOFLOW

Dataset preparation is one of the most important steps in detecting and segmenting images. ROBOFLOW is a cloud-based platform designed to facilitate the preparation of visual data for computer vision tasks, especially for AI training in object detection, Image Segmentation, and Image Classification. In addition, ROBOFLOW offers data management capabilities, including data import into the platform, image annotation, image augmentation, and the creation of datasets suitable for model training in formats such as YOLO, COCO, Pascal VOC, or TFRecord. This makes ROBOFLOW an important tool that effectively reduces the technical workload and increases the speed of AI model development [12]. ROBOFLOW also supports end-to-end model training on the cloud. Users can quickly bring the datasets obtained from annotation into the training process with popular models such as YOLOv5, YOLOv8, Detectron2, or Segment Anything, as shown in Figure 2. It also supports releasing models via API immediately after annotation, which is ideal for researchers, developers, and entrepreneurs who want to experiment with it or use it in systems that require image processing, such as detecting defects in production lines or counting customers in stores. This has made it very popular in the AI industry.

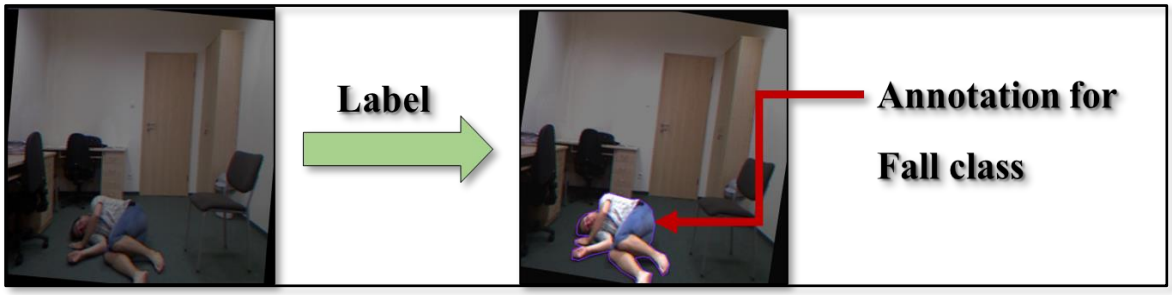

Figure 2. Annotation process.

2.3 Model evaluation

To evaluate the model, Precision (P), Recall (R), mPA@0.5, and F1-scores are used to assess its performance. Three YOLOv11-seg models were used in the test: YOLOv11s-seg, YOLOv11n-seg, and YOLOv11m-seg [13]. The Precision (P) value represents the accuracy of the prediction, which is calculated by

the number of true positives (TP) divided by the sum of the number of true positives (TP) and false positives (FP), as shown in equation 1. The Recall (R) value is used to evaluate the performance of a model that affects an object of interest. It is calculated as the number of true positives (TP) divided by the sum of true positives (TP) and false negatives (FN), as shown in equation 2. The mean Average Precision at an IoU threshold of 0.5 (mAP@0.5) represents the overall detection and segmentation performance across all classes by jointly considering localization and classification accuracy. As shown in equation 3. [14, 15]

$$P = TP / (TP + FP) \tag{1}$$

$$R = TP / (TP + FN) \tag{2}$$

$$mPA@0.5 = \frac{1}{N} \sum_{i=1}^{N} AP_i \tag{3}$$

where N is the number of classes, and AP denotes the Average Precision of class iii, obtained from the area under the Precision–Recall curve at an IoU threshold of 0.5. The mAP@0.5 metric balances detection robustness and localization tolerance and is therefore commonly adopted in real-time and edge-based detection systems. More stringent metrics, such as mAP@0.5:0.95, were not employed in this study because extremely strict localization accuracy is not essential for practical fall detection decisions. F1-Scores combines recall and precision to find the harmonic mean to solve the imbalanced classification problem, as shown in equation 4. [16,17]

$$F1\text{-}Scores = 2 \times P \times R / (P + R) \tag{4}$$

Together, these evaluation metrics provide a comprehensive assessment of the proposed system in terms of detection precision, robustness, and suitability for real-time deployment in IoT-based healthcare monitoring applications.

2.4 Integration with IoT and Real-Time Notification

To enhance the practical usability of the proposed fall detection system, the system integrates Internet of Things (IoT) technology with a real-time notification mechanism. After the YOLOv11-seg model detects a fall and confirms that the individual remains motionless for more than 10 seconds, an alert is automatically transmitted to a caregiver or designated recipient. All detection and notification processes are executed locally on an edge device, such as a Jetson Nano, a personal computer, or a Raspberry Pi, without relying on cloud-based inference, thereby reducing latency and preserving data privacy [18]. Alert notifications are delivered via LINE Notify, a messaging API widely used in Thailand, Japan, and Taiwan. The system transmits messages containing the detection timestamp, fall status, and optionally a snapshot image of the incident to the recipient's smartphone, enabling timely awareness and rapid response [19]. The end-to-end notification latency consists of three components: frame-level detection and instance segmentation, posture confirmation, and message transmission. The YOLOv11-seg model operates in real time with an average inference time of less than 500 ms per frame. A fixed 10-second immobility threshold is applied to reduce false alarms, after which the alert is sent via a secure HTTPS POST request. Under normal network conditions, message delivery latency ranges between 1 and 3 seconds [20–22]. Consequently, the total end-to-end notification latency is consistently within approximately 12 seconds, confirming the suitability of the proposed system for real-time IoT-based fall detection applications.

3. Experiment

In this study, experiments were conducted to evaluate the performance of the proposed instance segmentation–based human fall detection system using the YOLOv11-seg model. The dataset used for detection and segmentation was collected from two primary sources. The first source consisted of images captured within the Thaksin University, Phatthalung Campus, representing real-world indoor and outdoor environments with varying illumination conditions, backgrounds, and camera viewpoints. The second source

comprised curated images obtained from the Roboflow platform, selected to enhance posture diversity and scene variation. The dataset was categorized into two posture classes: Stand and Fall. The raw dataset contained 1,778 images in the Stand class and 3,878 images in the Fall class, as summarized in Table 1. To improve model robustness and generalization, data augmentation techniques were applied, including brightness and exposure adjustments. These augmentations were designed to simulate lighting variations commonly encountered in practical deployment scenarios, such as indoor environments and low-light conditions. After augmentation, the dataset was expanded to 10,169 images. The augmented dataset was divided into three subsets following an 85:10:5 ratio: 8,622 images for training, 994 images for validation, and 553 images for testing. An overview of the dataset composition is presented in Table 2, while the software tools and hardware environment used for model training and evaluation are summarized in Table 3. This data partitioning strategy was selected to ensure sufficient training samples while maintaining independent validation and testing sets for unbiased performance assessment. All experiments were conducted on a workstation equipped with an Intel Core i5-10300H CPU, an NVIDIA GTX 2060 GPU, and 16 GB of RAM. The models were implemented using Python 3.10 with CUDA 11.8 support. Due to hardware constraints, experiments were performed on a single-GPU platform. Although this configuration limits large-scale scalability evaluation, it is representative of edge-level deployment environments targeted by the proposed system, where computational resources are typically constrained.

Table 1. Data of Raw images

Class	Number of Raw images
Stand	1,778
Fall	3,878

Table 2. An overview of the dataset

Title	Description
Number of Classes	2
Total Number of Input Images	10,169
Training Images	8,622
Validation Images	994
Testing Images	553
Brightness	±13%
Exposure	±15%

Table 3. Environments used to train the model

Operating environment	Version
Operating System	Window 11
Language	Python 3.10
CUDA	11.8
GPU	GTX2060
CPU	Intel(R) Core(TM) i5-10300H

Table 4 summarizes the key training hyperparameters used for all YOLOv11-seg model variants in this study. To ensure a fair and consistent comparison, a unified training configuration was applied across all models. The input image resolution was fixed at 640 × 640 pixels, and the batch size was set to 16 samples per iteration. All models were trained for 100 epochs using the Adam optimizer with an initial learning rate of 0.01, with cosine learning rate decay to promote stable convergence. Standard YOLOv11-seg loss components, including bounding box loss, classification loss, and mask loss, were employed during training. Data augmentation techniques, such as random scaling and color adjustment, were enabled to improve generalization under varying illumination and environmental conditions. By maintaining identical hyperparameter settings for all YOLOv11-seg variants, observed performance differences can be attributed primarily to architectural variations rather than training-related bias.

Table 4. Training Hyperparameters

Hyperparameter	Value
Input image size	640 × 640
Batch size	16
Optimizer	Adam
Initial learning rate	0.01
Number of epochs	100
Loss functions	Box, Class, Mask loss

In the design of the fall detection system in this study, the working principle is clearly defined in stages. This is illustrated in Figure 3, which provides an overview of the process from inception to notification. In the design of the fall detection system in this study, the working principle is clearly defined in stages. This is illustrated in Figure 3, which provides an overview of the process from inception to notification. When the system starts, a pre-trained YOLOv11-seg model is loaded and trained on a dataset divided into "standing" and "falling" classes. The model has been adjusted using various parameters and weights from the training process to accurately distinguish a person's behavior in the image at the pixel level using the Instance Segmentation technique. After the image or video is sent to the system, the model continuously analyzes each image frame to detect a person's posture in the scene. If the system detects that a person is in a posture consistent with the nature of the fall, the person is in a position that corresponds to that nature. The system will begin the automatic timer process. If within 10 seconds after the fall. The person remains in the same position, without any movements indicating recovery, such as supporting or getting up. The system concludes that it is a fall case requiring assistance and immediately sends a notification to the administrator or relevant person via a defined system, such as an application, an IoT device notification, or a messaging system. The entire sequence of steps for this system is designed to be easy to apply in a real environment and to offer a high degree of flexibility in deployment across different devices. Image Analysis Decisions and alerts are collected and displayed in a flowchart format, as shown in Figure 4, to provide a clear overview of all mechanisms.

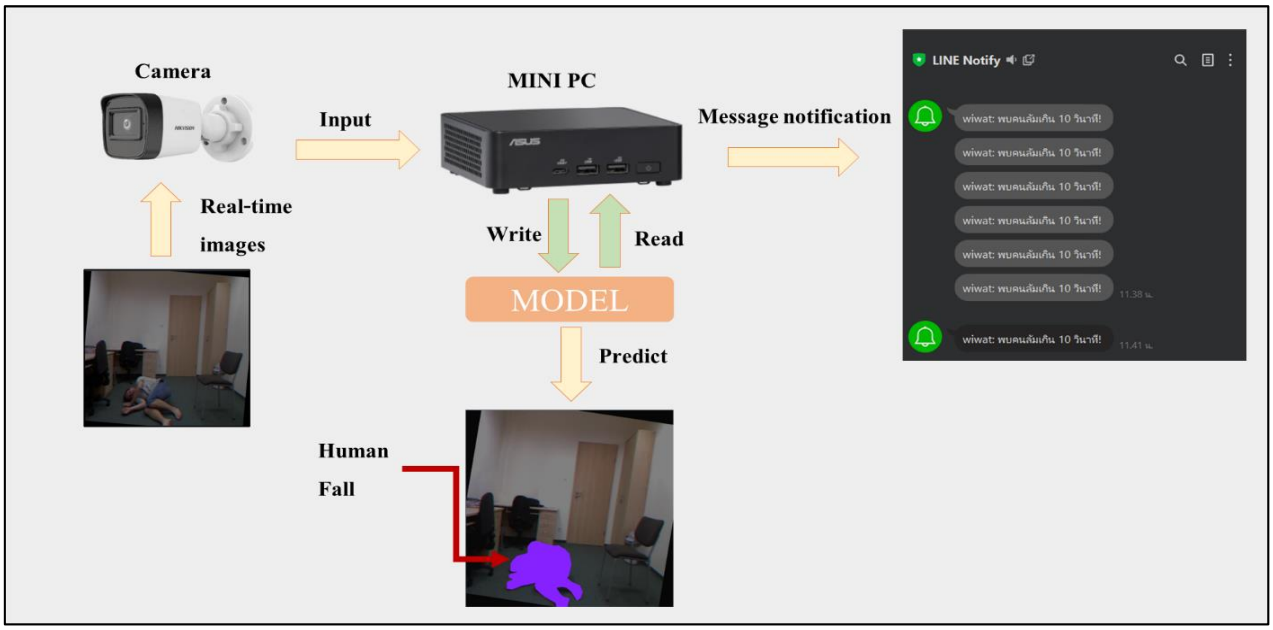

Figure 3. Principle of operation.

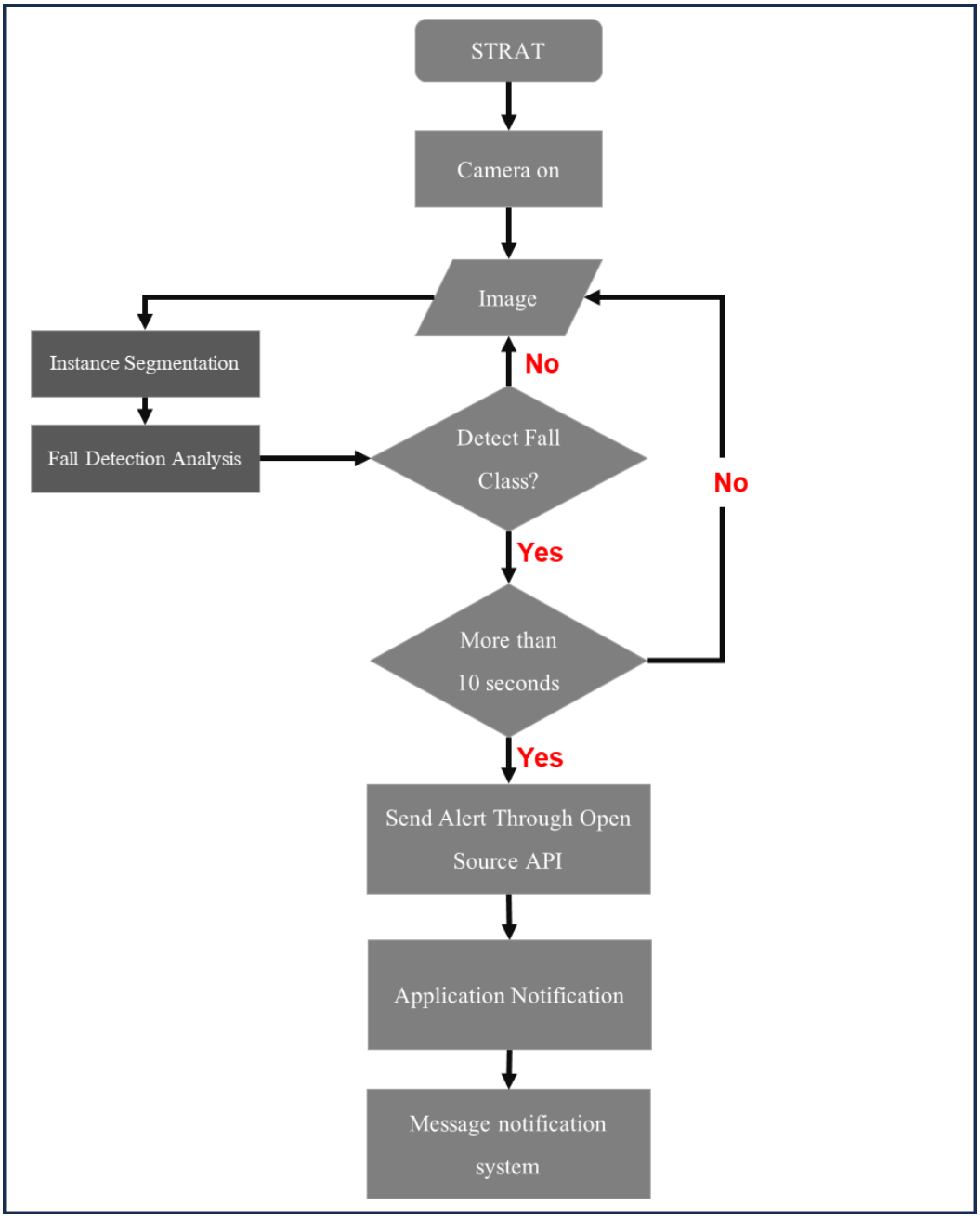

Figure 4. Flowchart.

4. Results and Discussion

In this paper, we propose the detection of fallen people by an instance segmentation method using the YOLOv11-seg model, which compares three models, namely YOLOv11s-seg, YOLOv11n-seg, and YOLOv11m-seg, by using Precision (P), Recall (R), mPA@0.5, and F1-scores to evaluate models and choose the right model for the research. The Precision (P) values of each model are 0.996, 0.929, and 0.934. The Recall (R) values are 0.850, 0.847, and 0.836, and the mPA0.5 values are 0.906, 0.906, and 0.763, respectively, as shown in Table 5. The results show that the suitable model is YOLOv11s-seg, as it achieves higher Precision, Recall, and mPA@0.5 than other models. In addition, there are fewer internal parameters than in other models. This makes the processing faster.

Table 5. Model Evaluation Results

Model	P	R	mAP@0.5
Yolov11s	0.996	0.850	0.906
Yolov11n	0.929	0.847	0.906
Yolov11m	0.934	0.836	0.763

To further analyze model behavior, Precision–confidence, Recall–confidence, and F1-score curves were examined, as shown in Figures 5–7. Across all three models, the Precision curves increase with higher confidence thresholds, while the F1-score curves decrease. This behavior reflects the expected trade-off between detection confidence and recall and indicates consistent and stable prediction characteristics across different model variants.

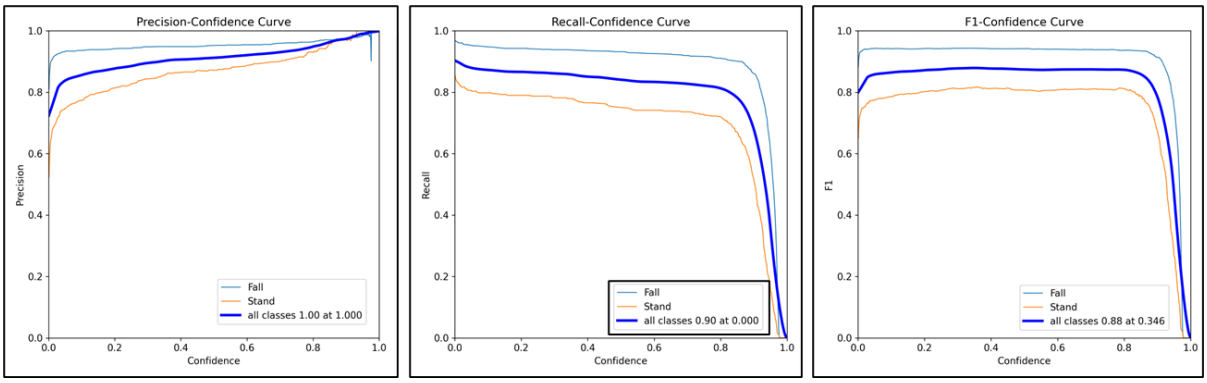

Figure 5. P-curve, R-curve, and F1-Scores curve of the YOLOv11s-seg model.

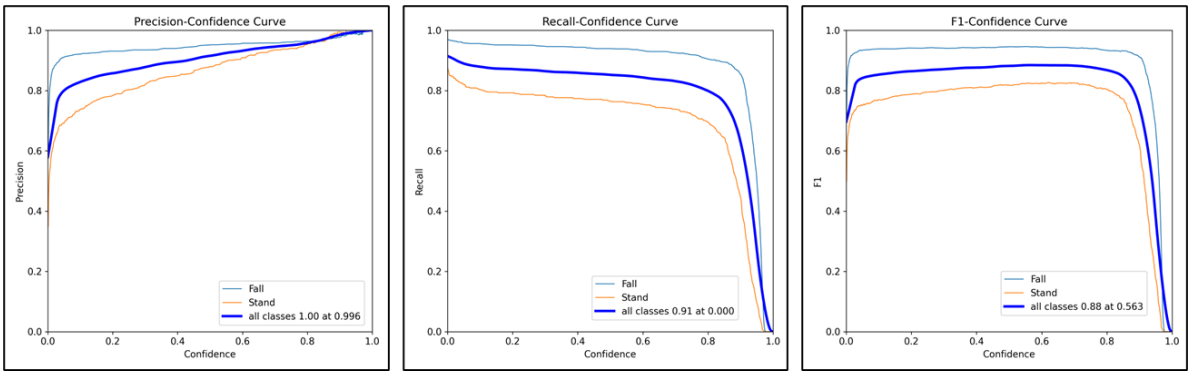

Figure 6. P-curve, R-curve, and F1-Scores curve of the YOLOv11n-seg model.

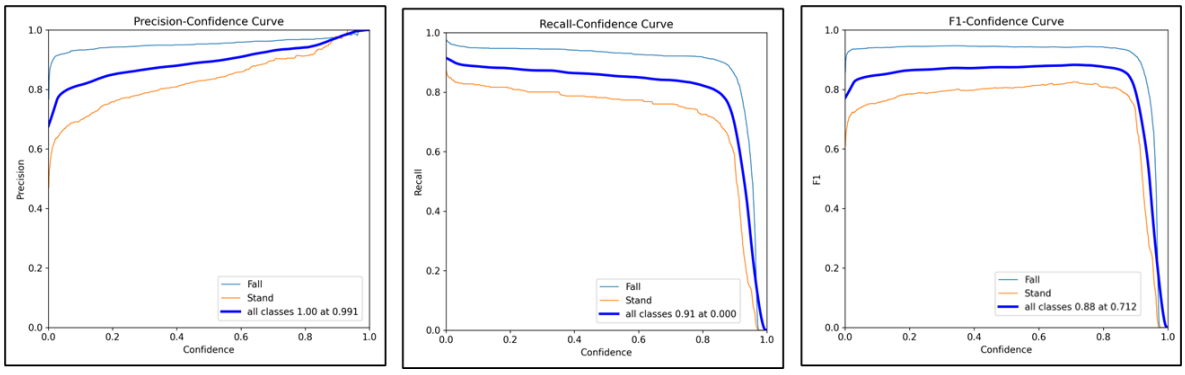

Figure 7. P-curve, R-curve, and F1-Scores curve of the YOLOv11m-seg model.

Qualitative evaluation results demonstrate that the proposed system can reliably distinguish between standing and falling postures under various environmental conditions. The system remains effective in challenging scenarios, including overlapping individuals and low-light environments. Representative detection results are illustrated in Figures 8 and 9, which show standing posture detection under normal and low-light conditions, respectively. Figures 10 and 11 present examples of fall detection for different fall orientations, including backward and inverted falls, under both lighting conditions. In all cases, the system visualizes the detected posture using segmentation masks and displays the corresponding confidence score, allowing users to assess detection reliability.

To position the proposed system within the broader context of fall detection research, Table 6 compares it with representative categories of existing fall detection approaches. Traditional computer vision–based methods offer low computational cost but suffer from limited robustness under illumination changes and occlusion. Wearable sensor–based systems achieve high detection accuracy but require continuous user compliance and device usage. Pose estimation–based and temporal deep learning approaches improve posture understanding and motion modeling, but introduce sensitivity to occlusion or increased computational complexity and latency. In contrast, the proposed YOLOv11-seg–based instance segmentation approach achieves high detection performance with real-time inference by directly analyzing pixel-level posture information, making it well-suited for edge and IoT-based fall detection applications.

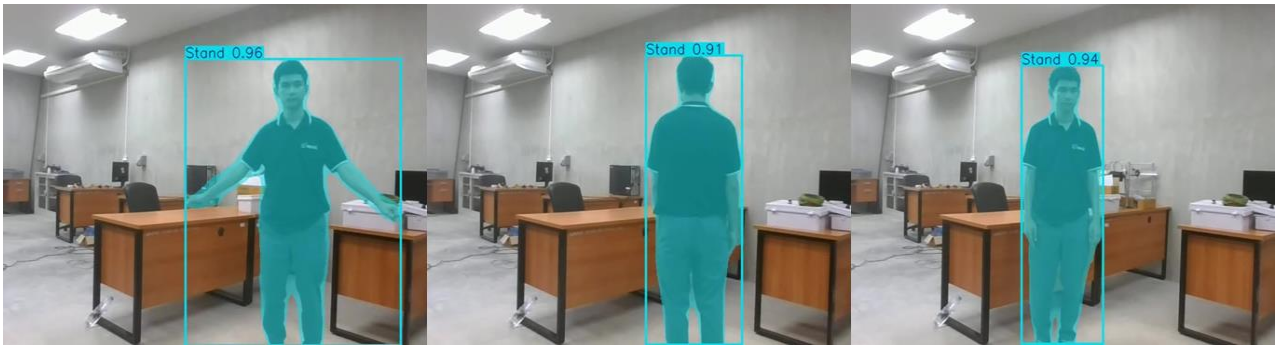

Figure 8. Human standing Detection in normal environmental conditions.

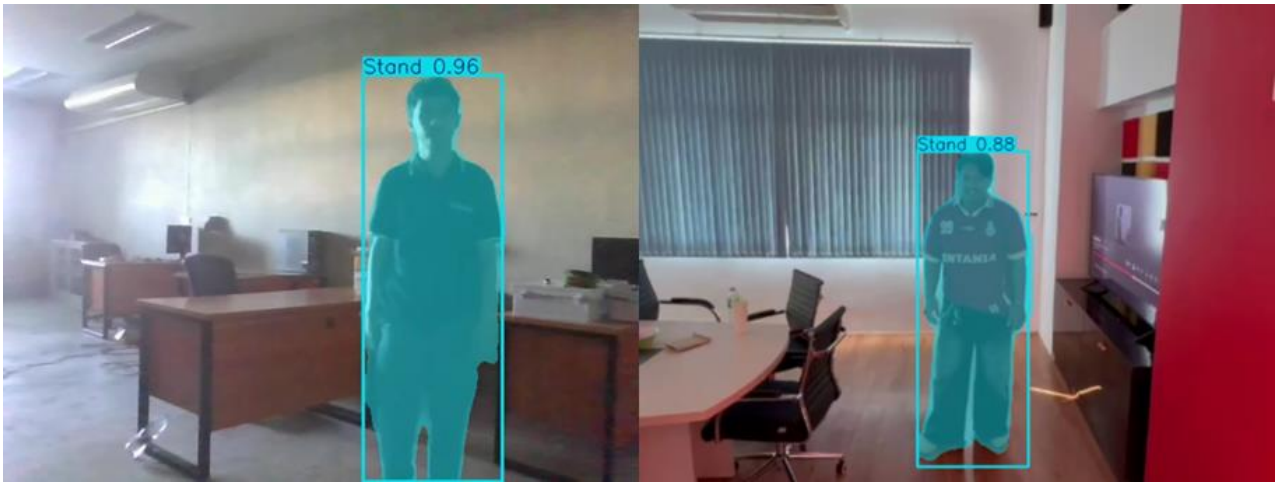

Figure 9. Human standing detection in low-light environmental conditions.

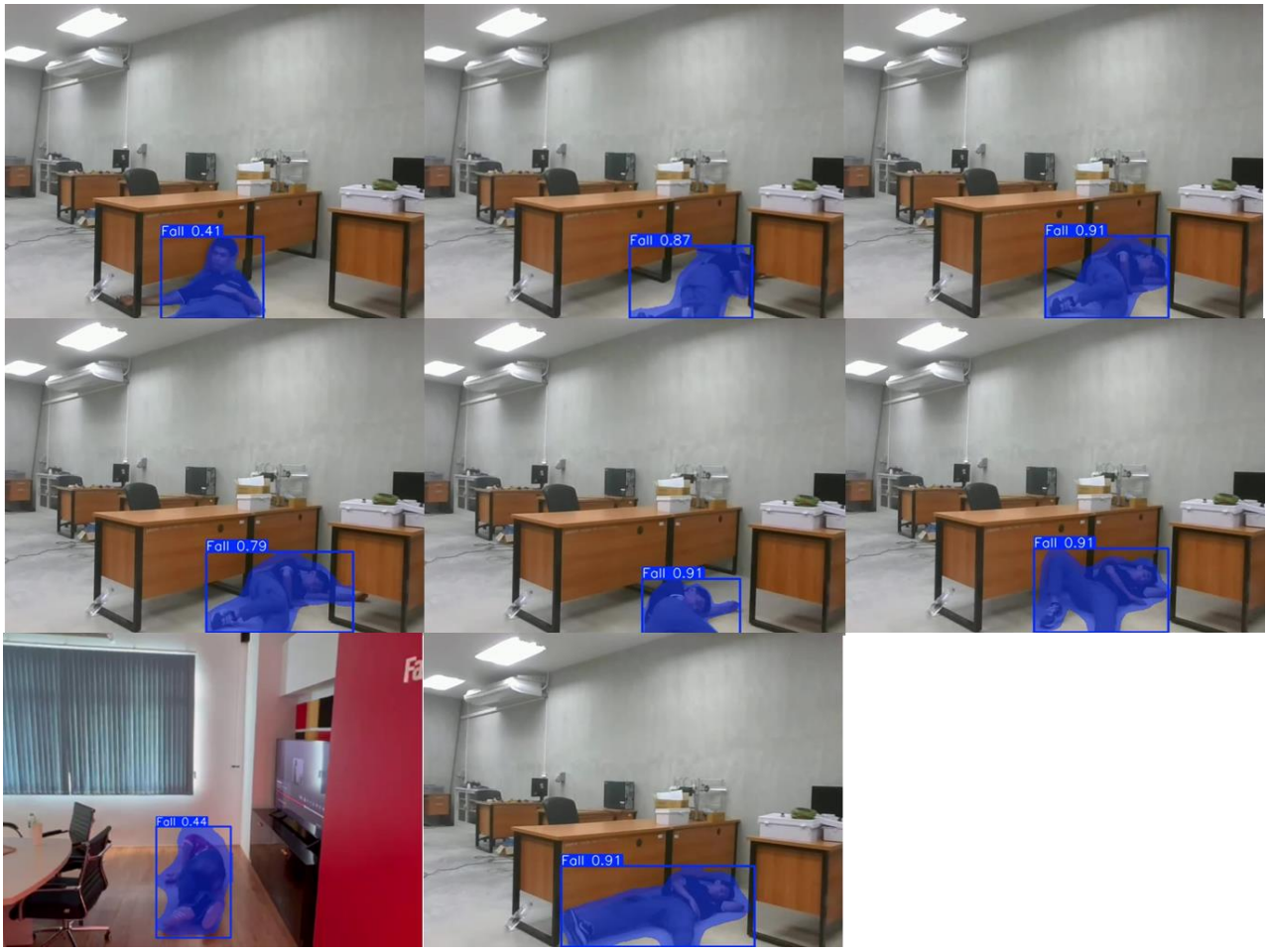

Figure 10. Detecting falls in various postures in normal environmental conditions.

Figure 11. Detecting falls across various postures in low-light environments.

In terms of performance reliability, the experimental results show that the model produces consistent outcomes across the training, validation, and testing datasets, indicating stable behavior when applied to unseen data. An analysis of detection errors reveals that false positive cases mainly occur during transitional human motions, such as bending or sitting, which may temporarily resemble falling postures. In contrast, false negatives are primarily observed in situations with partial occlusion or uncommon camera viewpoints, where the full body posture cannot be clearly captured.

Table 6. Comparison with Existing Fall Detection Approaches.

Approach Category	Representative Methods	Key Characteristics	Limitations	Suitability for Real-Time Deployment
Traditional Computer Vision [23]	Background subtraction, Optical flow, Motion history images	Low computational cost; simple implementation	Highly sensitive to illumination changes, occlusion, and background dynamics; limited robustness	Limited
Wearable Sensor-Based [24, 25]	Accelerometer, Gyroscope-based systems	Direct motion sensing; independent of visual conditions	Requires user compliance, discomfort, battery constraints, and privacy concerns	Moderate
Pose Estimation-Based [26]	OpenPose-based, skeleton tracking methods	Explicit posture and joint analysis; interpretable features	Degraded performance under occlusion, low resolution, or inaccurate key-point detection	Moderate
Temporal Deep Learning Models [27]	CNN–LSTM, TCN-based approaches	Captures motion dynamics over time; improved temporal consistency	Requires sequential buffering, higher computational overhead, and increased latency	Limited to Moderate
Proposed Method	YOLOv11-seg (Instance Segmentation)	Pixel-level posture representation; frame-level decision; robust to occlusion and illumination variation	Limited dataset diversity; absence of temporal modeling	High

5. Conclusions

This study presented a real-time human fall detection system based on instance segmentation using the YOLOv11-seg model. By analyzing human posture at the pixel level, the proposed system can distinguish between standing and falling postures under various environmental conditions. The integration of edge-based processing with an IoT notification mechanism enables timely alert delivery after a fall event is confirmed. A comparative evaluation of YOLOv11s-seg, YOLOv11n-seg, and YOLOv11m-seg showed that YOLOv11s-seg offers the best balance between detection performance and computational efficiency. The model achieved higher Precision, Recall, and mAP@0.5 values while maintaining a lower parameter count, making it appropriate for real-time deployment on edge devices. Several limitations should be acknowledged. The dataset was collected mainly from a university environment and includes only two posture classes, which may limit generalizability. In addition, the current system lacks temporal modeling, and formal statistical validation was not conducted. Future work will focus on expanding the dataset, incorporating additional posture classes and temporal information, and further evaluating the system in more diverse real-world environments.

6. Acknowledgements

We are grateful to the Faculty of Engineering, Thaksin University, Phatthalung Campus, for allowing the location for this research experiment.

Author Contributions: The following are the contributions of each author in this research: Conceptualization: Tanawat Srirugsa and Saowanee Singsarothai; Methodology: Tanawat Srirugsa and Tawat Chuchit; Software: Wiwat Su-hren and Supachai Kaewpoung; Writing—review and editing: Tawat Chuchit and Wiwat Su-hren; Project administration: Tawat Chuchit.

Funding: This work was supported by the Fundamental Fund for fiscal year 2025, provided by the Science, Research and Innovation Promotion Fund, for the project "Design and Development of a Smart Vegetable Plot Prototype with Internet of Things (IoT) Technology for the Elderly" at Thaksin University.

Conflicts of Interest: The authors of this study hereby state that they have no conflicts of interest.

References

[1] World Health Organization. Falls. https://www.who.int/news-room/fact-sheets/detail/falls (accessed 2026-02-23).

[2] He, K.; Gkioxari, G.; Dollár, P.; Girshick, R. Mask R-CNN. *Proc. IEEE Int. Conf. Comput. Vis.* **2017**, 2980–2988. https://doi.org/10.1109/ICCV.2017.322

[3] Zhang, S.-H.; Li, R.; Dong, X.; Rosin, P. L.; Cai, Z.; Han, X.; Yang, D.; Huang, H.-Z.; Hu, S.-M. Pose2Seg: Detection Free Human Instance Segmentation. *Proc. IEEE Conf. Comput. Vis. Pattern Recognit.* **2019**, 8811–8819. https://doi.org/10.1109/CVPR.2019.00902

[4] Lu, N.; Wu, Y.; Feng, L.; Song, J. Deep Learning for Fall Detection: Three-Dimensional CNN Combined With LSTM on Video Kinematic Data. *IEEE J. Biomed. Health Inf.* **2019**, *23*(1), 314–323. https://doi.org/10.1109/JBHI.2018.2808281

[5] Yao, L.; Yang, W.; Huang, W. A Fall Detection Method Based on a Joint Motion Map Using Double Convolutional Neural Networks. *Multimed. Tools Appl.* **2022**, *81*, 4551–4568. https://doi.org/10.1007/s11042-020-09181-1

[6] Su, S.; Wu, S.-S.; Chen, S.-Y.; Duh, D.-J. Multi-view Fall Detection Based on Spatio-temporal Interest Points. *Multimed. Tools Appl.* **2016**, *75*, 8469–8492. https://doi.org/10.1007/s11042-015-2766-3

[7] Gao, M.; Li, J.; Zhou, D.; Zhi, Y.; Zhang, M.; Li, B. Fall Detection Based on OpenPose and MobileNetV2 Network. *IET Image Process.* **2023**, *17*(3), 722–732. https://doi.org/10.1049/ipr2.12667

[8] Alam, E.; Sufian, A.; Dutta, P.; Leo, M. Vision-Based Human Fall Detection Systems Using Deep Learning: A Review. *Comput. Biol. Med.* **2022**, *146*, 105626. https://doi.org/10.1016/j.compbiomed.2022.105626

[9] Li, L.; Fang, M.; Fu, F. Instance Segmentation Based on Improved YOLACT. *Proc. Int. Conf. Virtual Real. Vis. (ICVRV)* **2020**, 165–170. https://doi.org/10.1109/ICVRV51359.2020.00042

[10] Khanam, R.; Hussain, M. YOLOv11: An Overview of the Key Architectural Enhancements. *arXiv* **2024**, arXiv:2410.17725. https://doi.org/10.48550/arXiv.2410.17725

[11] He, L.; Zhou, Y.; Liu, L.; Ma, J. Research and Application of YOLOv11-Based Object Segmentation in Intelligent Recognition at Construction Sites. *Buildings* **2024**, *14*(12), 3777. https://doi.org/10.3390/buildings14123777

[12] Deepa, D.; Sivasangari, A.; Roonwal, R.; Nayan, R. Pothole Detection using Roboflow Convolutional Neural Networks. *Proc. 7th Int. Conf. Intell. Comput. Control Syst. (ICICCS)* **2023**, 560–564. https://doi.org/10.1109/ICICCS56967.2023.10142700

[13] Su-Hren, W.; Chuchit, T.; Kaewpoung, S. Development of an Autonomous EV Navigation System Using Instance Segmentation for Medical Supply Delivery. *Proc. 13th Int. Electr. Eng. Congr. (iEECON)* **2025**, 1–6. https://doi.org/10.1109/iEECON64081.2025.10987580

[14] Babila, I. F. E.; Villasor, S. A. E.; Dela Cruz, J. C. Object Detection for Inventory Stock Counting Using YOLOv5. *Proc. IEEE 18th Int. Colloq. Signal Process. Appl. (CSPA)* **2022**, 304–309. https://doi.org/10.1109/CSPA55076.2022.9782028

[15] Mostafa, M.; Sadi, S.; Anamika, S. A.; Hussain, M. S.; Khan, R. Automatic Vehicle Classification and Speed Tracking. *Proc. 2nd Int. Conf. Appl. Artif. Intell. Comput. (ICAAIC)* **2023**, 972–977. https://doi.org/10.1109/ICAAIC56838.2023.10140935

[16] Pornpanomchai, C. Image Based Papaya (*Carica papaya* Linn.) Seed Germination Evaluation by ResNet50. *ASEAN J. Sci. Technol. Rep.* **2025**, *28* (1), e254804. https://doi.org/10.55164/ajstr.v25i1.245292

[17] Elaanba, A.; Ridouani, M.; Hassouni, L. Automatic Detection Using Deep Convolutional Neural Networks for Abnormal Positioning of Tubes and Catheters in Chest X-ray Images. *Proc. IEEE World AI IoT Congr. (AIIoT)* **2021**, 7–12. https://doi.org/10.1109/AIIoT52608.2021.9454205

[18] Ahmed, S.; Rahman, M. J.; Razzak, M. A. Design and Development of an IoT-Based LPG Gas Leakage Detector for Households and Industries. *Proc. IEEE World AI IoT Congr. (AIIoT)* **2023**, 762–767. https://doi.org/10.1109/AIIoT58121.2023.10174377

[19] Karar, M. E.; Shehata, H. I.; Reyad, O. A Survey of IoT-Based Fall Detection for Aiding Elderly Care: Sensors, Methods, Challenges and Future Trends. *Appl. Sci.* **2022**, *12*(7), 3276. https://doi.org/10.3390/app12073276

[20] Mrozek, D.; Koczur, A.; Małysiak-Mrozek, B. Fall Detection in Older Adults with Mobile IoT Devices and Machine Learning in the Cloud and on the Edge. *Inf. Sci.* **2020**, *537*, 132–147. https://doi.org/10.1016/j.ins.2020.05.070

[21] Yacchirema, D.; de Puga, J. S.; Palau, C.; Esteve, M. Fall Detection System for Elderly People Using IoT and Ensemble Machine Learning Algorithm. *Pers. Ubiquitous Comput.* **2019**, *23*, 801–817. https://doi.org/10.1007/s00779-018-01196-8

[22] Stanivuk, I.; Bjelić, V.; Samardžić, T.; Simić, Đ. Expanding Lua Interface to Support HTTP/HTTPS Protocol. *Proc. 13th Int. Conf. Adv. Technol., Syst. Serv. Telecommun. (TELSIKS)* **2017**, 407–410. https://doi.org/10.1109/TELSKS.2017.8246311

[23] Rougier, C.; Meunier, J.; St-Arnaud, A.; Rousseau, J. Fall Detection from Human Shape and Motion History Using Video Surveillance. *Proc. 21st Int. Conf. Adv. Inf. Netw. Appl. Workshops (AINAW)* **2007**, 875–880. https://doi.org/10.1109/AINAW.2007.181

[24] Mubashir, M.; Shao, L.; Seed, L. A Survey on Fall Detection: Principles and Approaches. *Neurocomputing* **2013**, *100*, 144–152. https://doi.org/10.1016/j.neucom.2011.09.037

[25] Noury, N.; Fleury, A.; Rumeau, P.; Bourke, A. K.; Laighin, G. O.; Rialle, V.; Lundy, J. E. Fall Detection – Principles and Methods. *Proc. 29th Annu. Int. Conf. IEEE Eng. Med. Biol. Soc. (EMBS)* **2007**, 1663–1666. https://doi.org/10.1109/IEMBS.2007.4352627

[26] Cao, Z.; Simon, T.; Wei, S.-E.; Sheikh, Y. Realtime Multi-Person 2D Pose Estimation Using Part Affinity Fields. *Proc. IEEE Conf. Comput. Vis. Pattern Recognit. (CVPR)* **2017**, 1302–1310. https://doi.org/10.1109/CVPR.2017.143

[27] Yang, G.; Zhao, J.; Guo, J. Research on Fall Detection Algorithm Based on CNN and LSTM. *Proc. 3rd Int. Conf. Nat. Lang. Process. (ICNLP)* **2021**, 190–195.

ASEAN
Journal of Scientific and Technological Reports
Online ISSN:2773-8752

Research article

Deep Learning-Based Classification of Apple Leaf Diseases under Field Conditions

Supakit Mamart[1], Sumalee Sangamuang[1*], and Prompong Sugunnasil[1]

[1] Faculty of Engineering, Chiang Mai University, 50200, Thailand
* Correspondence: sumalee.sa@cmu.ac.th

Citation:
Mamart, S.; Sangamuang, S.; Sugunnasil, P. Deep learning-based classification of apple leaf diseases under field conditions. *ASEAN J. Sci. Tech. Report.* **2026**, *29*(3), e260960. https://doi.org/10.55164/ajstr.v29i3.260960.

Article history:
Received: September 14, 2025
Revised: January 16, 2026
Accepted: January 25, 2026
Available online: February 28, 2026

Abstract: Accurate identification of apple leaf diseases in field conditions is essential for sustaining crop yield and supporting precision agriculture. Variable illumination, cluttered backgrounds, and co-occurring symptoms complicate diagnosis in real orchards. This study applies a deep learning approach using a fine-tuned MobileNetV2 model to classify apple leaf diseases from a heterogeneous dataset derived from the Plant Pathology 2021 (FGVC8) benchmark. The original five labels were expanded by subdividing the "multiple disease" category into expert-defined compound subclasses, yielding 12 disease categories encompassing both single and compound infections. Data augmentation and transfer learning were employed to improve robustness, while interpretability was assessed through Grad-CAM and LIME visualizations. Results show that the model performs well on distinct single-disease categories such as rust, scab, and frogeye leaf spot, but struggles to detect overlapping or compound infections. These findings highlight both the potential and the challenges of lightweight CNN architectures for agricultural image classification. The study contributes evidence that explainable, compact deep learning models can support future efforts to build reliable tools for plant health monitoring in diverse field conditions.

Keywords: Deep learning; mobileNetV2; apple leaf disease; explainable AI; agriculture

1. Introduction

Apple cultivation is a cornerstone of temperate agriculture, contributing significantly to food security, rural livelihoods, and international trade [1]. However, apple orchards are highly susceptible to foliar diseases such as frogeye leaf spot, powdery mildew, rust, and scab. These diseases often occur simultaneously and share overlapping symptoms, complicating timely and accurate diagnosis. Early detection is essential to reduce yield losses, yet conventional monitoring relies on manual inspection by human experts, a process that is labor-intensive, time-consuming, and prone to subjective variation [2]. Recent advances in mobile imaging technologies and edge computing have therefore stimulated interest in automated, vision-based diagnostic systems powered by deep learning to support faster and more reliable decision-making in agriculture [3].

In recent years, Convolutional Neural Networks (CNNs) have emerged as a powerful tool for plant disease recognition. Architectures such as ResNet, Inception, and EfficientNet have demonstrated high diagnostic accuracy under controlled laboratory conditions [4]. However, their large memory footprint and

high computational requirements restrict their use on mobile or embedded systems, which are more practical for field-based applications. In contrast, lightweight models such as MobileNetV2 offer a promising balance between efficiency and accuracy [5], making them suitable for real-time inference on portable devices without reliance on continuous cloud connectivity. The need for offline-capable solutions is particularly acute in many parts of the Global South. In rural and mountainous regions of Southeast Asia—including northern Thailand, Laos, and Vietnam—farmers often operate in areas with unreliable internet access or intermittent electricity supply. Such constraints make cloud-dependent systems impractical in real-world scenarios. To address this gap, self-contained diagnostic models that can operate locally are required. Moreover, interpretable lightweight AI systems are essential to promote equitable access to smart agriculture technologies, especially for smallholder farmers in underserved communities [6, 7].

Despite the progress of deep learning in plant disease diagnostics, several challenges remain. First, most models are trained on curated datasets collected under ideal conditions, which do not represent the variability of field environments where images often include noise, occlusion, or uneven lighting. Second, apple leaves frequently exhibit compound infections, and standard classifiers—typically designed for single-label prediction—struggle to disambiguate overlapping lesion patterns, particularly in minority or hybrid classes. Third, the computational demands of state-of-the-art CNNs limit their use in resource-constrained settings. Without compact, interpretable models that can operate offline, the benefits of AI-driven plant disease detection remain inaccessible to the farmers who need them most. These considerations motivate the development of a lightweight, interpretable deep learning system tailored for robust performance across heterogeneous field conditions. Figure 1 outlines the conceptual framework of this study, illustrating the challenges addressed and the proposed approach. Building on this foundation, the next subsection states the problem formally and situates the research within the broader context of deep learning applications in agriculture.

The objectives of this study are to develop a lightweight MobileNetV2-based classifier for apple leaf disease recognition under real field conditions, to evaluate the robustness of the model under environmental distortions such as illumination variation, occlusion, and background clutter, and to analyze misclassification behavior using explainable AI (Grad-CAM and LIME) to understand model attention on lesion regions and compound symptoms.

1.1 Deep Learning for Plant Disease Detection

The early success of deep learning in computer vision has naturally extended to agriculture, particularly for plant disease recognition. Convolutional Neural Networks (CNNs) have proven especially effective in extracting discriminative features from leaf imagery, enabling accurate classification of disease symptoms. Mohanty et al. [3] demonstrated this capability using a CNN trained on 26 diseases across 14 crops, achieving high accuracy under controlled conditions. Ferentinos [4] further explored multiple CNN architectures—including VGG and GoogLeNet—achieving average accuracies above 93% across 58 crop-disease pairs. However, these conventional architectures are computationally demanding and thus ill-suited for real-time, in-field use. To mitigate this limitation, Too et al. [5] and Barbedo [8] investigated the use of lightweight CNNs and stressed the importance of dataset diversity for robust generalization. These developments provide the technical foundation for exploring more efficient, deployable models, as discussed next.

1.2 Lightweight CNN Architectures in Agriculture

Lightweight CNN architectures have gained attention as a practical solution for precision agriculture, where computing power is often limited.

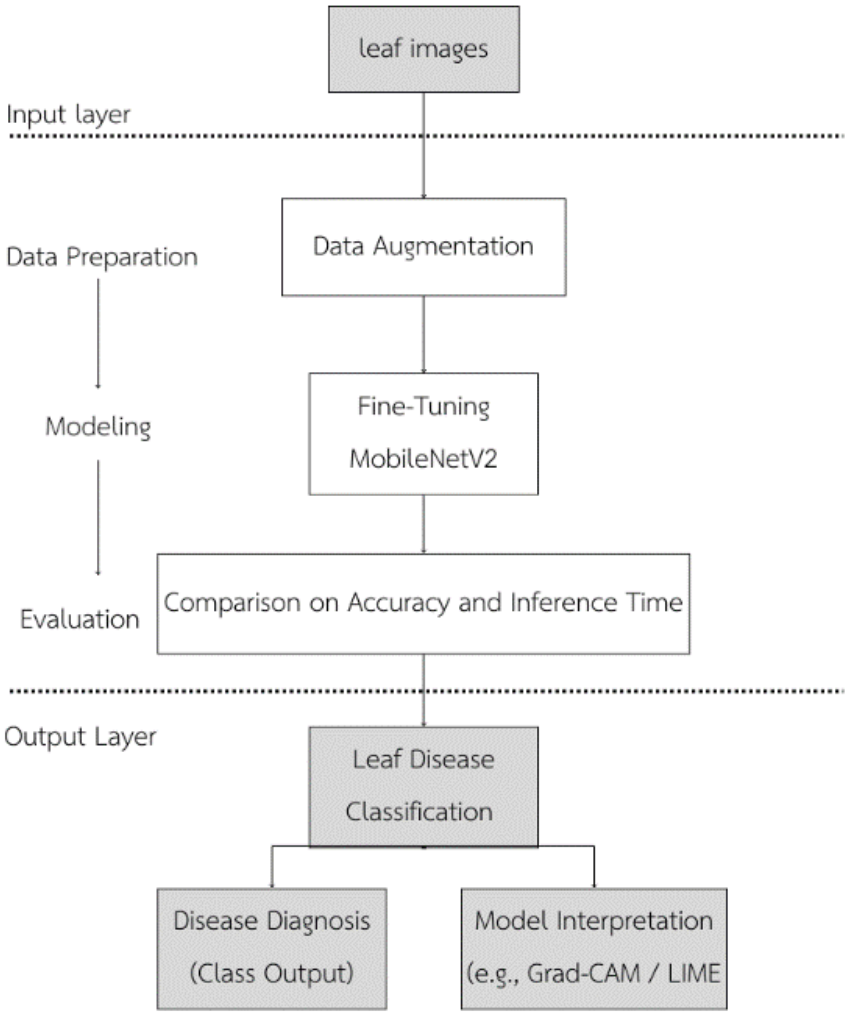

Figure 1. Conceptual framework for lightweight, interpretable, and deployable deep learning-based apple leaf disease classification. The model aims to address key challenges in real-world agricultural contexts, including compound symptoms, limited resource availability, and the need for interpretability.

Traditional networks like VGG and ResNet, though accurate, demand high memory and processing resources. In contrast, models such as MobileNet, SqueezeNet, and ShuffleNet employ parameter-efficient designs—e.g., depthwise separable convolutions—to achieve competitive accuracy while reducing complexity. Too et al. [5] found that MobileNet and SqueezeNet matched the performance of deeper models while being significantly more deployable. Fuentes et al. [9] confirmed the viability of these models for detecting tomato disease in natural environments. Kamilaris and Prenafeta-Bold'u [6] emphasized the role of lightweight CNNs in enabling real-time smart farming tools. Nevertheless, as Barbedo [8] noted, training on diverse and representative datasets remains essential for maintaining robustness. Among these options, MobileNetV2 has emerged as a particularly promising model for edge-based diagnosis, motivating further discussion in the following subsection.

1.3 MobileNetV2 in Field Applications

MobileNetV2 is increasingly adopted for field applications in agriculture due to its efficient inverted-residual architecture and linear bottlenecks. This architecture reduces model size and latency while preserving classification accuracy, making it well-suited for mobile and embedded systems. Xu et al. [10] applied MobileNetV2 to tomato leaf disease detection, achieving high performance and low inference delay under

real-world conditions. Similarly, Fuentes et al. [9] utilized MobileNet for tomato pest recognition in uncontrolled environments. Thapa et al. [11] demonstrated MobileNetV2's capacity to classify apple leaf diseases using transfer learning, while Albahli [12] reported that optimized variants of MobileNetV2 outperform deeper CNNs on mobile hardware. These applications validate MobileNetV2's suitability for edge deployment in smart agriculture. Our study builds upon these findings by customizing the model to a diverse apple leaf dataset, as further justified in the next subsection.

Table R1. Summary of related studies on plant disease classification under field conditions.

Study	Crop	Model	Dataset	Field conditions	Accuracy
Mohanty et al. (2016)	Multiple crops	AlexNet/GoogLeNet	PlantVillage	No	>99%
Ferentinos (2018)	Multiple crops	VGG/GoogLeNet	Lab images	No	>93%
Fuentes et al. (2018)	Tomato	Faster R-CNN	Field images	Yes	83–92%
Xu et al. (2022)	Tomato	MobileNetV2	Field images	Yes	94%
Thapa et al. (2020)	Apple	MobileNetV2/EfficientNet	Mixed	Limited	90%+
This study	Apple	MobileNetV2	FGVC8 + compound relabeling	Yes	65% (12-class), 71% (5-class)

This comparison highlights that most prior studies focus on single-disease labels, whereas our work explicitly analyzes compound infections and deployability constraints.

1.4 Limitations in Prior Work and Motivation

Despite the growing body of research applying deep learning to plant disease diagnosis, several key limitations hinder effective deployment in field settings. First, many existing studies rely on curated datasets captured under controlled laboratory conditions. These datasets often fail to capture the heterogeneity of real agricultural environments, including inconsistent lighting, occlusion, complex backgrounds, and compound symptoms. As Barbedo [8] notes, this lack of visual diversity limits model generalizability. Second, conventional classifiers are typically designed for single-label prediction, assuming that each leaf image contains only one disease. In practice, however, multiple infections often co-occur, leading to overlapping lesion patterns that challenge standard CNN-based methods. This limitation is particularly pronounced in apple leaf pathology, where visually ambiguous symptom combinations are common. Third, although several lightweight CNN architectures have been proposed for edge deployment, few studies provide a comprehensive evaluation that includes both classification accuracy and practical metrics such as inference latency, model size, and robustness under noisy conditions. While MobileNetV2 has shown promise in prior work [10, 12], its performance under real-world deployment constraints remains insufficiently characterized, especially for complex, multi-symptom categories. These limitations highlight the need for a field-adapted, interpretable, and computationally efficient diagnostic system that can operate reliably in resource-constrained environments. In response, this study **fine-tunes MobileNetV2** on a heterogeneous dataset of apple leaf diseases and systematically evaluates its performance under real-world deployment conditions. This includes assessing classification robustness to noise, evaluating interpretability with Grad-CAM and LIME, and benchmarking against deeper CNNs to establish a lightweight yet accurate solution for on-device agricultural diagnostics.

2. Materials and Methods

This section details the experimental methodology used to develop and evaluate the fine-tuned MobileNetV2 classifier for multi-class apple leaf disease detection. The process follows a modified CRISP-DM framework, encompassing data understanding, preprocessing, model training, and evaluation, with emphasis on field-readiness and interpretability. An overview of the workflow is illustrated in Figure 1.

2.1 Dataset and Preprocessing

The primary dataset used in this study is derived from the Plant Pathology 2021–FGVC8 competition on Kaggle [13]. It contains 18,600 high-resolution images of apple leaves, each originally annotated into one of five diagnostic categories: Apple Scab, Black Rot, Cedar Apple Rust, Healthy, and Multiple Disease, as illustrated in Figure 6. In this study, the "Multiple Disease" category was further subdivided into expert-defined compound subclasses (e.g., scab + frog eye leaf spot, rust + frog eye leaf spot, and higher-order combinations), yielding a total of 12 classes for model training and evaluation. This relabeling reflects realistic co-infection patterns observed under field conditions. Plant pathology experts manually verified all labels to ensure annotation quality and class integrity. Each disease class exhibits distinct lesion morphology and visual patterns, which are critical for both human interpretation and machine learning-based classification [8]. A brief description of the five categories is provided below:

- **Apple Scab**: Caused by Venturia inaequalis, this disease presents as olive-brown to dark circular lesions with sharply defined margins. Infected leaves often deform or drop prematurely [14].
- **Black Rot**: Induced by Botryosphaeria obtusa, black rot appears as necrotic lesions that typically originate at leaf edges and expand inward in concentric patterns [15].
- **Cedar Apple Rust**: Caused by Gymnosporangium juniperi-virginianae, this heteroecious rust produces vivid orange lesions with raised centers and chlorotic halos [16].
- **Healthy**: Leaves without visible disease symptoms are uniformly green with no deformation or lesion markings. They serve as control samples in diagnostic classification tasks [3].
- **Multiple Disease**: Co-infected leaves exhibit overlapping lesion types from two or more diseases, complicating classification due to mixed visual cues [8].

To prepare the dataset for training, all images were resized to 224 × 224 pixels using bilinear interpolation, under the input dimensions required by MobileNetV2. Pixel values were normalized using the ImageNet dataset's mean and standard deviation to ensure compatibility with pretrained weights. A set of data augmentation techniques was implemented using the torchvision transforms module. These included random horizontal flipping, cropping, jittering brightness and contrast, and illumination shifts. Each transformation was applied probabilistically to increase robustness against visual variability encountered in real-world field conditions. An 80:20 stratified sampling strategy was used to split the dataset into training and test sets, preserving the class distribution across both splits. This split was selected because of the relatively large dataset size and the high computational cost of repeated training with deep CNNs. While k-fold cross-validation can provide more stable estimates, a stratified hold-out set is commonly adopted in large-scale vision benchmarks and was considered sufficient for comparative evaluation in this study. Cross-validation is planned as future work. These processed and well-annotated images form the input to the deep learning models discussed in the next section, where we describe the network architecture, transfer learning strategy, and baseline comparisons.

2.2 Model Architecture and Transfer Learning

Based on the preprocessed image dataset, this study employed MobileNetV2 as the backbone architecture for apple leaf disease classification. MobileNetV2 is a lightweight convolutional neural network (CNN) optimized for deployment in resource-constrained environments, such as smartphones, drones, or IoT devices commonly used in agricultural field settings. Its design incorporates inverted residual blocks and depthwise separable convolutions, effectively reducing model size and computational complexity while preserving high representational capacity. The network was initialized with pretrained ImageNet weights to leverage generalized visual feature extraction. To adapt the model to the domain-specific task, the final fully

connected classification head was replaced with a softmax layer configured for five disease classes. A transfer learning strategy was applied: the first two inverted residual stages of MobileNetV2 were frozen to retain generic low-level features, while the remaining higher-level layers were fine-tuned to specialize in distinguishing lesion patterns unique to apple leaf diseases. Regularization components—including batch normalization for training stability, dropout to prevent overfitting, and ReLU activation for non-linear transformation—were retained from the original MobileNetV2 design.

2.3 Experimental Setup and Baseline Models

An 80/20 stratified split was used to divide the dataset into training and test sets, ensuring balanced class distribution across both subsets. A consistent data augmentation pipeline—comprising resizing, horizontal flipping, color jittering, and random cropping—was applied to all models using the torchvision transforms module. To evaluate the effectiveness of our proposed fine-tuned MobileNetV2 model, we compared its performance against three widely adopted deep CNN baselines: ResNet50, InceptionV3, and EfficientNetV2L. These architectures are commonly used in plant pathology and serve as benchmarks for assessing the trade-off between diagnostic accuracy and computational cost. To enhance model transparency and support error analysis, we applied two explainable AI (XAI) techniques—Grad-CAM and LIME, which produce saliency maps and feature attribution visualizations. These methods help verify that predictions are grounded in biologically relevant lesion regions, thereby improving model interpretability.

2.4 Training and Evaluation Protocol

All models were trained using the Adam optimizer with an initial learning rate of 1×10^{-4} and categorical cross-entropy loss. A ReduceLROnPlateau scheduler was applied with a factor of 0.1 and patience of 3 epochs. Training used early stopping based on validation loss, with a patience of 5 epochs, to prevent overfitting. Model performance was evaluated using accuracy, precision, recall, and F1-score on a per-class basis. Additionally, model size (MB) and inference latency (seconds per image) were measured to assess edge deployability. A confusion matrix was constructed to analyze class-specific performance and misclassification patterns. Particular attention was given to distinguishing between visually ambiguous and compound symptom classes.

2.5 Implementation Details

All experiments were implemented in PyTorch and executed on a GPU-enabled system with 16 GB of RAM and an NVIDIA RTX 3060. The batch size was set to 32, and training continued for up to 50 epochs with an early stopping patience of 5. No explicit class balancing (e.g., weighted loss or oversampling) was used during initial training to preserve dataset realism; an ablation study on class reweighting is presented in Section 5.

3. Results and Discussion

3.1 Results

This section presents the empirical findings of our study, structured to evaluate the model from five perspectives: classification performance, benchmarking, robustness, and efficiency.

3.1.1 Classification Performance

To evaluate the per-class predictive behavior of the MobileNetV2-based classifier, a confusion matrix is presented in Figure 2. This matrix provides a detailed summary of classification outcomes across the 12 disease categories by mapping true labels against predicted ones. The results reveal strong performance for clearly defined disease categories such as healthy, frog eye leaf spot, and rust, with high diagonal values indicating precise predictions. For instance, the healthy class was correctly identified in 902 out of 1061 cases, and frog eye leaf spot achieved 484 correct predictions out of 641 samples.

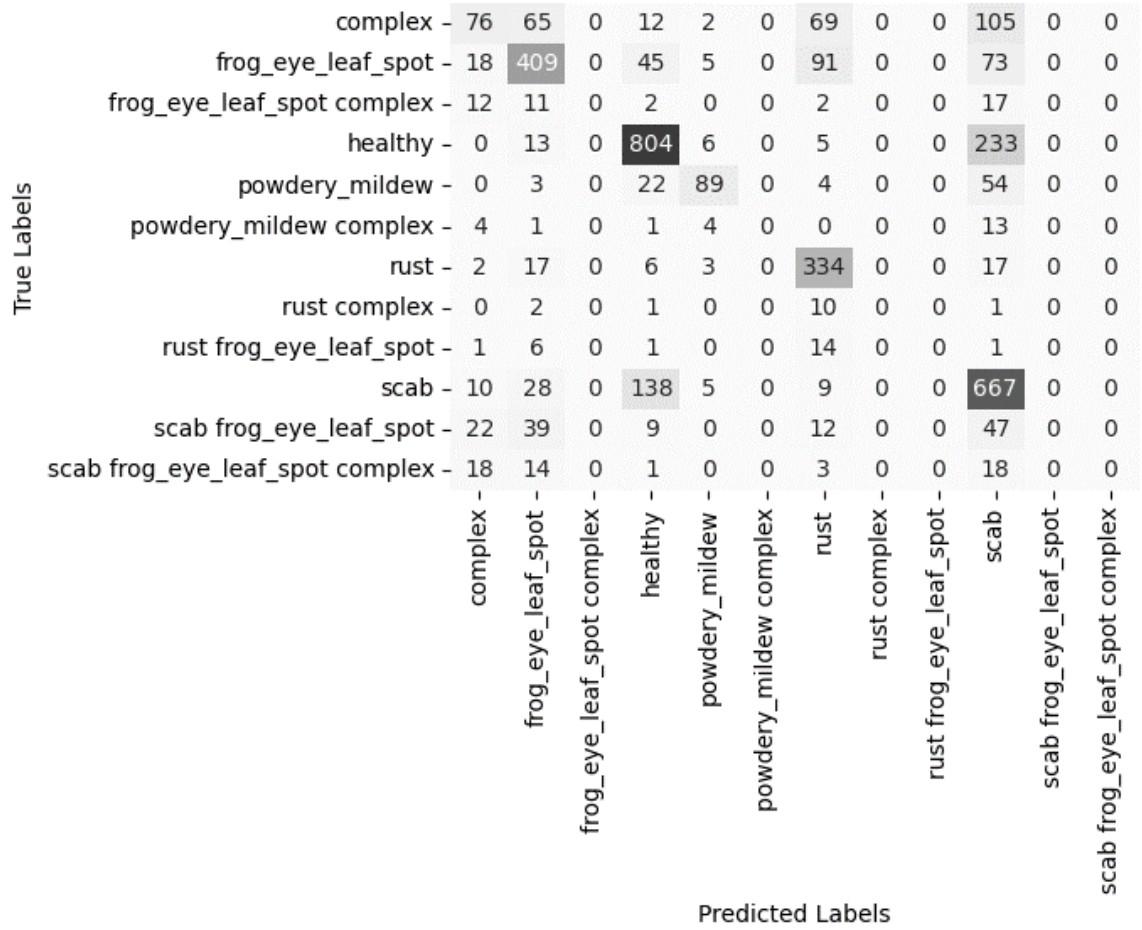

Figure 2. Confusion matrix for 12-class plant disease classification. Rows represent true labels, columns represent predicted labels.

In contrast, compound and visually ambiguous classes—such as powdery mildew complex, scab frog eye leaf spot, and rust complex—exhibited high misclassification rates. These categories were often confused with visually similar but simpler base classes (e.g., scab, rust, or frog eye leaf spot), indicating limitations in the model's ability to disentangle overlapping or co-occurring symptoms. Notably, the complex class was frequently misclassified as scab or frog eye leaf spot, yet this misclassification was not symmetric, suggesting potential dominance of base-class features or dataset imbalance. To gain further insight into the model's decision rationale, we incorporated explainable AI techniques. Figure 3 displays a Grad-CAM visualization for a leaf image predicted as powdery mildew with moderate confidence (31.61%). The heatmap indicates that the model focuses attention on the lesion regions, even under uncertainty, confirming the spatial relevance of the learned features.

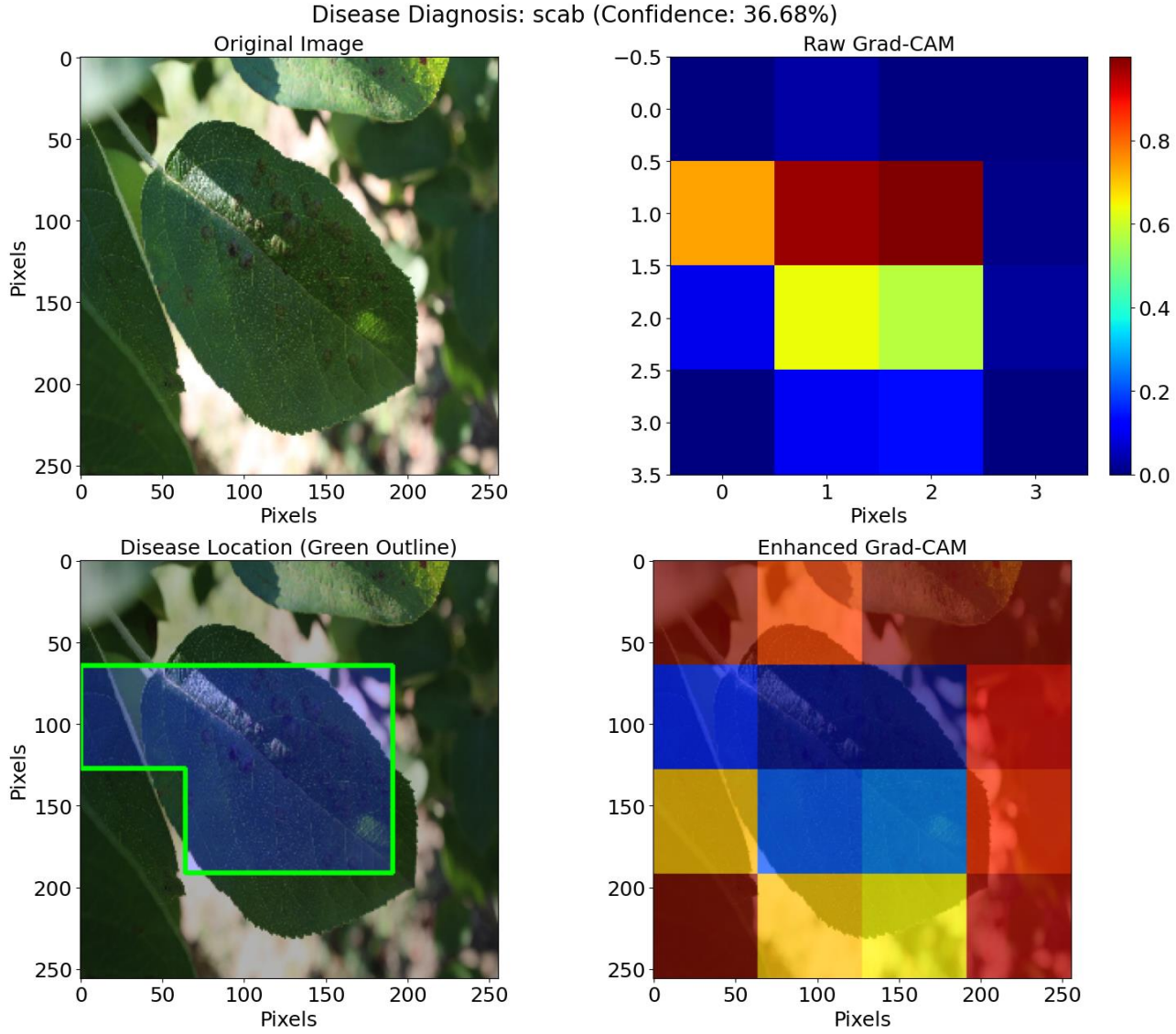

Figure 3. Grad-CAM visualization for a leaf classified as scab. The top-right panel shows raw Grad-CAM activations; the bottom-right panel shows the enhanced overlay on the original image. The green-outlined region denotes expert-annotated lesion zones. Despite moderate confidence, the model highlights relevant regions, supporting valid spatial attribution.

Figure 4 presents a LIME explanation for the same image, which the model also associated with frog eye leaf spot (35.47%). The highlighted superpixels demonstrate that visual patterns associated with necrotic lesions influenced the classifier's decision, offering a plausible explanation for inter-class confusion between visually overlapping symptoms.

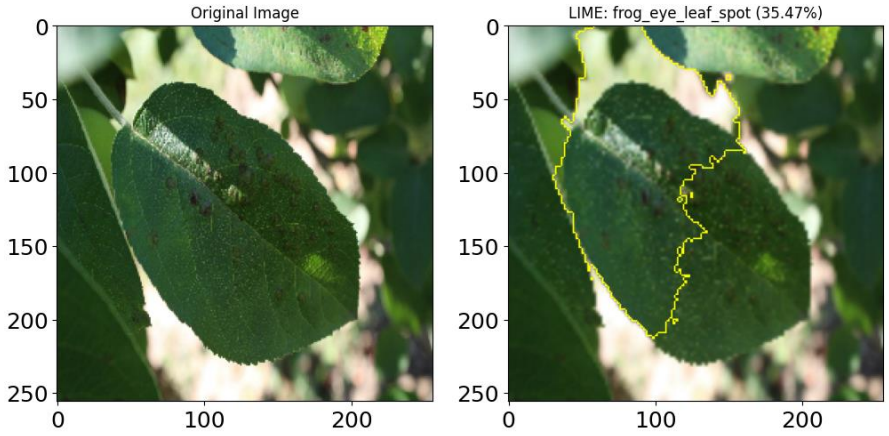

Figure 4. LIME explanation for the same apple leaf image. The right panel shows super pixels (outlined in yellow) that contributed most to the model's prediction of frog eye leaf spot. Overlapping lesion-like regions between disease classes may lead to misclassification.

Together, these interpretability tools validate that the model's attention aligns with lesion-relevant features, increasing trust in its predictions for well-defined classes. Simultaneously, they provide diagnostic insights into misclassification cases, especially among ambiguous categories, underscoring the need for future work in multi-label classification, improved data balancing, and domain-specific augmentation strategies.

3.1.2 Classification Accuracy and Metrics

To quantitatively assess the classifier's performance, standard metrics—including precision, recall, and F1-score—were computed for each of the 12 disease categories. The results are summarized in Table 1. While the overall accuracy reaches 65% for the 12-class (expanded-label) task, the macro-averaged F1-score drops to 0.32, indicating considerable variation in model performance across different classes, particularly among compound infection categories. Well-separated, visually distinct categories such as healthy, rust, and powdery mildew exhibit strong predictive performance, with F1-scores of 0.78, 0.77, and 0.63, respectively. The frog eye leaf spot class also demonstrates high discriminability (F1 = 0.68), benefiting from both larger support size and clear lesion morphology. In stark contrast, compound and structurally ambiguous classes—including frog eye leaf spot complex, powdery mildew complex, rust complex, and scab frog eye leaf spot complex—exhibit near-zero precision and recall. These findings are consistent with the confusion matrix analysis in Section 4.1, where misclassification was concentrated along off-diagonal cells for these hybrid labels. Particularly, the low F1-scores highlight the model's difficulty in recognizing co-occurring or overlapping symptom patterns, as further supported by the Grad-CAM and LIME visualizations presented earlier. Additionally, rare classes with limited support, such as rust frog eye leaf spot (support = 3), also suffer from negligible recall, underscoring the challenges of class imbalance and sparse representation in training data. The performance gap between simple and compound categories suggests a need for more sophisticated modeling strategies. Potential improvements include adopting multi-label training objectives, incorporating class-weighted or focal loss functions, and applying targeted data augmentation to enrich underrepresented visual patterns. Overall, while the model is effective for dominant, single-disease categories with distinct visual cues, substantial refinement is required to improve its generalization to rare, compound, or ambiguous disease instances.

3.1.3 Model Comparison with ResNet50, InceptionV3, and EfficientNetV2L

To evaluate the effectiveness of the proposed fine-tuning MobileNetV2 model, we conducted a comparative study against four widely used CNN architectures: MobileNetV3, ResNet50, InceptionV3, and EfficientNetV2L. All models were trained and tested under the same conditions to ensure a fair comparison in terms of classification performance, inference latency, and model size. As shown in Table 2, our fine-tuning MobileNetV2 model achieved the highest classification accuracy (71.04%) on the original 5-class FGVC8 label setting. At the same time, the detailed 12-class analysis is reported separately in Table 1 and Figure 2 while

maintaining a low inference time of 0.00195 seconds per image and a moderate model size of 12.79 MB. In contrast, deeper models such as ResNet50 and InceptionV3 achieved lower accuracy (26.89% and 53.78%, respectively) while having significantly larger parameter sizes (96.46 MB and 89.96 MB, respectively). Although EfficientNetV2L is known for its high capacity, it underperformed in both accuracy (28.26%) and speed, exhibiting the longest inference time (0.00773 seconds) and largest model size (455.32 MB). These findings suggest that the fine-tuned MobileNetV2 model offers a favorable trade-off among accuracy, efficiency, and deployability, making it well-suited for edge computing environments with limited computational resources.

Table 1. Classificationreportfor12categories.

Class	Precision	Recall	F1-score	Support
complex	0.42	0.18	0.25	329
frogeyeleafspot	0.58	0.82	0.68	641
frogeyeleafspotcomplex	0.00	0.00	0.00	44
healthy	0.71	0.88	0.78	1061
powderymildew	0.71	0.56	0.63	172
powderymildewcomplex	0.00	0.00	0.00	23
rust	0.84	0.70	0.77	379
rustcomplex	0.00	0.00	0.00	17
rustfrogeyeleafspot	0.00	0.00	0.00	3
scab	0.64	0.65	0.63	857
scabfrogeyeleafspot	0.25	0.03	0.06	129
scabfrogeyeleafspotcomplex	0.00	0.00	0.00	54
Accuracy			0.65	3726
Macroavg	0.34	0.32	0.32	3726
Weightedavg	0.61	0.65	0.62	3726

Table 2. Model Comparison on Accuracy and Inference Time

Model	Accuracy (%)	Inference Time (sec/image)	Model Size (MB)
Fine-TuningMobileNetV2	71.04	0.00195	12.79
MobileNetV3	26.89	0.00178	5.68
ResNet50	26.89	0.00248	96.46
InceptionV3	53.78	0.00287	89.96
EfficientNetV2L	28.26	0.00773	455.32

3.1.4 Robustness under Field-Like Conditions

To assess the robustness of the proposed model under realistic agricultural scenarios, we simulated four types of visual disturbances commonly encountered in the field: low illumination, partial occlusion, background clutter, and a composite of all three. These perturbations were applied to the test set to evaluate generalization performance beyond controlled conditions.

Table 3 summarizes the classification accuracy across noise settings. Under normal conditions, the model achieved 65.2% accuracy. Performance declined to 59.9% under low illumination, indicating moderate sensitivity to lighting. A more pronounced drop was observed under partial occlusion (48.0%) and complex backgrounds (26.6%), suggesting a reliance on unoccluded lesion features and consistent visual context. When all distortions were combined, accuracy fell to 30.2%, reflecting the compounding effect of multiple sources of noise. These results indicate that while MobileNetV2 performs reasonably well under mild degradation, its predictive stability is challenged by severe or compound noise. The findings highlight the need to integrate robust augmentation strategies and interpretability tools, such as Grad-CAM, to enhance model reliability for field deployment.

Table 3. Model Accuracy under Simulated Field Conditions

Condition	Accuracy (%)
Normal (baseline)	65.2
Low Illumination	59.9
Partial Occlusion	48.0
Complex Background	26.6
Combined Noise	30.2

3.1.5 Efficiency and Edge Readiness

The proposed MobileNetV2 model was evaluated for model size and inference latency to assess its feasibility for future deployment on resource-constrained platforms. The trained model occupies 13.6 MB of storage and achieves an average inference time of 0.00195 seconds per image on a CUDA-enabled GPU, suggesting suitability for low-latency applications. While these metrics indicate that the model is computationally efficient compared to deeper architectures such as ResNet50 and EfficientNetV2L, it is important to note that no real-world hardware deployment was conducted in this study. The reported performance metrics serve as reference indicators for potential use in edge computing environments such as mobile devices or embedded systems. Additional testing under hardware-specific constraints is required to validate real-time feasibility in practice.

3.2 Discussion

This section analyzes the empirical findings with the model's predictive behavior, interpretability, robustness, and deployability in real-world agricultural scenarios.

3.2.1 Interpretation of Findings

The results confirm that a fine-tuned MobileNetV2 can accurately classify visually distinct apple leaf diseases, especially for dominant single-disease classes such as healthy, rust, and frog eye leaf spot. These classes benefited from larger sample sizes, clearer symptom morphology, and lower intra-class variation, enabling effective feature extraction with lightweight convolutional layers. Conversely, the model consistently underperformed on compound classes with overlapping symptoms. These categories exhibited near-zero F1 Scores, highlighting the model's difficulty in disentangling co-occurring visual cues in a single-label classification setup. Explainability tools—Grad-CAM and LIME—confirmed that in such cases, attention maps often prioritized dominant lesion regions, while ignoring subtle secondary features. This reveals an attention collapse phenomenon, in which dominant disease patterns overshadow minority cues in multi-infection samples. Moreover, the asymmetry in misclassification patterns—where compound classes are misidentified as simpler ones but not vice versa—suggests that the model has implicitly learned to default to majority class prototypes. This indicates a distributional bias reinforced by class imbalance in the training data.

3.2.2 Deployment Feasibility and Use Cases

The fine-tuned MobileNetV2 model demonstrates favorable computational characteristics for potential use on edge devices. With a compact size of 13.6 MB and an average inference latency of less than 2 milliseconds per image on a GPU, the model demonstrates efficiency suitable for offline diagnostic scenarios in bandwidth-limited or rural agricultural contexts. Although physical deployment on platforms such as Raspberry Pi or mobile system-on-chips (SoCs) was not conducted in this study, the reported performance metrics provide preliminary evidence supporting the feasibility of such environments. Further validation through on-device testing will be required to confirm compatibility under real-world constraints, including thermal, energy, and input variability considerations. In practical use, the model may be integrated into mobile applications or drone-based crop monitoring tools to assist field workers or smallholder farmers. The inclusion of Grad-CAM and LIME facilitates visual interpretation of the model's decisions, offering an added layer of transparency and trust in high-stakes agricultural decision-making.

3.2.3 Scalability to Other Crops and Datasets

The proposed pipeline, based on transfer learning and image-based augmentation, is transferable to other crops, provided that annotated image datasets with sufficient inter-class diversity are available. For example, fine-tuning on tomato, rice, or grapevine datasets is feasible using the same backbone architecture. Explainability tools also aid in rapid domain adaptation, enabling visual validation across new phenotypes.

3.2.4 Ablation Study on Class Rebalancing

A weighted loss function was employed to assess its impact on class imbalance. The results indicate notable performance gains in previously underperforming compound classes, particularly in recall. For example, rust complex and powdery mildew complex showed a substantial increase in detection after reweighting, as illustrated in Table 4. However, this improvement often came at the cost of reduced performance in the dominant classes, underscoring the trade-off between minority-class recall and majority-class precision. To better illustrate the improvements, Figure 5 visualizes the change in F1-score across minority classes. Notably, several compound classes showed meaningful gains after applying weighted loss, reinforcing the importance of class balancing in agricultural datasets.

Table 4. Impact of Class Rebalancing on Minority Class Performance. The weighted loss improves recall and F1-score for compound and minority disease classes.

Class	Original Model			With Weighted Loss		
	Precision	**Recall**	**F1-score**	**Precision**	**Recall**	**F1-score**
complex	0.4653	0.2036	0.2833	0.2453	0.3191	0.2774
Frog eye leaf spot	0.6748	0.6443	0.6592	0.5294	0.3651	0.4321
Frog eye leaf spot complex	0.0000	0.0000	0.0000	0.2727	0.0682	0.1091
healthy	0.7767	0.7738	0.7753	0.7029	0.8096	0.7525
Powdery mildew	0.7830	0.4826	0.5971	0.5977	0.6041	0.6012
Powdery mildew complex	0.0000	0.0000	0.0000	0.1765	0.1304	0.1500
rust	0.5963	0.8575	0.7035	0.7522	0.4655	0.5681
Rust complex	0.0000	0.0000	0.0000	0.0166	0.6429	0.0324
Rust frog eye leaf spot	0.0000	0.0000	0.0000	0.0357	0.0870	0.0506
scab	0.5437	0.7993	0.6471	0.7010	0.3459	0.4629
Scab frog eye leaf spot	0.0000	0.0000	0.0000	0.1321	0.1628	0.1458
Scab frog eye leaf spot complex	0.0000	0.0000	0.0000	0.0714	0.0370	0.0488
Macro avg (all)	0.3200	0.3134	0.3055	0.3528	0.3354	0.3023

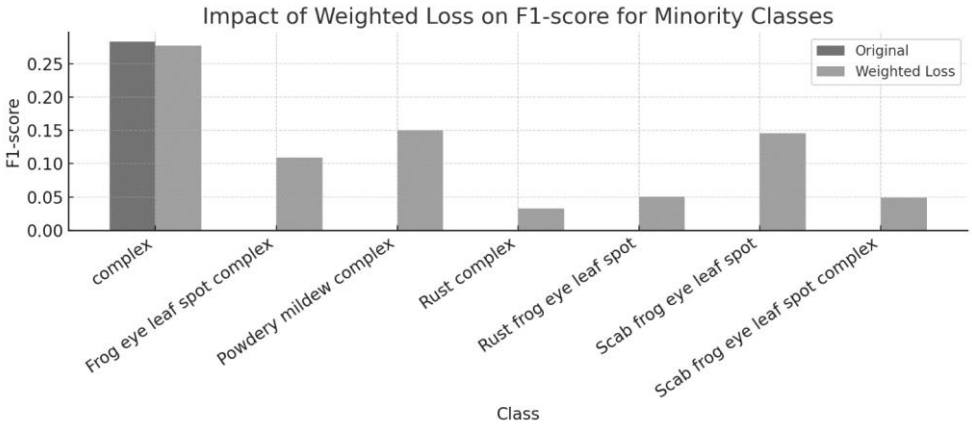

Figure 5. Per-class F1-score comparison before and after applying class weighting. Minority classes with zero F1 Scores in the original model showed notable improvements. Note that several previously underperforming compound classes (e.g., rust complex, powdery mildew complex) exhibit significant improvements in recall after class weighting.

3.2.5 Limitations, Deployment Challenges, and Ethical Considerations

Despite improved classification accuracy and explainability, several limitations remain in the proposed system. The model's performance degrades significantly under compounded visual disturbances—such as occlusion combined with low illumination—revealing sensitivity to high-entropy image conditions. In addition, the use of a single-label training framework limits the system's ability to capture real-world complexities, particularly in cases involving co-infections or overlapping symptom regions. These challenges constrain diagnostic performance in field scenarios where image quality and lesion presentation vary widely. To address these limitations, future work should explore multi-label classification frameworks that explicitly model multiple disease types within a single image. Incorporating uncertainty-aware learning objectives—such as focal loss or label smoothing—can enhance robustness in the presence of ambiguous or imbalanced class distributions. Lesion severity estimation and segmentation techniques could also support early-stage intervention and increase interpretability. Hardware benchmarking on ARM-based mobile platforms will be necessary to validate the system's practical viability for offline use in rural, low-connectivity agricultural environments. From an ethical standpoint, while automated plant disease diagnostics can offer significant value to smallholder farmers and agritech practitioners, it is important to recognize the limitations of imperfect AI systems. Misclassifications—particularly false negatives in early disease stages—may result in inaction and crop losses. Therefore, future deployments should consider human-in-the-loop frameworks that supplement AI-generated outputs with expert review or local agricultural advisory systems. Additionally, interpretability techniques such as Grad-CAM and LIME should be made accessible through user interfaces to enhance user trust and facilitate informed decision-making. These human-centered safeguards are essential to ensure responsible, reliable, and equitable deployment of AI systems in agriculture.

4. Conclusions

This study investigated a MobileNetV2-based model for apple leaf disease classification under heterogeneous field conditions. The model demonstrated strong performance in well-defined single-disease categories but struggled with compound or overlapping infections, reflecting the challenges posed by imbalanced and visually ambiguous classes. Grad-CAM and LIME confirmed that the model focused on biologically relevant lesion areas, increasing trust in predictions while revealing sources of misclassification. Key contributions of this study include: (1) the development of a lightweight MobileNetV2-based classifier tailored for heterogeneous field conditions, (2) explicit evaluation of compound infection categories derived from FGVC8 multiple-disease labels, and (3) integration of XAI methods to interpret misclassification behavior. Although physical deployment was not conducted, the results underline the value of lightweight deep learning models combined with interpretability methods for agricultural disease recognition. Future work should explore multi-label learning to capture co-infections better, employ class-balancing strategies to improve minority categories, and extend validation to larger, more diverse datasets. These steps will help advance the development of practical and trustworthy diagnostic systems to support sustainable crop management.

Appendix A: Disease Class Descriptions

This appendix provides comprehensive descriptions and pathological characteristics of the 12 apple leaf disease categories considered in this study. These categories were annotated by plant pathology experts using the PlantVillage dataset and encompass both single-disease manifestations and compound symptom co-occurrences commonly observed in real-world field conditions. Figure .6 presents representative examples of each category, illustrating the diversity in lesion morphology, co-infection patterns, and background complexity that challenge automated classification.

- **Complex** — Hybrid or unclassified symptoms: Leaves in this category exhibit multiple overlapping lesion types without a dominant visual pattern, often arising from ambiguous or advanced-stage infections. These are the most visually heterogeneous and challenge standard classifiers due to non-distinct lesion edges and color blending.

- **frog eye leaf spot** — Cercospora spp.: Characterized by circular gray lesions with purple margins, primarily affecting mature leaves. As illustrated in Figure 6., lesions are discrete, with sharply defined boundaries that make them visually separable under standard illumination.
- **frog eye leaf spot complex** — Mixed infection: Frogeye Leaf Spot present alongside one or more additional diseases, producing lesion zones with color gradients or merged edges. Visual identification becomes more difficult due to interference from adjacent pathogen effects.
- **Healthy** — Control class: Leaves in this category are free of visible infections, exhibiting uniform green pigmentation, intact structure, and no lesion formations. They serve as negative controls in training and are clearly separable in both visual and feature space.
- **powdery mildew** — Erysiphales fungi: Exhibits as white or gray powder-like growth on the upper leaf surface. This class is visually distinct due to the uniform texture and desaturation effect, as shown in the middle-left panel of Figure 6.
- **powdery mildew complex**—Compoundinfection: PowderyMildew occurring with another disease, often resulting in visually conflicting regions—e.g., powdery overlay on necrotic or chlorotic patches. Boundary regions are often misclassified due to overlapping visual signatures.
- **rust** — Gymnosporangium spp.: Manifests as bright orange or reddish pustules, often on the underside of leaves. Figure 6. shows typical rust pustules with well-demarcated circular morphology.
- **rust complex** — Co-infection class: Rust symptoms co-occur with another pathogen, often resulting in mixed orange-brown lesions with diffuse borders or color bleeding. Co-localization complicates visual separation and feature-based segmentation.
- **rust frog eye leaf spot** — Dual infection: Co-presence of Rust and Frogeye Leaf Spot in the same leaf area. Lesions may appear as rust-colored pustules surrounded by necrotic halos, leading to spatial ambiguity in model attention maps.
- **scab** — Venturia inaequalis: Distinguished by dark, scab-like lesions with a rough surface and irregular margins. They typically appear near leaf tips or edges. The structural roughness is an important cue for both human experts and deep learning models.
- **scab frog eye leaf spot** — Compound lesion type: Visual overlap between Scab and Frogeye Leaf Spot, sometimes with concentric lesion patterns or discoloration zones that reflect both fungal pathologies. Grad-CAM heatmaps often highlight only one dominant feature, leading to misclassification.
- **Scab frog eye leaf spot complex** — Ternary or ambiguous combination: Leaves showing features of both Scab and Frogeye Leaf Spot, along with additional visual noise or secondary infection. This is one of the most challenging categories for both annotation and classification, often appearing in the lower-confidence prediction regions of LIME visualizations.

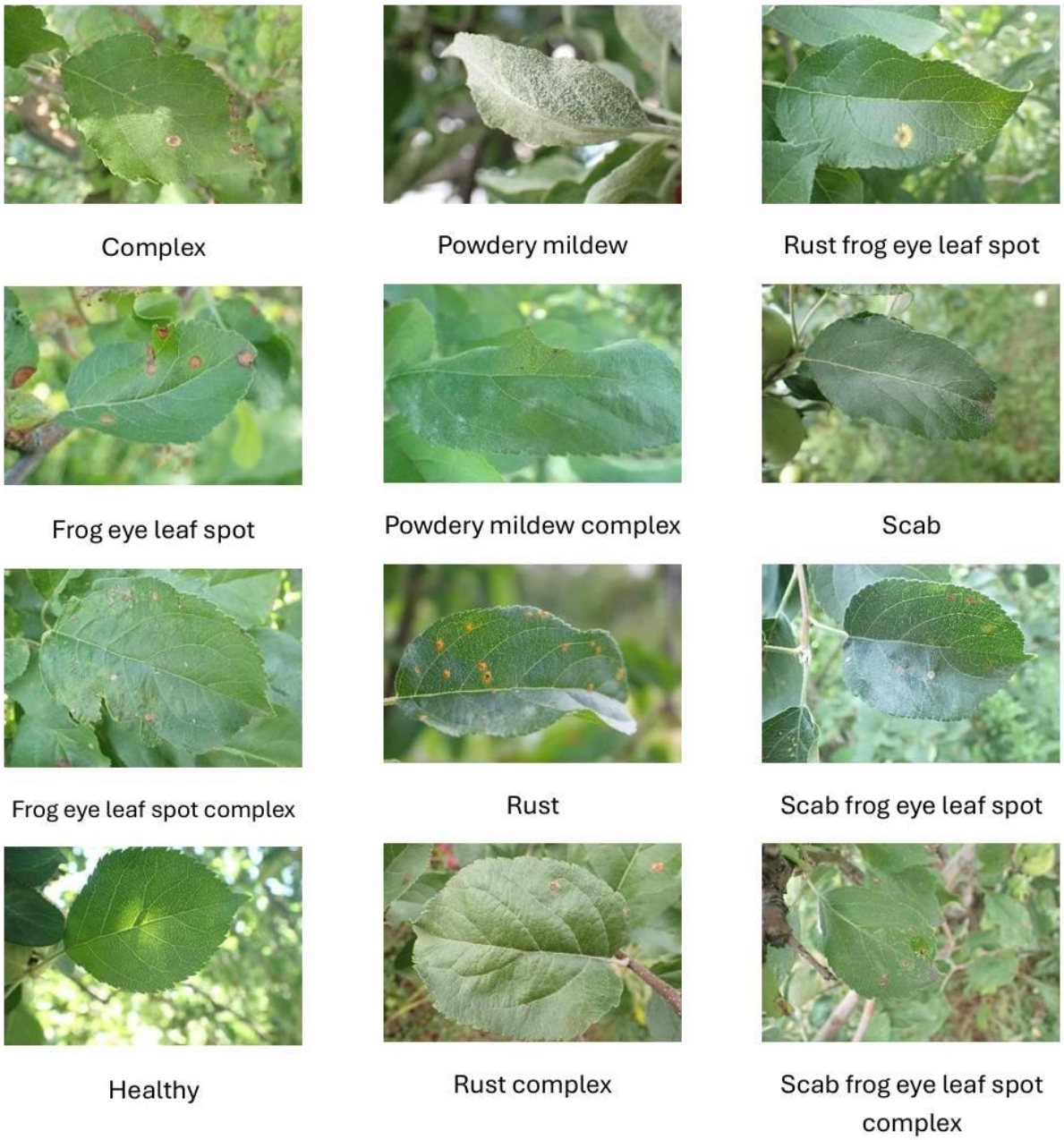

Figure 6. Representative examples of the 12 apple leaf disease categories classified by the proposed model. These include single-disease classes (e.g., scab, rust, powdery mildew, frog eye leaf spot, healthy) and compound classes (e.g., scab frog eye leaf spot, rust complex, powdery mildew complex, frog eye leaf spot complex, rust frog eye leaf spot, scab frog eye leaf spot complex, complex). The annotated images illustrate diverse lesion morphologies, co-infection interactions, and heterogeneous backgrounds, all of which significantly influence classification accuracy under real-world field conditions.

5. Acknowledgements

Funding: This research received no external funding.

Conflicts of Interest: The authors declare no conflict of interest.

References

[1] Mahlein, A.-K. Plant Disease Detection by Imaging Sensors–Parallels and Specific Demands for Precision Agriculture and Plant Phenotyping. *Plant Dis.* **2016**, *100*(2), 241–251. https://doi.org/10.1094/PDIS-03-15-0340-FE

[2] Yamamoto, K.; Togami, T.; Yamaguchi, N. Super-resolution of Plant Disease Images for the Acceleration of Image-based Phenotyping and Vigor Diagnosis in Agriculture. *Sensors* **2017**, *17*(11), 2557. https://doi.org/10.3390/s17112557

[3] Mohanty, S. P.; Hughes, D. P.; Salathé, M. Using Deep Learning for Image Based Plant Disease Detection. *Front. Plant Sci.* **2016**, *7*, 1419. https://doi.org/10.3389/fpls.2016.01419

[4] Ferentinos, K. P. Deep Learning Models for Plant Disease Detection and Diagnosis. *Comput. Electron. Agric.* **2018**, *145*, 311–318. https://doi.org/10.1016/j.compag.2018.01.009

[5] Too, E. C.; Yujian, L.; Njuki, S.; Yingchun, L. A Comparative Study of Fine-tuning Deep Learning Models for Plant Disease Identification. *Comput. Electron. Agric.* **2019**, *161*, 272–279. https://doi.org/10.1016/j.compag.2018.03.032

[6] Kamilaris, A.; Prenafeta-Boldú, F. X. Deep Learning in Agriculture: A Survey. *Comput. Electron. Agric.* **2018**, *147*, 70–90. https://doi.org/10.1016/j.compag.2018.02.016

[7] Xu, J.; Gu, B.; Tian, G. Review of Agricultural IoT Technology. *Artif. Intell. Agric.* **2022**, *6*, 10–22. https://doi.org/10.1016/j.aiia.2022.01.001

[8] Barbedo, J. G. A. Impact of Dataset Size and Variety on the Effectiveness of Deep Learning and Transfer Learning for Plant Disease Classification. *Comput. Electron. Agric.* **2018**, *153*, 46–53. https://doi.org/10.1016/j.compag.2018.08.013

[9] Udiani, O.; Mason, S.; Smith, G.; Riviere, J. E.; Baynes, R. E. Automation and Applications of the Tolerance Limit Method in Estimating Meat Withdrawal Periods for Veterinary Drugs. *Comput. Electron. Agric.* **2018**, *146*, 125–135. https://doi.org/10.1016/j.compag.2018.02.005

[10] Paul, K.; Chatterjee, S. S.; Pai, P.; Bhadra, B.; Dasgupta, S. Viable Smart Sensors and Their Application in Data Driven Agriculture. *Comput. Electron. Agric.* **2022**, *198*, 107096. https://doi.org/10.1016/j.compag.2022.107096

[11] Agu, C. M.; Menkiti, M. C.; Ekwe, E. B.; Agulanna, A. C. Modeling and Optimization of *Terminalia catappa* L. Kernel Oil Extraction Using Response Surface Methodology and Artificial Neural Network. *Artif. Intell. Agric.* **2020**, *4*, 1–11. https://doi.org/10.1016/j.aiia.2020.01.001

[12] Lu, M.; Chen, C.-L. Detection and Classification of Bearing Surface Defects Based on Machine Vision. *Appl. Sci.* **2021**, *11*(4), 1825. https://doi.org/10.3390/app11041825

[13] Thapa, R.; Zhang, K.; Snavely, N.; Belongie, S.; Khan, A. *Plant Pathology 2021 - FGVC8*. Kaggle Competition. https://kaggle.com/competitions/plant-pathology-2021-fgvc8 (accessed 2026-02-24).

[14] MacHardy, W. E. *Apple Scab: Biology, Epidemiology, and Management*; APS Press: St. Paul, MN, **1996**.

[15] Kim, Y. K.; Kwak, J. H.; Aguilar, C. G.; Xiao, C. L. First Report of Black Rot on Apple Fruit Caused by *Diplodia seriata* in Washington State. *Plant Dis.* **2016**, *100*(7), 1499. https://doi.org/10.1094/PDIS-12-15-1463-PDN

[16] Glawe, D. A. The Powdery Mildews: A Review of the World's Most Familiar (Yet Poorly Known) Plant Pathogens. *Annu. Rev. Phytopathol.* **2008**, *46*, 27–51. https://doi.org/10.1146/annurev.phyto.46.081407.104740

[17] Zhang, S.; Wu, X.; You, Z.; Zhang, L. Leaf Image Based Cucumber Disease Recognition Using Sparse Representation Classification. *Comput. Electron. Agric.* **2017**, *134*, 135–141. https://doi.org/10.1016/j.compag.2017.01.014

[18] Wang, S.; Xu, D.; Liang, H.; Su, C.; Wei, W. Advances in Deep Learning Applications for Plant Disease and Pest Detection: A Review. *Remote Sens.* **2025**, *17*(4), 698. https://doi.org/10.3390/rs17040698

[19] Pacal, I.; Kunduracioglu, I.; Alma, M. H.; Slany, V.; Martinek, R. A Systematic Review of Deep Learning Techniques for Plant Diseases. *Artif. Intell. Rev.* **2024**, *57*, 304. https://doi.org/10.1007/s10462-024-10944-7

[20] Das, P. K.; Rupa, S. S.; Pumrin, S.; Das, U. C.; Hossen, M. K. Deep Learning for Plant Disease Detection and Classification: A Systematic Analysis and Review. *Curr. Agric. Sci. Technol.* **2024**, *24*, 259016. https://doi.org/10.55003/cast.2024.259016

[21] Yang, B.; Li, M.; Li, F.; Li, C.; Wang, J. A Novel Plant Type, Leaf Disease and Severity Identification Framework Using CNN and Transformer with Multi-label Method. *Sci. Rep.* **2024**, *14*, 11664. https://doi.org/10.1038/s41598-024-62452-x

[22] Nnamdi, U. V.; Abolghasemi, V. Optimised MobileNet for Very Lightweight and Accurate Plant Leaf Disease Detection. *Sci. Rep.* **2025**, *15*, 43690. https://doi.org/10.1038/s41598-025-27393-z

[23] Islam, M.; Azad, A. K. M.; Arman, S. E.; Alyami, S. A.; Hasan, M. M. PlantCareNet: An Advanced System to Recognize Plant Diseases with Dual-mode Recommendations for Prevention. *Plant Methods* **2025**, *21*, 52. https://doi.org/10.1186/s13007-025-01366-9

[24] Prince, R. H.; Mamun, A. A.; Peyal, H. I.; Khandakar, A.; Ayari, M. A. CSXAI: A Lightweight 2D CNN-SVM Model for Detection and Classification of Various Crop Diseases with Explainable AI Visualization. *Front. Plant Sci.* **2024**, *15*, 1412988. https://doi.org/10.3389/fpls.2024.1412988

[25] Toda, Y.; Okura, F. How Convolutional Neural Networks Diagnose Plant Disease. *Plant Phenomics* **2019**, *2019*, 9237136. https://doi.org/10.34133/2019/9237136

[26] Wang, G.; Sun, Y.; Wang, J. Automatic Image-based Plant Disease Severity Estimation Using Deep Learning. *Comput. Intell. Neurosci.* **2017**, *2017*, 2917536. https://doi.org/10.1155/2017/2917536

[27] Parashar, P.; Johri, P. Enhancing Apple Leaf Disease Detection: A CNN-based Model Integrated with Image Segmentation Techniques for Precision Agriculture. *Int. J. Math. Eng. Manage. Sci.* **2024**, *9*(4), 943–964. https://doi.org/10.33889/IJMEMS.2024.9.4.050

[28] Bhatti, M.; Zeeshan, Z.; Ms, S.; Asif, M.; Afzal, T. Advanced Plant Disease Segmentation in Precision Agriculture Using Optimal Dimensionality Reduction With Fuzzy C-Means Clustering and Deep Learning. *IEEE J. Sel. Top. Appl. Earth Obs. Remote Sens.* **2024**, *17*, 18264–18277. https://doi.org/10.1109/JSTARS.2024.3437469

ASEAN
Journal of Scientific and Technological Reports
Online ISSN:2773-8752

Research article

Data-Driven Design of an Automatic Shower for the Elderly: Integrating the Kano Model and K-Means Clustering

Rattawut Vongvit[1], and Anyapat Kongwattananan[2*]

[1] Faculty of Engineering, Thammasat School of Engineering, Thammasat University, Pathumthani 12120, Thailand
[2] Academic Division, Chulachomklao Royal Military Academy, Nakhon Nayok, 26001, Thailand
* Correspondence: anyapat.crma@gmail.com

Citation:
Vongvit, R.; Kongwattananan, A. Data-driven design of an automatic shower for the Elderly: integratin the kano model and K-means clustering . *ASEAN J. Sci. Tech. Report.* **2026**, *29*(3), e261496. https://doi.org/10.55164/ajstr.v29i3.261496.

Article history:
Received: September 24, 2025
Revised: January 14, 2026
Accepted: February 5, 2026
Available online: February 28, 2026

Abstract: Automated devices designed for elderly users have become increasingly important in supporting independent living and addressing age-related challenges. Among these technologies, automatic shower devices play a key role in enhancing personal hygiene and reducing safety risks associated with conventional showering. This study applied the Kano model to identify factors influencing customer satisfaction with an automated shower device designed for older adults. Expert input was used to define and evaluate 25 quality elements across six dimensions, including washing, cleaning, safety, customer service, product-friendliness, and software–hardware integration. The results indicate that safety- and cleaning-related features—such as automatic disinfection, machine self-cleaning, automated emergency calls, emergency stop functions, and fall detection—exhibit high satisfaction coefficients, highlighting their importance in meeting elderly users' expectations. To further explore variation in user preferences, K-means clustering was used to segment respondents based on their Kano response patterns. Three distinct user clusters were identified, each demonstrating different feature prioritization strategies. One cluster emphasized comfort-enhancing features, such as body massage and automatic warm-air drying, while another placed greater importance on essential safety functions, including fall detection and emergency alerts. By integrating the Kano model with K-Means clustering, this study proposes a data-driven, customer-centric design framework that supports informed decision-making in assistive technology development. The findings enable designers and manufacturers to balance core safety requirements with differentiated features tailored to diverse elderly user segments, ultimately enhancing usability, independence, and overall user satisfaction.

Keywords: Kano model; K-mean clustering; customer satisfaction; data-driven design; automated devices

1. Introduction

Recently, automated devices designed explicitly for older adults have gained significant importance [1, 2]. As technological advancements continue to transform various aspects of our lives, healthcare and assistance for older adults are no exception. The development of automated devices catering to the specific needs of the elderly population holds immense potential to improve their overall quality of life and independence [2, 3]. The aging population faces unique challenges related to mobility,

health, and daily tasks that are often physically demanding [4-6]. Automated devices offer innovative solutions to these challenges by incorporating advanced technologies and intelligent features [7]. Such devices are designed to assist older adults with daily activities, promoting safety, convenience, and a sense of empowerment [8, 9]. The importance of automated devices for older adults goes beyond mere convenience. They contribute significantly to the physical and emotional well-being of seniors, allowing them to maintain independence and dignity [10]. By reducing physical strain and potential hazards, these devices promote a sense of confidence and self-sufficiency, leading to improved mental health and overall satisfaction [11, 12]. Furthermore, automated devices can provide peace of mind for caregivers and family members who may have concerns about the safety and well-being of their elderly loved ones. With the assistance provided by these devices, caregivers can be reassured that their elderly relatives receive the necessary support and care they need while minimizing the risk of accidents and injuries [13, 14].

Automated devices address mobility and health challenges among older adults by providing creative solutions to support daily tasks and increase independence. These devices enable a higher quality of life for the elderly by streamlining and simplifying tasks such as medication management [15, 16], home monitoring [17-19], and personal assistance [20, 21]. One area where the development of automated devices has shown great promise is personal hygiene [22, 23], particularly in automatic shower devices. Traditional showering can be physically strenuous and pose risks for elderly individuals, such as slips and falls [24]. Elderly individuals often face challenges with bathing, including difficulty getting in and out of the bathtub and the need for assistance due to safety concerns, highlighting the importance of innovative solutions that can provide greater independence and support [25]. A mechanical shower device can alleviate these concerns by incorporating automatic soaping, temperature control, and safety mechanisms [25, 26]. Despite the growing importance of automated devices designed for older people and their potential to enhance their quality of life and independence, a greater understanding is needed concerning the specific customer satisfaction factors that should be prioritized in designing such devices [27, 28]. While existing studies have explored the benefits of automated devices for older adults, few have applied a systematic approach [25, 26]. Therefore, more research is needed to fill the knowledge gap and to comprehensively understand the unique needs and preferences of older adults regarding automated devices, particularly for personal hygiene.

This study aims to bridge this gap by applying the Kano model to identify and evaluate the coefficients of customer satisfaction and dissatisfaction for key features of an automated shower device for older adults. K-Means clustering is further applied to segment users by their Kano response patterns, revealing distinct groups with shared preferences and expectations. While the combined use of the Kano model and clustering techniques has been explored in previous studies, the novelty of this research lies in its application to an elderly-centered automated shower system, supported by expert-driven feature elicitation and cluster-level interpretation explicitly linked to design implications for assistive technologies. This integrated approach enables a data-driven understanding of heterogeneous user needs across elderly subpopulations and supports more targeted, user-centered design strategies. The findings provide practical guidance for developing automated shower devices that enhance safety, usability, and overall well-being among elderly users.

2. Literature review

2.1 Application of the Kano Model in Data-Driven Design

The Kano model is widely recognized as an effective method for identifying and prioritizing customer needs by assessing their impact on overall satisfaction. The Kano model enables developers to discern essential, expected, and potentially agreeable elements by categorizing features into basic, performance, and agreeable categories [29-31]. A BERT-TCBAD-Kano-based method was developed to extract and prioritize user requirements from online reviews [32]. By combining sentiment analysis, complaint classification, and Kano evaluation, the study achieved a 30% improvement in prediction accuracy over the traditional Kano model, supporting more effective user-centered product design. Wang et al. [33] integrate the Kano model into a UGC-driven framework to identify how different product attributes influence user satisfaction and dissatisfaction. By analyzing user-generated content and clustering user needs, the Kano model categorizes factors that affect continuance and discontinuance intentions, offering a data-driven approach to

understanding the user experience. Cavacece et al. [34] apply the Kano model to explore the nonlinear relationship between digital health service quality and user satisfaction, highlighting that distinct service attributes affect satisfaction and dissatisfaction differently. It advances prior research by moving beyond linear assumptions and emphasizing user-centered design in digital health contexts. Li et al. [35] apply the Kano model, along with satisfaction and sensitivity coefficients, to evaluate functional requirements for health-focused e-sports chairs. By identifying essential, one-dimensional, and attractive features, the research offers a hierarchical design strategy that enhances user satisfaction while optimizing production through non-differentiated functions. These studies reinforce the methodological grounding of our research and highlight the growing trend of using Kano-based frameworks to guide the design of personalized, health-supportive technologies.

2.2 K-Means clustering

K-Means clustering is widely used for customer segmentation due to its simplicity and efficiency. This algorithm operates by grouping customers into distinct clusters based on similarities in their behaviors, preferences, or usage patterns, making it a powerful tool for uncovering hidden structures in large datasets [36]. Its core strengths lie in its computational speed and ease of implementation, enabling it to handle high-dimensional data efficiently. K-Means is particularly effective in applications such as market segmentation [37], personalized marketing, and behavioral profiling, where identifying homogeneous groups within diverse customer bases can lead to more targeted strategies and optimized service offerings. Despite its simplicity, it often yields meaningful insights that can drive decision-making in both business and engineering contexts. To enhance the traditional approach by introducing a nearest-neighbor density matrix and adaptive cluster selection [38], overcoming limitations such as sensitivity to initial centers and predefined cluster numbers. The improved method offers higher accuracy and stability, making it well-suited for analyzing customer behavior and demand patterns in power systems. Zhao et al. [39] enhance customer segmentation by extending the traditional K-Means clustering method with an elastic net penalty term, addressing challenges in high-dimensional data arising from weekly RFM variables. The improved method offers better clustering accuracy and variable selection, making it more effective for analyzing online customer behavior in omnichannel retail settings. Fang and Liu [40] applies and improves the K-Means algorithm for customer segmentation, aiming to enhance CRM effectiveness. It introduces a customer value evaluation system using AHP and clustering to classify customers. To address limitations of traditional K-Means, the study proposes two improved algorithms—one that automatically determines the optimal number of clusters, and another that boosts efficiency by combining sampling and agglomeration. The approach supports more accurate customer value analysis and decision-making in enterprise environments.

The review of prior research supports the suitability of both the Kano model and K-Means clustering as methodological foundations for this study. The Kano model has been widely used to classify user requirements into Must-Be, One-Dimensional, Attractive, Indifferent, and Reverse categories, enabling systematic feature prioritization based on their impact on user satisfaction. Its application across diverse domains demonstrates its effectiveness in capturing nonlinear relationships between product attributes and user perceptions. In the context of automated shower design for older adults, the Kano model provides a user-centered framework for distinguishing essential safety-related features from value-adding functions. The integration of K-Means clustering further enhances this approach by identifying latent user segments with differing expectations. Prior studies have shown that clustering techniques are effective for preference-based segmentation, supporting more targeted and inclusive design strategies. When combined with the Kano framework, clustering reveals how different user groups prioritize feature categories, offering deeper insight for design decision-making. Overall, the combined use of the Kano model and K-Means clustering aligns with best practices in user-centered product development and strengthens the analytical depth of this study. Together, these methods support a design approach that is both functionally responsive and adaptive to demographic diversity, making them well-suited to the research objectives.

3. Methods

3.1 Kano model

The Kano model considers both the subjective aspects of satisfaction and dissatisfaction as well as the objective elements of functionality [41-43]. It seeks to understand how a product or service's features and attributes influence user acceptance and satisfaction. The Kano model is critical and can be divided into five categories, as shown in Figure 1. These classifications are based on the varying levels of acceptance and satisfaction they provide users [44-46].

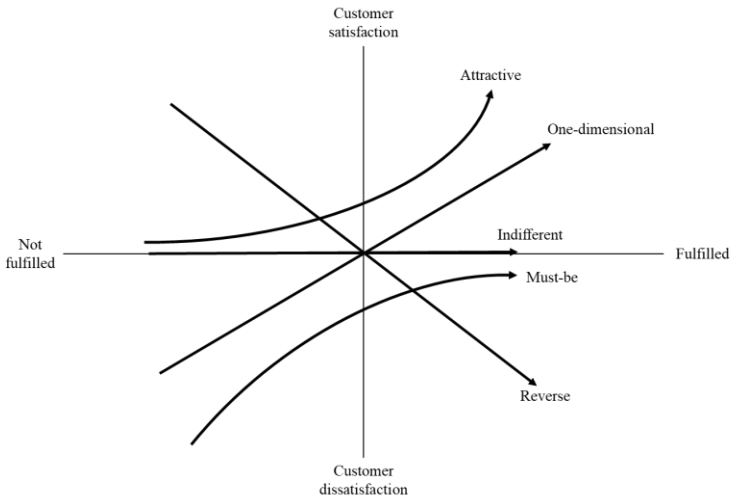

Figure 1. The Kano model [28]

Based on their characteristics, the Kano model systematically classifies user requirements and ranks them by the importance of achieving user satisfaction [47, 48]. This model offers a helpful framework for recognizing and satisfying users' needs and expectations. The Kano model can be used by businesses to categorize user requirements by their impact on customer satisfaction. The Kano model helps prioritize resource allocation and effort in product development by categorizing user requirements [49]. It enables companies to identify and focus on the key factors that significantly impact user satisfaction. This strategy allows businesses to allocate resources wisely and deliver goods and services that meet or exceed customer expectations [50]. The Kano model also offers a deeper comprehension of the dynamic nature of user requirements. It acknowledges that user satisfaction is influenced by various factors, including users' perceptions and expectations, as well as the presence or absence of attributes. Overall, the Kano model provides a comprehensive framework for categorizing and prioritizing user requirements based on their impact on user satisfaction. Businesses can use this model to make informed decisions about resource allocation and product development strategies, ultimately improving user satisfaction and gaining a competitive advantage in the market [51, 52].

3.2 Participants

A comprehensive participant study was conducted, specifically targeting adults aged 60 or older. This study was conducted as a non-invasive, questionnaire-based investigation of design requirements and user preferences for an automatic shower system for elderly users, using the Kano model. A total of 63 elderly participants were recruited using convenience sampling from local community centers and public residential areas. Inclusion criteria required participants to be aged 60 years or older, in generally good physical condition, and capable of independently understanding and completing the questionnaire. The study did not involve medical treatment, physical experimentation, or prototype testing, nor did it collect sensitive personal or health-related information. Participation was voluntary, and all participants were clearly informed of the study objectives and procedures before participation. Informed consent was obtained before data collection. Participant anonymity and data confidentiality were strictly maintained throughout the study. This cross-sectional study aimed to evaluate their unique requirements and preferences in depth. Subsequently, the

collected data were analyzed using the widely recognized Kano model, a methodology commonly used for evaluating customer satisfaction. To further explore patterns in user expectations, K-Means clustering was applied to segment participants into distinct groups based on their Kano response profiles. This combined approach enabled a deeper understanding of the heterogeneity among elderly users, offering actionable insights for the development of more personalized and effective automated shower device designs.

3.3 Developing quality evaluation dimensions and characteristics

The initial set of product features was identified through a structured expert brainstorming process involving a multidisciplinary panel with expertise in product design, mechanical engineering, and elderly care-related system design. The expert panel consisted of five professionals selected using purposive sampling based on their domain expertise and practical experience relevant to assistive shower system design. The panel included specialists in human factors engineering, automation engineering, and elderly care nursing, ensuring coverage of ergonomic design, system functionality, and user safety considerations. Experts were selected based on the following criteria: (1) a minimum of five years of professional or research experience in their respective fields, (2) direct involvement in product design, automation systems, or elderly care services, and (3) familiarity with assistive technologies or safety-oriented system design. The panel size was considered appropriate for early-stage feature identification and was consistent with exploratory engineering design practices. The process was conducted iteratively. In the first round, experts independently proposed potential features based on prior experience, relevant literature, and practical design considerations. These features were then reviewed collectively, and redundant or technically infeasible items were merged or removed through group discussion. Consensus was achieved through iterative deliberation, focusing on features that were relevant, easy to understand for elderly users, and suitable for Kano-based evaluation. The process continued until no new features emerged, yielding a final set of 25 product features for the Kano survey. A total of 25 quality evaluation elements across six dimensions were identified. The six dimensions of functional requirements include washing, cleaning, safety, customer service and support, product-friendliness, and software-hardware integration. The 25 quality evaluation elements and six dimensions are shown in Table 1.

Table 1. Quality evaluation elements and dimensions of customer requirements

Dimensions	Elements		Description
Washing Function	A1	Automatic soaping	Automatic dispensing and application of soap to reduce manual effort
	A2	Automatic water temperature control	Automatic regulation of water temperature for comfort and safety
	A3	Automatic warm air drying	Integrated warm air system for body drying after showering
	A4	Manual control	User-operated controls allowing manual adjustment of shower functions
	A5	Surround water jets	Multi-directional water jets provide full-body water coverage
	A6	Shower heads	Adjustable or multiple shower heads for improved washing efficiency
	A7	Body massage	Water pressure–based massage function to enhance comfort and relaxation
	A8	Ozone therapy	Use of ozone-treated water for hygiene and odor reduction
	A9	Color therapy lights	An integrated lighting system intended to enhance relaxation or mood
Cleaning Function	B1	Automatic Disinfection	Automated disinfection process to maintain hygiene after use
	B2	Automatic Machine self-cleaning	Self-cleaning mechanism to reduce maintenance requirements

Table 2. Quality evaluation elements and dimensions of customer requirements (continue)

Dimensions	Elements		Description
Safety Function	C1	Automated emergency call	Automatic alert system activated during emergencies
	C2	Automated emergency stop	An immediate system shutdown function to prevent accidents
	C3	Fall Detection	Sensor-based system to detect user falls and trigger safety responses
Customer Service and Support	D1	Safety assurance	Measures ensuring compliance with safety standards and user protection
	D2	Product guarantee	Warranty and assurance covering product performance and reliability
	D3	On-site service	Availability of maintenance and repair services at the user's location
Product-friendliness	E1	Easy to set up	Simple installation process requiring minimal effort or tools
	E2	Lightweight	Design emphasizing reduced weight for easier handling and installation
	E3	Duration	Expected service life and durability of the product
	E4	Comfortable seat	Ergonomically designed seating to support comfort and stability
Software-Hardware Integration	F1	Mobile application control	Smartphone-based control interface for system operation
	F2	Music Player	Integrated audio system for entertainment during use
	F3	Voice command	Voice-activated control for hands-free operation
	F4	Memory setup	System capability to store and recall personalized user settings

Table 3. Demand attribute definitions

Demand attribute	Definitions
Must-be (M)	Customers tend to be more dissatisfied with less functional products. However, even if the product becomes highly active, customer satisfaction remains at a neutral level.
One-dimensional (O)	Increased functionality typically results in greater customer satisfaction.
Attractive (A)	Customers generally experience higher satisfaction with more functional products, but achieving greater functionality requires more effort.
Indifferent (I)	Customers tend to exhibit a neutral level of satisfaction regardless of whether the product is fully functional or dysfunctional.
Reverse (R)	Customers are likely to experience a decrease in satisfaction if a product's functionality is reduced, and the level of satisfaction is typically inversely proportional to the extent of the reduction.

The Kano questionnaire is a structured survey tool used to assess customer needs and the importance of product or service quality to users. The two-way Kano questionnaire is an effective tool for comprehensively understanding consumer demands and preferences, including individual quality elements (demand attributes) and overall satisfaction. Table 3 illustrates the Kano two-way questionnaire format. The

questionnaire utilized a Kano two-dimensional model of quality, which organizes customer preferences into five distinct categories. These categories were thoroughly examined to understand their implications. Each quality element being investigated is associated with positive and negative questions. Participants are provided with five options to select from for each question. The questionnaire was designed to capture the product's basic requirements, desired features, and any surprises or delights that could exceed customer expectations, taking a comprehensive approach. This allowed for a more thorough evaluation of customer satisfaction and helped identify key areas for product improvement. The Kano quality attribute determination matrix was utilized to classify the quality level of each demand attribute. To ensure content validity and clarity, the questionnaire items were adapted from established Kano model studies and reviewed for relevance to the context of automatic shower system design for elderly users. All questions were presented in clear, simple language appropriate for elderly respondents. Before the main data collection, the questionnaire was reviewed for clarity and completeness to minimize ambiguity and misunderstanding, as presented in Table 4.

Table 4. The Kano two-way questionnaire format

Customer Requirement	Question	Answer
Automatic water temperature control	What would you think of an automatic shower device for the elderly that controls water temperature?	□ Satisfying □ Should be so □ Does not matter □ Tolerable □ Disagreeable
	What would you think of an automatic shower device for the elderly that has no automatic water temperature control?	□ Satisfying □ Should be so □ Does not matter □ Tolerable □ Disagreeable

Table 5. Kano evaluation matrix

	Available / Unavailable	Satisfying	Should be so	Does not matter	Tolerable	Disagreeable
		Negative				
Positive	Satisfying	Q	A	A	A	O
	Should be so	R	I	I	I	M
	Does not matter	R	I	I	I	M
	Tolerable	R	I	I	I	M
	Disagreeable	R	R	R	R	Q

3.5 Importance coefficients

Importance coefficients, such as customer satisfaction and dissatisfaction values, are employed to compare the significance of different demands classified under the same attribute. These coefficients help determine which features are essential for raising customer satisfaction and allow a more accurate assessment of customer preferences. The customer satisfaction coefficient is used to assess the impact of customer satisfaction and dissatisfaction, and can be calculated as

$$\text{Satisfaction Coefficient (SC)} = \frac{(A+O)}{(\text{A+O+M+I})} \quad (1)$$

$$\text{Dissatisfaction Coefficient (DC)} = \frac{(O+M)}{(\text{A+O+M+I})} \quad (2)$$

The satisfaction and dissatisfaction values range from 0 to 1. A higher satisfaction value, closer to 1, indicates that providing the attribute can enhance satisfaction. On the other hand, a higher dissatisfaction value, closer to 1, indicates that not providing the attribute can lead to greater dissatisfaction [55]. Note that

the dissatisfaction coefficient (DC) is reported as a negative value to indicate the direction of dissatisfaction, consistent with conventional Kano model interpretations. In this study, the negative sign is retained to explicitly indicate the potential decrease in customer satisfaction when a feature is absent. For interpretation purposes, a larger absolute DC value indicates a stronger effect of dissatisfaction.

3.6 K-Means clustering

K-Means clustering is one of the most widely used unsupervised machine learning algorithms for data partitioning. The algorithm aims to divide a set of *n* data points into *k* distinct, non-overlapping clusters, where each data point belongs to the cluster with the nearest mean (centroid). This method is particularly suitable for customer segmentation, behavioral analysis, and feature preference grouping, especially when the objective is to explore underlying patterns in large-scale data without prior labels. K-Means minimizes the within-cluster sum of squares (WCSS) [56], also known as inertia, which represents the variance within each cluster. The objective is to locate:

$$arg\ \min \sum_{i=1}^{k} \sum_{x \in S_i} \|x - \mu_i\|^2 \quad (3)$$

Where:
$k = number\ of\ clustering.$
$S_i =$ $set\ of\ data\ point\ assigned\ to\ cluster\ i$
$\mu_i =$ $mean\ (centroid)\ of\ cluster\ i$
$\|x - \mu_i\|^2 =$ $squared\ Euclidean\ distance\ between\ data\ point\ x\ and$
$its\ cluster\ centroid.$
Algorithmic Steps:

Initialization: Select k initial centroids, either randomly or using an improved method such as K-Means++ to improve convergence. Assignment Step: Assign each data point x_j to the cluster whose centroid μ_i is closest, based on the Euclidean distance:

$$Cluster(x_j) arg_i \min \|x - \mu_i\| \quad (4)$$

Update Step: Recalculate each cluster's centroid by taking the mean of all points assigned to that cluster:

$$\mu_i = \frac{1}{|S_i|} \sum_{x \in S_i} x \quad (5)$$

Iteration and Convergence: Repeat the assignment and update steps until the centroids no longer change significantly or a predefined maximum number of iterations is reached. Choosing the Optimal Number of Clusters (k). One of the key challenges in K-Means clustering is determining the most appropriate number of clusters. Common techniques include: the Elbow Method: plotting the WCSS for different values of k and identifying the "elbow" point where the rate of decrease changes sharply. Silhouette Score: Measuring how similar an object is to its own cluster compared to other clusters. Domain Knowledge: Leveraging prior understanding of the user base or problem context to select a meaningful k. In this research, K-Means clustering was applied to numerically encoded Kano response data (e.g., A = 1, O = 2, M = 3, I = 4, R = 5) to segment elderly participants based on their preference patterns across 25 features of an automatic shower device. The optimal number of clusters was determined using a combination of the elbow method and interpretability of the output. This enabled the identification of distinct user groups, each with specific preferences for Must-Be, Attractive, or One-Dimensional features. By incorporating K-Means clustering alongside the Kano model, this study offers a robust approach to user segmentation, enabling designers to prioritize feature sets according to specific needs and latent patterns within different elderly subgroups.

4. Results and Discussion

4.1 Classification and analysis of Kano demand attributes

A total of 63 valid questionnaires were collected, with participants comprising 54% men and 46% women. The participants were aged 60 or older, with a mean age of 70.85 years (SD = 3.29). For the Kano two-dimensional quality analysis, respondents were instructed to indicate their perceived satisfaction with six

dimensions comprising 25 quality elements. For each quality element, the Kano category was determined by the response category with the highest percentage: Attractive (A), One-Dimensional (O), Must-Be (M), Indifferent (I), or Reverse (R). This dominant category was assigned as the representative Kano classification, reflecting the predominant user perception of each feature in accordance with standard Kano model practices. A total of 25 quality elements were evaluated, as given in Table 5. Out of these, seven were identified as "Attractive" to customers, meaning they positively impacted customer satisfaction and loyalty. Another seven elements were classified as "One-Dimensional," meaning they were considered essential by customers but did not necessarily increase customer loyalty or satisfaction. Four elements were identified as "Must-Be," meaning they were crucial to meeting customer expectations, and their absence would lead to dissatisfaction. Seven other elements were classified as "Indifferent," meaning customers did not consider them positive or negative in terms of their impact on satisfaction and loyalty. Finally, none of the 25 quality elements were classified as "Reverse," indicating that none negatively impacted customer satisfaction or loyalty.

Table 6. Kano quality element percentage and classification

Dimensions		Elements	A (%)	O (%)	M (%)	I	R (%)	Kano
Washing Function	A1	Automatic soaping	48	24	22	6	0	A
	A2	Automatic water	22	13	43	22	0	M
	A3	Automatic warm air drying	22	38	25	14	0	O
	A4	Manual control	21	43	21	16	0	O
	A5	Surround water jets	17	48	19	16	0	O
	A6	Shower heads	43	8	19	30	0	A
	A7	Body massage	54	5	3	38	0	A
	A8	Ozone therapy	37	2	2	60	0	I
	A9	Color therapy lights	30	2	2	67	0	I
Cleaning Function	B1	Automatic Disinfection	59	19	6	16	0	A
	B2	Automatic Machine self-	54	16	10	21	0	A
Safety Function	C1	Automated emergency call	21	48	22	10	0	O
	C2	Automated emergency stop	17	51	19	13	0	O
	C3	Fall Detection	44	29	19	8	0	A
Customer Service and Support	D1	Safety assurance	13	60	22	5	0	O
	D2	Product guarantee	22	13	43	22	0	M
	D3	On-site service	25	44	22	8	0	O
Product-friendliness	E1	Easy to set up	32	19	29	21	0	A
	E2	Lightweight	27	2	16	56	0	I
	E3	Duration	21	30	37	13	0	M
	E4	Comfortable seat	21	19	41	19	0	M
Software–Hardware Integration	F1	Mobile application control	19	2	10	60	10	I
	F2	Music Player	38	5	10	48	0	I
	F3	Voice command	25	5	3	63	3	I
	F4	Memory setup	27	8	10	56	0	I

4.1.1 Attractiveness

Seven quality elements were identified as attractive to customers, which positively affected their satisfaction and loyalty. Elements such as "Automatic Soaping" and "Shower Heads" can enhance the shower experience by providing convenience and comfort. "Body Massage" is an added feature that helps customers relax and reduce stress while showering [57]. "Automatic Machine Self-Cleaning" and "Automatic Disinfection" help customers maintain hygiene and cleanliness without manual cleaning. A "Fall Detection"

safety feature can help prevent accidents and ensure customers' well-being. Lastly, "Ease of Setup" can help customers quickly and easily install and use the product, increasing their satisfaction.

4.1.2 One-dimensional

"Automatic Warm Air Drying," "Manual Control," "Surround Water Jets," "Automated Emergency Call," "Automated Emergency Stop," "Safety Assurance," and "On-Site Service" were all classified as one-dimensional; increasing functionality can typically result in greater customer satisfaction. While these one-dimensional quality elements are essential for meeting customer expectations, companies should continue offering these critical features. They should enhance these elements by adding functionality, which can lead to greater customer satisfaction and loyalty. For example, "Automatic Warm Air Drying" is an essential feature for drying off after a shower, but a more advanced feature could be an adjustable temperature setting, which would enable the customer to customize the drying temperature. Similarly, "Surround Water Jets" can be enhanced by adding different pressure settings or patterns, offering customers a more customized shower experience. "Automated Emergency Call" and "Automated Emergency Stop" are essential safety features customers expect to include in the product. However, offering additional safety features can help differentiate a product from its competitors. "Safety Assurance" can be enhanced by providing certifications or warranties that assure customers that the product is safe and reliable. "On-Site Service" can be improved by offering additional services, such as installation or maintenance, to enhance the customer experience further.

4.1.3 Must-be

The quality elements "Automatic Water Temperature Control," "Product Guarantee," "Duration," and "Comfortable Seat" were all classified as must-be, indicating that their absence can lead to customer dissatisfaction. The must-be quality elements are customers' basic requirements for the product. Customers will likely be dissatisfied with the product if any of these elements need to be added or are not up to standard. For example, "Automatic Water Temperature Control" is a must-have feature, ensuring customers can shower comfortably and safely without manually adjusting the temperature. "Product Guarantee" is another must-have element, as customers expect a certain level of quality and reliability from the product. A guarantee can provide them with confidence and peace of mind. "Duration" is also a must-have element, as customers expect the product to last for a reasonable amount of time without requiring frequent repairs or replacement. A product that fails to meet this requirement is likely to result in customer dissatisfaction. Similarly, a "Comfortable Seat" is a must-have feature, especially for customers with disabilities or elderly customers who may require additional support and comfort. While these must-be quality elements are essential for meeting customer expectations and preventing dissatisfaction, they do not necessarily increase customer satisfaction or loyalty. Companies should also focus on enhancing the quality of their products to differentiate themselves from competitors and improve customer satisfaction and loyalty.

4.1.4 Indifferent

The quality elements of "Ozone Therapy," "Color Therapy Lights," "Lightweight," "Mobile Application Control," "Music Player," "Voice Command," and "Memory Setup" were all classified as indifferent, indicating that their presence or absence would not likely affect customer satisfaction in any significant way. Indifferent quality elements do not significantly impact customer satisfaction, and their presence or absence does not significantly affect a customer's purchase decision. For example, "Ozone Therapy" and "Color Therapy Lights" can provide additional health benefits and relaxation, but they are not essential for a satisfactory shower experience. Similarly, "Lightweight" is a desirable feature, but it is unlikely to significantly affect customer satisfaction because it has no direct effect on the product's functionality. "Mobile Application Control," "Music Player," "Voice Command," and "Memory Setup" are additional features that can enhance the overall shower experience. However, their absence is likely to still result in customer satisfaction. These features may appeal to some customers, but they are optional for meeting the basic requirements of a shower.

4.1.5 Reverse

The Reverse classifications for mobile application control and voice command indicate that these features were perceived as undesirable by some elderly users. Mobile application control may increase

usability complexity and cognitive load, requiring familiarity with smartphones and application management, thereby reducing perceived ease of use. Similarly, voice command functions may be viewed as unreliable or uncomfortable in bathroom environments due to speech recognition issues, background noise, or privacy concerns. These findings suggest that advanced digital interaction features may conflict with elderly users' preferences for simplicity and predictability and should therefore be treated as optional rather than core design elements in assistive technologies.

4.2 Results of customer satisfaction and dissatisfaction coefficients

The Kano model is a framework for understanding customer satisfaction and prioritizing features based on how customers perceive them. The dimensions and elements listed in the result are the various features that could be included in an automatic shower device for the elderly. The satisfaction and dissatisfaction coefficients indicate the perceived importance of each feature and the level of satisfaction or dissatisfaction it would evoke in a customer. In Figure 2, the X-axis center line represents the average extent of satisfaction for the 25 quality elements, while the Y-axis center line represents moderate dissatisfaction. The satisfaction and dissatisfaction coefficients indicate the magnitude of these factors, with values ranging from 0 to 1. When the quality element improves, a customer satisfaction coefficient close to 1 indicates a significant increase in perceived satisfaction. If the quality element remains unsatisfactory, an extent of dissatisfaction coefficient closer to -1 indicates a significant increase in perceived dissatisfaction [53]. Based on the coefficients listed in Table 6, clear product development priorities can be identified. Safety and cleaning functions should be treated as first-level priorities, as they exhibit high satisfaction coefficients and strong dissatisfaction effects when absent. In particular, automatic disinfection and Machine self-cleaning (B1 and B2), together with automated emergency call, emergency stop, and fall detection (C1–C3), represent core system requirements that directly influence user trust and acceptance. The second level of prioritization includes washing-related features with high satisfaction coefficients, such as automatic soaping (A1), surround water jets (A5), shower heads (A6), and body massage (A7), which primarily enhance comfort and perceived value. In contrast, features such as automatic water temperature control (A2) and color therapy lights (A9) show limited impact on satisfaction. Customer service and support features, particularly safety assurance (D1) and on-site service (D3), also contribute strongly to satisfaction and should be integrated into the overall product–service strategy. Product-friendliness attributes, including easy setup (E1) and product duration (E3), support usability and lifecycle performance and can be treated as secondary priorities. By comparison, software–hardware integration features (F1–F4) exhibit relatively low satisfaction coefficients and should be considered optional enhancements rather than core design requirements. Overall, the satisfaction coefficient analysis supports a structured prioritization strategy that emphasizes safety and hygiene first, followed by comfort-related features, while deprioritizing low-impact digital functions.

4.3 Cluster Analysis of User Requirements Using K-Means

To explore distinct patterns in user preferences for an Automatic Shower Device for the Elderly, K-Means clustering was employed. This unsupervised learning method was selected due to its effectiveness in partitioning users based on multidimensional categorical response data—in this case, the Kano responses (Attractive, One-dimensional, Must-be, Indifferent, and Reverse) to 25 product features. Based on the elbow method and interpretability considerations, the analysis was conducted with three clusters (k=3). The optimal number of clusters was determined using the elbow method by examining the relationship between the number of clusters (k) and the within-cluster sum of squares (WCSS). As shown in the elbow plot in Figure 3, WCSS decreased substantially from 10,483.28 at k = 1 to 2,660.81 at k = 3, after which the rate of reduction became less pronounced (e.g., 1,396.01 at k = 4 and 996.80 at k = 5). This noticeable change in the rate of WCSS reduction indicates an elbow at k = 3. Beyond this point, increasing the number of clusters yields only marginal improvements at the expense of interpretability. Therefore, k = 3 was selected as an appropriate balance between clustering performance and practical interpretability. To further assess cluster quality and robustness, internal validation was conducted using silhouette analysis. For the selected solution with k = 3, the average silhouette score was 0.47, indicating acceptable cluster separation and supporting the suitability of the clustering structure for exploratory, design-oriented analysis. The analysis revealed three distinct user

clusters, as shown in Table 7, each representing a unique pattern of prioritization of product requirements. The validity of the clustering results was reinforced through multiple observations. First, a clear separation in response patterns was evident when the data were projected into a two-dimensional space using Principal Component Analysis (PCA)[56], indicating that the clusters captured meaningful variance among respondents. The distribution of Kano response types—Attractive (A), One-dimensional (O), Must-be (M), Indifferent (I), and Reverse (R)—was analyzed across the three identified clusters to gain a deeper understanding of each user group's underlying preferences. The results are summarized in Table 7. Each cluster exhibits a distinct prioritization pattern, reflecting the diversity of user expectations regarding the product features.

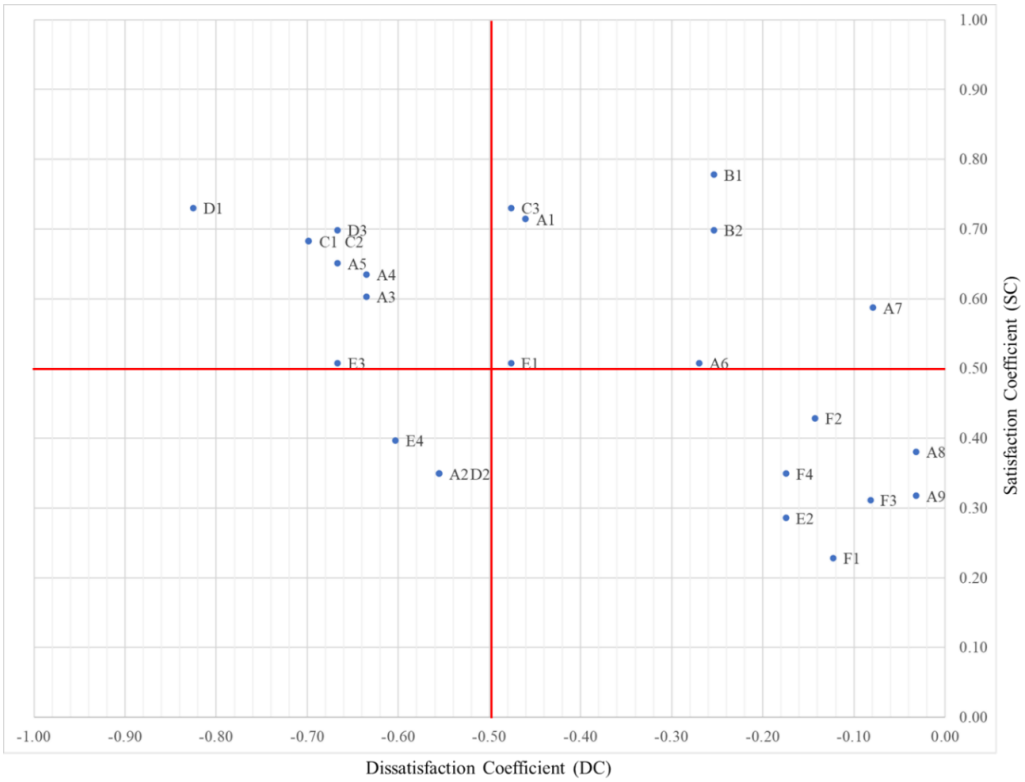

Figure 2. Customer satisfaction matrix

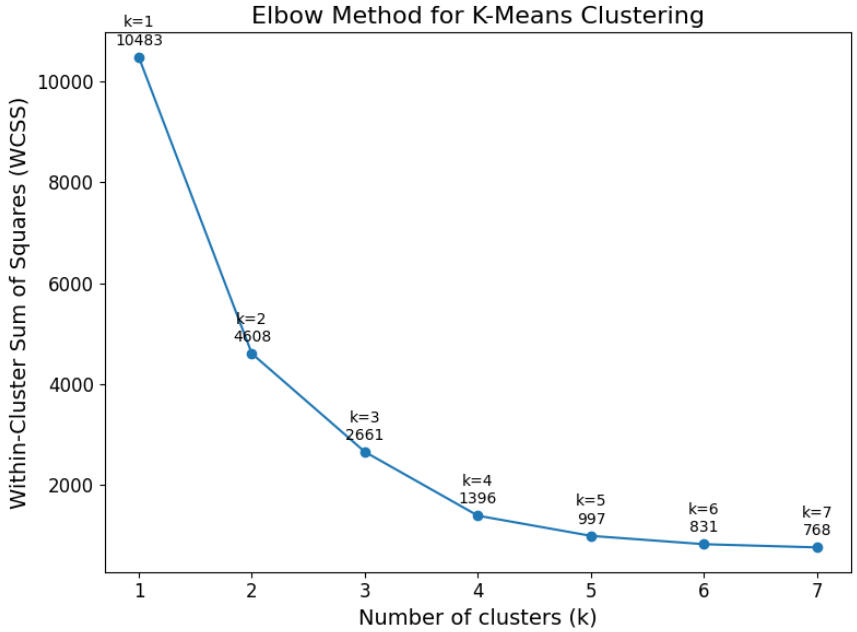

Figure 3. The elbow method is used to determine the optimal number of clusters for K-Means analysis.

Table 7. Customer satisfaction coefficients

Dimensions		Elements	Kano Classification	SC	DC
Washing Function	A1	Automatic soaping	A	0.71	-0.46
	A2	Automatic water temperature control	M	0.35	-0.56
	A3	Automatic warm air drying	O	0.60	-0.63
	A4	Manual control	O	0.63	-0.63
	A5	Surround water jets	O	0.65	-0.67
	A6	Shower heads	A	0.51	-0.27
	A7	Body massage	A	0.59	-0.08
	A8	Ozone therapy	I	0.38	-0.03
	A9	Color therapy lights	I	0.32	-0.03
Cleaning Function	B1	Automatic Disinfection	A	0.78	-0.25
	B2	Automatic Machine self-cleaning	A	0.70	-0.25
Safety Function	C1	Automated emergency call	O	0.68	-0.70
	C2	Automated emergency stop	O	0.68	-0.70
	C3	Fall Detection	A	0.73	-0.48
Customer Service and Support	D1	Safety assurance	O	0.73	-0.83
	D2	Product Guarantee	M	0.35	-0.56
	D3	On-site service	O	0.70	-0.67
Product-friendliness	E1	Easy to set up	A	0.51	-0.48
	E2	Lightweight	I	0.29	-0.17
	E3	Duration	M	0.51	-0.67
	E4	Comfortable seat	M	0.40	-0.60
Software-Hardware Integration	F1	Mobile application control	I	0.23	-0.12
	F2	Music Player	I	0.43	-0.14
	F3	Voice command	I	0.31	-0.08
	F4	Memory setup	I	0.35	-0.17

Table 8. Results of Cluster Analysis

Cluster	Male (60-69 yrs.)	Male (70-79 yrs.)	Female (60-69 yrs.)	Female (70-79 yrs.)	Attractive (A)	One-dimensional (O)	Must-Be (M)	Indifferent (I)	Reverse (R)
0	10.53%	42.11%	21.05%	26.32%	34.53%	21.89%	18.74%	24.84%	0.00%
1	14.29%	38.10%	14.29%	33.33%	27.62%	25.33%	19.81%	27.05%	0.19%
2	21.74%	34.78%	13.04%	30.43%	29.39%	18.96%	18.26%	32.17%	1.22%

Cluster 0 consists predominantly of older males aged 70–79 years (42.11%) and females aged 70–79 years (26.32%), indicating a strong representation of users in the advanced elderly stage. This cluster demonstrates the highest proportion of Attractive responses (34.53%), suggesting that these users are especially responsive to features that deliver enjoyment, comfort, or an enhanced experience—such as body massage and automatic warm-air drying. Their relatively lower emphasis on Must-be (18.74%) suggests that their satisfaction may not depend solely on basic functionality but rather on emotionally engaging enhancements. The Indifferent rate (24.84%) further suggests that while these users value certain advanced features, they also consider several others as non-essential. Cluster 1 is more evenly distributed across gender and age groups, with a notable proportion of females aged 70–79 years (33.33%) and males aged 70–79 years (38.10%). This group reflects a balanced Kano distribution, with One-dimensional (25.33%) and Indifferent (27.05%) categories slightly dominating. This implies that users in this segment are more performance-oriented—placing value on features that deliver proportional satisfaction but also holding neutral views on many aspects of the system. Their Must-be rate (19.81%) is the highest among the three clusters, reflecting a

cautious expectation for basic reliability and functionality. Cluster 2 exhibits the highest percentage of users aged 60–69 years, both male (21.74%) and female (13.04%), and a strong representation of females aged 70–79 years (30.43%). This cluster is particularly defined by a high proportion of Indifferent responses (32.17%), indicating a group that is less responsive to both essential and advanced features. These users may prioritize simplicity and familiarity over innovation, and are likely to reject features that feel unnecessary or overwhelming. Their Reverse response rate (1.22%), although low overall, is the highest among the clusters, potentially signifying some resistance to certain technological elements. Taken together, these findings highlight the heterogeneity of user needs within the elderly population. Segmenting by cluster provides a more nuanced understanding than age or gender alone. For instance, while older males tend to dominate Cluster 0 and prefer appealing, non-essential features, younger seniors in Cluster 2 appear more indifferent or resistant to feature complexity. Such insights are critical for guiding inclusive design, feature prioritization, and marketing strategies in assistive technology for aging populations.

4.4 Heatmap Analysis of Kano Responses by User Cluster

To gain deeper insight into how different user groups perceive and prioritize the features of the Automatic Shower Device for the Elderly, this study employed a heatmap visualization. Heatmaps are particularly effective for displaying patterns of categorical data across multiple dimensions, allowing simultaneous observation of both intensity and distribution. In this analysis, heatmaps were generated for three specific Kano response types—Must-Be (M), Attractive (A), and One-Dimensional (O), as shown in Figure 4, to identify which features were most frequently associated with each type across the clusters derived from K-Means clustering. Each cell in the heatmap represents the frequency count of a particular Kano response (e.g., "Must-Be") for a given feature within a specific cluster, with color gradients indicating the relative intensity of responses. This approach enables a visual, comparative understanding of user expectations, desires, and satisfaction drivers across distinct elderly user segments. By observing the patterns in these heatmaps, design teams and developers can prioritize which features to include, enhance, or simplify to better align with the differentiated needs of target user groups.

Features categorized as Must-Be (M) represent essential expectations that users assume will be included by default. While their presence may not significantly enhance satisfaction, their absence typically results in dissatisfaction. Analysis of the heatmap reveals that across all clusters, "Automatic water temperature control" consistently ranks as a critical Must-Be requirement, underscoring the fundamental importance of thermal safety and comfort among elderly users. Additionally, features such as "Product guarantee" and "Comfortable seat" appear prominently in Clusters 1 and 2, suggesting shared expectations regarding product reliability and ergonomic support. Interestingly, Cluster 2, which consists of a higher proportion of younger elderly individuals (aged 60–69), more frequently designates features such as "Fall Detection" and "Automated emergency call" as Must-Be than Cluster 0. This pattern implies a heightened awareness of safety and emergency preparedness in the early stages of aging. These findings highlight that such core features should be regarded as non-negotiable elements in the product's design and functionality, and must be clearly emphasized in product communication, instructional materials, and marketing strategies. Attractive (A) features are elements that users do not explicitly expect, yet, when present, create a sense of surprise and delight, significantly enhancing user satisfaction. Cluster 0 demonstrates strong preferences for features such as "Body massage," "Shower heads," and "Automatic warm air drying," indicating that this group places high value on spa-like, comfort-enhancing experiences. In contrast, Cluster 1 exhibits a different trend, with a high concentration of Attractive responses for "Ozone therapy" and "Mobile application control," reflecting a more progressive attitude and openness toward innovative or digital features. Meanwhile, Cluster 2 shows a more moderate pattern, with appreciation for basic conveniences like "Easy to set up" and "Voice command," but generally records fewer Attractive responses overall. This may suggest that users in Cluster 2 exhibit lower emotional engagement or enthusiasm for optional or luxurious enhancements. These patterns highlight the importance of Attractive features as key differentiators in design and marketing—particularly for Cluster 0, where such features could be promoted as wellness-oriented or premium add-ons to enhance user appeal and product satisfaction.

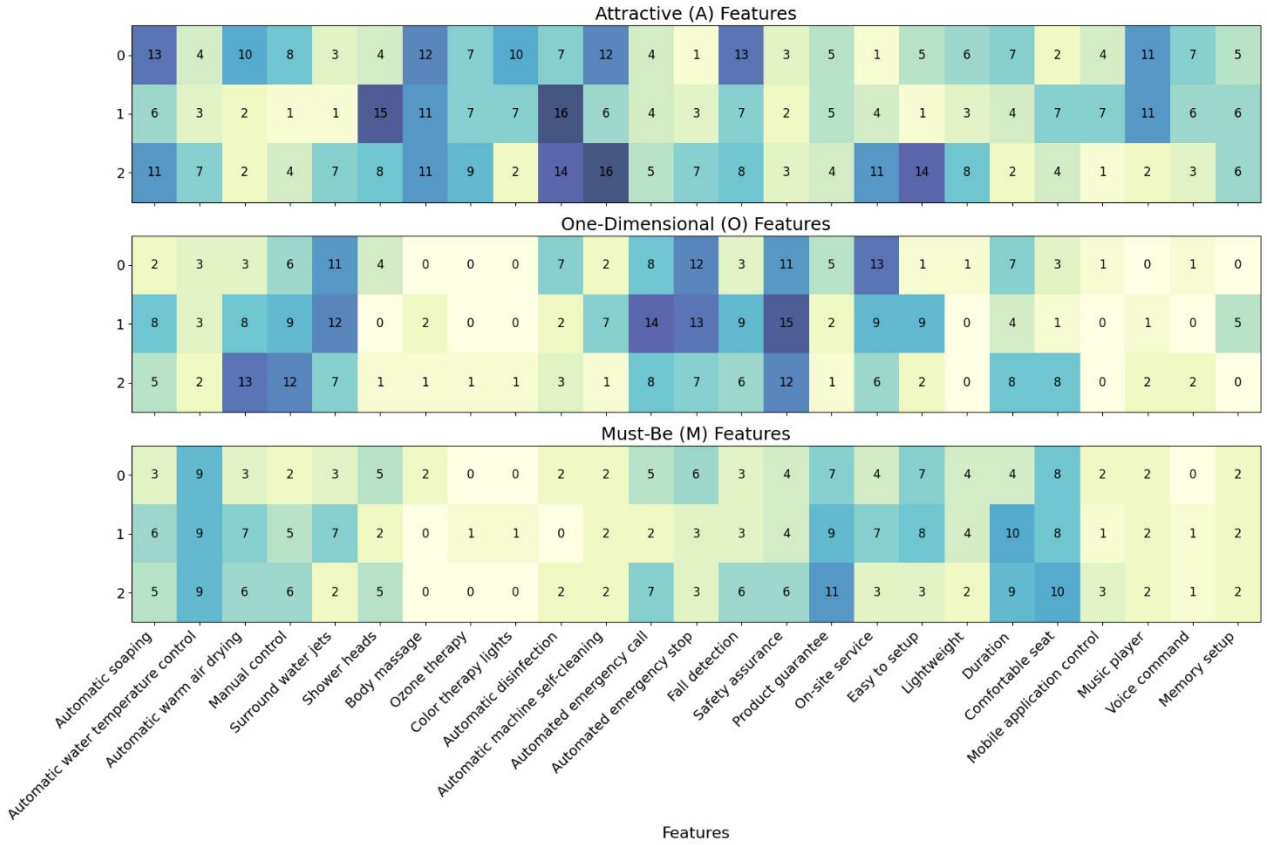

Figure 4. Heatmaps of Attractive (A), One-Dimensional (O), and Must-Be (M) features across user clusters.

One-Dimensional (O) features are those that contribute to user satisfaction in a directly proportional manner—the better these features perform or the more of them are present, the greater the user's satisfaction. As revealed in the heatmap analysis, "Automated emergency stop" and "Fall Detection" are consistently rated highly across Clusters 1 and 2, underscoring their critical role as performance-driven safety functions. Cluster 1, in particular, places considerable emphasis on "Product guarantee" and "On-site service," suggesting that users in this group prioritize dependable service and long-term support as key components of product performance. Meanwhile, Cluster 2 assigns relatively high value to features such as "Manual control" and "Automatic warm air drying," indicating appreciation for hands-on functionality and immediate physical comfort. These results affirm that One-Dimensional features represent a significant avenue for gaining a competitive advantage, as focused enhancements in these areas can translate directly into increased user satisfaction. Prioritizing the performance and reliability of these features can thus yield measurable improvements in product perception and user loyalty. The results of this study are consistent with prior research on assistive technology design, which identifies safety, reliability, and ease of use as key factors influencing elderly user acceptance. Previous studies have emphasized the importance of fall-prevention and emergency-response functions in building trust in assistive systems, particularly in personal care applications [58, 59]. The present findings reinforce these observations by showing that safety and hygiene-related features generate the strongest effects on satisfaction and dissatisfaction [60]. While existing literature often highlights the potential of advanced digital interfaces to enhance engagement, the results indicate that software-based features have limited perceived value compared with fundamental safety and comfort requirements. This highlights the need for user-centered rather than technology-driven design approaches. By combining Kano analysis with clustering techniques, this study contributes a data-driven engineering design framework that complements prior qualitative research and supports systematic feature prioritization in assistive technology development.

4.5 Limitations and Future Research

Despite providing valuable insights into user preferences and satisfaction through the integration of the Kano model and K-Means clustering, this study has several limitations that should be acknowledged. First,

the sample size and demographic composition may not fully represent the heterogeneity of the elderly population. Factors such as age subgroups (e.g., early elderly versus advanced elderly), health conditions, and prior experience with assistive technologies were not explicitly modeled as moderating variables, which may limit the generalizability of the findings across broader populations or cultural contexts. Second, the identification of product features was based solely on expert input and did not directly involve elderly users or caregivers at the initial feature generation stage. While expert-driven brainstorming is suitable for early-stage engineering design, the absence of direct end-user participation may limit the completeness of the identified feature set. Future studies should incorporate participatory design approaches, such as co-design workshops or interviews with elderly users and caregivers, to further validate and refine the feature dimensions. Third, this study employed a static Kano model, which assumes that user perceptions remain stable over time. In practice, preferences for assistive technologies may evolve as users gain experience, receive caregiver support, or improve digital literacy. In addition, the use of K-Means clustering introduces methodological constraints, as the algorithm assumes spherical cluster structures and relies on distance-based calculations. Given that Kano categories are categorical in nature and were numerically encoded for clustering, this approach may not fully capture more complex or non-spherical preference patterns. Furthermore, clustering results are sensitive to the predefined number of clusters (k). Although the elbow method and silhouette analysis were used to support the selection of k, the relatively small sample size may still affect cluster stability and reproducibility. Therefore, the clustering results should be interpreted as exploratory rather than definitive population-level segmentation. Future studies may benefit from larger samples and alternative clustering techniques, such as hierarchical clustering or density-based methods (e.g., DBSCAN), to validate or complement the segmentation outcomes. Future research should consider larger, more diverse samples, including elderly users from home care, assisted living, and clinical settings. Longitudinal designs may further reveal how satisfaction and expectations change over time. Additionally, hybrid analytical approaches that combine qualitative methods (e.g., interviews or observations) with quantitative clustering could provide a more comprehensive understanding of user needs. Finally, incorporating adaptive or real-time feedback mechanisms into assistive device design may support dynamic personalization and enhance long-term usability and engagement.

5. Conclusion

This study contributes to an engineering design framework for assistive shower systems by translating user satisfaction data into actionable insights for design and decision-making. By integrating the Kano model with K-Means clustering, the framework enables systematic feature prioritization based on user expectations, safety requirements, and ergonomic considerations. Must-Be attributes such as fall detection, automated emergency call, and emergency stop functions represent fundamental safety constraints. From an engineering design perspective, these features should be embedded as baseline requirements, as their absence directly undermines user trust and system acceptance. One-Dimensional features, including product guarantee and on-site service, emphasize the importance of reliability and lifecycle-oriented design, highlighting the relevance of product–service system thinking in assistive technologies. Attractive features, such as body massage and advanced shower functions, were valued by specific user segments and can be strategically implemented as optional or modular components. This enables cost–performance optimization while accommodating heterogeneous user needs. The clustering results further indicate that younger elderly users prioritize safety-related features, whereas older users place greater emphasis on comfort, reinforcing the need for adaptive and ergonomically scalable design strategies. Notably, software-based features were largely perceived as Indifferent across clusters, suggesting that increased technological complexity does not necessarily translate into higher perceived value. This underscores the importance of aligning digital functions with usability and user capability rather than pursuing technology-driven design. Overall, the proposed engineering design framework demonstrates how Kano-based classification and user segmentation can inform structured decision-making in assistive technology development, supporting safer, more acceptable, and user-centered design solutions for elderly populations.

6. Acknowledgements

This work was supported by 2epartment of Ordnance Engineering, Academic Division, Chulachomklao Royal Military Academy, and the Department of Industrial Engineering, Faculty of Engineering, Thammasat School of Engineering, Thammasat University.

Author Contributions: RV: Conceptualization, RV and AK; methodology, RV and AK; formal analysis,RV and AK; validation, RV; visualization, RV; resources, RV; writing—original draft, review, and editing, RV and AK. All authors have read and agreed to the published version of the manuscript.

Conflicts of Interest: The authors affirm that they are not affiliated with or involved in any organization or entity with any interest, financial or otherwise, in the subject matter or materials discussed in this manuscript.

References

[1] Harmo, P.; Taipalus, T.; Knuuttila, J.; Vallet, J.; Halme, A. Needs and solutions-home automation and service robots for the elderly and disabled. In *2005 IEEE/RSJ International Conference on Intelligent Robots and Systems*, **2005**; IEEE: pp 3201–3206. https://doi.org/10.1109/IROS.2005.1545387

[2] Marques, B.; McIntosh, J.; Valera, A.; Gaddam, A. Innovative and Assistive eHealth Technologies for Smart Therapeutic and Rehabilitation Outdoor Spaces for the Elderly Demographic. *Multimodal Technol. Interact.* **2020**, *4*(4), 76. https://doi.org/10.3390/mti4040076

[3] Baucas, M. J.; Spachos, P.; Gregori, S. Internet-of-Things Devices and Assistive Technologies for Health Care: Applications, Challenges, and Opportunities. *IEEE Signal Process. Mag.* **2021**, *38*(4), 65–77. https://doi.org/10.1109/MSP.2021.3075929

[4] Brouwer, D. M.; Sadlo, G.; Winding, K.; Hanneman, M. I. G. Limitations in Mobility: Experiences of Visually Impaired Older People. *Br. J. Occup. Ther.* **2008**, *71*(10), 414–421. https://doi.org/10.1177/030802260807101003

[5] Chen, Z.; Yu, J.; Song, Y.; Chui, D. Aging Beijing: Challenges and strategies of health care for the elderly. *Ageing Res. Rev.* **2010**, *9*, S2–S5. https://doi.org/10.1016/j.arr.2010.07.001

[6] Wang, H.-H.; Tsay, S.-F. Elderly and long-term care trends and policy in Taiwan: Challenges and opportunities for health care professionals. *Kaohsiung J. Med. Sci.* **2012**, *28*(9), 465–469. https://doi.org/10.1016/j.kjms.2012.04.002

[7] Subramaniyaswamy, V.; Vijayakumar, V.; Logesh, R.; Indraganti, V. An ontology-driven personalized food recommendation in IoT-based healthcare system. *J. Supercomput.* **2019**, *75*, 3184–3216. https://doi.org/10.1007/s11227-018-2331-8

[8] Wickramasinghe, A.; Torres, R. L. S.; Ranasinghe, D. C. Recognition of falls using dense sensing in an ambient assisted living environment. *Pervasive Mobile Comput.* **2017**, *34*, 14–24. https://doi.org/10.1016/j.pmcj.2016.06.004

[9] Selvaraj, S.; Sundaravaradhan, S. Challenges and opportunities in IoT healthcare systems: a systematic review. *SN Appl. Sci.* **2019**, *2* (1), 139. https://doi.org/10.1007/s42452-019-1925-y

[10] Sixsmith, A. Ethical challenges in aging and technology. Presented at the *15th International Conference on PErvasive Technologies Related to Assistive Environments (PETRA)*, Corfu, Greece, 2022. https://doi.org/10.1145/3529190.3534756

[11] Sixsmith, A. AgeTech: Technology-based solutions for aging societies. In *Promoting the health of older adults: the Canadian experience*; 2021; pp 135–151

[12] Morato, J.; Sanchez-Cuadrado, S.; Iglesias, A.; Campillo, A.; Fernández-Panadero, C. Sustainable Technologies for Older Adults. *Sustainability* **2021**, *13*(15), 8465. https://doi.org/10.3390/su13158465

[13] Haescher, M.; Höpfner, F.; Jähne-Raden, N.; Denker, K.; Koldrack, P.; Rostalski, P.; Kirste, T.; Bieber, G. Automated fall risk assessment of elderly using wearable devices. *J. Rehabil. Assist. Technol. Eng.* **2020**, *7*, 2055668320946209. https://doi.org/10.1177/2055668320946209

[14] Perez, A. J.; Siddiqui, F.; Zeadally, S.; Lane, D. A review of IoT systems to enable independence for the elderly and disabled individuals. *Internet Things* **2023**, *21*, 100653. https://doi.org/10.1016/j.iot.2022.100653

[15] Ramkumar, J.; Karthikeyan, C.; Vamsidhar, E.; Dattatraya, K. N. Automated pill dispenser application based on IoT for patient medication. In *IoT and ICT for Healthcare Applications*; Springer: **2020**; pp 231–253. https://doi.org/10.1007/978-3-030-42934-8_13

[16] Fernandes, N.; Amorim, A. R.; Silva, B.; Freitas, J.; Mendonça, J. P. TAB-Med: automated pill dispenser in residential environments. In *Innovations in Mechanical Engineering*; Springer: **2022**; pp 359–370. https://doi.org/10.1007/978-3-030-79165-0_34

[17] Maswadi, K.; Ghani, N. B. A.; Hamid, S. B. Systematic Literature Review of Smart Home Monitoring Technologies Based on IoT for the Elderly. *IEEE Access* **2020**, *8*, 92244–92261. https://doi.org/10.1109/ACCESS.2020.2992727

[18] Sokullu, R.; Akkaş, M. A.; Demir, E. IoT supported smart home for the elderly. *Internet Things* **2020**, *11*, 100239. https://doi.org/10.1016/j.iot.2020.100239

[19] Boumpa, E.; Kakarountas, A. Home supporting smart systems for elderly people. In *Convergence of ICT and Smart Devices for Emerging Applications*; Springer: 2020; pp 81–98. https://doi.org/10.1007/978-3-030-41368-2_4

[20] Salichs, M. A.; Castro-González, Á.; Salichs, E.; Fernández-Rodríguez, R.; Maroto-Gómez, M.; Gamboa-Montero, J. J.; Marques-Villarroya, S.; Castillo, J. C.; Alonso-Martín, F.; Malfaz, M. Mini: A New Social Robot for the Elderly. *Int. J. Soc. Rob.* **2020**, *12*(6), 1231–1249. https://doi.org/10.1007/s12369-020-00687-0

[21] de Barcelos Silva, A.; Gomes, M. M.; da Costa, C. A.; da Rosa Righi, R.; Barbosa, J. L. V.; Pessin, G.; De Paz, G. F.; Jose, V. R. Q. Intelligent personal assistants: A systematic literature review. *Expert Syst. Appl.* **2020**, *147*, 113193. https://doi.org/10.1016/j.eswa.2020.113193

[22] Fong, J. H.; Mitchell, O. S.; Koh, B. S. Disaggregating activities of daily living limitations for predicting nursing home admission. *Health Serv. Res.* **2015**, *50*(2), 560–578. https://doi.org/10.1111/1475-6773.12235

[23] Millán-Calenti, J. C.; Tubío, J.; Pita-Fernández, S.; González-Abraldes, I.; Lorenzo, T.; Fernández-Arruty, T.; Maseda, A. Prevalence of functional disability in activities of daily living (ADL), instrumental activities of daily living (IADL) and associated factors, as predictors of morbidity and mortality. *Arch. Gerontol. Geriatr.* **2010**, *50*(3), 306–310. https://doi.org/10.1016/j.archger.2009.04.017

[24] Golding-Day, M.; Whitehead, P.; Radford, K.; Walker, M. Interventions to reduce dependency in bathing in community dwelling older adults: a systematic review. *Syst. Rev.* **2017**, *6*, 1–6. https://doi.org/10.1186/s13643-017-0586-4

[25] Wang, W.; Chen, Y.; Zou, X.; Wang, S.; Ferreira, J. P.; Liu, T. Development of Bath Auxiliary Robot for the Disabled Elderly. In *2021 IEEE International Conference on Intelligence and Safety for Robotics (ISR)*, **2021**; pp 85–88. https://doi.org/10.1109/ISR50024.2021.9419499

[26] Zlatintsi, A.; Dometios, A. C.; Kardaris, N.; Rodomagoulakis, I.; Koutras, P.; Papageorgiou, X.; Maragos, P.; Asfour, T.; Lichtenthäler, R.; Reiser, U.; et al. I-Support: A robotic platform of an assistive bathing robot for the elderly population. *Robotics Auton. Syst.* **2020**, *126*, 103451. https://doi.org/10.1016/j.robot.2020.103451

[27] Wenninger, A.; Rau, D.; Röglinger, M. Improving customer satisfaction in proactive service design. *Electron. Mark.* **2022**, *32*(3), 1399–1418. https://doi.org/10.1007/s12525-022-00565-9

[28] Xi, L.; Zhang, H.; Li, S.; Cheng, J. Integrating fuzzy Kano model and fuzzy importance-performance analysis to analyse the attractive factors of new products. *Int. J. Distrib. Sens. Netw.* **2020**, *16*(5), 1550147720920222. https://doi.org/10.1177/1550147720920222

[29] Zhao, S.; Zhang, Q.; Peng, Z.; Fan, Y. Integrating customer requirements into customized product configuration design based on Kano's model. *J. Intell. Manuf.* **2020**, *31*(3), 597–613. https://doi.org/10.1007/s10845-019-01467-y

[30] Kohli, A.; Singh, R. An assessment of customers' satisfaction for emerging technologies in passenger cars using Kano model. *Vilakshan-XIMB J. Manag.* **2021**, *18*(1), 76–88. https://doi.org/10.1108/XJM-08-2020-0103

[31] Lu, M.-T.; Lu, H.-P.; Chen, C.-S. Exploring the Key Priority Development Projects of Smart Transportation for Sustainability: Using Kano Model. *Sustainability* **2022**, *14*(15), 9319. https://doi.org/10.3390/su14159319

[32] Yang, Y.; Li, Q.; Li, C.; Qin, Q. User requirements analysis of new energy vehicles based on improved Kano model. *Energy* **2024**, *309*, 133134. https://doi.org/10.1016/j.energy.2024.133134

[33] Wang, T.; Wang, W.; Feng, J.; Fan, X.; Guo, J.; Lei, J. A novel user-generated content-driven and Kano model focused framework to explore the impact mechanism of continuance intention to use mobile APPs. *Comput. Hum. Behav.* **2024**, *157*, 108252. https://doi.org/10.1016/j.chb.2024.108252

[34] Cavacece, Y.; Maggiore, G.; Resciniti, R.; Moretta Tartaglione, A. Evaluating digital health attributes for users' satisfaction: an application of the Kano model. *TQM J.* **2025**, *37*(3), 831–852. https://doi.org/10.1108/TQM-09-2023-0301

[35] Li, Z.-Q.; Cao, G.-P.; Cai, S.-Y.; Wang, D.-Y.; Zhang, X.-C. Functional requirements and design strategy of E-sports chair based on the KANO model. *BioResources* **2024**, *19*(3), 4679–4697. https://doi.org/10.15376/biores.19.3.4679-4697

[36] Tabianan, K.; Velu, S.; Ravi, V. K-means clustering approach for intelligent customer segmentation using customer purchase behavior data. *Sustainability* **2022**, *14*(12), 7243. https://doi.org/10.3390/su14127243

[37] Chiu, C.-Y.; Chen, Y.-F.; Kuo, I.-T.; Ku, H. C. An intelligent market segmentation system using k-means and particle swarm optimization. *Expert Syst. Appl.* **2009**, *36*(3), 4558–4565. https://doi.org/10.1016/j.eswa.2008.05.029

[38] Chen, Y.; Tan, P.; Li, M.; Yin, H.; Tang, R. K-means clustering method based on nearest-neighbor density matrix for customer electricity behavior analysis. *Int. J. Electr. Power Energy Syst.* **2024**, *161*, 110165. https://doi.org/10.1016/j.ijepes.2024.110165

[39] Zhao, H.-H.; Luo, X.-C.; Ma, R.; Lu, X. An extended regularized K-means clustering approach for high-dimensional customer segmentation with correlated variables. *IEEE Access* **2021**, *9*, 48405–48412. https://doi.org/10.1109/ACCESS.2021.3067499

[40] Fang, C.; Liu, H. Research and application of improved clustering algorithm in retail customer classification. *Symmetry* **2021**, *13*(10), 1789. https://doi.org/10.3390/sym13101789

[41] Yin, S.; Cai, X.; Wang, Z.; Zhang, Y.; Luo, S.; Ma, J. Impact of gamification elements on user satisfaction in health and fitness applications: A comprehensive approach based on the Kano model. *Comput. Hum. Behav.* **2022**, *128*, 107106. https://doi.org/10.1016/j.chb.2021.107106

[42] Jin, J.; Jia, D.; Chen, K. Mining online reviews with a Kansei-integrated Kano model for innovative product design. *Int. J. Prod. Res.* **2022**, *60*(22), 6708–6727. https://doi.org/10.1080/00207543.2021.1949641

[43] He, C.; Li, Z.; Liu, D.; Zou, G.; Wang, S. Improving the functional performances for product family by mining online reviews. *J. Intell. Manuf.* **2023**, *34*(6), 2809–2824. https://doi.org/10.1007/s10845-022-01961-w

[44] Pandey, A.; Sahu, R.; Joshi, Y. Kano Model Application in the Tourism Industry: A Systematic Literature Review. *J. Qual. Assur. Hosp. Tour.* **2022**, *23*(1), 1–31. https://doi.org/10.1080/1528008X.2020.1839995

[45] Shi, Y.; Peng, Q. Enhanced customer requirement classification for product design using big data and improved Kano model. *Adv. Eng. Inf.* **2021**, *49*, 101340. https://doi.org/10.1016/j.aei.2021.101340

[46] Dou, R.; Zhang, Y.; Nan, G. Application of combined Kano model and interactive genetic algorithm for product customization. *J. Intell. Manuf.* **2019**, *30*, 2587–2602. https://doi.org/10.1007/s10845-016-1280-4

[47] Fofan, A. C.; Oliveira, L. A. B.; Melo, F. J. C.; Jerônimo, T. B.; Medeiros, D. D. An Integrated Methodology Using PROMETHEE and Kano's Model to Rank Strategic Decisions. *Eng. Manage. J.* **2019**, *31*(4), 270–283. https://doi.org/10.1080/10429247.2019.1655351

[48] Shen, Y.; Kokkranikal, J.; Christensen, C. P.; Morrison, A. M. Perceived importance of and satisfaction with marina attributes in sailing tourism experiences: A kano model approach. *J. Outdoor Recreat. Tour.* **2021**, *35*, 100402. https://doi.org/10.1016/j.jort.2021.100402

[49] Cai, M.; Wu, M.; Luo, X.; Wang, Q.; Zhang, Z.; Ji, Z. Integrated framework of Kansei engineering and Kano model applied to service design. *Int. J. Hum.–Comput. Interact.* **2023**, *39*(5), 1096–1110. https://doi.org/10.1080/10447318.2022.2102301

[50] Tang, L.-L.; Chen, S.-H.; Lin, C.-C. Integrating FMEA and the Kano Model to Improve the Service Quality of Logistics Centers. *Processes* **2021**, *9*(1), 51. https://doi.org/10.3390/pr9010051

[51] Bhardwaj, J.; Yadav, A.; Chauhan, M. S.; Chauhan, A. S. Kano model analysis for enhancing customer satisfaction of an automotive product for Indian market. *Mater. Today: Proc.* **2021**, *46*, 10996–11001. https://doi.org/10.1016/j.matpr.2021.02.093

[52] Madzík, P.; Budaj, P.; Mikuláš, D.; Zimon, D. Application of the Kano Model for a Better Understanding of Customer Requirements in Higher Education-A Pilot Study. *Adm. Sci.* **2019**, *9*(1), 11. https://doi.org/10.3390/admsci9010011

[53] Ma, M.-Y.; Chen, C.-W.; Chang, Y.-M. Using Kano model to differentiate between future vehicle-driving services. *Int. J. Ind. Ergon.* **2019**, *69*, 142–152. https://doi.org/10.1016/j.ergon.2018.11.003

[54] Palumbo, F. Developing a new service for the digital traveler satisfaction: The Smart Tourist App. *Int. J. Digit. Account. Res.* **2015**, *15*. https://doi.org/10.4192/1577-8517-15_2

[55] Violante, M. G.; Vezzetti, E. Kano qualitative vs quantitative approaches: An assessment framework for products attributes analysis. *Comput. Ind.* **2017**, *86*, 15–25. https://doi.org/10.1016/j.compind.2016.12.007

[56] Minh, H.-L.; Sang-To, T.; Wahab, M. A.; Cuong-Le, T. A new metaheuristic optimization based on K-means clustering algorithm and its application to structural damage identification. *Knowl.-Based Syst.* **2022**, *251*, 109189. https://doi.org/10.1016/j.knosys.2022.109189

[57] Elshaaer, N. I.; Elsayed, S. F. Improving Spa Services to a Better Customers' Attraction (A Case Study on Red Sea Resorts). *J. Assoc. Arab Univ. Tour. Hosp.* **2016**, *13*(1), 167–182. https://doi.org/10.21608/jaauth.2016.49970

[58] Friedrich, P.; Schmid, S.; Fuchs, D. Acceptance of assistive fall prevention technologies: an online survey. *Procedia Comput. Sci.* **2024**, *246*, 4582–4591. https://doi.org/10.1016/j.procs.2024.09.322

[59] Nyrop, K. A.; Zimmerman, S.; Sloane, P. D.; Bangdiwala, S. Fall prevention and monitoring of assisted living patients: an exploratory study of physician perspectives. *J. Am. Med. Dir. Assoc.* **2012**, *13*(5), 429–433. https://doi.org/10.1016/j.jamda.2011.08.003

[60] Li, J.; Mo, Y.; Jiang, S.; Ma, L.; Zhang, Y.; Wei, S. Bathing assistive devices and robots for the elderly. *Biomimetic Intell. Rob.* **2025**, 100218. https://doi.org/10.1016/j.birob.2025.100218

ASEAN
Journal of Scientific and Technological Reports
Online ISSN:2773-8752

Research article

The combination of different carriers in producing plant-based seasoning powder from oyster mushroom (*Pleurotus sajor-caju*)

Nguyen Thi Ngoc Giang[1, 3*], Tran Van Khai[2, 3], and Ho Thi Ngan Ha[2, 3]

[1] Experimental-practical Area, An Giang University, Vietnam
[2] Faculty of Agriculture and Natural Resource, An Giang University, Vietnam
[3] Vietnam National University, Ho Chi Minh City, Vietnam
* Correspondence: ntngiang@agu.edu.vn

Citation:
Giang, N.T.N; Khai, T.V; Ha, H.T.N. The combination of different carriers in producing plant-based seasoning powder from oyster mushroom (*Pleurotus sajor-caju*). *ASEAN J. Sci. Tech. Report.* **2026**, *29*(3), e261864. https://doi.org/10.55164/ajstr.v29i3.261864.

Article history:
Received: October 13, 2025
Revised: January 27, 2026
Accepted: February 5, 2026
Available online: February 28, 2026

Abstract: The increasing popularity and prioritization of plant-based nutritional foods have heightened the focus on research and the diversification of plant-derived products. Therefore, this paper centers on producing a plant-based seasoning powder from oyster mushroom, an available commodity, using its concentrated extract and various carriers to maximize retention of bioactive nutrients and ensure compliance with the product's physicochemical and microbiological quality standards. The optimal ratio of the combination between maltodextrin (MD) and gum arabic (GA) was obtained through a range of investigated ratios, which was a completely randomized setup with concentrations of 5, 10, 15, and 20% for MD, and 0, 0.5, 1.0, 1.5, and 2% for GA. The outcome has shown that MD combined with GA significantly affected the seasoning powder product; at a mixing ratio of 10% MD and 1% GA, it exhibited the highest stability and optimal physicochemical properties. The high retention of key bioactive compounds, including flavonoids, phenolics, lysine, glutamic acid, and β-glucan, with respective contents of 0.0034 g QE, 0.28 g TAE, 0.0052 mg, 2.32 mg, and 10.86 mg per 100 g dry matter. The powder demonstrated satisfactory yield and solubility, and the brightness index was the highest among all tested formulations. Moreover, the water activity reached 0.42, ensuring the product's enzymatic and microbiological stability.

Keywords: Carrier; gum arabic; maltodextrin; physicochemical properties; plant-based products

1. Introduction

Oyster mushroom (*Pleurotus sajor-caju*) is favored for consumption not only for its affordable price but also for its nutritional and functional benefits. Many studies have highlighted that it contains high levels of proteins, essential amino acids, dietary fiber, and diverse bioactive constituents [1]. These bioactive compounds include polysaccharides and phenolic compounds, which are associated with antioxidant, antihypertensive, antidiabetic, antiviral, and immunomodulatory properties [2, 3]. However, this fresh crop has a high respiration rate and high water content and lacks an epidermal structure [4]. As a result, they are prone to mechanical damage, bacterial spoilage, weight loss, and enzymatic browning, leading to rapid deterioration in quality after harvesting. Moreover, the cultivation conditions for oyster mushrooms are relatively simple, with high annual yields; thereby, without appropriate preservation methods, this nutrient-rich resource is prone to significant wastage

[4, 5]. Traditional preservation methods, such as thermal treatment or cold storage, are commonly used to prolong shelf life, but they still have shortcomings, especially in retaining nutritional content during storage [6]. Instead of applying a single approach solely for a single purpose, such as storage or processing, a combination of multiple processing methods can enhance nutrient retention in the raw material while generating value-added products, thereby diversifying mushroom-based product lines and providing additional income for mushroom growers.

Nowadays, demand for vegan-based products has been on the rise due to their health benefits. Numerous studies have reported that plant-based diets provide high levels of dietary fiber, vitamins, and beneficial micronutrients, while also containing abundant phytochemicals with antioxidant, anti-inflammatory, and metabolic-supporting properties [7, 8]. A study further demonstrated that individuals following plant-based diets exhibited significant improvements in glycemic control, reduced insulin resistance, and lower serum cholesterol levels compared with those following omnivorous diets [9]. This study focused on producing a vegetarian seasoning powder derived from oyster mushrooms, which undergo extraction and concentration to maximize nutrient retention, followed by drying to produce a seasoning product that meets quality and nutritional standards. During drying, the use of carriers for microencapsulation is essential to protect core compounds from adverse environmental factors such as pH, temperature, oxygen, and light. Choosing an appropriate carrier (also referred to as wall material) is particularly critical, as it forms a protective barrier for thermally sensitive bioactive ingredients, reduces moisture content, extends shelf life, and helps preserve functional activity [10, 11]. Current research trends emphasize the use of food-grade, naturally derived carriers, most notably maltodextrin (MD), a starch-based polysaccharide, and gum arabic (GA) or acacia resin [12]. A substantial body of evidence indicates that incorporating maltodextrin and gum arabic, either individually or in combination, during drying enhances microencapsulation efficiency and minimizes antioxidant losses [13, 14]. A comparison of spray-dried chokeberry juice reported that, with maltodextrin and gum arabic, the powder achieved high retention rates of bioactive compounds ranging from 63% to over 97% [15]. Another study strongly demonstrated that a combination of maltodextrin and gum arabic effectively protected and retained bioactive constituents from an extract of palmyra palm peel, which aligns with its antioxidative characteristics [16]. Collectively, these findings underscore that selecting suitable natural carriers in drying is highly effective for retaining phenolic, flavonoids, and antioxidant compounds in plant-based materials. Therefore, the objective is to obtain the most effective ratio in combining MD and GA to enhance the stability as well as chemical and nutritional properties of the oyster mushroom's seasoning powder. The product is designed to follow the concept of sustainable development, emphasizing the valorization of abundant, locally available raw materials, while aligning with the emerging global trend toward healthy vegetarian diets by promoting customer choice diversification.

2. Materials and Methods

2.1 Materials

Freshly harvested oyster mushroom (*Pleurotus sajor-caju*) from a My Thoi farm, without physical damage or insect defects, was transported to An Giang University and Vietnam University, Ho Chi Minh City (Vietnam). Maltodextrin (DE < 15%) and gum arabic were bought from My Uc Science & Technology JSC (Vietnam), and other analytical-grade chemicals were sourced from Sinopharm Chemical Reagent Co., Ltd.

2.2 Experimental design

Fresh oyster mushrooms were pretreated according to the procedure described in the doctoral dissertation of Giang Nguyen [17] before their use in the production of vegetarian seasoning powder as follows. Fresh oyster mushrooms were cleaned and dried in a solar dryer until the moisture content was reduced to below 10%. The dried mushrooms were then ground into powder and subjected to enzyme-assisted extraction of nutritional and bioactive compounds using cellulase. The extraction was performed at a water-to-material ratio of 20:1 (v/w), with 4% (w/w) cellulase, pH 5.5, at 50°C for 8 h. The resulting extract was concentrated under vacuum at 80°C and 600 mmHg for 60 min. The concentrated oyster mushroom extract was then subsequently used as a raw material for the study, according to the experimental design described below. To identify an optimal concentration of each investigating carrier in the combination of maltodextrin

and gum arabic to produce powder. The concentrations of the carriers under examination were set up completely randomized with three replications as follows: maltodextrin (in a ratio of 5, 10, 15, and 20%) and gum arabic (in a ratio of 0, 0.5, 1, 1.5, and 2%) based on the wet weight of the concentrated oyster mushroom solution. Specifically, 500 mL of the concentrated solution for each sample was dried using a spraying dryer (Yamato ADL311-A, Japan) at an inlet air temperature of 150°C with an input flow rate of 3 mL/min. The obtained powder product was kept in glass jars with lids for further quality analyses. For each test, 10-15 g of the powder product was dissolved in 500 mL of hot water and analyzed.

2.3 Physical properties analysis

2.3.1 Color analysis: L* (representing the brightness), a* (red-green section), b* (yellow-blue section) parameters of the powder after drying were measured using a colorimeter (Konica Minolta CR400).

2.3.2 Powder yield determination: the yield (Y) was defined by a ratio obtained from the weight of powder after drying (m_1) to the weight of the extraction before drying (m_2).

$$Y\ (\%) = (m_1/m_2) \times 100$$

2.3.3 Water activity (a_w): Each sample (1.0 g) was measured using digital water activity meters Aqualab (4TEV, USA). All samples were measured at 28-30 °C.

2.3.4 Solubility: The ability to dissolve the sample powder was checked based on the procedure carried out by Cano-Chauca et al. [18] with some adjustments. Following a series of steps, including dissolving, centrifuging, and drying to obtain a constant weight. Solubility was calculated as the ratio between the mass of dry matter in the constant weight and the initial sample mass.

2.4 Chemical properties analysis

The glutamic acid content (mg/100 g dry matter) was approached by following the method of Stauß et al. [19]. Briefly, a 0.2 mL aliquot of the sample was reacted with phosphate buffer (pH 6.0) and 2% ninhydrin, heated at 90°C for 15 min, diluted to 25 mL with distilled water, and quantified as glutamic acid using a standard curve $y = 4.1191x + 0.0814$ ($R^2 = 0.9999$).

The level of lysine (mg/100 g dry matter) in the powder was detected following the assay outlined by Hasani et al. [20] through the reaction of the sample with buffer (pH 8.0) and 1,2-naphthoquinone-4-sulfonate (NQS), diluting to 5 mL with distilled water, and measuring absorbance at 480 nm. Lysine concentration was quantified using a lysine standard curve, $y = 0.0009x + 0.139$ ($R^2 = 0.980$).

The concentration of β-glucan (mg/100 g dry matter) was assessed based on the Phenol-Sulfuric method [21]. Briefly, samples were ethanol-precipitated (96%, 4°C, 24 h), filtered, alkaline-treated (1 M NaOH, 60°C, 1 h), reacted with phenol and sulfuric acid, and the absorbance was measured at 490 nm. β-Glucan concentration was quantified using a standard glucan curve $y = 2745.61x + 0.0003$ (R^2=0.9999).

The content of flavonoid (g QE/100 g dry matter) and ***phenolic*** (g TAE/100 g dry matter) was identified relying on the colorimetric method described by Sumaiyah et al. [22]. Total flavonoid content was determined using the aluminum chloride colorimetric method through the reaction of samples with $NaNO_2$, $AlCl_3 \cdot H_2O$, and NaOH to form a stable yellow complex, and absorbance was measured at 510 nm using a UV–Vis spectrophotometer (V730, Jasco, Japan), its content was quantified using a quercetin calibration curve $y = 8.2634x + 0.0182$ ($R^2 = 0.9999$). Total phenolic content was determined using the Folin–Ciocalteu reagent. Samples were reacted with Folin–Ciocalteu reagent and Na_2CO_3, and absorbance was measured at 750 nm using a UV–Vis spectrophotometer (V730, Jasco, Japan). The content was quantified using a tannic acid calibration curve ($y = 0.0021x + 0.0064$; $R^2 = 0.9999$).

Note: Where y represents absorbance and x represents concentration for all standard curves.

2.5 Data analysis

Statgraphics Centurion XVI software (USA) was used to analyze the statistics of this study; the LSD test was used to identify differences between trial averages at a 5% confidence level (P = 0.05), and Microsoft Excel was used for computation and graphing. The suitability of the predicted model during optimization was

evaluated using the R^2 correlation coefficient. The equation for optimizing the response surface method (RSM) was derived from general form experiments, as indicated below.

$$Y = \beta_0 + \sum_{i=1}^{k} \beta_i X_i + \sum_{i=1}^{k} \beta_{ii} X_i^2 + \sum_{i=1}^{k} \sum_{j=1}^{k} \beta_{ij} X_i X_j$$

In the equation, Y represents the objective function, β_0 stands for the constant term, β_i denotes the linear coefficient, β_{ii} represents the squared coefficient, β_{ij} indicates the interaction coefficient, and X_i and X_j represent the survey variables.

3. Results and Discussion

3.+1 Effects of different mixing ratios between maltodextrin and gum arabic on the product's physical properties

3.1.1 Recovery yield

This parameter is one of the critical indicators for evaluating the economic and efficient potential of the entire process. According to Table 1, the interaction between the two carriers was not statistically significant ($P > 0.05$), indicating that their combination did not produce a synergistic or antagonistic effect beyond their individual effects ($P < 0.05$). The results revealed that the recovery yield increased in direct proportion to the concentration of added MD, with the highest yield of 19.20% at 20% MD addition. However, the difference between 15 and 20% was not statistically significant ($P > 0.05$). In addition, GA had a considerable impact on recovery yield: it initially rose with increasing concentration, then decreased when the addition exceeded 1%, but the highest yield was obtained at 2% GA (18.55%). The mechanisms of each carrier can explain this during the drying process: they both reduce stickiness and wall deposition within the drying chamber. Moreover, they enhance particle formation and structural stability due to their high glass transition temperature, which facilitates the formation of stable powder particles during drying, thereby minimizing product loss [23]. Carrier supplementation also contributes to reducing the final moisture content and improving powder flowability, thereby increasing the recovery of dry product. Furthermore, carriers act as protective agents for heat-sensitive compounds, such as proteins and vitamins, by reducing their degradation during drying, thereby further enhancing the effective recovery yield [24].

Table 1. Physical properties of seasoning powder from oyster mushroom

The ratio of MD (%)	**Recovery yield (%)**	**a_w**	**Solubility (%)**
5	10.95^{c}	0.337^{c}	94.55^{a}
10	14.81^{b}	0.403^{a}	94.10^{b}
15	19.08^{a}	0.403^{a}	93.77^{c}
20	19.20^{a}	0.398^{b}	93.73^{c}
Level of significance	**	**	**
The ratio of GA (%)	**Recovery yield (%)**	**a_w**	**Solubility (%)**
0	13.73^{e}	0.383^{c}	94.22^{b}
0.5	15.75^{c}	0.400^{b}	94.64^{a}
1.0	16.78^{b}	0.398^{b}	93.87^{c}
1.5	15.25^{d}	0.407^{a}	93.74^{c}
2	18.55^{a}	0.336^{d}	93.73^{c}
Level of significance	**	**	**
Significance level of interaction	NS	**	NS

The superscripts offer the statistical difference at 1% significance level; NS indicates no statistically significant difference at the 5% level ($P > 0.05$).

3.1.2 Water activity (a_w)

Despite the low moisture content (MC) of the powder after drying (2-3%), which was consistent with previous studies on similar dried powder products [23-25]. Different food products have similar MC but remain significantly different in terms of safety and spoilage susceptibility; thus, MC should be measured in parallel with a_w to provide a comprehensive moisture analysis [26]. According to the results, the water activity

(a_w) of the powder was greatly affected by the concentration of added carriers, both in the individual factors (main effects) and in their interaction ($P < 0.01$). There was a fluctuation in the aw with increases in the levels of added MD and GA. It initially rose gradually, but when the MD content exceeded 15%, and the GA content exceeded 1.5%, the product's aw declined significantly. The a_w increase can be explained due to the molecular structure of MD with the large number of branches bearing hydrophilic groups, which enhances the holding water ability of MD [27], or it is partly attributable to the higher porosity of the powder, which facilitates the absorption of water from the surrounding environment into the pores of the powder after drying [28]. This finding was similar to previous related studies; Cao et al. [29] also reported a decrease in a_w values from 0.25 to 0.23 while increasing MD concentration to 30%. Powder products with a_w values below 0.60 are considered microbiologically safe, which indicates the condition is insufficient to support the growth or survival of microorganisms, as the available water is too limited for cellular metabolic activity. This threshold is widely used in food microbiology to ensure microbial stability and safety [30]. The absence of total aerobic microorganisms in the analysis further confirmed this microbiological safety result. However, the range of 0.2-0.4 is considered the most favorable, as it provides enhanced stability against undesirable reactions, including oxidation, browning, hydrolysis, and enzymatic activity [31].

3.1.3 Solubility

The powder's soluble capacity depends on several factors, including drying methods, drying temperature and duration, thermal treatment during concentration, and the type of carrier [32,33,34]. Both individual and cooperative effects of MD and GA on powder's solubility were in the range of 93.73–94.64% (Table 1). Results show that, with a gradual increase in the proportion of added carriers in both MD and GA, the solubility of the seasoning powder decreased significantly ($P < 0.05$). However, the differences among MD and GA ratio combinations were not statistically significant ($P > 0.05$). This can be explained by the effects of the carriers on the powder structure, which usually become denser and less porous after drying, thereby reducing the particles' surface area and water permeability [23]. At the same time, the high concentration of the carrier may reduce the bulk density and lead to a more compact particle structure, which significantly affects solubility [35]. Moreover, GA is characterized by its high molecular weight, which limits its solubility; therefore, excessive addition can reduce the dissolution rate or result in incomplete solubility of the powder [36]. In addition, a previous study on spray-dried apple juice powder noted that, among the produced samples, formulations containing GA as the carrier had higher moisture content than those prepared with MD. This may be attributed to the higher water-retention capacity of hydrocolloids relative to starch derivatives, thereby reducing the powder's solubility and increasing caking and stickiness, which decrease the surface area for contact and reduce particle porosity [37]. Therefore, determining an appropriate blending ratio of MD and GA is essential to ensure stable MC in the dried powder, minimize particle agglomeration, and maintain flowability and dispersibility when reconstituted in water [27].

3.1.4 Color

Table 2 presents the color index values under the influence of different carriers and their combinations. Significant differences ($P < 0.05$) were observed in L* and a* values in color parameters among samples with varying concentrations of MD and GA. For instance, powders containing MD exhibited higher L* values compared to those produced with GA. Conversely, powders produced with GA as the carrier displayed a darker color than those produced with MD. However, the combination of MD and GA did not have a significant effect on brightness or the red/green hue coordination values ($P > 0.05$). This difference may be attributed to the intrinsic color of the carriers, which affects the final product's color characteristics. The b* values of samples with higher GA concentrations were greater than those of the other samples. This difference can be attributed to the inherently reddish color of GA compared to MD. In a similar study, the effects of pectin type and concentration, GA, and MD as carriers for tamarind powder on color indices were investigated. Among the different carriers, powders produced with Whey Protein Concentrate (WPC) and GA exhibited higher a* and b* values [38]. Maillard reactions between reducing sugars may explain these color variations, as may the protein components present either in GA itself or in the raw material, which in this case was the concentrated extract of oyster mushrooms. Gum arabic is a mixture of glycoproteins and polysaccharides, with

protein content ranging from 1 to 3% [23]. However, the extent of non-enzymatic browning and the resulting color indices depend strongly on the drying chamber's processing time and temperature. A study by Shishir and Chen [24] reported that the increase in powder color was due to higher temperatures and intensified non-enzymatic browning reactions.

Table 2. Color observation at different mixing ratios between MD and GA of seasoning powder from oyster mushrooms

The ratio of MD (%)	**L**	**a**	**b**
5	64.03^{d}	-4.95^{a}	10.18^{a}
10	70.63^{b}	-5.54^{b}	10.46^{a}
15	69.15^{c}	-5.61^{b}	10.12^{a}
20	75.00^{a}	-6.22^{c}	9.65^{b}
Level of significance	**	**	NS
The ratio of GA (%)	**L**	**a**	**b**
0	66.83^{d}	-5.59^{c}	9.92^{ab}
0.5	65.68^{d}	-5.24^{a}	9.91^{b}
1.0	70.45^{c}	-5.41^{b}	10.05^{ab}
1.5	73.83^{a}	-5.90^{e}	10.23^{ab}
2	71.72^{b}	-5.75^{d}	10.39^{a}
Level of significance	**	**	NS
Significance level of interaction	NS	NS	**

The superscripts offer the statistical difference at 1% significance level; NS indicates no statistically significant difference at the 5% level ($P > 0.05$).

3.2 Effects of different mixing ratios between maltodextrin and gum arabic on the product's chemical properties

3.2.1 Phenolic compounds

The negative regression coefficients of both maltodextrin and gum arabic in all equations (first-order and second-order) indicate an inverse effect. As the concentration of either carrier or the combination of these two carriers increased, the phenolic compounds tended to decline (Figure 1). The highest phenolic content was recorded at 10% maltodextrin, and the lowest concentrations of gum arabic were 0.28 and 0.33, respectively. This trend indicated that using too much carrier above the optimal concentration can cause dilution, leading to a decrease in active compounds in the dry powder or an increase in solution viscosity. Moreover, prolonging the drying time leads to greater degradation of phenolic compounds [39,40]. Maltodextrin and gum arabic, when mixed with the extract, formed a matrix that encapsulated the phenolic molecules, thereby reducing their exposure to high temperatures and oxygen during the spray-drying process [41,42]. Maltodextrin is a commonly used carrier due to its low cost, high solubility at high solid concentrations, and its ability to increase the glass transition temperature of the dried product, reduce adhesion, and retain volatile compounds [43].

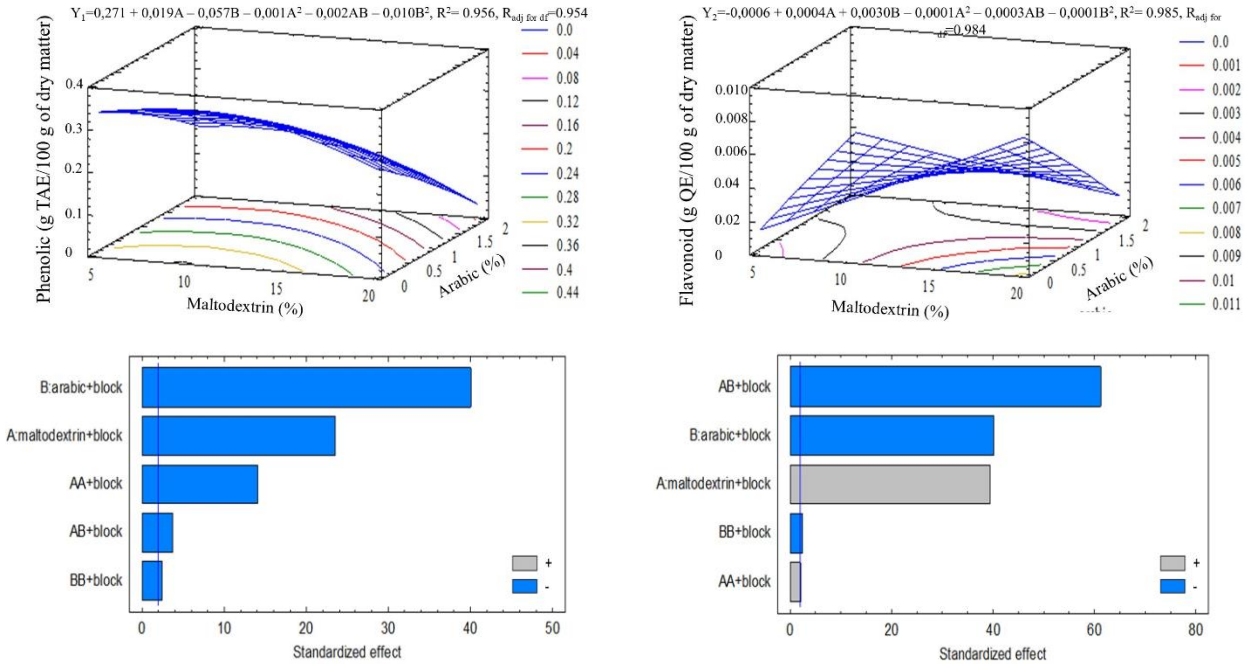

(a) Phenolic (b) Flavonoid

Figure 1. The content of phenolic and total flavonoid compounds at different mixing ratios between MD and GA

3.2.2 Flavonoid compounds

The regression equation for flavonoids showed a positive first-order coefficient for maltodextrin, indicating that increasing maltodextrin concentration significantly enhanced total flavonoid content after drying (Figure 1). This showed that maltodextrin has the ability to retain flavonoids during drying, due to its encapsulating and limiting exposure to high temperatures and oxygen. However, the first-order coefficient of gum arabic was negative, which indicated that further increases in its concentration caused a great loss in the flavonoid recovery. A similar trend was observed in the interaction between both carriers, indicating that the flavonoid level reached a maximum at the optimum point and then decreased with further increases in both carrier levels. Indeed, the maximum flavonoid content (approximately 0.0034 g QE/100 g) was obtained at 10% maltodextrin and 1% gum arabic. Both carriers had a statistically significant impact on flavonoids ($P < 0.05$). Specifically, maltodextrin creates a solid protective frame surrounding flavonoid molecules, preventing evaporation or interacting with oxygen, while gum arabic acts as a durable coating layer to support the efficiency of maltodextrin's mechanism [44]. Therefore, the highest flavonoid recovery after drying was obtained when integrating maltodextrin and gum arabic at their respective optimal levels. Previous studies have observed comparable protective effects of flavonoids when they were microencapsulated using polysaccharide-based carriers. For instance, Gomes et al. [45] found that spray-dried papaya powder supplemented with 14% MD contained significantly higher levels of polyphenols and flavonoids than freeze-dried papaya. This increase was attributed to the shorter drying duration, which effectively retained these compounds within the carrier matrix. However, if the concentration of gum arabic was too high, the flavonoids could be diluted, causing a decline in their content. The results clearly showed that using more than 1% gum arabic significantly reduced flavonoid content.

3.2.3 Glutamic acid

It is a non-essential amino acid, but is crucial for cellular metabolism, protein synthesis, and brain function, acting as an excitatory neurotransmitter involved in learning and memory [18]. The results indicate that the ratios of maltodextrin and gum arabic significantly influenced the glutamic acid content of the seasoning powder extracted from oyster mushrooms. The positive first-order regression coefficient for gum arabic in the equation indicates that, as concentration increased from low levels, the glutamic acid content

obtained after spray drying increased significantly (Figure 2). Results show that the addition of gum arabic effectively helped to limit the loss of glutamic acid content during drying due to its features as a good emulsifying and film-forming agent, helping to evenly coat the glutamic acid molecules in the microcapsules, before they undergo intramolecular cyclization to form pyroglutamic acid (5-oxoproline) or maillard reactions, especially under heat and low water activity [46]. However, maltodextrin and the combination of both carriers showed opposite influences (negative order coefficients), indicating that the concentrations continuously increased beyond the optimal degree of the carriers, while the glutamic acid content began to decrease (Figure 2). Excessive addition of carriers can cause a dilution effect, increase the viscosity of the extracted solution, prolong drying time, and accelerate glutamic acid degradation [39,40]. Especially, MD can trap water molecules for longer, leading to higher internal temperatures near the end of drying [33]. Indeed, glutamic acid content increased to an optimal value and subsequently declined with further increases in both carriers. Specifically, glutamic acid content reached its peak at 2.32 g/100 g dry matter with 10% maltodextrin and 2.34 mg/100 g dry matter with 1.5% gum arabic.

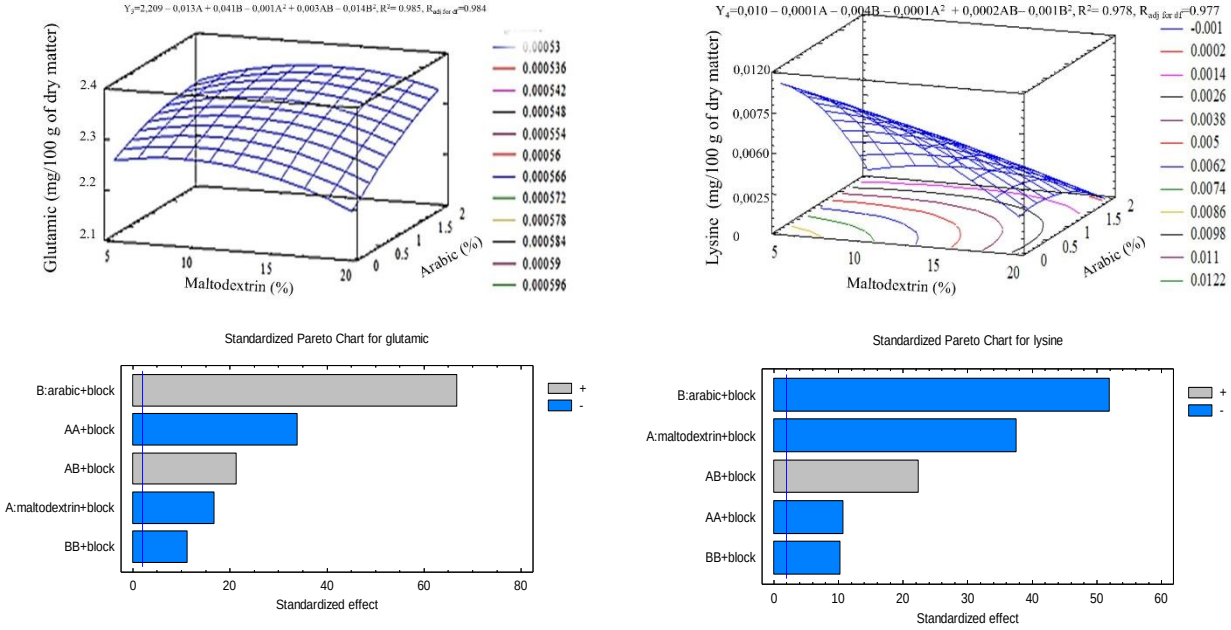

(a) Glutamic acid (b) Lysine

Figure 2. The content of glutamic acid and lysine at different mixing ratios between MD and GA

3.2.4. Lysine

The regression model showed that maltodextrin and gum arabic both negatively affected the obtained lysine content. While the positive interaction coefficient implies that the combination of these two carriers enhances lysine retention more effectively than using them individually, this effect was similar to that of the glutamic compound. In particular, with a relatively high concentration of maltodextrin and a small amount of gum arabic, lysine content was efficiently increased. The highest content was 0.0052 mg/100 g dry matter, obtained at a 10% maltodextrin and 1% gum arabic concentration. However, the negative quadratic coefficients for both carriers still indicated a tendency for lysine content to decrease with excessive carrier use. The findings were similar to prior relevant studies. Kurek & Pratap-Singh [47] and Pérez-Pérez et al. [48] reported that excessive single use of maltodextrin or gum arabic may dilute proteins and lead to lower lysine retention compared to more balanced carrier systems.

The mechanism by which the combination of GA and MD protects amino acid compounds is the formation of a polysaccharide matrix through hydrogen/ionic bonding with their polar regions, which keeps the amino acids within the matrix and reduces their direct exposure to oxygen and heat. This can lower the

rate of degradation or Maillard reactions involving glutamic and lysine [49]. However, the similarity in the results between glutamic and lysine contents showed that excessive carrier concentrations can enhance solidification and reduce moisture, but at the same time increase molecular mobility, which may facilitate the migration of hydrolyzed compounds to the capsule surface and decrease mechanical stability. In addition, too much carrier's supplement can dilute the amino acid, thereby reducing the encapsulation and core-protection efficiency, due to weaker matrix hardening, poorer structural homogeneity, or more pronounced reverse diffusion (from the core to the surface). In general, the results obtained are consistent with the microencapsulation theory, which states that the polysaccharide carriers create an outer layer that protects target compounds from degrading agents (heat, oxygen). However, it is necessary to optimize the amount of each carrier to ensure both protection efficiency and to avoid diluting the active ingredient content in the final product [50, 51].

3.2.5. β-glucan

Maltodextrin had positive interactions with the content of β-glucan in the seasoning powder after drying, the highest content was recorded at 15% of maltodextrin concentration with 8.77 mg/100 g dry matter, but when the concentration to 20%, β-glucan significantly reduced to 7.90 mg/100 g dry matter (Figure 3). This may be affected by the negative quadratic coefficients for both carriers (especially gum arabic), which still showed a tendency for β-glucan content to decrease with excessive carrier use. Especially, gum arabic: when the amount added exceeds 1%, the β-glucan content in the product decreased significantly from its highest value of 11.43 to 2.24 mg/100 g dry matter.

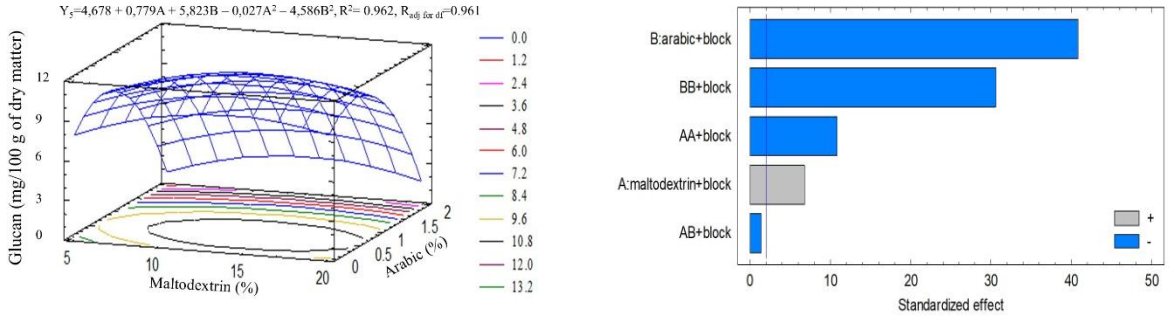

Figure 3. The content of β-glucan at different mixing ratios between MD and GA

During drying, β-glucan under high-temperature conditions may undergo chain scission, reducing molecular weight through thermal degradation. According to the analysis, maltodextrin showed a strong protective effect on β-glucan content, which is consistent with its characteristic. In particular, MD is a hydrophilic polysaccharide composed of D-glucose units primarily linked by α-(1→4) glycosidic bonds. The increase in β-glucan concentration in our microencapsulated samples may be due to the glucose units of MD interacting with the β-glucan functional groups in the powder during the coating process, thereby increasing the β-glucan content in the dried samples [27,52]. According to previous studies by Giang et al. [53, 54] on the bioactive compound content of oyster mushroom extracts, on a dry matter basis the levels of phenolics, flavonoids, β-glucan, lysine, and glutamic acid were reported as 5.74 g TAE, 0.73 g QE, 2.13 g, 8.28 mg, and 32.45 mg per 100 g dry matter, respectively. In comparison, the seasoning powder obtained in the present study still contained detectable amounts of these bioactive compounds, with corresponding values of 0.28 g TAE, 0.0034 g QE, 10.86 mg, 0.0052 mg, and 2.32 mg per 100 g dry matter. These results indicate a certain degree of reduction during processing. On a dry matter basis, the estimated retention ranged from approximately 0.5–5% for phenolics, flavonoids, and β-glucan, while glutamic acid showed a relatively higher retention of about 7%, supporting the functional and sensory relevance of the final product. These results indicate a certain degree of reduction during processing, which was not completely lost and remained detectable in the final product, confirming the retention of bioactive constituents. In particular, the presence of glutamic acid contributes not only to the nutritional value but also to the product's umami-related sensory properties, while the residual phenolic compounds and β-glucan suggest potential antioxidant and functional benefits. Therefore, despite the observed reductions compared with the original mushroom extract, the oyster

mushroom–based seasoning powder retains functional relevance as a value-added food product rather than serving solely as a flavoring agent. Furthermore, the product's physical properties, including color, water activity, and absorption capacity, meet the quality standards and microbiological safety requirements for seasoning granule products currently available on the market [55,56]. Along with the presence of bioactive compounds such as phenolics, flavonoids, and β-glucan, as well as a certain amount of naturally occurring amino acids (lysine and glutamic acid) extracted from oyster mushrooms, without the addition of synthetic monosodium glutamate (MSG). These findings demonstrate that the developed seasoning product not only ensures quality stability but also has strong potential to be developed as a natural and safe seasoning, aligning with current consumer trends toward functional foods and clean-label products.

4. Conclusions

At a 10% maltodextrin and 1% gum arabic mixing ratio, the dried powder showed the greatest benefit, resulting in powders with low stickiness and hygroscopicity, enhanced stability, and desirable functional properties. Notably, key bioactive compounds, including flavonoids, phenolics, lysine, glutamic acid, and β-glucan, were retained at the highest levels, with concentrations of 0.0034 g QE, 0.28 g TAE, 0.0052 mg, 2.32 mg, and 10.86 mg per 100 g dry matter, respectively. In terms of the physicochemical properties, the seasoning powder obtained after drying exhibited a relatively high recovery yield and solubility, reaching 14.86% and 93.76%, respectively. The product showed the highest brightness, as indicated by the L* color parameter, which was optimal compared to other mixing ratios. The water activity (a_w) of the seasoning powder was 0.42, indicating enzymatic and microbiological stability, with no total aerobic bacterial count detected. The study powder meets basic physicochemical standards and also exhibits considerable nutritional content and bioactive compounds. Future research is recommended to focus on comprehensive investigations of particle size distribution and morphological characteristics to elucidate the microencapsulation properties, storage stability, and practical applications of the product, particularly in relation to optimal usage levels and daily nutrient intake recommendations.

5. Acknowledgements

Author Contributions: All authors contributed to the conception and design of the study; methodology, Giang, N.T.N., and Ha, H.T.N.; data analysis and curation, Giang, N.T.N., and Khai, T.V.; writing–original draft preparation, Giang, N.T.N; writing–review and editing, Giang, N.T.N., and Khai, T.V.; all authors have read and agreed to the published version of the manuscript.

Funding: This research was funded by Vietnam National University Ho Chi Minh City (VNU-HCM) under Grant C2024-16-11.

Conflicts of Interest: The authors declare that they hold no competing interests.

References

[1] Giang, N. T. N.; Khai, T. V.; Thuy, N. M. Changes in yield and quality of *Pleurotus sajor-caju* by seasons, harvest times and during maturation. *Vietnam J. Agric. Rural Dev.* **2021**, *1*, 39–47.

[2] Galappaththi, M. C. A.; Dauner, L.; Madawala, S.; Karunarathna, S. C. Nutritional and medicinal benefits of oyster (*Pleurotus*) mushrooms: a review. *Fungal Biotec.* **2021**, *1*(2), 65–87. https://doi.org/10.5943/FunBiotec/1/2/5

[3] Fogarasi, M.; et al. Bioactive secondary metabolites in mushrooms: A focus on polyphenols, their health benefits and applications. *Food Biosci.* **2024**, *62*, 105166. https://doi.org/10.1016/j.fbio.2024.105166

[4] Subramaniam, S.; Jiao, S.; Zhang, Z.; Jing, P. Impact of post-harvest processing or thermal dehydration on physiochemical, nutritional and sensory quality of shiitake mushrooms. *Compr. Rev. Food Sci. Food Saf.* **2021**, *20*(3), 2560–2595. https://doi.org/10.1111/1541-4337.12738

[5] Giang, N. T. N.; Thuy, N. M. Effects of drying methods on the characteristics of *Pleurotus sajor-caju* mushroom. *Malays. Appl. Biol.* **2020**, *49*(3), 31–36. https://doi.org/10.55230/mabjournal.v49i3.1538

[6] Giang, N. T. N.; Khai, T. V.; Thuy, N. M. The influence of packaging and storage temperature on the chemical composition of fresh oyster mushrooms (*Pleurotus sajor-caju*) during storage. *Acta Sci. Pol. Technol. Aliment.* **2022**, *21*(3), 261–269. https://doi.org/10.17306/J.AFS.2022.1007

[7] Nolden, A. A.; Forde, C. G. The nutritional quality of plant-based foods. *Sustainability* **2023**, *15*(4), 3324. https://doi.org/10.3390/su15043324

[8] Xue, J.; Yin, Y. Plant-based food: From nutritional value to health benefits. *Foods* **2024**, *13*(22), 3595. https://doi.org/10.3390/foods13223595

[9] Medawar, E.; Huhn, S.; Villringer, A.; Witte, A. V. The effects of plant-based diets on the body and the brain: a systematic review. *Transl. Psychiatry* **2019**, *9*(1), 226. https://doi.org/10.1038/s41398-019-0552-0

[10] Jiménez-González, O.; Guerrero-Beltrán, J. Á. Extraction, microencapsulation, color properties, and experimental design of natural pigments obtained by spray drying. *Food Eng. Rev.* **2021**, *13*(4), 769–811. https://doi.org/10.1007/s12393-021-09288-7

[11] Pudžiuvelytė, L.; Petrauskaitė, E.; Stabrauskienė, J.; Bernatonienė, J. Spray-drying microencapsulation of natural bioactives: Advances in sustainable wall materials. *Pharmaceuticals* **2025**, *18*(7), 963. https://doi.org/10.3390/ph18070963

[12] Kandasamy, S.; Naveen, R. A review on the encapsulation of bioactive components using spray-drying and freeze-drying techniques. *J. Food Process Eng.* **2022**, *45*(8), e14059. https://doi.org/10.1111/jfpe.14059

[13] Ribeiro, A. M.; Shahgol, M.; Estevinho, B. N.; Rocha, F. Microencapsulation of vitamin A by spraydrying, using binary and ternary blends of gum arabic, starch and maltodextrin. *Food Hydrocoll.* **2020**, *108*, 106029. https://doi.org/10.1016/j.foodhyd.2020.106029

[14] Sukri, N.; Multisona, R. R.; Zaida; Saputra, R. A.; Mahani; Nurhadi, B. Effect of maltodextrin and arabic gum ratio on physicochemical characteristic of spray dried propolis microcapsules. *Int. J. Food Eng.* **2021**, *17*(2), 159–165. https://doi.org/10.1515/ijfe-2019-0050

[15] Bednarska, M. A.; Janiszewska-Turak, E. The influence of spray drying parameters and carrier material on the physico-chemical properties and quality of chokeberry juice powder. *J. Food Sci. Technol.* **2020**, *57* (2), 564–577. https://doi.org/10.1007/s13197-019-04088-8

[16] Thanh, D. V.; Ha, H. T. N.; Tan, N. D.; Giang, N. T. N. Combining carrier materials for spray-drying antioxidant extracts from Palmyra palm peel (*Borassus flabellifer*): optimization using RSM and ANN-GA. *Acta Sci. Pol. Technol. Aliment.* **2025**, *24*(3), 427–440.

[17] Giang, N. T. N. Study on the production of concentrated extracts and their application in the production of mushroom-based sauce from oyster mushrooms (*Pleurotus* spp.). Ph.D. Dissertation, Can Tho University, Can Tho, Vietnam, 2023 (In Vietnamese).

[18] Cano-Chauca, M.; Stringheta, P. C.; Ramos, A. M.; Cal-Vidal, J. Effect of the carriers on the microstructure of mango powder obtained by spray drying and its functional characterization. *Innov. Food Sci. Emerg. Technol.* **2005**, *6*(4), 420–428. https://doi.org/10.1016/j.ifset.2005.05.003

[19] Stauß, A. C.; Fuchs, C.; Jansen, P.; Repert, S.; Alcock, K.; Ludewig, S.; Rozhon, W. The ninhydrin reaction revisited: Optimisation and application for quantification of free amino acids. *Molecules* **2024**, *29*(14), 3262. https://doi.org/10.3390/molecules29143262

[20] Hasani, M.; Yaghoubi, L.; Abdollahi, H. A kinetic spectrophotometric method for simultaneous determination of glycine and lysine by artificial neural networks. *Anal. Biochem.* **2007**, *365*(1), 74–81. https://doi.org/10.1016/j.ab.2007.02.010

[21] Fournier, E. Colorimetric quantification of carbohydrates. *Curr. Protoc. Food Anal. Chem.* **2001**, *1*(1), E1.1.1–E1.1.8. https://doi.org/10.1002/0471142913.fae0101s00

[22] Sumaiyah; Masfria; Dalimunthe, A. Determination of total phenolic content, total flavonoid content, and antimutagenic activity of ethanol extract nanoparticles of *Raphidophora pinnata* (L.F) schott. Leaves. *Rasayan J. Chem.* **2018**, *11*(2), 505–510. https://doi.org/10.31788/RJC.2018.1122068

[23] Sarabandi, K.; et al. Effect of different carriers on microstructure and physical characteristics of spray dried apple juice concentrate. *J. Food Sci. Technol.* **2018**, *55*(8), 3098–3109. https://doi.org/10.1007/s13197-018-3235-6

[24] Shishir, M. R.; Chen, W. Trends of spray drying: A critical review on drying of fruit and vegetable juices. *Trends Food Sci. Technol.* **2017**, *65*, 49–67. https://doi.org/10.1016/j.tifs.2017.05.002

[25] Bazaria, B.; Kumar, P. Effect of whey protein concentrate as drying aid and drying parameters on physicochemical and functional properties of spray dried beetroot juice concentrate. *Food Biosci.* **2016**, *14*, 21–27. https://doi.org/10.1016/j.fbio.2015.11.002

[26] Escobedo-Avellaneda, Z.; Rodríguez-Martínez, V.; Serment-Moreno, V.; Velázquez, G.; Welti-Chanes, J.; Torres, J. A. Selected applications of water activity management in the food industry. In *Water Activity in Foods: Fundamentals and Applications*, 2nd ed.; Barbosa-Cánovas, G. V., Fontana, A. J., Schmidt, S. J., Labuza, T. P., Eds.; Wiley: Hoboken, NJ, USA, 2020; pp 465–482

[27] Valková, V.; et al. Impact of freeze- and spray-drying microencapsulation techniques on β-glucan powder biological activity: A comparative study. *Foods* **2022**, *11*(15), 2267. https://doi.org/10.3390/foods11152267

[28] Michalska, A.; Lech, K. The Effect of carrier quantity and drying method on the physical properties of apple juice powders. *Beverages* **2018**, *4*(1), 2. https://doi.org/10.3390/beverages4010002

[29] Cao, X.; Zhang, M.; Qian, H.; Mujumdar, A. S.; Wang, Z. Physicochemical and nutraceutical properties of barley grass powder microencapsulated by spray drying. *Dry. Technol.* **2017**, *35*(11), 1358–1367. DOI: 10.1080/07373937.2017.1332074

[30] Barbosa-Cánovas, G. V.; Fontana, A. J., Jr.; Schmidt, S. J.; Labuza, T. P. *Water Activity in Foods: Fundamentals and Applications*, 2nd ed.; John Wiley & Sons: Hoboken, NJ, 2020.

[31] Nurhidajah; Boby, P.; Muhammad, Y.; Yunan, K. S.; Diode, Y. Microencapsulation of Umami Flavor Enhancer from Indonesian Waters Brown Seaweed. *Curr. Res. Nutr. Food Sci.* **2022**, *10*(1), 349–359. https://doi.org/10.12944/CRNFSJ.10.1.29

[32] Sharma, A.; Jana, A. H.; Chavan, R. S. Functionality of milk powders and milk-based powders for end use applications: a review. *Compr. Rev. Food Sci. Food Saf.* **2012**, *11*(5), 518–528. https://doi.org/10.1111/j.1541-4337.2012.00199.x

[33] Lee, J. K. M.; Taip, F. S.; Abdullah, Z. Effectiveness of additives in spray drying performance: a review. *Food Res.* **2018**, *2*(6), 486–499. https://doi.org/10.26656/fr.2017.2(6).134

[34] Toikkanen, O.; Outinen, M.; Malafrante, L.; Rojan, O. J. Formation and structure of insoluble particles in reconstituted model infant formula powders. *Int. Dairy J.* **2018**, *82*, 19–27. https://doi.org/10.1016/j.idairyj.2018.03.001

[35] Etzbach, L.; Meinert, M.; Faber, T.; Klein, C.; Schieber, A.; Weber, F. Effects of carrier agents on powder properties, stability of carotenoids, and encapsulation efficiency of goldenberry (*Physalis peruviana* L.) powder produced by co-current spray drying. *Curr. Res. Food Sci.* **2020**, *3*, 73–81. https://doi.org/10.1016/j.crfs.2020.03.002

[36] Chavan, G. M.; et al. Enhancing functional and physical properties of spray dried mixed fruit juices using composite carrier agents. *Ital. J. Food Sci.* **2025**, *37*(4), 34–46. https://doi.org/10.15586/ijfs.v37i4.3122

[37] Ho, T. M.; Chan, S.; Yago, A. J. E.; Shravya, R.; Bhandari, B. R.; Bansal, N. Changes in physicochemical properties of spray-dried camel milk powder over accelerated storage. *Food Chem.* **2019**, *295*, 224–233. https://doi.org/10.1016/j.foodchem.2019.05.122

[38] Bhusari, S. N.; Muzaffar, K.; Kumar, P. Effect of carrier agents on physical and microstructural properties of spray dried tamarind pulp powder. *Powder Technol.* **2014**, *266*, 354–364. https://doi.org/10.1016/j.powtec.2014.06.038

[39] Nordin, N. L.; Bakar, J.; Adzahan, N. M.; Razis, A. F. A.; Ismail, N.; Sulaiman, R. Microencapsulation of bioactive volatile compounds from MD2 pineapple peel Extract using spray-drying and foam-mat drying. *J. Agric. Food Res.* **2024**, *18*, 101539. https://doi.org/10.1016/j.jafr.2024.101539

[40] Thuy, N. M.; Hao, H. V.; Duong, L. T. T.; Giau, T. N.; Minh, V. Q.; Tai, N. V. Foam-mat drying of lucuma powder: Mathematical and artificial modeling of drying kinetics, physicochemical and microstructural properties. *J. Agric. Food Res.* **2025**, *19*, 101656. https://doi.org/10.1016/j.jafr.2025.101656

[41] Laureanti, E. J. G.; Paiva, T. S.; de Matos-Jorge, L. M.; Jorge, R. M. M. Microencapsulation of bioactive compound extracts using maltodextrin and gum arabic by spray and freeze-drying techniques. *Int. J. Biol. Macromol.* **2023**, *253*, 126969. https://doi.org/10.1016/j.ijbiomac.2023.126969

[42] Parhizkary, M.; Hasanpour, R.; Assadpour, E.; Jafari, S. M. Spray-drying encapsulation of jujube extract: Enhancing bioactivity and stability via maltodextrin-based carriers with polysaccharides and proteins. *Carbohydr. Polym. Technol. Appl.* **2025**, *10*, 100869. https://doi.org/10.1016/j.carpta.2025.100869

[43] Xu, Y.; et al. The application of encapsulation technology in the food Industry: Classifications, recent advances, and perspectives. *Food Chem. X* **2024**, *21*, 101240. https://doi.org/10.1016/j.fochx.2024.101240

[44] Iesa, N. B.; et al. Effects of maltodextrin and gum arabic composition on the physical and antioxidant activities of dewaxed stingless bee cerumen. *Foods* **2023**, *12*(20), 3740. https://doi.org/10.3390/foods12203740

[45] Gomes, W. F.; et al. Effect of freeze- and spray-drying on physico-chemical characteristics, phenolic compounds and antioxidant activity of papaya pulp. *J. Food Sci. Technol.* **2018**, *55*(6), 2095–2102. https://doi.org/10.1007/s13197-018-3124-z

[46] Rahman, M. M. A.; Ranganathan, T. V. Encapsulation of isoflavone with milk, maltodextrin and gum acacia improves its stability. *Curr. Res. Food Sci.* **2020**, *2*, 77–83. https://doi.org/10.1016/j.crfs.2019.12.003

[47] Kurek, M. A.; Pratap-Singh, A. Plant-based (hemp, pea and rice) protein-maltodextrin combinations as wall material for spray-drying microencapsulation of hempseed (*Cannabis sativa*) oil. *Foods* **2020**, *9*(11), 1707. https://doi.org/10.3390/foods9111707

[48] Pérez-Pérez, V.; Jiménez-Martínez, C.; González-Escobar, J. L.; Corzo-Ríos, L. J. Exploring the impact of encapsulation on the stability and bioactivity of peptides extracted from botanical sources: trends and opportunities. *Front. Chem.* **2024**, *12*, 1423500. https://doi.org/10.3389/fchem.2024.1423500

[49] Rao, P. S.; Bajaj, R. K.; Mann, B.; Arora, S.; Tomar, S. K. Encapsulation of antioxidant peptide enriched casein hydrolysate using maltodextrin-gum arabic blend. *J. Food Sci. Technol.* **2016**, *53*(10), 3834–3843. https://doi.org/10.1007/s13197-016-2376-8

[50] Buljeta, I.; Pichler, A.; Šimunović, J.; Kopjar, M. Polysaccharides as carriers of polyphenols: comparison of freeze-drying and spray-drying as encapsulation techniques. *Molecules* **2022**, *27*(16), 5069. https://doi.org/10.3390/molecules27165069

[51] Rezvankhah, A.; Emam-Djomeh, Z.; Safari, M.; Salami, M.; Askari, G. Investigating the effects of maltodextrin, gum arabic, and whey protein concentrate on the microencapsulation efficiency and oxidation stability of hemp seed oil. *J. Food Process. Preserv.* **2022**, *46*(6), e16554. https://doi.org/10.1111/jfpp.16554

[52] Li, R. Y.; Shi, Y. Microencapsulation of borage oil with blends of milk protein, β-glucan and maltodextrin through spray drying: physicochemical characteristics and stability of the microcapsules. *J. Sci. Food Agric.* **2018**, *98*(3), 896–904. https://doi.org/10.1002/jsfa.8535

[53] Giang, N. T. N.; Tan, N. D.; Ha, H. T. N.; Thanh, D. V.; Diem, L. T. T.; Khai, T. V.; Quyen, D. K. Sustainable and novel approach for valorizing nutritional component in oyster mushrooms (*Pleurotus sajor-caju*) hydrolysates: An optimization study by ANN-GA. *J. Agric. Food Res.* **2025**, *24*, 102351. https://doi.org/10.1016/j.jafr.2025.102351

[54] Giang, N. T. N.; Tan, N. D.; Ha, H. T. N.; Thanh, D. V.; Diem, L. T. T.; Khai, T. V.; Diem, M. L.; et al. Artificial intelligence prediction the desirable moisture content of dried oyster mushroom (*Pleurotus sajor-caju*) for enhancing the cellulase-assisted extraction efficiency. *J. Agric. Food Res.* **2025**, *19*, 101561. https://doi.org/10.1016/j.jafr.2024.101561

[55] Gayathry, K. S.; John, J. A. Physical, functional and bioactive properties of microencapsulated powders from banana pseudostem and inflorescence extracts. *Food Prod. Process and Nutr.* **2024**, *6*(1), 74. https://doi.org/10.1186/s43014-024-00251-7

[56] Fournaise, T.; Petit, J.; Gaiani, C. Main powder physicochemical characteristics influencing their reconstitution behavior. *Powder Technol.* **2021**, *383*, 65–73. https://doi.org/10.1016/j.powtec.2021.01.056

ASEAN
Journal of Scientific and Technological Reports
Online ISSN:2773-8752

Research article

Service Life Prediction of Natural Rubber/Reclaimed Rubber Blends through Thermogravimetric Analysis

Sutiwat Thumrat[1], Weerawut Naebpetch[2], Sitisaiyidah Saiwari[1], and Nabil Hayeemasae[1*]

[1] Faculty of Science and Technology, Prince of Songkla University, Pattani Campus, Pattani, 94000, Thailand
[2] Faculty of Engineering, Thaksin University, Phatthalung Campus, Phatthalung, 93210, Thailand
* Correspondence: nabil.h@psu.ac.th

Citation:
Thumrat, S.; Naebpetch, W.; Saiwari, S.; Hayeemasae, N. Service Life Prediction of Natural Rubber/Reclaimed Rubber Blends through Thermogravimetric Analysis. *ASEAN J. Sci. Tech. Report.* **2026**, *29*(3), e261676. https://doi.org/10.55164/ajstr.v29i3.261676.

Article history:
Received: October 1, 2025
Revised: January 28, 2026
Accepted: February 5, 2026
Available online: February 28, 2026

Abstract: The rubber products containing reclaimed rubber may have influenced the service life due to their prior degradation history. However, not many rubber compounders know their service life until they have used it for a certain period. This study breaks this barrier by proposing a simple, cost-effective prediction method based on thermogravimetric analysis (TGA). It focused on blends of Natural Rubber (NR) and Reclaimed Rubber (RR) at various blending ratios. The Ozawa–Flynn–Wall (OFW) Method was applied to the TGA outputs. The results showed that NR/RR blends at all ratios had slightly lower lifetimes than virgin NR over the temperature range of 30-600 °C. When considering a service temperature of 70 °C, the use of RR at 50 phr could reduce the service life from 195 years to 2.01 years. This indicates that the addition of RR may severely affect the service life of the products. The results of this study are useful information for rubber compounders when using RR in their formulations.

Keywords: Lifetime prediction; service life; reclaimed rubber; natural rubber; thermogravimetric analysis

1. Introduction

The problem of waste from worn-out rubber items like tires is growing rapidly, with around 1 billion tires discarded each year. It is anticipated that this figure will increase to 1.2 billion by the year 2030 [1]. Disposing of these rubber products by incineration or landfilling causes significant environmental pollution in the air and soil, as vulcanized rubber is non-biodegradable and not easily recyclable [2]. Accumulated tires are prone to catching fire, causing long-lasting environmental damage and air pollution [3,4]. A significant portion of waste tires is disposed of illegally, contributing to environmental degradation [5]. This poses a significant difficulty in eco-friendly rubber waste management. A potential approach is the creation of reclaimed rubber (RR), in which old vulcanized rubber is heated and treated with chemicals to break molecular chains, enabling it to undergo re-vulcanization. Nonetheless, reclaimed rubber usually shows reduced mechanical properties, such as tensile strength and elongation at break, compared to virgin rubber because the reclamation process randomly cuts chains, which may affect the main chain and result in a lower molecular weight [6, 7, 8]. But at the same time, researchers have continuously sought to increase the efficiency of RR use by applying advanced recycling methods, such as ultrasonic grinding [9], microbial devulcanization [10], and microwave devulcanization [11], to name a few. However, these methods have

not been widely scaled up at the industrial level, so the resulting performance decrease limits the potential use of recycled rubber in demanding applications such as tires or high-quality rubber products.

As mentioned, rubber products containing RR may have a shorter service life due to their inherent properties. Not many rubber manufacturers know their service life until they observe the products after a certain period of use. Therefore, predicting the lifetime of rubber products containing RR is challenging and essential for accurately utilizing recovered rubber to address these constraints. The Arrhenius equation is commonly used to predict product lifetime by relating degradation mechanisms to temperature, as reaction rates increase with temperature [12]. This study applied this equation to the outputs from Thermogravimetric Analysis (TGA). The reliability of TGA-based kinetics for lifetime prediction has been validated in various material systems. For instance, Núñez et al. [13] successfully utilized this technique for epoxy resin systems, while Viorel et al. [14] applied it to catalytic materials. In the context of rubber, Ngudsuntear et al. [15] employed TGA kinetics for hydrogenated epoxidized natural rubber (HENR), and Ahn et al. [16] demonstrated strong agreement between TGA predictions and accelerated aging tests for automotive rubber composites. These applications are grounded in the foundational theory established by Toop [17], confirming that non-isothermal TGA is a robust tool for estimating material longevity. To date, there has been limited discussion of the lifetime prediction of NR/RR blends, and it remains unclear whether variations in RR loading have a positive or negative effect on the long-term durability of the final product. This study offers a simple, cost-effective method for predicting the service life of materials. This is unlike other experiments, which require more time and a larger budget. TGA can be performed for a short time, during which the data obtained from its outputs is sufficient to estimate the lifetime. The findings from this research will serve as a foundation for the development of RR-based rubber products.

2. Materials and Methods

2.1 Materials

This study primarily utilized natural rubber (NR) and reclaimed rubber (RR). The NR was of RSS3 grade, prepared in accordance with Thai industrial standards. Yupphadirubber Part., Ltd manufactured the RSS3. The RR was supplied by Union Commercial Development Co., Ltd., Bangkok, Thailand. The RR used was a UCD-105 grade in bulk form (slabs), with a thermo-mechanical process in the presence of a reclaiming agent. According to TGA analysis, RR contained 56.92% rubber hydrocarbon, 10.54% oil, 27.39% carbon black, and 5.15% inorganic matter. Other compounding ingredients, such as Zinc oxide, were purchased from Thai-Lysaght Co., Ltd., Phra Nakhon Si Ayutthaya, Thailand. Stearic acid was purchased by Permata Group Pte. Ltd., Sumatra Utara, Indonesia. Paraffin wax and Paraffinic oil were purchased by H&R Chem Pharm (Thailand) Co., Ltd., Bangkok, Thailand. $CaCO_3$ was purchased by Phatthana Chemical Co., Ltd., Songkhla, Thailand, with an average particle size of 45-50 μm. Carbon black (N550) grade was purchased by Thai Tokai Carbon Product Co., Ltd., Bangkok, Thailand, having a primary particle size of approximately 40–60 nm. N-Cyclohexyl-2-Benzothiazol Sulfenamide (CBS) was purchased by Kawaguchi, Co., Ltd., Tokyo, Japan. Sulfur was purchased by Siam Chemical, Co., Ltd., Bangkok, Thailand. All these materials and chemicals were used as received.

2.2 Preparation of rubber blends

Table 1 shows the blending formulation for NR and RR. The blending ratios were 100/0, 90/10, 70/30, and 50/50 phr/phr. Later, these blending ratios were abbreviated as RR0, RR10, RR30, and RR50, respectively. The content of hydrocarbon rubber, carbon black, and other additives in RR was analyzed using Thermogravimetric analysis (TGA) in accordance with ASTM D6370-99. These data were used to adjust the amounts of virgin NR and fillers in the formulations to ensure that the total content of rubber hydrocarbon and fillers remained consistent across all blends and was comparable to the control (RR0). The entire amount of ingredients, except for CBS and sulfur, was compounded in a 50-L dispersion kneader at a controlled temperature of 75-80 °C for 60 minutes. Subsequently, the compounds were passed through the two-roll mill to add the CBS and sulfur. Finally, the resultant compounds were compression-molded at 150 °C. The time consumed was based on the curing times measured by a moving-die rheometer (MDR), as described in the

following section. Notably, these formulations were derived from a commercial rubber wheel stopper compound, which requires high filler loading for dimensional stability and cost-effectiveness under static loading conditions.

Table 1. Compounding ingredients for preparing NR/RR blends.

Material	Role	Amount (phr)			
		RR0	**RR10**	**RR30**	**RR50**
Natural rubber	Rubber matrix	100	90	70	50
Reclaimed rubber	Rubber matrix	0	10	30	50
Zinc Oxide	Activator	3	3	3	3
Stearic acid	Activator	1	1	1	1
Paraffin wax	Antiozonant	2	2	2	2
$CaCO_3$	Filler	100	100	100	100
N550	Filler	40	40	40	40
Paraffinic oil	Plasticizer	15	15	15	15
CBS	Accelerator	1.5	1.5	1.5	1.5
Sulfur	Vulcanizing agent	1	1	1	1

Note: The amounts of Paraffinic oil, Carbon Black (N550), and Calcium Carbonate ($CaCO_3$) added were adjusted based on the composition of RR to maintain a constant total filler loading.

2.3 Measurement of Mooney viscosity

The Mooney viscosity of the rubber blends was determined using a Mooney viscometer (ML1+4, 100 °C) in accordance with ASTM D1646. The tests were conducted on three samples to measure the Mooney viscosity of the rubber blends before vulcanization**.**

2.4 Measurement of Curing Characteristics

The vulcanization properties of the rubber blends were analyzed using a moving die rheometer (MDR) at 150 °C for 30 minutes, in accordance with ASTM D5289. To find Scorch time (t_{s1}), Cure time (t_{c90}), Maximum torque (M_H), Minimum torque (M_L), Torque difference ($M_H - M_L$), and Cure rate index (CRI).

2.5 Measurement of mechanical properties

Tensile properties were measured using a Universal Testing Machine in accordance with ASTM D412. Test specimens were fabricated in five replicates, each having a gage length of 25 mm. The crosshead velocity was established at 500 mm/min. The tensile strength and elongation at break were recorded for each specimen. The tear strength was evaluated in accordance with ASTM D624 (Die C), utilizing an angular-shaped test specimen. The examination was performed at a crosshead velocity of 500 mm/min with a force of 500 N. The hardness was assessed utilizing an Automatic Rubber Hardness Tester fitted with a Shore A durometer. Test specimens were fabricated as square samples measuring 6 x 6 cm and 0.9 cm in thickness, in accordance with ASTM D2240. To evaluate the durability of the rubber blends, aging tests were conducted under two conditions: thermal aging and oil-swollen aging. For thermal aging, dumbbell-shaped specimens were placed in a hot-air oven at 100 °C for 7 days (168 h), in accordance with ASTM D573. For oil-swelling aging, the specimens were immersed in SAE 5W-30 oil at 100 °C for 7 days (168 h) in accordance with ASTM D471. After aging, the samples were allowed to rest at room temperature for at least 24 h before testing for mechanical properties.

2.6 Thermogravimetric analysis

A Perkin-Elmer Pyris 6 TGA analyzer was used to perform a thermogravimetric analysis (TGA) on samples weighing approximately 9.263 mg. The samples were heated at 5, 10, 15, and 20 °C/min in a nitrogen flow while being scanned from 30 °C to 600 °C.

2.7 Thermal Kinetics Analysis

TGA is essential for predicting material lifetime by modeling degradation processes. These models help analyze phase transitions and chemical reactions under heat, determining key kinetic parameters such as

activation energy (E_a), Arrhenius pre-exponential factor (A), and reaction order (n). For non-isothermal conditions, the reaction rate constant (k) is temperature-dependent and follows the Arrhenius equation [18]. The fundamental kinetic relationship of the degradation process is described in Equation (1):

$$\frac{d\alpha}{dt} = k(T) \cdot f(\alpha) \tag{1}$$

Where $k(T)$ is the temperature-dependent reaction rate constant, and $f(\alpha)$ represents the reaction model.

The degradation of polymers is measured by the decline in their properties, where the degradation rate depends on temperature. Higher temperatures accelerate the reaction rate and increase the rate constant (k) according to the Arrhenius equation, [18] as described in Equation (2):

$$k(T) = A \cdot e^{-\frac{E_a}{RT}} \tag{2}$$

Where: A is Arrhenius pre-exponential factor, E_a is Activation energy (J/mol), R is Gas constant (8.314 J/mol/K), T is Absolute temperature (K).

To eliminate the time dependence in Equation (1), which relies on temperature (T) and conversion rate (α), the equation can be transformed by dividing the differential form by the heating rate [18]. This results in Equation (3):

$$\frac{d\alpha}{dT} = \frac{A}{\beta} \cdot e^{-\frac{E_a}{RT}} \cdot f(\alpha) \tag{3}$$

Where β is the heating rate (°C/min).

The Friedman's Method (FRD) is an isoconversion differential technique used to analyze the kinetic parameters of thermal degradation. It can be derived by applying the natural logarithm (ln) to both sides of Equation (1), [15,16] leading to the simplified expression shown in Equation (4).

$$ln\left(\frac{d\alpha}{dT}\right) = constant \cdot -\frac{E_a}{RT} \tag{4}$$

The Kissinger–Akahira–Sunose (KAS) method is an isoconversion technique used to evaluate the kinetic parameters of thermal degradation. It can be calculated using the Coats−Redfern equation [15,16] as expressed in Equation (5).

$$ln\left(\frac{\beta}{T^2}\right) = constant \cdot -\frac{E_a}{RT} \tag{5}$$

The Ozawa–Flynn–Wall (OFW) method is an integral isoconversion technique used to determine the activation energy (E_a). This method analyzes the relationship between the heating rate (β) and temperature (T) at a constant conversion rate. By plotting $ln(\beta)$ against $1000/T$, the slope of the resulting straight line corresponds to E_a/R [15,16]. The mathematical expression for this relationship is shown in Equation (6):

$$ln(\beta) = \ln\left(\frac{AE_a}{f(a)R}\right) - 5.331 - 1.052\frac{E_a}{R}\left(\frac{1}{T}\right) \tag{6}$$

By combining Toop's equation with the activation energy (E_a) obtained from the OFW method, the lifetime of the material can be predicted [15,16,17]. The relationship is expressed in Equation (7):

$$\ln(t_f) = \frac{E_a}{RT_f} + \ln\left(\frac{E_a}{\beta R} \cdot P(x_f)\right) \quad (7)$$

Where t_f is Thermal life (min), T_f is Operating temperature (K), $P(x_f)$ is Doyle approximation integral.

3. Results and Discussion

3.1 Mooney viscosity

Figure 1 shows the Mooney viscosity of NR/RR blends. To characterize the starting material, the viscosity of neat reclaimed rubber (RR100) was measured at 21.80 MU. As observed, the viscosity of the blends decreases with increasing RR content. It is well known that the reclaiming process for RR involves breaking crosslinking bonds to restore the condition as close as possible to the original rubber. However, during the reclaiming process, especially under mechanical force, the main molecular chains are also damaged, so when re-vulcanized, their strength will be reduced accordingly. In addition, in other research, it was found that the phase-separation factors of NR and RR also decreased the Mooney viscosity of the blends compared to pure NR or pure RR [8].

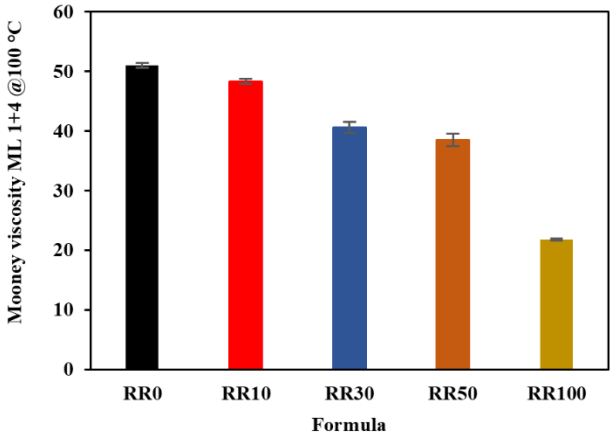

Figure 1. Mooney viscosity of NR/RR blends at ratios of 100/0, 90/10, 70/30, 50/50, and 0/100.

3.2 Curing characteristics

Figure 2 presents the rheometric curves of the NR/RR blends, and the summarized data are listed in Table 2. It can be observed that t_{s1} showed marginal variations across the blends, indicating that the addition of reclaimed rubber did not significantly alter the premature vulcanization safety of the compounds. However, t_{c90} increased slightly, resulting in a lower cure rate as the amount of reclaimed rubber increased. This retardation in curing is attributed to the lower degree of unsaturation (lower carbon-carbon double bond concentration) in reclaimed rubber compared to virgin NR [19]. Since the RR has previously undergone vulcanization and reclaiming, a significant portion of its double bonds has been consumed. Consequently, the depletion of available reactive sites for sulfur crosslinking decreases the overall reaction rate, requiring a longer time to reach the optimal cure state. In addition, as the amount of RR increases, the minimum torque (ML), maximum torque (MH), and delta torque (MH-ML) decrease, indicating a decrease in linkage density due to shortened molecular chains resulting from the reclaiming process [20].

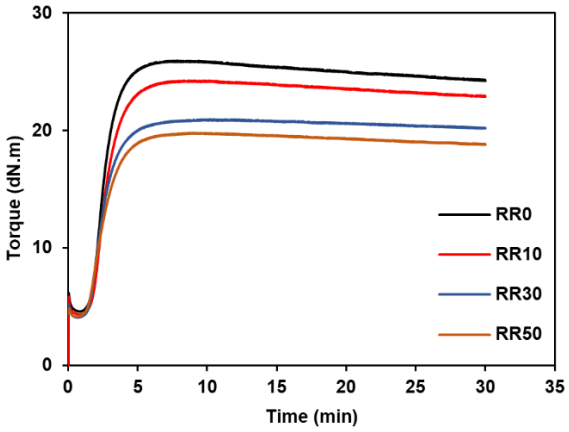

Figure 2. Curing characteristics of NR/RR blends at ratios of 100/0, 90/10, 70/30, and 50/50.

Table 2. Minimum torque (M_L), maximum torque (M_H), torque difference ($M_H - M_L$), and cure rate index (CRI) for NR/RR blends at ratios of 100/0, 90/10, 70/30, and 50/50.

Sample	t_{s1} (min)	t_{c90} (min)	M_H (dN.m)	M_L (dN.m)	M_H-M_L (dN.m)	CRI (min^{-1})
RR0	1.58	4.06	25.95	4.57	21.38	40.34
RR10	1.64	4.39	24.26	4.31	19.95	36.38
RR30	1.49	4.27	20.95	4.08	16.87	35.91
RR50	1.40	4.33	19.80	4.13	15.67	34.07

3.3 Mechanical properties of NR/RR blends

Figures 3 and 4 show the tensile properties, tear strength, and hardness of NR/RR blends. It showed that tensile strength decreased with increasing reclaimed rubber (RR) content. It is widely known that RR was originally cured before undergoing the reclaiming process. So, there was a crosslinking precursor. Such a crosslink precursor can cause catastrophic failure of the sample during stretching, reducing stress transfer. As a result, the tensile strength is reduced. This also affected the elongation at break of the blends (see Figure 3b). The higher RR content eventually reduced the flexibility of the blends. The tensile strength and elongation at break appear to be influenced by the virgin NR. This behavior can be explained by the high strength associated with strain-induced crystallized (SIC) of NR [21]. The ability of NR to undergo SIC decreased with increasing RR content. Furthermore, the tear strength also exhibited the same trend, decreasing with the addition of RR. A similar reason also applies here, as tear strength depends on the SIC of NR. Furthermore, other studies indicate that combinations of NR and RR frequently fail to form a homogenous phase, resulting in inconsistent dispersion within the material [6-8]. This structural inhomogeneity additionally exacerbates the decline of mechanical characteristics. However, Figure 4b shows that the hardness of the blends increased with increasing RR content. The addition of RR to the rubber matrix increased the vulcanizates' stiffness, as hardness is an indicator of material stiffness. As more RR was incorporated into the NR, the flexibility and elasticity of the rubber chains decreased, resulting in greater rigidity and hardness in the rubber vulcanizates.

The properties of the blends after aging are also observed in this study. It was done under normal thermal aging conditions and oil-swollen aging conditions. Both types of thermal aging reduced the overall properties of the blends. The decline in overall mechanical properties can be attributed to oxidation of the polymer, which leads to chain scissions. The breaking of larger molecular chains increased the number of shorter chains, resulting in fewer entanglements and, consequently, a reduction in the mechanical properties. Moreover, the reduction was highest for the thermal aging in oil. The decrease in various properties when immersed in oil is due to NR, which is mainly composed of hydrocarbons, and the RR in this study also has NR as its main component, which is low in polarity. Therefore, when it comes into contact with oil, which is also a hydrocarbon with low polarity, it permeates into the structure, causing the molecular chains to swell and reduce various mechanical properties [15]. To strictly evaluate the durability of the blends, the percentage

retention of tensile strength after aging was calculated and presented in Figure 5. Interestingly, after thermal aging at 100 °C for 7 days, the RR50 blend exhibited the highest retention of approximately 59%, whereas RR0 showed a retention of 50%. This suggests that the presence of reclaimed rubber, which contains carbon black and crosslinked gel precursors, enhances the thermal stability of the rubber matrix, thereby retarding degradation better than virgin NR alone. However, for oil-swollen aging, all blends showed a significant reduction in tensile strength, with retention values dropping below 20%. This drastic decrease is attributed to the non-polar nature of natural rubber, which readily absorbs non-polar oil, leading to severe swelling and the disruption of physical entanglements, regardless of RR content.

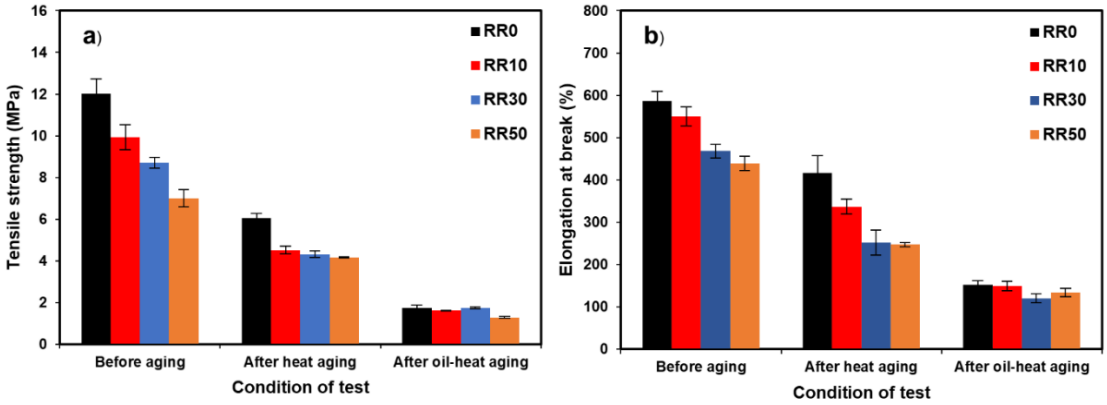

Figure 3. Tensile properties of NR/RR Blend at ratios of 100/0, 90/10, 70/30, and 50/50, including a) Tensile strength and b) Elongation at break.

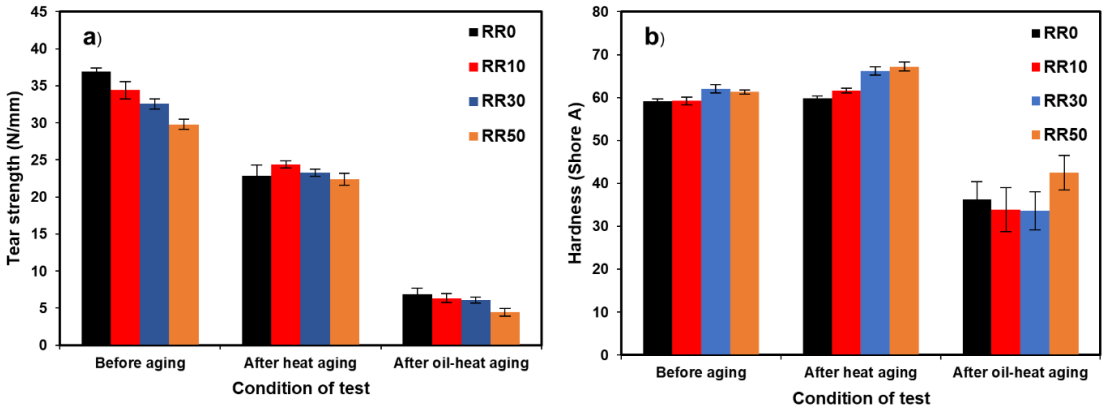

Figure 4. a) Tear strength and b) Hardness of NR/RR Blend at ratios of 100/0, 90/10, 70/30, and 50/50.

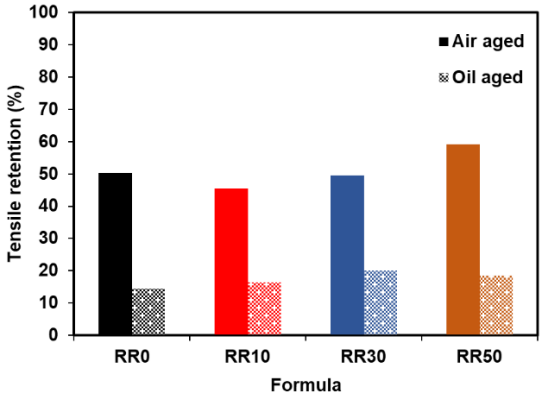

Figure 5. Percentage retention of tensile strength for NR/RR blends after thermal aging (100 °C, 7 days) and oil-swollen aging (100 °C, 7 days).

3.4 Thermal stability

Thermogravimetric analysis (TGA) measures the change in mass of a sample and its rate (velocity) of change in response to temperature or time in a controlled environment. This technique is primarily used to assess the thermal and oxidative stabilities of materials, as well as their compositional properties. The thermal decomposition behavior of NR/RR blends is shown in Figure 6. The decomposition temperatures at different weight losses and various stages are also summarized in Table 3. The initial slight weight loss observed around 180–200 °C was attributed to volatile substances, such as stearic acid, and to adsorbed water around 300 °C [22]. The main degradation process of the blends began at approximately 330 °C and was completed around 450 °C. This decomposition was due to the breakdown of NR segments, as evidenced by the major peak observed in the DTG curve. The degradation of NR is particularly sensitive to the presence of oxidized structures and the depletion of sulfur crosslinks. Notably, the decomposition temperatures at 5, 10, 20, and 30% weight loss for the blends were higher as the RR content increased. This increase in thermal stability is attributed to two factors: the physical shielding effect of carbon black and inorganic fillers in the reclaimed rubber, which acts as a thermal barrier, and the presence of thermally stable mono- and di-sulfidic crosslinks (C-S-C, C-S_2-C) generated during the reclaiming process, which possess higher bond dissociation energy than the polysulfidic bonds predominant in virgin NR. The char residue obtained for both blends at the final temperature exhibited behavior that was essentially the same as a function of the RR phase concentration. As noted, the RR composition was analyzed by TGA before formulating the rubber ingredients. So, the rubber, hydrocarbon, and filler content were controlled. This has led to the unchanged residue remaining in the rubber formulations.

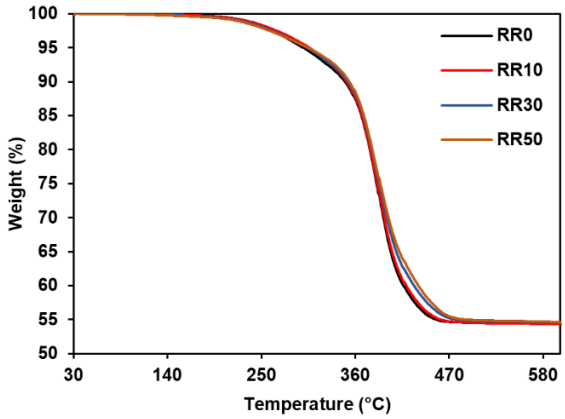

Figure 6. TGA of NR/RR blends at ratios of 100/0, 90/10, 70/30, and 50/50 at a heating rate of 15 °C/min.

Table 3. Temperature at 5%, 10%, 20% and 30% weight loss and char residue of NR/RR blend.

Sample	Decomposition temperature (°C)				Char residue (%)
	T-5%	T-10%	T-20%	T-30%	
RR0	298.5	348	376.5	392.25	54.3070
RR10	306	349.5	377.25	393	54.3077
RR30	303	351	378.75	396.75	54.5472
RR50	304.5	353.25	379.5	398.25	54.6205

3.5 Activation energy

Figure 7 shows the thermogram of the blends at various heating rates. A lower heating rate caused faster degradation of the rubber. This is simply due to the time the resident spends degrading the rubber. A longer time has led to faster chain scission due to its heat storage, resulting in faster decomposition. The data from Figure 7 were utilized to determine the activation energy (Ea) according to Equation (6) by graphing ln(β) versus 1000/T for conversion rates that ranged from 0.05 to 0.45, in increments of 0.05. The outcomes are presented in Figure 8. It was then computed into activation energy using the OFW, KAS, and FRD methods. A comparison of activation energy (Ea) values obtained from the OFW, KAS, and FRD methods is shown in

Figure 9. The Ea is higher for RR0 because of its virgin rubber. Higher Ea indicates that more energy is required to break the specific bonds in the rubber molecules. The activation energy trends across all approaches exhibit strong consistency, with smooth, stable curves indicating negligible variation. This consistency validates the precision and dependability of the computed activation energies [23, 24].

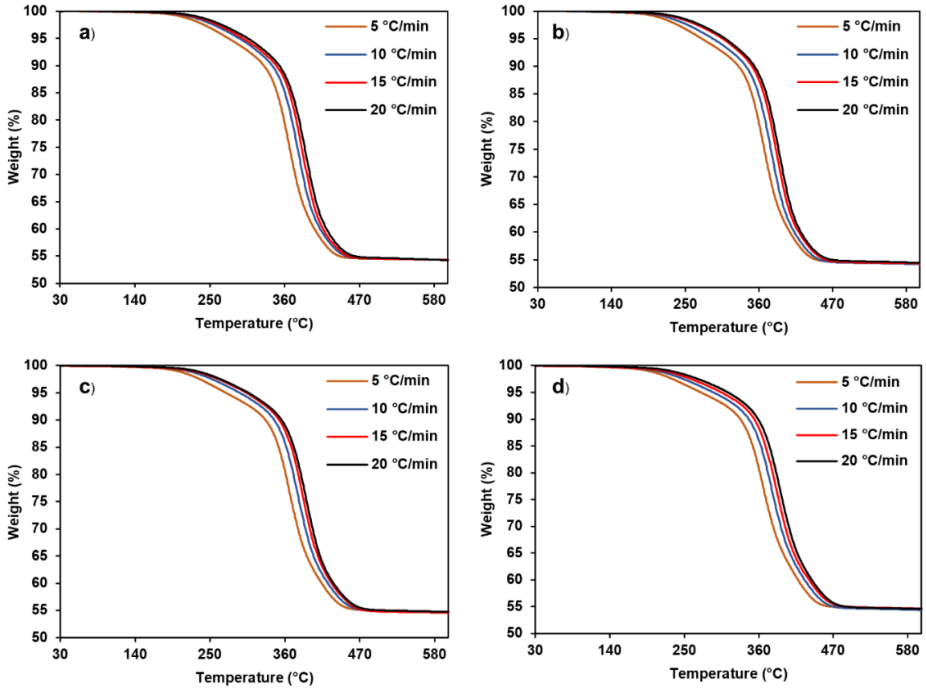

Figure 7. Thermogravimetric analysis (TGA) of NR/RR blends with ratios of a) 100/0, b) 90/10, c) 70/30, and d) 50/50 was conducted at heating rates of 5, 10, 15, and 20 °C/min. The analysis was performed in the temperature range of 30–600 °C under a nitrogen atmosphere.

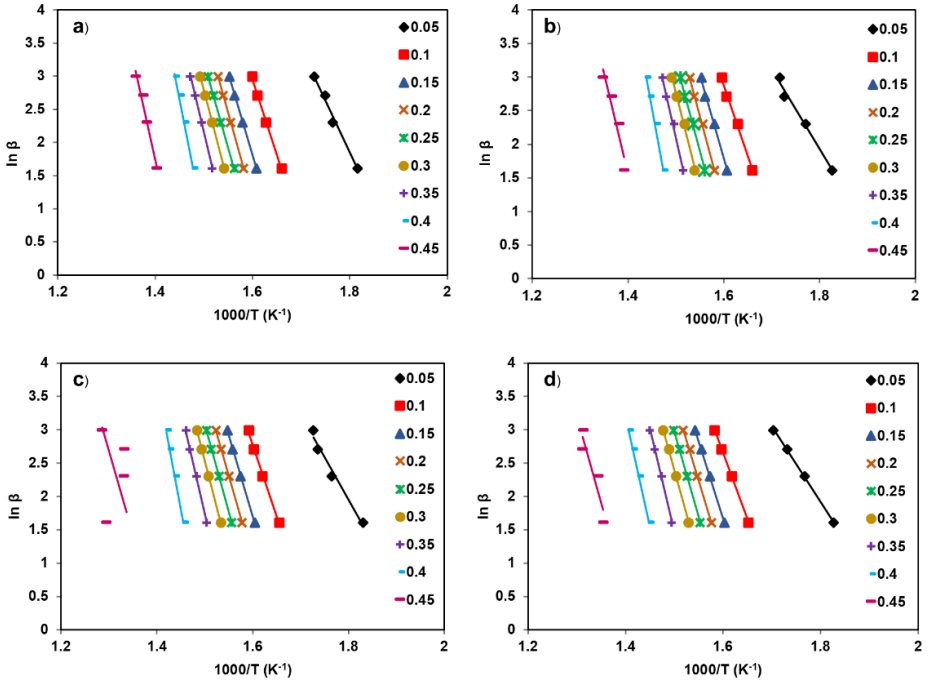

Figure 8. Plot derived from TGA curves at various conversion rates (0.05–0.45) for NR/RR blends with ratios of a) 100/0, b) 90/10, c) 70/30, and d) 50/50 using the Ozawa–Flynn–Wall (OFW) method.

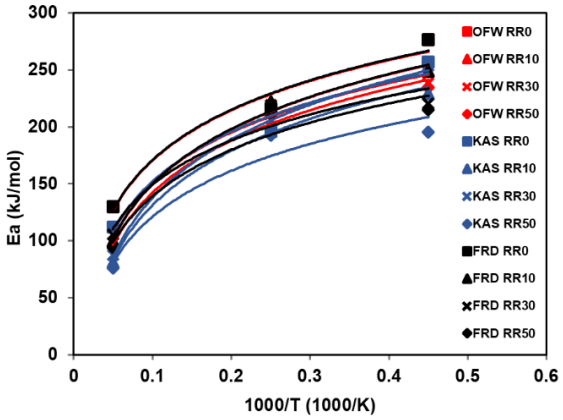

Figure 9. The activation energy relationships of RR0 (rectangle), RR10 (triangle), RR30 (cross), and RR50 (square) as a function of the transformation extent obtained by the OFW method (red symbols), KAS method blue symbols), and FRD method (black symbols) applied to the thermal decomposition.

3.6 Lifetime prediction of NR/RR blends

As shown in Table 4, the high correlation coefficients ($R^2 > 0.97$) obtained from the linear regression of the OFW plots further confirm the reliability of the kinetic data at this conversion level. Additionally, a heating rate of 20 °C/min was employed as the reference condition to simulate a rigorous thermal history, ensuring that the predicted service life provides a conservative estimate under accelerated thermal stress.

Table 4. Kinetic parameters used for lifetime prediction based on the OFW method at the failure criterion ($\alpha = 0.05$).

Sample	Linear Equation (y = mx + c)	Correlation Coefficient (R^2)	Activation Energy (E_a) [kJ/mol]
RR0	y = -15.649x + 30.015	0.9882	130.10
RR10	y = -11.934x + 23.412	0.9854	99.32
RR30	y = -12.685x + 24.786	0.9759	105.46
RR50	y = -11.308x + 22.271	0.9993	94.01

Predicting a material's lifetime is essential for accident prevention and for ensuring optimal product performance by mitigating premature degradation. For the lifetime calculation, the kinetic parameters were determined at a conversion degree of 0.05, consistent with the methodology reported by [15]. This specific conversion level was selected as the failure criterion because it corresponds to the onset of the degradation process. Although a 5% mass loss may appear minimal, in practice, such a degree of chemical change can lead to a significant degradation in the material's mechanical properties. Therefore, lifetime prediction at this threshold is essential for accurately assessing the material's durability and safety in real-world applications. The lifetime was computed using Equation (7) with the acquired data and the previously calculated activation energy. Figure 10 shows the predicted lifetime of NR/RR blends with ratios of 100/0, 70/30, and 50/50, respectively. The results show a persistent reduction in lifetime as temperatures increase. For example, as the temperature increases from 70 °C to 100 °C, the lifetime of RR0 decreases from 195 years to 5.15 years, RR10 lifetime decreases from 3.77 years to 0.24 years, RR30 lifetime decreases from 7.65 years to 0.40 years, and RR50 lifetime decreases from 2.01 years to 0.15 years. Temperature significantly affects the durability of rubber due to the direct relationship between activation energy and temperature. The RR composition substantially affects the lifetime [16]. At lower temperatures, such as 30 °C, increased RR content results in shorter lifetimes. This behavior is attributed to the presence of shortened molecular chains and pre-oxidized structures in the reclaimed rubber, which accelerate degradation kinetics. Conversely, at elevated temperatures, specifically above 250 °C, blends with higher RR content show extended lifetimes due to a crossover phenomenon. This behavior is attributed to the dominance of stable monosulfidic and disulfidic crosslinks and to the physical shielding effect of carbon black, which enhances thermal stability in the later phases [25]. It should be noted

that the lifetime predicted in this study (e.g., >195 years at 70 °C) represents a theoretical thermal lifetime under an inert nitrogen atmosphere. In real-world service conditions, rubber products are simultaneously exposed to oxygen, ozone, UV radiation, and mechanical stress, which significantly accelerate degradation. Therefore, the actual service life will be considerably shorter than the TGA-based predictions. However, this method remains valuable for comparing the relative thermal stability of different rubber formulations under controlled thermal stress.

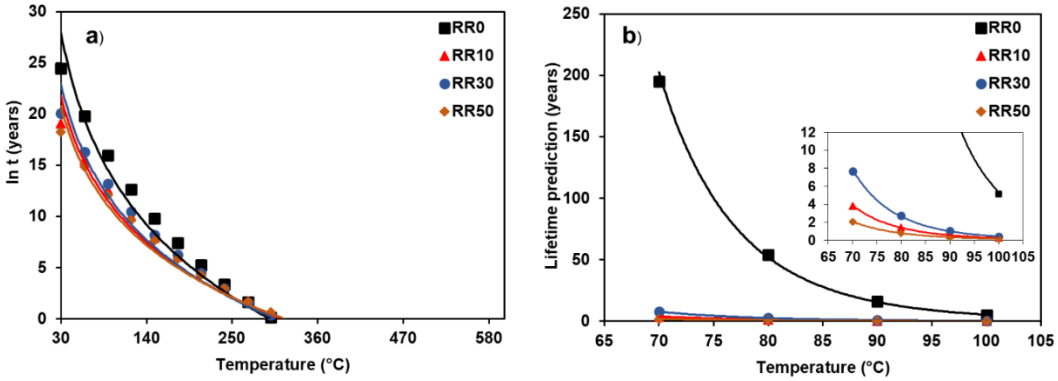

Figure 10. OFW lifetime prediction curves of NR/RR blends at ratios of (RR0) 100/0, (RR10) 90/10, (RR30) 70/30, and (RR50) 50/50: (a) prediction over the full temperature range, and (b) expanded view at 70–100 °C. (Calculated with a heating rate of 5 °C/min at conversion α = 0.05).

4. Conclusions

The experimental results showed that the mechanical properties of NR/RR blends tended to decrease continuously with increasing amounts of reclaimed rubber due to the decreasing molecular weight of the RR due to chain break during the reclaiming process and the inhomogeneity of the phases in the NR/RR blends, resulting in a decrease in the mechanical properties of NR upon the addition of reclaimed rubber. However, the hardness increased due to the remaining filler in the reclaimed rubber. The thermal degradation of NR/RR blends was studied using TGA. The obtained experimental TGA data were used to calculate the activation energy (Ea) using the Ozawa–Flynn–Wall (OFW) Method. It was found that vulcanized rubber without RR addition had the highest activation energy, due to its natural origin. The results showed that NR/RR blends at all ratios had slightly lower lifetimes than NR vulcanized in the temperature range of 30-600 °C and at a service temperature of 70 °C. When comparing the NR/RR blends at different ratios, the values ranged from 195 years to 2.01 years. This indicates that the addition of RR may affect the service life of the products. The results of this study provide useful information and a foundation for rubber compounders when using RR in their formulations.

5. Acknowledgements

We gratefully acknowledge the financial support from Prince of Songkla University, Pattani Campus, through Grant No. SAT6703029S. The first author wishes to thank the Faculty of Science and Technology, Prince of Songkla University, Pattani Campus, for providing a personal scholarship under Grant No. 013/2566.

Author Contributions:

- **Conceptualization** – Nabil Hayeemasae; Weerawut Naebpetch
- **Methodology** – Nabil Hayeemasae; Weerawut Naebpetch; Sitisaiyidah Saiwari
- **Software** – NA
- **Validation –** Nabil Hayeemasae; Weerawut Naebpetch; Sitisaiyidah Saiwari
- **Formal analysis** – Sutiwat Thumrat
- **Investigation** – Sutiwat Thumrat
- **Resources** – Nabil Hayeemasae; Weerawut Naebpetch
- **Data curation** – Sutiwat Thumrat; Nabil Hayeemasae

- **Writing – original draft preparation** – Sutiwat Thumrat; Nabil Hayeemasae
- **Writing – review & editing** – Nabil Hayeemasae
- **Visualization** – Nabil Hayeemasae; Weerawut Naebpetch; Sitisaiyidah Saiwari
- **Supervision** – Nabil Hayeemasae; Weerawut Naebpetch; Sitisaiyidah Saiwari
- **Project administration** – Nabil Hayeemasae
- **Funding acquisition** – Nabil Hayeemasae

Funding: This research was funded by Prince of Songkla University, Pattani Campus, grant number SAT6703029S, and the APC was funded by the same grant.

Conflicts of Interest: The authors declare no conflict of interest.

References

[1] Formela, K. Waste tire rubber-based materials: Processing, performance properties and development strategies. *Adv. Ind. Eng. Polym. Res.* **2022**, *5*(4), 234–247. https://doi.org/10.1016/j.aiepr.2022.06.003

[2] [2] Ali, F.; Denis, R. Waste Rubber Recycling: A Review on the Evolution and Properties of Thermoplastic Elastomers. *Materials* **2020**, *13*(3), 782. https://doi.org/10.3390/ma13030782

[3] Daniele, R.; Andrea, D. Novel uses of recycled rubber in civil applications. *Adv. Ind. Eng. Polym. Res.* **2022**, *5*(4), 214–233. https://doi.org/10.1016/j.aiepr.2022.08.005

[4] Pranay, G.; Sukhanand, S. B.; Rohit, S.; Praful, S.; Ajay, G. D. Use of waste rubber tyre in construction of bituminous road. *Int. Res. J. Mod. Eng. Technol. Sci.* **2023**, https://doi.org/10.56726/irjmets44098

[5] Dennis, G. The value of different recycling technologies for waste rubber tires in the circular economy—A review. *Front. Sustain.* **2024**, https://doi.org/10.3389/frsus.2023.1282805

[6] Said, S.; Lucía, A.; Morena, R. M.; Nourredine, A. H. Thermo-mechanical devulcanization and recycling of rubber industry waste. *Resour. Conserv. Recycl.* **2019**, *144*, 180–186. https://doi.org/10.1016/j.resconrec.2019.01.047

[7] Zhao, X.; Hu, H.; Zhang, D.; Zhang, Z.; Peng, S.; Sun, Y. Curing behaviors, mechanical properties, dynamic mechanical analysis and morphologies of natural rubber vulcanizates containing reclaimed rubber. *e-Polymers* **2019**, *19*(1), 482–488. https://doi.org/10.1515/epoly-2019-0051

[8] Darestani, F. T.; Bakhshandeh, G. R.; Abtahi, M. Mechanical and Viscoelastic properties of natural rubber/reclaimed rubber blends. *Polym. Bull.* **2006**, *56*(4-5), 495–505. https://doi.org/10.1007/s00289-006-0508-4

[9] Aditya, R.; Pranav, K. S.; Prashant, P.; Nimisha, R. S. Minimization and Utilization of Byproduct. *Int. J. Innov. Eng. Sci.* **2023**, *8*(5), https://doi.org/10.46335/IJIES.2023.8.5.8

[10] Mishel, P. F.; Steffi, P. F.; Vijayalakshmi, S. Conventional and modern waste treatment approaches – bioremediation of rubber waste. In *Sustainable Bio-Remediation of Waste Rubber*, Elsevier: **2023**; pp 97–113. https://doi.org/10.1016/B978-0-443-15206-1.00007-4

[11] Tao, Z.; Lucia, A.; Michel, G.; Nourredine, A. H. An overview on waste rubber recycling by microwave devulcanization. *J. Environ. Manage.* **2024**, *353*, 120122. https://doi.org/10.1016/j.jenvman.2024.120122

[12] Woo, C. S.; Park, H. S. Useful lifetime prediction of rubber component. *Eng. Fail. Anal.* **2011**, *18*(7), 1645–1651. https://doi.org/10.1016/j.engfailanal.2011.01.003

[13] Núñez, L.; Villanueva, M.; Núñez, M. R.; Rial, B. Lifetime prediction of the epoxy system DGEBA (n= 0)/1, 2-DCH modified with an epoxy reactive diluent by thermogravimetric analysis. *J. Appl. Polym. Sci.* **2003**, *89*(14), 3835–3839. https://doi.org /10.1002/app.12536

[14] Viorel, S.; Orsina, V.; Alexandru, P. The estimation of thermal endurance for some heteropoly acidic catalysts from thermogravimetric decomposition data. *J. Therm. Anal. Calorim.* **2017**, *127*(1), 273–282. https://doi.org/10.1007/s10973-016-5479-6

[15] Ngudsuntear, K.; Limtrakul, S.; Vatanatham, T.; Arayapranee, W. Mechanical and aging properties of hydrogenated epoxidized natural rubber and its lifetime prediction. *ACS Omega* **2022**, *7*(41), 36448–36456. https://doi.org/10.1021/acsomega.2c04225

[16] Ahn, W.; Lee, J. M.; Lee, H. S. A Study on Life Time Prediction of ACM Rubber Composite Using Accelerated Test and Thermogravimetric Analysis. *Elastomers Compos.* **2014**, *49*(2), 144–148. https://doi.org/10.7473/EC.2014.49.2.144

[17] Toop, D. Theory of Life Testing and Use of Thermogravimetric Analysis to Predict the Thermal Life of Wire Enamels. *IEEE Trans. Electr. Insul.* **1971**, *EI-6*(1), 2–14. https://doi.org/10.1109/TEI.1971.299128

[18] Plota, A.; Masek, A. Lifetime Prediction Methods for Degradable Polymeric Materials—A Short Review. *Materials* **2020**, *13*(20), 4507. https://doi.org/10.3390/ma13204507

[19] Saiwari, S.; Lohyi, E.; Nakason, C. Application of NR Gloves Reclaim: Cure and Mechanical Properties of NR/Reclaim Rubber Blends. *Adv. Mater. Res.* **2013**, *844*, 437–440. https://doi.org/10.4028/www.scientific.net/AMR.844.437

[20] https://doi.org/Thitithammawong, A.; Hayichelaeh, C.; Nakason, W.; Jehvoh, N. The use of reclaimed rubber from waste tires for production of dynamically cured natural rubber/reclaimed rubber/polypropylene blends: Effect of reclaimed rubber loading. *J. Met. Mater. Miner.* **2019**, *29* (2), 85–94. https://doi.org/10.14456/jmmm.2019.24

[21] Candau, N.; Chazeau, L.; Chenal, J. M.; Gauthier, C.; Ferreira, J.; Munch, E.; Thiaudière, D. Strain induced crystallization and melting of natural rubber during dynamic cycles. *Phys. Chem. Chem. Phys.* **2015**, *17*(23), 15331–15338. https://doi.org/10.1039/C5CP00384A

[22] Lu, L.; Lu, L.; Cai, J.; Frost, R. L. Desorption of stearic acid upon surfactant adsorbed montmorillonite: A thermogravimetric study. *J. Therm. Anal. Calorim.* **2010**, *100*(1), 141–144. https://doi.org/10.1007/s10973-009-0169-2

[23] Ammineni, S. P.; Nagaraju, C.; Lingaraju, D. Thermal degradation of naturally aged NBR with time and temperature. *Mater. Res. Express* **2022**, *9*(6), 065305. https://doi.org/10.1088/2053-1591/ac7302

[24] Mohit, A.; Remya, N. Pyrolysis characteristics and kinetics study of native polyculture microalgae using thermogravimetric analysis. *Biomass Convers. Biorefin.* **2024**, *14*(16), 19825–19833. https://doi.org/10.1007/s13399-023-04175-z

[25] Joseph, A. M.; George, B.; Alex, R. Effect of devulcanization on crosslink density and crosslink distribution of carbon black filled natural rubber vulcanizates. *Rubber Chem. Technol.* **2016**, *89*(4), 653–670. https://doi.org/10.5254/rct.16.84819

ASEAN
Journal of Scientific and Technological Reports
Online ISSN:2773-8752

Research article

Electron Spin Resonance (ESR) Signal Analysis of Fossil Teeth from Mae Moh Mine, Thailand

Tidarut Vichaidid[1*], and Sumaiyah Kortor[1]

[1] Faculty of Science and Technology, Prince of Songkla University, Pattani Campus, Pattani, 94000, Thailand
* Correspondence: tidarut.v@psu.ac.th

Citation:
Vichaidid, T.; Kortor, S. Electron spin resonance (ESR) signal analysis of fossil teeth from Mae Moh Mine, Thailand. *ASEAN J. Sci. Tech. Report.* **2026**, *29*(3), e260951. https://doi.org/10.55164/ajstr.v29i3.260951.

Article history:
Received: August 21, 2025
Revised: January 26, 2026
Accepted: February 5, 2026
Available online: February 28, 2026

Abstract: This study investigates the characteristics of Electron Spin Resonance (ESR) signals in fossil tooth enamel collected from the Mae Moh lignite mine in Lampang Province, Thailand. ESR spectra were recorded at room temperature (298 K) using a Bruker EMX Premium spectrometer operating at X-band (9.85 GHz) with a modulation frequency of 100 kHz and a modulation amplitude of 0.3 mT. The most prominent signal was observed at g ≈ 2.002, attributable to trapped carbonate radicals within the hydroxyapatite crystal lattice. By applying the Multiple-Aliquot Additive Dose (MAAD) protocol, the ESR intensity at g ≈ 2.002 exhibited a strong linear relationship with laboratory-administered gamma doses (0–2000 Gy), yielding a dose-response slope of 0.2185 a.u./Gy (R^2 = 0.907). From this calibration, the natural accumulated dose for the fossil teeth was determined to be 550 ± 30 Gy. These findings demonstrate the reliability of ESR signal analysis for quantifying accumulated radiation dose in fossil enamel and support its application for future geochronological investigations in the Mae Moh basin.

Keywords: ESR signal intensity; fossil tooth enamel; multiple-aliquot additive dose (MAAD); accumulated dose

1. Introduction

Electron Spin Resonance (ESR) spectroscopy is a powerful analytical method for detecting unpaired electrons and free radicals in paramagnetic materials, offering high sensitivity and specificity [1]. It has been extensively applied in archaeometry and geosciences to characterize fossil, bone, and tooth samples and to assess radiation-induced defect centers [2]. Tooth enamel, composed primarily of hydroxyapatite $(Ca_{10}(PO_4)_6(OH)_2)$ and organic inclusions, undergoes structural defect formation and radical entrapment during prolonged burial. The most prominent ESR-active center in fossil enamel is the carbonate radical (CO_2^-), which produces a characteristic signal at g ≈ 2.002, making it an ideal probe for dosimetric and microstructural studies [3]. The Mae Moh lignite mine in Lampang Province, Thailand, is a key Miocene depositional basin (15–20 Ma) known for abundant mammalian fossils, including well-preserved tooth and bone specimens. This geological context offers a unique archive of diagenetic processes and paleoenvironmental conditions in northern Thailand [4]. ESR-based dosimetry and dating commonly employ the MAAD protocol to calibrate signal intensity against known $\gamma-$ray doses. Standardized procedures, as outlined by Dennis [5] and Said et al. [6], ensure reliable assessment of accumulated radiation doses in enamel, providing groundwork for subsequent

age estimation. This study presents a detailed analysis of ESR signals in fossil tooth enamel from the Mae Moh mine, focusing on signal amplitude, line shape, and the precise determination of the g ≈ 2.002 component. We establish a dose–response calibration, derive the natural accumulated dose, and evaluate the potential of ESR signal analysis for paleodosimetric applications and future geochronological research in the Mae Moh basin [6].

2. Materials and Methods

2.1 Study Area and Sample Collection

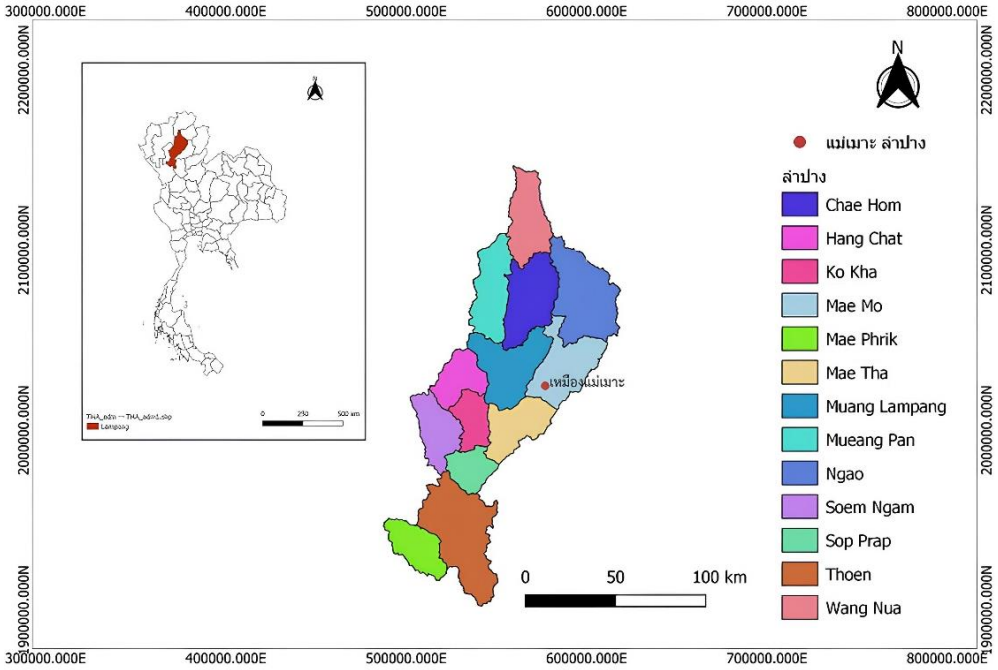

Figure 1. Map of the Mae Moh lignite mine showing sampling locations (red dots) within the Miocene graben basin [7-8].

The study was conducted in the Mae Moh lignite mine (18°20′–18°27′ N, 99°40′–99°46′ E) in Lampang Province, northern Thailand (Figure 1). This mine lies within the Miocene Mae Moh Graben Basin, a fault-bounded depression with more than 1,000 m of fluvio-lacustrine sediments that have yielded diverse vertebrate fossils [7]. The stratigraphy of the Mae Moh Group comprises three lithostratigraphic members—Huai King, Nakhaem, and Huai Luang—each characterized by alternating coal seams and clastic units (Figure 2) [7]. Fossil tooth enamel specimens were discovered in the Nakhaem member, specifically within the interburden between coal seams K-3 and K-4, at an elevation of approximately 332 m above sea level and beneath ~18 m of overburden (Figure 3). Field sampling followed established ESR-dating guidelines: GPS coordinates, stratigraphic position, overburden thickness, and sedimentological context were recorded at each find [9]. To prevent photobleaching of trapped radicals, each tooth was immediately wrapped in opaque aluminum foil and stored under dim red light (<5 lx) until laboratory processing [9-10].

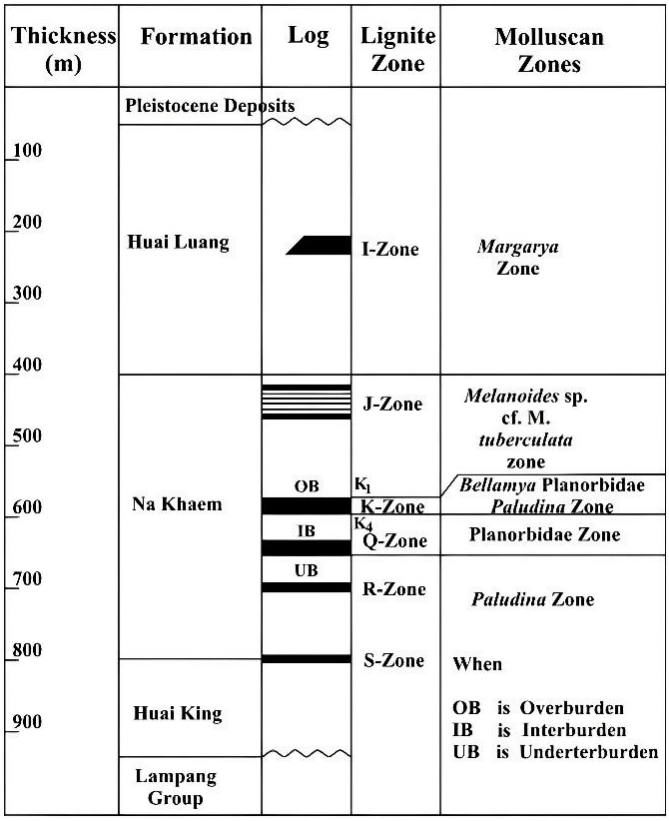

Figure 2. Simplified stratigraphic column of the Mae Moh Group, indicating the Huai King, Nakhaem, and Huai Luang members with fossil-bearing horizons between coal seams K-3 and K-4 [7].

Figure 3. Fossil molar tooth recovered from the sediment between coal seams K-3 and K-4 at the Mae Moh lignite mine, Lampang Province, Thailand, showing the occlusal surface. (scale bar = 1 cm).

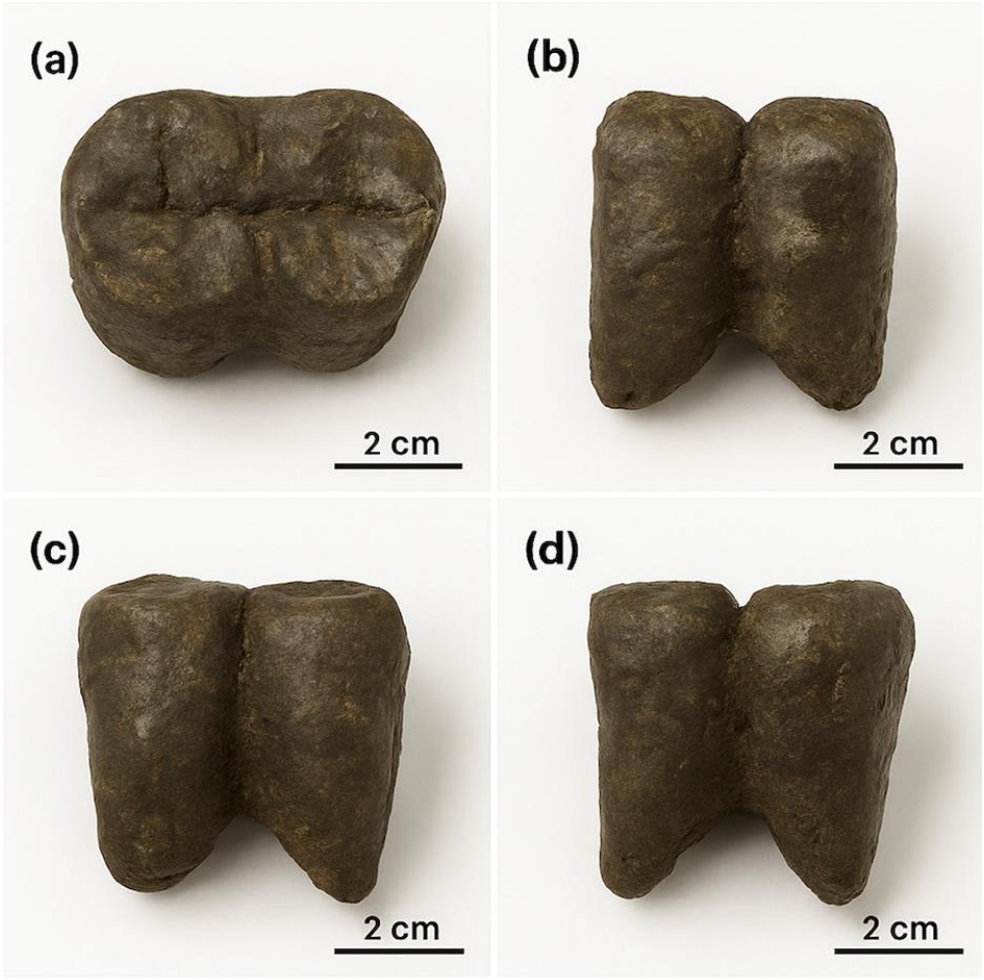

Figure 4. Simulated four-view presentation of the fossilized molar tooth pair recovered from the member (between coal seams K-3 and K-4) at the Mae Moh lignite mine, Lampang Province, Thailand. Panels show (a) occlusal surface, (b) frontal aspect, (c) buccal aspect, and (d) distal aspect. Scale bars = 2 cm. This illustration was digitally generated for illustrative purposes and does not depict the actual specimen.

2.2 Sample Preparation

To preserve the radicals formed during burial, freshly excavated fossil teeth were wrapped in light-proof foil and stored under dim red light (<5 lx) until laboratory preparation. In the laboratory, the enamel layer was separated from dentine under red light and processed for ESR measurements. The surrounding sediment does not alter the spectral shape or intensity of the ESR signal in enamel, as the detected ESR response reflects the concentration and stability of trapped paramagnetic centers within the hydroxyapatite lattice, which are primarily governed by the cumulative radiation dose and defect structure of the enamel. Therefore, sediment analyses were not considered within the scope of this study, which focuses on ESR signal characterization rather than external dose-rate modeling. The outer ~3 mm was removed following International Atomic Energy Agency (IAEA) recommendations [11]. The resulting powder (90–150 μm) was obtained by gentle crushing and sieving. Chemical etching was not performed to avoid alteration of trapped radicals, in agreement with studies showing minimal benefit of additional HF treatment for ESR signals in well-preserved samples [9, 12].

2.3 ESR Measurements

Before measurement, powdered enamel (90–150 μm) was transferred into quartz ESR tubes and rinsed sequentially in 48 % HF (60 min), 10 % HCl, deionized water, and acetone to remove residual silicates and organic matter. Spectra were acquired at room temperature (298 K) on a Bruker EMX Premium X-band spectrometer (9.85 GHz) fitted with a high-Q dielectric cavity. Instrument settings were optimized to maximize signal-to-noise while avoiding power saturation: microwave power = 0.1002 mW, modulation frequency = 100 kHz, modulation amplitude = 0.3 mT, sweep width = 20 mT, center field = 351 mT, sweep time = 10.51 s, and a single scan per aliquot. Each spectrum was baseline-corrected and normalized using the manufacturer's software, and the g ≈ 2.002 carbonate radical signal was verified by comparison with a standard tooth-enamel reference [3]. Reproducibility was confirmed by repeated measurements (n = 3) on selected samples, yielding intensity variations below 5 % [13]. These procedures follow best practices for ESR dosimetry in enamel as outlined by Formela [1] and Viorel et al. [14].

2.4 Data Analysis

All ESR spectra were first subjected to baseline correction and a five-point moving-average smoothing using Bruker Xenon software to remove low-frequency noise and enhance the signal-to-noise ratio [15]. The CO_2^- signal at g ≈ 2.002 was isolated by spectral deconvolution employing Maximum Likelihood Common Factor Analysis (MLCFA), following the procedure of [15]. Peak-to-peak amplitudes were determined by integrating the first-derivative line shape between 350.9 and 352.0 mT.

The g-factor for each spectrum was calculated as

$$g = h\nu / \mu_B B \quad (1)$$

where h is Planck's constant, ν the microwave frequency, μ_B the Bohr magneton, and B the magnetic field at resonance. Dose–response curves were constructed by plotting integrated signal intensities against administered $\gamma-$ray doses (0–2000 Gy) and fitting a weighted linear regression constrained through the origin to obtain the calibration slope and coefficient of determination (R^2) [15]. To quantify uncertainty, we evaluated contributions from spectral noise, dose delivery (±2%), and regression fitting. Combined standard uncertainties and 95% confidence intervals for the natural accumulated dose were calculated using the analytical framework of Ahn et al. [16], which propagates error sources through dose determination to yield interval estimates rather than single values.

3. Results and Discussion

3.1 ESR Signal Characteristics

The room-temperature X-band ESR spectrum of fossil tooth enamel from the Mae Moh mine (Figure 5) is characterized by a sharp, single-component line centered at g ≈ 2.002, attributable to the CO_2^- in the hydroxyapatite lattice [17-18]. This narrow line (peak-to-peak width ≈ 0.6 mT) indicates a homogeneous microenvironment around the radical sites and minimal spectral overlap with other defect centers [19]. Recent advances in ESR spectral processing [17] have improved deconvolution accuracy, confirming that the CO_2^- signal dominates the spectrum with reproducibility better than 5% across multiple scans. Carbonate radicals form when the environment liberates electrons that become trapped in lattice vacancies during prolonged burial and diagenesis. Their geological stability and linear dose–response make the g ≈ 2.002 signal an ideal dosimetric marker for retrospective dose assessment in enamel [18].

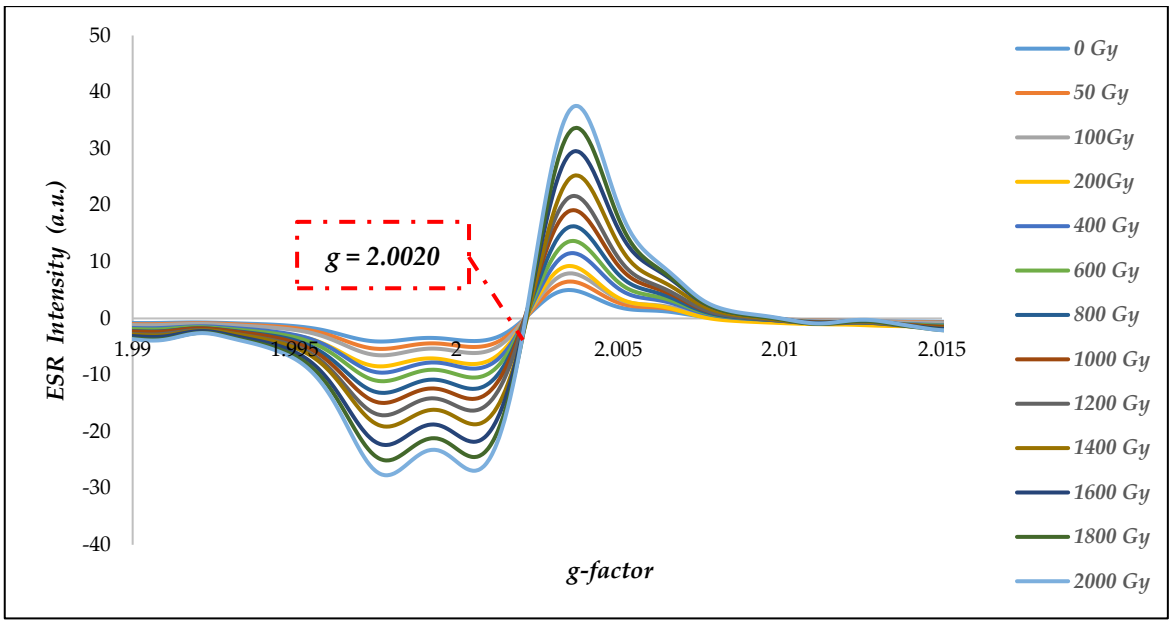

Figure 5. X-band ESR spectrum (first-derivative) of fossil tooth enamel from Mae Moh mine at 298 K, showing the dominant CO_2^- radical signal at g ≈ 2.002 (peak-to-peak width ≈ 0.6 mT)—inset: deconvoluted line shape used for amplitude extraction.

3.2 ESR Signal Intensity

The peak-to-peak ESR intensity of the CO_2^- signal at g ≈ 2.002 shows a strong linear relationship with administered $\gamma-$ray doses from 0 to 2000 Gy (Figure 6). A weighted linear regression constrained through the origin yields a calibration slope of 0.2185 ± 0.005 a.u./Gy and a coefficient of determination (R^2) of 0.9066, indicating that over 90% of the variance in signal intensity is explained by the applied dose. The y-intercept (120.49 a.u.) reflects the background contribution from intrinsic paramagnetic centers and instrument baseline; this offset is subtracted from all measured intensities before dose calculation. From this calibration, the natural accumulated dose (AD) in the fossil enamel is determined to be 550 ± 30 Gy. The uncertainty was derived by propagating three main error sources—spectral noise, dose-delivery error (±2%), and regression fitting uncertainty—using the analytical framework of viorel et at. [14] and Ahn et al. [16]. These results demonstrate that ESR intensity measurements provide a reliable and quantitative basis for retrospective dose assessment in tooth enamel, underpinning future paleodosimetric and geochronological applications.

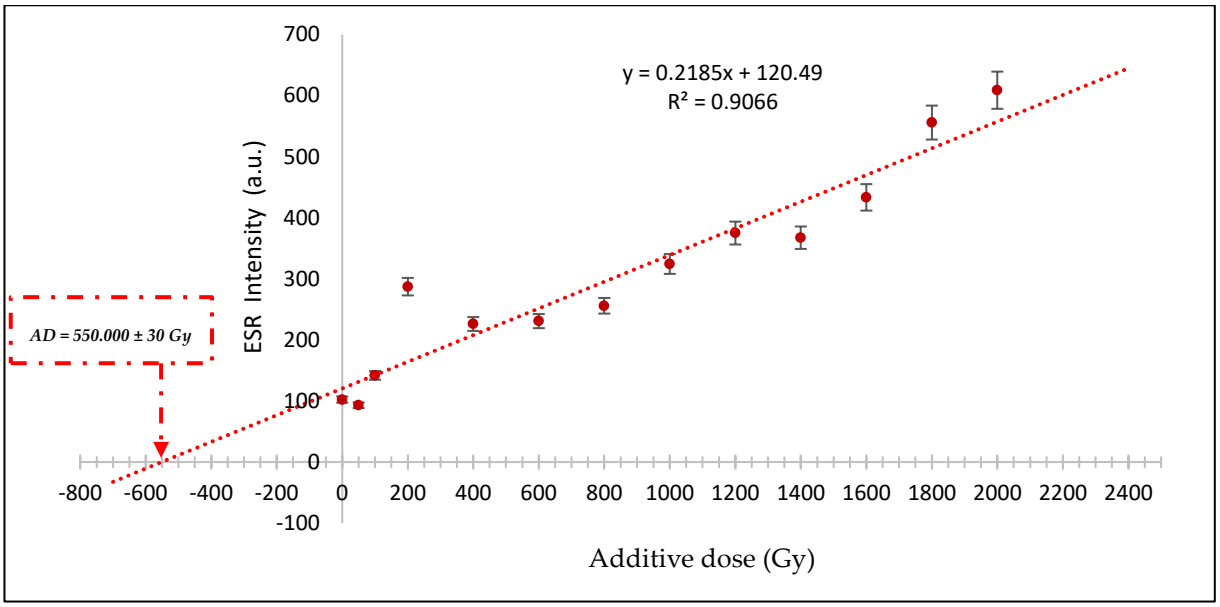

Figure 6. Dose–response calibration for the CO_2^- ESR signal at g ≈ 2.002 in fossil tooth enamel. The dashed line represents the weighted linear regression (slope = 0.2185 a.u./Gy; R^2 = 0.9066). The extrapolated natural accumulated dose is 550 ± 30 Gy.

3.3 Limitations and Potential Applications

While the MAAD protocol offers a robust approach for reconstructing accumulated dose (AD) from ESR measurements on fossil enamel, several methodological limitations remain. The accuracy of AD estimation depends on the quality of the dose–response curve and the reproducibility of the carbonate radical signal at g ≈ 2.002, which may vary among fossil specimens and diagenetic settings [5]. In addition, the lack of a complete external dose-rate model in the present study prevents AD values from being converted into numerical age estimates, as ESR dating requires integrating both internal and external radiation components, including sediment radioelements and moisture content [6, 22]. Analytical uncertainties related to spectral noise, dose delivery, and regression fitting must also be considered when interpreting AD results [14]. Despite these limitations, ESR enamel dosimetry holds promising applications in radiation and geochronological research. In palaeodosimetry, ESR signal intensities provide a direct proxy for long-term environmental radiation exposure in biological tissues and complement other retrospective dosimetry techniques [20]. Furthermore, ESR-based AD values can be integrated with U-series or luminescence chronometers to cross-validate burial ages and refine Quaternary stratigraphic frameworks [6]. Continued methodological improvements in signal processing, dose-response modeling, and dose-rate assessment will further enhance the utility of ESR enamel dosimetry in geochronological and radiation exposure studies.

4. Conclusions

This study demonstrates that fossil tooth enamel from the Mae Moh lignite mine exhibits a remarkably stable ESR signal at g ≈ 2.002, characterized by a narrow peak-to-peak width (~0.6 mT) and highly reproducible intensities across additive doses up to 2000 Gy, yielding a linear dose–response calibration (slope = 0.2185 a.u./Gy, R^2 = 0.9066) and a natural accumulated dose of 550 ± 30 Gy. The persistence and sharpness of this g ≈ 2.002 signal reflect the deep-trap stability of the CO_2^- center within the carbonated hydroxyapatite lattice, which has been shown to retain its paramagnetic properties with less than 4% signal variation over 360 days in analogous synthetic systems [2] and to resist diagenetic alteration in natural enamel samples [20]. Future research should prioritize refining environmental dose-rate models through comprehensive field-based measurements of radionuclide concentrations (U, Th, K) and sediment moisture content, enabling accurate quantification of both internal and external dose-rate components [5, 21]. Coupling these geochemical datasets with advanced MAAD protocols will improve the precision of ESR calibration curves. At the same time,

integration of ESR-derived doses with complementary chronometers—such as U-series and luminescence dating—will allow cross-validation of age estimates and the construction of a robust multi-method geochronological framework [22]. This integrated approach promises high-resolution reconstructions of Miocene sedimentation dynamics and vertebrate evolutionary history in northern Thailand.

5. Acknowledgements

The authors wish to express their sincere gratitude to the Department of Mineral Resources for its invaluable assistance in conducting field surveys and collecting samples at the Mae Moh mine in Lampang Province. We are also grateful to the National Standard Radiation Laboratory (NSRL), Office of Atoms for Peace (OAP), for providing the gamma irradiation support and for kindly granting access to the Electron Spin Resonance instrumentation. Finally, we would like to thank the Nuclear Physics Laboratory, Faculty of Science and Technology, Prince of Songkla University, Pattani Campus, for generously allowing us to use their research facilities.

Author Contributions: Conceptualization, Tidarut Vichaidid and Sumaiyah Kortor; methodology, Tidarut Vichaidid and Sumaiyah Kortor; software, Tidarut Vichaidid; validation, Tidarut Vichaidid; formal analysis, Tidarut Vichaidid; investigation, Tidarut Vichaidid; resources, Tidarut Vichaidid; data curation, Tidarut Vichaidid; writing—original draft preparation, Tidarut Vichaidid and Sumaiyah Kortor; writing—review and editing, Tidarut Vichaidid; visualization, Tidarut Vichaidid; supervision, Tidarut Vichaidid; project administration, Tidarut Vichaidid. All authors have read and agreed to the published version of the manuscript.

Funding: This research received no external funding

Conflicts of Interest: The authors declare no conflict of interest.

References

[1] Formela, K. Waste tire rubber-based materials: Processing, performance properties and development strategies. *Adv. Ind. Eng. Polym. Res.* **2022**, *5*(4), 234–247. https://doi.org/10.1016/j.aiepr.2022.06.003

[2] Ali, F.; Denis, R. Waste Rubber Recycling: A Review on the Evolution and Properties of Thermoplastic Elastomers. *Materials* **2020**, *13*(3), 782. https://doi.org/10.3390/ma13030782

[3] Daniele, R.; Andrea, D. Novel uses of recycled rubber in civil applications. *Adv. Ind. Eng. Polym. Res.* **2022**, *5*(4), 214–233. https://doi.org/10.1016/j.aiepr.2022.08.005

[4] Pranay, G.; Sukhanand, S. B.; Rohit, S.; Praful, S.; Ajay, G. D. Use of waste rubber tyre in construction of bituminous road. *Int. Res. J. Mod. Eng. Technol. Sci.* **2023**, *5*(8), 1395–1401. https://doi.org/10.56726/irjmets44098

[5] Dennis, G. The value of different recycling technologies for waste rubber tires in the circular economy—A review. *Front. Sustain.* **2024**, *4*, 1282805. https://doi.org/10.3389/frsus.2023.1282805

[6] Said, S.; Lucía, A.; Morena, R. M.; Nourredine, A. H. Thermo-mechanical devulcanization and recycling of rubber industry waste. *Resour. Conserv. Recycl.* **2019**, *144*, 180–186. https://doi.org/10.1016/j.resconrec.2019.01.047

[7] Zhao, X.; Hu, H.; Zhang, D.; Zhang, Z.; Peng, S.; Sun, Y. Curing behaviors, mechanical properties, dynamic mechanical analysis and morphologies of natural rubber vulcanizates containing reclaimed rubber. *e-Polymers* **2019**, *19*(1), 482–488. DOI: 10.1515/epoly-2019-0051

[8] Darestani, F. T.; Bakhshandeh, G. R.; Abtahi, M. Mechanical and Viscoelastic properties of natural rubber/reclaimed rubber blends. *Polym. Bull.* **2006**, *56*(4-5), 495–505. https://doi.org/10.1007/s00289-006-0508-4

[9] Aditya, R.; Pranav, K. S.; Prashant, P.; Nimisha, R. S. Minimization and Utilization of Byproduct. *Int. J. Innov. Eng. Sci.* **2023**, *8*(5), 38–41. https://doi.org/10.46335/IJIES.2023.8.5.8

[10] Mishel, P. F.; Steffi, P. F.; Vijayalakshmi, S. Conventional and modern waste treatment approaches – bioremediation of rubber waste. In *Sustainable Bio-Remediation of Waste Rubber*, Elsevier: **2023**; pp 97–113. https://doi.org/10.1016/B978-0-443-15206-1.00007-4

[11] Tao, Z.; Lucia, A.; Michel, G.; Nourredine, A. H. An overview on waste rubber recycling by microwave devulcanization. *J. Environ. Manage.* **2024**, *353*, 120122. https://doi.org/10.1016/j.jenvman.2024.120122.

[12] Woo, C. S.; Park, H. S. Useful lifetime prediction of rubber component. *Eng. Fail. Anal.* **2011**, *18*(7), 1645–1651. https://doi.org/10.1016/j.engfailanal.2011.01.003

[13] Núñez, L.; Villanueva, M.; Núñez, M. R.; Rial, B. Lifetime prediction of the epoxy system DGEBA (n= 0)/1, 2-DCH modified with an epoxy reactive diluent by thermogravimetric analysis. *J. Appl. Polym. Sci.* **2003**, *89*(14), 3835–3839. https://doi.org/10.1002/app.12536

[14] Viorel, S.; Orsina, V.; Alexandru, P. The estimation of thermal endurance for some heteropoly acidic catalysts from thermogravimetric decomposition data. *J. Therm. Anal. Calorim.* **2017**, *127*(1), 273–282. https://doi.org/10.1007/s10973-016-5479-6

[15] Ngudsuntear, K.; Limtrakul, S.; Vatanatham, T.; Arayapranee, W. Mechanical and aging properties of hydrogenated epoxidized natural rubber and its lifetime prediction. *ACS Omega* **2022**, *7*(41), 36448–36456. https://doi.org/10.1021/acsomega.2c04225

[16] Ahn, W.; Lee, J. M.; Lee, H. S. A Study on Life Time Prediction of ACM Rubber Composite Using Accelerated Test and Thermogravimetric Analysis. *Elastomers Compos.* **2014**, *49*(2), 144–148. https://doi.org/10.7473/EC.2014.49.2.144

[17] Toop, D. Theory of Life Testing and Use of Thermogravimetric Analysis to Predict the Thermal Life of Wire Enamels. *IEEE Trans. Electr. Insul.* **1971**, *EI-6*(1), 2–14. https://doi.org/10.1109/TEI.1971.299128.

[18] Plota, A.; Masek, A. Lifetime Prediction Methods for Degradable Polymeric Materials—A Short Review. *Materials* **2020**, *13* (20), 4507. DOI: 10.3390/ma13204507

[19] Saiwari, S.; Lohyi, E.; Nakason, C. Application of NR Gloves Reclaim: Cure and Mechanical Properties of NR/Reclaim Rubber Blends. *Adv. Mater. Res.* **2013**, *844*, 437–440. https://doi.org/10.4028/www.scientific.net/AMR.844.437

[20] Thitithammawong, A.; Hayichelaeh, C.; Nakason, W.; Jehvoh, N. The use of reclaimed rubber from waste tires for production of dynamically cured natural rubber/reclaimed rubber/polypropylene blends: Effect of reclaimed rubber loading. *J. Met. Mater. Miner.* **2019**, *29*(2), 85–94. https://doi.org/10.14456/jmmm.2019.24

[21] Candau, N.; Chazeau, L.; Chenal, J. M.; Gauthier, C.; Ferreira, J.; Munch, E.; Thiaudière, D. Strain induced crystallization and melting of natural rubber during dynamic cycles. *Phys. Chem. Chem. Phys.* **2015**, *17* (23), 15331–15338. https://doi.org/10.1039/C5CP00384A

[22] Lu, L.; Lu, L.; Cai, J.; Frost, R. L. Desorption of stearic acid upon surfactant adsorbed montmorillonite: A thermogravimetric study. *J. Therm. Anal. Calorim.* **2010**, *100*(1), 141–144. https://doi.org/10.1007/s10973-009-0169-2

[23] Ammineni, S. P.; Nagaraju, C.; Lingaraju, D. Thermal degradation of naturally aged NBR with time and temperature. *Mater. Res. Express* **2022**, *9*(6), 065305. https://doi.org/10.1088/2053-1591/ac7302.

[24] Mohit, A.; Remya, N. Pyrolysis characteristics and kinetics study of native polyculture microalgae using thermogravimetric analysis. *Biomass Convers. Biorefin.* **2024**, *14*(16), 19825–19833. https://doi.org/10.1007/s13399-023-04175-z

[25] Joseph, A. M.; George, B.; Alex, R. Effect of devulcanization on crosslink density and crosslink distribution of carbon black filled natural rubber vulcanizates. *Rubber Chem. Technol.* **2016**, *89*(4), 653–670. https://doi.org/10.5254/rct.16.84819

ASEAN
Journal of Scientific and Technological Reports
Online ISSN:2773-8752

Research article

Conflict Victimization Model in Southern Thailand: An Event-Level Analysis Using Multinomial Logistic Regression

Abdunfatah Masamae[1], and Rhysa McNeil[2*] and Mayuening Eso[2]

[1] College of Digital Science, Prince of Songkla University, Songkhla, 90110, Thailand
[2] Faculty of Science and Technology, Prince of Songkla University, Pattani, 94000, Thailand
* Correspondence: rhysa.m@psu.ac.th

Citation:
Masamae, A.; Mcneil, R.; Eso, M. Conflict victimization model in southern Thailand: An event level analysis using multinomial logistic regression . *ASEAN J. Sci. Tech. Report.* **2026**, *29*(3), e261780. https://doi.org/10.55164/ajstr.v29i3.261780.

Article history:
Received: October 7, 2025
Revised: January 27, 2026
Accepted: February 5, 2026
Available online: February 28, 2026

Abstract: This study investigates the determinants of conflict-related victimization severity in Thailand's southernmost provinces using event-level data from 9,310 southern unrest incidents recorded between 2004 and 2020. Victimization outcomes were classified into three ordered severity categories—safe, injured, and dead—and analyzed using Multinomial Logistic Regression (MLR) to capture differentiated risk mechanisms. The dataset, compiled by the Deep South Coordination Center (DSCC), integrates police, military, and administrative records to provide comprehensive coverage of subnational conflict events. Feature selection was conducted using chi-squared screening followed by backward refinement, yielding nine key predictors encompassing temporal, spatial, contextual, and tactical dimensions. Model estimation was performed under both baseline and imbalance-adjusted weighted specifications, with robustness assessed through cross-validation and sensitivity analyses. Results indicate that non-residential locations, particularly public places, roads, and agricultural areas, substantially increase the likelihood of injury and fatal outcomes. At the same time, rural settings are associated with lower severity risk, and attacks targeting military personnel exhibit markedly elevated injury and fatality odds relative to civilian targets. Shooting attacks emerge as the most lethal modality, with an estimated 15.8-fold increase in fatal risk compared to bombings. Predictive evaluation demonstrates strong discrimination for safe outcomes (AUC = 0.94), with good to moderate performance for injury (AUC = 0.80) and fatal events (AUC = 0.75). The findings highlight the dominant roles of spatial context and attack modality in shaping victimization severity and demonstrate the value of interpretable statistical modeling for informing targeted security planning and conflict-prevention strategies.

Keywords: Multinomial logistic regression; conflict victimization; southern Thailand; imbalanced classification; event-level analysis

1. Introduction

Correctly classifying the outcomes of violent events is an increasingly important operation in conflict analytics and security informatics. Policymakers and practitioners require analytical tools that can distinguish between incidents resulting in no casualties, injuries, and fatalities. These distinctions directly affect emergency preparedness, resource allocation, and long-term planning. From a data science perspective, such problems are typically multiclass and imbalanced, meaning that some outcomes occur far more frequently than others. At the same time, stakeholders often demand interpretability in addition to predictive

accuracy, so that statistical models can both guide immediate decision-making and justify resource allocation transparently. Southern Thailand provides a unique case study for evaluating such models. Since 2004, the southernmost provinces, including Pattani, Yala, Narathiwat, and parts of Songkhla, have experienced more than 7,000 conflict-related deaths linked to protracted insurgency. Unlike many global conflict datasets, the Deep South Coordination Center (DSCC) has consolidated reports from multiple administrative sources, including police, military, and local government. This is resulting in a comprehensive event-level dataset of 9,310 southern unrest incidents covering 2004–2020. This dataset, with its temporal, spatial, and tactical attributes, enables systematic analysis of victimization outcomes at the incident level and represents one of the most complete longitudinal records of subnational violence in Southeast Asia.

To analyze such data, Multinomial Logistic Regression (MLR) offers an interpretable baseline. MLR is widely used in political science, epidemiology, and risk modeling to classify categorical outcomes with more than two categories. Its coefficients, expressed as odds ratios, provide policymakers with interpretable effect sizes that are more transparent than those from many machine learning models. However, MLR is not without limitations: it assumes independence of irrelevant alternatives (IIA), can be sensitive to class imbalance, and may underperform compared to nonparametric classifiers such as decision trees, random forests, or support vector machines. Our approach treats MLR not as a novel methodology, but as an interpretable benchmark against which more complex learners can be evaluated. Prior research in conflict and civil war modeling has employed a variety of approaches to assess event outcomes and risk factors. Competing risks and survival models have been used to examine the duration and escalation dynamics of civil war [1]. More recently, ensemble learning models and spatial econometric approaches have been applied to predict terrorism incidents and conflict clustering [2]. At the same time, a growing literature in data science has emphasized handling imbalanced classification problems through resampling, class weighting, and evaluation metrics beyond simple accuracy. Yet, there remains a gap in systematically applying these imbalanced multiclass methods to subnational conflict event datasets, balancing predictive accuracy with interpretability.

This study addresses that gap by presenting a reproducible data science workflow for multiclass victimization classification. This study focuses on outcomes of southern unrest events in Southern Thailand to demonstrate how transparent preprocessing, model benchmarking, and assumption testing can improve both research credibility and policy relevance. Rather than making causal claims about insurgent strategy, we emphasize the descriptive and predictive utility of our models for real-world decision-support systems.

2. Materials and Methods

2.1 Data Cleaning

The dataset used in this study comprises 9,310 southern unrest events recorded between 2004 and 2020 in Thailand's southernmost provinces, including Pattani, Yala, Narathiwat, and neighboring districts in Songkhla. These records were consolidated and validated by the Deep South Coordination Center (DSCC), Faculty of Science and Technology, Prince of Songkhla University, Pattani Campus, through triangulation from three sources: police, military, and local administrative offices. The original dataset contained 33,312 victim-level observations and 199 variables. To focus on event-level dynamics, several filtering and aggregation steps were applied. First, 7,864 records were excluded as they were associated with self-accidents, criminal disputes, or other non-conflict incidents. Second, since multiple victims could be linked to a single southern unrest incident, 14,083 victim-level records collapsed to avoid duplication, ensuring that each observation represents one unique event. After this process, the final dataset consisted of 9,310 unique southern unrest events, each coded with situational, temporal, and spatial attributes relevant to conflict analysis, as shown in Table 1.

Table 1. Variable descriptions.

Variable	Definition / Categories	Rationale
Outcome	*Safe* (no casualties), *Injured* (≥1 injury, no deaths), *Dead* (≥1 death)	Defines victimization outcome at the event level.
Month	January–December (categorical)	Captures seasonal/temporal variations in event frequency and severity.
Day	Monday–Sunday	Tests for weekly activity patterns.
Time	morning (06.00–11.59), afternoon (12.00–17.59), evening (18.00–23.59), night (00.00–05.59)	Identifies operational timing of events.
Province	Pattani, Yala, Narathiwat, Songkhla	Captures regional heterogeneity
Zone	residential, public space, road, business, agricultural, military/police base, checkpoint, others	Differentiates exposure risks across everyday and strategic locations.
Area	urban/rural	Reflects differences in density, surveillance, and protection
Target	civilian, civil officer, police, military	Captures differential victimization risk.
Festival	religious holiday, public holiday, none	Explores symbolic timing and crowding effects.
Season	wet/dry	Environmental context for mobility and exposure.
Attack	bombing, shooting, other	Identifies tactical modality of insurgent operations: bombing, gun-shooting, arson, and nail-trapping.

The unit of analysis in this study is therefore a single southern unrest event. Although the original dataset contains victim-level observations, this study's analytical focus is on event-level victimization severity. Because a single southern unrest event may involve multiple victims with different injury outcomes, victim-level information was aggregated into a single event-level outcome using a maximum-severity rule. Specifically, an event was classified as "dead" if at least one fatality occurred; if no fatalities occurred but at least one individual was injured, the event was classified as "injured"; otherwise, the event was classified as "safe." This aggregation strategy prioritizes the most severe consequence for each event and is commonly used in conflict and injury research to avoid double-counting while preserving operational relevance. While this approach may obscure within-event heterogeneity in casualty counts, it enables a consistent and interpretable event-level outcome suitable for multinomial modeling. Of the 199 original variables, 11 were retained based on both empirical relevance and theoretical grounding in insurgent strategy. Temporal factors include the month, day, time of day, season, and whether the event coincided with a festival, capturing possible symbolic timing or the event's operational opportunities. Spatial factors include the province, the specific zone of occurrence (such as residential area, public place, road, or checkpoint), and whether the area was classified as rural or urban, reflecting geographical exposure and risk contexts. Finally, situational and tactical factors include the type of target (civilian, military, police, or civil officer) and the method of attack (such as bombing, shooting, or other tactics; arson and nail-trapping), which represent insurgents' strategic choices to maximize impact or convey political messages. Together, these structured variables form the basis for the multinomial logistic regression analysis, allowing for systematic assessment of how temporal, spatial, and tactical dimensions shape the likelihood of different victimization outcomes.

2.2 Feature Selection

Depending on the categorical data of the independent variables, filter-based feature selection was performed using the chi-squared test, and the results are summarized in Table 2.

$$\chi^2 = \sum_{i=1}^{r} \sum_{j=1}^{c} \frac{(O_{ij}-E_{ij})^2}{E_{ij}} \quad (1)$$

where *Oij* is the observed frequency, therefore, the actual count in cell *i* and *j* of the contingency table. While *Eij* is the expected frequency, it's the count expected if the variables are independent. This is explained below:

$$E_{ij} = \frac{(Row\ total_i) \times (Column\ total_j)}{N} \quad (2)$$

where *N* is the total of southern unrest, *r* is the number of categories in the predictor, and *c* is the number of outcome classes.

Table 2. Chi-squared features selection

Variable	Chi-squared		
	Degree of freedom	test value	p-value
Month	22	93.39	< 0.001
Day	12	39.11	< 0.001
Time	6	141.81	< 0.001
Province	6	85.33	< 0.001
Zone	12	662.12	< 0.001
Area	2	35.47	< 0.001
Target	6	689.28	< 0.001
Festival	4	62.53	< 0.001
Season	2	17.77	< 0.001
Attack	4	3,309.00	< 0.001

The feature selection results in Table 2 revealed 10 statistically significant independent variables (all $p < 0.05$). Consistent with the model-prediction principle, these variables were excluded because they were not significant ($p > 0.05$). Thus, these eight advanced to the final model analytical process.

2.3 Multinomial Logistic Regression Analysis

The outcome variable in this study was categorical with multiple classes. The MLR was employed as an analytical method. The MLR is specially designed for modeling multiclass categorical outcomes. Let a dependent variable *Y* with *K* classes, and *p* predictor variables, the probability $P(Y = k \mid x)$ that an observation belongs to class *k* is modeled as:

$$P(Y=k|x) = \frac{e^{\beta_0^{(k)} + \beta_1^{(k)} x_1 + \ldots + \beta_p^{(k)} x_p}}{\sum_{j=1}^{K} e^{\beta_0^{(j)} + \beta_1^{(j)} x_1 + \ldots + \beta_p^{(j)} x_p}} \quad (3)$$

where $\beta_0^{(k)} + \beta_1^{(k)} x_1 + \cdots + \beta_p^{(k)} x_p$ is the linear combination of predictors for class *k*, $\beta_0^{(k)}$ is the intercept for class *k* and $\beta_i^{(k)}$ is the coefficient for predictors x_i for class *k*. This was a normalization probability that sums to 1 across all classes. Although the outcome categories (safe, injured, dead) exhibit a natural severity ordering, they were treated as nominal in the MLR framework to avoid imposing the proportional odds assumption required by ordinal models. The connection emerged when it was compared to one class of *k* to the reference class *K*. The ratio of probability is as follows:

$$\frac{P(Y=k \mid x)}{P(Y=K \mid x)} = e^{\beta_0^{(k)} + \beta_1^{(k)} x_1 + \ldots + \beta_p^{(k)} x_p} \quad (4)$$

Then, this was taken to the natural logarithm to get log-odds:

$$ln\left(\frac{P(Y=k \mid x)}{P(Y=K \mid x)}\right) = e^{\beta_0^{(k)} + \beta_1^{(k)} x_1 + \cdots + \beta_p^{(k)} x_p} \quad (5)$$

MLR has been widely applied across diverse studies, including health science, social sciences, and education [3]. Implemented MLR to generate real-time non-invasive vibrotactile feedback signals in operating rooms using field-programmable gate arrays, while [4] employed MLR to analyze electronic medical record audit logs across three clinical groups (primary care, surgical, and non-surgical medical). During the training period, k-fold cross-validation was applied only to the training dataset to assess model stability while preserving temporal separation between training and test data.

2.4 Study Mechanism

This study follows a structured analytical mechanism designed to predict event-level victimization severity while ensuring methodological rigor and preventing information leakage. The mechanism is as follows: Figure 1

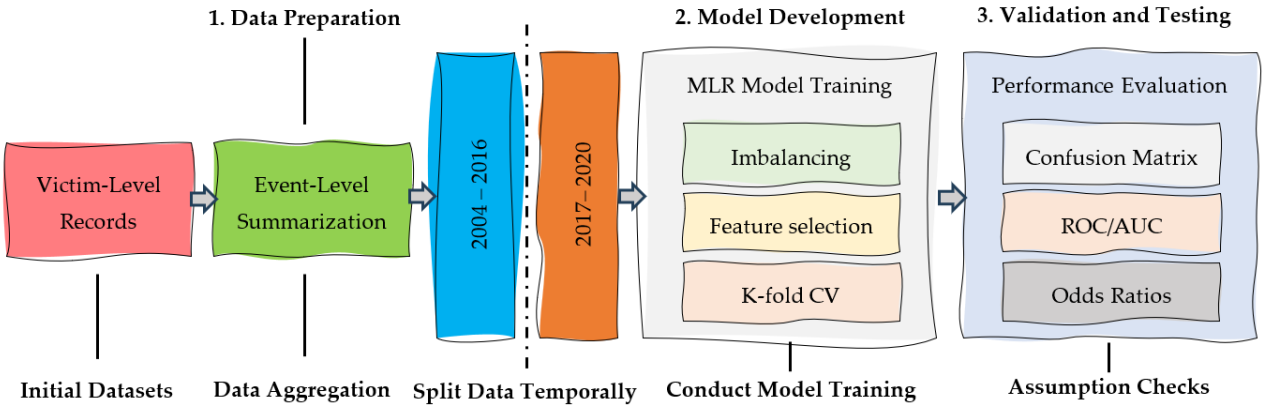

Figure 1. Analytical framework

First, victim-level records were aggregated into event-level outcomes using a maximum-severity rule, yielding three mutually exclusive categories: safe, injured, and dead. The analysis then adopted a temporal validation strategy, with events from 2004–2016 used for model development and events from 2017–2020 reserved for independent testing. Within the training period, class distributions were examined to assess imbalance across outcome categories. To mitigate the influence of class imbalance on parameter estimation and predictive performance, inverse-frequency class weighting was applied during model training. Feature selection was conducted exclusively on the training dataset using univariate screening methods, including chi-square tests for categorical predictors and nonparametric tests for numerical predictors, followed by multivariable model refinement. MLR models were subsequently estimated to examine the associations between temporal, spatial, and contextual predictors and event-level victimization severity. Model stability was evaluated using k-fold cross-validation within the training period, while key model assumptions—particularly the IIA—were assessed using diagnostic tests. Final model performance was evaluated on the held-out test dataset using multiple complementary metrics, including confusion matrices expressed as percentages, macro-averaged performance measures, and one-vs-rest receiver operating characteristic (ROC) curves. Model interpretability was enhanced by estimating odds ratios with 95% confidence intervals and by graphical visualization of effect sizes. Together, this analytical mechanism integrates predictive accuracy, statistical inference, and methodological transparency to support robust interpretation of conflict-related victimization outcomes.

2.5 Validation

2.5.1 Data Splitting

To evaluate the model's ability to generalize to future southern unrest events, a temporal hold-out validation strategy was employed. Specifically, southern unrest events occurring between 2004 and 2016 were used as the training dataset, while events from 2017 to 2020 were reserved as an independent test dataset. This time-based split reflects a realistic prediction setting and prevents information leakage from future events into model estimation.

All model development procedures—including feature screening, class imbalance handling, and k-fold cross-validation—were conducted exclusively on the training dataset. The held-out test dataset was used only for final model evaluation.

2.5.2 Model Assessment

Model assessment in this study involved confusion matrices, model accuracy, F1-score, and ROC curves. The confusion matrix for multi-classification is described:

$$\text{CM}= \begin{bmatrix} TP_1 & FP_{12} & FP_{13} \\ FP_{21} & TP_2 & FP_{23} \\ FP_{31} & FP_{32} & TP_3 \end{bmatrix} \tag{6}$$

where TP_k is a true positive prediction of class k while FP_{kj} It is a false positive prediction where class j was predicted as k class. Model accuracy was calculated:

$$Accuracy = \frac{\sum_{k=1}^{K} TP_k}{N} \tag{7}$$

where N is the total sample size. Next, the F1-score was calculated:

$$F1_k = 2 \times \frac{Precision_k \times Recall_k}{Precision_k + Recall_k} \tag{8}$$

where

$$Precision_k = \frac{TP_k}{TP_k + \sum_{j \neq k} FP_{jk}} \tag{9}$$

$$Recall_k = \frac{TP_k}{TP_k + \sum_{j \neq k} FN_{jk}} \tag{10}$$

Moreover, the ROC curve was applied to illustrate the fitted model as performed by this equation:

$$TPR_k = \frac{TP_k}{TP_k + FN_k} \quad , \quad FPR_k = \frac{\sum_{j \neq k} FP_{jk}}{\sum_{j \neq k} TN_{jk}} \tag{11}$$

2.6 Statistical Software

All statistical analyses were conducted using R (version 4.5.0). MLR models were estimated with the nnet package, and model evaluation and cross-validation were performed with *caret*. Receiver operating characteristic (ROC) curves and area under the curve (AUC) statistics were computed using the *pROC* package, and data visualization was carried out using *ggplot2*. All analyses were conducted with a fixed random seed to ensure reproducibility.

3. Results and Discussion

3.1 Descriptive Overview

The final dataset comprises 9,310 conflict-related events recorded between 2004 and 2020 in Thailand's southernmost provinces. Event-level victimization severity was classified into three categories: safe, injured, and dead. The distribution of outcomes reveals a pronounced imbalance across severity levels. Of the total recorded incidents, 45.06% resulted in fatalities, 43.15% led to injuries, and only 11.79% were classified as safe events. This distribution indicates that the vast majority of unrest incidents involved human casualties, with fatal outcomes occurring slightly more frequently than injuries. The relatively small proportion of safe events

underscores the high overall severity of conflict episodes in the region and highlights the non-random nature of victimization outcomes. This substantial imbalance in outcomes motivates the use of imbalance-aware modeling strategies in subsequent analyses to ensure reliable estimation and evaluation of severity-specific risk factors. Figure 2 illustrates the distribution of outcome classes over time.

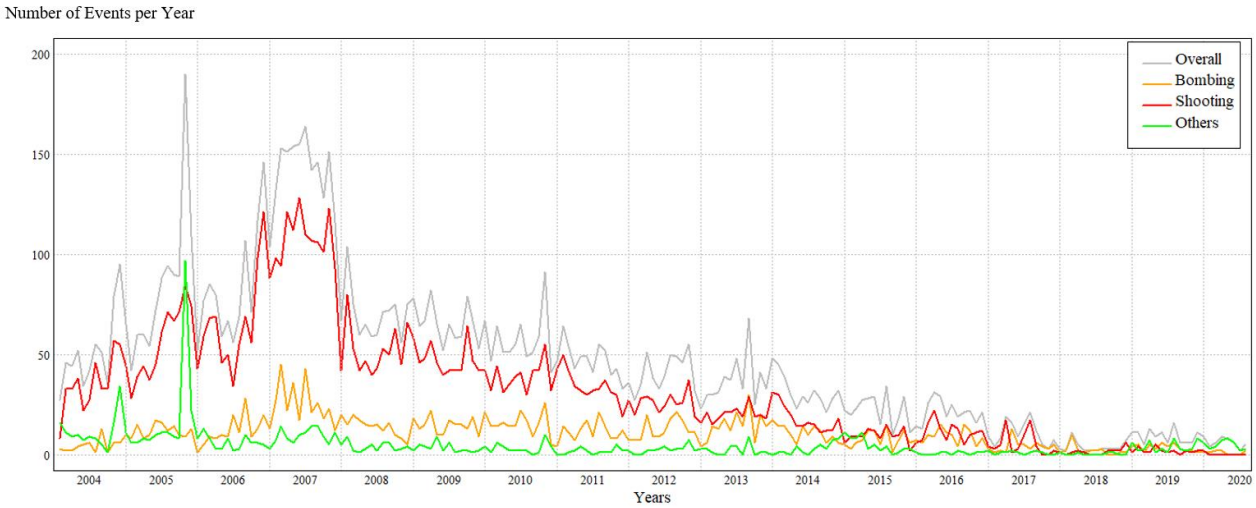

Figure 2. Trends of southern unrest in the southernmost provinces of Thailand

Figure 2 depicts the frequency of southern unrest events in Southern Thailand across different attack types: bombings, shootings, and others over the 17 years. Overall event frequency (gray line) peaked sharply between 2004 and 2007, reflecting the escalation phase of the conflict following its resurgence in early 2004. During this period, shooting incidents (red line) dominated, reaching more than 150 events per year, while bombings (orange line) were comparatively fewer but still frequent. After 2008, all attack types show a gradual, sustained decline, indicating a reduction in large-scale, coordinated violence. By 2015, annual frequencies fell below 20 incidents per year across all categories, suggesting the conflict entered a low-intensity phase. The "other" attack types (green line) include arson, nail trapping, and other weapons. These remained consistently low throughout, rarely exceeding 10 events annually. Overall, this temporal pattern illustrates a high-intensity outbreak phase (2004 – 2007) followed by a steady stabilization and de-escalation trend. The predominance of shootings throughout the period underscores their central role in the conflict's tactical profile, consistent with the model findings that shootings carry the highest lethality odds.

3.2 Model Estimation

Feature selection and model estimation were conducted sequentially using the training dataset to ensure methodological consistency and to prevent information leakage. Candidate predictors were first screened using univariate association tests to identify variables significantly related to event-level victimization severity. These predictors were subsequently refined using backward stepwise selection based on the Akaike Information Criterion (AIC), which balances model goodness-of-fit and model complexity. This procedure yielded a parsimonious set of predictors for multivariable modeling: Month, Day, Time, Province, Zone, Area, Target, Festival, and Attack. Using this final predictor set, multinomial logistic regression models were estimated with the safe outcome specified as the reference category. To assess model adequacy and the impact of outcome imbalance, goodness-of-fit was evaluated using likelihood-based indices, including the Akaike Information Criterion (AIC), Bayesian Information Criterion (BIC), McFadden's pseudo-R^2, and likelihood ratio tests comparing the fitted models with their corresponding null specifications. The results indicate that the estimated models provide a statistically significant improvement over the null model, as summarized in Table 3.

Table 3. Model estimation

Component	MLR Model
Outcome categories	safe, injured, dead
Selected predictors	Month, Day, Time, Province, Zone, Area, Target, Festival, and Attack
AIC	14,403.96
BIC	14,985.02
McFadden's pseudo-R^2	0.18
LR χ^2 (df)	3,077.65 (df)
LR p-value	< 0.001

The effects of selected predictors on event-level victimization severity were examined using odds ratios (ORs) with 95% confidence intervals derived from the MLR models. Odds ratios greater than one indicate an increased likelihood of experiencing injury or fatal outcomes relative to the safe reference category, while odds ratios less than one indicate a decreased likelihood. To assess the influence of outcome imbalance on effect estimation, odds ratios derived from the estimated models were examined. Several predictors exhibit heterogeneous effects across outcome categories, indicating that factors associated with injury do not necessarily translate directly into fatal outcomes. This finding underscores the importance of modeling victimization severity using a multinomial framework, rather than collapsing outcomes into a binary specification, as illustrated in Tables 4 and 5.

Table 4. MLR model ref. safe vs. injured

	Estimate	SE	OR	CI Lower	CI Upper	p-value
Constant	-60.608	0.000	0.000	0.000	0.000	< 0.001
Month						
January*	0.326	0.041	1.386	1.278	1.503	< 0.001
February	0.274	0.040	1.316	1.215	1.424	< 0.001
March	-0.049	0.041	0.953	0.879	1.032	0.234
April	0.000	-	-	-	-	-
May	0.077	0.042	1.080	0.996	1.172	0.063
June	-0.011	0.041	0.989	0.912	1.072	0.782
July	0.177	0.040	1.194	1.104	1.291	< 0.001
August	0.036	0.040	1.037	0.960	1.120	0.358
September	0.240	0.040	1.271	1.174	1.376	< 0.001
October	-0.188	0.038	0.829	0.769	0.893	< 0.001
November	-0.142	0.039	0.868	0.804	0.937	< 0.001
December	-0.104	0.043	0.901	0.829	0.981	0.016
Day						
Sunday*	0.000	-	-	-	-	-
Monday	-0.049	0.029	0.952	0.900	1.008	0.090
Tuesday	0.087	0.029	1.091	1.031	1.155	0.003
Wednesday	-0.234	0.029	0.791	0.748	0.837	< 0.001
Thursday	0.138	0.029	1.148	1.085	1.216	< 0.001
Friday	0.152	0.031	1.165	1.097	1.236	< 0.001
Saturday	0.103	0.030	1.109	1.045	1.176	0.001

Table 4. MLR model ref. safe vs. injured (continus)

	Estimate	SE	OR	CI Lower	CI Upper	p-value
Time						
morning*	0.000	-	-	-	-	-
afternoon	-0.009	0.028	0.991	0.938	1.048	0.756
evening	0.096	0.028	1.101	1.042	1.163	0.001
night	-0.202	0.015	0.817	0.794	0.842	< 0.001
Province						
Pattani*	0.000	1.000	-	-	-	-
Narathiwat	0.179	0.029	1.196	1.131	1.265	< 0.001
Yala	0.096	0.031	1.100	1.036	1.168	0.002
Songkhla	-0.326	0.006	0.722	0.713	0.730	< 0.001
Zone						
resident*	0.000	-	-	-	-	-
bases and checkpoints	1.396	0.004	4.040	4.012	4.069	< 0.001
public places	1.613	0.035	5.018	4.683	5.378	< 0.001
road	1.319	0.023	3.738	3.572	3.912	< 0.001
business	0.829	0.039	2.292	2.123	2.474	< 0.001
agriculture	0.520	0.008	1.682	1.657	1.707	< 0.001
others	2.061	0.036	7.850	7.312	8.428	< 0.001
Area						
urban*	0.000	-	-	-	-	-
rural	-0.422	0.035	0.655	0.612	0.702	< 0.001
Target						
civil*	0.000	-	-	-	-	-
civil officer	-0.006	0.031	0.994	0.935	1.057	0.850
police	0.321	0.045	1.378	1.262	1.506	< 0.001
military	1.521	0.038	4.578	4.246	4.936	< 0.001
Festival						
religious*	0.000	-	-	-	-	-
public holiday	0.375	0.015	1.455	1.413	1.498	< 0.001
general	0.486	0.034	1.626	1.520	1.738	< 0.001
Attack						
bombing*	0.000	-	-	-	-	-
shooting	0.719	0.029	2.052	1.939	2.170	< 0.001
others	-2.180	0.018	0.113	0.109	0.117	< 0.001

The multinomial logistic regression results in Table 4 indicate that the likelihood of injury, relative to safe outcomes, varies systematically across temporal, spatial, and contextual factors. Several months, particularly January, February, July, and September, are associated with significantly higher odds of injury compared to April, while October through December show reduced injury risk, suggesting seasonal variation in event severity. Day-of-week effects further reveal that incidents later in the week are more likely to result in injury, whereas Wednesday and nighttime events are associated with lower odds of injury. Together, these temporal patterns indicate that injury severity is not uniformly distributed across calendar or daily cycles. Spatial and situational characteristics exert stronger and more consistent effects. Events occurring in

Narathiwat and Yala provinces are more likely to result in injury than those in Pattani, while Songkhla exhibits a substantially lower risk. Incidents in non-residential zones—particularly public places, roads, business areas, and security-related locations—are associated with markedly higher injury odds, highlighting the heightened vulnerability of these settings. Attacks targeting police and military personnel also display substantially elevated injury risk relative to civilian targets. In addition, shooting incidents are associated with more than twice the odds of injury compared to bombings, whereas other attack types are linked to significantly lower injury likelihood. Overall, the results underscore the importance of considering contextual and tactical heterogeneity when modeling victimization severity, reinforcing the suitability of a multinomial framework for capturing differentiated outcome patterns. On the other hand, the likelihood of death, which is related to safe outcomes, is presented in Table 5.

Table 5. MLR model ref. safe vs. dead

	Estimate	SE	OR	CI Lower	CI Upper	p-value
Constant	-189.767	0.000	0.000	0.000	0.000	< 0.001
Month						
January	0.596	0.041	1.816	1.674	1.969	< 0.001
February	0.425	0.040	1.529	1.414	1.653	< 0.001
March	0.175	0.040	1.191	1.100	1.289	< 0.001
April*	0.000	-	-	-	-	-
May	0.378	0.041	1.459	1.346	1.582	< 0.001
June	0.434	0.041	1.544	1.425	1.673	< 0.001
July	0.443	0.039	1.558	1.442	1.683	< 0.001
August	0.408	0.039	1.505	1.393	1.625	< 0.001
September	0.420	0.040	1.521	1.406	1.646	< 0.001
October	-0.004	0.038	0.996	0.925	1.072	0.918
November	0.117	0.039	1.124	1.041	1.214	0.003
December	0.185	0.043	1.203	1.107	1.309	< 0.001
Day						
Sunday*	0.000	-	-	-	-	-
Monday	-0.093	0.029	0.911	0.861	0.963	0.001
Tuesday	0.227	0.029	1.255	1.186	1.328	< 0.001
Wednesday	-0.134	0.028	0.875	0.827	0.925	< 0.001
Thursday	0.049	0.029	1.050	0.993	1.111	0.086
Friday	0.148	0.030	1.159	1.093	1.230	< 0.001
Saturday	0.135	0.030	1.145	1.080	1.214	< 0.001
Time						
morning*	0.000	-	-	-	-	-
afternoon	-0.137	0.028	0.872	0.825	0.922	< 0.001
evening	-0.252	0.028	0.777	0.736	0.820	< 0.001
night	-0.449	0.015	0.638	0.620	0.658	< 0.001
Province						
Pattani*	0.000	1.000	-	-	-	-
Narathiwat	0.108	0.028	1.114	1.054	1.177	< 0.001
Yala	0.061	0.031	1.063	1.001	1.129	0.047
Songkhla	-0.460	0.006	0.631	0.624	0.639	< 0.001

Table 5. MLR model ref. safe vs. dead (continus)

	Estimate	SE	OR	CI Lower	CI Upper	p-value
Zone						
resident*	0.000	-	-	-	-	-
bases and checkpoints	0.551	0.004	1.735	1.723	1.747	< 0.001
public places	1.535	0.035	4.642	4.338	4.966	< 0.001
road	1.058	0.023	2.880	2.752	3.013	< 0.001
business	0.822	0.036	2.275	2.120	2.441	< 0.001
agriculture	0.938	0.009	2.556	2.512	2.600	< 0.001
others	1.540	0.035	4.663	4.355	4.992	< 0.001
Area						
urban*	0.000	-	-	-	-	-
rural	-0.270	0.034	0.763	0.714	0.815	< 0.001
Target						
civil*	0.000	-	-	-	-	-
civil officer	0.169	0.032	1.184	1.112	1.261	< 0.001
police	-0.115	0.041	0.891	0.823	0.965	0.005
military	0.908	0.036	2.480	2.309	2.664	< 0.001
Festival						
religious*	0.000	-	-	-	-	-
public holiday	0.183	0.014	1.201	1.168	1.235	< 0.001
general	0.381	0.034	1.463	1.370	1.562	< 0.001
Attack						
bombing*	0.000	-	-	-	-	-
shooting	2.762	0.028	15.826	14.988	16.710	< 0.001
others	-0.446	0.020	0.640	0.615	0.666	< 0.001

Table 5 presents the multinomial logistic regression results comparing fatal versus safe outcomes, with safe events specified as the reference category. Strong and consistent temporal patterns are evident. Relative to April, almost all months are associated with significantly higher odds of fatal outcomes, particularly during the first three quarters of the year, indicating a pronounced seasonal escalation in lethality. Day-of-week effects further reveal elevated fatal risk for incidents occurring on Tuesdays, Fridays, and Saturdays, whereas Mondays and Wednesdays are associated with reduced odds of death. Time-of-day effects show a clear gradient, with incidents occurring in the afternoon, evening, and especially at night exhibiting substantially lower odds of fatality compared to morning events, suggesting that the most lethal incidents tend to occur earlier in the day. Spatial and situational factors emerge as the dominant determinants of fatal outcomes. Compared to Pattani province, events in Narathiwat and Yala show modestly higher odds of death, while Songkhla consistently exhibits substantially lower fatal risk. Incidents occurring outside residential areas are markedly more lethal: public places, roads, business areas, agricultural zones, and security-related locations such as bases and checkpoints all demonstrate dramatically elevated odds of death relative to residential settings, with effect sizes far exceeding those observed for injury outcomes. Rural areas are associated with lower fatal risk than urban areas, highlighting important contextual differences in escalation dynamics. Target characteristics further differentiate severity, with attacks against military targets showing more than double the odds of fatality compared to civilian targets, while police targets exhibit slightly lower fatality risk. Finally, attack modality displays the strongest effect in the model: shooting incidents are associated with an exceptionally large increase in the odds of death relative to bombings, underscoring the extreme lethality of

direct-fire tactics. Collectively, these findings indicate that fatal outcomes are driven primarily by location, target type, and attack modality, reinforcing the importance of modeling severity as a multinomial process rather than collapsing outcomes into a binary framework.

Taken together, the results from Tables 4 and 5 reveal several common structural patterns governing both injury and fatal outcomes, albeit with differing magnitudes. Across both severity levels, victimization risk exhibits clear temporal regularities, with elevated odds concentrated in specific months and on particular days of the week, indicating that conflict severity is shaped by recurring patterns of activity and exposure rather than random occurrence. While temporal effects are more pronounced for fatal outcomes, both models consistently demonstrate that severity varies across calendar cycles, reflecting systematic shifts in operational intensity over time. This temporal factor finding aligns with Summer et al. [5], who found that successful incidents were more likely to be perpetrated by individuals living more than 100 miles from the target location. Most notably, spatial and situational factors emerge as the dominant shared determinants of injury and fatal outcomes. In both models, incidents occurring in non-residential environments—such as public places, roads, business districts, agricultural zones, and security-related locations—are associated with substantially higher odds of harm relative to residential areas. These settings often involve greater population exposure and a higher potential for property damage, particularly during large-scale or coordinated attacks, which, in turn, increases the likelihood of casualties [6]. Spatial patterns also converge across provinces, with events in Narathiwat and Yala consistently exhibiting higher severity risk than those in Pattani, while Songkhla demonstrates a persistently lower risk, suggesting important regional differences in conflict dynamics and security control.

Target characteristics further reinforce shared escalation mechanisms. Attacks directed at military targets are consistently associated with elevated odds of both injury and fatal outcomes compared to civilian targets, reflecting the inherently confrontational nature of engagements involving security forces as represented in [7, 8]. While bombing attacks frequently result in substantial property damage and widespread disruption, their association with human casualties is more moderate relative to shooting incidents, which emerge as the most severe attack modality across both models. Shooting attacks significantly increase the likelihood of injury and, more strongly, fatal outcomes, highlighting the heightened lethality of direct-fire methods and their shared risk determinants across attack modalities and temporal patterns [9]. Collectively, these shared findings indicate that while injury and fatal outcomes differ in intensity, they are driven by a largely overlapping set of contextual, target-specific, and tactical factors, reinforcing the importance of modeling victimization severity using a multinomial framework that captures both common escalation pathways and outcome-specific effects. Next, Figures 3 and 4 present a log-scale forest plot of odds ratios with confidence intervals, facilitating comparison of effect magnitude and statistical uncertainty across predictors and outcome contrasts.

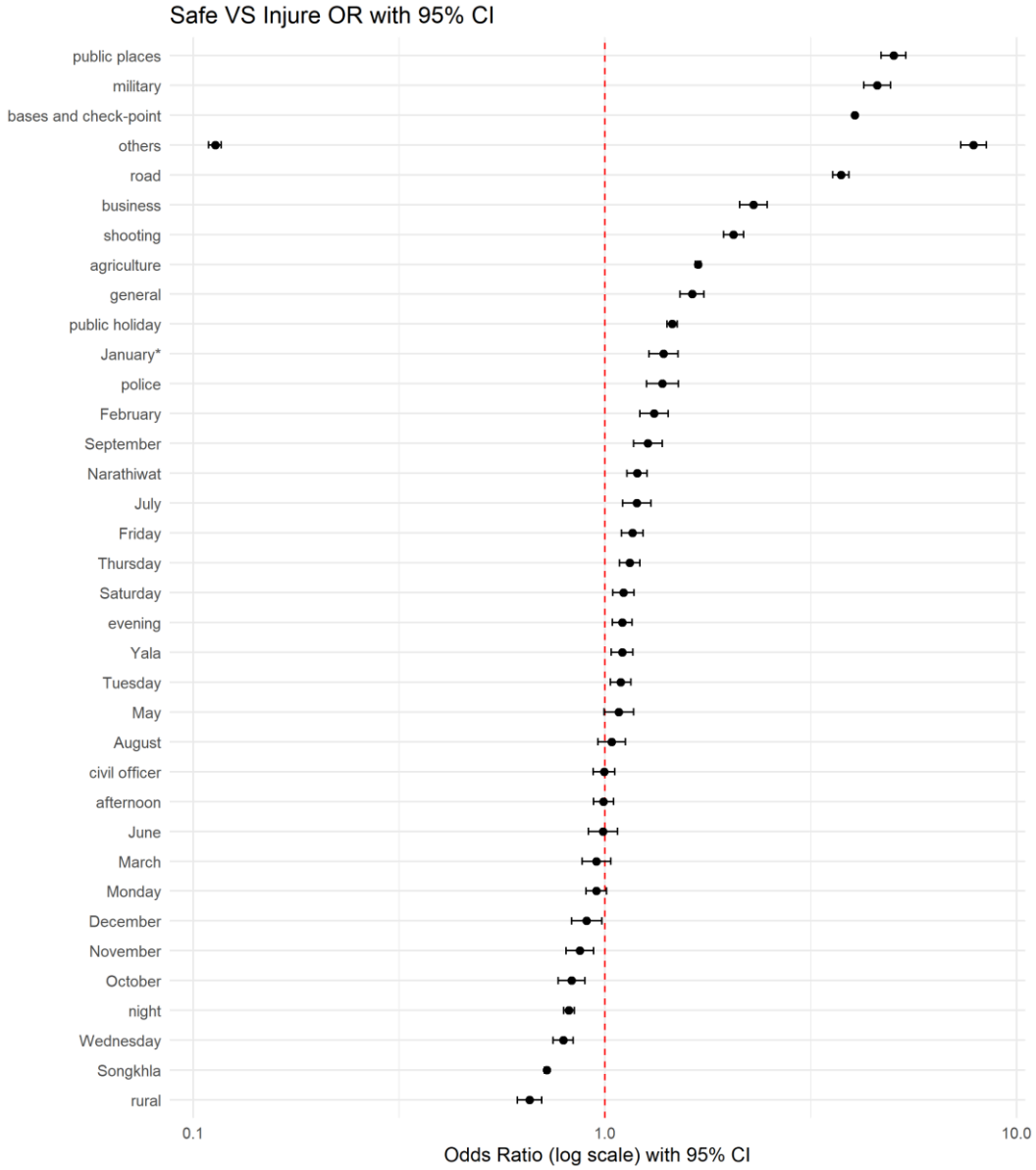

Figure 3. The 95% CI plot of Safe vs Injured

Figure 3 presents a log-scale forest plot of odds ratios with 95% confidence intervals for the injured versus safe comparison. Predictors with confidence intervals entirely above one indicate an increased likelihood of injury relative to safe outcomes, while those with intervals below one are associated with reduced injury risk. The plot shows that location- and target-related factors, particularly incidents in non-residential zones and attacks against security forces, exhibit the strongest positive associations with injury. In contrast, several temporal factors and rural settings are associated with a lower likelihood of injury. The width of some confidence intervals reflects uncertainty arising from data sparsity and outcome imbalance, but the overall pattern reinforces the importance of situational and contextual determinants in shaping injury severity.

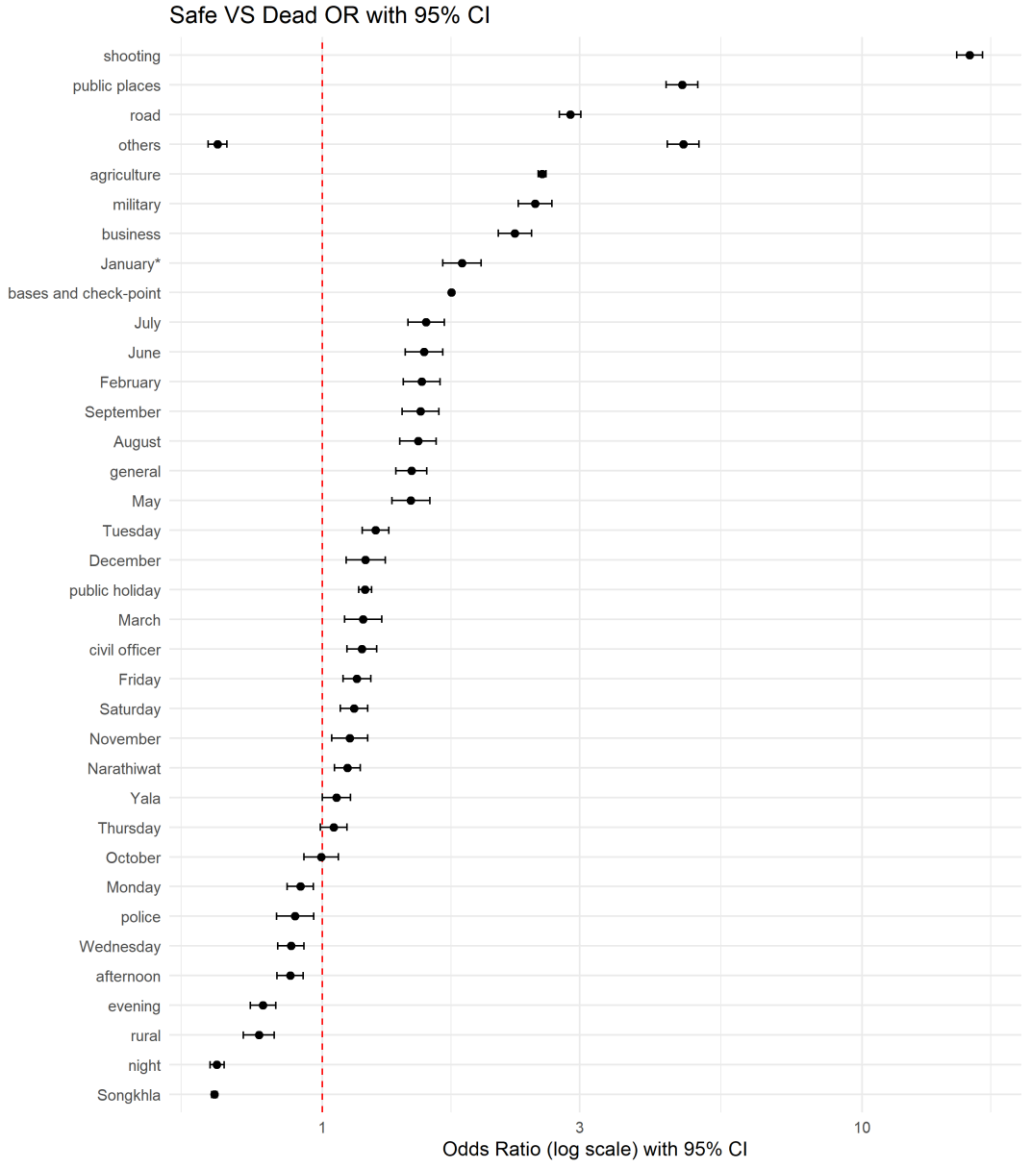

Figure 4. The 95% CI plot of Safe vs Dead

The dead versus safe comparison, Figure 4, indicates that fatal outcomes are driven primarily by situational and tactical factors, with the largest increases in odds observed for shooting incidents, non-residential locations (particularly public places and roads), and security-related targets. These effects are substantially stronger than those observed for injury outcomes, highlighting a clear escalation mechanism associated with attack modality and location. In contrast, several temporal factors, rural settings, and specific provinces exhibit odds ratios below one, indicating reduced likelihood of fatal outcomes relative to safe events. Although some confidence intervals are wide—reflecting the rarity of fatal events—the overall pattern demonstrates that lethality is dominated by where and how attacks occur, rather than by timing alone.

3.3 Performance Evaluation

The predictive performance of the multinomial logistic regression models was evaluated using classification-based metrics, with particular attention to outcome imbalance across severity categories. Model discrimination was assessed using receiver operating characteristic (ROC) curves and the corresponding area under the curve (AUC), computed separately for each outcome category as presented in Figure 5. In addition, confusion matrices expressed as row-wise percentages were used to evaluate classification accuracy conditional on the true outcome class, providing an interpretable assessment of model performance under imbalanced class distributions.

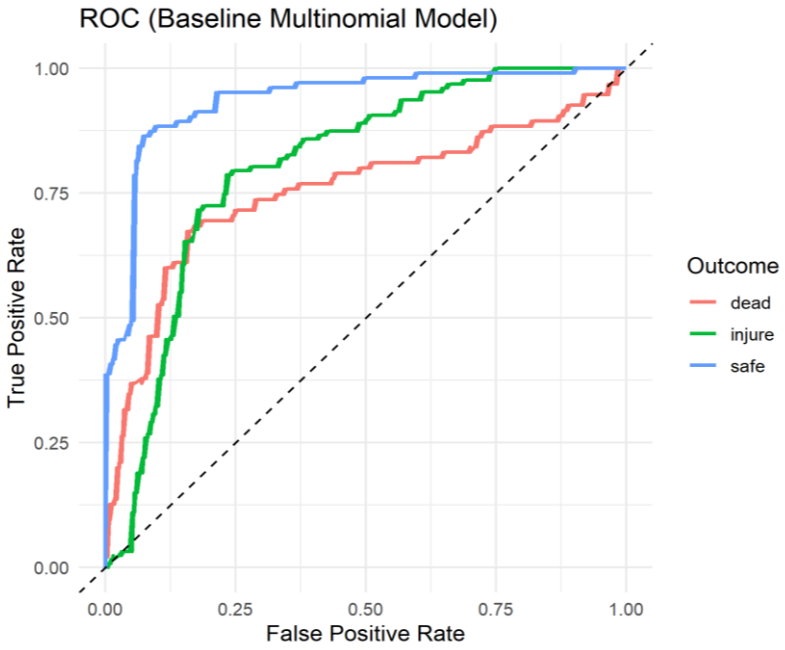

Figure 5. ROC curve model discrimination

The area under the ROC curve (AUC) values in Figure 2 indicate that the baseline multinomial logistic regression model demonstrates strong overall discriminatory ability, with performance varying across outcome categories. The model achieves an AUC of 94% for the safe outcome, indicating excellent discrimination and indicating that safe events are identified with high accuracy. This result is expected given that safe cases constitute the majority of observations and exhibit more stable patterns. For the injured outcome, the AUC of 80% suggests good discrimination, indicating that the model can reasonably distinguish injury events from other outcome categories. While performance is lower than for safe outcomes, the AUC remains well above conventional thresholds for acceptable classification, demonstrating that the model meaningfully captures injury-related patterns. The dead outcome yields an AUC of 75%, representing moderate but informative discrimination. This comparatively lower value reflects the inherent difficulty of predicting rare, heterogeneous fatal events. Importantly, the AUC remains substantially above the random classification benchmark (0.5), indicating that the model retains predictive value even for the most severe outcome category. Overall, the decreasing AUC values across severity levels reveal a clear severity gradient in predictive performance, with the strongest discrimination for non-severe outcomes and reduced—but still meaningful—performance for fatal events. This pattern underscores both the challenges posed by class imbalance and the necessity of complementary evaluation using weighted models and additional performance metrics. Next, the confusion matrix results further reveal that misclassification primarily occurs between adjacent severity categories, with fewer extreme errors between safe and fatal outcomes. This suggests that while prediction uncertainty remains—especially for rare fatal events—the model captures meaningful structure in severity differentiation. Collectively, these findings indicate that the weighted multinomial model provides a balanced and robust predictive framework for modeling event-level victimization severity in the presence of substantial class imbalance.

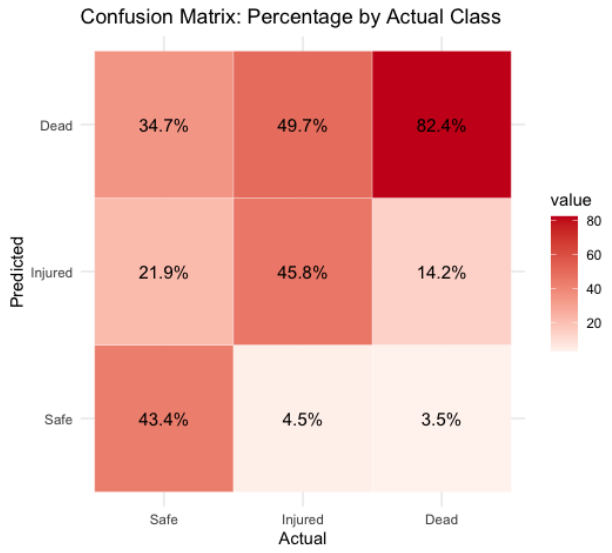

Figure 6. Confusion matrix of southern unrest victimization

The confusion matrix in Figure 6 reveals significant variation in the model's ability to classify outcomes across the three categories of southern unrest victimization: safe, injured, and dead. For dead, the model demonstrates strong performance with a recall of 82.4%, indicating it successfully identifies over 80% of actual fatalities. However, its precision for dead is moderate (59.3%), meaning that nearly 40% of predicted "dead" cases were false alarms (misclassified as safe or injured). This suggests the model errs on the side of caution for fatalities, which could be critical for emergency response but may strain resources due to overprediction. For Injured, precision was the highest among all classes (68.8%), showing that when the model predicts an injury, it is correct ~69% of the time. However, its recall is notably lower (45.8%), revealing that over half of actual injuries are missed (often misclassified as Dead). This gap signals a need to improve sensitivity to injury cases, possibly by addressing class imbalance or refining feature selection. The Safe category performs poorly across both metrics, with the lowest recall (43.4%) and modest precision (59.4%). This means the model fails to detect more than half of truly safe cases (mislabeling them as injured/dead) and incorrectly predicts safety in ~40% of cases.

Such errors could undermine trust in the system, especially if used for risk assessment. A series of sensitivity analyses was conducted to assess the robustness of the estimated effects and predictive performance. First, to evaluate the impact of outcome imbalance, all analyses were performed using both a baseline multinomial logistic regression model and an imbalance-adjusted weighted specification. While the weighted model yielded improved sensitivity for injury and fatal outcomes, the overall direction and relative magnitude of estimated effects remained consistent across model specifications, indicating that the weighting strategy does not drive the substantive conclusions. Second, the IIA assumption underlying the multinomial framework was examined using the Hausman–McFadden test. As commonly observed in imbalanced outcome settings, the test produced numerically unstable statistics, limiting definitive inference regarding strict adherence to IIA. To mitigate this limitation, additional robustness checks were conducted, including alternative predictor specifications and comparison with an ordinal logistic regression model. The consistency of results across these analyses suggests that potential deviations from the IIA assumption do not materially affect the study's conclusions. Third, model stability was assessed using k-fold cross-validation, with performance metrics averaged across folds. The cross-validated results demonstrate stable discrimination across outcome categories, with only modest fold-to-fold variability, supporting the generalizability of the fitted models. Collectively, these robustness checks indicate that the findings are stable across alternative modeling choices and are not sensitive to specific assumptions or estimation procedures.

3.3 Discussion and Limitation

Beyond the empirical findings, this study contributes methodologically and contextually to the understanding of victimization severity in subnational conflict settings. The application of multinomial logistic regression (MLR) enables explicit differentiation between safe, injured, and fatal outcomes, allowing severity-specific risk mechanisms to be examined without collapsing heterogeneous outcomes into a binary framework. While ensemble machine learning approaches such as Random Forests or Support Vector Machines have been widely applied in terrorism and conflict risk modeling [2, 10]. MLR offers a distinct advantage in terms of interpretability, providing transparent estimates of effect size and direction that can be clearly communicated to policymakers. This transparency is particularly important in conflict-affected regions, where security decisions require justification and accountability. From a behavioral perspective, the heightened vulnerability of military personnel to both injury and fatal outcomes likely reflects the symbolic and strategic value of such targets to insurgent groups. This finding aligns with theories in the civil war literature that conceptualize selective violence as a form of strategic communication intended to undermine state authority or morale [11]. The distinction between the elevated injury risk for police personnel and the lack of a corresponding increase in fatality risk further suggests differentiated targeting logics, potentially influenced by perceived threat levels, engagement rules, or operational constraints [12].

The spatial dynamics observed in this study also resonate with geographic theories of conflict vulnerability. Incidents occurring in public places, roads, business districts, and agricultural areas exhibit substantially higher odds of severe victimization, reflecting increased exposure, population flow, and limited protective infrastructure. Such environments are also more prone to property damage, particularly during coordinated or high-impact attacks. Prior research on African civil wars has similarly documented that violence often clusters in accessible, high-traffic locations where territorial control is contested or shifts frequently [13]. These findings underscore the importance of geographically targeted intervention strategies, including infrastructural reinforcement and surveillance in transit corridors and economic zones. Temporal variations further reveal meaningful escalation patterns. The finding that nighttime attacks are significantly less lethal suggests constraints related to tactical visibility, logistics, or coordination after dark. This pattern is consistent with evidence from other conflict regions, where nighttime engagement tends to be lower due to operational limitations and heightened detection risk [14]. Counterinsurgency planning and public safety operations could therefore be optimized by aligning patrol intensity and surveillance resources with time-specific risk profiles, particularly during morning and daytime periods when fatal outcomes are more likely. Despite these contributions, several limitations should be acknowledged. First, the analysis relies on event-level aggregation using a maximum-severity rule, in which the most severe observed outcome is used to classify each incident. While this approach preserves operational relevance and aligns with common practice in conflict event analysis, it necessarily obscures within-event variation in casualty counts and injury severity. Future research could extend this framework using count-based, ordinal, or hierarchical models to capture casualty intensity more granularly while retaining event-level interpretability.

Second, although multinomial logistic regression provides a flexible and interpretable framework, it relies on the independence of irrelevant alternatives (IIA) assumption. Formal diagnostic testing yielded numerically unstable results, a known limitation in imbalanced multiclass conflict data. To address this concern, robustness checks using alternative model specifications, including ordinal logistic regression, were conducted and yielded substantively consistent findings. Nonetheless, future studies may consider modeling approaches that explicitly relax the IIA assumption, such as nested or mixed logit models, where data availability permits. Third, the dataset exhibits substantial imbalance in outcomes, with injury and fatal events accounting for the majority of observations. Although imbalance-aware modeling strategies were implemented and predictive performance was evaluated using multiple metrics, including ROC curves and confusion matrices, classification performance for rare and heterogeneous outcomes—particularly fatal events—remains constrained by data sparsity. Expanding the temporal scope or integrating additional conflict datasets may further enhance model stability and predictive accuracy. Finally, while this study focuses on incident-level characteristics, future research should incorporate demographic risk factors, such as age, gender, and occupation, to better understand which groups are most vulnerable. Reports from global conflict

databases, including the Geneva Declaration Secretariat and the Uppsala Conflict Data Program, have highlighted the uneven burden of violence among civilian populations, which may be masked in aggregate models [15]. Integrating such disaggregated information would enhance humanitarian targeting and resource allocation. Taken together, these contextual and methodological discussions extend the policy relevance of the findings and position this study as both an interpretable predictive tool and a framework for deeper causal inquiry into subnational conflict dynamics.

4. Conclusions

This study examined the determinants of conflict-related victimization severity in Thailand's southernmost provinces using event-level data from 9,310 unrest incidents recorded between 2004 and 2020. By applying multinomial logistic regression, the analysis explicitly differentiated between safe, injured, and fatal outcomes, allowing severity-specific risk mechanisms to be identified without collapsing heterogeneous outcomes into a binary framework. The results demonstrate that victimization severity is shaped primarily by spatial context, target type, and attack modality, with temporal factors playing a secondary but consistent role. Incidents occurring in non-residential locations—particularly public places, roads, agricultural areas, and security-related zones—are associated with substantially elevated risks of both injury and fatality. Attacks targeting military personnel exhibit markedly higher odds of severe outcomes, reflecting the confrontational nature and strategic salience of such targets. Among attack modalities, shooting incidents emerge as the most lethal, exhibiting an order-of-magnitude increase in fatal risk compared to bombings, underscoring the extreme lethality of direct-fire tactics. From a predictive perspective, the multinomial framework demonstrates strong discrimination for safe events and moderate but informative performance for injury and fatal outcomes, despite substantial class imbalance. Sensitivity analyses confirm that the substantive findings are robust across baseline and weighted model specifications, alternative predictor sets, and validation strategies. Although formal testing of the independence of irrelevant alternatives (IIA) assumption yielded unstable results—common in imbalanced multiclass settings—comparative analyses indicate that potential deviations do not materially affect the study's conclusions. Methodologically, this study reinforces the value of multinomial logistic regression as an interpretable benchmark for conflict analytics. While more complex machine learning models may achieve higher predictive accuracy, the transparency of odds ratios and confidence intervals provides policymakers with actionable insights for resource allocation, patrol planning, and civilian protection. The proposed analytical workflow—combining transparent preprocessing, imbalance-aware modeling, and comprehensive performance evaluation—offers a reproducible framework applicable to other subnational conflict settings. Several limitations warrant acknowledgment. Aggregating victimization-level records into event-level outcomes using a maximum-severity rule prioritizes operational relevance but obscures within-event variation in casualties. Future research could extend this framework using hierarchical, count-based, or ordinal models to capture casualty intensity more granularly. Additionally, integrating real-time geospatial data, demographic attributes, and dynamic conflict indicators may further enhance predictive performance and policy relevance. Overall, this study provides empirical evidence and methodological guidance for modeling conflict related to victimization severity. By demonstrating how interpretable statistical models can capture differentiated escalation pathways, the findings support the integration of data-driven analytics into evidence-based security planning and early-warning systems in conflict-affected regions.

5. Acknowledgements

The author would like to express sincere gratitude to the Department of Engineering Science, Faculty of Engineering, The University of Auckland, for their generous support and guidance throughout the practicum and research thesis. Their valuable advice, technical assistance, and academic insights greatly contributed to the successful completion of this study. The department's encouragement and resources were instrumental in shaping the research process and enhancing the quality of the outcomes.

Author Contributions: Conceptualization, A.M., R.M., and M.E.; Methodology, A.M., R.M., and M.E.; Formal analysis and investigation, A.M., R.M., and M.E.; Writing–original draft preparation, A.M. and R.M.; Writing–

review and editing, A.M. and R.M.; Supervision, R.M. and M.E.; Project administration, R.M.; Funding acquisition, A.M., R.M., and M.E.

Funding: This research was funded by the Digital Science for Economy, Society, Human Resources, Innovative Development, and Environment Project by Reinventing Universities & Research Institutes, under grant no. 2046735, Ministry of Higher Education, Science, Research and Innovation, Thailand, and the Overseas Thesis Research grant, Graduate School, Prince of Songkla University, under the grant no. OTR2566-008.

Conflicts of Interest: The authors declare no conflict of interest.

References

[1] Brandt, P. T.; Mason, T. D.; Gurses, M.; Petrovsky, N.; Radin, D. *When and How the Fighting Stops: Explaining the Duration and Outcome of Civil Wars. Def. Peace Econ.* **2008**, *19*(6), 415–434. https://doi.org/10.1080/10242690701823267

[2] Olabanjo, O. A.; Aribisala, B. S.; Mazzara, M.; Wusu, A. S. *An Ensemble Learning Model for the Prediction of Danger Zones: Towards a Global Counter-Terrorism. J. Soft Comput. Lett.* **2021**, *3*, 1–6. https://doi.org/10.1016/j.socl.2021.100020

[3] Erbas, I.; Vargas, D. A.; Guclu, B. *FPGA Implementation of Multinomial Logistic Regression for Vibrotactile Feedback in a Robotic Hand.* In *2020 International Conference on e-Health and Bioengineering (EHB)*; IEEE, 2020; pp 1–4. https://doi.org/10.1109/EHB50910.2020.9280239

[4] Wilkinson, K.; Seo, K.; Pierce, R.; Tonellato, P.; Kim, J. H.; Myers, D. *Electronic Medical Record Specialty Group Comparison by Multinomial Logistic Regression.* In *2021 IEEE 9th International Conference on Healthcare Informatics (ICHI)*; IEEE, 2021; pp 415–421. https://doi.org/10.1109/ICHI52183.2021.00067

[5] Summer, J.; Ratcliff, K.; Smith, B. *Spatial Analysis of U.S. Terrorism Incidents.* National Consortium for the Study of Terrorism and Responses to Terrorism (START), 2017. 1-4.

[6] Miller, E. *Use of Firearms in Terrorist Attacks in the United States, 1970–2014.* START, 2015. http://www.start.umd.edu/pubs/START_FirearmsinTerrorism_BackgroundReport_July2015.pdf

[7] Boonthep, N.; Intharachat, S.; Iemsomboon, T. *Factors Influencing Injury Severity Score Regarding Thai Military Personnel Injured in Mass Casualty Incident April 10, 2010: Lessons Learned from Armed Conflict Casualties: A Retrospective Study. BMC Emerg. Med.* **2012**, *12*(1), 1-7. https://doi.org/10.1186/1471-227X-12-1

[8] Eso, M.; McNeil, R.; Masamae, A. *Factors Associated with Severe Violent Events in the Southernmost Provinces of Thailand. Adv. Appl. Stat.* **2020**, *63*(1), 59–74. https://doi.org/10.17654/AS063010059

[9] Stelmach, J.; Moch, N. *Time in Responding to Terrorist Attacks in Cities. Sustainability* **2022**, *14* (21), 1-19. https://doi.org/10.3390/su142416643

[10] Peng, A. *An Integrated Machine Learning Approach to Studying Terrorism.* B.S. Thesis, Department of Computer Science, Yale University, New Haven, CT, 2018.

[11] Kalyvas, S. N. *The Logic of Violence in Civil War*; Cambridge University Press: Cambridge, 2006. https://doi.org/10.1017/CBO9780511818462

[12] Shapiro, J.; Siegel, D. A. *Coordination and Security: How Mobile Communications Affect Insurgency. J. Peace Res.* **2015**, *52* (3), 312–322. https://doi.org/10.1177/0022343314559624

[13] Buhaug, H.; Rod, J. K. *Local Determinants of African Civil Wars, 1970–2001. Polit. Geogr.* **2006**, *25*(3), 315–335. https://doi.org/10.1016/j.polgeo.2006.02.005

[14] Lafree, G.; Dugan, L. *Introducing the Global Terrorism Database. Terror. Polit. Violence* **2007**, *19*(2), 181–204. https://doi.org/10.1080/09546550701246817

[15] Geneva Declaration Secretariat. *Global Burden of Armed Violence.* September 2008. https://www.refworld.org/reference/research/gds/2008/en/64390

ASEAN
Journal of Scientific and Technological Reports
Online ISSN:2773-8752

Research article

An Academic Extension-Driven Solution for Enhancing Local Governance

Dawn Iris Calibo-Senit[1*]

[1] College of Technology, Siquijor State College, Larena, Siquijor, 6226, Philippines
* Correspondence: dawniriscalibo@gmail.com

Citation:
Calibo-Senit, DI.; An academic extension-driven solution for enhancing local governance. *ASEAN J. Sci. Tech. Report.* **2026**, *29*(3), e261914. https://doi.org/10.55164/ajstr.v29i3.261914.

Article history:
Received: October 16, 2025
Revised: January 27, 2026
Accepted: February 5, 2026
Available online: February 28, 2026

Abstract: Despite the rise of the e-governance agenda in supporting local government operations, the involvement of higher education in promoting a collaborative extension initiative supporting such an agenda remains scarce in the literature, especially in rural communities with low digital literacy. Thus, this work details the development and implementation of the Cangbagsa Digital Barangay Information System (CDBIS), an academically driven extension solution that addresses inefficiencies in barangay (i.e., the Philippines' smallest administrative unit) operations. Prior challenges included processing documents within 2–3 days, data inaccuracies, and limited service accessibility. This study aims to digitize local governance, improve efficiency, ensure data integrity, and create a scalable model for community innovation. The system was developed using a web-based, multi-tier architecture that integrates a user-friendly interface, role-based business logic, a centralized database, and secure server infrastructure to support efficient barangay data management and decision-making. The post-implementation evaluation uses the Updated DeLone and McLean Information System Success Model and a 22-item survey for system users, using a 7-point Likert scale. Data from the survey were analyzed through descriptive statistics and stepwise regression to identify predictors of user satisfaction. Respondents rated all constructs highly. Regression analysis shows System Quality as the strongest predictor of satisfaction (β=0.361), followed by Service (β=0.295) and Information Quality (β=0.287), explaining 65% of the variance. CDBIS significantly improved governance, reducing processing time by 75% and improving data accuracy by 88%. Sustaining success requires ongoing optimization, training, and user engagement. The system offers a replicable model for digital transformation in other rural communities.

Keywords: Barangay information system; e-governance; digital transformation; system development; local governance

1. Introduction

Barangays, the Philippines' smallest administrative units, are the frontline of local government, as they directly interact with citizens and provide basic services. However, a significant number of these units, including Barangay Cangbagsa, a residential coastal community with 1,042 residents in 2024 and about 198 households, continue to use outdated manual systems, which undermine their capacity to manage records and provide prompt, efficient services. This dependence on paper-based procedures results in operational

bottlenecks, data inconsistencies, and restricted accessibility, ultimately affecting the quality of services they deliver to their residents. The issues at Cangbagsa, including the 2- to 3-day processing time for simple document requests, frequent data errors, and susceptibility to data loss, are symptomatic of a broader need for digital transformation in local governance.

Siquijor State College, a higher educational institution within the reach of Cangbagsa, in pursuit of its mandate for instruction, research, extension, and production, sees the urgent need for digitization in local government units. As a faculty member in Information Technology and a resident of the locality, the researcher heeded the Barangay Chief's request to address operational inefficiencies, data inconsistencies, and restricted service accessibility in Cangbagsa through a focused extension project: the design and implementation of a Digital Barangay Information System (DBIS). This project aims to transition the barangay's processes from manual to digital, streamlining administrative procedures, maintaining data integrity, and enhancing service availability, thereby demonstrating the practical application of technology to facilitate responsive and efficient local governance and to provide a replicable model for broader community innovation. Also, this project demonstrates the system's effectiveness through documentation of the processes in system design and its corresponding deliverables, offering a worthwhile model for other local government and barangay units interested in streamlining their operations and enhancing service delivery by embracing an information system solution.

In the literature, numerous studies highlight the continued reliance of local government on manual and paper-based procedures; inefficiencies, data fragmentation, and limited transparency arise from these practices [1-5]. These issues are associated with several persistent challenges at the local government level, including limited ICT infrastructure, budgetary constraints, digital skills gaps, and concerns about data privacy and security. These are supported by prior works of Islam *et al.* [6], Heidlund and Sundberg [7], and Nafi'ah [8]. Such problems highlight the desirability of systematically applying established information systems to support local e-governance initiatives. In the Philippines, for instance, Garcia *et al.* [9] highlight the challenges that persist at the grassroots level, noting that only 15% of barangays have fully adopted digital systems. This disparity underscores a critical gap that necessitates further investigation and action to bridge the technological divide in local governance.

Nevertheless, the concept of e-governance in the Philippines has gained significant traction in recent years, as government efforts aim to digitize public services for enhanced efficiency. Notably, Alampay [10] conducted a comprehensive analysis discussing the current government initiative to harmonize e-government projects. They coined it as the Medium-term Information Technology Harmonization Initiative, which prioritizes system interoperability, development of critical registries, and alignment with priority development strategies. This indicates a successful move towards modernizing government services. On the other hand, a growing body of developmental studies focuses on the design and evaluation of barangay information systems or related systems, document and issuance systems, geographic information systems, and health information platforms [11-13]. Empirical evaluations consistently indicate a high level of usability, acceptance, and perceived effectiveness of these systems in reducing administrative workload, improving data accuracy, and enhancing service delivery [14-17]. These align with national digitization efforts and legislative directions, such as the e-Governance Act of 2022, which emphasizes interoperability, cybersecurity, and digital inclusion.

When examining barangay-specific digital solutions, current literature appears limited, particularly in addressing the needs of rural barangays. Most studies focus on urban settings, with Cruz and Reyes [18] documenting several successful implementations in Metro Manila, the Philippine capital. Yet Roberts and Hernandez [19] emphasize the unique challenges rural barangays face in adopting digital technologies. It emphasizes that most marginalised communities are often the least connected and participate least in digital citizenship programmes. The application of Agile methodology within government systems has been recognized as a means to enhance digital transformation projects. The literature reveals several advantages of employing Agile practices in this context, e.g., Kupi and McBride [20]. For instance, Agile enables the faster deployment of essential features within digital platforms, significantly improving service delivery [21]. Moreover, it fosters improved stakeholder engagement throughout the development process, ensuring that

users' needs and feedback are prioritized [22]. This adaptability to changing requirements keeps government projects relevant and responsive. Lastly, the iterative nature of Agile development reduces project risks, allowing for continuous evaluation and improvement [21]. Such methodologies could be instrumental in addressing the performance issues currently faced by various e-governance initiatives in the Philippines. Despite these efforts, the agenda of involving higher education institutions in assisting digitization initiatives in rural communities draws limited attention in the literature. The involvement brings a collaborative platform that enables the productive exchange of expertise to promote the e-governance agenda, which could leapfrog future initiatives in nearby communities. Demonstrating how such development and collaboration efforts work provides critical insights into promoting e-governance in rural communities, especially in developing countries where digitization is still emerging and leaves much to be desired.

Thus, this work intends to contribute to the domain literature in three ways. First, it designs an information system that accounts for the intricacies and idiosyncrasies of Barangay Cangbagsa, a rural community. Aside from the overarching components of the proposed information system, which include the resident database, project and program monitoring, barangay directory, and analytics reports, it embeds analytics capabilities to support more informed decision-making. Second, it demonstrates the deployment of the information system to Cangbagsa, given their existing IT infrastructure and the technical expertise of their human resources. Third, it evaluates the adoption of the information system in the community and identifies specific gaps that could serve as a salient feedback mechanism for future system development efforts in similar communities.

To assess the adoption of the proposed CDBIS, the updated DeLone & McLean Information Systems Success Model [23] is deployed. This multidimensional framework examines the interdependent success metrics across distinct performance categories. This study integrates such an established model to develop a comprehensive analytical structure for interpreting findings that inform the adoption of the proposed information system and, by extension, similar systems. The model encompasses six critical dimensions of information system effectiveness: system quality, information quality, service quality, usage quality, usage patterns, user satisfaction, and net benefits. As illustrated in Figure 1, these components are interconnected: Technical attributes (system, information, and service quality) directly influence both adoption behaviors (Usage/intent) and satisfaction levels. Subsequent system engagement generates tangible benefits that later create a feedback loop, affecting continued usage and stakeholder satisfaction.

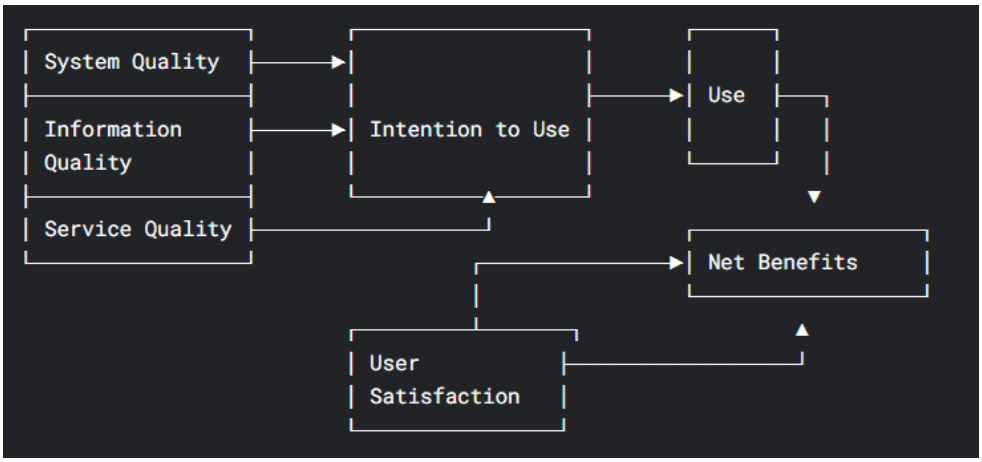

Figure 1. Updated Information Systems Success Model

In addition, the DeLone & McLean model [23] was applied in the study to support the specific objectives of assessing the CDBIS. Although the full model encompasses the elements of "Use" and "Net Benefits," these aspects were not given much emphasis, as the system's implementation is still new and its use is mandatory for all barangay officials and personnel. Therefore, assessing the "Use" of the system would not yield much variation, since all respondents (or project beneficiaries) are required to use it. Likewise, "Net

Benefits" was not considered since this study focused on the initial perceptions of the respondents regarding the quality of the system, information, and service, and not on the long-term effects of the system on the organization and community, which would require a longer period of observation and comparison of baseline data. Through the use of the contextualized model, the assessment of the system is made more practical and context-specific, focusing on the aspects that were most relevant to the initial assessment of the proposed system while recognizing that future studies could use the full DeLone & McLean model to assess the usage and socio-economic benefits of the system. Consequently, Pitt et al. [24] adapted Delone & McLean's Updated Information System Success Model for clientele retention contexts. Following Jeyaraj [25], they streamlined the framework to three core quality dimensions that collectively determine system effectiveness. This modified structure is visually presented in Figure 2. Driven by this modified structure, the study applies the adapted framework to assess the effectiveness of CDBIS as an e-governance solution. Correspondingly, the model incorporates three core dimensions: system quality (i.e., alignment with user specifications and satisfaction benchmarks), information quality (i.e., content value and utility), and service quality (i.e., technical performance against user expectations).

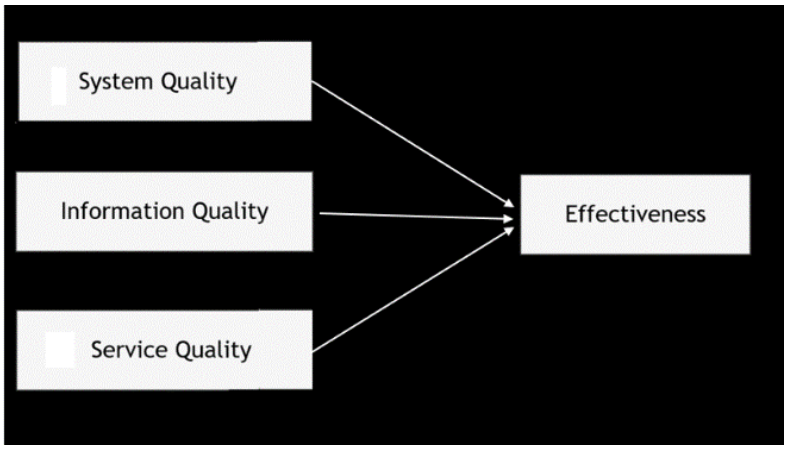

Figure 2. The Factors on the Quality of CBIS Systems' Effectiveness

2. Materials and Methods

2.1 Research Design

This study employed a developmental and descriptive approach. Specifically, it focused on the design, development, deployment, and assessment of the CDBIS as a technology-based extension initiative. The approach is appropriate for information systems research that aims to produce an operational system and empirically evaluate its effectiveness upon its implementation.

2.2 Development Paradigm

The system development follows the Agile software development methodology, which emphasizes flexibility, iterative development, and continuous stakeholder involvement. The Agile approach was selected due to the evolving requirements of barangay operations and the need for frequent feedback from barangay end users. The development process is divided into iterative cycles consisting of five phases: (1) pre-development, (2) development, (3) iteration, (4) feedback, lessons, and refining, and (5) deployment. These phases are represented in Figure 3.

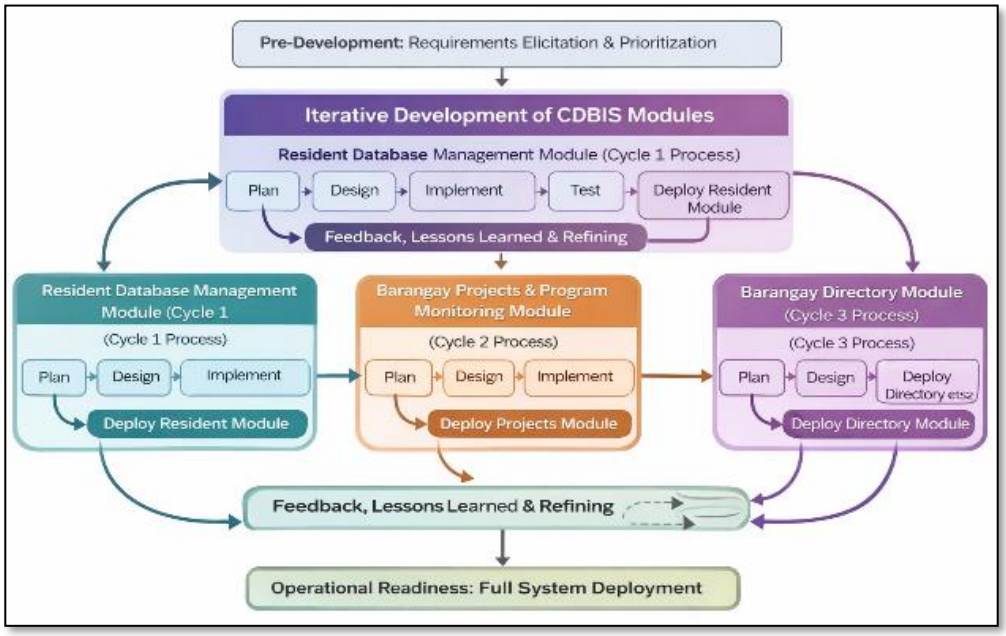

Figure 3. Iterative Development Life Cycle of the CBDIS

The CDBIS development process follows a systematic, iterative approach based on the Agile Software Development paradigm. The first stage is pre-development, where the main stakeholders or end users, including the barangay secretary, barangay captain (or Chief), selected residents, and the developer, are involved in requirements gathering and prioritization. The stage ensures that the system aligns with the community's genuine needs and that specific goals are set for the system's capabilities. Next, the project moves through three iterative development stages (sprints), each focusing on a different module. The first sprint focused on the Resident Database Management Module, which underwent planning, design, implementation, testing, and deployment. The second sprint highlights the Barangay Projects and Program Monitoring Module, which also went through the iterative development process, while the third sprint focuses on the Barangay Directory Module. The iterative processes in each of the three sprints lasted two weeks, allowing sufficient time for development, testing, and stakeholder feedback. Throughout the three sprints, continuous feedback from barangay officials and some residents was incorporated to improve the system's functionality and usability, with a user-centered approach. The development team includes the developer, the extension director, the barangay secretary, the barangay chief, IT experts, and selected residents who were actively involved in decision-making, testing, and reviewing. The system was developed using web technologies such as HTML, CSS, and JavaScript for front-end development, a relational database management system (RDBMS) for data storage, and PHP for server-side scripting. The system is hosted on a secure server environment with regular backups to ensure availability and functionality at all times. After the refinement and successful deployment of all modules, the system entered the operational readiness stage, indicating full deployment and community use.

2.3 System Architecture and Technology Stack

The CDBIS was developed as a web-based, multi-tier information system architecture to ensure accessibility, scalability, and maintainability. Its system infrastructure is illustrated in Figure 4.

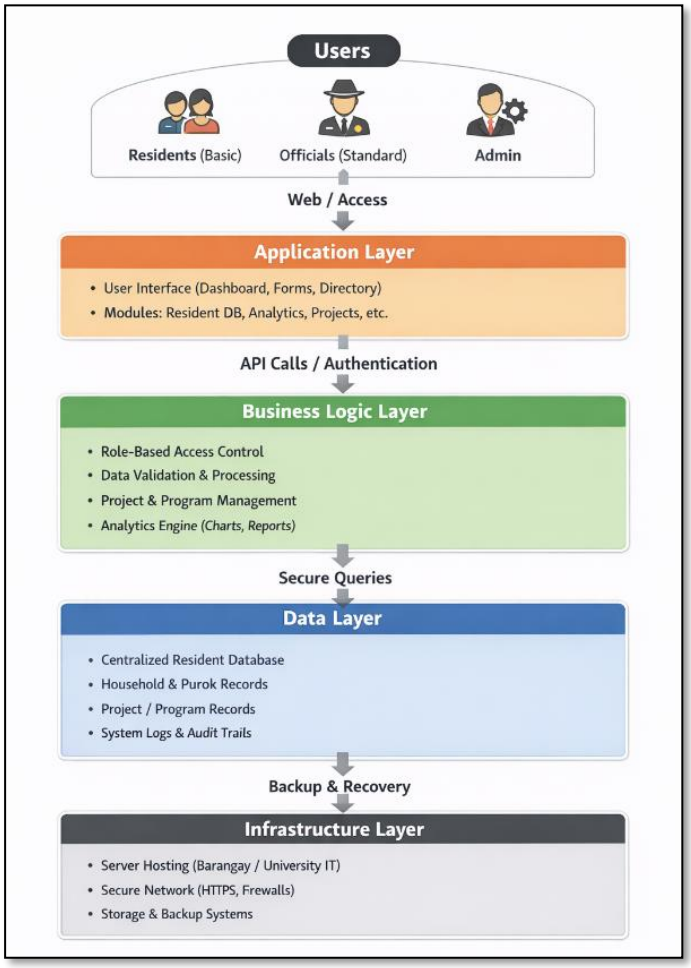

Figure 4. Cangbagsa Barangay Digital Information System Architecture

Details of the system infrastructure are provided as follows:

2.3.1 Presentation Layer

The presentation layer is the system user interface. It was built using standard web technologies like HTML, CSS, and JavaScript to ensure compatibility with most web browsers. This layer provides community and barangay officials with accessible tools, including dashboards, digital forms, and directories. Focusing on usability and responsiveness, it allows users to seamlessly engage with the system by inputting resident information, checking project updates, or searching directories.

2.3.2 Application and Business Logic Layer

This layer is the central engine of the CDBIS. It handles critical operations such as user authentication and role-based access control, ensuring that only authorized users can access confidential information. It also handles resident record management, project monitoring, and analytics processing, allowing barangay officials to make informed decisions based on real-time data. Server-side processing in this layer handles user requests and securely communicates with the database via application programming interfaces (APIs), ensuring system efficiency and security.

2.3.3 Data Layer

The data layer stores and manages structured data. Using an RDBMS, it stores data for resident profiles, household information, barangay projects, user accounts, and system logs. This structured data enables fast, precise information retrieval, supporting accurate reporting and monitoring. By centralizing community data, the system provides a solid platform for evidence-based planning and governance.

2.3.4 Infrastructure Layer

The infrastructure layer is the technical backbone of the CDBIS. It runs the system in a secure server environment and is aided by network services that provide connectivity. The system has routine backup processes integrated to eliminate data loss and ensure availability, reliability, and recoverability in the event of disruptions. This layer also provides system resilience and reliability, which allows barangay officials and residents to depend on the system for their day-to-day activities.

2.4 Security and Data Privacy Measures

To ensure the protection of personal and sensitive data, the CDBIS was developed in compliance with the Philippine Data Privacy Act of 2012 (Republic Act No. 10173). In addition, various security features were also integrated to ensure the confidentiality, integrity, and availability of data. First, Role-Based Access Control (RBAC) was implemented to ensure that users can access only data relevant to their roles, thereby minimizing the risk of unauthorized disclosure. Second, secure data transfer is also ensured through HTTPS encryption, which protects data as it is transmitted between users and the system. Third, the data integrity is also safeguarded through input validation and system checks, which prevent the entry of invalid and inconsistent data. Fourth, audit trails and logging systems are also integrated to monitor activities within the system, thus promoting accountability and transparency in system operations. And lastly, to further enhance the system's resilience, data backups and a secure server setup are also employed to ensure the system can recover in the event of failure or data loss.

2.5 Limitations

Aside from the success of the design, deployment, and evaluation of CDBIS, a few challenges hindered its deployment and evaluation. First, a good number of barangay officials and household residents have limited digital literacy skills, so additional orientation and hands-on training are deemed necessary to enable them to use the system fully. Additionally, there are some IT infrastructure limitations, such as internet connectivity and the availability of compatible devices, that occasionally affect the system's performance and usability. However, most of these challenges have been resolved and mitigated through additional user training and constant troubleshooting aided by the extension project initiated by Siquijor State College.

2.6 Sustainability

The sustainability of the CDBIS depends on clear provisions for maintenance, costs, and technical support. The system's maintenance will be addressed through regular updates and database backups to ensure reliability and security within the framework. In addition, the cost structure is mainly composed of regular software updates, network and connectivity, electricity, and minimal user training costs, which can be addressed through funding from the local government. Technical support will be provided by the faculty of the College of Technology at Siquijor State College, in coordination with the barangay through a Memorandum of Understanding, and as part of the Technology Transfer Agreement between the college and the community, ensuring that troubleshooting, updates, and user support are always available. This sustainability plan outlines the directions for the project's long-term sustainability.

2.7 System Pages

The CDBIS is a robust, web-based system designed to make barangay operations easier and more efficient. When users log in, they are presented with a clean and simple homepage that showcases the system's key features. Designed with accessibility in mind, the system's homepage provides easy access to key areas, including resident analysis, household information, project and program tracking, and the barangay directory. This one-stop access makes it convenient for barangay officials, employees, and residents to access information, manage records, and track barangay initiatives. Moreover, the homepage is not only clean and organized; it is also role-aware, dynamically changing what users see depending on their access level to ensure the security of the system's data and the smooth flow of operations. In addition to the homepage shown in Figure 5, four other modules work seamlessly together to support a particular aspect of barangay management.

Figure 5. Cangbagsa Digital Barangay Information System Homepage

These modules are presented in the following:

2.7.1 Resident Database Management Module

Figure 6 shows the Resident Database Management Page, Barangay Cangbagsa's central demographic repository. This module enables authorized personnel to easily insert, modify, search for, and view all resident and household information. Designed for processing data in real time, this module ensures that all data is up to date and accurate, helping make well-informed decisions and improve service delivery. It also enables the direct generation of official documents such as the barangay census report, making administrative processes easier and more transparent. The module is user-friendly and accounts for user roles, enabling system administrators to navigate resident, household, and voter information seamlessly.

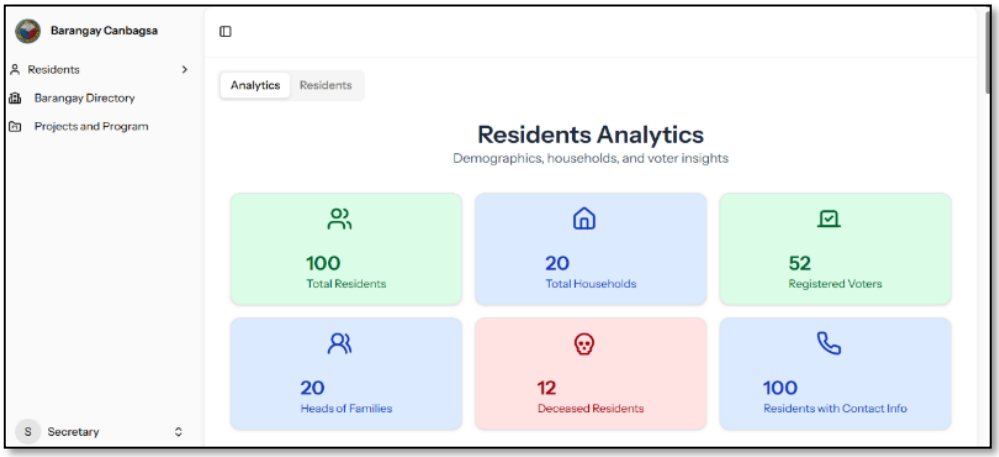

Figure 6. Resident Database Management Page

2.7.2 Barangay Projects and Program Monitoring Module

The Barangay Projects and Program Monitoring Page, as shown in Figure 7, is a dynamic, transparent platform for barangay development monitoring. It is a real-time dashboard that provides vital project information: status, timeline, and budget allocation. With this system, barangay officials and personnel can monitor project developments in real time, making informed decisions. The module can generate comprehensive reports that provide stakeholders with a complete understanding of project outcomes and ensure responsible resource management. Through its clean and interactive design, the monitoring page enhances transparency and facilitates data-driven decision-making.

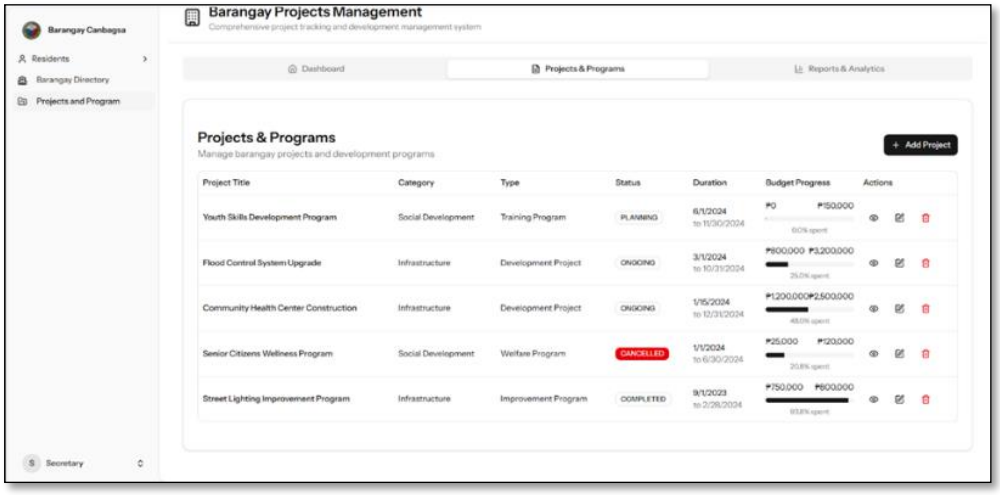

Figure 7. Barangay Projects and Program Monitoring Page

2.7.3 Barangay Directory Module

Figure 8 presents the Barangay Directory Page, a dedicated section of the information system designed to enhance transparency and foster public accessibility. This module serves as a centralized digital repository of elected barangay officials and appointed personnel, providing essential contact details, office roles, and service information in compliance with the Philippine Data Privacy Act of 2012. By making this data readily available, the directory promotes open governance and strengthens community engagement. The page also highlights key service features, including organized recordkeeping, secure system access, efficient community management, and streamlined digital services. These elements ensure that residents can easily connect with barangay offices for inquiries, transactions, and support. With clearly displayed office hours, hotline numbers, and email contacts, the directory empowers citizens to access public services with ease and confidence.

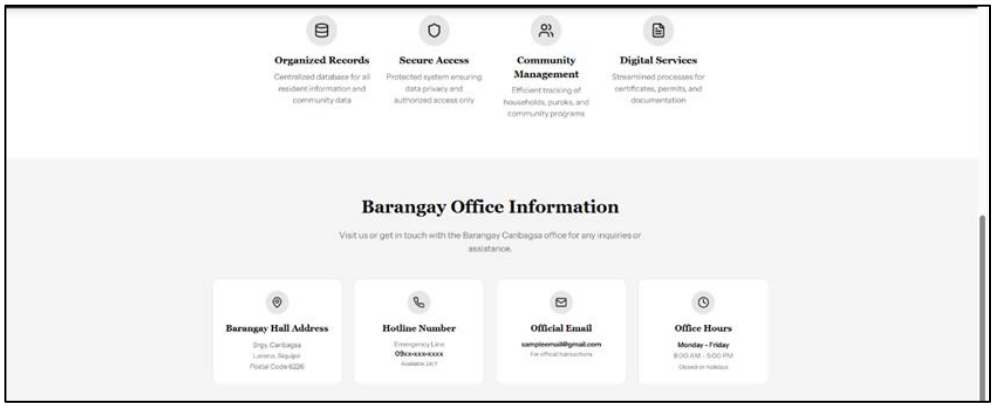

Figure 8. Barangay Directory Page

2.7.3 Analytics and Reporting Module

The Analytics and Reporting Page is the central location for data visualization and reporting within the system, designed to support evidence-based barangay governance. The page enables users to extract real-time summaries, identify trends, and generate operational reports that accurately reflect the performance of various community projects and programs. Using simple graphs and essential data points such as the number of projects, completion rates, and budget utilization, the page provides a comprehensive view of development achievements and resource allocation. Category- and status-based graphs enable barangay leaders to identify areas where progress is being made, where projects are stalled or canceled, and to adjust strategies accordingly.

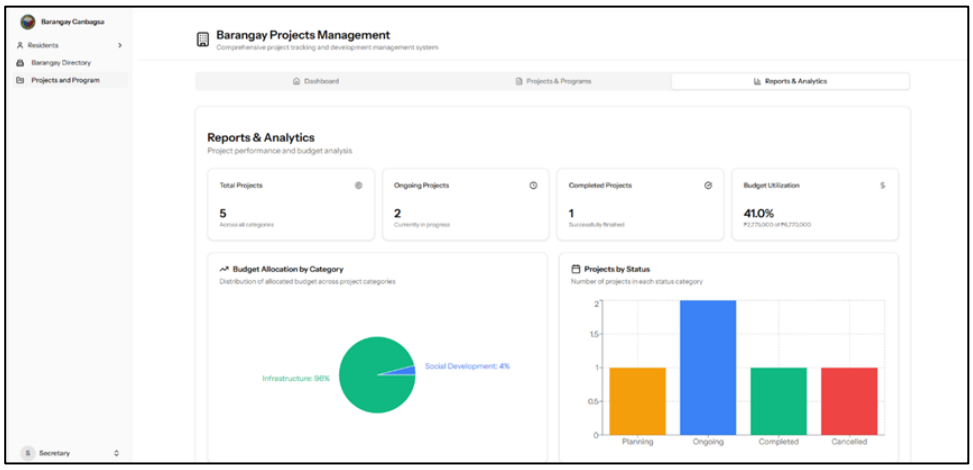

Figure 9. Analytics and Reporting Page

2.8 System Evaluation

After system implementation, a quantitative adoption evaluation was conducted to assess user satisfaction and system effectiveness. The evaluation was guided by the updated DeLone and McLean Information Systems Success Model.

2.8.1 Respondents and Data Collection

A total of 50 respondents took part in the assessment of the CDBIS. The sample includes six of eight barangay officials and personnel actively utilizing the system, accounting for 75% of the total population, and 44 household heads out of 198, representing 22% of the sample. The barangay officials offered administrative insights, while the household heads provided community-level insights. The choice of these respondent profiles ensures that the assessment was conducted properly, reflecting the experiences of both those who implement the system and those who benefit from its services. The CDBIS was assessed six months after its launch in April 2025. This allows sufficient hands-on experience for the users of the system, namely the barangay officials and the household heads, so that their feedback would be based on experience with the functional system. Before administering the survey, all respondents were reoriented to the system's characteristics and the constructs of the Updated Delone & McLean Information System Success Model to ensure they provided accurate, informed answers. Additionally, the research bias toward the local and the researcher has been eliminated, as the respondents were well-informed about the system and received hands-on experience. Pilot testing of the model's measures (or items) was deliberately skipped, as a standardized evaluation tool was adopted and the instrument had been tested for reliability in similar settings in the literature. The tool was reviewed for contextualization by three information technology experts and two barangay officials who were not part of the main survey. They maintained that the instrument was appropriate for deployment in the study environment but suggested translating it into the local dialect to facilitate better understanding by the respondents. The translation was conducted by the researcher in collaboration with the Siquijor State College Research Office to ensure it was culturally and linguistically appropriate. Informed consent was obtained from all participants before data collection to ensure they understood the purpose of the study, that their participation was voluntary, and that the information gathered would be kept confidential.

2.8.2 Instrument and Data Analysis

Based on the constructs of the Updated Delone & McLean Information System Success Model, the evaluation includes a 22-item survey questionnaire structured around four (4) constructs. System quality is evaluated through seven (7) measures: design, navigation response, response time, system security, system availability, functionality, and error-free transactions. Information quality assessment focuses on seven (7) measures: content variety, completeness, detail, accuracy, timeliness, reliability, and appropriateness. Service quality incorporates six (6) measures: responsiveness, reliability, confidence, empathy, follow-up service, and competence. Meanwhile, the user satisfaction construct involves two (2) measures: perceived user acceptance and perceived user satisfaction.

This methodological approach provides valid measurement parameters for evaluating the CDBIS. Survey responses were analyzed using a 7-point Likert Scale (i.e., strongly disagree, disagree, somewhat disagree, neutral, somewhat agree, agree, and strongly agree) to assess user agreement with each model construct. For quantification, the weighted mean was computed for each indicator, each construct, and the overall system evaluation. The mean scores were analyzed using the following descriptive scale: 6.50-7.00: Strongly Agree (Very High); 5.50-6.49: Agree (High); 4.50-5.49: Somewhat Agree (Moderately High); 3.50-4.49: Neutral (Moderate); 2.50-3.49: Somewhat Disagree (Low); 1.50-2.49: Disagree (Very Low); and 1.00-1.49: Strongly Disagree (Extremely Low). This quantitative method enables the generation of measurable, comparable parameters for evaluating the effectiveness, usability, and acceptability of the CDBIS.

3. Results and Discussion

In this section, the evaluation results of the CDBIS using the Updated Delone & McLean Information System Success Model are discussed in sufficient detail. The evaluation spans four constructs: system quality, information quality, service quality, and user satisfaction. Table 1 presents the results for the system quality construct, including the mean evaluation score for each measure, its corresponding Standard Error of the Mean (SEM), and the corresponding interpretation of the score, as defined in Section 2.8.2. It suggests that all mean scores are above 5.86 ("Strongly Agree" is at 6.24), with Error-Free Transactions scoring highest (6.24 ± 0.150) and System Availability lowest (5.86 ± 0.151). All items are interpreted as "Agree" except the highest, which is "Strongly Agree". The composite mean is 6.02±0.124.

Table 1. System Quality

Measures	Mean ± SEM	Interpretation
Design	6.08 ± 0.137	Agree
Navigation Response	5.92 ± 0.134	Agree
Response Time	6.12 ± 0.147	Agree
System Security	6.04 ± 0.137	Agree
System Availability	5.86 ± 0.151	Agree
Functionality	5.88 ± 0.133	Agree
Error Free Transaction	6.24 ± 0.150	Strongly Agree
Composite	**6.02 ± 0.124**	**Agree**

These results show that the CDBIS achieves high ratings across all system quality measures. Error-Free Transactions receives the highest score (6.24), followed by Response Time (6.12), indicating that users strongly value reliable, smooth, and efficient performance. The composite mean of 6.02 confirms that respondents agree the system consistently meets their expectations for technical quality. These findings align with the DeLone and McLean Information System Success Model [23] and studies by Gable *et al.* [26], which highlight that system reliability and fast response times are key drivers of user satisfaction. However, other research, such as Livari [27] and Shareef et al. [28], suggests that technical quality alone does not entirely predict satisfaction, as users also expect relevant information and responsive support. This implies that while CDBIS has established a strong technical foundation, continuous effort is needed to maintain system stability and performance. At the same time, complementing technical improvements with adequate user support and content relevance would help sustain high levels of trust and satisfaction among barangay users.

Meanwhile, Table 2 shows that users rated the quality of information provided by the CDBIS at 5.67. The highest score, 5.92, is for Accurate Information, indicating that most people consider the data generated by the CDBIS reliable and correct. Following close behind, Detailed Information receives a 5.88, suggesting that the system provides enough useful details to meet users' requirements. Also, mean evaluation scores across categories such as Content Variety, Complete Information, Timely Information, and Appropriate Information all fall between 5.62 and 5.64, indicating that users believe the system is relevant, thorough, and up-to-date. Moreover, Reliable Information receives the lowest score, 5.36, yet it still fits within the Agree range. This indicates minor concerns about consistency, but overall, users still demonstrate confidence in the system's generated information. These findings align with Lee *et al.* [29], who emphasized that accuracy and

detail are critical components of perceived information quality. At the same time, studies such as those by Wang and Strong [30] found that reliability and timeliness are equally important in building user confidence, and lower reliability scores can affect overall trust. Furthermore, these imply that while the system delivers useful and accurate information, improvements are needed to ensure that the data is consistently reliable. Strengthening data entry quality control, training staff in information management, and adopting automated validation tools will help address these concerns and further enhance user trust.

Table 2. Information Quality

Measures	Mean ± SEM	Interpretation
Content Variety	5.62 ± 0.151	Agree
Complete Information	5.62 ± 0.148	Agree
Detailed Information	5.88 ± 0.139	Agree
Accurate Information	5.92 ± 0.142	Agree
Timely Information	5.64 ± 0.151	Agree
Reliable Information	5.36 ± 0.189	Agree
Appropriate Information	5.62 ± 0.156	Agree
Composite	**5.67 ± 0.144**	**Agree**

As shown in Table 3, respondents have a high regard for the service quality of the CDBIS. In aggregate, the mean of the composite is 6.18, which is a "Strongly Agree", and is indicative of a decisively satisfied perspective. The highest mean scores correspond to Empathy (6.34), Follow-Up Service (6.32), and Competence (6.32), indicating that users believe in a clear understanding of the system staff, appropriate attention, and highly effective staff. Confidence (6.16) and Reliability (6.12) also obtain higher mean scores, indicating that users trust the services and rely on them. Responsiveness is marginally lower at 5.82, but not yet at the level of "Undecided," indicating that the system is responsive with efficient support. Altogether, these findings validate that CDBIS is indeed viewed as a reliable, competent, and user-focused service platform. These insights show that users feel well-supported and understood when interacting with the system's personnel. As confidence and reliability are highly rated, this further confirms trust in the service provided. These findings are consistent with the SERVQUAL model as cited by Davis [31], which emphasizes that empathy, responsiveness, and assurance are critical drivers of user satisfaction. Prior research by Zeithaml *et al.* [32] similarly found that consistent, professional support strongly influences perceptions of service quality in public sector systems. The implication is that strong service interactions are a key factor in sustaining satisfaction with the CDBIS. Barangay management should continue prioritizing staff training focused on empathy, communication skills, and problem resolution to maintain the high standards users expect and value. This is supported by the comment of the Barangay Secretary, one of the system administrators, who noted that, "The system helps me in processing reports faster and more organized compared to the manual system." In addition, an IT graduate and one of the household heads and respondents also highlighted that, "Before we had to go back to the barangay several times for our Brgy. Certificate to be released. Today, we received it in just a few minutes of processing."

Table 3. Service Quality

Measures	Mean ± SEM	Interpretation
Responsiveness	5.82 ± 0.161	Agree
Reliability	6.12 ± 0.145	Agree
Confidence	6.16 ± 0.141	Agree
Empathy	6.34 ± 0.147	Strongly Agree
Follow-Up Service	6.32 ± 0.147	Strongly Agree
Competence	6.32 ± 0.150	Strongly Agree
Composite	**6.18 ± 0.139**	**Strongly Agree**

Table 4 shows that users generally have a positive perception of their satisfaction with the CDBIS. The composite mean score of 5.99 indicates that respondents are satisfied with the system's overall performance. Perceived user acceptance receives a mean of 6.08, suggesting that most users have willingly accepted and adopted the system in their daily transactions. Perceived user satisfaction scored 5.90, showing that users are pleased with their experience using CDBIS. These results demonstrate that the system meets user expectations and effectively supports their needs, contributing to high levels of acceptance and satisfaction among barangay constituents and indicating that most users have integrated the system into their regular activities and view it positively. These findings align with the Technology Acceptance Model [31], which highlights that perceived usefulness and ease of use are strong predictors of user satisfaction and continued adoption. Similar studies in e-governance by Shareef *et al. [28] have shown that when digital systems are relevant and easy to use, users are more likely to embrace them in the* long term. Thus, CDBIS has successfully gained community trust, and its integration is pivotal in barangay operations. Management can build on this momentum by introducing additional features, offering refresher orientations, and promoting active user feedback to further strengthen satisfaction and long-term engagement. In summary, the results demonstrate consistently high mean scores across all measured constructs, supporting the working hypothesis that the CDBIS would be positively received and that higher perceptions of quality would correspond to higher user satisfaction.

Table 4. User Satisfaction

Measures	Mean ± SEM	Interpretation
Perceived user acceptance	6.08 ± 0.145	Agree
Perceived user satisfaction	5.90 ± 0.141	Agree
Composite	**5.99 ± 0.135**	**Agree**

The collinearity diagnostics in Table 5 indicate no serious multicollinearity among the predictors. Tolerance values for system quality (0.512), service quality (0.593), and information quality (0.558) are well above the minimum acceptable level of 0.10, indicating each variable contributes unique variance to the model. Variance inflation factors (VIF) ranging from 1.688 to 1.925 remain substantially below the critical threshold of 10, confirming that multicollinearity is minimal and does not compromise the stability or interpretability of the regression coefficients. The regression results in Table 5 reveal that System Quality ($\beta = 0.361$) has the strongest influence on User Satisfaction, followed by Service Quality ($\beta = 0.295$) and Information Quality ($\beta = 0.287$). The model explains 65% of the variance in satisfaction ($R^2 = 0.650$), indicating a substantial predictive power. All predictors were statistically significant, confirming their relevance to user experience. These findings align with the DeLone and McLean Information System Success Model [23], which identifies system, service, and information quality as key contributors to system success. Supporting studies also emphasize that improvements in these areas directly influence user satisfaction and overall system effectiveness. The implication is that system performance should remain a top priority to achieve the most significant impact on satisfaction. However, a balanced approach that also enhances service interactions and information consistency will ensure more comprehensive and sustainable improvements in user experience. The absence of multicollinearity confirms the stability of these findings.

Table 5. Stepwise regression estimates of constructs with influence on user satisfaction of the CDBIS

Construct	β	SE	t-value	95% CI		Collinearity	
				Lower	Upper	Tol	VIF
System Quality	0.361**	0.132	2.96	0.125	0.658	0.512	1.925
Service Quality	0.295*	0.110	2.60	0.065	0.509	0.593	1.688
Information Quality	0.287*	0.109	2.46	0.049	0.489	0.558	1.793

[a] Probability of F to enter ≤0.05 and probability of F to remove ≥0.01.

[b] Influential factor/construct: constant + system quality + service quality + information quality. F change = 6.046, Sig F change = 0.018. Regression and Residual ANOVA: F =28.481, p = 0.000. $R^2 = 0.650$.

* significant at p≤0.05, **significant at p < 0.001

Finally, based on barangay secretary data logs, the CDBIS significantly improved the system's efficiency. The average processing time per document, which took 2-3 days (i.e., 2.5 days on average), was reduced by 75%, to ~0.625 days (~5 hours). This enabled the system to process 20 clients per day, up from 5 previously. Moreover, the system's accuracy improved from 90% to 98-99%, which is an 88% error reduction in processing. Together, the results suggest that the CDBIS is a successful example of a digital governance platform. However, sustained efforts in system reliability, service responsiveness, and information consistency are critical to maintaining user trust and satisfaction as the system upgrades.

4. Conclusions

Dependence on paper-based procedures in local government units has been found to have adverse impacts on operational efficiency, data quality, information accessibility, and service quality. The rise of e-governance platforms helped bridge these gaps, demonstrating effectiveness in minimizing administrative workload, enhancing data quality, and improving service delivery, all deemed critical to governance. Although significant attention has been paid in the literature to the design and implementation of these e-governance systems, the involvement of higher education in carrying out extension projects to promote a collaborative platform for the e-governance agenda remains a gap in practice, particularly in developing countries with rural communities where digital literacy is relatively low. Thus, this work demonstrates the design and deployment of CDBIS, an information system that transitions processes from manual to digital, streamlines administrative procedures, maintains data integrity, and enhances service availability. Furthermore, aside from the design and implementation of the CDBIS in a case barangay, this study reports an evaluation of the adoption efficacy of the CDBIS from the lens of the Updated DeLone & McLean Information Systems Success Model. Results of the adoption evaluation found strong positive perceptions across system quality, information quality, service quality, and user satisfaction constructs of the model. System Quality scores highest overall, highlighting the importance of reliable, efficient performance. While Information Quality is rated positively for accuracy and detail, some concerns about reliability suggest the need for improved data consistency. Measures such as maintaining data entry quality control, training staff on information management, and adopting automated validation tools would address these concerns. Service Quality achieves excellent ratings, especially for empathy and competence, confirming that responsive support significantly enhances satisfaction. Findings also revealed that the system met user expectations and effectively supported their needs, contributing to high levels of user satisfaction among stakeholders and end users. Regression results showed that System Quality had the most significant impact on User Satisfaction, followed by Service and Information Quality, consistent with established information systems success models. Collinearity diagnostics confirm the stability of these findings. Overall, CDBIS has been effectively integrated into barangay operations and demonstrates strong potential as a model for e-governance. Sustaining this success requires continuous system improvements, staff training, and active user engagement to build long-term trust and satisfaction. Finally, this work offers a practical application of technology to facilitate effective local governance, which can be adopted for broader innovation in rural communities. Future research could explore long-term usage patterns and the impact of additional features on community engagement. Also, as the adoption evaluation survey covers only a limited number of respondents, the generalizability of the results to other barangays or communities may need further examination in future work.

5. Acknowledgements

The author would like to acknowledge the support and collaboration between Siquijor State College and Barangay Cangbagsa for successfully implementing the said research-based extension project. The author would like to extend his sincerest gratitude to Dr. Lanndon Ocampo for his invaluable mentorship, which has significantly improved the manuscript. His mentorship has been instrumental in addressing reviewers' comments and improving the manuscript's overall quality.

Conflicts of Interest: The author declares no conflict of interest in the collection, analysis, or interpretation of data; in the writing of the manuscript, or in the decision to publish the results.

References

[1] Correa, J. M.; Garcia, R. J.; Mutas, J.; D Bañez, J. G.; Nava, M. Strategies and mechanisms of local government units for e-Governance. *SSRN* **2022**, 5602071.

[2] Okudolo, I. P. T.; Ojakorotu, V. Digitalization of local governance for fostering accelerated attainment of the SDGs: Challenges and prospects from a Nigerian perspective. *Afr. J. Dev. Stud.* **2021**, 177. https://doi.org/10.31920/2634-3649/2021/SIv1a9

[3] Herasymiuk, K.; Zabolotenko, D.; Baimuratov, M.; Kofman, B.; Bobrovnik, D. Public governance at the local level in the context of digital transformation. Repository of National Pirogov Memorial Medical University, Vinnytsia, **2024**. https://doi.org/10.33543/1401399499

[4] Mustafa, K.; Mustafa, R.; Ahmedi, D. B. The impact of the COVID-19 pandemic on the digitalization of municipal administration, the development of e-governance. *Asian J. Res. Comput. Sci.* **2021**, 1–21. https://doi.org/10.9734/ajrcos/2021/v10i230236

[5] Gallera, J. M.; Salvador, A. S. Assessment of digital information systems for local barangays. *Int. Res. J. Adv. Eng. Sci.* **2023**, *8*(2), 112–115.

[6] Islam, M. R.; Sayem, M. A.; Makhdum, N.; Bhuiyan, M. L. Barriers to effective digital local governance: a qualitative insight on municipalities in Bangladesh. *Bangladesh J. Public Adm.* **2025**, *32*(1).

[7] Heidlund, M.; Sundberg, L. What is the value of digitalization? strategic narratives in local government. *Inf. Polity* **2023**, *28*(4), 523–539. https://doi.org/10.3233/IP-220063

[8] Nafi'ah, B. A. Challenges of implementing an electronic-based government system in local governments. *KnE Soc. Sci.* **2022**, 117–127. https://doi.org/10.18502/kss.v7i9.10932

[9] Garcia, M.; Reyes, I.; Santos, F. Barriers to the adoption of e-governance in local governance: A barangay perspective. *Philipp. J. Public Adm.* **2022**, *66*(3), 123–145.

[10] Alampay, E. A. Harmonizing e-government initiatives in the Philippines. In *Proceedings of the 7th International Conference on Theory and Practice of Electronic Governance*, ACM: **2013**; pp 260–263. https://doi.org/10.1145/2591888.2591935

[11] Carpio, C. O. Barangay management system. *Int. J. Multidiscip. Res. Publ.* **2020**, *3*(2), 26–32.

[12] Villones, T. T. Barangay constituents information and services management system. *Int. J. Comput. Sci. Mobile Comput.* **2021**, *10*(4), 63–66. https://doi.org/10.47760/ijcsmc.2021.v10i04.009

[13] Altura, K. A. P.; Madjalis, H. E. C.; Sungahid, M. D. G.; Serrano, E. A.; Rodriguez, R. L. Development of a web-portal health information system for barangay. In *2023 11th International Conference on Information and Education Technology (ICIET)*, IEEE: Fujisawa, Japan, **2023**; pp 544–550. https://doi.org/10.1109/ICIET56899.2023.10111439

[14] Jamis, M. N.; et al. One barangay: a mobile and web barangay management system. In *2022 2nd International Conference in Information and Computing Research (iCORE)*, IEEE: **2022**; pp 202–207. https://doi.org/10.1109/iCORE58172.2022.00055

[15] Del Pilar, C. G. E.; et al. B-GIS: Modernizing local governance through a web-based barangay geographic information system for Barangay 99, Tondo, Manila. In *2024 International Conference on Intelligent Cybernetics Technology & Applications (ICICyTA)*, IEEE: Bali, Indonesia, **2024**; pp 161–166. https://doi.org/10.1109/ICICYTA64807.2024.10912845

[16] Gazuda, M.; et al. The impact of digitalization and e-governance on transformation of state management mechanisms of the regional development. *J. Theor. Appl. Inf. Technol.* **2024**, *103*(3), 956–968.

[17] Regondola-Baltazar, J. Evaluation of public information system: a narrative review of objectives, vision, pillars, best practices and challenges with a case study of barangay management information system in the Philippines. *Vision, Pillars, Best Practices and Challenges*, **2025**. https://doi.org/10.2139/ssrn.5248917

[18] Cruz, M. A.; Reyes, L. G. e-Governance implementation in Metro Manila Barangays: a model for local government efficiency. *Philipp. J. Public Adm.* **2020**, *64*(2), 45–62.

[19] Roberts, T.; Hernandez, K. Digital access is not binary: the 5'a's of technology access in the Philippines. *Electron. J. Inf. Syst. Dev. Ctries.* **2019**, *85*(4), e12084. https://doi.org/10.1002/isd2.12084

[20] Kupi, M.; McBride, K. Agile development for digital government services: challenges and success factors. *Lect. Notes Comput. Sci.* **2021**, *12849*, 139–150. https://doi.org/10.1007/978-3-030-82824-0_11

[21] Silva, J.; Silva, A.; Araujo, A.; Silva, A. Agile project management in government software development: addressing challenges in education public policy. Computing Institute, Federal University of Alagoas, **2023**.

[22] Neumann, O.; Kirklies, P.-C.; Schott, C. Adopting Agile in Government: A Comparative Case Study. *Public Manage. Rev.* **2024**, *26*(12), 3692–3714. https://doi.org/10.1080/14719037.2024.2354776

[23] DeLone, W. H.; McLean, E. R. The DeLone and McLean model of information systems success: a ten-year update. *J. Manage. Inf. Syst.* **2003**, *19*(4), 9–30. https://doi.org/10.1080/07421222.2003.11045748

[24] Pitt, L. F.; Watson, R. T.; Kavan, C. B. Service quality: a measure of information systems effectiveness. *MIS Q.* **1995**, *19*(2), 173–187. https://doi.org/10.2307/249687

[25] Jeyaraj, A. DeLone & McLean models of information system success: critical meta-review and research directions. *Int. J. Inf. Manage.* **2020**, *54*, 102139. https://doi.org/10.1016/j.ijinfomgt.2020.102139

[26] Gable, G. G.; Sedera, D.; Chan, T. Re-conceptualizing information system success: The IS-impact measurement model. *J. Assoc. Inf. Syst.* **2008**, *9*(7), 377–408. https://doi.org/10.17705/1jais.00164

[27] Iivari, J. An empirical test of the DeLone–McLean model of information system success. *Database Adv. Inf. Syst.* **2005**, *36*(2), 8–27. https://doi.org/10.1145/1066149.1066152

[28] Shareef, M. A.; Kumar, V.; Kumar, U.; Dwivedi, Y. K. E-government adoption model (GAM): differing service maturity levels. *Gov. Inf. Q.* **2011**, *28*(1), 17–35. https://doi.org/10.1016/j.giq.2010.05.006

[29] [29] Lee, Y. W.; Strong, D. M.; Kahn, B. K.; Wang, R. Y. AIMQ: A methodology for information quality assessment. *Inf. Manage.* **2002**, *40*(2), 133–146. https://doi.org/10.1016/S0378-7206(02)00043-5

[30] Wang, R. Y.; Strong, D. M. Beyond accuracy: what data quality means to data consumers. *J. Manage. Inf. Syst.* **1996**, *12*(4), 5–34. https://doi.org/10.1080/07421222.1996.11518099

[31] Davis, F. D. Perceived usefulness, perceived ease of use, and user acceptance of information technology. *MIS Q.* **1989**, *13* (3), 319–340. https://doi.org/10.2307/249008

[32] Zeithaml, V. A.; Parasuraman, A.; Malhotra, A. Service quality delivery through websites: a critical review of extant knowledge. *J. Acad. Mark. Sci.* **2002**, *30*(4), 362–375. https://doi.org/10.1177/009207002236911

ASEAN
Journal of Scientific and Technological Reports
Online ISSN:2773-8752

Research article

Impact of Marine Fish Amino Acid on Yield Parameters and Preventive Antioxidant in Okra

Nopparat Tatmala[1], Pimchana Hoktha[2], Mohd Syafik Mohamad Hamdan[3], and Sorapong Benchasri[4]

[1] Faculty of Agricultural Technology, Rajamangala University of Technology Thanyaburi, Pathumthani, 12110, Thailand
[2] Faculty of Science and Digital Innovation, Thaksin University, Phatthalung Province, 93210, Thailand
[3] Faculty of Agroscience, University College of Agroscience Malaysia, Ayer Pa'abas, 78000, Malaysia
[4] Faculty of Technology and Community Development, Thaksin University, Phatthalung, 93210, Thailand
* Correspondence: sorapong@tsu.ac.th

Citation:
Tatmala, N.; Hoktha, P.; Hamdan, M.S.M.; Benchasri, S. Impact of marine fish amino acid on yield parameters and preventive antioxidant in okra. *ASEAN J. Sci. Tech. Report.* **2026**, *29*(3), e260960. https://doi.org/10.55164/ajstr.v29i3.260960.

Article history:
Received: August 22, 2025
Revised: January 16, 2026
Accepted: January 25, 2026
Available online: March 1, 2026

Abstract: A field experiment was carried out to evaluate the effects of foliar-applied marine fish amino acids (MFA) on the growth, yield, yield components, and preventive antioxidant capacity of okra, as well as the interaction between okra varieties and MFA concentrations. The study used a split-plot design with four replications. Three okra varieties — RED FINGER, KN–OYV–02, and LUCKY FILE 473 — were assigned to main plots. Five concentrations were tested in the subplots (0.00, 1.50, 3.00, 4.50, and 6.00 ml/l). Yield per plant — a key indicator for growers — did not differ significantly among the three varieties but responded to MFA levels-plants treated with 3.00, 4.50, or 6.00 ml/l. MFA showed no significant differences among these higher concentrations; however, all produced higher yields than the untreated control and the 1.50 ml/l treatment. The greatest yield (1,271.49 g/plant) was obtained at 3.00 ml/l, followed by 4.50 ml/l (1,251.22 g/plant) and 6.00 ml/l (1,215.51 g/plant). Reducing sugar content did not vary significantly among the okra varieties but was influenced by MFA levels. LUCKY FILE 473 recorded the highest reducing sugar (~1.77 mg/ml). The concentrations 3.00, 4.50, and 6.00 ml/l yielded the highest reducing sugar levels (1.89, 1.84, and 1.77 mg/ml, respectively), with no significant difference among them, while the control plants had the lowest value (1.53 mg/ml). Among pigment traits, RED FINGER exhibited the lowest chlorophyll a, chlorophyll b, and total chlorophyll contents (2.96, 1.51, and 4.47 mg/g FW, respectively) but had the highest carotenoid concentration (0.50 μg/g FW).

Keywords: Antioxidant; marine fish amino acid (MFA); okra; yield

1. Introduction

The okra (*Abelmoschus esculentus* L.) is widely cultivated in tropical and subtropical regions. It is recognized by diverse local names such as "bhindi" in India, "krajiab kheaw" in Thailand, "bamia" in the Middle East, "gumbo" in the USA and France, "lady's finger" in England, "quiabo" in Portuguese-speaking areas including Angola, "quimbombo" in Cuba, "guino-gombo" in Spain, and "okura" in Japan [1-3]. Species within the *genus Abelmoschus exhibit* notable variation in chromosome numbers, reflecting broad genetic diversity [4, 5]. Okra is cultivated both commercially and in home gardens, with major producing regions including India, Turkey, Iran, West Africa, Pakistan, Myanmar, Japan, Malaysia, Thailand, and the southern United States [6]. Okra is considered

economically important and nutritionally valuable [7]. Fresh pods provide carbohydrates, proteins, vitamin C, and minerals such as calcium and phosphorus in relatively high amounts compared with other fruit vegetables [8]. They also contain mucilage, which influences texture and functional properties. Besides its dietary role, okra has long been used in traditional medicine, and pharmacological studies confirm its antidiabetic, antioxidant, antihyperlipidemic, and antihyperglycemic activities [9-11]. These bioactivities are attributed mainly to phenolic compounds [12].

Marine fish–derived amino acids, commonly formulated as fish amino acid or fish hydrolysate fertilizers, have been widely reported as effective biostimulants in various crop species. Previous studies demonstrated that foliar application of fish-derived amino acids enhanced vegetative growth, nutrient uptake, and yield in vegetables and field crops, including okra, chilli, lettuce, tomato, and wheat. These positive effects have been associated with improved photosynthetic capacity, increased chlorophyll content, enhanced antioxidant metabolism, and better nitrogen assimilation [13]. Given its nutritional and health-promoting properties, demand for okra is increasing in Thailand and elsewhere [3, 6]. However, okra production faces several challenges, including inconsistent yields, pest and disease outbreaks, pesticide residues, and rising costs of synthetic fertilizers [6]. Consequently, there is growing interest in alternative nutrient sources, particularly liquid amino acid fertilizers. MFA, produced through fermentation of fish-processing byproducts, provides readily available amino acids that can enhance plant growth and yield [13]. Although fish amino acid application has been shown to significantly improve growth and yield attributes of okra, wheat, and leafy vegetables under organic farming systems, plant responses vary across crop species, cultivars, and application rates. Despite these reported benefits, information regarding the optimal concentration of MFAs and varietal responses in okra, particularly in relation to yield components and preventive antioxidant traits under tropical field conditions, remains limited. Therefore, this study aimed to evaluate the effects of foliar MFA application on growth, yield, and preventive antioxidant capacity of three okra varieties, contributing to sustainable production and value-added utilization of marine byproducts within a circular economy framework. Consequently, there is growing interest in alternative nutrient sources that can improve productivity while supporting sustainable agriculture in line with SDG 2 (Zero Hunger). MFAs are produced by fermenting fish-processing byproducts to release plant-available amino acids that enhance growth and yield. Therefore, this study aimed to evaluate the effects of foliar MFA application on the growth, yield, and preventive antioxidant capacity of okra varieties, thereby generating evidence to support sustainable production practices.

2. Materials and Methods

2.1 Area research

Field experiments were conducted at the Department of Plant Science, Faculty of Technology and Community Development, Thaksin University, Phatthalung Campus, Thailand (7°37′N, 100°5′E). The study area has a tropical climate suitable for okra cultivation.

2.2 Plant material and fish amino acid spray

Three okra varieties — KN–OYV–02, LUCKY FILE 473, and RED FINGER — were cultivated as main plots. Seeds were sown at 3–4 seeds per hill and later thinned to one seedling per hole after two weeks. Planting beds measured 1 m × 7 m, with 75 cm spacing between rows and plots. Manure was incorporated at 1,000 kg/ha, and a basal application of 15-15-15 fertilizer was applied at 20 kg/ha. Routine cultural practices included hand weeding every two weeks and morning-evening irrigation. MFAs were obtained from PLANEAT FARM CO., LTD. MFA is a liquid organic nutrient derived from the fermentation of marine fish byproducts, containing essential amino acids that enhance plant metabolism and yield [13]. Foliar spraying began in the second week after emergence and continued twice weekly. Five concentrations were tested (0.00, 1.50, 3.00, 4.50, and 6.00 ml/l), with 0.00 ml/l serving as the control. The MFA level is calculated by dividing the initial amount of amino acids by the volume of the solution (water, in liters).

2.3 Yield and yield component record

Morphological and yield parameters—including Morphological aspects, plant height, leaf width,

canopy width, first date of flowering, firmness, number of good pods, good pod weight, total yield, number of pods/plant, yield/plant, harvesting index, and major elements—were measured.

2.4 Chemical analysis

MFAs were applied to okra plants as foliar sprays at 2-week intervals throughout the growing period. Quality and biochemical traits included pod firmness, carotenoid content, reducing sugar, dietary fiber, chlorophyll a, chlorophyll b, and total chlorophyll content.

Leaf pigments were determined using spectrophotometry adapted from standard protocols [14–16]. Chlorophyll content was estimated after extraction with 80% acetone; absorbance was recorded at key wavelengths (A645, A646, A663) using a UV–Vis spectrophotometer. Carotenoids were quantified following Rebecca et al. [15]. Anthocyanin content was determined by the pH differential method [16], and reducing sugars were analyzed by the Nelson–Somogyi method [17].

A. chlorophyll a (μg/mL) = -1.93A646 + 11.93A663
   chlorophyll b (μg/mL) = 20.36A646 – 5.50A663
   total chlorophyll (μg/mL) = 6.43A663 + 18.43A646
B. chlorophyll a (μg/mL) = 12.7 (A663) – 2.69 (A645)
   chlorophyll b (μg/mL) = 22.9 (A645) - 4.8 (A663)
   total chlorophyll (μg/mL) = 20.2 (A645) + 8.02 (A663)

2.5 Statistical analysis

The study employed a split-plot design with four replications and 20 plants per replicate. Okra varieties were assigned to main plots, and MFA concentrations to subplots. The design was based on a randomized complete block arrangement to minimize field variability. The growth and all data (plant height, leaf width, canopy diameter, first date of flowering, firmness, pod number, pod weight, total yield, harvest index, sugar content, and various essential elements) from the 4 replications of all varieties and concentrations were subjected to a variance analysis (ANOVA) using SPSS 16.0 for Windows. Significant treatment differences were separated using Duncan's new multiple range test (DMRT) at the 0.05 probability level

3. Results and Discussion

The Physicochemical properties of the soil before and after plantation are provided in Table 1. The total nitrogen content in the soil during okra planting was low (0.16% and 0.14%). Similarly, the soil exhibited a medium level of phosphorus (35.33 and 36.01 mg/kg) with a corresponding low level of potassium (81.35 and 63.01 mg/kg) before and after plantation, respectively. Organic matter was low in both years (1.15% and 1.15%), while the water pH was weakly acidic at about 4.57 and 4.58 before and after the season, respectively.

Table 1. Physicochemical properties of soil

Soil properties	Soil properties		Method of analysis
	Before planting	After planting	
Organic matter (%)	1.15	1.15	Walkley-Black method
Nitrogen (%)	0.16	0.14	McKenzie method
P_2O_5 (mg/kg)	35.33	36.01	Flame photometric
K (mg/kg)	81.35	63.01	Oxidation
pH (H2O)	4.57	4.58	pH meter method
EC (dS./m)	0.08	0.08	

In this experiment, amino acids were derived from the fermentation of various species of marine fish, including *Caesio erythrogaster*, *Sardinella gibbosa*, purple-spotted bigeye *Priacanthus tayenus*, and *Pyjama cardinalfish*. These fish were fermented to extract amino acids, which were subsequently tested in a standardized laboratory. The analysis confirmed the presence of 21 essential amino acids, including alanine, arginine, aspartic acid, cystine, glutamic acid, glycine, histidine, hydroxylysine, hydroxyproline, isoleucine, leucine,

lysine, methionine, phenylalanine, proline, serine, threonine, tryptophan, tyrosine, valine, and glutamine. Furthermore, when examining other parameters such as electrical conductivity, acidity-alkalinity, total nitrogen content, total phosphorus content, total potassium, total calcium, total magnesium, and sulfur, the values were determined to be 23.77, 4.26, 0.33, 0.71, 0.75, 0.76, 0.12, and 0.01 percent, respectively (Figure 1).

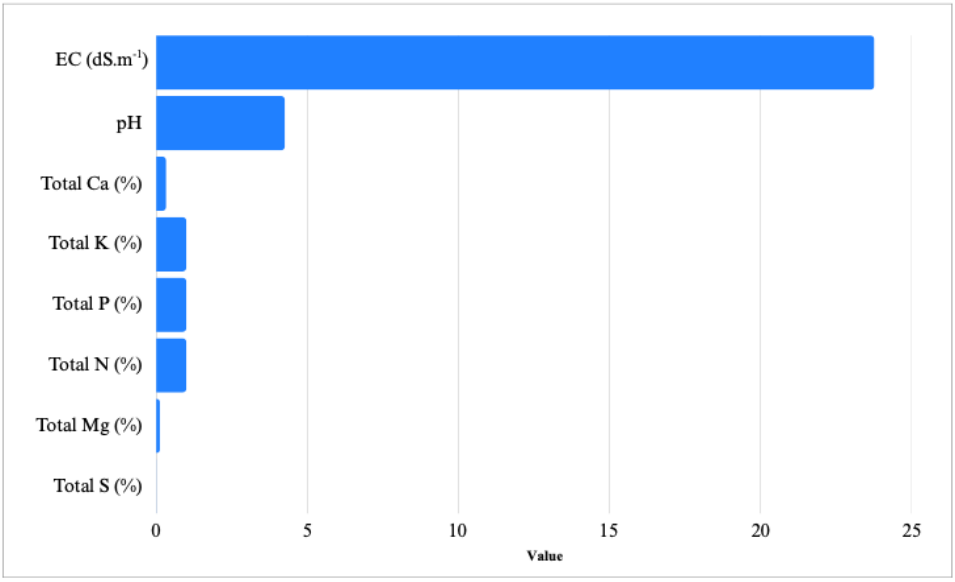

Figure 1. Acidity-alkalinity, electrical conductivity, and mineral content.

The MFAs were sprayed on the okra plant's foliage. Morphological aspects, leaf width, canopy width, first date of flowering, number of good pods, good pod weight, total yield, firmness, number of pods/plant, yield/plant, harvesting index, carotenoid, reducing sugar, fiber content, chlorophyll a, chlorophyll b, and total chlorophyll content were measured. It was found that each trait exhibited statistically significant differences across the various characteristics studied. Table 1 shows the physicochemical properties of soil, and the morphology of pod size, pod color, and pod length (Figure 2). The application of MFAs to the foliage of okra plants at 2-week intervals demonstrated a substantial influence on various aspects of plant physiology. Significant effects were observed on morphological characteristics [18], cell structure [6], trichome development [20], plant height and leaf width [19, 21], and canopy width [22]. Moreover, the application of MFAs significantly affected the first flowering date of bean plants. These findings underscore the multifaceted influence of MFAs on the overall growth and development of okra plants. Three okra varieties (KN–OYV–02, LUCKY FILE 473, and RED FINGER) were sprayed with MFAs twice per week at five concentration levels. Significant differences were observed in growth, yield, and yield components, as well as in preventive antioxidant traits, depending on okra variety, MFA concentration, and their interaction. Plant height differed significantly among okra varieties and MFA concentration levels (Table 2). Leaf width, an indicator of leaf size, showed a response pattern similar to that of plant height, with significant differences among varieties, MFA concentrations, and their interaction. KN–OYV–02 exhibited the widest leaf width (29.17 cm), while the highest mean leaf width across MFA treatments (27.89 cm) was recorded at an MFA concentration of 4.50 ml/L. Canopy width, reflecting the size of the mature okra canopy, was also significantly affected by both okra variety and MFA concentration. KN–OYV–02 recorded the largest canopy width (81.43 cm), whereas the highest mean canopy width among MFA concentrations (79.67 cm) was obtained at 3.00 ml/l. The interaction between okra varieties and MFA concentrations for leaf width and canopy width was statistically significant ($p < 0.05$)

Three varieties of okra, consisting of KN – OYV – 02, LUCKY FILE 473, and RED FINGER, were sprayed 2 times a week. The concentrations of MFAs were divided into 5 levels. Statistical analysis revealed significant differences in growth, yield, and yield components; preventive antioxidant levels; interaction between varieties; and amino acid content of okra. Statistical differences in plant height were observed between the okra varieties and MFA concentration levels. (Table 2). Leaf width, indicating leaf size pod after

MFA injection, had a similar effect as the height characteristics. Statistical differences were observed between the two okra varieties and the MFA concentrations. KN-OYV-02 displayed the widest leaf width (29.17 cm), while the highest value (27.89 cm) occurred at an MFA concentration of 4.50 ml/l. The canopy width, which measured the size of the mature okra canopy, showed statistical differences after spraying with MFA, affecting both okra varieties and MFA concentrations. KN-OYV-02 had the largest canopy width (81.43 cm), while the highest value (79.67 cm) was recorded at an MFA concentration of 3.00 ml/l. The interaction between varieties and MFA levels concerning leaf width and canopy width of okras showed a statistically significant difference ($p < 0.05$).

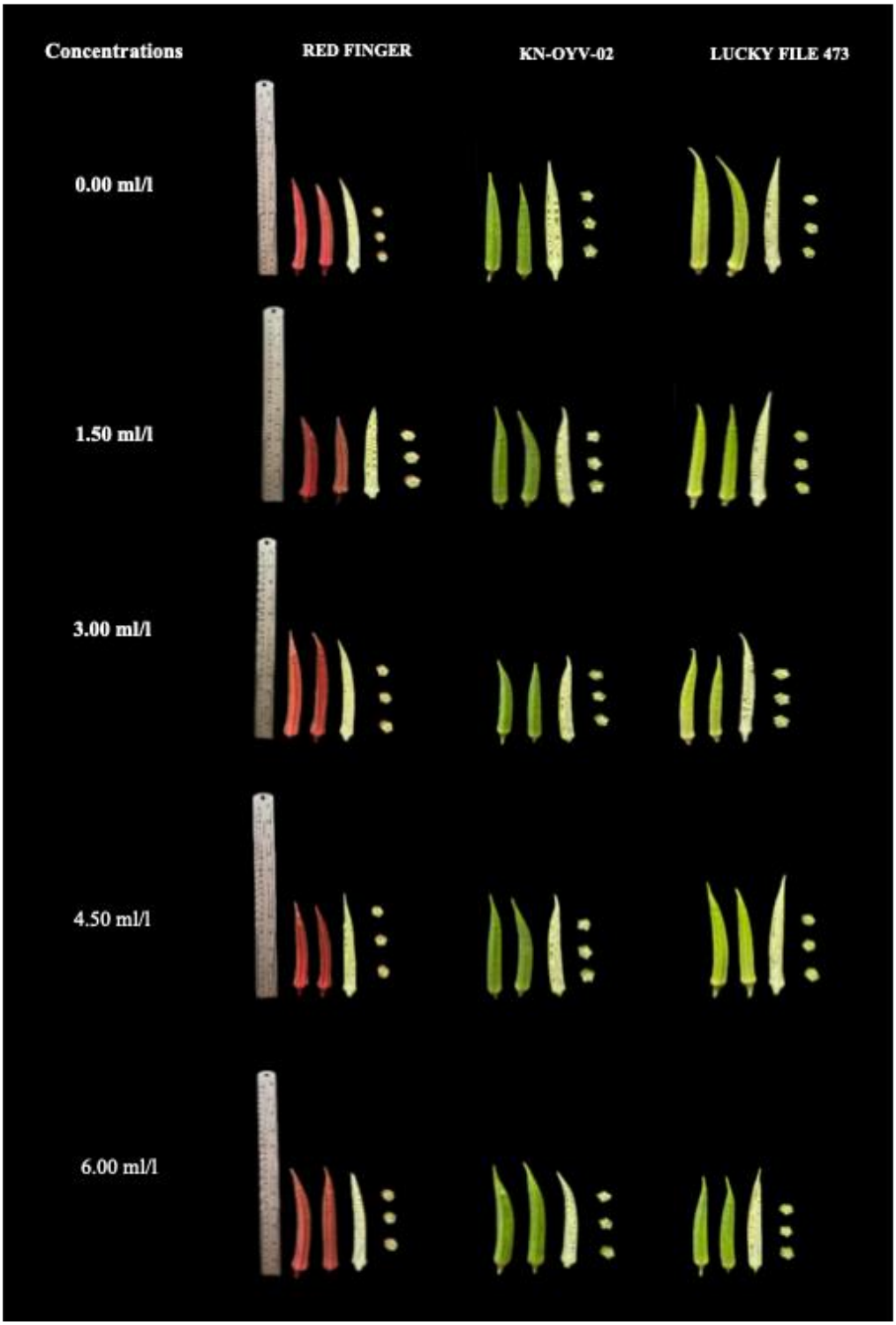

Figure 2. Pod size and pod color of okra sprayed with different concentrations of MFAs.

Table 2. Plant height, leaf width, and canopy width of okra after being sprayed by MFAs

Plant height (cm)	Concentrations (ml/l)					
	0.00	**1.50**	**3.00**	**4.50**	**6.00**	**Varieties (V)**
RED FINGER	162.67	170.33	171.33	164.50	177.83	169.33a
KN-OYV-02	147.66	163.16	163.26	167.00	172.00	162.62b
LUCKY FILE 473	131.50	166.50	124.83	145.33	155.17	144.67b
Concentrations Means (A)	147.28B	166.66A	153.14AB	158.94A	168.33A	
P-VALUE (F-TEST)						
VARIETIES (V)	= 0.0028*					
AMINO ACID (A)	= 0.0022*					
VxA	= 0.0024*					
(CV.%)	= 7.1394					
Leaf width (cm)	**Concentrations (ml/l)**					
	0.00	**1.50**	**3.00**	**4.50**	**6.00**	**Varieties (V)**
RED FINGER	25.00	25.83	21.50	19.83	23.33	23.10b
KN-OYV-02	24.67	24.50	25.33	35.66	35.68	29.17a
LUCKY FILE 473	28.50	30.50	27.00	28.17	16.17	26.07ab
Concentrations Means (A)	26.06A	26.94A	24.61B	27.89A	25.06AB	
P-VALUE (F-TEST)						
VARIETIES (V)	= 0.0021*					
AMINO ACID (A)	= 0.0046*					
VxA	= 0.0064*					
(CV.%)	=12.0521					
Wide canopy (cm)	**Concentrations (ml/l)**					
	0.00	**1.50**	**3.00**	**4.50**	**6.00**	**Varieties (V)**
RED FINGER	74.17	73.33	74.67	78.00	73.33	74.70b
KN-OYV-02	77.00	86.16	86.00	78.66	79.33	81.43a
LUCKY FILE 473	71.67	79.17	78.33	79.33	87.50	79.20a
Concentrations Means (A)	74.27B	79.55A	79.67A	78.66AB	80.05A	
P-VALUE (F-TEST)						
VARIETIES (V)	=0.0435*					
AMINO ACID (A)	=0.0012*					
VxA	=0.0031*					
(CV.%)	=5.4912					

Uppercase letters are horizontal comparison, lowercase letters are vertical comparison, ns, and * means not significant, significant at 0.05 level of probability.

Table 3 shows the characteristics of the first date of flowering and firmness. No statistical difference in the first flowering date was found among the okra cultivars, but a statistical difference in the concentrations of MFAs received by each plant was observed. RED FINGER exhibited the earliest first date of flowering at 38.20 days, while the MFA concentration was 3.00 ml/l. The earliest first date of flowering was 40.67 days. The harvest showed statistically significant differences among the cultivated okra varieties and the MFA concentration levels administered at each level. Specifically, KN-OYV-02 demonstrated the longest harvest period, lasting 48 days. Firmness, a crucial characteristic indicating consumer preference, showed no statistical differences in the traits of the cultivated okra cultivars. However, there were statistical differences in MFA concentrations across levels. KN-OYV-02 had the lowest firmness at 918.16 g with an MFA concentration of 3.00 ml/L, a value not statistically different from those at 4.50 and 6.00 ml/L.

Table 3. First date of flowering and firmness of okra after MFAs were sprayed

First date of flowering (day)	Concentrations (ml/l)					Varieties mean (V)
	0.00	**1.50**	**3.00**	**4.50**	**6.00**	
RED FINGER	37.00	37.00	39.00	39.00	39.00	38.20
KN-OYV-02	39.33	43.01	43.02	42.00	41.00	41.67
LUCKY FILE 473	41.00	39.12	40.00	40.00	40.00	40.02
Concentrations Means (A)	39.11B	39.71AB	40.67A	40.33A	40.00A	
P-VALUE (F-TEST)						
VARIETIES (V)	=0.3485ns					
AMINO ACID (A)	=0.0031*					
VxA	=0.0066*					
(CV.%)	=12.0014					

Harvest index (d)	Concentrations (ml/l)					Varieties mean(V)
	0.00	**1.50**	**3.00**	**4.50**	**6.00**	
RED FINGER	40.15	42.15	42.48	45.15	43.59	42.70b
KN-OYV-02	44.00	48.00	50.00	51.00	47.00	48.00a
LUCKY FILE 473	40.25	42.35	45.25	45.16	44.25	43.45b
Concentrations Means (A)	41.47C	44.17B	45.91A	47.10A	44.95AB	
P-VALUE (F-TEST)						
VARIETIES (V)	=0.0001*					
AMINO ACID (A)	=0.0085*					
VxA	=0.0042*					
(CV.%)	=4.6884					

Firmness (g)	Concentrations (ml/l)					Varieties mean(V)
	0.00	**1.50**	**3.00**	**4.50**	**6.00**	
RED FINGER	1012.35	999.14	982.15	989.30	979.58	992.50
KN-OYV-02	989.81	989.07	842.73	878.92	890.25	918.16
LUCKY FILE 473	1011.60	1003.12	990.25	989.68	998.25	998.58
Concentrations Means (A)	1004.59A	997.11AB	938.38C	952.63C	956.3BC	
P-VALUE (F-TEST)						
VARIETIES (V)	=0.2158ns					
AMINO ACID (A)	=0.0097*					
VxA	=0.0262*					
(CV.%)	=7.1658					

Uppercase letters are horizontal comparison, lowercase letters are vertical comparison, ns, and * means not significant, significant at 0.05 level of probability.

Yield/plant was the most important factor in farmers' decision-making. The results of this experiment indicated that there was no statistical difference in the characteristics of the Okra cultivars planted across all three species. However, there were statistical differences in the concentrations of MFAs obtained at each level: 3.00, 4.50, and 6.00 ml/l. No statistical difference was obtained among these levels. Nevertheless, a statistical difference was noted between the non-injection of MFA and the infusion of MFAs at a concentration of 1.50 ml/l. Injection of MFAs at a concentration of 3.00 ml/l resulted in the highest yield at 1,271.49 g/plant, followed by the application of MFAs at concentrations of 4.50 and 6.00 ml/l, with mean values of 1,251.22 and 1,215.51 g/plant, respectively (Figure 3A). The number of pods/plant, which was an important component of the three varieties, showed no statistical differences in the characteristics of the three okra varieties after spraying with MFA. However, there were statistical differences in MFA concentrations across levels. KN-OYV-02 had the number of pods/plant (67.99 pods). At an MFA concentration of 3.00 ml/l, the number of pods/plant (73.55

pods) was recorded, which was statistically different from MFA concentrations of 6.00, 1.50, and 0.00 ml/l, where the number of pods/plant was 67.72, 63.66, and 55.02 pods, respectively (Figure 3B). The number of pods/plant, a critical parameter for all okra varieties, showed no statistical differences in its characteristics after spraying with MFAs. However, there were significant variations in MFA concentrations at each level. KN-OYV-02 had the highest number of pods/plant (67.99). At an MFA concentration of 3.00 ml/l, the highest number of pods/plant (73.55 pods) was recorded, presenting a statistically significant difference from MFA concentrations of 6.00, 1.50, and 0.00 ml/l, where the number of pods/plant was 67.72, 63.66, and 55.02 pods, respectively and Yield/plant emerged as the most influential factor in farmers' decision-making. Findings from this experiment indicated no statistical difference in the characteristics of Okra cultivars planted, encompassing all three species. However, there were statistical differences in the concentrations of MFAs obtained at each level: 3.00, 4.50, and 6.00 ml/l. No statistical difference was noted among these levels. Nevertheless, a statistical difference was observed between the non-injection of MFA and the infusion of MFAs at a concentration of 1.50 ml/l. Injection of MFAs at a concentration of 3.00 ml/l resulted in the highest yield at 1,271.49 g/plant, followed by the application of MFAs at concentrations of 4.50 and 6.00 ml/l, with mean values of 1,251.22 and 1,215.51 g/plant, respectively. Similarly, Seyedi et al. [23] reported that amino acids affect growth and yield in many plants [24]. The weight per pod, an important constituent, showed that after MFAs were inoculated, there was no statistical difference in the characteristics of okra cultivars, but there were statistical differences in the concentrations of MFAs at each level. A statistical difference was observed in the absence of MFA intake. KN-OYV-02 had the highest weight per pod (17.99 g) at an MFA concentration of 0.00 ml/l, while it had the lowest weight per pod (16.85 g) at 0.00 ml/l (Figure 3C). The harvesting index, a biomarker of okra harvest time, showed that after inoculation with MFAs, there were significant differences in okra cultivar characteristics and MFAs concentrations at each level. KN-OYV-02 had the longest harvest index time at 48 days, while the MFA concentration of 4.50 ml/l had the longest harvest time of 47.10 days, but was not statistically different from the MFAs of 3.00 and 6.00 ml/l (Figure 3D).

Statistical analyses of plants, as documented in various studies [21,6], revealed substantial variation in growth, yield, yield components, antioxidant levels, interactions among varieties, and amino acid content of okra. Differences were notable in plant height among okra varieties and MFA concentration levels [25]. Leaf width, an indicator of leaf size post-MFA injection, showed effects similar to those of height characteristics, with statistical differences observed between okra varieties and MFA concentrations [26]. KN-OYV-02 exhibited the widest leaf width at 29.17 cm, with the highest value (27.89 cm) recorded at an MFA concentration of 4.50 ml/l. In terms of canopy width, the mature okra canopy size showed significant differences after MFA spraying, with effects on both okra varieties and MFA concentrations. KN-OYV-02 displayed the largest canopy width (81.43 cm), while the highest value (79.67 cm) was noted at an MFA concentration of 3.00 ml/l. The interaction between varieties and MFA levels regarding leaf width and canopy width of okra exhibited statistically significant differences. The first date of flowering and firmness indicated that although no statistical difference was found in the first date of flowering among okra cultivars, there was a significant difference in the concentrations of MFAs received by each plant. RED FINGER displayed the earliest first date of flowering at 38.20 days, with the MFA concentration at 3.00 ml/l, while the earliest first date of flowering was 40.67 days. Regarding firmness, a critical consumer preference indicator, there were no statistical differences in the traits of the cultivated okra cultivars. However, statistical differences were observed in the concentrations of MFAs obtained at each level. KN-OYV-02 had the lowest firmness at 918.16 g when the MFA concentration was 3.00 ml/l, a value not statistically different from those at 4.50 and 6.00 ml/l. This is consistent with the report of Baqir and Naqeeb [27], who reported that amino acid extracts had an effect on growth in wheat or tested the influence of marine fish amino extracts on okra yield [23]. Moreover, MFA of okra proteins shows that glutamic acid is predominantly present, with values ranging from 12.01 to 19.31 mg/100 g protein. This finding agrees with other previous studies, which reported that glutamic acid is always present in abundance in plant-based foods [28, 29]

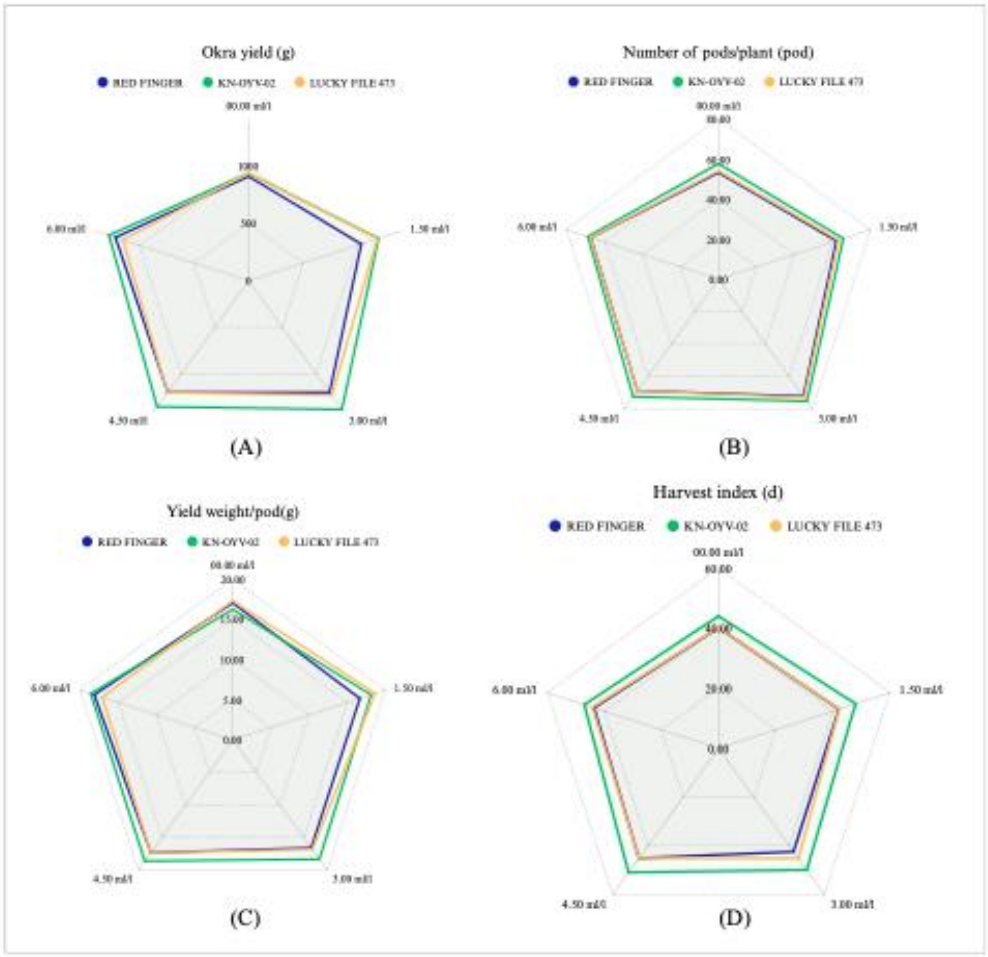

Figure 3. Yield and yield components of okra as affected by MFA treatments.

Carotenoids are yellow, orange, red, and orange-red pigments commonly found in plants. Organisms capable of photosynthesis use chlorophyll, a green pigment that absorbs energy from sunlight for photosynthesis and provides protection against light as an antioxidant. Statistical differences in carotenoid levels were obtained. RED FINGER showed the highest carotenoid content at 0.50 μg/g fresh weight, while KN-OYV-02 and LUCKY FILE 473 showed similar values at 0.06 and 0.07 μg/g fresh weight, respectively. The optimal value was found at MFA levels at 3.00 ml/l, with 0.26 μg/g fresh weight. However, there was no statistical difference in MFA intake at 4.50 and 6.00 ml/l, which were 0.22 and 0.23 ml/l, respectively, while non-injected MFA carotenoids contained the least number of carotenoids, 0.16 μg/g fresh weight (Figure 4). The determination of reducing sugar was performed using the 3,5-dinitrosalicylic acid (DNS) method. The results showed that reducing sugar levels was not different between varieties. However, a statistical difference was observed among the MFA levels used to treat okra. LUCKY FILE 473 showed the highest amount of reducing sugar, approximately 1.77 mg/ml. The optimal values were obtained with MFA intake at 3.00, 4.50, and 6.00 ml/l, with no statistical difference among them. The corresponding values were 1.89, 1.84, and 1.77 mg/mL, while the lowest reducing sugar content was 1.53 mg/mL. Dietary fiber, mainly found in fruits, vegetables, whole grains, and legumes, is well known for its ability to relieve constipation. The dietary fiber content of okra, after the infusion of MFA, exhibited statistical differences among the characteristics of okra varieties and the MFA at each level. LUCKY FILE 473 recorded the highest dietary fiber content at 1.22 g/100 g of solvent, while MFA levels of 1.50, 3.00, 4.50, and 6.00 ml/l showed no statistical difference. However, a statistical difference was observed compared to the control. MFA at 4.50 ml/l showed the highest dietary fiber content (1.21 g/100 g of solvent), followed by 3.00, 1.50, and 6.00 ml/l. with a dietary fiber content of 1.20, 1.18, and 1.17 g/100 g of solvent, respectively.

Chlorophyll a, chlorophyll b, and total chlorophyll content are important factors in farmers' decision-making. The RED FINGER variety had the lowest chlorophyll A content, averaging 2.96 mg/g fresh weight, while the concentrations of MFA obtained at each level showed statistical differences. The control treatment with MFA had the lowest value (5.04 mg/g fresh weight). The chlorophyll b content and total chlorophyll content varied among the cultivated okra varieties. KN-OYV-02 had the highest chlorophyll b (4.66 mg/g fresh weight). MFA treated at 3.00, 4.50, and 6.00 ml/l were the best and did not differ statistically. The values of chlorophyll b were 3.60, 3.92, and 4.15 mg/g fresh weight, respectively. In contrast, the control treatment (non-injection MFA) found that chlorophyll b contained the lowest amount of chlorophyll b (2.69 mg/g fresh weight). The total chlorophyll content was similar to the results shown in Figure 4. Statistical differences were observed in carotenoid levels, reducing sugar, fiber content, and chlorophyll among okra varieties. RED FINGER exhibited the highest carotenoid content at 0.50 μg/g fresh weight, while KN-OYV-02 and LUCKY FILE 473 showed similar values at 0.06 and 0.07 μg/g fresh weight, respectively. The optimum carotenoid value was observed at MFA levels of 3.00 ml/l, corresponding to 0.26 μg/g fresh weight. However, no statistical difference was observed in MFA intake at 4.50 and 6.00 ml/l, which were 0.22 and 0.23 μg/g, respectively, while the non-injected MFA carotenoids contained the fewest carotenoids, 0.16 μg/g fresh weight. Reducing sugar analysis revealed no differences between okra varieties. However, a statistical difference was observed among the MFA levels used to treat okra. LUCKY FILE 473 exhibited the highest reducing sugar content, approximately 1.77 mg/mL, as reported by Wiedemair et al. [30]. The optimal values were obtained with MFA intake at 3.00, 4.50, and 6.00 ml/l, with no statistical difference among them. The dietary fiber content of okra, after MFA infusion, showed statistical differences among okra varieties and MFA concentrations at each level. LUCKY FILE 473 recorded the highest dietary fiber content at 1.22 g/100 g of solvent, while MFA levels of 1.50, 3.00, 4.50, and 6.00 ml/l showed no statistical difference compared to the control. MFA at 4.50 ml/l demonstrated the highest dietary fiber content (1.21 g), followed by MFA concentrations of 3.00, 1.50, and 6.00 ml/l, with dietary fiber contents of 1.20, 1.18, and 1.17 g, respectively, as reported by [26]. The RED FINGER variety had the lowest chlorophyll A content, averaging 2.96 mg/g fresh weight, while MFA concentrations at each level showed statistical differences. The control treatment with MFA had the lowest value (5.04 mg/g fresh weight). The chlorophyll b content and total chlorophyll content varied among the cultivated okra varieties. KN-OYV-02 had the highest chlorophyll b (4.66 mg/g fresh weight). MFA treated at 3.00, 4.50, and 6.00 ml/l did not differ statistically, with values of 3.60, 3.92, and 4.15 mg/g fresh weight, respectively. In contrast, the control treatment (non-injection MFA) found that chlorophyll b contained the lowest amount of chlorophyll b (2.69 mg/g fresh weight). Ofosu-Anim and Leitch [31] reported that Microbes also play a role in chlorophyll levels, and the effects of microbes have been previously reported. demonstrated a significantly higher chlorophyll content in barley leaves, reflecting differences in the N content and uptake of organic manures. Moreover, Reghuvaran and Das Ravindranath [32] also reported that leaf chlorophyll content is important because photosynthetic activity and crop yields might increase with higher leaf chlorophyll.

Research on organic farming and organic food production is rapidly increasing worldwide because organic agricultural products are generally considered safer and healthier than conventionally grown food [24]. The current report confirms that MFA is the best form of liquid organic nutrients for maintaining soil fertility, as it supports a higher microbial population and promotes a more sustainable system of food production with a high nutritive value. This low-cost liquid technology could play a major role in protecting the environment, increasing the number of living biota in cultivable soil, and increasing yields in future agricultural practices. Moreover, the preparation of this MFA is quite simple, and every farmer can follow it; the ingredients are available in their farmyard at a low cost.

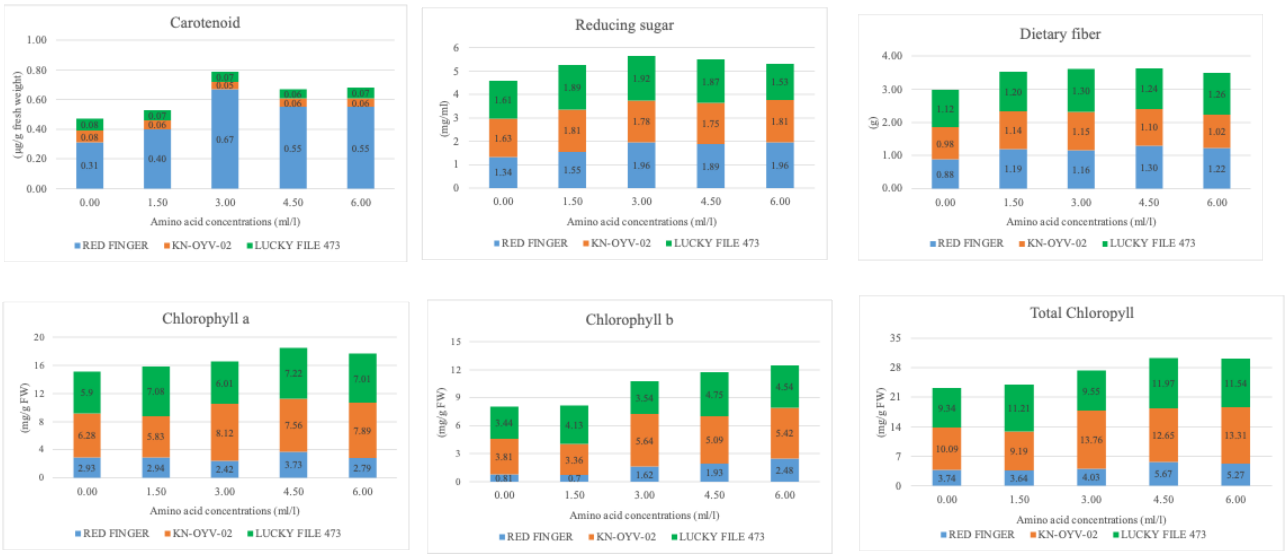

Figure 4. Carotenoid, reducing sugar, fiber, and chlorophyll contents of okra as affected by MFA concentrations.

4. Conclusions

The present study sheds light on the potential impact of MFA foliar applications on okra plant growth, yield, and antioxidant levels. Recognized for its pharmacological and health benefits, okra has shown promise for further enhancement through strategic MFA use. Key findings indicate that MFA at 3 ml/l had the most substantial effect on increasing plant growth, pod morphology, and yield. Additionally, notable improvements in various yield parameters, including plant height, pod length and width, yield/pod, and yield/plant, were observed in plants treated with 3.00, 4.50, and 6.00 ml/l, emphasizing their practical significance for yield enhancement. Furthermore, those dosages exhibited higher dietary fiber and reduced sugar concentrations, along with higher concentrations of carotenoids, anthocyanins, and total Chl, underscoring the potential of MFA composition to facilitate the biosynthesis of those phytochemical compounds. These outcomes reveal the promising potential of MFA foliar sprays to maximize okra growth, yield, and photosynthesis-related phytochemical concentrations. The practical implications of our research are noteworthy, offering a strategic approach for enhancing okra cultivation. This study has significant implications for sustainable agriculture practices and enhances the agricultural and pharmaceutical industries by improving both the nutritional and therapeutic qualities of this exceptional crop.

5. Acknowledgements

The authors are highly grateful to the Faculty of Technology and Community Development, Thaksin University. The Research and Innovation Fund at Thaksin University supported this work. Lastly, the authors would like to express their sincere gratitude to PLANEAT FARM CO., LTD. for providing the amino acids used in this experiment.

Author Contributions: For research articles with several authors, a short paragraph specifying their individual contributions must be provided. The following statements should be used "Conceptualization, S.B. methodology, S.B., P.H., M.S.M.H. and N.T.; software, S.B.; validation, S.B. and M.S.M.H.; formal analysis, S.B.; investigation, S.B.; resources, S.B. and N.T.; data curation, S.B..; writing—original draft preparation, S.B., P.H., M.S.M.H. and N.T; writing—review and editing, S.B.; visualization, S.B. and N.T.; supervision, S.B..; project administration, S.B. All authors have read and agreed to the published version of the manuscript.

Funding: This research was funded by the Faculty of Technology and Community Development, Thaksin University; the Research and Innovation Institute, Thaksin University; and the National Research Council of Thailand (NRCT).

Conflicts of Interest: The authors declare no conflict of interest.

References

[1] Benchasri, S.; Pruthikanee, P. Genetic Variability for Yield and Yield Components of Thai Chilli (*Capsicum* spp.) Landraces under Inorganic and Organic Agricultural Systems. *Aust. J. Crop Sci.* **2018**, *12*, 126–134. https://doi.org/10.21475/ajcs.18.12.01.pne778

[2] Liu, J.; Lin, X.; Wang, X.; Feng, L.; Zhu, S.; Tian, R.; Fang, J.; Tao, A.; Fang, P.; Qi, J.; Zhang, L.; Huang, Y.; Xu, J. Genomic and Cytogenetic Analyses Reveal Satellite Repeat Signature in Allotetraploid Okra (*Abelmoschus esculentus*). *BMC Plant Biol.* **2024**, *24*, 71. https://doi.org/10.1186/s12870-024-04739-9

[3] Benchasri, S. Okra (*Abelmoschus esculentus* (L.) Moench) as a Valuable Vegetable of the World. *Field Veg. Crop Res.* **2012**, *49*, 105–112. https://doi.org/10.5937/ratpov49-1172

[4] Dantas, T. L.; Buriti, F. C. A.; Florentino, E. R. Okra (*Abelmoschus esculentus* L.) as a Potential Functional Food Source of Mucilage and Bioactive Compounds with Technological Applications and Health Benefits. *Plants* **2021**, *10* (8), 1683. https://doi.org/10.3390/plants10081683

[5] Hamdan, Y. A. S.; Hawamda, A. I. M.; Salimia, R. B.; Salman, M. Genetic Diversity Assessment of Palestinian Okra Landraces (*Abelmoschus esculentus* L.) through RAPD Marker. *Genet. Resour. Crop Evol.* **2024**, in press. https://doi.org/10.21203/rs.3.rs-3536240/v1

[6] Benchasri, S.; Simla, S.; Harakotr, B. The Effect of Genotypic Variability on the Yield and Yield Components of Okra (*Abelmoschus esculentus* L. Moench) in Thailand. *Asian J. Agric. Biol.* **2020**, *8*(4), 480–490.

[7] Sun, J.; Xu, G.; Hu, Y.; Zheng, Y.; Wang, X.; Yang, J.; Yang, M.; Xie, D.; Dai, Z. Genome-Wide Assessment of Genetic Diversity and Association Mapping for Salt Tolerance Traits in Okra (*Abelmoschus esculentus* L. Moench) Using Genotyping-by-Sequencing. *Sci. Hortic.* **2023**, *313*, 111922. https://doi.org/10.1016/j.scienta.2023.111922

[8] Coban, S. N.; Polatoglu, I.; Eroglu, E. M. Methyl Cellulose/Okra Mucilage Composite Films, Functionalized with *Hypericum perforatum* Oil and Gentamicin, as a Potential Wound Dressing. *Int. J. Biol. Macromol.* **2024**, *251* (1), 127757. https://doi.org/10.1016/j.ijbiomac.2023.127757

[9] Graham, J. O.; Agbenorhevi, J. K.; Kpodo, F. M. Total Phenol Content and Antioxidant Activity of Okra Seeds from Different Genotypes. *Am. J. Food Nutr.* **2015**, *5*, 90–94. https://doi.org/10.12691/ajfn-5-3-2

[10] Zhang, T.; Xiang, J.; Zheng, G.; Yan, R.; Min, X. Preliminary Characterization and Antihyperglycemic Activity of a Pectic Polysaccharide from Okra (*Abelmoschus esculentus* (L.) Moench). *J. Funct. Foods* **2018**, *41*, 19–24. https://doi.org/10.1016/j.jff.2017.12.028

[11] Elkhalifa, A. E.; Alshammari, E.; Adnan, M.; Alcantara, J. C.; Awadelkareem, A. M.; Eltoum, N. E.; Mehmood, K.; Panda, B. P.; Ashraf, S. A. Okra (*Abelmoschus esculentus*) as a Potential Dietary Medicine with Nutraceutical Importance for Sustainable Health Applications. *Molecules* **2021**, *26*(3), 696. https://doi.org/10.3390/molecules26030696

[12] Jiang, N.; Liu, C.; Li, D.; Zhang, Z.; Liu, C.; Wang, D.; Niu, L.; Zhang, M. Evaluation of Freeze Drying Combined with Microwave Vacuum Drying for Functional Okra Snacks: Antioxidant Properties, Sensory Quality, and Energy Consumption. *LWT–Food Sci. Technol.* **2017**, *82*, 216–226. https://doi.org/10.1016/j.lwt.2017.04.015

[13] Hildebrandt, T. M.; et al. Amino Acid Catabolism in Plants. *Mol. Plant* **2015**, *8*(11), 1563–1579. https://doi.org/10.1016/j.molp.2015.09.005

[14] Sarojnee, D. Y.; Navindra, B.; Chandrabose, S. Effect of Naturally Occurring Amino Acid Stimulants on the Growth and Yield of Hot Peppers (*Capsicum annuum* L.). *J. Anim. Plant Sci.* **2009**, *5*(1), 414–424.

[15] Rebecca, L. J.; Sharmila, S.; Paul Das, M.; Seshiah, C. Extraction and Purification of Carotenoids from Vegetables. *J. Chem. Pharm. Res.* **2014**, *6* (4), 594–598.

[16] Giusti, M. M.; Wrolstad, R. E. Characterization and Measurement of Anthocyanins by UV–Visible Spectroscopy. *Curr. Protoc. Food Anal. Chem.* **2001**, F1.2.1–F1.2.13. https://doi.org/10.1002/0471142913.faf0102s00

[17] Somogyi, M. Notes on Sugar Determination. *J. Biol. Chem.* **1952**, *195*, 19–23. https://doi.org/10.1016/S0021-9258(19)50870-5

[18] Andrade, N. J. P.; Monteros-Altamirano, A.; Bastidas, C. G. T.; Sørensen, M. Morphological, Sensorial and Chemical Characterization of Chilli Peppers (*Capsicum* spp.) from the CATIE Genebank. *Agronomy* **2020**, *10* (11), 1732. https://doi.org/10.3390/agronomy10111732

[19] Karem, M. H.; Haidery, A. A. A. Induced Systemic Resistance of Okra (*Abelmoschus esculentus* L.) against Okra Yellow Vein Mosaic Virus Using Amino Acid and Algae Extracts. *Pak. J. Phytopathol.* **2022**, *34*(2), 213–220. https://doi.org/10.33866/phytopathol.034.02.0799

[20] Han, G.; Li, Y.; Yang, Z.; Wang, C.; Zhang, Y.; Wang, B. Molecular Mechanisms of Plant Trichome Development. *Front. Plant Sci.* **2022**, *13*, 910228. https://doi.org/10.3389/fpls.2022.910228

[21] Khan, S.; Yu, H.; Li, Q.; Gao, Y.; Sallam, B. N.; Wang, S.; Liu, P.; Jiang, W. Exogenous Application of Amino Acids Improves the Growth and Yield of Lettuce by Enhancing Photosynthetic Assimilation and Nutrient Availability. *Agronomy* **2019**, *9*, 266. https://doi.org/10.3390/agronomy9050266

[22] Shekari, G.; Javanmardi, J. Effects of Foliar Application of Pure Amino Acid and Amino Acid-Containing Fertilizer on Broccoli (*Brassica oleracea* L. var. *italica*) Transplant. *Adv. Crop Sci. Technol.* **2017**, *5*, 280. https://doi.org/10.4172/2329-8863.1000280

[23] Seyedi, A.; Fathi, S.; Movlodzadeh, R. The Effect of Biostimulants Based on Free Amino Acids on Some Growth and Physiological Parameters of *Dracocephalum moldavica* L. under Salinity Stress. *J. Med. Plants By-Prod.* **2023**, in press.

[24] Krishnamoorthy, R.; Alshatwi, A. A.; Subbarayan, S.; Bharathi. Impact of Farm-Made Liquid Organic Nutrients Jevamirtham and Fish Amino Acid on Growth and Nutritional Status in Different Seasons of *Abelmoschus esculentus*: A Self-Sustainable Field Trial. *Org. Agric.* **2019**, *9*(3–4), 333–344. https://doi.org/10.1007/s13165-018-0205-2

[25] Koukounaras, A.; Tsouvaltzis, P.; Siomos, A. S. Effect of Root and Foliar Application of Amino Acids on the Growth and Yield of Greenhouse Tomato under Different Fertilization Levels. *J. Food Agric. Environ.* **2013**, *11*, 644–648.

[26] Teixeira, W. F.; Fagan, E. B.; Soares, L. H.; Umburanas, R. C.; Reichardt, K.; Neto, D. D. Foliar and Seed Application of Amino Acids Affects the Antioxidant Metabolism of the Soybean Crop. *Front. Plant Sci.* **2017**, *8*, 327. https://doi.org/10.3389/fpls.2017.00327

[27] Baqir, A.; Naqeeb, A. Effect of Some Amino Acids on Tillering and Yield of Three Bread Wheat Cultivars. *Iraqi J. Agric. Sci.* **2019**, *50*, 20–30. https://doi.org/10.36103/ijas.v50iSpecial.173

[28] Ijarotimi, O. S.; Akinola-Ige, A. O.; Oluwajuyitan, T. D. Okra Seed Proteins: Amino Acid Profile, Free Radical Scavenging Activities and Inhibition of Diabetes- and Hypertension-Converting Enzyme Indices. *Measurement: Food* **2023**, *11*, 100101. https://doi.org/10.1016/j.meafoo.2023.100101

[29] Esmaeilzadeh, D.; Razavi, B. M.; Hosseinzadeh, H. Effect of *Abelmoschus esculentus* (Okra) on Metabolic Syndrome: A Review. *Phytother. Res.* **2020**, *34* (9), 2192–2202. https://doi.org/10.1002/ptr.6679

[30] Wiedemair, V.; Scholl-Bürgi, S.; Karall, D.; Huck, C. W. Amino Acid Profiles and Compositions of Different Cultivars of *Panicum miliaceum* L. *Chromatographia* **2020**, *83*, 829–837. https://doi.org/10.1007/s10337-020-03899-8

[31] Ofosu-Anim, J.; Leitch, M. Relative Efficacy of Organic Manures in Spring Barley (*Hordeum vulgare* L.) Production. *Aust. J. Crop Sci.* **2009**, *3*(1), 13–19.

[32] Reghuvaran, A.; Das Ravindranath, A. Efficacy of Biodegraded Coir Pith for Cultivation of Medic. **2010**.

ASEAN
Journal of Scientific and Technological Reports
Online ISSN:2773-8752

Research article

A Comprehensive Literature Review on Greenhouse Gas Mitigation in Thailand's Building and Industrial Sectors: Technical, Economic, and Policy Insights from Recent Studies

Jirawong Siribrahmanakul[1*], and Somying Ngarmpornprasert[1]

[1] College of Engineering and Technology, Dhurakij Pundit University, Bangkok, 10210, Thailand
* Correspondence: j.siribrahmanakul@gmail.com; somying.ngt@dpu.ac.th

Citation:
Siribrahmanakul, J.; Ngarmpornprasert, S. A comprehensive literature review on greenhouse gas mitigation in Thailand's building and industrial sectors: technical, economic, and policy insights from recent studies. *ASEAN J. Sci. Tech. Report.* **2026**, *29*(3), e261277. https://doi.org/10.55164/ajstr.v29i3.261277.

Article history:
Received: September 15, 2025
Revised: January 22, 2026
Accepted: January 25, 2026
Available online: March 1, 2026

Publisher's Note:
This article is published and distributed under the terms of Thaksin University

Abstract: This scoping review examines greenhouse gas (GHG) mitigation options in Thailand's industrial and building sectors, synthesizing findings from 26 peer-reviewed articles and five national policy documents. The review is structured around three themes: technical viability, financial performance, and policy alignment of key mitigation strategies. Results indicate that energy-efficiency retrofitting, renewable energy integration, carbon capture and storage (CCS), and life-cycle assessment (LCA)-guided design – particularly when combined with Building Information Modeling (BIM) – can substantially reduce both operational and embodied emissions. Many of these approaches demonstrate strong financial attractiveness, characterized by high internal rates of return (IRR) and short payback periods. However, widespread deployment remains constrained by policy fragmentation, insufficient incentive mechanisms, and weak stakeholder coordination. The review also exposes critical gaps in sectoral strategies, including the absence of tailored energy conservation measures for certain building typologies. The limited uptake of local green certification schemes, such as TREES, which cover fewer than 15% of certified green buildings nationwide, further reflects structural barriers in Thailand's regulatory and market environments. To address these challenges, this study proposes a sectoral strategy matrix that maps appropriate technologies to specific building types alongside relevant economic indicators. It also recommends harmonizing existing frameworks – EEP2015, AEDP2015, and BEC2021 – with Thailand's 2022 Nationally Determined Contribution (NDC) and Long-Term Low Emissions Development Strategy (LT-LEDS). Future research should explore integrated models incorporating ESG criteria, stakeholder capacity-building, and carbon tracking linked to Science-Based Targets (SBTs). By bridging technical rigor with policy relevance, this review offers actionable guidance for researchers, policymakers, and industry practitioners.

Keywords: Energy efficiency; carbon mitigation; life cycle assessment; science-based targets; Thailand

1. Introduction

Climate change mitigation has become a priority in modern society, forcing national governments and industries to adopt more effective GHG-reduction policies aligned with scientific advice. The paths for global warming levels adopted at 1.5°C and 2.0°C – defined in the Paris Agreement and advocated by programs like Science-Based Targets (SBTs) – call for immediate

action from all industries, with a focus on decarbonization. In Thailand, where industrial and building energy use accounts for a major share of the country's total emissions, effective action in these areas is not only a critical environmental imperative but also a potential economic opportunity. The industry sector accounts for nearly 40% of Thailand's total emissions, mostly from fossil fuel combustion [1]. In contrast, the building sector, including residences, offices, retail buildings, and public institutions, accounts for approximately 15% of emissions, primarily from electricity consumption for cooling, lighting, and operations [2]. This is further supported by office LCA studies that highlight high operational loads, particularly HVAC and lighting [3]. These figures characterize the imperative for effective, scalable mitigation measures.

To address these issues, Thailand has put forward a series of policies for energy and climate, including the Energy Efficiency Plan (EEP2015) [4], Alternative Energy Development Plan (AEDP2015) [5], Power Development Plan (PDP2015) [6], and Building Energy Code (BEC2021) [7]. In addition, the Energy Conservation Promotion Act B.E.2535 (1992) [8] has created a long-term legislative foundation for energy conservation measures. Furthermore, Thailand has recently committed to updated international goals under the 2022 Nationally Determined Contribution (NDC) and the Long-Term Low Emissions Development Strategy (LT-LEDS), reinforcing the need to integrate new strategies for deep decarbonization. However, even with the strength of these tools, they require revision to capture advancements in technology, innovative financial instruments, and global climate targets. For one, policies currently on the books often aim to reduce energy use; yet they don't incorporate life-cycle emissions data, carbon trading schemes, or harmonization between private-sector activities and Net Zero targets. Previous academic studies have put forward numerous mitigation measures that include energy efficiency retrofitting improvements, integration with renewable energy technologies, carbon capture and storage (CCS) technologies, and design principles based on life cycle assessment (LCA), often supplemented with digital tools like Building Information Modeling (BIM) [3, 9, 10, 11, 12]. While they provide estimates of both technical and economic aspects, limited academic work connects these findings with Thailand's evolving policy and institutional environment.

This review consolidates evidence from 26 peer-reviewed research articles and five official policy documents to examine the intersection of technical feasibility, economic viability, and policy relevance in Thailand's efforts to reduce GHG emissions.

2. Methodology

This study employed a scoping literature review approach to synthesize measures for reducing GHG emissions in Thailand's construction and industrial sectors. The review aimed to link technological knowledge with economic feasibility and policy harmonization, thereby facilitating the identification of replicable, context-appropriate strategies for national application.

2.1 Literature Selection

A total of 26 peer-reviewed scholarly articles published between 2006 and 2024 were selected based on predefined inclusion criteria. These criteria included (1) direct relevance to GHG mitigation, (2) application within Thailand's building or industrial sectors, (3) inclusion of quantitative or model-based findings, and (4) publication in peer-reviewed journals. The 2006–2024 timeframe was chosen to reflect the evolution of Thailand's energy and climate frameworks, covering both the pre-Paris Agreement period and the post-BEC2021 implementation context. This allowed the review to capture shifts in technology availability, policy direction, and methodological practice over time, including the emergence of BIM-LCA and SBTi-aligned studies in the 2020s. To mitigate selection bias, articles were identified through a combination of database search (ScienceDirect, SpringerLink, TCI), backward reference tracking, and citation-based relevance filtering. The screening was performed independently using the stated criteria to ensure consistency and thematic saturation across the sample. In parallel, five national-level policy documents were selected based on their legal status, current applicability, and foundational role in shaping Thailand's energy and climate strategies. These include the Energy Efficiency Plan (EEP2015) [4], the Alternative Energy Development Plan (AEDP2015) [5], the Power Development Plan (PDP2015) [6], the Building Energy Code (BEC2021) [7], and the Energy Conservation Promotion Act B.E.2535 (1992) [8]. While other planning documents, such as Thailand's NDC and National Climate Change Master Plan, exist, they were not included due to their non-binding nature or

insufficient detail for building-sector implementation at the time of writing. In alignment with the PRISMA-ScR framework, the initial search process involved querying Scopus and ThaiJo databases using a combination of keyword strings, including: "greenhouse gas mitigation," "GHG reduction," "building sector," "industrial sector," "energy efficiency," "carbon neutrality," "carbon capture and storage," "life cycle assessment," "BIM," and "Thailand." Boolean operators (AND, OR) were used to enhance the sensitivity and specificity of search results. This process identified 223 articles from Scopus and 13 from ThaiJo. After removing duplicates and conducting an initial screening of titles and abstracts, 108 articles were selected for full-text assessment. Finally, 26 articles were retained for synthesis based on relevance, methodological rigor, and alignment with the inclusion criteria (Figure 1).

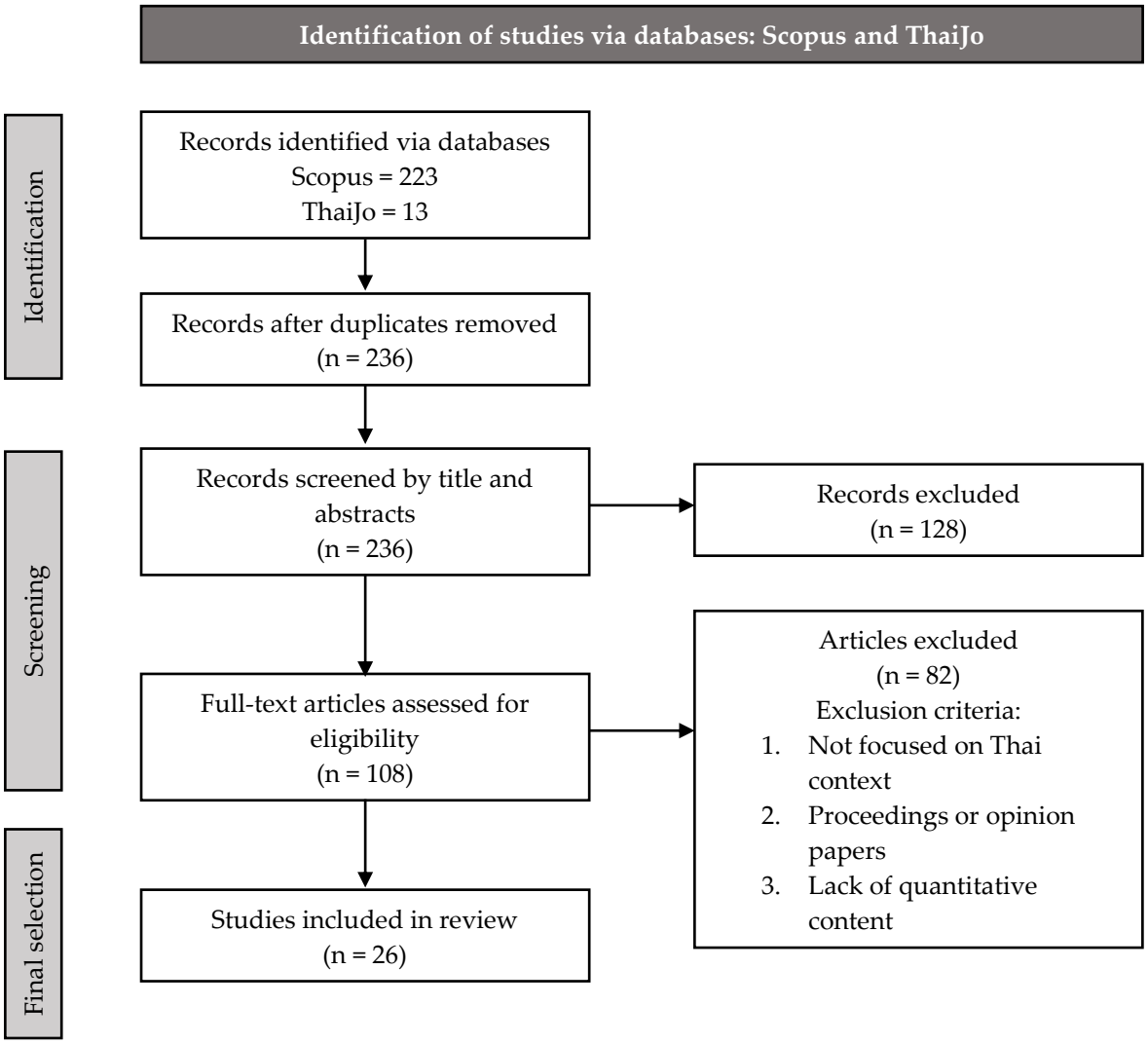

Figure 1. PRISMA-ScR flow diagram illustrating the identification, screening, and selection process of articles for inclusion in the scoping review.

2.2 Classification and Summary of Literature

Table 1 provides a structured summary of the 26 academic articles that were analyzed, including information on year of publication, methodologies applied, sector focus, and breadth of analysis. The articles were categorized based on underlying methodologies, including:

- Life Cycle Assessment (LCA)
- Energy simulation and modeling (e.g., LEAP, CGE)
- Techno-economic analysis
- Policy assessment or scenario-based modeling

These methodological groupings were used to understand not only the scope of technical and economic findings but also the kinds of questions each approach is suited to address. For example, LCA studies generally emphasized embodied versus operational carbon tradeoffs, while LEAP and CGE models captured system-level implications and macroeconomic outcomes. Techno-economic and sensitivity analyses focused on financial feasibility, while policy modeling helped to frame alignment with national and international targets. This categorization informed subsequent data extraction and thematic synthesis, ensuring that each mitigation approach was assessed across multiple dimensions: technical effectiveness, financial feasibility, and policy relevance.

2.3 Data Extraction and Grouping

Quantitative measures such as energy savings, percentage decrease in GHG emissions, IRR, payback time, and marginal abatement cost (MAC) were obtained from individual studies. Likewise, qualitative remarks regarding implementation barriers, policy deficiencies, and stakeholder concerns were also noted.

Data from each article were extracted into structured tables and matrices to enable comparison across metrics and methods.

It was categorized in terms of thematic dimensions in accordance with their main contributions:

- Technical effectiveness of specific measures (e.g., HVAC retrofits, rooftop PV, CCS)
- Economic performance and financial viability
- Regulatory frameworks and institutional readiness

This thematic clustering was essential for identifying performance trends, context-dependent barriers, and sector-specific policy implications, which were subsequently integrated into the comparative synthesis presented in the Results section.

2.4 Analytical Synthesis Approach

The synthesis procedure consisted of two main phases:

1. Comparative Analysis: Different tools were analyzed with respect to what they specifically address (e.g., Life Cycle Assessment for embodied carbon and LEAP for long-term national scenarios). Similarities and distinctions between these tools were noted to identify how different tools complement one another. This phase enabled identification of methodological strengths, data limitations, and sector-specific insights, which informed the structure of the final comparative synthesis across strategies.
2. Policy Integration Mapping: The findings from the technical-economic analysis were aligned with the five main national policies [4 - 8] to identify gaps and potential avenues for strategic alignment. This also included considering how mitigation measures could enable Thailand's transition to Net Zero, as well as determining where future modeling should align with methodologies such as the Science Based Targets initiative (SBTi). Rather than employing a rigid, systematic protocol, the synthesis followed a structured scoping review process that enabled thematic integration across technical, financial, and policy domains.

Table 1. Summary of Reviewed Articles by Year, Method, and Focus.

Reference	Author (s) / Year	Methodology	Sector Focus	Analytical Scope
[1]	Pradhan et al. (2022)	LCA+BIM	Housing	Early-stage carbon optimization
[2]	Tangprasert & Leeprechanon (2023)	LEAP	Industry	LEAP scenario analysis
[3]	Kofoworola & Gheewala (2009)	LCA	Office Buildings	Embodied & Operational emissions
[9]	Tevis et al. (2019)	Scenario modeling	Residential	Behavioral scenarios
[10]	Viriyaroj et al. (2024)	GHG accounting	Industry	Carbon footprint estimation
[11]	Tulevech et al. (2018)	Techno-economic	Industry	Energy-cost trade-off
[12]	Inharwararak & Stravoravdis (2023)	Techno-economic	Industry	BEMS & lighting systems
[13]	Kofoworola & Gheewala (2008)	LCA	Office Building	Embodied & Operational emissions
[14]	Phyo Zaw Oo et al. (2021)	LCA	Materials	Low-carbon cement
[15]	Seeley & Dhakal (2021)	Policy review	Policy	Energy law analysis
[16]	Ananwattanaporn et al. (2021)	LCA + GHG inventory	Industrial Buildings	EF benchmarking
[17]	Yamtraipat et al. (2006)	LCA	Residential	Life cycle GHG evaluation
[18]	Jareemit et al. (2022)	Policy analysis	Policy	Policy coherence
[19]	Boonpanya & Masui (2020)	Policy review	Policy	Power sector strategy
[20]	Rajbhandari et al. (2019)	LCA	Buildings	Material intensity hotspots
[21]	Thepkhun et al. (2013)	Policy evaluation	Policy	Implementation barriers
[22]	Kongwanarat & Limmeechokchai (2016)	Techno-economic	Industrial	Investment decision modeling
[23]	Limmeechokchai et al. (2024)	Techno-economic	Industry	Efficiency adoption modeling
[24]	Rajbhandari & Limmeechokchai (2020)	LEAP	Residential	Long-term energy demand
[25]	Limmeechokchai et al. (2017)	Energy simulation	Commercial Buildings	Cooling energy modeling
[26]	Chaichaloempreecha et al. (2019)	LEAP + MAC modeling	Multi-sector Policy	National Plan Scenario Modeling
[27]	Lohmeng et al. (2017)	Policy Review	Certification	Green Building Rating Systems
[28]	Rahong & Prapaspongsa (2022)	LCA	Construction	Green materials innovation
[29]	Inazumi et al. (2011)	Environmental Accounting	Urban Waste	Waste Stream GHG Accounting
[30]	Limmeechokchai et al. (2023)	Policy analysis	Policy	Policy incentive analysis
[31]	Saranrom et al. (2023)	Scenario modeling	Residential	Technology adoption & policy

3. Literature Review

3.1 Embodied Carbon and Life Cycle Assessment (LCA)

Recent years have seen growing scholarly interest in applying Life Cycle Assessment (LCA) to quantify embodied carbon in buildings, aiming to capture the hidden GHG footprint associated with materials and the construction stage, not just operational use. This subsection reviews key LCA studies across Thailand's building typologies and interprets their implications for decarbonization strategies. The use of Life Cycle Assessment (LCA) to assess embodied carbon in Thailand's construction industry has shown a continued upward trend in research activity. LCA provides a structured methodology for assessing cumulative greenhouse gas (GHG) emissions associated with building operations and material changes throughout a building's life cycle. A series of studies investigated embodied emissions across different building types, construction phases, and energy systems. Kofoworola and Gheewala [3] performed one of the earliest LCA-oriented analyses of a typical office building in Bangkok. They found that embodied emissions from concrete and steel accounted for a significant share of the overall life-cycle contribution. Subsequent research by the same authors [13] on a larger commercial building validated that these materials continue to dominate the embodied carbon footprint. For industrial buildings, Tulevech et al. [11] conducted a multi-scenario LCA study of a low-energy facility. The results showed that approximately 71% of total emissions originated from embodied energy, while operational energy contributed only 17%. This trend was similarly observed in the residential sector by Viriyaroj et al. [10], who found that operational emissions accounted for 72–78% of total life-cycle GHGs in standard detached houses, while embodied emissions comprised 19–23%, primarily from concrete and insulation. The study done by Tevis et al. [9] involved a life cycle assessment (LCA) of different alternative energy supply scenarios for office buildings. The study showed that rooftop photovoltaic (PV) systems with ice thermal storage could reduce reliance on grid electricity by up to 38%, while the strategy might increase metal depletion and resource use in upstream activities. Under the design integration framework, Inharwararak and Stravoravdis [12] used a Building Information Modeling–Life Cycle Assessment (BIM-LCA) approach to examine a low-rise residential complex in Thailand. The study findings revealed that material optimization at early stages, using BIM software, resulted in a 42.4% reduction in embodied emissions. To enhance methodological accuracy in Thai-specific contexts, Phyo Zaw Oo et al. [14] proposed a localized set of normalization factors for LCA. These country-specific metrics were developed to improve the comparability and relevance of LCA results, particularly when applied to construction systems and material supply chains in Thailand. While both Tulevech et al. [11] and Viriyaroj et al. [10] used LCA to evaluate life-cycle emissions, their findings differ substantially – one emphasizes embodied emissions, the other operational emissions. This discrepancy is likely due to differences in building type, system boundary, and occupancy assumptions. Industrial facilities often have large structural footprints with low energy loads, while residential homes have lighter construction but high cooling demands. Furthermore, the modeling boundary (e.g., cradle-to-gate vs cradle-to-grave) and assumed usage profiles significantly affect the outcome. More broadly, methodological limitations were observed across studies. Not all LCA models used the same emission factors or normalization methods; some relied on global datasets, while others incorporated region-specific parameters. Only one study [14] proposed Thai-specific normalization factors. This inconsistency limits cross-comparability of results and weakens policy translation. Additionally, BIM-LCA integration remains in the early stages, with limited adoption beyond academic pilots. Despite these limitations, the reviewed LCA studies consistently highlight the carbon dominance of concrete and steel in embodied emissions and underscore the mitigation potential of early design intervention, material optimization, and locally adapted emission factors.

Table 2. Summary of Key Findings from LCA Studies in Thailand.

Study Focus	Sector	Main Findings & Implications	Reference
Office Building LCA (Bangkok)	Commercial	Operational energy (HVAC ~56%, lighting ~15%) is dominant; high embodied emissions from concrete (64%) and steel (17%)	[3]
Operational Energy Supply (Office)	Commercial	Rooftop PV with ice thermal storage reduced grid dependency (~38%); caution metal depletion impacts	[9]
Standard Residential Houses	Residential	Operational emissions dominate life-cycle (72–78%); notable embodied emissions (19–23%)	[10]
Low-Energy Industrial Buildings	Industrial	Embodied energy (materials ~71%) exceeds operational energy (~17%); renewables and recycled materials are recommended	[11]
BIM-LCA for Housing Estates	Residential	Early design integration of BIM-LCA reduces embodied emissions by ~42.4%	[12]
Office Building LCA (Extended)	Commercial	Embodied emissions dominated by concrete and steel; findings consistent with earlier Bangkok office study [6]	[13]
Thai Normalization Factors	General	Development of Thai-specific normalization factors enhances the accuracy and applicability of local LCAs	[14]

3.2 Energy Use and GHG Emission Reduction in Thailand's Building Sector

An increasing number of studies in Thailand have been investigating energy conservation and GHG mitigation strategies in the building sector. These studies primarily focus on retrofitting existing systems, enhancing energy efficiency in commercial and residential buildings, and integrating renewable energy solutions such as photovoltaic (PV) systems. The reviewed articles assessed technical performance, financial viability, and regulatory alignment, particularly in relation to the Building Energy Code (BEC2021). Seeley and Dhakal [15] analyzed HVAC and lighting system retrofits in commercial buildings and reported energy savings of approximately 18.1%, an internal rate of return (IRR) of 19%-20%, and a payback period of 4 years. Ananwattanaporn et al. [16] evaluated BEC-compliant retrofits in low-rise residential buildings and found energy savings of approximately 49.4%, with an IRR of 19.3% and a payback period of 4.36 years. Yamtraipat et al. [17] showed that increasing indoor temperature setpoints from 24°C to 26°C in offices reduced electricity usage by 12.3%, offering a no-cost behavioral mitigation option. Jareemit et al. [18] explored Zero Energy Office Building (ZEB) investment and confirmed its strong financial viability, particularly when supported by dedicated incentives and policy mechanisms. Tevis et al. [9] found that rooftop PV systems with thermal storage reduced grid electricity reliance by 38% in commercial buildings, though metal depletion impacts were noted. Across these studies, retrofit interventions in residential buildings yielded higher energy savings than in commercial settings, due in part to lower baseline efficiency and greater insulation potential in detached housing stock. However, commercial retrofits demonstrated superior financial indicators (e.g., IRR, payback) due to economies of scale and operating hour advantages. Collectively, these findings suggest that retrofit strategies must be customized by building type, with residential retrofits focusing on thermal performance and envelope measures, while commercial buildings may prioritize HVAC system upgrades and control systems. Policy incentives should reflect these differences to maximize return on investment and GHG reductions.

Table 3. Summary of Key Findings from Energy Efficiency and Renewable Energy Studies in Thailand's Building Sector.

Study Focus Group	Building Type	Main Findings and Economic Implications	Reference
Renewable Energy Integration (PV)	Commercial & Residential	Rooftop PV reduced grid dependency by ~38% and is economically viable with appropriate incentives.	[9]
HVAC and LED Retrofits	Commercial	Average energy savings ~18.1%; IRR ~19–20%; payback period ~4 years	[15]
Residential Retrofits (BEC compliance)	Residential	Energy savings up to ~49.4%; IRR ~19.3%; payback period ~4.36 years	[16]
Indoor Temperature Setpoint Adjustments	Commercial (Offices)	Increasing temperatures from 24°C to 26°C reduced energy consumption ~12.3% nationwide	[17]
Zero Energy Office Buildings (ZEB)	Commercial	Integration of renewable energy and energy-efficient design is highly economically viable with policy support	[18]

Note: Table includes only empirical or techno-economic studies with measured or modeled outcomes.

3.3 GHG Reduction in the Industrial and Commercial Sectors through Energy Efficiency and CCS Technologies

Several studies have examined the prospects for GHG mitigation in Thailand's commercial and industrial sectors through advanced energy efficiency measures and carbon capture and storage (CCS) technology. These options are typically assessed for both technical potential and economic viability, particularly in light of the nation's changing policy environment and long-term decarbonization objectives. Seeley and Dhakal [15] studied retrofitting energy efficiency measures in a range of commercial buildings. Their study focused on heating, ventilation, and air conditioning (HVAC) systems, lighting upgrades, and building energy management systems (BEMS). Their results showed that operational energy savings were around 18%, with internal rates of return (IRR) of 19%-20%, a payback period of about 4 years, and negative marginal abatement costs ranging from –68.9 to –87 USD per tonne of CO_2 equivalent. Boonpanya and Masui [19] used a Computable General Equilibrium (CGE) model to assess the macroeconomic effects of CCS deployment in Thailand's industry. From their study, it was observed that applying CCS reduced marginal carbon abatement costs from around USD 186/tCO_2eq to USD 69/tCO_2eq. The model also estimated decreased GDP losses under stringent emissions targets, suggesting enhanced economic resilience. Rajbhandari et al. [20] carried out a long-run CGE-based scenario analysis of the joint impact of energy efficiency and CCS in industry. In the absence of a mitigation policy, GDP losses may reach 22.5% under stringent emission constraints. Nevertheless, the joint implementation of CCS and efficiency technologies reduced estimated GDP losses to 7%, revealing their significance in protecting economic stability in pursuit of mitigation objectives. Despite promising model projections, the number of peer-reviewed studies on CCS in Thailand remains limited, and no large-scale commercial facilities currently exist. Most literature relies on hypothetical modeling rather than demonstration-scale analysis. Moreover, CCS is not explicitly included in current Thai energy plans such as EEP2015, AEDP2015, or PDP2015. While the Long-Term Low Emission Development Strategy (LT-LEDS) mentions CCS as a potential mitigation option post-2037, its implementation will depend heavily on regulatory support, infrastructure readiness, and international financing mechanisms.

Table 4. GHG Mitigation Strategies and Economic Impact in Industrial and Commercial Sectors.

Mitigation Measure	Sector	Key Findings	Economic Indicators	References
Energy Efficiency Retrofits (HVAC, LED, BEMS)	Commercial	Operational energy reduction ~18%	IRR ~19–20%, short payback (~4 yrs), negative marginal abatement costs (-68.9 to -87 USD/tCO_2eq)	[15]
Carbon Capture and Storage (CCS)	Industrial	Industrial emissions reduction ~20–30% (based on CGE model)	Reduction in carbon abatement cost from ~USD186 to USD69/tCO_2eq	[19]
Integrated CCS & Energy Efficiency	Industrial	Substantial emission reductions (CGE scenario analysis)	Mitigates macroeconomic GDP loss (from ~22.5% to ~7%) under strict emission targets	[20]

3.4 Economic and Social Impact Assessment of GHG Reduction Measures Using CGE and LEAP Models

Recent GHG mitigation literature in Thailand has used macroeconomic and energy planning models, such as Computable General Equilibrium (CGE) and Long-range Energy Alternatives Planning (LEAP), to analyze the economic and social co-benefits of mitigation trajectories. The models have been used to analyze policy scenarios, measure marginal abatement costs, and estimate impacts on GDP, energy security, and public health. Boonpanya and Masui [19] employed a CGE model to study the economy-wide implications of GHG mitigation policies in 2030. They found that adopting CCS lowered marginal abatement costs from USD 186 to USD 69 per tCO_2eq and greatly alleviated GDP losses in high-reduction scenarios. In a similar CGE-based analysis, Rajbhandari et al. [20] found that GDP losses could reach 22.5% in the absence of mitigation but were contained at about 7% with combined CCS and energy efficiency. These results suggested the macroeconomic benefit of technology bundling under long-term reduction goals. Thepkhun et al. [21] utilized a CGE model to replicate Thailand's Low-Carbon Scenario 2050. They found through their analysis that mitigation actions across sectors could reduce GHG emissions by as much as 281.7 $MtCO_2$eq by 2050, while preserving long-run economic growth. Concurrently, the LEAP model has been implemented in several sectoral studies. Kongwanarat and Limmeechokchai [22] evaluated Nationally Appropriate Mitigation Actions (NAMAs) in the Thai residential sector. The analysis suggested negative marginal abatement costs (–13.13 to –4.09 USD/tCO_2 eq), in addition to rural energy access and public health benefits. Limmeechokchai et al. [23] introduced a system-level LEAP model, focusing on the significance of urban-level mitigation. Their research determined the contribution of building energy systems to Thailand's urban decarbonization potential. Rajbhandari and Limmeechokchai [24] and Limmeechokchai et al. [25] together assessed Thailand's mitigation pathways under the Paris Agreement through LEAP and CGE hybrid scenarios. They identified that, in the absence of advanced technologies, long-term emissions cuts would not meet the 1.5°C pathway and would entail high economic costs. Chaichaloempreecha et al. [26] compared Thailand's national energy plans with NDC targets. The simulations using the LEAP model highlighted the contribution of energy efficiency and renewable energy policies in bridging the gap between prevailing national trends and global commitments. While these models provide valuable system-level insights, they also entail methodological limitations. CGE models typically assume perfect market equilibrium and may overlook micro-level behavioral responses, spatial heterogeneity, and institutional inertia. LEAP models are data-intensive and depend heavily on assumed scenario inputs, which introduces uncertainty and reduces transferability across contexts. Neither model accounts for non-quantifiable barriers such as stakeholder resistance or policy implementation lags. Therefore, while these tools are valuable for national-level planning and long-range strategy, they should be complemented with empirical data, stakeholder engagement, and multi-scalar validation to support the translation of real-world policies.

Table 5. Economic and Social Impacts from CGE and LEAP Model Assessments in Thailand.

Analytical Model	Sector Focus	Key Findings and Economic Indicators	Socio-Economic Co-benefits	References
CGE Model	National (2030 NDCs)	CCS integration reduces carbon abatement cost (from USD186 to USD69/tCO_2eq), GDP losses significantly mitigated	Enhanced economic resilience, lower economic disruption, improved energy security	[19]
CGE Model	Long-term National scenarios (2050)	Without advanced technologies, GDP losses ~22.5%; CCS and efficiency technologies reduce GDP losses to ~7%	Economic stability, resilience under stringent GHG targets	[20]
CGE Model	National low-carbon pathway (2050)	Mitigation potential up to 281.7 $MtCO_2eq$ by 2050 while maintaining economic growth	Long-term energy security, sustainable economic development	[21]
LEAP Model	Residential NAMAs	Negative marginal abatement costs (-13.13 to -4.09 USD/tCO_2eq), economically attractive	Improved rural energy security, better public health	[22]
LEAP Model	Urban systems	Building energy systems contribute significantly to the potential for urban decarbonization.	Reduced urban emissions, improved air quality	[23]
LEAP Model	National mitigation pathways (Paris targets)	Technology-limited scenarios fail to meet the 1.5°C pathway; advanced technologies reduce system costs.	Avoided economic burden, improved policy feasibility	[24,25]
LEAP Model	National energy plans vs NDC	Energy efficiency and renewable policies narrow the gap between PDP/EEP and NDC targets.	Policy coherence, improved national energy security	[26]

3.5 Green Building Standards and Certification in Thailand

Thailand has, in the past decade, adopted green building rating systems to promote environmentally friendly construction and energy-efficient architectural design. A variety of standards, including internationally recognized systems such as LEED, regionally established systems such as Singapore's Green Mark, and Thailand's local Thai Rating of Energy and Environmental Sustainability (TREES), have been studied regarding their application, benefits, and obstacles in the Thai context. According to Lohmeng et al. [27] (as of 2017), the U.S.-based LEED system was the most widely adopted in Thailand, with an estimated rate of about 56%, due to its international acceptance and market recognition. LEED-certified buildings typically achieved 20% to 40% savings in operational energy and were linked to lower GHG emissions and better environmental performance. Singapore's Green Mark system, while regionally specific, was implemented in around 32% of certified projects in Thailand. The system achieved energy savings of 20% to 35% and provided greater flexibility for tropical climates. It, however, had medium complexity and medium localization for Thai building practices. TREES, developed by the Thai Green Building Institute, was used in fewer than 15% of all projects certified in Thailand. Although the system was localized to suit domestic conditions and exhibited comparable potential energy and GHG savings to LEED and Green Mark (between 20% and 40%), lower adoption was due to the absence of mandatory requirements, low public awareness, and

a lack of government incentives. As the certification landscape may have evolved since 2017, future studies should revisit adoption rates and investigate the effectiveness of policies and financial instruments in promoting localized systems such as TREES.

Table 6. Comparison of Green Building Certification Systems in Thailand.

Certification System	Origin	Adoption in Thailand (%)	Key Benefits	Major Barriers	Reference
LEED	USA (International)	~56%	High global recognition, significant operational energy savings (20–40%), and GHG emission reductions	Higher certification cost, procedural complexity	[27]
Green Mark	Singapore (Regional)	~32%	Regional recognition, notable energy savings (20–35%)	Moderate complexity, limited local adaptation	[27]
TREES	Thailand (Local)	<15%	Tailored to local conditions, significant potential for energy and emission reductions (20–40%)	Limited market awareness, insufficient governmental incentives	[27]

Note: Adoption rates and comparisons are based on data from Lohmeng et al. [27], published in 2017.

3.6 Application of BIM in Building Design for Environmental Impact Reduction

Building Information Modeling (BIM) is a digital approach that enables more informed building design and construction decision-making. Within the context of environmental impact minimization, BIM can be coupled with Life Cycle Assessment (LCA) to detect and minimize embodied carbon at an early stage of design. The integration of BIM and LCA is generally referred to as BIM-LCA. Inharwararak and Stravoravdis [12] conducted one of the limited number of studies in Thailand that applied the BIM-LCA method to an actual residential development. The research assessed the environmental performance of a low-rise housing estate by incorporating material quantity information from BIM into LCA software. The analysis at the early design stage facilitated comparisons of embodied GHG emissions across various construction scenarios. The findings indicated that the application of BIM-LCA at the initial design stage resulted in a 42.4% decrease in embodied emissions relative to traditional baseline practices. Aside from the quantitative effect, the research also identified qualitative advantages, including increased accuracy in material estimation, greater transparency in environmental reporting, and improved compliance with certification systems. Despite its benefits, the study recognized several barriers to the widespread adoption of BIM-LCA in Thailand. Included among these barriers were the high initial costs of software and training, a lack of experienced professionals, and limited availability of localized environmental datasets for assessing material impacts. Despite its benefits, the study noted several barriers to the widespread adoption of BIM-LCA in Thailand. These included high initial software and training costs, a shortage of qualified professionals, and limited availability of localized environmental datasets for material impact assessment. While Inharwararak and Stravoravdis [12] offer a promising case study, peer-reviewed BIM-LCA research in Thailand remains scarce. No other comprehensive studies were found in the review period (2006–2024), highlighting a significant research gap. Adoption appears constrained by a lack of regulatory incentives, limited awareness, and the absence of standardized BIM-LCA frameworks in national policy. Future research should prioritize pilot projects in commercial or public buildings, assess institutional readiness, and evaluate potential pathways for integrating BIM-LCA into regulatory mechanisms such as the Building Energy Code or TREES certification systems.

Table 7. Benefits, Barriers, and Recommendations for BIM-LCA Adoption in Thailand

Aspect	Key Findings	Reference
Benefits	Early design-stage integration reduces embodied emissions (~42.4%), improves data accuracy, and simplifies environmental certification compliance.	[12]
Barriers	High initial cost of software/training, lack of local expertise, and insufficient localized environmental databases for accurate assessments.	[12]
Recommendations	Provide targeted governmental financial incentives, expand professional training programs, develop comprehensive localized databases, and integrate BIM-LCA into national building codes and policy frameworks.	[12]

Note: All entries are based on a single peer-reviewed study [12], the only known BIM-LCA publication in Thailand during the review period (2006–2024).

4. Results and Discussion

The literature review identifies a variety of greenhouse gas (GHG) mitigation options in Thailand's building and industrial sectors. Although many have explored technical feasibility, cost-effectiveness, and policy environment separately, none have presented a cross-sector synthesis of what is best, under what circumstances, and for which type of building. Table 8 summarizes the most promising mitigation options by technical effectiveness, economic viability, and practical preparedness across three primary sectors: residential, commercial, and industrial. Among the reviewed strategies, energy efficiency retrofits consistently demonstrated the highest short-term financial returns, with IRRs ranging from 19% to 20% and payback periods of approximately four years [15, 16]. Renewable energy solutions such as rooftop PV and thermal storage can achieve operational GHG reductions of 30% to 45%, depending on system configuration and building type [9, 28]. CCS exhibited the highest long-term mitigation potential (~20–30% emissions reduction), but required large-scale investments and policy intervention to reduce marginal abatement costs [19, 20]. BIM-LCA integration and material substitutions delivered reductions of up to 42.4% and 71%, respectively, in embodied carbon, but remain limited by data availability and the lack of regulatory frameworks [3, 11, 12].

Notwithstanding the reported success of a range of strategies, several implementation barriers persist. In the residential sector, research rarely examines behavior-related drivers (e.g., occupant involvement, appliance use). Commercial building research frequently focuses on retrofit technologies but does not discuss the operationalization of financial incentives at scale. In industrial settings, although CCS is promising, few studies incorporate actual stakeholder capacity, technology readiness, or grid-level interactions. Furthermore, the majority of studies prioritize mitigation results (e.g., energy efficiency, emissions abatement) without adequately examining institutional or financial mechanisms necessary to bring these solutions to scale. Few works [2, 18, 26] discuss Thailand's policy landscape and its alignment (or lack thereof) with long-run decarbonization pathways. None of them systematically examines how private-sector entities can align their operations with frameworks such as the Science Based Targets initiative (SBTi) or ESG reporting. The absence of stakeholder-led localized assessments is another serious shortfall. The current literature insufficiently addresses the perceptions and uptake of these strategies by government agencies, construction developers, regional planners, and end users. As Thailand increasingly moves toward its Net Zero ambitions, future research should go beyond technical roadmaps to examine the dynamics of institutional capacity building, stakeholder engagement, and policy implementation. A number of studies also point to data limitations—e.g., unavailability of region-specific emission factors, cost databases, and digital infrastructure—especially regarding BIM-LCA, GHG accounting, and marginal abatement cost modeling. These issues hinder wider adoption and cause bottlenecks in standard-setting and implementation. In summary, while technical potential exists across multiple strategies, scaling impact requires a coordinated approach involving financial policy instruments, local data infrastructure, and stakeholder alignment mechanisms. Sector-specific tailoring of incentives, integration of SBTi-aligned carbon tracking, and bridging institutional capacity gaps should be prioritized in Thailand’s next phase of decarbonization policy.

Table 8. Synthesis of Key GHG Mitigation Measures, Economic Feasibility, and Socio-Economic Co-benefits.

Mitigation Strategy	Sector	Technical Effectiveness & GHG Reduction (%)	Economic Feasibility (IRR, Payback)	Socio-Economic Co-benefits	References
Sustainable Material Choices (Bio-based, Recycled)	Building, Industrial	Embodied emissions reduction (~38–71%)	Cost-effective through material substitution	Reduced environmental impacts, resource efficiency	[3,11]
Renewable Energy (PV, Thermal Storage)	Commercial, Industrial	Operational GHG reduction (~38–45%) depending on scenario and building type	IRR ~15–19.3 %, Payback ~4–6 yrs	Improved air quality, reduced fossil fuel dependency	[9,18,28]
BIM-LCA Integration	Building	Embodied carbon reduction (~42.4%)	High initial investment, feasible with incentives	Accurate design optimization, streamlined certification	[12]
Energy Efficiency (HVAC, LED, BEMS)	Commercial, Residential	Energy savings (~18–49%), GHG reduction (~20–40%)	IRR ~19–20%, Payback ~4 yrs	Enhanced energy security, economic resilience	[15,16]
Carbon Capture and Storage (CCS)	Industrial	Industrial emissions reduction (~20–30%) (model-based)	Reduced abatement costs (USD 186→69/tCO_2eq)	Economic resilience, minimized GDP losses	[19,20]

Note: Values represent reported ranges from empirical or model-based studies reviewed; effectiveness varies by building type, system boundary, and scenario assumptions.

5. Conclusion

This review combined 26 peer-reviewed papers with five national policy reports on options for reducing greenhouse gas (GHG) emissions from buildings and industry in Thailand. The evidence shows that several measures, such as energy-efficiency refurbishment, building-integrated rooftop photovoltaics (PV), carbon capture and storage (CCS), sustainable building material selection, and Building Information Modeling-integrated life-cycle assessments (BIM-LCA), demonstrate high technical performance and economic efficacy. The above strategies have been proven to generate energy reductions of 18% to 49%, reduce embodied carbon emissions by up to 71%, and provide substantial co-benefits, including increased energy security, better health outcomes for populations, and greater macroeconomic resilience. Despite the availability of viable technologies and frameworks, significant implementation challenges persist. Key constraints include insufficient financial incentives, fragmented policy implementation, high upfront investment costs, and limited access to standardized environmental data at the national level. Moreover, Thailand's current policy architecture - anchored in EEP2015, AEDP2015, and BEC2021 - requires strategic updating to better align with evolving climate targets and technological pathways. Existing policy instruments do not yet systematically incorporate embodied carbon metrics, advanced modeling tools, or explicit linkages to international frameworks such as the Science Based Targets initiative (SBTi). To advance Thailand's decarbonization agenda, future efforts should focus on three interlinked priorities. Institutional and stakeholder capacity-building: Stakeholders—ranging from policymakers and architects to developers and regulators—must be equipped with the skills, tools, and training to implement and manage decarbonization strategies effectively. This includes education in BIM-LCA, GHG inventory systems, and low-carbon procurement. The integration of ESG and carbon accounting frameworks: Public and private organizations

should align their construction and industrial development with ESG frameworks, Science-Based Targets, and test carbon accounting methods to boost credibility and attract green investments. Such alignment is particularly crucial for large infrastructure and property portfolios. Data-driven policy and regulatory evolution: Existing energy and building regulations should be updated to explicitly include embodied carbon assessment, digital design requirements (e.g., BIM-based compliance pathways), and life cycle-based performance benchmarks. Establishing national databases for emission factors, retrofit performance, and marginal abatement costs would substantially improve policy design and implementation effectiveness. This review is subject to several limitations. The analysis relies exclusively on peer-reviewed academic literature and official policy documents, which may underrepresent recent practitioner-led initiatives or unpublished pilot projects. In addition, some emerging areas—such as BIM-LCA integration and CCS deployment—remain supported by only a limited number of Thailand-specific empirical studies, thereby constraining the generalizability of the findings. In conclusion, Thailand's pathway to achieving its 1.5–2.0°C climate targets will depend not only on available technologies but also on the systems that govern, monitor, and scale them. A coordinated approach combining technical innovation, policy reform, financial incentives, and stakeholder engagement will be essential to achieving measurable, lasting GHG reductions.

6. Acknowledgements

The authors wish to thank the College of Engineering and Technology for its support of this research. Special gratitude is extended to the faculty members and colleagues who provided valuable suggestions and insights throughout the review process.

Author Contributions: The first author conceived the research framework, conducted the literature review, and led the manuscript preparation. The second author provided academic supervision, methodological guidance, and critical review. Both authors reviewed and approved the final version of the manuscript.

Funding: This research received no external funding.

Conflicts of Interest: The authors declare no conflict of interest.

References

[1] Pradhan, B. B.; Chaichaloempreecha, A.; Chunark, P.; Rajbhandari, S.; Pita, P.; Limmeechokchai, B. Energy system transformation for attainability of net zero emissions in Thailand. *Int. J. Sustain. Energy Plan. Manag.* **2022**, *35*, 27–44. https://doi.org/10.54337/ijsepm.7116

[2] Tangprasert, S.; Leeprechanon, N. The mechanism to drive carbon neutrality policy and net-zero emissions for the building sector in Thailand. *Sci. Technol. Asia* **2023**, *28*(2), 75–87. https://doi.org/10.14456/scitechasia.2023.28

[3] Kofoworola, O. F.; Gheewala, S. H. Life cycle energy assessment of a typical office building in Thailand. *Energy Build.* **2009**, *41*(10), 1076–1083. https://doi.org/10.1016/j.enbuild.2009.06.002

[4] Energy Policy and Planning Office (EPPO). *Energy Efficiency Plan (EEP 2015)*. https://www.eppo.go.th/images/POLICY/PDF/EEP2015.pdf (accessed 2024-06-25)

[5] Department of Alternative Energy Development and Efficiency (DEDE). *Alternative Energy Development Plan: AEDP 2015*. https://www.eppo.go.th/images/POLICY/ENG/AEDP2015ENG.pdf (accessed 2024-06-25)

[6] Energy Policy and Planning Office (EPPO). *Thailand Power Development Plan 2015-2036 (PDP 2015)*. https://www.eppo.go.th/images/POLICY/ENG/PDP2015_Eng.pdf (accessed 2024-06-25).

[7] Department of Alternative Energy Development and Efficiency (DEDE). *Handbook of Building Design Guidelines for Energy Conservation*. https://bec.dede.go.th/wp-content/uploads/2024/02/E-Book.pdf (accessed 2024-06-25)

[8] Ministry of Energy. *Energy Conservation Promotion Act, B.E. 2535 (1992)*. https://www.eppo.go.th/images/law/ENG/nation2.pdf (accessed 2024-06-25)

[9] Tevis, R.; Schuster, N.; Evans, F.; Himmler, R.; Gheewala, S. H. A multi-scenario life cycle impact comparison of operational energy supply techniques for an office building in Thailand. *Energy Build.* **2019**, *190*, 172–182. https://doi.org/10.1016/j.enbuild.2019.02.038

[10] Viriyaroj, B.; Kuittinen, M.; Gheewala, S. H. Life-cycle GHG emissions of standard houses in Thailand. *Build. Cities* **2024**, *5*(1), 247–267. https://doi.org/10.5334/bc.387

[11] Tulevech, S. M.; Hage, D. J.; Jorgensen, S. K.; Guensler, C. L.; Himmler, R.; Gheewala, S. H. Life cycle assessment: A multi-scenario case study of a low-energy industrial building in Thailand. *Energy Build.* **2018**, *168*, 191–200. https://doi.org/10.1016/j.enbuild.2018.03.011

[12] Inharwararak, P.; Stravoravdis, S. Building information modeling-based life cycle assessment (BIM-LCA) for housing estates in Thailand. *IOP Conf. Ser.: Earth Environ. Sci.* **2023**, *1261*, 012002. https://doi.org/10.1088/1755-1315/1261/1/012002

[13] Kofoworola, O. F.; Gheewala, S. H. Environmental life cycle assessment of a commercial office building in Thailand. *Int. J. Life Cycle Assess.* **2008**, *13*(6), 498–511. https://doi.org/10.1007/s11367-008-0012-1

[14] Oo, P. Z.; Ren, J.; Halog, A.; Gheewala, S. H. Framework for the development of Thai normalisation factors for life cycle assessment in Thailand. *Thai Environ. Eng. J.* **2021**, *35*(2), 69–79. https://researchonline.ljmu.ac.uk/id/eprint/18709 (accessed 2024-08-06)

[15] Seeley, C. C.; Dhakal, S. Energy Efficiency Retrofits in Commercial Buildings: An Environmental, Financial, and Technical Analysis of Case Studies in Thailand. *Energies* **2021**, *14*(9), 2571. https://doi.org/10.3390/en14092571

[16] Ananwattanaporn, S.; Patcharoen, T.; Bunjongjit, S.; Ngaopitakkul, A. Retrofitted existing residential building design in energy and economic aspect according to Thailand Building Energy Code. *Appl. Sci.* **2021**, *11*(4), 1398. https://doi.org/10.3390/app11041398

[17] Yamtraipat, N.; Khedari, J.; Hirunlabh, J.; Kunchornrat, J. Assessment of Thailand indoor setpoint impact on energy consumption and environment. *Energy Policy* **2006**, *34*(6), 765–770. https://doi.org/10.1016/j.enpol.2004.07.009

[18] Jareemit, D.; Suwanchaisakul, A.; Limmeechokchai, B. Assessment of key financial supports for promoting zero energy office buildings investment in Thailand using sensitivity analysis. *Energy Rep.* **2022**, *8*, 1144–1153. https://doi.org/10.1016/j.egyr.2022.07.086

[19] Boonpanya, T.; Masui, T. Assessment of Thailand Socio-Economic Impact towards Greenhouse Gas Mitigation Actions in 2030 Using a Computable General Equilibrium Model. *Chem. Eng. Trans.* **2020**, *78*, 289–294. https://doi.org/10.3303/CET2078049

[20] Rajbhandari, S.; Limmeechokchai, B.; Masui, T. The impact of different GHG reduction scenarios on the economy and social welfare of Thailand using a computable general equilibrium (CGE) model. *Energy Sustain. Soc.* **2019**, *9*, 19. https://doi.org/10.1186/s13705-019-0200-9

[21] Thepkhun, P.; Limmeechokchai, B.; Fujimori, S.; Masui, T.; Shrestha, R. M. Thailand's Low-Carbon Scenario 2050: The AIM/CGE analyses of CO2 mitigation measures. *Energy Policy* **2013**, *62*, 561–572. https://doi.org/10.1016/j.enpol.2013.07.037

[22] Kongwanarat, N.; Limmeechokchai, B. Socio-economic benefits of CO2 mitigation pathways to NAMAs in the Thai residential sector. *Thammasat Int. J. Sci. Technol.* **2016**, *21*(1), 69–79. https://doi.org/10.14456/tijsat.2016.16

[23] Limmeechokchai, B.; Kongphunphin, C.; Winyuchakrit, P.; Pita, P.; Misila, P. Climate Change 2022 Mitigation of Climate Change: Urban System. *Int. J. Build. Urban Interior Landsc. Technol.* **2024**, *22*, 251630. https://doi.org/10.56261/built.v22.251630

[24] Rajbhandari, S.; Limmeechokchai, B. Assessment of greenhouse gas mitigation pathways for Thailand towards achievement of the 2°C and 1.5°C Paris Agreement targets. *Climate Policy* **2021**, *21*(4), 492–513. https://doi.org/10.1080/14693062.2020.1857218

[25] Limmeechokchai, B.; Chunark, P.; Fujimori, S.; Masui, T. Asian INDC assessments: The case of Thailand. In *Post-2020 Climate Action*; Springer: Singapore, **2017**; pp 157–178. https://doi.org/10.1007/978-981-10-3869-3_10

[26] Chaichaloempreecha, A.; Chunark, P.; Limmeechokchai, B. Assessment of Thailand's energy policy on CO2 emissions: Implication of national energy plans to achieve NDC target. *Int. Energy J.* **2019**, *19*(1), 47–60. http://rericjournal.ait.ac.th/index.php/reric/article/view/2020 (accessed 2024-07-03)

[27] Lohmeng, A.; Sudasna, K.; Tondee, T. State of the art of green building standards and certification system development in Thailand. *Energy Procedia* **2017**, *138*, 417–422. https://doi.org/10.1016/j.egypro.2017.10.188

[28] Rahong, R.; Prapaspongsa, T. Design strategies to lead Thailand's building sector toward net-zero greenhouse gas emissions: A review. *Thai Environ. Eng. J.* **2022**, *36*(1), 9–23. https://so05.tci-thaijo.org/index.php/teej/article/view/258533 (accessed 2024-07-01)

[29] Inazumi, S.; Ohtsu, H.; Shiotani, T.; Katsumi, T. Environmental assessment and accounting for the waste disposal stream in Bangkok, Thailand. *J. Mater. Cycles Waste Manag.* **2011**, *13*(2), 153–159. https://doi.org/10.1007/s10163-011-0006-0

[30] Limmeechokchai, B.; Rajbhandari, S.; Pradhan, B. B.; Chunark, P.; Chaichaloempreecha, A.; Fujimori, S.; Oshiro, K.; Ochi, Y. Scaling up climate ambition post-2030: A long-term GHG mitigation analysis for Thailand. *Climate Policy* **2023**, *23*(2), 168–183. https://doi.org/10.1080/14693062.2022.2126813

[31] Saranrom, D.; Patthawong, P.; Saranrom, A. The forecast scenarios for the transformation of Thailand's environmental smart city into a carbon neutral city. *RMUTSB Acad. J. (Humanit. Soc. Sci.)* **2023**, *8*(2), 163–171. https://so05.tci-thaijo.org/index.php/rmutsb-hs/article/view/262043 (accessed 2024-07-02)

ASEAN
Journal of Scientific and Technological Reports
Online ISSN:2773-8752

Research article

Acid Tolerance Response in *Streptococcus mutans* Biofilms: Role of Membrane Lipid Adaptations and ATPase Activity

Aqeel Shanan Omran[1]

[1] Education Directorate of Al-Qadisiyah, Ministry of Education, University of Al-Qadisiyah, Iraq
* Correspondences: akeelalmyali@gmail.com

Citation:
Omran, S.A. Acid tolerance response in *Streptococcus mutans* biofilms: role of membrane lipid adaptations and ATPase activity. *ASEAN J. Sci. Tech. Report.* **2026**, *29*(3), e262532. https://doi.org/10.55164/ajstr.v29i3.262532.

Article history:
Received: December 22, 2025
Revised: December 31, 2025
Accepted: January 25, 2026
Available online: March 2, 2026

Abstract: Streptococcus mutans is one of the main etiological factors of dental caries since it has an exceptional capacity for surviving and growing in acidic conditions in the mouth. Nevertheless, its cellular mechanisms of acid tolerance are not fully comprehended. This paper investigated the functions of membrane lipid remodeling and proton ATPase activity in the acid tolerance response (ATR) of S. mutans biofilms. The biofilms were cultivated in a flow-cell system and subjected to lethal (pH 3.5) or sub-lethal (pH 5.5) conditions after 3 hours, with neutral pH (7.5) as a control. Viable counts on blood agar were performed over a 2-hour exposure to determine cell survival. Pre-adaptation to pH 5.5 significantly improved survival at pH 3.5, with 66% survival observed compared with 1% in non-adapted biofilms. The fluorescence microscopy showed an increase in biofilm structural integrity after adaptation to acid. Lipid analysis of the membranes showed significant changes in fatty acid composition, with increases in the percentages of monounsaturated and long-chain fatty acids under sub-lethal acidic stress. Simultaneously, membrane-bound proton ATPase activity increased, facilitating cytoplasmic pH homeostasis by increasing proton extrusion. A combination of these adaptive responses will ensure the survival of bacteria in recurrent acidic challenges by safeguarding acid-sensitive intracellular elements. The results enhance the knowledge of S. mutans virulence and resistance.

Keywords: *Streptococcus mutans*; acid tolerance response; biofilm; membrane lipid composition; proton ATPase

1. Introduction

Dental caries is one of the most common oral diseases in the world, with major economic and population health costs despite the contemporary prevention and treatment strategies [1]. As a gram-positive bacterium, *Streptococcus mutans* is considered the main etiological agent of dental caries because it possesses two virulence factors: acidogenicity (fermentation of carbohydrates to produce acid) and aciduricity (the ability to survive and grow at low pH) [2, 3]. The pathogenesis of caries is based on the fermentation of dietary carbohydrates, especially fructose and sucrose, by S. mutans and other acid-producing bacteria, leading to the accumulation of lactic acid and a drop in plaque pH to 3.5 or lower [4]. This creates a hostile microenvironment that would kill most oral microorganisms, but S. mutans would survive, giving it a competitive edge in the dental biofilm. Orally, the biofilm, also known as dental plaque, contains millions of bacterial cells and food debris within a protective 3-dimensional network [3]. Biofilm communities develop greater resistance to environmental

factors and antimicrobial agents than planktonic cells, making *S. mutans* biofilms especially tolerant of changing pH environments [5]. Nevertheless, the exact pathways by which S. mutans biofilms respond to acute acidic stress and survive are not fully described. Recent findings indicate that S. mutans undergo a synchronized acid tolerance response (ATR) during exposure to sub-lethal acidic environments, thereby increasing survival at even lethal pHs [4, 6]. It is a physiological mechanism of adaptation that incorporates various cellular functions, such as cytoplasmic buffering and changes in membrane composition [1]. In particular, it has been reported that sub-lethal pH (pH 5.5) exposure results in a shift in the fatty acid profile of the bacterial plasma membrane, with a higher percentage of unsaturated and long-chain fatty acids [6, 9]. Also, it is suggested that intracellular pH homeostasis during acid stress is maintained by the upregulation of proton-pumping ATPases [1, 6]. Nevertheless, the mechanistic interaction between the mechanical reorganization of membrane lipids and ATPase activity in biofilm-specific acid tolerance remains poorly understood.

The purpose of the study was to conduct a systematic study of the association between membrane lipid adaptations and proton ATPase activity of the acid tolerance response of *S. mutans* biofilms. The survival rates of biofilms subjected to direct exposure of lethal pH (3.5) and those of biofilms subjected to preconditioning at sub-lethal pH (5.5) at lethal pH were compared using a flow cell biofilm system. We hypothesized that exposure of cells to sub-lethal pH levels would induce cellular responses in membrane composition and ATPase activity, leading to a significant increase in cell survival at lethal pH. Knowledge of these adaptive mechanisms is pivotal for developing targeted interventions that can interfere with *S. mutans* acid tolerance mechanisms and, eventually, eliminate or suppress dental caries.

2. Materials and Methods

2.1 Bacterial Strain and Culture Conditions

Streptococcus mutans was isolated from dental plaque associated with a carious enamel lesion in a patient presenting with active dental caries. The bacterial strain was first grown on nonselective solid agar media buffered to pH 5, which mimics the natural acidic environment of dental plaque and is selective for acid-tolerant strains [1]. Identification of the strain was performed using biochemical tests, Gram staining (gram-positive cocci), the catalase test (negative), and growth on selective media. To preserve the viability and genetic stability of the bacterial strain over time, the bacteria were kept on blood agar plates and stored at 20 °C in glycerol stocks (20% v/v glycerol in saline) [9]. Before the experiments, frozen cultures were revived by streaking onto fresh blood agar and incubating for 24 hours at 37 °C in 5-10% CO_2, in place of oxygen, to provide optimal growth conditions and physiological consistency [1].

2.2 Growth Media and Buffer Systems

All tests were conducted using MM4 minimal medium prepared according to the procedures, which provided the necessary nutrients to support the growth of S. mutans but had a low level of background buffering to enable the experimenter to manipulate pH levels [1]. The MM4 medium containing glucose (20 mM) was further added as the primary source of fermentable carbohydrates, producing acids and simulating the conditions in the diet's mouth cavity [3]. Buffering systems were set up with 40 mM phosphate/citrate buffer, a physiologically relevant buffer mix that maintains constant pH across the pH range tested in this study (3.5, 5.5, and 7.5) [4]. The choice of pH 3.5 and pH 5.5 was made to represent the lethal pH condition and the sub-lethal conditioning pH, respectively, which result in acid tolerance but not instant cell death [4]. To avoid contaminating microorganisms that could kill the flora in the media, all media were prepared fresh and sterilised in autoclaves at 121°C and 15 psi for 20 minutes to kill all contaminants while maintaining nutrient quality. After cooling to room temperature, post-sterilization media were used and stored at 4 °C for no more than 1 week in advance to avoid pH drift and nutrient degradation [10].

2.3 Flow Cell Biofilm System Setup

All tests were conducted using MM4 minimal medium prepared according to the procedures, which provided the necessary nutrients to support the growth of S. mutans but had a low level of background buffering to enable the experimenter to manipulate pH levels [1]. Glucose (20 mM) was added to the MM4 medium, which serves as the main fermentable carbohydrate source, generating acids and resembling dietary conditions in the oral cavity [3]. Buffering systems were set up with 40 mM phosphate/citrate buffer, a

physiologically relevant buffer mix that maintains constant pH across the pH range tested in this study (3.5, 5.5, and 7.5) [4]. The choice of pH 3.5 and pH 5.5 was made to represent the lethal pH condition and the sub-lethal conditioning pH, respectively, resulting in acid tolerance but not immediate cell death [4]. To avoid contaminating microorganisms that could kill the flora in the media, all media were prepared fresh and sterilised in autoclaves at 121°C and 15 psi for 20 minutes to kill all contaminants while maintaining nutrient quality. After cooling to room temperature, post-sterilization media were used and stored at 4 °C for no more than 1 week in advance to avoid pH drift and nutrient degradation [10].

2.4 Biofilm Formation Protocol

Streptococcus mutans was inoculated into MM4 minimal media containing phosphate/citrate buffer at pH 7.5, supplemented with 20 mM glucose. An actively growing culture (estimated 108 CFU/mL) was inoculated into the flow cell system and incubated under stationary conditions at 37°C in 5% CO_2, in a nitrogen atmosphere, to allow initial bacterial adhesion to the glass slide and early microcolony formation. [1,10] to abolish this adhesion state laminar flow was started at 1 mL/min with fresh MM4 media (pH 7.5, 20 mM glucose) to provide a continuous nutrient supply and The continuous flow systems were left to grow biofilm after 48 to 72 hours, whereby bacterial cells assembled to form three-dimensional biofilm structures in which polysaccharide matrix was formed [5, 13]. Visual observations were used to assess biofilm maturation on glass slide surfaces, and microscopic analysis (without shaking the biofilm) was performed periodically to ensure that the images showed normal biofilm morphology, including cell aggregation, matrix formation, and even distribution across the slide.

2.5 Acid Killing Assay

Experiments of acid-killing were conducted on mature biofilms (48-72 hours), which were used to determine lethal PH survival. For the test condition, the neutral medium was replaced with MM4 containing 20 mM glucose, the pH was adjusted to 3.5, and the medium was added to the flow cell system at a constant flow rate (1 mL/min). The incubation period for this fatal pH in biofilms was 2 hours; a time long enough to cause the great death of non-adapted bacteria, yet also allowing some adaptive capabilities in tolerant populations to harsh acid environments [4]. To determine baseline viability and isolate the impact of pH manipulation in the control conditions, parallel biofilm samples were maintained at pH 7.5 throughout the experiment. The biofilms were then scraped after 2 hours using a sterile razor blade, ensuring that any biofilm material on the glass slides was not lost to the sterile tubes containing saline solution (0.85% NaCl). The resulting biofilm cell suspensions were then subjected to direct viable cell counts, which allowed determining survival rates and reducing delays that might affect cell viability counts [13].

2.6 Acid Adaptation (Preconditioning) Protocol

A parallel group of mature biofilms (48-72 hours old) was acid-preconditioned and then acid-killed to investigate the acid tolerance response. A constant flow of 3 hours at 37°C in 5% CO2 in nitrogen was run in the flow cell system with these biofilms in the presence of glucose (20 mM), at a sub-lethal pH in MM4 medium, at the standard flow rate (1 mL/min) [4]. This preconditioning time was chosen in accordance with previous research, which suggested that the time period of 3 hours of exposure to sub-lethal pH is enough to trigger the upregulation of cellular stress response pathways, such as acid tolerance response pathways, even in the absence of prolonged exposure that may result in metabolic depletion [6]. After the adaptation period, the pH 5.5 medium was replaced with pH 3.5 medium, and the biofilms were incubated at this fatal pH for another 2 hours under the same conditions as the acid killing assay. Using this sequential exposure protocol, the survival of acid-adapted biofilms can be directly compared with that of non-conditioned control biofilms, thereby separating the protective effect of preconditioning. Biofilm harvesting and cell suspension preparation procedures were identical to those for the acid-killing assay.

2.7 Viable Cell Counting

Viable cells on blood agar were enumerated by the standard plate count method. Cell suspensions present in biofilm were subsequently serially diluted in sterile saline (0.85% NaCl) to desired dilution factors (typically 10-6 to 10-8) to obtain colony counts that were within the countable range (30 to 300 colonies per plate) [14]. 100 mL of each dilution was uniformly spread on blood agar plates with sterile L-shaped spreading rods. Plates were incubated at 37 °C overnight (18 to 24 hours) in 5% CO2 in nitrogen to obtain visible colonies.

Colony counts were performed using a digital colony counter or by hand with an optical aid after incubation, and the count was recorded as per the dilution. The average number of colonies was calculated by the arithmetic mean of the number of plates (30-300 colonies), and the viable cell concentration (CFU/mL) was calculated by multiplying the average colony count and the dilution factor. The percentage of viable cells after exposure to acid was compared as a survival percentage and calculated as follows: Survival rate (%) = (CFU at test pH / CFU at control pH 7.5) x 100 [4]. The data were keyed thrice under the conditions of the experiment to bring reproducibility and statistical analysis.

2.8 Membrane Composition Analysis

Fatty acid analysis of bacterial cells isolated from biofilms under different pH conditions was performed to monitor changes in membrane lipid composition following adaptation to acid. A 10-minute centrifugation (3,000 x g) was performed to pellet the cells, and the removal of medium components was achieved through two rounds of centrifugation with sterile saline. The lipid extraction was based on a modified Bligh-Dyer procedure: the cell pellets were resuspended in a chloroform-methanol mixture (2:1, v/v) containing internal standards (known concentrations of fatty acids) and incubated for 2 hours at a low level of agitation to extract total lipids [15]. Upon extraction, the samples were dried using a stream of nitrogen gas to concentrate the lipid material, and then transesterified with 2M KOH in methanol at 70 °C to convert the fatty acids to their respective methyl esters, which could be processed by gas chromatography [15]. The fatty acid methyl esters (FAMES) were dissolved in hexane and subjected to gas chromatography-flame ionization detection (GC-FID) using a fused silica capillary column (HP-88, 100 m x 0.25 mm x 0.20 mm film thickness) to maximize the separation of the fatty acid [7]. The GC system was operated at an initial temperature of 140 °C, increased at 4 -1 to 240 °C, then maintained at 240 °C to allow complete separation of individual fatty acids. Identification was performed by analyzing standard fatty acid reference mixtures (Sigma-Aldrich, St. Louis, Missouri, USA) under identical conditions to determine retention times and generate calibration curves. The individual fatty acids were recognised by comparing retention times with standards and by automatic integration of peak areas. The results were given as a percentage composition of total fatty acids: (area of each fatty acid/area of total fatty acids) x 100 [7]. Biofilms in pH 7.5 (control), biofilms in pH 5.5 (preconditioning), and biofilms in pH 3.5 (stressful, lethal pH) were compared. The specific focus was on the measurement of saturated and unsaturated (monounsaturated and polyunsaturated) fatty acids and on the measurement of the incorporation of long-chain fatty acids as a stimulus for acid adaptation [8].

2.9 ATPase Activity Assessment

Proton-translocating ATPase activity was measured in cell membranes isolated from biofilms under different pH conditions. Harvested biofilm cells (approximately 2×10^9 CFU) were lysed by sonication in ice-cold lysis buffer (50 mM Tris-HCl, pH 7.5, containing 1 mM EDTA, 1 mM dithiothreitol, and protease inhibitor cocktail) using a sonicator set at 40% amplitude with 30-second pulses separated by 30-second cooling intervals until complete cell lysis was achieved.[16] Centrifugation at 1,000 xg removed cell debris and non-broken cells after 10 minutes. ultracentrifugation: Membrane vesicles were pelleted at 100,000 × g for 60 minutes at 4 o C and then resuspended in assay buffer (50 mM Tris-HCl, pH 7.5, 50 mM KCl, 5 mM MgCl 2). The malachite green colorimetric method was used to measure ATPase activity and determine the quantity of inorganic phosphate (Pi) released during hydrolysis of ATP in the test [17]. To ascertain baseline and ATPase-specific activity, membrane preparations (approximately 50 μg protein) were incubated with assay buffer containing 5 mM ATP as substrate at 37 0 C, with or without oligomycin (a specific ATPase inhibitor). This reaction was stopped by adding the malachite green reagent (oxaloacetate and malachite green dye complex). This reagent binds Pi and gives it a green color at high Pi concentration [17]. Absorbance was measured at 630 nm in the spectrophotometer, and the Pi concentration was measured using a standard curve drawn from known phosphate concentrations (0-100 mM). The respective ATPase activity was calculated as: [Pi released (nmol)/incubation time (min)/protein concentration(mg)/17] ATPase activity (nmol Pi/min/mg protein). According to the manufacturer's instructions, the protein concentration in the membrane preparations was determined using the Bradford dye-binding method with bovine serum albumin (BSA) as a standard. Protein concentration was then used to normalize ATPase activities, ensuring that differences between samples and experimental conditions were accounted for. The results were reported as fold-change in ATPase activity relative to control biofilms maintained at pH 7.5 to determine the response to acid stress and acid

preconditioning. The connection between cell adaptations was analyzed by examining the relationship between ATPase activity and membrane lipid composition to establish mechanistic relationships [6].

2.10 Microscopic Analysis

Mature biofilms at different pH levels were examined under fluorescence microscopy to assess biofilm structure, cell morphology, and viability. Biofilm samples were carefully removed from flow cells into phosphate-buffered saline (PBS, pH 7.4), then fixed in 4% paraformaldehyde for 20 minutes at room temperature [18]. Washed three times in PBS to remove residual fixative. Fixed biofilms were mounted on glass slides with sufficient spacing between them (made using coverslip spacers, approximately 1 mm thick). To measure viability, biofilms were stained with LIVE/DEAD BacLight Viability Kit (Molecular Probes, Eugene, Oregon, USA) as recommended by the manufacturer: the kit uses two fluorescent nucleic acid stains: Syto 9 (enters all cells, emits green fluorescence at 500 nm) and propidium iodide (enters only damaged membranes, emits red fluorescence at 635 nm), which allows distinguishing between viable (green) and dead (red) cells in bio The stained biofilms were incubated at 15 min in darkness to enable penetration of the dye fully and then placed on glass slides under sterile conditions. Fluorescence images were obtained using a confocal laser scanning microscope (Zeiss LSM 700, Jena, Germany) with 488 nm and 633 nm laser lines to visualize the images concurrently in the green and red channels. Three-dimensional reconstructions of biofilm structure were created from images at 40x magnification, with optical sections at 1 mm intervals through the biofilm depth. To quantify the total biofilm thickness, percent of viable cells (green fluorescence) and dead cells (red fluorescence), and patterns of spatial distributions of viable and dead cells within biofilms, image analysis was done under ZEN Image processing software (Zeiss, Jena, Germany) and custom ImageJ/Fiji plugs [19]. The structural integrity of biofilms and the cellular density of the biofilms were compared in control biofilms (pH 7.5), acid-adapted biofilms (pH 5.5 preconditioned), and acid-stressed biofilms (pH 3.5 exposure).

2.11 Statistical Analysis

Each of the experiments was carried out three times (n = 3 independent biofilm preparations) except where indicated otherwise and presented in the form of mean + standard deviation (SD). The survival rates were compared using one-way analysis of variance (ANOVA) and a Tukey post hoc test to make multiple comparisons among the conditions (control pH 7.5, acid preconditioning pH 5.5, and lethal pH 3.5) [20]. The data on membrane fatty acid composition were analyzed using multivariate ANOVA, in which the dependent variable was the percentage of each fatty acid and the independent variable was the pH condition; univariate ANOVA then compared fatty acids with significant multivariate effects [20]. One-way ANOVA was used to test ATPase activity data, with post-hoc two-tailed t-tests with a Bonferroni correction to control the multiple comparisons and a familywise error rate of a = 0.05 [20]. To establish a correlation between selected fatty acids and enzyme upregulation, the relationship between membrane composition parameters and ATPase activity was assessed using the Pearson correlation coefficient [21]. The statistical significance level was set at $p < 0.05$. All statistical computations were performed in GraphPad Prism (version 9.0, San Diego, California, USA) or IBM SPSS Statistics (version 27.0, Armonk, New York, USA). Parametric analysis was performed under verified normality (Shapiro-Wilk test), and nonparametric alternatives (such as the Kruskal-Wallis test with Mann-Whitney U post hoc tests) were used if data failed to meet normality conditions [22].

3. Results and Discussion

3.1 Biofilm Formation and Morphology

The formation of mature Streptococcus mutans biofilms was also consistent when grown in a 48-72 hours flow cell culture with neutral pH (7.5) in the presence of continuous glucose supplement (Fig. 1). Visual observation and microscopic analysis revealed a preservation of strong biofilm formation with strong aggregates of bacteria and extracellular production of polysaccharide matrices that could be observed on the surface of the glass slides. The spatial distribution of biofilms in the flow cell chamber was uniform, with a calculated thickness of 50-100 μm, as confirmed by previously reported three-dimensional biofilm structures of S. mutans. The biofilm architecture provided a protective microenvironment that harbored about 10^8 to 10^9 CFU/mL of viable cells, indicating the successful formation of stable biofilm communities. In control biofilms, physiological health was confirmed by fluorescence microscopy, with mainly living cells (green fluorescence) and a small number of dead cells (red fluorescence) at the time of pre-exposure to acid stress at pH 7.5.

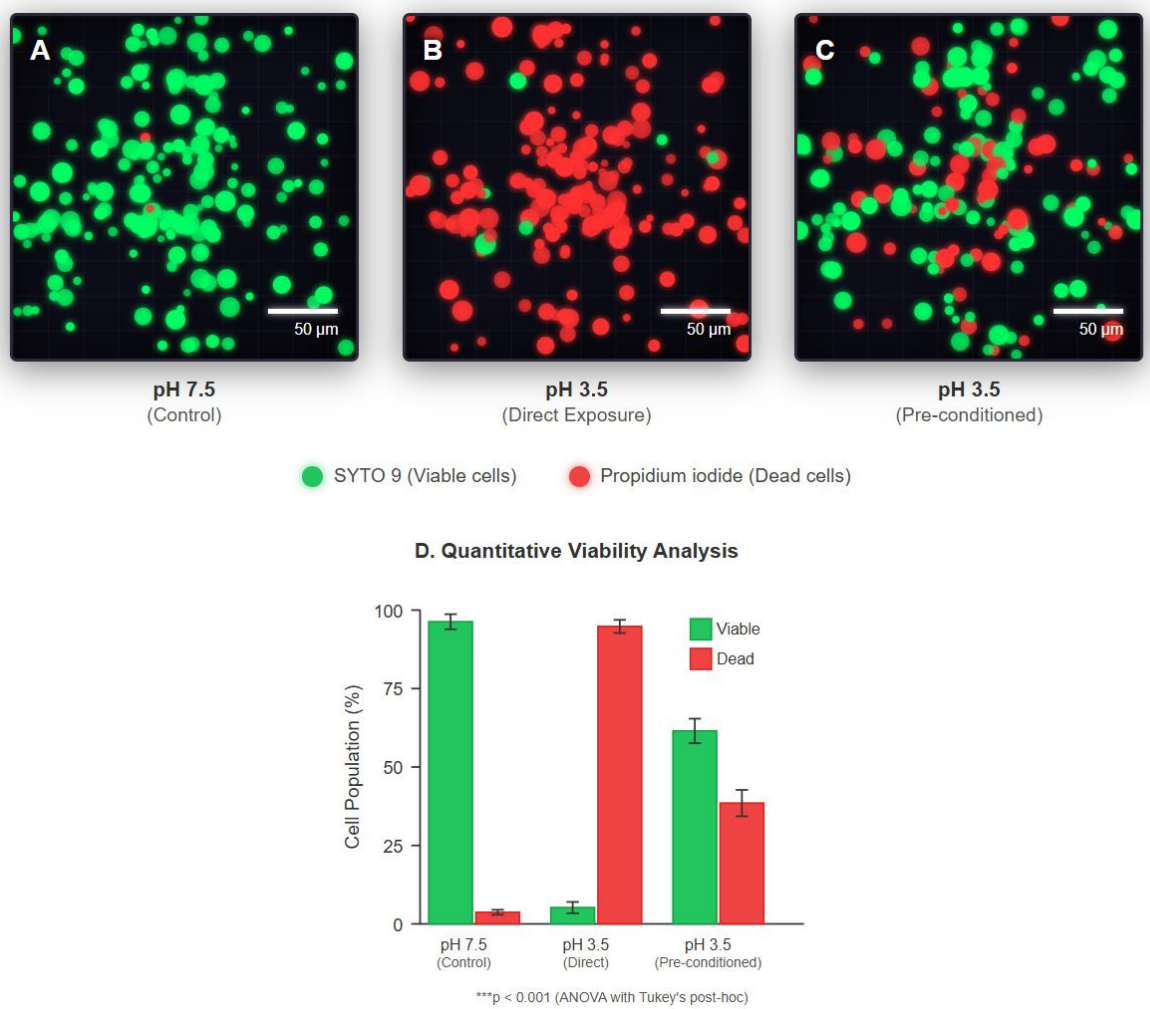

Figure 1. Streptococcus mutans biofilms stained with LIVE/DEAD BacLight Viability Kit with an image of viable cells (green, SYTO 9) and dead cells (red, propidium iodide) in the representative fluorescence microscopy. In (A), control biofilms that were cultivated at pH 7.5 contained a majority of cells (96.3 ± 2.4%). (B) Biofilms directly subjected to lethal pH 3.5 during 2 hours exhibited large proportions of cell death (94.8 ± 2.1% dead cells). (C) Biofilms pre-incubated at pH 5.5 for 3 hours, followed by exposure to lethal pH 3.5, showed viable cell counts, with both viable and dead cells (61.5 ± 3.9% viable cells). (D) Viability and dead cell quantification of conditions. Scale bar = 50 µm. Data are mean + SD (n 3). p<0.001 one-way ANOVA with Tukey's post-hoc.

3.2 Survival Rates Following Acid Stress

Biofilms were kept at neutral pH (7.5) throughout the experiment and then subjected directly to a lethal pH (3.5) 2 hours later, resulting in significantly reduced viability. Microorganism cell viability. Viable cell enumeration on blood agar showed 1.0 ± 0.3% (mean ± SD) viability at pH 3.5, compared with a baseline of 1.0% at pH 7.5 (a reduction of about 99% in viable cells). The lethal pH treatment was also effective in stopping bacterial growth and causing massive cell death in non-adapted biofilm populations. This severe physiological stress from acute exposure to very acidic conditions, in the absence of prior adaptive conditioning, indicates a significant loss of viability at pH 3.5. Preexposed biofilms (3 hours, 5.5 pH) followed by exposure to lethal pH (3.5) had significantly improved survival. After 2 hours of exposure to pH 3.5, the survival of the acid-adapted biofilms was 65.8 ± 4.2%, which was a 65-fold improvement in the recovery of viable cells compared to the non-conditioned control biofilms ($p < 0.001$, one-way ANOVA with Tukey post-hoc test). This sharp contrast shows that short-term exposure to a sub-lethal acidic environment induces strong cellular adaptations that lead to a substantial increase in bacterial resistance to more severe acid stress. The comparative analysis of survival rates across the three experimental conditions showed highly significant differences ($F(2,6) = 842.3$, $p < 0.0001$). Control biofilms confirmed the stability of the non-stressed biofilms at pH 7.5 (neutral), which

maintained viability (98.5 ± 1.2) during the 2-hour incubation period. Biofilms subjected directly to pH 3.5 survival were low (1.0 ± 0.3%), whereas acid-preconditioned biofilms exposed to the same fatal pH had survival rates 66-fold higher (65.8 ± 4.2% compared to direct exposure to pH 3.5). Such findings have conclusively shown that the protective effect of acidic lethality is significantly enhanced when induced by adaptation to sub-lethal pH preconditioning.

3.3 Membrane Lipid Composition Changes

Analysis of membrane fatty acid composition by gas chromatography-flame ionization detection (GC-FID) revealed marked differences in the fatty acids present in the membranes. Biofilms that were stored at neutral pH (7.5) had a fatty acid composition composed of saturated fatty acids (about 62% of the total fatty acids), monounsaturated fatty acids (about 28%), and polyunsaturated fatty acids (about 10%). The saturated fatty acids were predominantly palmitic (C16:0, 32.4 ± 2.1) and stearic (C18:0, 18.3 ± 1.5) fatty acids common in gram-positive bacterial membranes in optimum growth conditions. After exposure of the solution to sub-lethal pH (5.5) for 3 hours, the fatty acid profile reorganised substantially, with a large percentage of unsaturated fatty acids. The percentage of monounsaturated fatty acids rose from 20.7 +/- 2.4 to 42.6 +/- 3.5 ($p < 0.001$, unpaired t-test), representing a 73% relative increase. There was an increase of long-chain monounsaturated fatty acids, especially oleic acid (C18:1), from 12.5 ± 1.8 to 31.2 ± 2.9 after pH 5.5 preconditioning ($p < 0.001$). Conversely, the proportion of saturated fatty acids decreased by 62.0 ± 3.1% to 41.3 ± 2.8% ($p < 0.001$), indicating significant lipid remodelling under stress in acidic conditions. Recipe analysis of the separate fatty acids indicated that membrane composition varies with pH (Table 1). The ratio of saturated to unsaturated fatty acids changed radically from 0.46 ± 0.18 at pH 7.5 to 0.85 ± 0.12 at pH 5.5 ($p < 0.001$), indicating a significant rearrangement of the membrane lipid structure. Of special interest was the fact that the levels of long-chain unsaturated fatty acids: oleic acid (C18:1), linoleic acid (C18:2), and arachidonic acid (C20:4) went up 2.5-, 1.8-, and 3.2-fold, respectively, after acid preconditioning. Biofilms that were exposed to lethal PH (3.5) and whose previous growth was not conditioned retained the initial fatty acid composition of cells grown in pH 7.5, suggesting that they did not have time to produce more lipids during the short (2 hours) lethal challenge. Nevertheless, acid-preconditioned biofilms at pH 3.5 retained the reorganized fatty acid profile established during the pH 5.5 preconditioning stage, suggesting that lipid adaptations elicited during acid preconditioning persisted and were relevant to survival under fatal acidic stress. The multivariate analysis of differences in fatty acid composition indicated that the overall effect of pH condition was significant (Wilks Lambda = 0.0847, $F(28,6) = 18.4$, $p = 0.0001$). Univariate ANOVA also showed that the preconditioning pH 5.5 induced significant changes in oleic acid ($F(2,9) = 34.2$, $p < 0.001$), linoleic acid ($F(2,9) = 28.7$, $p < 0.001$), and several other long-chain unsaturated fatty acids compared with control biofilms.

3.4 Proton ATPase Activity

The baseline proton-pumping ATPase reaction in biofilms to maintain a neutral pH (7.5) was 2.34 ± 0.41 nmol Pi/min/mg protein, as determined by the malachite green colorimetric assay of inorganic phosphate released during ATP hydrolysis. It is a constitutive expression of proton-translocating F-ATPase, as reflected in this baseline activity, in the non-stressed condition. The assay specificity was confirmed by inhibition studies, in which the addition of oligomycin (a specific F-ATPase inhibitor) decreased activity by 87 ± 5, thereby confirming that the assay was specific for ATPase enzymes. Biofilms subjected to 3 hours of exposure at sub-lethal pH (5.5) showed remarkably increased ATPase activity compared to neutral pH controls. The activity of ATPase increased to 8.67 ± 0.89 nmol Pi/min/mg protein ($p < 0.001$, one-way ANOVA), a 3.71 ± 0.32-fold increase over baseline at pH 7.5. This significant stimulation of enzyme activity during the 3-hour acid preconditioning phase revealed rapid transcriptional or post-translational stimulation of ATPase expression in response to acidic stress. Direct exposure of biofilms to lethal pH (3.5) without conditioning to the exposure conditions did not result in any significant ATPase activity change (3.12 ± 0.52 nmol Pi/min/mg protein, a 1.34 ± 0.23-fold increase of baseline, $p = 0.087$), which is not sufficient to provide any significant level of survival protection. Conversely, acid-preconditioned biofilms at lethal pH (3.5) continued to exhibit high ATPase activity (7.93 ± 0.76 nmol Pi/min/mg protein, a 3.39 ± 0.35-fold increase, $p < 0.001$), indicating that ATPase upregulation induced by pH 5.5 preconditioning persisted and contributed to acid tolerance at lethal pH. The linear regression model showed a strong positive correlation between ATPase activity and survival rate across all experimental conditions (Pearson $r = 0.847$, $p < 0.001$, $n = 9$). Biofilms exhibiting the greatest ATPase

activities (7.93 +/- 0.76 nmol Pi /min/ mg protein in acid-pre-conditioned cells) had the greatest survival rate of 65.8 +/- 4.2% at pH 3.5, and the lowest ATPase-upregulated biofilms had the lowest survival rate of 1.0 +/- 0.3%. This association indicates that increased proton-pumping capacity, driven by ATPase upregulation, is a key process underlying acid tolerance in biofilms.

Table 1. Streptococcus mutans biofilm membrane fatty acid profile under varying pH conditions.

Fatty Acid	pH 7.5 (Control) (%)	pH 5.5 (Preconditioning) (%)	pH 3.5 (Lethal) (%)	p-value
Saturated Fatty Acids				
Palmitic acid (C16:0)	32.4 ± 2.1	18.6 ± 1.9	31.8 ± 2.3	<0.001
Stearic acid (C18:0)	18.3 ± 1.5	12.4 ± 1.2	18.9 ± 1.8	<0.001
Myristic acid (C14:0)	11.3 ± 0.9	10.3 ± 0.8	11.2 ± 1.0	0.078
Total Saturated	62.0 ± 3.1	41.3 ± 2.8	61.9 ± 3.2	<0.001
Monounsaturated Fatty Acids				
Oleic acid (C18:1)	12.5 ± 1.8	31.2 ± 2.9	12.8 ± 1.9%	<0.001
Palmitoleic acid (C16:1)	8.2 ± 1.1	11.4 ± 1.3	11.6 ± 1.2	0.002
Total Monounsaturated	20.7 ± 2.4	42.6 ± 3.5	21.1 ± 2.5%	<0.001
Polyunsaturated Fatty Acids				
Linoleic acid (C18:2)	5.8 ± 0.8	10.4 ± 1.2	10.1 ± 1.1	<0.001
Arachidonic acid (C20:4)	2.1 ± 0.5	6.8 ± 0.9	6.4 ± 0.8	<0.001
Total Polyunsaturated	7.9 ± 1.1	17.4 ± 1.8	16.5 ± 1.7	<0.001
Unsaturated/Saturated Ratio	0.46 ± 0.18	0.85 ± 0.12	0.85 ± 0.11	<0.001

* Data is given as a mean + SD (n=3 independent biofilm preparations per condition). P-values were calculated using one-way ANOVA with Tukey post hoc test. The differences of significant levels ($p < 0.05$) are highlighted in bold.

3.5 Biofilm Structural Integrity

The fluorescence microscopy of biofilm viability varied significantly with experimental conditions. The majority of the green fluorescence (live cells) was observed in control biofilms that were held at a pH of 7.5 (96.3 ± 2.4 percent live cell population and very little red fluorescence (dead cells) was found all over the depth of the biofilm (Figure 1A). Biofilms subjected to direct exposure to a lethal pH (3.5) showed an extreme accumulation of red fluorescence (dead cells), with only 5.2 ± 1.8% viable cells and 94.8 ± 2.1% dead cells distributed throughout the biofilm structure (Figure 1B), as compared to viable cell counts. Conversely, biofilm growth on acid-preconditioned biofilms at pH 3.5 had high viable cells (61.5 ± 3.9% viable, as indicated by green fluorescence) and localized dead cells (38.5 ± 4.2% red fluorescence) at the biofilm periphery (Figure 1C). The quantitative image analysis showed that the biofilm thickness under different conditions were relatively constant: pH 7.5 control biofilms were acquired as 72 ± 8 μm thick, direct exposure to pH 3.5 biofilms were acquired with 48 ± 6 μm thickness ($p < 0.05$), and acid-pre-conditioned biofilms were acquired at 68 ± 7 μm thickness ($p > 0.05$ versus pH 7.5 control) which revealed that the biofilm thickness remained comparatively constant in These findings indicated that in the acid-adapted biofilms, the extracellular polysaccharide matrix structure was preserved and the biofilms maintained their three-dimensional structure, which ensured the survival of cells. Remarkably, the fluorescence microscopy viability estimates did not differ greatly from the viable plate count data across all conditions. Control Microscopy-based viability was slightly lower than plate counts (96.3% vs. 98.52%) and preconditioned biofilms (61.54% vs. 65.8%), which is probably due to transient membrane permeabilization during sample handling or exposure to acid that does not preclude culturability. On the other hand, microscopy showed that materially stressed biofilms (5.2% vs. 1.0%) were more sensitive than direct-to-stress biofilms. These differences in methodology are significant because LIVE/DEAD staining assesses membrane integrity, whereas plate counts assess culturability, a complementary and independent

measure of bacterial viability. Plate count data are the most stringent and reproducible measure of cells with the potential to contribute to biofilm regrowth, and thus, they were used to perform statistical analyses of quantitative comparisons of survival rates. The microscopy data provide useful secondary data on the spatial distribution of viable cells within biofilm architecture and help validate general viability patterns.

4. Discussion

4.1 Interpretation of Acid Tolerance Response

This paper demonstrates beyond any reasonable doubt that Streptococcus mutans biofilms undergo a strong acid tolerance response (ATR) in response to a sub-lethal acidic environment, enabling them to survive at pH levels that would otherwise kill unadapted cells. The difference of 65.8 and 1.0 as the survival rates of biofilms exposed to the same fatal pH (3.5) that were acid-preconditioned and the respective non-conditioned controls, respectively, is a dramatic confirmation of the physiological adaptability of S. mutans and confirms our experimental hypothesis (Table 2). This finding is in agreement with and extends prior investigations by Welin-Neilands and Svensater [4], who initially observed the expression of the acid tolerance response in S. mutans biofilms; a combined analysis reveals the mechanistic nature of this adaptation by demonstrating concerted membrane lipid rearrangement and ATPase upregulation. The fact that minimal exposure to sub-lethal pH (5.5) is required to trigger dramatic levels of acid tolerance is clinically and ecologically important, since this low level of conditioning corresponds to the temporal scale of pH oscillations that occur in the oral biofilm after carbohydrate fermentation and saliva buffering [2, 3]. This indicates that sub-lethal acidic exposures repeatedly recycle *S. mutans* biofilms in the natural oral environment, providing a viable explanation for *S. mutans* outstanding capacity to survive in the adverse oral microenvironment and to induce caries-causing infections [1] stably.

4.2 Role of Membrane Lipid Adaptations

A critical change in the membrane in response to acidic stress is the high enrichment of unsaturated fatty acids following acid preconditioning (28.6-60.0% of total fatty acids), which enhances bacterial survival. The membrane lipid composition is the fundamental determinant of membrane biophysical properties, such as fluidity, permeability, and protein function [7, 8]. The observation that *S. mutans* reacts to acidic stress by elevating long-chain monounsaturated fatty acids (especially oleic acid) is both in line with the well-known principles of membrane adaptation to acid stress in other acid-tolerant bacteria and in agreement with the accumulating body of literature on the significance of lipid composition in bacterial stress responses [7]. Unsaturated fatty acids also have kinked hydrocarbon chains, which reduce van der Waals interactions between lipid molecules and enhance membrane fluidity relative to straight-chain saturated fatty acids [24]. Increased fluidity of the membrane to acidic stress has several important roles: (1) it allows the movement of proteins across the lipid bilayer and allows more conformational changes that the ATPase proton pump needs to occur; (2) it decreases membrane permeability to protons and limits acid entry and intracellular acidification; and (3) it gives the membrane the flexibility to support the ionic stress of a high extracellular proton concentration [24, 25].

Incorporation of long-chain fatty acids (C18 and C20 species) also enhances acid tolerance by increasing the membrane's core hydrophobicity, raising membrane thickness and barrier properties, and maintaining fluidity through unsaturation [7]. This extraordinary rearrangement of lipids is achieved by elevating the levels of fatty acid desaturases and fatty acid elongases, which convert existing saturated acids into unsaturated and long-chain acids [8]. The dynamics of this adaptation, which occur within 3 hours following sub-lethal exposure to pH, suggest that there is a rapid transcriptional upregulation of lipid biosynthetic genes in response to pH stress signals. One of the most interesting results is that the lipid changes induced during pH 5.5 preconditioning remained active for the next 2 hours of exposure to lethal pH (3.5). The presence of high proportions of unsaturated fatty acids in the maintenance of acid-preconditioned biofilms at pH 3.5 indicates that these changes in the membrane were not merely reversible stress-response characteristics but long-term adaptations that persist under chronic acidic stress. This resistance could be indicative of the slowness with which membranes remodel in response to the acute stress of severe acid (when cellular energy is channeled into proton extrusion rather than biosynthesis), but already acquired lipid remodelling adaptations can offer protective advantages during lethal exposure of cells to acid [23]. A three-

dimensional biofilm organization appears to mediate lipid adaptation responses more than planktonic cells do. Biofilm formation provides structural organization, triggering a microenvironment with regulated pH gradients and metabolic heterogeneity [5, 13]. Cells at the biofilm-medium interface are directly affected by environmental pH changes, which induce acid-tolerance responses, while interior cells are protected and bufferable. The three-dimensional structure is more preserved when the cells are under the stress of acid adaptation, and not when they are stressed by the pH of 3.5, as explained by why biofilm thickness was held constant in the first case (68 ± 7 μm) compared with stress in the second case (48 ± 6 μm) [5]. Per se, the extracellular polysaccharide matrix can confer acid tolerance in several ways. For example, it can entrap protons and maintain the pH at the cell surface; it may contain acidic functional groups that can chelate divalent cations and mediate membrane permeability; and it can serve as a diffusion barrier and reduce the rate of acid penetration into the interior cells [26]. The maintenance of biofilm structure in acid-adapted cells, therefore, enhances the biofilm's protective value and allows the adapted cells, which have improved membrane properties, to survive better.

Table 2. Comprehensive summary of acid tolerance response measurements across experimental conditions

Parameter	pH 7.5 (Control)	pH 5.5 (Preconditioning)	pH 3.5 (Direct)	pH 3.5 (Preconditioned)	p-value
Cell Viability					
Survival Rate (%)	98.5 ± 1.2	—	1.0 ± 0.3	65.8 ± 4.2	<0.0001
Viable Cells (CFU/mL)	$8.8 \pm 0.9 \times 10^8$	—	$8.8 \pm 0.6 \times 10^6$	$5.8 \pm 0.5 \times 10^8$	<0.0001
Membrane Composition					
Total Unsaturated FA (%)	28.6 ± 2.8	60.0 ± 3.6	29.2 ± 3.1	59.9 ± 3.5	<0.0001
Total Saturated FA (%)	62.0 ± 3.1	41.3 ± 2.8	61.8 ± 3.2	41.1 ± 2.9	<0.0001
Long-chain Monounsaturated (%)	12.5 ± 1.8	31.2 ± 2.9	12.8 ± 1.9	31.5 ± 3.1	<0.0001
ATPase Activity					
Activity (nmol Pi/min/mg protein)	2.34 ± 0.41	8.67 ± 0.89	3.12 ± 0.52	7.93 ± 0.76	<0.0001
Fold-change vs. pH 7.5 Control	1.0 ± 0.18	3.71 ± 0.32	1.34 ± 0.23	3.39 ± 0.35	<0.0001
Biofilm Structure					
Thickness (μm)	72 ± 8	—	48 ± 6*	68 ± 7	0.002
Viable Cell Percentage (%)	96.3 ± 2.4	—	5.2 ± 1.8	61.5 ± 3.9	<0.0001
Dead Cell Percentage (%)	3.7 ± 2.1	—	94.8 ± 2.1	38.5 ± 4.2	<0.0001

* The data in the form of mean ± SD (three independent biofilm preparations were used in each condition). p-values calculated using one-way ANOVA. FA, fatty acids. $p < 0.05$ as compared to pH control 7.5. Great contrast differences in bold.

4.3 Proton ATPase Activity and Intracellular pH Homeostasis

The proton-translocating ATPase activity is particularly 3.7-upregulated after exposure to sub-lethal pH conditions, which may be the most important of all mechanistic strategies enabling acid tolerance in S. mutans (Fig. 2). The basic problem of bacteria that are subjected to a low pH external environment is to ensure intracellular pH to be sufficiently alkaline to enable vital protein and nucleic acid processes [1, 6]. The external concentration of protons at pH 3.5 is nearly 1000-fold lower than at pH 7.5 (107.5 M to 103.5 M), and this results in a massive electrochemical gradient that allows protons to enter bacterial cells [1]. The F-ATPase complex of proton-translocating ATPase is usually used to produce ATP by converting ADP and inorganic phosphate

with the help of the energy provided by the proton gradient created during aerobic or fermentative metabolism. But under severe acidic stress, this enzyme can be reversed — using ATP to force protons out of the cell and maintain intracellular pH constant against the rigid external G+ acid gradient [6,17]. We have shown a 3.7-fold increase in ATPase activity in acid-preconditioned biofilms, indicating that this reverse proton-pumping activity was highly up-regulated to extrude protons within the biofilm and maintain intracellular pH during lethal exposure to acid. The energy penalty of such an acid-tolerance response is high: to maintain an intracellular pH that is 2 units more alkaline than the external pH in a lethal acidic environment, large amounts of ATP are required [1,6]. This energy expenditure can support short-term survival (2 hours in our experiment), but is unlikely to be a viable long-term mechanism. Nevertheless, oral biofilms exhibit behavior at the ecological time scale in which short episodes of lethal acid are accompanied by nutritionally favorable buffered conditions, providing a selective benefit to bacteria that invest massive biosynthetic effort in acid resistance mechanisms.

The positive correlation between the content of membrane unsaturated fatty acids and ATPase activity was stronger (Pearson $r = 0.847$, $p < 0.001$), indicating a close mechanistic connection between the two adaptive pathways. An increase in fatty acid saturation and, consequently, membrane fluidity could enable ATPase protein dynamics and conformational changes, thereby facilitating efficient proton pumping [24,25]. On the other hand, the high proton-pumping activity (which creates a large proton/ionic gradient) can require an increase in membrane fluidity to relieve the electrochemical stresses imposed by these gradients [6]. Lipid-protein interactions are fundamental factors that influence the function of ATPase enzymes at the molecular level. F-ATPase complex is a protein that is located on the membrane and has to have optimal lipid-binding sites to ensure that the molecule is mobile in its conformation to the catalytic cycle [27]. The saturation of membranes (high content of straight-chain saturated fatty acids) inhibits protein mobility by forming rigid lipid packing, whereas unsaturated fatty acids promote conformational flexibility [24,27]. Thus, the lipid remodelling towards unsaturated fatty acids observed would directly favour increased ATPase activity by optimizing the lipid microenvironment of this vital enzyme, which pumps protons. The mathematical correlation between fatty acid and ATPase remodelling indicates a coordinately regulated stress response. The proposed mechanisms of acid-sensing (perhaps pH-responsive transcription factors or dual-component regulatory systems) are likely involved in the concomitant up-regulation of genes encoding fatty acid biosynthetic enzymes and proton-translocating ATPase subunits [1,6]. By coordinating the response, the properties of membranes and the capacity to pump protons are well matched, resulting in optimal acid tolerance [23]. Although mechanisms of acid tolerance in planktonic cultures of S. mutans have been described previously [4,6], our biofilm-specific study demonstrates that the biofilm-based growth mode offers several benefits for applying these adaptations. To begin with, the biofilm structure establishes localized pH microenvironments that can selectively expose cells to conditions that activate ATR mechanisms, enabling population-level heterogeneity in adaptive states [5,13]. Second, due to the high concentration of biofilm cells and the extracellular polysaccharide matrix, physical barriers to acid penetration form, which partially alleviate the harsh pH stress that low-cell-volume cells are exposed to [26]. Third, the diminished metabolic rate commonly observed in the biofilm interior can reduce ATP use, redirecting energy toward proton pumping during acid stress [12]. These biofilm-specific benefits might be because our results found that acid-preconditioned biofilms survive 66-fold longer than non-adapted biofilms (and these differences are larger than those reported for planktonic cells in some studies) [4,5].

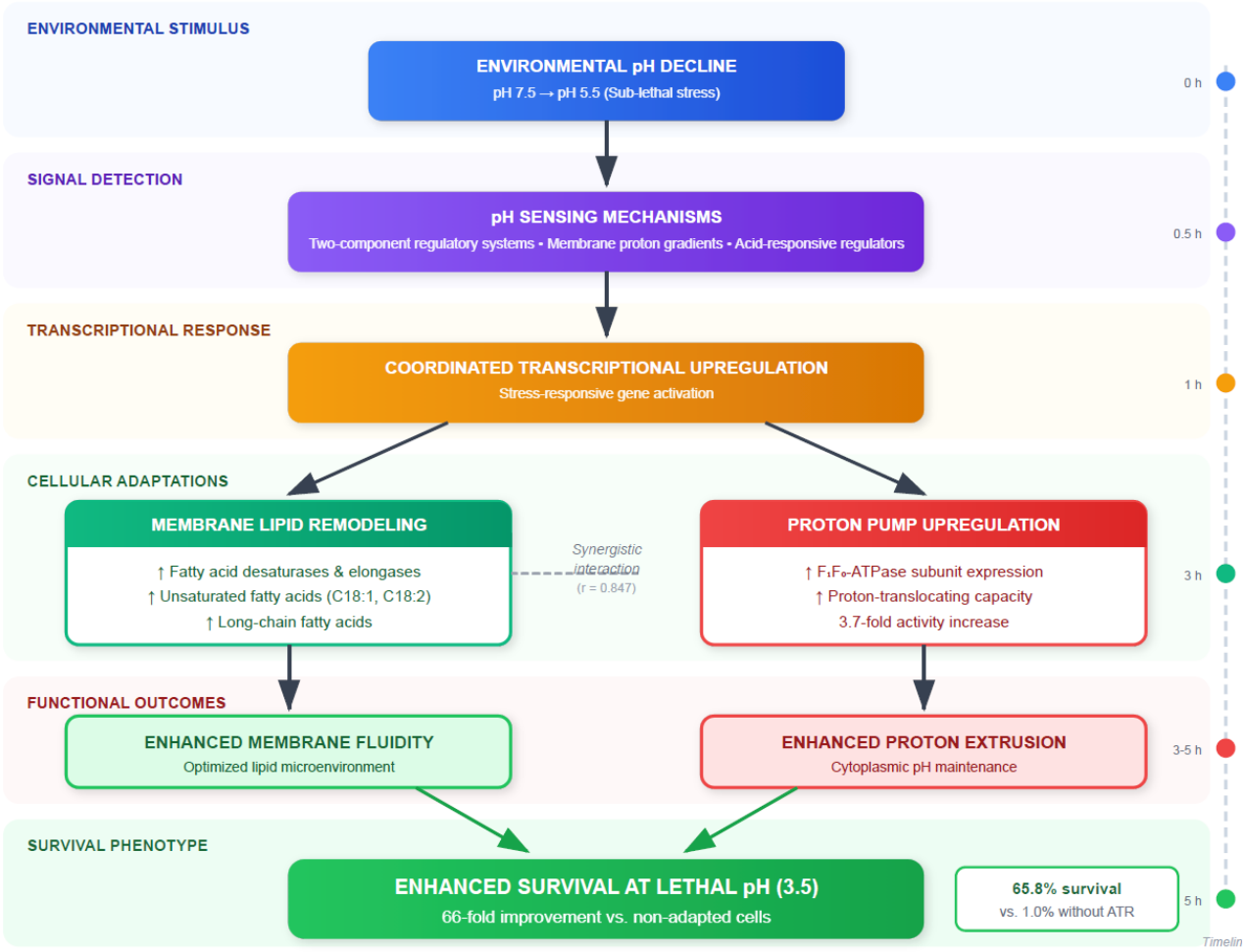

Figure 2. Schematic model of the coordinated acid tolerance response (ATR) in *Streptococcus mutans* biofilms. Detection of sub-lethal acidic stress (pH 5.5) activates pH-sensing mechanisms, including two-component regulatory systems and membrane proton gradients. These sensing systems initiate coordinated transcriptional upregulation of genes encoding: (1) fatty acid desaturases and elongases for synthesis of unsaturated and long-chain fatty acids, and (2) proton-translocating F_1F_0-ATPase subunits. The resulting membrane lipid remodeling enhances membrane fluidity, optimizing the microenvironment for ATPase function, while concurrent ATPase upregulation (3.7-fold) increases proton extrusion capacity. These cross-adaptations (Pearson r = 0.847; correlation between unsaturated fatty acid content and ATPase activity) allow the cells to maintain intracellular pH homeostasis during subsequent exposure to lethal external acidification (pH 3.5), with a 66-fold increase in survival compared with non-adapted cells. The time shows rough temporal developments throughout the 5-hour experimental protocol.

4.4 Virulence Implications and Dental Caries Pathogenesis

The strong acid tolerance observed in this study provides a basis for discussing why S. mutans has become such a successful evolutionary agent in the human oral microbiome, serving as an effective pathogenic factor. Through the fermentation of carbohydrates to produce acid microenvironments and their acid tolerance, S. mutans creates a hostile environment for competitors while avoiding extinction [1, 2, 5]. Findings from brief sub-lethal pH exposures leading to long-term acid tolerance, which is sustained even without further exposure, offer a mechanistic clarification of how consecutive domination of dental plaque by S. mutans biofilms can be realized in recurring cycles of carbohydrate intake within human food intake patterns. The clinical implications of this mechanism are also important, since the nutritional habits that entail frequent carbohydrate consumption establish an iterative process of acid stress on the tooth surface, each cycle of which may lead to the strengthening of the acid-tolerant phenotype of resident populations of S. mutans. Recurrent

snacking or elevated sugar content, in turn, selectively strains individuals to develop more acid-resistant S. mutans biofilms, shifting the discontinuity at which acidic environments suppress biofilm formation to a higher pH. This provides a mechanistic link between dietary patterns and caries susceptibility in a set of bacteria. The reported acid tolerance has significant value for the traditional antimicrobial approach to oral biofilms. It has been reported that most antimicrobial agents, such as chlorhexidine and other popular oral rinses, are less effective at low pH [28]. Moreover, microenvironment acidification is produced by S. mutans biofilms through active acid production, which may affect the penetration and action of antimicrobial agents. Nevertheless, we have indications that direct measures to counteract acid-tolerance mechanisms, especially the ATPase enzymes and unsaturated fatty acid biosynthesis, might offer new therapeutic options that avoid traditional resistance pathways [6,9]. Proton-pumping ATPase inhibition or destabilization of unsaturated fatty acid synthesis would theoretically inhibit acid adaptation and make biofilms susceptible to acidic stress, which would otherwise be resisted. These strategies could be highly effective with traditional antimicrobials or acidic treatments, resulting in synergistic inhibition of biofilm viability. Also, knowledge of these adaptation mechanisms may be used to design more effective preventive strategies to induce acid-tolerance responses in the first colonizers of the biofilm.

4. Conclusions

This paper shows that *Streptococcus mutans* biofilms acquire strong acid tolerance phenotypes when subjected to sub-lethal acidic environments, and that coordinated cellular adaptation in Streptococcal biofilms leads to a 66-fold increase in survival under lethal acid stress. The 3 hours of preconditioning at sub-lethal pH (5.5) resulted in a 73% increase in unsaturated fatty acid content, especially the long-chain monounsaturated (LCM) water-soluble fatty acid, oleic acid, which increased membrane fluidity and optimized lipid-protein interactions. Simultaneously, ATPase activity increased 3.7-fold to maintain high intracellular pH homeostasis under harsh external acid conditions at pH 3.5. These adaptations are an integrated mechanism against acidic stress, as the positive correlation between membrane lipid reorganization and ATPase upregulation is significant (Pearson $r = 0.847$, $p < 0.001$). The three-dimensional biofilm lifestyle has biofilm-specific capabilities, such as maintaining structural integrity and preserving lipid modifications during exposure to lethal pH, suggesting that the advantages of acid-tolerance mechanisms in cells are significantly enhanced by their existence in a three-dimensional biofilm. These results offer a mechanistic disposition of the outstanding evolutionary achievement of S. mutans as the chief etiological agent of dental caries. The fact that repeated sub-lethal exposures to acid lead to long-term tolerance justifies the selection of more acid-resistant biofilm populations during repeated cycles of dietary carbohydrate consumption. The identification of specific molecular targets, such as proton-pumping ATPases, and the biosynthesis of unsaturated fatty acids, offers hope for new therapeutic approaches to interfere with acid-tolerance mechanisms. Future studies that combine mechanistic lessons with clinical interventions must help improve the prevention and treatment of dental caries.

5. Acknowledgements

The author hereby wishes to thank the Education Directorate of Al-Qadisiyah, Ministry of Education, Iraq, for its continued support.

Author Contributions: Conceptualization, A.S.O.; methodology, A.S.O.; software, A.S.O.; validation, A.S.O.; formal analysis, A.S.O.; investigation, A.S.O.; resources, A.S.O.; data curation, A.S.O.; preparation of original draft, A.S.O.; editing and reviewing, A.S.O.; visualization, A.S.O.; supervision, A.S.O.; project administration, A.S.O.; funding acquisition, A.S.O. All authors have read and agreed to the published version of the manuscript.

Funding: Not applicable.

Conflicts of Interest: The authors declare no conflict of interest.

References

[1] Lemos, J. A.; Palmer, S. R.; Zeng, L.; Wen, Z. T.; Kajfasz, J. K.; Freires, I. A.; Abranches, J.; Burne, R. A. The Biology of *Streptococcus mutans*. *Microbiol. Spectr.* **2019**, *7*(1). https://doi.org/10.1128/microbiolspec.GPP3-0051-2018

[2] Wilkins, J. C.; Homer, K. A.; Beighton, D. Analysis of *Streptococcus mutans* Proteins Modulated by Culture under Acidic Conditions. *Appl. Environ. Microbiol.* **2002**, *68*(5), 2382–2390. https://doi.org/10.1128/AEM.68.5.2382-2390.2002

[3] Forssten, S. D.; Björklund, M.; Ouwehand, A. C. *Streptococcus mutans*, Caries and Simulation Models. *Nutrients* **2010**, *2*(3), 290–298. https://doi.org/10.3390/nu2030290

[4] Welin-Neilands, J.; Svensäter, G. Acid Tolerance of Biofilm Cells of *Streptococcus mutans*. *Appl. Environ. Microbiol.* **2007**, *73*(17), 5633–5638. https://doi.org/10.1128/AEM.01049-07

[5] Krzysciak, W.; Jurczak, A.; Kościelniak, D.; Bystrowska, B.; Skalniak, A. The Virulence of *Streptococcus mutans* and the Ability to Form Biofilms. *Eur. J. Clin. Microbiol. Infect. Dis.* **2014**, *33*(4), 499–515. https://doi.org/10.1007/s10096-013-1993-7

[6] Baker, J. L.; Faustoferri, R. C.; Quivey, R. G., Jr. Acid-Adaptive Mechanisms of *Streptococcus mutans*—The More We Know, the More We Don't. *Mol. Oral Microbiol.* **2017**, *32*(2), 107–117. https://doi.org/10.1111/omi.12162

[7] Bojanich, M. A.; Calderón, R. O. *Streptococcus mutans* Membrane Lipid Composition: Virulence Factors and Structural Parameters. *Arch. Oral Biol.* **2017**, *81*, 74–80. https://doi.org/10.1016/j.archoralbio.2017.04.023

[8] Fozo, E. M.; Scott-Anne, K.; Koo, H.; Quivey, R. G., Jr. Role of Unsaturated Fatty Acid Biosynthesis in Virulence of *Streptococcus mutans*. *Infect. Immun.* **2007**, *75*(3), 1537–1539. https://doi.org/10.1128/IAI.01938-06

[9] Madigan, M. T.; Martinko, J. M.; Bender, K. S.; Buckley, D. H.; Stahl, D. A. *Brock Biology of Microorganisms*, 16th ed.; Pearson: Upper Saddle River, NJ, **2018**.

[10] Cvitkovitch, D. G.; Li, Y.-H.; Ellen, R. P. Quorum Sensing and Biofilm Formation in Streptococcal Infections. *J. Clin. Invest.* **2003**, *112*(11), 1626–1632. https://doi.org/10.1172/JCI200320430

[11] Heydorn, A.; Nielsen, A. T.; Hentzer, M.; Sternberg, C.; Givskov, M.; Ersbøll, B. K.; Molin, S. Quantification of Biofilm Structures by the Novel Computer Program COMSTAT. *Microbiology* **2000**, *146*(10), 2395–2407. https://doi.org/10.1099/00221287-146-10-2395

[12] Koo, H.; Xiao, J.; Klein, M. I.; Jeon, J. G. Biofilm Formation and Control in Cariology. *Dent. Clin. North Am.* **2011**, *55*(1), 1–16.

[13] Snoep, J. L.; Maloolaka, P.; Kholodenko, B. N.; Westerhoff, H. V.; Barber, J. Safety Assessment and Risk Management for the Intentional Release of Organisms with Altered Traits. *J. Biotechnol.* **2009**, *138*(2–4), 91–98.

[14] Sutton, S. Measurement of Microbial Cells by Optical Density. *J. Validat. Technol.* **2011**, *17*(1), 46–50.

[15] Bligh, E. G.; Dyer, W. J. A Rapid Method of Total Lipid Extraction and Purification. *Can. J. Biochem. Physiol.* **1959**, *37*(8), 911–917. https://doi.org/10.1139/o59-099

[16] Matsui, R.; Cvitkovitch, D. Acid Tolerance Mechanisms Utilized by *Streptococcus mutans*. *Future Microbiol.* **2010**, *5*(3), 403–417. https://doi.org/10.2217/fmb.09.129

[17] Ames, B. N. Assay of Inorganic Phosphate, Total Phosphate and Phosphatases. *Methods Enzymol.* **1966**, *8*, 115–118. https://doi.org/10.1016/0076-6879(66)08014-5

[18] Valm, A. M.; Mark Welch, J. L.; Rieken, C. W.; Hasegawa, Y.; Sogin, M. L.; Oldenbourg, R.; Dewhirst, F. E.; Borisy, G. G. Systems-Level Analysis of Microbial Community Organization. *Proc. Natl. Acad. Sci. U. S. A.* **2011**, *108*(12), 4152–4157. https://doi.org/10.1073/pnas.1101134108

[19] Heydorn, A.; Nielsen, A. T.; Hentzer, M.; Sternberg, C.; Givskov, M.; Ersbøll, B. K.; Molin, S. Quantification of Biofilm Structures by the Novel Computer Program COMSTAT. *Microbiology* **2000**, *146*(10), 2395–2407. https://doi.org/10.1099/00221287-146-10-2395

[20] Field, A. P. *Discovering Statistics Using IBM SPSS Statistics*, 5th ed.; Sage Publications: London, **2017**.

[21] Pearson, K. Notes on the History of Correlation. *Biometrika* **2020**, *13*(1), 25–45. https://doi.org/10.1093/biomet/13.1.25

[22] Shapiro, S. S.; Wilk, M. B. An Analysis of Variance Test for Normality. *Biometrika* **1965**, *52*(3–4), 591–611. https://doi.org/10.1093/biomet/52.3-4.591

[23] Kirk, P. L. *Quantitative Ultramicroanalysis*, 3rd ed.; Academic Press: New York, **1968**.

[24] Cevc, G.; Marsh, D. *Phospholipid Bilayers: Physical Principles and Models*; Wiley-Interscience: New York, **1987**.

[25] de Kruijff, B. Lipid Polymorphism and Membrane Function. *Curr. Opin. Chem. Biol.* **1997**, *1*(4), 564–569. https://doi.org/10.1016/S1367-5931(97)80053-1

[26] Steinberg, D. A.; Zabriskie, J. B. Bacterial Cell Wall-Remodeling Enzymes as Targets for Antimicrobial Therapy. *Curr. Opin. Microbiol.* **1998**, *1*(5), 579–584.

[27] Müller, V.; Hess, V. Minimum Biological Energy Quantum. *Front. Microbiol.* **2017**, *8*, 2019. https://doi.org/10.3389/fmicb.2017.02019

[28] McDonnell, G.; Russell, A. D. Antiseptics and Disinfectants: Activity, Action, and Resistance. *Clin. Microbiol. Rev.* **1999**, *12*(1), 147–179. https://doi.org/10.1128/CMR.12.1.147

[29] Burne, R. A.; Penders, J. M. Oral Anaerobes, Oral Candidosis, and Denture Stomatitis. *Crit. Rev. Oral Biol. Med.* **2002**, *13*(2), 141–154.

ASEAN
Journal of Scientific and Technological Reports
Online ISSN:2773-8752

Research article

Nitrogen Uptake at Different Growth Stages of Corn and Its Effect on Important Yield Parameters

Melissa I. Canunayon[1], Grecila B. Nedamo[1], Elvira D. Jamio[1], Daniel B. Tangpos[1], Julius D. Caritan[1], Noriel Jay A. Magsayo[1], and Pet Roey L. Pascual[2]

[1] Graduate School, Cebu Technological University-Barili Campus, Barili, 6306 Cebu, Philippines
[2] Agribusiness and Development Communication, Cebu Technological University-Barili Campus, Barili, 6306 Cebu, Philippines
* Correspondence: melissacanunayon30@gmail.com

Citation:
Canunayon, I.M.; Nedamo, B.G.; Jamio, D.E.; Tangpos, B.D.; Caritan, D.J.; Magsayo, J.A.N.; Pascual, L.R. Nitrogen uptake at different growth stages of corn and its effect on important yield parameters. *ASEAN J. Sci. Tech. Report.* **2026**, *29*(3), e259741. https://doi.org/10.55164/ajstr.v29i3.259741.

Article history:
Received: June 11, 2025
Revised: November 17, 2025
Accepted: February 7, 2026
Available online: March 2, 2026

Abstract: Nitrogen is the primary nutrient governing corn yield. This study compares the contrasting nitrogen dynamics of open-pollinated (OPV) and hybrid corn varieties and their consequential impact on overall yield. However, limited research exists comparatively evaluating the nitrogen uptake and utilization efficiency of these varieties under uniform fertilization rates across distinct growth stages. The study employed a Randomized Complete Block Design (RCBD) with three replications, and all treatment plots received the same fertilizer rate to guarantee unbiased experimental results. All collected data were analyzed using the Statistical Package for the Social Sciences (SPSS) and the Statistical Tool for Agricultural Research (STAR) software. These analyses include One-way Analysis of Variance, Independent Sample T-tests, and Pearson's correlation. The results show that nitrogen uptake in hybrid corn declined gradually and steadily across all growth stages (V8: 3.17%, R1: 2.92%, R3: 2.88%, and R5: 2.27%), contrasting with the fluctuating absorption pattern of the OPV. This superior N management is supported by Nitrogen Utilization Efficiency (NUtE), in which the hybrid (31.55 ± 1.36) achieved a higher NUtE than the OPV (28.09 ± 1.38). The two varieties exhibited a statistically significant difference in N uptake at the R1 stage ($p = 0.048$), with the hybrid maintaining a higher N concentration (2.92%) than the OPV (2.58%). Interestingly, OPV N uptake at R1 exhibited a strong correlation with kernel weight (0.638), unshelled weight (0.676), ear weight (0.643), and grain yield (0.576), but showed the inverse trend for hybrid corn. These contrasting results confirm that the OPV exhibits lower nitrogen uptake efficiency while the hybrid displays rapid nitrogen absorption, necessitating precision, variety-specific fertilization strategies for yield and environmental stewardship.

Keywords: Nitrogen content; nitrogen utilization efficiency; hybrid corn; open-pollinated variety (OPV)

1. Introduction

Corn (*Zea mays* L.) is globally recognized as a fundamental staple crop, with annual production exceeding 1 billion tons, making it one of the most consumed grains worldwide [1]. As a major cereal crop, corn plays a fundamental part in Philippine agriculture. In Visayas and Mindanao, 20% of the population relies on it as a staple food, showcasing its significance for the nation's economic and food security [2]. Despite its importance, corn production,

along with that of other cereals, is linked to environmental concerns, accounting for around 30% of all synthetic nitrogen (N) fertilizers used worldwide in crop production [1].

Nitrogen (N) is the primary nutrient that determines the final grain output of corn [3]. An adequate N supply is essential, as it enhances photosynthetic rate and prolongs leaf functional life, thereby positively influencing grain filling and yield [4]. However, the global use of nitrogen fertilizer has escalated significantly and has the potential to increase four to five times by 2050, with developing nations accounting for two-thirds of this growth [5]. This trend results in the excessive and disproportionate application of chemical fertilizers, often utilized to maximize yields and alleviate food insecurity [6, 7]. According to [8], nearly half of the nitrogen fertilizer input isn't consumed by crops and is instead released into the environment through gas emissions or waterbody pollution. For instance, inefficient nitrogen use results in significant environmental contamination through surface runoff, denitrification, leaching, and volatilization [9].

The government has been implementing various corn varieties, including hybrids, genetically modified varieties, and open-pollinated varieties (OPVs) [10-12]. Each corn variety absorbs nitrogen differently, and its nitrogen demand changes as it matures. What's more, how corn reacts to applied nitrogen fertilizer isn't fixed; it shifts quite a bit depending on the variety, the location where it's planted, and the presence of other available nutrients [13]. Therefore, recognizing these varying nitrogen requirements is essential, especially since some varieties inherently possess superior efficiency, requiring less N to achieve maximum output. This study investigates the performance of an open-pollinated variety (OPV) relative to a hybrid corn variety with modern genetic traits, comparing their N absorption and capacity to convert absorbed N into grain yield. Nitrogen Utilization Efficiency (NUtE) is defined as the plant's capacity to convert the N already absorbed into economic yield [14]. Limited information exists comparing the N uptake and utilization efficiencies of OPV and hybrid corn varieties under uniform fertilizer regimes, particularly within tropical field conditions. Understanding these varietal differences in N assimilation across growth stages remains a major gap that constrains precise nitrogen management in maize production.

Addressing these differences is crucial for sustainable agriculture, helping farmers optimize fertilizer application and achieve higher yields, lower operational costs, and reduced environmental impact. The primary aim of this study is to analyze the total nitrogen content in two corn varieties during their vegetative and reproductive stages. Specifically, it intends to compare the Nitrogen content and N utilization Efficiency (NUtE) of OPV and hybrid corn varieties, determine the growth stages when nitrogen assimilation is highest for both, measure yield components across the two varieties, and investigate the relationship between N content and key yield parameters.

2. Materials and Methods

2.1 Location

The study was conducted at the production farm of Cebu Technological University–Barili Campus, located at 10°7'56" N and 123°32'56" E. The experiment spanned four months, from October 2024 to January 2025. The experimental site measured approximately 50 m^2, and meticulous preparation ensured optimal conditions for crop growth. Furthermore, the soil analysis conducted by Puyod et al. [15] in the same experimental area indicated that the soils have a high clay content, ranging from 46-70%, which provides a water-holding capacity of more than 40%.

2.2 Planting Materials

The experiment utilized two genetically distinct corn varieties: an open-pollinated variety, IPB Var 11 ck, and a hybrid variety, 1038B339-44, with advanced genetic traits.

2.3 Field Preparation and Planting

A systematic approach was established. Initially, plowing was done after the previous crop was harvested to prevent weed growth and enrich the soil with organic matter. Thereafter, to provide an improved soil surface for planting operations, harrowing was carried out to create a fine seedbed and reduce clodding in the field. The last step was furrowing, which involved creating hills 0.25 meters apart and rows 0.75 meters apart throughout the study area. The study setup included three blocks, each 5 m long and 2.25 m wide,

separated by 1 m-wide alleyways to minimize interaction effects and promote uniformity. As soon as the area was laid out, the study began. Lastly, to attain a 100% germination rate, two to three seeds were sown in each hill.

2.4 Experimental Design and Treatments

The experiment was set up with three replications using a Randomized Complete Block Design (RCBD) to ensure reliable results. Fertilizer was applied equally across all treatment plots to maintain consistent nutrient levels and avoid bias during analysis. This allows a comparative assessment of their nitrogen uptake and its potential influence on yield.

2.5 Fertilizer Application

One week before sowing, organic fertilizer (Microbial Compost) was applied to the soil as a basal nutrient source. Subsequently, a split application of commercial nitrogen-rich fertilizers was implemented. The first split was applied 15 days after planting (DAP) with complete fertilizer (14-14-14), followed by the second split at 30 DAP with a mixture of complete and urea fertilizer (46-0-0). These early applications ensured the plants received adequate nitrogen during their vegetative growth stage. Additionally, a third top-dress application of complete fertilizer and potash was applied at 45 DAP to support reproductive development. All fertilizer amounts adhered to the recommended application rates for the area, ensuring proper nutrient management.

2.6 Thinning and Weeding

Thinning was carried out 12 days after sowing, leaving one healthy seedling per hill. For hills where germination did not occur, healthy seedlings from extra hills were transplanted to fill the gaps. Weeds were promptly removed through hand-weeding to ensure the corn had full access to soil nutrients without competition. Additionally, the soil was hilled up around the base of the plants to enhance plant stability and support growth.

2.7 Destructive Sampling Analysis

The samples were gently extracted from the soil during the cooler parts of the day, either early in the morning or late in the afternoon, to reduce the effects of environmental stress, such as heat and strong sunlight, which can impact the plant's physiological processes. Following their removal, they were carefully rinsed with running tap water to remove any dirt that might have adhered to the roots. Then, a second rinse with distilled water was performed to ensure no tap-water residues or contaminants remained that could affect the nitrogen analysis or introduce unintended variables. The samples were then oven-dried according to the method described by Zhao et al. [9], which involved an initial drying phase at 105°C for 30 minutes, followed by a secondary drying stage at 80°C for 8 hours. Once fully dried, the dry weight was recorded, and the samples were carefully stored in labeled plastic zip-lock bags for total nitrogen analysis.

2.8 Data Collection

Nitrogen Content Analysis. Corn samples from both GMO and OPV varieties were collected at four distinct growth stages (V8, R1, R3, and R5). At each stage, the corn tissue was analyzed using the Kjeldahl method at F.A.S.T. Laboratories.

Ear Weight (g). After harvesting, each part of the corn—the husk, cob, and kernels—was carefully weighed with a digital weighing scale.

Unshelled Weight (g). The husk was carefully stripped away from the corn, revealing the cob and grains. These were then weighed to the nearest gram using a digital scale, ensuring accurate measurements for the analysis.

Shelled Weight (g). The grains were separated from the cob through hand-shelling. Afterwards, each sample was individually weighed.

Moisture Content. The kernels were weighed using a moisture meter, which measures moisture content.

Grain Yield. Computed using this formula.

$$= Grain\ Yield\ \left(\frac{t}{ha}\right) = \left(SW\ (g) x\ \frac{100-MC}{100-18}\right) x\ \left(\frac{10{,}000}{Harvest\ Area\ (m2)}\right) \text{ x } \left(\frac{1}{1{,}000{,}000}\right)$$

Where:

- Grain yield (t/ha) = Grain Yield in tons per hectare
- SW (g) = Total Shelled Weight (g)
- MC = Actual Harvest Moisture (%)
- 18 = Standard Moisture Basis (%)
- 10,000 = Conversion factor from square meters to hectares (1ha=10,000m^2)
- Harvest Area (m2) = actual physical area of the crop rows that were cut, collected, and weighed to obtain the raw yield data.
- 1,000,000 = Conversion factor from grams to metric tons (1t=1,000,000g)

Nitrogen Utilization Efficiency. Computed by following the formula of [16].

$$NUtE = \frac{Grain\ Yield\ \left(\frac{kg}{ha}\right)}{Total\ N\ Content}$$

Where:

- Grain yield (kg/ha) = Grain Yield in kilograms per hectare
- N Content = Nitrogen Uptake at Reproductive Stage 5

2.9 Statistical Analysis

All collected data underwent a comprehensive, combined statistical analysis using Statistical Package for the Social Sciences (SPSS) and Statistical Tool for Agricultural Research (STAR) software. The initial phase involved a careful examination of nitrogen content in both OPV and hybrid corn varieties, specifically during their vegetative (V8) and reproductive (R1, R3, R5) stages. Using a One-way Analysis of Variance (ANOVA) in STAR software, this preliminary step aimed to detect significant differences in nitrogen absorption as plant development progressed. Following this, independent-samples t-tests were performed in SPSS to directly compare nitrogen content between the hybrid and OPV corn varieties at each distinct growth stage. The same analytical approach was then applied to evaluate several key yield parameters. As a final step, Pearson's correlation analysis thoroughly examined the strength and direction of the relationships between the observed final yield traits and the corresponding nitrogen absorption patterns.

3. Results and Discussion

The findings indicate a variability in nitrogen (N) uptake between the two corn varieties across different growth stages. Nitrogen uptake in hybrid corn peaks during the vegetative stage, reaching 3.17%, thereby promoting the plant's early active growth. As the plant advanced to the reproductive stages, its nitrogen absorption gradually declined, with silking and milking stages showing comparable uptake rates of *2.92%* and *2.88%*, respectively. Subsequently, the dent stage (R5) marks the lowest nitrogen absorption, at 2.27%, indicating it is close to complete maturity. In contrast, OPV corn exhibits a distinct pattern of nitrogen absorption across its growth stages. Nitrogen absorption reaches its maximum during the vegetative stage at *3.40%*, giving the plant the nutrients it requires for rapid early growth. After declining to an average of *2.58%* during the silking phase, uptake increases again during the milking stage to 3.04%, a value similar to that during the vegetative period. As the corn reaches the dent stage, nitrogen absorption declines further, settling at *2.13%*, signaling its progression toward full maturity. Furthermore, the independent sample t-test results (Table 2) showed a statistically significant difference in nitrogen uptake between the two corn varieties at the R1 growth stage ($p = 0.048$). This finding may indicate that the genetic disparities and nitrogen absorption characteristics between the two varieties could affect nitrogen absorption during the early stages of

reproductive development. Moreover, no significant differences were observed in the V8, R3, and R5 growth stages (p-values of 0.24, 0.242, and 0.476, respectively).

Table 1. Total Nitrogen Content of OPV and Hybrid Corn Varieties per 100g of Dried Samples.

Source: The First Analytical Services and Technical Cooperative Laboratories

Growth Stages	HYBRID	OPV
V8 (Vegetative)	3.17 [a]	3.40 [a]
R1 (Silking)	2.92 [b]	2.58 [b]
R3 (Milking)	2.88 [b]	3.04 [a]
R5 (Dent)	2.27 [c]	2.13 [c]

Means with the same letter are not significantly different.

Table 2. Independent Sample T-tests Result on Nitrogen Content in Hybrid and OPV corn at V8, R1, R3, and R5.

Growth Stages	Significance (2-tailed)
V8 (Vegetative)	0.240
R1 (Silking)	0.048
R3 (Milking)	0.242
R5 (Dent)	0.476

3.1 Peak N uptake at V8 (Vegetative Stage)

During the vegetative growth phase, both varieties typically exhibit their highest nitrogen (N) uptake rate, a crucial process for establishing substantial aboveground biomass. This pattern is corroborated by the research of Khan et al. [12], which documented that corn exhibits its highest N uptake during the early developmental stages, particularly up to the V8 leaf stage. Likewise, [17] found that leaves and roots function as sinks for N uptake and utilization during the early vegetative stage. Agricultural practices often emphasize fertilizer application between the V6 and V8 stages to align with the plant's peak N requirements. Interestingly, corn can accumulate N beyond its immediate needs during this time, a phenomenon described as "luxury consumption" [18]. The slightly higher N concentration observed in the OPV variety at V8 (3.40%) compared to the hybrid variety (3.17%) may reflect a greater capacity for luxury consumption during this early growth phase. This early-accumulated N functions as a reserve pool, primarily stored in stalks and leaves [16]. This supply provides a buffer against potential N deficiencies and supports grain development and overall plant health if N uptake after silking becomes restricted [18]. The contrasting early nitrogen absorption sets the stage for the different strategies these varieties employ during grain filling.

3.2 Genetic Difference and Acute N stress at R1 (Silking)

The tissue analysis shows that the OPV corn experienced an acute drop in N content, from its vegetative peak of 3.40% to 2.58% at R1. This represents a drastic decline in tissue N during the transition to the most demand-intensive phase of reproduction. This reduction implies that the N supply fails to meet the crop's peak requirement at the onset of silking. The R1 stage marked the point of greatest physiological and statistical divergence between the two varieties. The independent sample t-test revealed a statistically significant difference in N uptake at R1 ($p=0.048$), the only stage to show such a difference. At R1, the OPV variety demonstrated a sharp decline in tissue N concentration. Conversely, the hybrid variety exhibited a more modest decline to 2.92% N, maintaining a significantly higher relative N status than the OPV variety. The plant's early capacity for substantial nitrogen uptake underscores its effective nutrient utilization strategy throughout its life cycle. However, N deficiency during the critical tasseling and silking stages can substantially increase the risk of crop failure [19]. To satisfy the notable N requirements of grain development, a considerable quantity of N is progressively redistributed from vegetative tissues during the reproductive phase [20]. As evident from the sharp decline in OPV's tissue N (Table 1), an influential decline in N availability likely stressed the plants. This N deficit during R1 in OPV could lead to compromised pollination, reduced kernel formation, and increased kernel abortion, as research has established that successful spikelet development relies on pollination, and severe N stress during this process can impede pollination success [16]. On the other hand, the observed modest decrease in N uptake in hybrid corn at the R1 stage suggests a relative

resilience to significant yield loss from N stress at this critical point. A study demonstrated superior nitrogen use efficiency (NUE) and grain yield of Topcross corn compared with open-pollinated varieties (OPVs) under both limited and ample N conditions [21], which may support a broader trend of improved N management in more advanced corn varieties compared with OPVs under stress.

3.3 Compensatory Uptake and Remobilization at R3 (Milking)

The pattern reversed dramatically at the R3 (Milking) stage. The milking stage, characterized by rapid starch accumulation, milky kernel contents, and completed endosperm cell division [26], showed a significant recovery in OPV, increasing its N concentration from 2.58% (R1) back up to 3.04%. Meanwhile, the hybrid variety continued a gradual, stable decline in N content (2.88%). Ultimately, scientific literature confirms that the developing ear's massive N requirements during reproductive stages cannot be met solely through new soil uptake; the plant heavily relies on remobilized N from its stalks and leaves [22]. Since the OPV suffered an acute R1 deficit, its subsequent recovery at R3 must be interpreted, at least in part, as a desperate survival mechanism: the plant aggressively transferred remaining N reserves from its vegetative structures (source organs like stalks and older leaves) to the developing kernels (sink organs) to continue grain filling and survive further growth stages. This aligns with the research of Ruiz et al. [23], showing corn's ability to redistribute remaining stalk nitrogen to the grain. Therefore, the increased nitrogen content observed in OPV at the milking stage likely reflects this enhanced movement and uptake aimed at making up for the earlier deficit during R1 and supporting grain development. While this remobilization demonstrates the corn plant's adaptive capacity, it comes at a physiological cost, often resulting in premature senescence of vegetative tissues. Crucially, because the yield potential (kernel number) was already significantly reduced by the N limitation that occurred at R1, this late-stage N recovery cannot repair the structural yield losses. The resulting weak or negative correlation between R3 N content and final grain yield demonstrates this. Conversely, the nitrogen uptake pattern in the hybrid variety suggests potentially better nitrogen utilization efficiency (NUtE), indicating a more stable and more effective allocation of nitrogen to support critical reproductive stages.

3.4 Overall Superiority in Yield Parameters

The outcomes of this investigation unequivocally demonstrate that the hybrid corn exhibits greater production capacity across nearly all metrics than the OPV. The visual data in Figure 1, where the bar heights for the hybrid variety are consistently greater than those for the OPV, are statistically supported by the Independent Samples T-test results. The hybrid corn demonstrated statistically superior Shelled Weight performance (p=0.000) compared to the Open-Pollinated Variety (OPV). The hybrid achieved a significantly higher weight of 196.10 ± 8.49 g, while the OPV recorded 152.73 ± 6.68 g. Since shelled weight is the primary determinant of final grain mass, this superiority suggests that the hybrid corn was genetically more robust in kernel setting (kernel number). Further supporting the yield difference, the hybrid variety achieved significantly higher Unshelled Weight and Ear Weight. Specifically, the hybrid recorded 227.43 ± 10.32 g (Unshelled Weight) and 243.12 ± 10.63 g (Ear Weight). In comparison, the OPV only yielded 187.79 ± 9.00 g (Unshelled) and 199.36 ± 10.93 g (Ear Weight). These results provide comprehensive proof that the advanced genetics in the hybrid variety successfully translated resources into greater physical biomass in the final harvestable ear structure compared to the OPV. Most importantly, the calculated Grain Yield (t/ha) was statistically superior for the hybrid variety (p=0.004). This finding provides the fundamental justification for the conclusion that the hybrid variety has a substantially higher yield potential under these specific conditions. The only yield parameter that appears to have a counterproductive effect on the hybrid is moisture content. Consistent with our findings, previous research has also documented significant variations in grain moisture content across different corn varieties [24-26]. Furthermore, [27] noted that earlier-maturing cultivars dry their grains more quickly before physiological maturity, while later-maturing ones dry more slowly. Additionally, [28] found that increased nitrogen levels and rice biomass were associated with higher moisture content and a longer time to reach harvest dryness, a pattern also observed in corn [27]. Likewise, [29] reported a connection between larger leaf area (potentially due to higher nitrogen) and greater moisture content in maize. These established findings from other studies support our results, especially given the higher nitrogen utilization efficiency (NUtE) observed in the hybrid corn in this research.

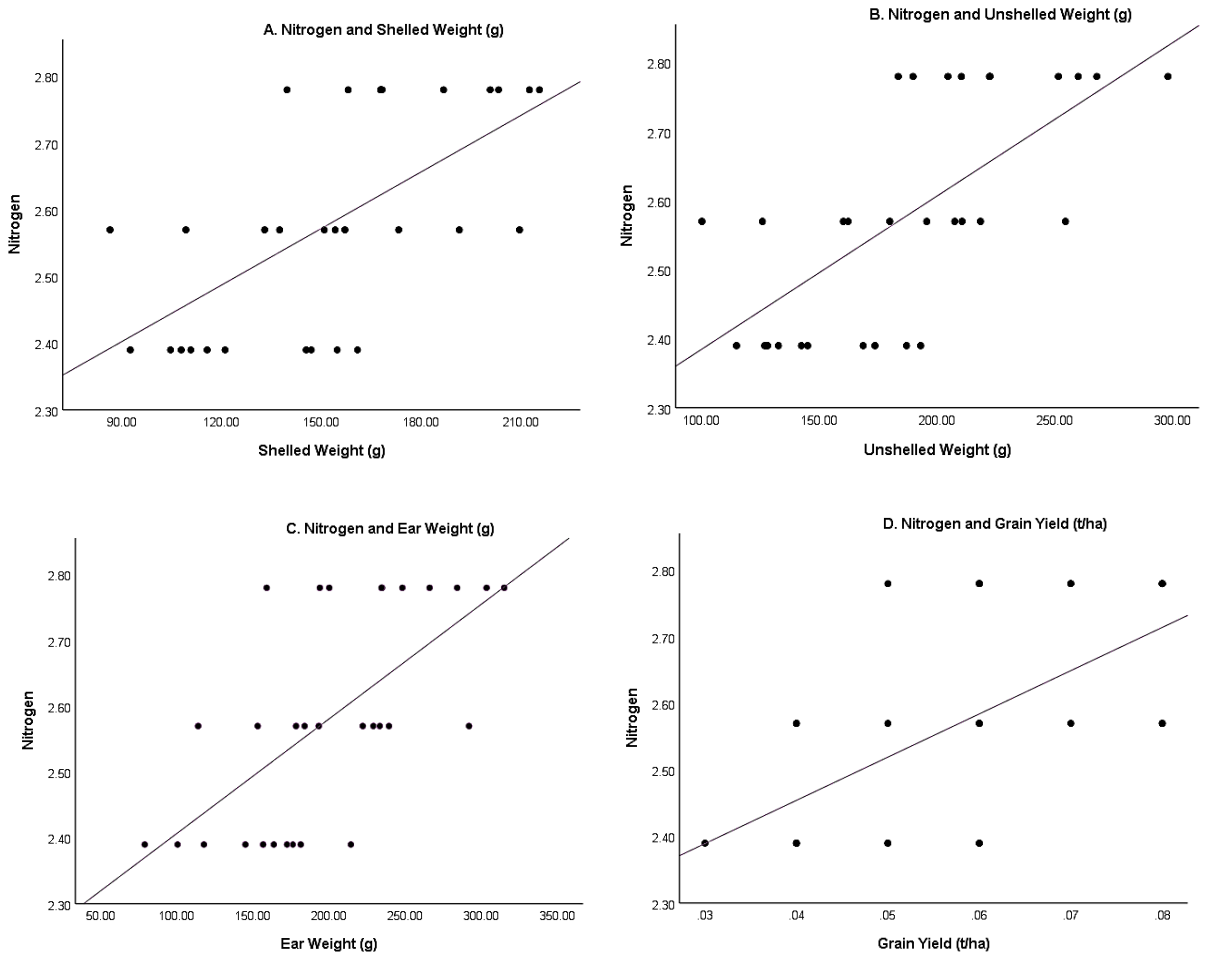

Figure 1. Pearson's correlation analysis showing the relationship between R1 tissue Nitrogen (N) concentration (%) and various yield components in the Open-Pollinated Variety (OPV) corn: A. Shelled Weight (g); B. Unshelled Weight (g); C. Ear Weight (g); and D. Final Grain Yield (t/ha). The positive slope of the trend lines indicates a strong positive correlation between R1 N uptake and final yield output.

Table 3. Corn Yield Parameters and Nitrogen Utilization Efficiency (NUtE) subjected to Independent Sample T-test

Yield Component	OPV	Hybrid	Sig. (2tailed)
Shelled Weight	152.73 ± 6.68	196.10 ± 8.49	0.000
Unshelled Weight	187.79 ± 9	227.43 ± 10.32	0.005
Ear Weight	199.36 ± 10.93	243.12 ± 10.63	0.006
Moisture Content	20.63 ± 0.50	25.67 ± 0.83	0.000
Grain Yield	0.60 ± 0.00	0.07 ± 0.00	0.004
Nitrogen Utilization Efficiency (NUtE)	28.09 ± 1.38	31.55±1.36	0.080

3.5 Superior Nitrogen Utilization Efficiency (NUtE)

NUtE is defined as the ratio of grain weight (yield) to the total amount of nitrogen accumulated in the mature plant. This metric measures the plant's capacity to convert absorbed nitrogen into final economic yield. As Figure 1 shows, the hybrid variety (31.55 ± 1.36) achieved a higher NUtE than the OPV (28.09 ± 1.38). This finding provides direct quantitative support for the view that hybrid corn's superior yield is fundamentally driven by better resource partitioning and conversion efficiency, rather than simply by higher N uptake. The ability to produce greater grain mass per unit of absorbed N mass highlights the hybrid's proactive, controlled genetic management of nitrogen, enabling it to achieve higher yields.

3.6 Positive Relationship of N and R1

Pearson's correlation analysis revealed a strong, positive relationship between nitrogen (N) uptake and yield at the R1 (silking) stage in the OPV. This finding strongly suggests that N supply was a limiting factor at R1. The OPV displayed high sensitivity to N stress at this stage, evidenced by a sharp drop in tissue N from V8 to R1, which subsequently required compensatory N remobilization at R3. Therefore, any variation that resulted in slightly higher tissue N content at R1 directly translated to a measurable increase in final grain output. Under the uniform fertilization regime, the OPV was operating below its N-saturation point, making its yield highly responsive to N availability at R1. Small increases in tissue N due to plot variability made the yield sensitive and directly translated into higher grain output, resulting in the observed positive correlation. Based on these results, the current split fertilizer timing failed to ensure adequate N availability for the OPV during R1. The OPV requires N inputs adjusted to ensure a higher, more stable N level is present leading up to and during R1. This necessitates more targeted, strategic fertilization (better timing) and potentially a higher total N rate to avoid N-limiting stress. In short, the OPV is a reactive, N-demanding variety that needs fertilizer management to be front-loaded and accurately timed to push its N status above the stress threshold, thus unlocking its full yield potential. In contrast, the hybrid variety exhibited an inverse correlation between N uptake and yield across all four growth stages (V8, R1, R3, and R5). This does not indicate poor productivity; instead, it suggests the hybrid variety, which is effective at accumulating N, surpassed its optimal N level for maximizing yield per unit of N absorbed under the current fertilizer inputs. This pattern signals a decline in Nitrogen Utilization Efficiency (NUtE) at very high N uptake levels. As N uptake increases beyond a certain point, its yield plateaus because excess N cannot translate into additional yield, as it has already reached its maximum potential. The same yield plateauing situation was observed in the OPV at the later R3 and R5 stages. This finding is particularly relevant for sustainable farming. It implies that applying the highest possible N rates might not be the most efficient or environmentally sound strategy for this hybrid corn. Excess absorbed N could instead be wasted, contributing to environmental issues through leaching or runoff. The plant maximized its yield potential at a specific N level; absorbing more N did not increase grain yield, so the efficiency of that additional N uptake appeared negative in terms of yield return. While N deficiency negatively impacts productivity, excessive N consumption can also compromise product quality.

Table 4. Pearson's Correlation Analysis Report from SPSS (Open-pollinated Variety)

Yield Component	Pearson Correlation (r)			
	Nitrogen (V8 Stage)	Nitrogen (R1 Stage)	Nitrogen (R3 Stage)	Nitrogen (R5 Stage)
Shelled Weight	-.629	.638	-.236	-.201
Unshelled Weight	-.675	.676	-.288	-.252
Ear Weight	-.615	.643	-.141	-.104
Moisture Content	-.157	.093	-.345	-.346
Grain Yield	-.553	.576	-.139	-.106

Table 5. Pearson's Correlation Analysis Report from SPSS (Hybrid Variety)

Yield Component	Pearson Correlation (r)			
	Nitrogen (V8 Stage)	Nitrogen (R1 Stage)	Nitrogen (R3 Stage)	Nitrogen (R5 Stage)
Shelled Weight	-.254	-.382	-.416	-.349
Unshelled Weight	-.152	-.269	-.315	-.293
Ear Weight	.039	-.081	-.161	-.236
Moisture Content	-.003	-.198	-.316	-.404
Grain Yield	-.254	-.319	-.316	-.219

4. Conclusion

The study conclusively demonstrates that the uniform fertilization regime revealed two fundamentally distinct physiological responses across the two varieties. The Open-Pollinated Variety (OPV) was confirmed as an N-limited, reactive genotype. The sharp decline in N tissue content at the R1 (silking) stage, coupled with a strong positive correlation between N uptake and final yield, provides empirical evidence that the uniform N rate was insufficient and imposed a yield-limiting stress. This stress mandates strategic intervention through improved timing and potentially higher N inputs to realize the OPV's full potential. In contrast, the hybrid variety demonstrated superior yield and high Nitrogen Utilization Efficiency (NUtE). The consistent inverse correlation between N uptake and yield proves that the uniform rate constituted over-fertilization, pushing the variety beyond its efficiency ceiling and leading to luxury N consumption that did not contribute to higher yields. This research confirms that the optimal agronomic strategy for modern, high-efficiency corn varieties is fundamentally different from that required for OPVs, mandating a move toward variety-specific N management.

5. Acknowledgements

The authors would like to express their gratitude to the DOST-Strand N and Cebu Technological University, Barili Campus, for their support and assistance in making this study successful.

Author Contributions: Conceptualization, M.C; methodology, M.C. and P.R.P.; software, M.C.; validation, M.C., G.N., and P.R.P.; formal analysis, M.C.; investigation, M.C., G.N., E.J., D.T., J.C., N.J.M.; resources, M.C., N.J.M., E.J., D.T., and J.C..; data curation, M.C.; writing—original draft preparation, M.C.; writing—review and editing, M.C., P.R.P, and G.N.; visualization, M.C.; supervision, P.R.P.; project administration, M.C., G.N., E.J., D.T., J.C, and N.J.M..; funding acquisition, M.C., G.N. All authors have read and agreed to the published version of the manuscript.

Conflicts of Interest: This research was made possible through the support of the Department of Science and Technology (DOST) STRAND N program and Cebu Technological University - Barili Campus. The authors declare no conflicts of interest, as the funding agency did not influence the study's design, methodology, data analysis, or conclusions.

References

[1] Galindo, F. S.; et al. Impact of nitrogen fertilizer sustainability on corn crop yield: the role of beneficial microbial inoculation interactions. *BMC Plant Biol.* **2024**, *24*(1), 446. https://doi.org/10.1186/s12870-024-04971-3

[2] Anuada, A. M. Effect of agro-climatic factors on the yield of corn (IPB Var 6) under rainfed conditions in the Philippines. *Philipp. e-J. Appl. Res. Dev.* **2022**, *12*, 45–56.

[3] Zhu, L.; et al. Optimizing crop yields while minimizing environmental impact through deep placement of nitrogen fertilizer. *J. Integr. Agric.* **2024**, https://doi.org/10.1016/jia.2024.05.012

[4] Fathi, A. Role of nitrogen (N) in plant growth, photosynthesis pigments, and N use efficiency: A review. *Zenodo* **2022**, https://doi.org/10.5281/zenodo.7143588

[5] Nadarajan, S.; Sukumaran, S. Chemistry and toxicology behind chemical fertilizers. In *Elsevier eBooks*; Elsevier: **2021**; pp 195–229. https://doi.org/10.1016/b978-0-12-819555-0.00012-1

[6] Bisht, N.; Chauhan, P. S. Excessive and Disproportionate Use of Chemicals Cause Soil Contamination and Nutritional Stress. In *IntechOpen eBooks*; IntechOpen: **2021**. https://doi.org/10.5772/intechopen.94593

[7] John, D. A.; Babu, G. R. Lessons From the Aftermaths of Green Revolution on Food System and Health. *Front. Sustain. Food Syst.* **2021**, *5*, 644559. https://doi.org/10.3389/fsufs.2021.644559

[8] Martínez-Dalmau, J.; Berbel, J.; Ordóñez-Fernández, R. Nitrogen Fertilization. A Review of the Risks Associated with the Inefficiency of Its Use and Policy Responses. *Sustainability* **2021**, *13*(10), 5625. https://doi.org/10.3390/su13105625

[9] Zhao, J.; Qi, Y.; Yin, C.; Liu, X. Effects of Nitrogen Reduction at Different Growth Stages on Maize Water and Nitrogen Utilization under Shallow Buried Drip Fertigated Irrigation. *Agronomy* **2024**, *14*(1), 63. https://doi.org/10.3390/agronomy14010063

[10] Alvarez, F.; Manalo, A.; Clarete, R. Economic Assessment of GM Corn Use in the Philippines. *Int. J. Food Sci. Agric.* **2021**, *5*(1), 115–128. https://doi.org/10.26855/ijfsa.2021.03.016

[11] Hapinat, H. L.; Montero, E. S. Development of Corn-based Farming System in Response to Climate Change. *FFTC-AP* **2022**. https://ap.fftc.org.tw/article/3235 (accessed 2025-03-08).

[12] Khan, S.; et al. Limited Nitrogen and Plant Growth Stages Discriminate Well Nitrogen Use, Uptake and Utilization Efficiency in Popcorn. *Plants* **2020**, *9*(7), 893. https://doi.org/10.3390/plants9070893

[13] Sharma, R.; Adhikari, P.; Shrestha, J.; Acharya, B. P. Response of maize (*Zea mays* L.) hybrids to different levels of nitrogen. *Arch. Agric. Environ. Sci.* **2019**, *4*(3), 295–299. https://doi.org/10.26832/24566632.2019.040306

[14] Jones, C. R.; Michaels, T. E.; Carley, C. S.; Rosen, C. J.; Shannon, L. M. Nitrogen uptake and utilization in advanced fresh-market red potato breeding lines. *Crop Sci.* **2020**, *61*(2), 878–895. https://doi.org/10.1002/csc2.20297

[15] Puyod, S. E. G.; Pascual, P. R. Varietal Performance of Hybrid Corn Fertilized with Ammonium Fertilizers in an Alkaline Soil Under Drought Conditions. *ASEAN J. Sci. Technol. Rep.* **2025**, *28*(4), e257403. https://doi.org/10.55164/ajstr.v28i4.257403

[16] Congreves, K. A.; et al. Nitrogen Use Efficiency Definitions of Today and Tomorrow. *Front. Plant Sci.* **2021**, *12*, 637108. https://doi.org/10.3389/fpls.2021.637108

[17] Kant, S.; Bi, Y. M.; Rothstein, S. J. Understanding plant response to nitrogen limitation for the improvement of crop nitrogen use efficiency. *J. Exp. Bot.* **2010**, *62*(4), 1499–1509. https://doi.org/10.1093/jxb/erq297

[18] Nasielski, J.; Earl, H.; Deen, B. Luxury vegetative nitrogen uptake in maize buffers grain yield under post-silking water and nitrogen stress: a mechanistic understanding. *Front. Plant Sci.* **2019**, *10*, 318. https://doi.org/10.3389/fpls.2019.00318

[19] Shrestha, J.; Yadav, D. N.; Amgain, L. P.; Sharma, J. P. Effects of Nitrogen and Plant Density on Maize (*Zea mays* L.) Phenology and Grain Yield. *Curr. Agric. Res. J.* **2018**, *6*(2), 175–182. https://doi.org/10.12944/carj.6.2.06

[20] Ning, P.; Yang, L.; Li, C.; Fritschi, F. B. Post-silking carbon partitioning under nitrogen deficiency revealed sink limitation of grain yield in maize. *J. Exp. Bot.* **2018**, *69*(7), 1707–1719. https://doi.org/10.1093/jxb/erx496

[21] Ige, S. A.; et al. Nitrogen Use Efficiency of Open-pollinated Maize Cultivars and Topcrosses under Low Nitrogen Soil. *Heliyon* **2024**, *10*(20), e39223. https://doi.org/10.1016/j.heliyon.2024.e39223

[22] Mueller, S. M.; Vyn, T. J. The Effects of Late-season Nitrogen Applications in Corn. *Purdue Extension* **2017**, AY-364-W.

[23] Ruiz, A.; Listello, A.; Trifunovic, S.; Archontoulis, S. V. Maize breeding enhances lodging resistance through vertical allocation changes of stem dry matter and nitrogen. *Front. Plant Sci.* **2025**, *16*, 1514045. https://doi.org/10.3389/fpls.2025.1514045

[24] Ward, J. K.; Henry, W. B.; Hock, M. W. Variability in harvest moisture and dry-down in multi-hybrid planting systems. *Trans. ASABE* **2016**, *59*(5), 1111–1115. https://doi.org/10.13031/trans.59.11572

[25] Xu, C. C.; et al. Grain yield and grain moisture associations with leaf, stem and root characteristics in maize. *J. Integr. Agric.* **2022**, *21*(7), 1941–1951. https://doi.org/10.1016/s2095-3119(20)63598-5

[26] Zhu, X.; Chi, R.; Ma, Y. Effects of Corn Varieties and Moisture Content on Mechanical Properties of Corn. *Agronomy* **2023**, *13*(2), 545. https://doi.org/10.3390/agronomy13020545

[27] Zhang, Y. M.; et al. Does nitrogen application rate affect the moisture content of corn grains? *J. Integr. Agric.* **2021**, *20*(10), 2627–2638. https://doi.org/10.1016/s2095-3119(20)63401-3

[28] Brinkhoff, J.; Dunn, B. W.; Dunn, T. The influence of nitrogen and variety on rice grain moisture content dry-down. *Field Crops Res.* **2023**, *302*, 109044. https://doi.org/10.1016/j.fcr.2023.109044

[29] Xu, C. C.; et al. Grain yield and grain moisture associations with leaf, stem and root characteristics in maize. *J. Integr. Agric.* **2022**, *21*(7), 1941–1951. https://doi.org/10.1016/s2095-3119(20)63598-5

ASEAN
Journal of Scientific and Technological Reports
Online ISSN:2773-8752

ASEAN
Journal of Scientific and Technological Reports
Online ISSN: 2773-8752

Article type

Type of the Paper (Article, Review, Communication, etc.) *about 8,000 words maximum*

Title (Palatino Linotype 18 pt, bold)

Firstname Lastname[1], Firstname Lastname[2] and Firstname Lastname[2*]

[1] Affiliation 1; e-mail@e-mail.com
[2] Affiliation 2; e-mail@e-mail.com
* Correspondence: e-mail@e-mail.com; (one corresponding authors, add author initials)

Citation:
Lastname, F.; Lastname, F.; Lastname, F. Title. *ASEAN J. Sci. Tech. Report.* **2023**, *26*(X), xx-xx. https://doi.org/10.55164/ajstr.vxxix.xxxxxx

Article history:
Received: date
Revised: date
Accepted: date
Available online: date

Abstract: A single paragraph of about 400 words maximum. Self-contained and concisely describe the reason for the work, methodology, results, and conclusions. Uncommon abbreviations should be spelled out at first use. We strongly encourage authors to use the following style of structured abstracts, but without headings: (1) Background: Place the question addressed in a broad context and highlight the purpose of the study; (2) Methods: briefly describe the main methods or treatments applied; (3) Results: summarize the article's main findings; (4) Conclusions: indicate the main conclusions or interpretations.

Keywords: keyword 1; keyword 2; keyword 3 (List three to ten pertinent keywords specific to the article yet reasonably common within the subject discipline.)

1. Introduction

The introduction should briefly place the study in a broad context and highlight why it is crucial. It should define the purpose of the work and its significance. The current state of the research field should be carefully reviewed and critical publications cited. Please highlight controversial and diverging hypotheses when necessary. Finally, briefly mention the main aim of the work. References should be numbered in order of appearance and indicated by a numeral or numerals in square brackets—e.g., [1] or [2, 3], or [4–6]. See the end of the document for further details on references.

2. Materials and Methods

The materials and methods should be described with sufficient details to allow others to replicate and build on the published results. Please note that your manuscript's publication implicates that you must make all materials, data, computer code, and protocols associated with the publication available to readers. Please disclose at the submission stage any restrictions on the availability of materials or information. New methods and protocols should be described in detail, while well-established methods can be briefly described and appropriately cited.

Interventional studies involving animals or humans, and other studies that require ethical approval, must list the authority that provided approval and the corresponding ethical approval code.

2.1 Subsection

2.1.1. Subsubsection

3. Results and Discussion

This section may be divided by subheadings. It should provide a concise and precise description of the experimental results, their interpretation, as well as the experimental conclusions that can be drawn.Authors should discuss the results and how they can be interpreted from previous studies and the working hypotheses. The findings and their implications should be discussed in the broadest context possible. Future research directions may also be highlighted.

3.1. Subsection

3.1.1. Subsubsection

3.2. Figures, Tables, and Schemes

All figures and tables should be cited in the main text as Figure 1, Table 1, etc.

Figure 1. This is a figure. Schemes follow the same formatting.

Table 1. This is a table. Tables should be placed in the main text near the first time they are cited.

Title 1	Title 2	Title 3
entry 1	data	data
entry 2	data	data [1]

[1] Table may have a footer.

3.3. Formatting of Mathematical Components

This is example 1 of an equation:

$$a = 1, \tag{1}$$

The text following an equation need not be a new paragraph. Please punctuate equations as regular text. This is example 2 of an equation:

$$a = b + c + d + e + f + g + h + i + j + k + l + m + n + o + p + q + r + s + t + u \tag{2}$$

The text following an equation need not be a new paragraph. Please punctuate equations as regular text. The text continues here.

4. Conclusions

Concisely restate the hypothesis and most important findings. Summarize the significant findings, contributions to existing knowledge, and limitations. What are the future directions? Conclusions MUST be well stated, linked to original research question & limited to supporting results.

5. Acknowledgements

Should not be used to acknowledge funders – funding will be entered as a separate. As a matter of courtesy, we suggest you inform anyone whom you acknowledge.

Author Contributions: For research articles with several authors, a short paragraph specifying their individual contributions must be provided. The following statements should be used "Conceptualization, X.X. and Y.Y.; methodology, X.X.; software, X.X.; validation, X.X., Y.Y. and Z.Z.; formal analysis, X.X.; investigation, X.X.; resources, X.X.; data curation, X.X.; writing—original draft preparation, X.X.; writing—review and editing, X.X.; visualization, X.X.; supervision, X.X.; project administration, X.X.; funding acquisition, Y.Y. All authors have read and agreed to the published version of the manuscript." Please turn to the CRediT taxonomy for the term explanation. Authorship must be limited to those who have contributed substantially to the work reported.

Funding: Please add: "This research received no external funding" or "This research was funded by NAME OF FUNDER, grant number XXX" and "The APC was funded by XXX". Check carefully that the details given are accurate and use the standard spelling of funding agency names at https://search.crossref.org/funding. Any errors may affect your future funding.

Conflicts of Interest: Declare conflicts of interest or state "The authors declare no conflict of interest." Authors must identify and declare any personal circumstances or interest that may be perceived as inappropriately influencing the representation or interpretation of reported research results. Any role of the funders in the design of the study; in the collection, analyses or interpretation of data; in the writing of the manuscript, or in the decision to publish the results must be declared in this section. If there is no role, please state "The funders had no role in the design of the study; in the collection, analyses, or interpretation of data; in the writing of the manuscript, or in the decision to publish the results".

References

References must be numbered in order of appearance in the text (including citations in tables and legends) and listed individually at the end of the manuscript. We recommend preparing the references with a bibliography software package, such as EndNote, ReferenceManager to avoid typing mistakes and duplicated references. Include the digital object identifier (DOI) for all references where available.

Citations and references in the Supplementary Materials are permitted provided that they also appear in the reference list here.

In the text, reference numbers should be placed in square brackets [ ] and placed before the punctuation; for example [1], [1–3] or [1, 3]. For embedded citations in the text with pagination, use both parentheses and brackets to indicate the reference number and page numbers; for example [5] (p. 100), or [6] (pp. 101–105).

Using the American Chemical Society (ACS) referencing style

[1] Author 1, A.B.; Author 2, C.D. Title of the article. *Abbreviated Journal Name* Year, *Volume*, page range.

[2] Author 1, A.; Author 2, B. Title of the chapter. In *Book Title*, 2nd ed.; Editor 1, A., Editor 2, B., Eds.; Publisher: Publisher Location, Country. **2007**, Volume *3*, pp. 154–196.

[3] Author 1, A.; Author 2, B. *Book Title*, 3rd ed.; Publisher: Publisher Location, Country, **2008**, pp. 154–196.
[4] Author 1, A.B.; Author 2, C. Title of Unpublished Work. *Abbreviated Journal Name* stage of publication (under review; accepted; in press).
[5] Author 1, A.B. (University, City, State, Country); Author 2, C. (Institute, City, State, Country). Personal communication, 2012.
[6] Author 1, A.B.; Author 2, C.D.; Author 3, E.F. Title of Presentation. In Title of the Collected Work (if available), Proceedings of the Name of the Conference, Location of Conference, Country, Date of Conference; Editor 1, Editor 2, Eds. (if available); Publisher: City, Country, Year (if available); Abstract Number (optional), Pagination (optional).
[7] Author 1, A.B. Title of Thesis. Level of Thesis, Degree-Granting University, Location of University, Date of Completion.
[8] Title of Site. Available online: URL (accessed on Day Month Year).

Reviewers sugestion

1. Name, Address, e-mail
2. Name, Address, e-mail
3. Name, Address, e-mail
4. Name, Address, e-mail

URL link:

Notes for Authors >>
https://drive.google.com/file/d/1r0zegnIVeQqe4iLQyT1xDEIinNggINPD/view?usp=sharing
https://drive.google.com/file/d/1r0zegnIVeQqe4iLQyT1xDEIinNggINPD/view?usp=sharing

Online Submissions >> https://ph02.tci-thaijo.org/index.php/tsujournal/user/register

Current Issue >> https://ph02.tci-thaijo.org/index.php/tsujournal/issue/view/16516

AJSTR Publication Ethics and Malpractice >> https://ph02.tci-thaijo.org/index.php/tsujournal/ethics

Journal Title Abbreviations >> http://library.caltech.edu/reference/abbreviations

ASEAN
Journal of Scientific and Technological Reports
Online ISSN:2773-8752

ASEAN
Journal of Scientific and Technological Reports
Online ISSN:2773-8752

ASEAN Journal of Scientific and Technological Reports (AJSTR)
Institute of Research and Innovation, Thaksin University, Phatthalung Campus
222 Moo. 2, Baan Prao Sub-District, Papayom District, Phatthalung, 93210, Thailand
Tel. +668 1540 7304